



Journal of Science

Volume: 17, Issue: 2, Year: 2021

Contact

Manisa Celal Bayar University
Institute of Natural and Applied Sciences
Campus of Şehit Prof Dr İlhan Varank 45140 Yunusmre – MANİSA, TURKEY
Tel: (00 90) 236 201 27 05
Fax: (00 90) 236 241 21 49
e-mail: cbujos@gmail.com
Web: <https://dergipark.org.tr/tr/pub/cbayarfbe>

“CBU Journal of Science is indexed by ULAKBIM-TUBITAK TR-DIZIN”



ISSN 1305-130X

E-ISSN 1305-1385

CBUJOS is published quarterly at Manisa Celal Bayar University Printing House

“CBU Journal of Science is a refereed scientific journal”



Celal Bayar University Journal of Science

Owner

Manisa Celal Bayar University,

Editors : Assoc. Prof. Dr. Kamil ŞİRİN

Assoc. Prof. Dr.. Emine KEMİKLİOĞLU

Assistant Editor: Assoc. Prof. Dr. Mustafa AKYOL

Layout Editor & Secretary

Dr. İlker Çetin KESKİN

International Scientific Advisory Board

Prof. Dr. Arianit REKA; State University of Tetova, Macedonia

Prof. Dr. Tomasz NIEMIEC; Warsaw University of Life Sciences, Poland

Prof. Dr. Alyani ISMAIL; Universiti Putra, Malaysia

Prof. Dr. Iuliana APRODU; Dunarea de Jos University, Romania

Assoc. Prof. Dr. Johanan Christian PRASANNA; Madras Christian College, South India

Assoc. Prof. Dr. Noureddine ISSAOUI; Université de Monastir, Tunisie.

Assoc. Dr. Edward Albert UECKERMANN; North-West University, South Africa

Assoc. Dr. Zhi-Qiang ZHANG; The University of Auckland, Holland

Assist. Prof. Dr. Young Ki KIM; Pohang University of Science and Technology, South Korea

Assist. Prof. Can BAYRAM; University of Illinois, USA

Assist. Prof. Dr. Mona MIRHEydARI; Rutgers University, USA

Assist. Prof. Dr. Donatella ALBANESE; Università Degli Studi Di Salerno, Italy

Assist. Prof. Dr. Jinghua JIANG; The University of Memphis, USA

Assist. Prof. Dr. Jens OLDELAND; University of Hamburg, Germany

Dr. Cheng CHENG; Apple Inc., USA

Dr. Sajedah AFGHAH; Microsoft Corporation, USA

Dr. Jinghua JIANG; The University of Memphis

National Scientific Advisory Board

Prof. Dr. Mustafa Ersöz; Selçuk University

Prof. Dr. Oğuz Gürsoy; Mehmet Akif University

Prof. Dr. Mehmet Çevik; İzmir Katip Çelebi University

Prof. Dr. Sezgin Çelik; Yıldız Teknik University

Prof. Dr. Osman Dayan; Çanakkale Onsekiz Mart University

Prof. Dr. Serdar İplikçi; Pamukkale University

Prof. Dr. Yasin Üst; Yıldız Teknik University

Prof. Dr. Mahmut Kuş; Konya Teknik University

Prof. Dr. Ertuğ Gundüz; Hacettepe University

Prof. Dr. Tülin Aydemir; Manisa Celal Bayar University

Prof. Dr. Sezai Taşkın; Manisa Celal Bayar University

Prof. Dr. Fatma Şaşmaz Ören; Manisa Celal Bayar University

Assoc. Prof. Dr. Fatih Doğan; Çanakkale Onsekiz Mart University

Assoc. Prof. Dr. Erol Akpınar; Abant İzzet Baysal University

Assoc. Prof. Dr. Yeliz Yıldırım; Ege University

Assoc. Prof. Dr. Serap Derman; Yıldız Teknik University

Assoc. Prof. Dr. Hayati Mamur; Manisa Celal Bayar University

Assoc. Prof. Dr. Fatih Selimefendigil; Manisa Celal Bayar University

Assoc. Prof. Dr. Özlem Çağındı; Manisa Celal Bayar University

Assoc. Prof. Dr. Osman Çulha; Manisa Celal Bayar University

Assoc. Prof. Dr. Ali Demir; Manisa Celal Bayar University

Assoc. Prof. Dr. Ali Konuralp; Manisa Celal Bayar University

Assist. Prof. Dr. Nil Mansuroğlu; Ahi Evran University

Assist. Prof. Dr. Zeynep Çipiloğlu Yıldız; Manisa Celal Bayar University



CBU Journal of Science

Celal Bayar University Journal of Science (CBUJOS) covers scientific studies in the fields of Engineering and Science and publishes accounts of original research articles concerned with all aspects of experimental and theoretical studies. CBU Journal of Science is a refereed scientific journal published four times annually (March, June, September and December) by Institute of Natural and Applied Sciences of Manisa Celal Bayar University. CBU Journal of Science considers the original research articles written in English for evaluation.

CBU Journal of Science is indexed by TUBİTAK ULAKBİM TR-DİZİN, and also is included in DOAJ, Cite Factor, Journal TOCS, Advanced Science Index and OAJI databases. Digital Object Identifier (DOI) number will be assigned for all the articles being published in CBU Journal of Science.

Instructions for Authors and Article Template can be found on the main page of MCBU Institute of Natural and Applied Sciences (<http://fbe.cbu.edu.tr>)





Vol: 17, Issue: 2, Year: 2021

Contents

Research Article

Pages

Positioning of Cubic Shaped Particles with Different Edge Structures in Nematic Medium

DOI: 10.18466/cbayarfbe.835483

Aslı Karausta, Emre Büküşoğlu

115-120

Geometric Characterization of Three-Dimensional (3D) Woven Jute Fiber Preforms for Composites

DOI: 10.18466/cbayarfbe.826090

Nesrin Şahbaz Karaduman

121-128

CFD Modelling of Non-Newtonian Fluid Flow in a Pipe Including Obstacle

DOI: 10.18466/cbayarfbe.865261

Mustafa Murat Yavuz, Pınar Sarı Çavdar

129-136

Deep Feature Generation for Author Identification

DOI: 10.18466/cbayarfbe.846016

Şükrü Ozan, D. Emre Taşar, Umut Özdil

137-143

Deep Feature Extraction for Detection of Tomato Plant Diseases and Pests based on Leaf Images

DOI: 10.18466/cbayarfbe.812375

Yahya Altuntaş, Adnan Fatih Kocamaz

145-152

Numerical Solutions of System of First Order Normalized Linear Differential Equations by Using Bernoulli Matrix Method

DOI: 10.780314/cbayarfbe.845017

Kübra Erdem Biçer, Mehmet Sezer, Mustafa Kazaz

153-158

Comparison of Cellular Autofluorescence Patterns of Two Model Microalgae by Flow Cytometry

DOI: 10.18466/cbayarfbe.827615

Uğur Uzuner

159-165

A Novel Donor- π -Acceptor Type Sensitizer for Dye Sensitized Photochemical Hydrogen Generation

DOI: 10.801544/cbayarfbe.844704

Emre Aslan

167-173

Fenoxycarb Effects 7th instar *Galleria mellonella* Larvae by Triggering Extra Larval Stages

DOI: 10.18466/cbayarfbe.823562

Esen Poyraz Tınartaş, Nesrin Ebru Göncü, Kamil Koç

175-179

Adhesive Behavior of the Pack-Borided AISI 304L Steel with Microwave Hybrid Heating

DOI: 10.18466/cbayarfbe.826118

Dilek Arslan, Recep Onur Uzun

181-191

Analysis of a Capacitor Modelled with Conformable Fractional Derivative under DC and Sinusoidal Signals

DOI: 10.18466/cbayarfbe.757813

Utku Palaz, Reşat Mutlu

193-198

Optimal placement of multiple DGs in radial distribution systems to minimize power loss using BSA

DOI: 10.18466/cbayarfbe.796140

Waleed Fadel, Ulaş Kılıç, Sezai Taşkın

199-207



Frame Detection with Deep Learning

DOI: 10.18466/cbayarfbe. 693942

209-213

Mete Yıldırım, Radosveta İvanova Sokullu

Anatomy of *Carlina corymbosa* L., *Carthamus dentatus* Vahl. and *Picnomon acarna* (L.) Cass.
(Asteraceae)

DOI: 10.18466/cbayarfbe. 785328

215-222

Ummahan Öz

Positioning of Cubic Shaped Particles with Different Edge Structures in Nematic Medium

Aslı Karausta¹, Emre Büküşoğlu^{1*}

¹ Department of Chemical Engineering, Middle East Technical University, Dumlupınar Bulvarı,
Çankaya, Ankara, Turkey

* emrebuk@metu.edu.tr

*Orcid: 0000-0002-3128-059X

Received: 9 November 2020

Accepted: 24 May 2021

DOI: 10.18466/cbayarfbe.835483

Abstract

Liquid crystals (LC) are phases of matter that possess long range orientational order while maintaining fluidic properties. LCs have been shown to provide a medium that result in self-assembly of the colloidal particles through elastic interactions. One parameter that affects the positioning of the particles in LC medium is the edge sharpness of the particles. Simulation studies in the literature suggests that the edge sharpness of the particles directly affect the LC director profile at the vicinity of the particles, and playing a critical role in the formation and the shapes of the topological defects. This article presents a systematic study to show the effects of the edge sharpness on the orientation and the defect structure around the cubic shaped particles. The particles were shown to orient with their diagonal preferably parallel to the direction of the far field nematic director when the particles mediate planar anchoring. Whereas the particles with homeotropic anchoring did not exhibit strong preference in their orientation. We also showed defect structures to form around the particles with homeotropic surface anchoring. The defect structure around the particles with round edges were ring shaped, whereas the defects with S-shapes were formed around sharp-edged or truncated particles. The findings herein were found to be consistent with the simulations present in literature. The findings would find use in next generation materials for optics, photonics and responsive systems.

Keywords: *Alignment, Colloids, Defects, Liquid Crystals.*

1. Introduction

Liquid crystals (LCs) are the phases of matter that exhibit both fluidic properties and molecular ordering which are currently being developed for emerging applications.[1–3] In the nematic phases, the molecules exhibit orientational order along a unique direction called the director.[1] When colloidal particles are dispersed in a LC medium, the director profile is affected due to the interfacial interactions, which leads to useful observations that are unique to LCs.[4, 5, 14–16, 6–13] These interfacial phenomena can be described using three generalized concepts, which can be classified as surface anchoring, elasticity and the formation of the defects.[2] When a LC medium is in contact with a surface, the interaction of the mesogenic molecules at the interface results in a preferred orientation of the LCs, called the easy axis, which is the outcome of the maintained minimum energy state. This orientation can then be shifted due to the external fields, which is penalized with a surface anchoring energy. The

long-range orientation of the LCs underlies the existence of the elastic properties of the LCs. When the natural orientation of the LC medium is affected by a geometric constraint, for example the presence of the colloids or surfaces, the director is strained that results in an energetic penalty. When LCs cannot satisfy the present surface anchoring in its medium via just elastic deformations, topological defects occur, which are defined as the local regions of low orientational ordering, or singularity. These three concepts were used in the current literature to define the positioning of the colloidal species dispersed in LC medium.

Studies in the literature showed that the surface anchoring and the director field around a particle is critically important in their positioning, and their interaction with the colloidal particles in a LC media.[4, 7, 11] For example, Poulin and Weitz demonstrated that the chaining of the spherical particles, which mediate planar anchoring of LCs on their surfaces, in a direction that is around an angle of 30° from the far-field

director.[7] Musevic and collaborators showed that spherical particles with homeotropic surface alignment which causes the formation of a satellite point or a Saturn ring to maintain straight chain or as kinked chains, respectively.[17] These different symmetries of the aggregates can be explained by the minimization of the elastic energy free energy.

The effect of particle shape on particle organization in LCs has not yet fully been studied in the literature.[5, 8, 9, 11, 18, 19] Recently, the experimental studies of Lapointe and his collaborators and the simulation studies of Hung and Bale demonstrated that the interaction of the particles that have different shapes (cube, triangle and pentagonal prism) is strongly related to the orientation of these particles towards each other.[9, 20] This effect varies depending on the orientation of the particles with respect to the far field director and the strain of the LC ordering at the vicinity of the particles. As a result, the organization of the particle in LC media is strongly affected. Lapointe and his collaborators also showed that these particles can form assemblies as the multiple (double and triple) organizations, with their shapes to critically effect the symmetry of the interactions. Thus, the studies presented in the literature highlights the critical importance of the particle shapes on their individual orientation and their interaction symmetry. Although the studies showed the importance of the particle shapes on their positioning, the experimental studies are currently limited to the particles with planar surface anchoring.[9] A recent simulation study by Beller et al. showed that the colloidal particles with homeotropic anchoring to mediate defect structures that are critically dependent on the shapes and sharpness of the particles.[21] For example, the cubic shaped particles maintain minimum energy state with their surface normal orientation of 45° with respect to the far field nematic director. In addition, the particles with curved edges maintain a ring-shaped defect, where increasing the sharpness of the edges resulted in the formation of the S-shaped defects that follow the sharp edges of the particles. The studies followed in this article would also be considered as an experimental that mimics a similar system to these simulation studies.

In this study, we experimentally investigated the positioning of the cubic shaped particles in nematic LC medium. We determined the effect of surface anchoring and the edge sharpness of the particles on their alignment in LC medium. In addition, we characterized the shapes of the defects formed around the colloidal particles dispersed in nematic medium. The study highlights the importance of the details of the particle geometry on their positioning in LC medium and suggests routes for the design of the self-assembled colloidal particles in LCs.

2. Materials and Methods

2.1. Materials

A room temperature nematic liquid crystal 4-cyano-4'-pentylbiphenyl (5CB) was purchased from HCCH Jiangsu Hecheng Chemical Materials Co., Ltd. (Nanjing, China). Dimethyloctadecyl [3-(trimethoxysilyl) propyl] ammonium chloride (DMOAP), polyvinyl alcohol (PVA), and anhydrous ethanol were obtained from Sigma-Aldrich Co. Ltd. (St. Louis, USA) and used without further purification. Glass slides were obtained from Marienfeld GmbH (Lauda-Königshofen, Germany). The cubic shaped zeolite A particles were obtained from Prof. Halil Kalıpçılar and Prof. Berna Topuz.

2.2. Methods

2.2.1. DMOAP Functionalization of the Particles

Approximately 2% wt particle (zeolite 4A) in 1 mL deionized water was prepared and placed into ultrasonic bath for 10 minutes to disperse the particles. Then, 100 μ l of DMOAP was added and the solution was kept in ultrasonic bath for another 10 minutes. The particles were then rinsed three times with deionized water and water was substituted with ethanol.

2.2.2. Functionalization of the Glass Surfaces

PVA coated surfaces were used for planar anchoring. Glass surfaces were coated with 5% wt PVA in water using a spincoater (5000 rpm for 2 minutes) and then rubbed with a velvet cloth to maintain unidirectional surface anchoring of LCs. DMOAP functionalization was used for the homeotropic anchoring. Before functionalization of the glass surfaces, O_2 plasma etching was applied to the glass slides using a Diener Electronics, Zepto Plasma Unit. Then, DMOAP was deposited on the glass surfaces from 10 minutes incubation in its 1% wt aqueous solution. The glass slides were finally rinsed with water and dried with nitrogen stream.

2.2.3. Preparation of the Liquid Crystal-Microparticle Suspensions

The particles (about 1 g/L) were dispersed in 5CB using a vortex mixer. 5CB, the particles and anhydrous ethanol was mixed in the isotropic phase until homogenous suspension is maintained. Then, ethanol was evaporated under vacuum to obtain a nematic suspension at room temperature. The suspension is then filled between two glass slides in the nematic phase and equilibrated for about an hour before the imaging.

2.2.4. Optical Microscopy

Optical characterizations of the films were performed using Olympus BX50 and BX53 microscopes (Olympus

Inc., Japan) equipped with a polarizer and an analyzer filter. Three independent samples were prepared to determine angle distribution of the particles. An average of around 100 images were collected from each sample. The images were analyzed using angle analysis of Fiji imagej, an open source image processing software.

2.2.5. Scanning Electron Microscopy

Quanta 400F Field Emission series scanning electron microscope was used to characterize the shapes of the particles at higher resolution.

3. Results and Discussion

We used cubic shaped particles to study the effect of the edge sharpness on the alignment and the LC director profiles around the particles. For the systematic studies, we obtained cubic shaped zeolite 4A particles with round, truncated and sharp edges as shown in the scanning electron micrographs in Figure 1. As shown, the sizes of the particles were in the range of 1 μm to 6 μm . This range is important and useful when considering the range 1 μm to 10 μm , where the interplay of the elasticity and the surface anchoring usually occur.[2] Although the sizes of the particles are within a range of interest in the field, the particles used in this study is not common in studying such interactions. Thus, we first performed studies to understand the surface anchoring of LCs on bare and functionalized particles in the first section below. Then, the next two sections are dedicated to the alignment and positioning of the particles in LCs and the investigation of the defect structures around the particles, respectively.

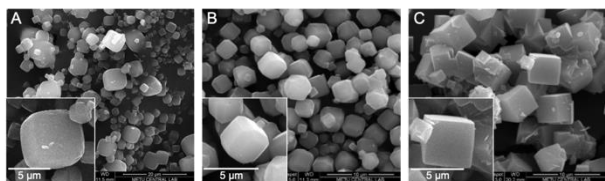


Figure 1. Scanning electron micrographs of zeolite 4A with (A) rounded edge, (B) truncated edge, (C) sharp edges. Insets showing the magnified images of the representative particles.

3.1. Determination of Surface Anchoring of LCs on the Surfaces of the Microparticles

The anchoring condition on the surface of the particles is one of the important parameters affecting the alignment of the particles in liquid crystalline media. Thus, we first analyzed the anchoring of the LCs on the surfaces of these particles since the anchoring of 5CB on the surfaces of the zeolite particles was not readily available in the literature. For this purpose, we dispersed zeolite 4A into 5CB in its nematic phase and collected images of the particles within the range of 2-6 μm using

a polarized microscope equipped with crossed polarizers and a first order retardation plate (FOP). As seen in Figure 2A, the far field director of the nematic 5CB was in the direction of one of the polarizers (shown as *R*, far from the particles), thus, dark appearance was observed under polarized light. However, the distortion of the nematic director around the particles due to the anchoring condition at the surface of the particle resulted in a bright transmitted light as shown by white arrows in the polarized micrographs of Figure 2A-*ii*. Also, when FOP was inserted into the light path, red and blue colors were observed (shown by blue and red arrows in Figure 2A-*iii*).[22] This coloring was consistent with the planar alignment of LCs at the sides of the particles. Using this characterization, the LC anchoring on particle surface was determined as planar and a sketch of the ordering profile of the LCs at the vicinity of the particles was shown in the right panel of Figure 2A-*iv*. Here we note that we observed ~80% of the zeolite 4A particles exhibited planar anchoring of the LCs on their surfaces.

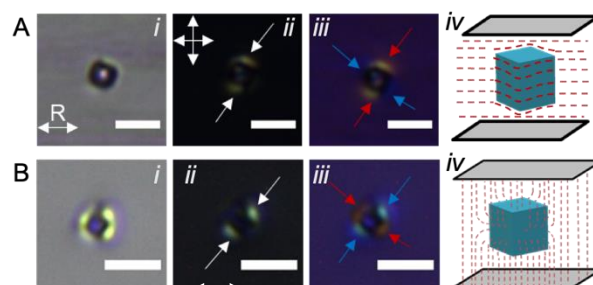


Figure 2. Optical characterizations of the (A) bare and (B) DMOAP functionalized zeolite particles. Brightfield (*i*), polarized light (*ii*) and polarized with first order retardation plate (*iii*) micrographs of single particles dispersed in nematic 5CB). The sketch in the right panel shows the schematic representation of the LC director profile around the particles determined from the micrographs. Double headed arrow indicates the rubbing direction of the two glass slides, R indicates the far field nematic director. Scale bars: 5 μm .

We then modified the LC surface anchoring of the particles with dimethyloctadecyl[3-(trimethoxysilyl)propyl] ammonium chloride (DMOAP) for the expectation of a homeotropic surface anchoring. After functionalization, we checked the anchoring from polarized light micrographs as shown in Figure 2B. The far field director in the images shown in Figure 2B-*ii* is perpendicular to the imaging plane (in-plane), so dark appearance was observed under polarized light. However, the distortion of the nematic director around the particles due to the anchoring condition at the surface of the particle resulted in a bright appearance as indicated by white arrows in the polarized micrographs of Figure 2B-*ii*. Also, when FOP was inserted (Figure 2B-*iii*), which is with a different symmetry compared with that of the planar

particles. When we compared the FOP micrographs of DMOAP coated particles and bare particles, it was seen that the red and blue colors around the particles were located at different sides that pointed out the difference in the anchoring conditions on the surface of the particles. This coloring suggested a homeotropic anchoring of LCs at the surfaces of particles, which would appear dark if particle surface mediated planar anchoring. Using this characterization, the LC anchoring on particle surface was determined as homeotropic and a sketch of the ordering profile of the LCs at the vicinity of the particles was shown in the right panel of Figure 2B-iv. We note that we observed ~90% of the zeolite 4A particles exhibited homeotropic anchoring of the LCs on their surfaces.

3.2. Particle Alignment in Nematic Liquid Crystals

After characterizing the surface anchoring of LCs on the surfaces of bare and DMOAP functionalized zeolite 4A particles, we next characterized the orientation of particles in nematic 5CB. For the analysis, orientations of the single zeolite 4A particles were examined by measuring the angles that the particles maintain in 5CB. When we analyzed bare zeolite 4A particles with sharp edges in planar and homeotropic cells, we evidenced the particles to maintain a position with an angle of 0° in planar medium whereas there was no significant tendency in the case of particles in homeotropic cells as shown in Figure 3.

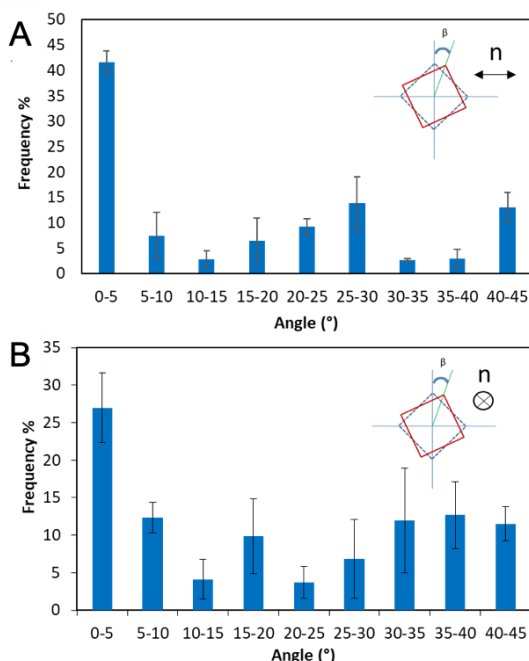


Figure 3. Angle distribution of the bare single zeolite 4A particles with sharp edges in a) planar cell b) homeotropic cell and schematic representation of orientations of the particles. β indicates the angle that the particle oriented in LC media.

As shown in Figure 3, the particles exhibited a preferred orientation along the nematic director, which was expected due to the elastic effects of the LC medium. However, that elastic anisotropy is missing in the direction orthogonal to the nematic director due to the lack of the elastic force anisotropy. Consistent with this, we also observed the same trend in the relative orientation of the DMOAP coated particles with respect to the far field nematic director.

In order to investigate the effect of the edge sharpness of the particles on their orientation in nematic medium, zeolite 4A with rounded and truncated edges were also used. When we analyzed the orientation of the single bare zeolite 4A with truncated edges (Figure 4, red data) and round edges (Figure 4, green data), we observed that the single particles dispersed in planar medium to generally maintain an orientation with an angle around 0° with respect to the far field nematic director, consistent with the observations described above for the particles with sharp edges. However, when compared among the three types of the particles, the frequency of the round-edged particles to maintain an angle of 0° is significantly lower than that of the other two particle shapes. This is expected when considering the loss of the shape anisotropy with the rounding of the edges of a cubic particle.

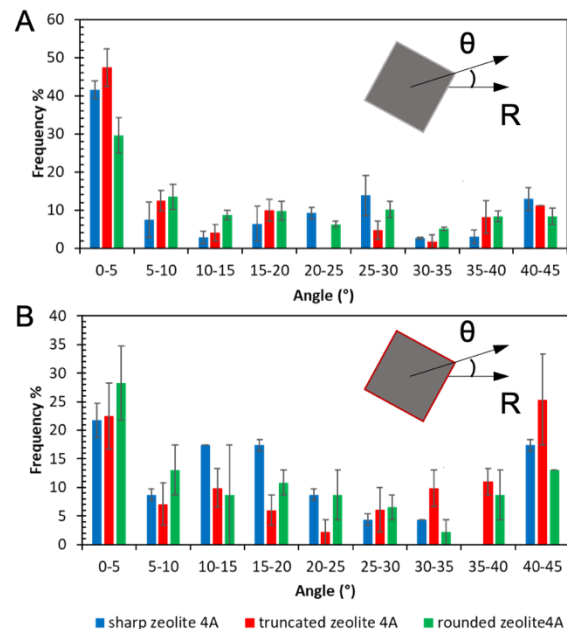


Figure 4. Angle distribution of (A) the bare and (B) the DMOAP coated single zeolite 4A particles with sharp, truncated and rounded edges in planar LC medium. The schematic representation of orientations of the particles are shown as insets where β indicates the angle that the particle oriented in LC media.

When the orientation of the DMOAP functionalized particles were quantified in nematic 5CB, we did not observe a significantly pronounced orientation of the particles with respect to the far field nematic director, independent of the particle shapes. As shown in Figure 4B, the particles maintaining an average orientation of 0 to 5° with respect to the nematic director were almost half of those observed in particles with planar surface anchoring. We reasoned that this significant difference in the distribution of the orientation of the particles would be due to the formation of defects around the particles with surfaces mediating homeotropic orientation, which we detailed below.

3.3. Defect Structures Around Cubic Particles Suspended in Nematic Medium

The literature suggested a range of defect shapes that could form around the cubic shaped particles.[21] Interestingly, simulation studies suggested that at the vicinity of the cubic particles mediating homeotropic orientations, defect loops form that wraps the particles.[21] When the sharpness of the particles at their edges are increased, they have found that the ring shapes of the defects were deformed and maintained shapes that follows the edges of the particles. Herein, we collected images of the three types of the DMOAP coated particles under the microscope to provide evidence of whether or not there are defects present, and whether or not their shapes are affected by the sharpness of the cubic particles.

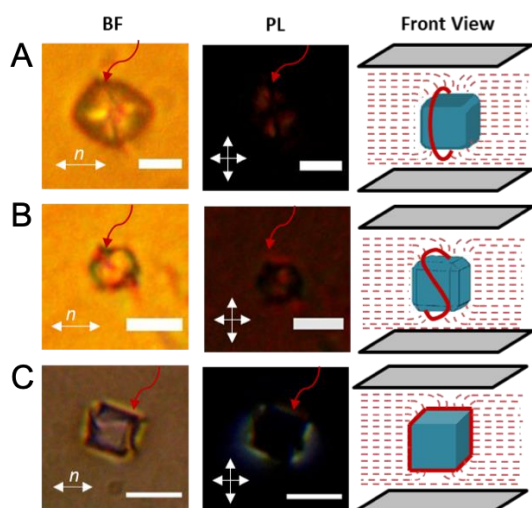


Figure 5. Brightfield (BF) and polarized light (PL) micrographs of DMOAP-coated zeolite 4A particles with (A) rounded, (B) truncated and (C) sharp edges and the corresponding schematic illustrations of the nematic director field and the shapes of the defects around the particles in nematic planar cell. Red arrows in micrographs indicate the defects around the particles. Dashed and solid red lines in schematic illustrations represent the director field and defects, respectively. Scale bars: $5 \mu\text{m}$

Figure 5A-B demonstrates the representative micrographs of the particles with round, truncated and sharp edges, respectively. Evidently, defect structures around DMOAP coated particles with rounded edges were in the shape of a ring (Figure 5A). Defects with S-shapes were formed around DMOAP coated, truncated particles (Figure 5B). As the sharpness of the particles is high (Figure 5C), the shapes of the disclinations (indicated with solid red lines) are deformed and maintained a shape that wrapped the edges of the particles. These observations of the sharpness-dependent shapes of the defects formed around the cubic particles provides the first experimental evidence to the findings of the simulations.[21]

After finding the evidence of the formation of the defects around particles mediating homeotropic surface anchoring, we revisited the alignment of the particles in nematic medium shown in Figure 4. When we compared the distributions of the alignments of the DMOAP coated particles, we did not observe a significant difference in their alignment with respect to the defect structures. However, when the alignment of the particles mediating homeotropic orientation were compared with that of the particles mediating planar anchoring, we found that the particles with homeotropic anchoring not to exhibit a strong preference in the alignment with respect to the far field nematic director. There exists a slight preference of the angles close to 0° and 45° , which is consistent with the literature.[21] However, it does not appear to be strong when compared with the planar particles.

4. Conclusion

We have investigated the positioning of the cubic shaped microparticles with different edge sharpness in nematic liquid crystals. Our results of this study are two-folds. First, we found a relationship between the edge sharpness and the alignment of the particles with respect to the far field director. Specifically, the planar particles with sharp edges to preferentially align with their diagonal parallel to the far field nematic director, which was lowered with the rounding of the particle edges. Second, from the imaging of the particles with homeotropic surface anchoring in the nematic LCs, we found that the defect structure around the particles to be affected by the edge sharpness of the particles. The defect structures observed around the rounded particles were close to a ring shapes, whereas the defects around the cubic particles with sharp edges to maintain a deformed ring with line defects following the proximity of the edges. The observations reached in this study is consistent with the simulations performed on similar systems in literature. The findings would find use in next generation materials for optics, photonics and responsive systems.

Acknowledgement

The authors thank the financial support provided by Scientific and Technological Research Council of Turkey (TÜBİTAK) under award number 116C093.

Author's Contributions

Aslı Karausta: Performed the experiment and result analysis.

Emre Bukusoglu: Assisted in analytical analysis on the structure, supervised the experiment's progress, result interpretation and helped in manuscript preparation.

Ethics

There are no ethical issues after the publication of this manuscript.

References

1. de Gennes, P. G., Prost, J., The Physics of Liquid Crystals; Second Edi, Oxford, New York, 1993.
2. Bukusoglu, E., Bedolla-Pantoja, M. A., Mushenheim, P. C., Wang, X., Abbott, N. L. 2016. Design of responsive and active (Soft) materials using liquid crystals. *Annual Review of Chemical and Biomolecular Engineering*; 7: 163–196.
3. Bai, Y., Abbott, N. L. 2011. Recent advances in colloidal and interfacial phenomena involving liquid crystals. *Langmuir*; 7: 5719–5738.
4. Loudet, J. C., Barois, P., Poulin, P. 2000. Colloidal ordering from phase separation in a liquid-crystalline continuous phase. *Nature*; 407: 611–613.
5. Mondiot, F., Chandran, S. P., Mondain-Monval, O., Loudet, J. C. 2009. Shape-induced dispersion of colloids in anisotropic fluids. *Physical Review Letters*; 103: 1–4.
6. Prathap Chandran, S., Mondiot, F., Mondain-Monval, O., Loudet, J. C. 2011. Photonic control of surface anchoring on solid colloids dispersed in liquid crystals. *Langmuir*; 27: 15185–15198.
7. Poulin, P., Weitz, D. A. 1998. Inverted and multiple nematic emulsions. *Physical Review E*; 57: 626–637.
8. Yuan, Y., Martinez, A., Senyuk, B., Tasinkevych, M., Smalyukh, I. I. 2018. Chiral liquid crystal colloids. *Nature Materials*; 17: 71–78.
9. Lapointe, C. P., Mason, T. G., Smalyukh, I. I. 2009. Shape-controlled colloidal interactions in nematic liquid crystals. *Science*; 326: 1083–1086.
10. Senyuk, B., Liu, Q., Bililign, E., Nystrom, P. D., Smalyukh, I. I. 2015. Geometry-guided colloidal interactions and self-tiling of elastic dipoles formed by truncated pyramid particles in liquid crystals. *Physical Review E*; 91: 1–8.
11. Yuan, Y., Liu, Q., Senyuk, B., Smalyukh, I. I. 2019. Elastic colloidal monopoles and reconfigurable self-assembly in liquid crystals *Nature*; 570: 214–218.
12. Wood, T. A., Lintuvuori, J. S., Schofield, A. B., Marenduzzo, D., Poon, W. C. K. 2014. A Self-Quenched Defect Glass in a Colloid-Nematic Liquid Crystal Composite. *Science*; 79: 79–83.
13. Koenig, G. M., de Pablo, J. J., Abbott, N. L. 2009. Characterization of the reversible interaction of pairs of nanoparticles dispersed in nematic liquid crystals. *Langmuir*; 25: 13318–13321.
14. Rahimi, M., Roberts, T. F., Armas-Pérez, J. C., Wang, X., Bukusoglu, E., Abbott, N. L., de Pablo, J. J. 2015. Nanoparticle self-assembly at the interface of liquid crystal droplets. *Proceedings of the National Academy of the Sciences of the U. S. A.*; 112: 5297–5302.
15. Wang, X., Miller, D. S., de Pablo, J. J., Abbott, N. L. 2014. Organized assemblies of colloids formed at the poles of micrometer-sized droplets of liquid crystal. *Soft Matter*; 10: 8821–8.
16. Wang, X., Miller, D. S., De Pablo, J. J., Abbott, N. L. 2014. Reversible switching of liquid crystalline order permits synthesis of homogeneous populations of dipolar patchy microparticles. *Advanced Functional Materials*; 24: 6219–6226.
17. Muševič, I., Škarabot, M., Tkalec, U., Ravnik, M., Žumer, S. 2006. Two-dimensional nematic colloidal crystals self-assembled by topological defects. *Science*; 313: 954–958.
18. Lapointe, C. P., Mayoral, K., Mason, T. G. 2013. Star colloids in nematic liquid crystals. *Soft Matter*; 9: 7843.
19. Lapointe, C., Hultgren, A., Silevitch, D. M., Felton, E. J., Reich, D. H., Leheny, R. L. 2004. Elastic Torque and the Levitation of Metal Wires by a Nematic Liquid Crystal. *Science*; 303: 652–655.
20. Hung, F. R., Bale, S. 2009. Faceted nanoparticles in a nematic liquid crystal: defect structures and potentials of mean force. *Molecular Simulation*; 35: 822–834.
21. Beller, D. A., Gharbi, A., Liu, I. B. 2015. Shape-controlled orientation and assembly of colloids with sharp edges in nematic liquid crystals. *Soft Matter*; 11: 1078–1086.
22. Miller, D. S., Carlton, R. J., Mushenheim, P. C., Abbott, N. L. 2013. Introduction to optical methods for characterizing liquid crystals at interfaces. *Langmuir*; 29: 3154–3169.

Geometric Characterization of Three-Dimensional (3D) Woven Jute Fiber Preforms for Composites

Nesrin Şahbaz Karaduman¹*

¹ Department of Textile, Footwear and Leather, Akdagmadeni Vocational High School, Yozgat Bozok University, 66300, Yozgat, Turkey
[*nesrin38@gmail.com](mailto:nesrin38@gmail.com)

*Orcid: 0000-0001-9555-7044

Received: 15 November 2020

Accepted: 30 March 2021

DOI: 10.18466/cbayarfbe.826090

Abstract

Fiber-reinforced composite materials have many advantages in various engineering applications when compared to traditional materials such as glass, metals, ceramics, and unreinforced plastics. Recently, textile-reinforced composites are increasingly used in various industries including aerospace, construction, and automotive. This study aims to investigate the geometric characteristics of three-dimensional (3D) woven preforms which are used as reinforcement materials in composites. To this end, 3D woven preforms with three different weave types were produced namely 3D orthogonal, 3D plain z-orthogonal, and 3D satin z-orthogonal. The effect of weave pattern and the number of layers on the geometric characteristics of the produced fabrics was investigated. For this purpose, yarn-yarn distances and density, yarn lengths, and yarn angles were measured. The effect of the number of layers on the geometric parameters was limited. Yarn-to-yarn distances in plain-weave fabrics were found to be greater when compared to other types of fabrics whereas the yarn density decreased in plain woven fabrics due to a large number of interlacements. This shows that in composite form, the fiber volume fraction in the filling and z-directions will be lower in the semi-interlaced fabrics when compared to the non-interlaced orthogonal structures. It was also shown that filling and warp angles are a function of weave type while z yarn angle is associated with the weaving operations such as beat-up, multi-layer filling insertion, and warp yarn let off.

Keywords: Geometric characterization, Jute fiber, Natural fiber composites, Three dimensional (3D) woven preform.

1. Introduction

Fiber-reinforced composites have many advantages over traditional materials such as metals, glass, ceramics, and plastics. These advantages include high strength and stiffness, low weight, tailorability, fracture toughness, and corrosion resistance. Fibers are the main load-bearing element in a composite system due to their high strength and stiffness whereas the matrix determines the final shape of the composite and protects the fibers against harmful environments. The matrix phase is also responsible for homogeneously dispersing applied loads to reinforcing fibers. Fiber and matrix type, fiber orientation/architecture, and fiber volume fraction determine the mechanical properties of a composite material.

Textile-reinforced composites are a group of materials that use a textile form as reinforcement such as yarns, woven, knitted, braided, nonwoven, and multiaxial fabrics. Textile fabrics can be manufactured in two-dimensional (2D) and three-dimensional (3D) forms. The main difference between the two is the use of through-the-thickness or z-yarns in the latter. The type and parameters of textile structure determine the fiber architecture and orientation as well as fiber volume fraction in composite materials.

The first application of textile fabrics was in the aerospace industry where carbon-carbon composites were produced using layered 2D textile fabrics. These composites were produced by simply stacking 2D woven fabrics one on top of the other and impregnating with the resin using one of the composite manufacturing methods. These composite structures were prone to

delamination and showed poor damage tolerance due to a lack of through-the-thickness reinforcement (z-yarns). The solution to these problems of layered structures was the development of 3D fabric manufacturing processes which incorporated z-yarns in the thickness direction to bind the fabric layers and create a compact 3D structure which has good interlaminar strength and damage tolerance [1]. Moreover, 3D fabrics eliminate the labor-intensive layering step in composite processing reducing the overall cost and allow net-shape manufacturing. For all these reasons, 3D textile-reinforced composite structures have been used in the aerospace industry since the 1960s. Nowadays 3D textile composites are used in various industries including aerospace, civil engineering, automotive, and sports [2].

In recent years, natural fibers have attracted considerable attention as composite reinforcement due to increased environmental concerns such as global warming and environmental pollution as well as economic reasons such as rising petroleum prices and depletion of fossil fuels. Natural bast fibers such as jute, hemp, flax, and kenaf are increasingly being used as reinforcement materials due to their low density and high strength/stiffness. Natural fibers are environmentally friendly, sustainable, renewable, and biodegradable [3-7]. Owing to these distinct advantages, natural fibers can compete with glass fibers in various composite applications [8-11].

A literature survey showed that the number of studies on the geometric parameters of 3D woven natural fiber fabrics is limited. This study aims to investigate the geometric characteristics of 3D woven jute preforms as a potential candidate as reinforcement in composites. For this purpose, non-interlaced and semi-interlaced 3D woven preforms with three different weave types were produced namely 3D orthogonal, 3D plain z-orthogonal, and 3D satin z-orthogonal. The effect of weave pattern and the number of layers on the geometric characteristics of the produced fabrics was investigated. For this purpose, yarn-yarn distances and density, yarn lengths, and yarn angles were measured. The results were evaluated taking into account the corresponding composite properties.

2. Materials and Methods

2.1. Materials Used

3D weaving requires three yarn sets such as warp, filling and, z-yarns (through-the-thickness yarns). In this study jute yarns with a linear density of 250 tex were used as warp, filling and z-yarns to make 3D woven preforms. Jute yarns were provided by Erkollar Ltd. (Gaziantep, Turkey).

2.2. 3D Woven Fabric Production

An in-house developed 3D weaving apparatus was used to produce the 3D woven jute fabrics. Two main groups of fabrics were produced such as a) Non-interlaced orthogonal and b) Semi-interlaced orthogonal fabrics. In non-interlaced fabrics, warp, filling, and z-yarns run along the length (x-axis), width (y-axis) and thickness (z-axis) of the fabric respectively without making interlacements with other yarn sets (Figure 1(a) and 2(a)). The production of this fabric requires six distinct steps such as warp let-off, 2D shedding, multilayer filling insertion, z-yarn insertion, beating, and fabric take-up [12]. Figure 3 shows 3D orthogonal weaving principle schematically. The second group of 3D fabrics produced in this study i.e. semi-interlaced fabrics were produced using two distinct weave patterns such as plain-weave and satin-weave. These patterns were chosen due to the fact that plain-weave fabrics contain a large number of interlacements when compared to satin-weave making it easier to observe the effect of any geometrical differences on fabric properties. In these fabrics, warp and filling yarns make interlacements according to 1/1 plain (Figure 1(b), 2(b)) and 1/4 satin (Figure 1(c), 2(c)) weave patterns while z-yarns run along the thickness of the fabrics between adjacent warp yarns without making any interlacements with other two yarn sets. Fabric production started with warp let-off. Then, z-yarns are divided into two groups, such that an odd number of yarns are laid in the +z direction while an even number of yarns are laid in -z direction. Then the filling yarn makes interlacements with warp yarns according to the weave pattern in every layer. Then z-yarns move in alternate directions to their first position such that an odd number of yarns are laid in the -z direction while an even number of yarns are laid in +z direction. This cycle of movements was repeated to make preforms. Two different number of layers such as 2 and 4 layers were used for the production of all the fabrics in this study. Table 1 lists the produced 3D fabric samples together with their sample codes.

Table 1. Produced 3D fabric samples.

Fabric Type	Number of Layers	Sample Code	
Orthogonal	2	3DWO	
	4		
Semi-interlaced	Plain	2	3DWP-ZO
		4	
	Satin	2	3DWS-ZO
		4	

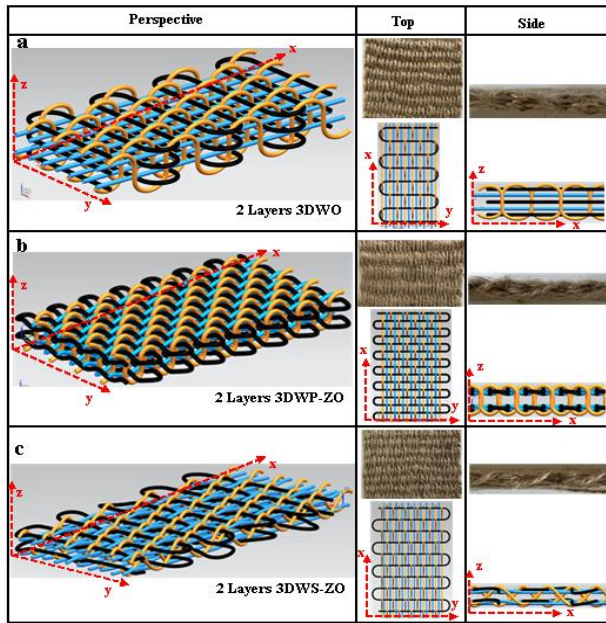


Figure 1. Two-layer fabric samples and their computer drawings (a) 3D orthogonal fabric; (b) 3D plain-weave z-orthogonal fabric; (c) 3D satin-weave z-orthogonal fabric.

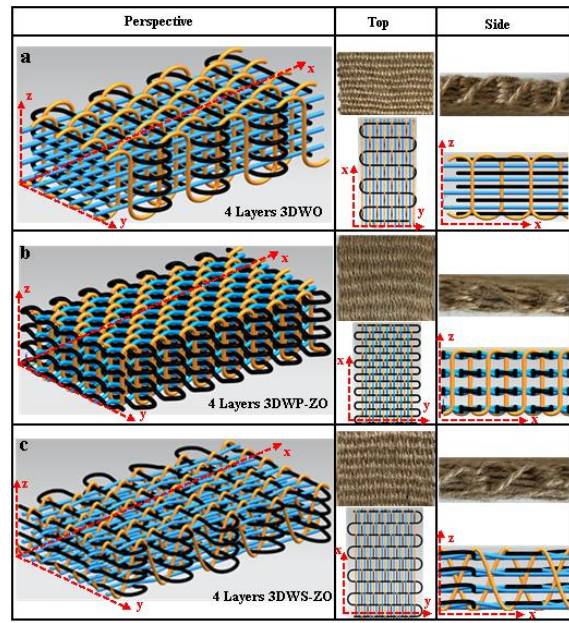


Figure 2. Four-layer fabric samples and their computer drawings (a) 3D orthogonal fabric; (b) 3D plain-weave z-orthogonal fabric; (c) 3D satin-weave z-orthogonal fabric.

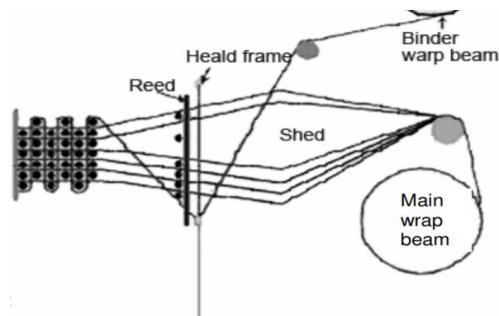


Figure 3. 3D orthogonal weaving principle [13].

2.3. Computer Modeling

The produced fabric samples were modeled using NX-Unigraphics 7.5 software to clearly demonstrate the yarn paths and interlacements in 3D structures and for future analysis.

2.4. Determination of Fabric Dimensions

In 3D woven fabrics, fabric length (Sl), width (Sw), and thickness (St) were measured. The fabric length was limited to 20 cm in all the fabrics. Figure 4 shows the fabric dimensions and yarn sets on actual fabric and computer model.

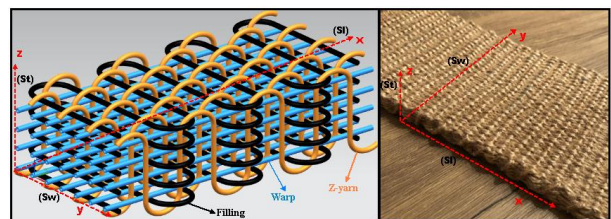


Figure 4. Demonstration of the fabric dimensions and yarn sets on computer model and actual fabric sample.

2.5. Determination of Yarn-to-Yarn Distances and Yarn Density

Yarn-to-yarn distances of adjacent yarns were measured on the 3D woven fabric samples. Warp-warp (w-w), filling-filling (f-f), and z-yarn-z-yarn (z-z) distances were measured on top side (x-y plane), side (x-z plane), and cross-section (y-z plane). Figure 5 highlights the yarn-to-yarn distances and other related parameters for measurements.

Yarn density measurements were carried out for warp, filling, and z-yarns on top, side, and cross-section planes of the fabrics. The number of yarns in 5 cm was considered for yarn density measurements.

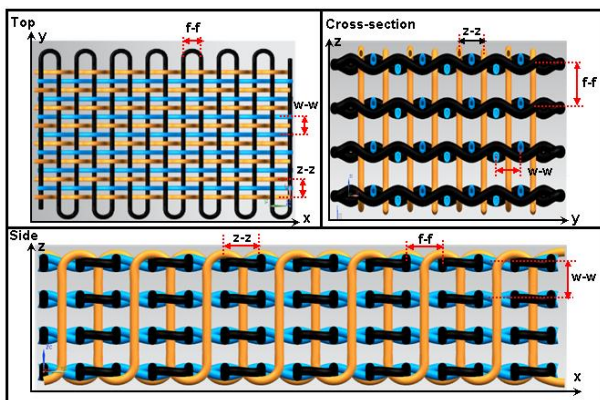


Figure 5. The illustration of the parameters considered in yarn-to-yarn distance measurements.

2.6. Determination of the Yarn Lengths

Uncrimped yarn lengths were measured in 3D woven fabrics. In fabric structure, especially at the interlacement points, warp, filling, and z-yarns follow curved paths and the yarns become curved. This is referred to as the “yarn crimp”. The length of the path that warp, filling, and z-yarns follow in the fabric structure is hence called the “uncrimped yarn length”. In this study, guide yarns were used in order to be able to measure the uncrimped yarn lengths. First, the guide yarn was inserted in the structure following the exact same yarn path as the yarn (i.e. warp, filling or z-yarn) whose uncrimped length is to be measured. Then the ends of this guide yarn were marked before it is withdrawn from the structure.

The distance between the markings on the straightened guide yarn gives the uncrimped yarn length. Uncrimped warp yarn length (l_w), uncrimped filling yarn length (l_f), and uncrimped z-yarn length (l_z) were measured for all fabric types (Figure 6).

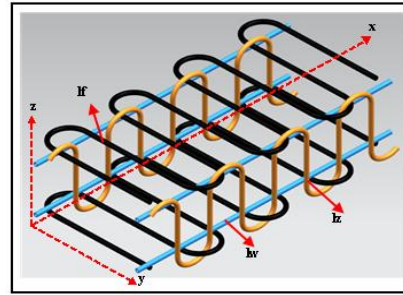


Figure 6. Illustration of uncrimped warp, filling, and z-yarn length on the computer model.

2.7. Determination of the Yarn Angles

The following yarn angle measurements were carried out in 3D woven fabric structures:

- The filling angle between the filling yarn and warp yarn in the fabric width direction (y-axis) (θ_f) (Figure 7(a))
- The filling trajectory angle between the filling yarn and z- yarn in the fabric thickness direction (z-axis) (θ_{fz}) (Figure 7(a))
- The warp angle between the warp yarn and filling yarn in the fabric length direction (x-axis) (θ_w) (Figure 7(b))
- The warp trajectory angle between the warp yarn and z- yarn in the fabric thickness direction (z-axis) (θ_{wz}) (Figure 7(b))
- The z-yarn angle between the z-yarn and warp yarn in the fabric length direction (x-axis) (θ_z) (Figure 8)
- The z-yarn trajectory angle between z-yarn and warp yarn in the thickness direction (z-axis) (θ_{zw}) (Figure 8)

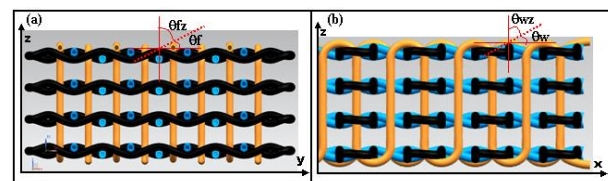


Figure 7. Demonstration of (a) θ_f and θ_{fz} angles (b) θ_w and θ_{wz} angles.

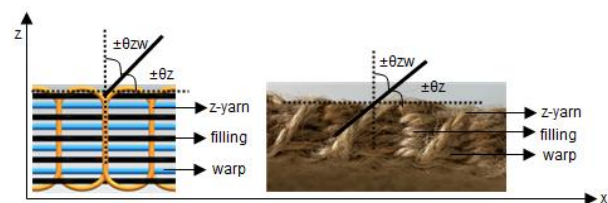


Figure 8. Demonstration of θ_z and θ_{zw} angles.

3. Results and Discussion

In the current study, the geometric characterization of 3D woven jute fabrics was carried out for their possible application in fiber-reinforced composites. For this purpose, 3D orthogonal, 3D plain z-orthogonal, and 3D satin z-orthogonal woven fabrics were produced (Figure 9).

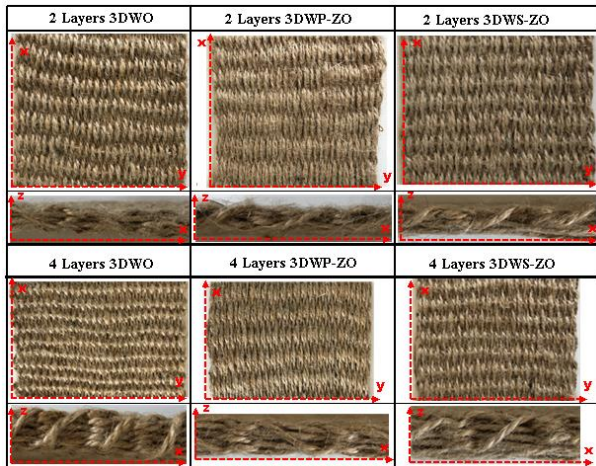


Figure 9. Fabric types produced in the current study.

3.1. Yarn-to-Yarn Distances and Yarn Density

Figure 10 shows the relation between the fabric type and the yarn-to-yarn distances measured on the fabric side (xz-plane). Filling-filling and z-yarn-z-yarn distances were found to be the same with each other and greater than the warp-warp distance. The number of layers did not have a significant effect on the yarn-to-yarn distances. When the semi-interlaced fabrics were compared with the non-interlaced structures, filling-filling and z-z yarn distances were found to be similar in satin-weave and non-interlaced orthogonal fabrics. In plain-weave fabrics, however, filling-filling and z-z yarn distances were found to be greater than other types of fabrics. This was attributed to relatively large number of warp-filling interlacements in plain-woven fabrics which prevent the adjacent filling yarns from approaching each other during the beat-up action. The same can be stated for the z-yarns. This effect was limited in satin-woven fabrics due to a smaller number of interlacement points in satin fabrics. Hence filling-filling and z-z distances were similar to those of the non-interlaced fabrics. When composite properties are considered, directional fiber volume fractions in filling and z directions will be lower in semi-interlaced structures when compared to non-interlaced fabric composites.

Figure 11 shows the relation between the fabric type and the yarn-to-yarn distances measured on the fabric cross section (yz-plane). Filling-filling, warp-warp and z-z distances measured on fabric cross section plane

were in a narrow range of 0.2 to 0.6 cm. As the number of layers was increased, warp-warp distance was found to decrease. Warp-warp and filling-filling distances (distances between the adjacent layers) were lower in semi-interlaced structures due to the more compact nature of the fabrics resulting from a large number of interlacements. z-z distance increased as the number of layers was increased. On the other hand, z-z distances were greater in semi-interlaced structures. In these structures, warp-filling interlacement points prevent the adjacent z-yarns from approaching each other, thus increasing the z-z yarn distances.

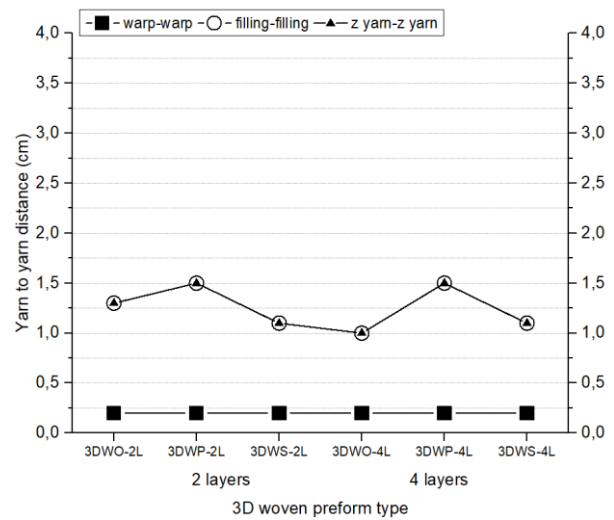


Figure 10. The relation between the fabric type and the yarn-to-yarn distances measured on the fabric side (xz-plane).

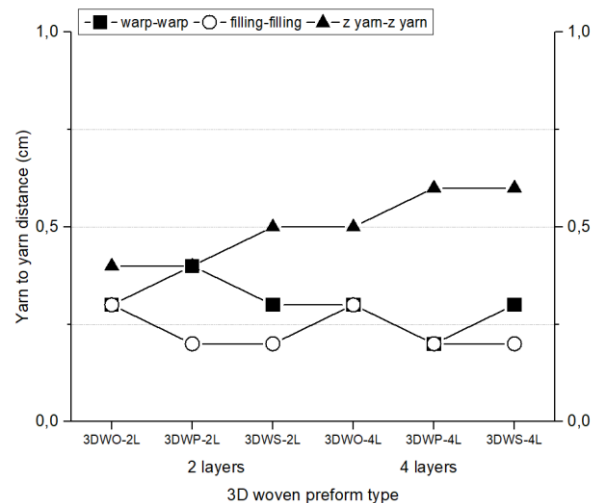


Figure 11. The relation between the fabric type and the yarn-to-yarn distances measured on the fabric cross section (yz-plane).

Figure 12 shows the relation between the fabric type and the filling and z-yarn densities measured on the

fabric side (xz-plane). It was observed that the filling and z-yarn density values are very similar to each other. (Figure 12). Filling-filling and z-z yarn densities were lower in plain-weave semi-interlaced fabrics in line with the increment observed in filling-filling and z-z yarn distances in these structures. As explained above, warp-filling interlacement points in plain-weave semi-interlaced fabrics prevent the adjacent filling yarns from approaching each other, thus increasing the yarn-to-yarn distances and lowering the yarn density values. However, the effect of warp-filling interlacements was minimized in satin-weave semi-interlaced fabrics due to a lower number of warp-filling interlacements in satin structure. Accordingly, yarn density values were similar to those of the non-interlaced fabrics and higher than those of the plain-weave fabric samples.

Figure 13 shows the relation between the fabric type and the warp and z-yarn densities measured on the fabric cross-section (yz-plane). Warp yarn density values were found to be twice as higher as the z-yarn densities (Figure 13). This is an expected result because one z yarn is placed between two adjacent warp yarns when producing 3D fabric structures. The measured yarn densities are indicative of a successful 3D fabric weaving operation which resulted in uniform fabric structures. In semi-interlaced fabrics, z-yarn densities were lower due to increasing z-z distance. z-directional fiber volume fraction in these structures should be expected to be lower.

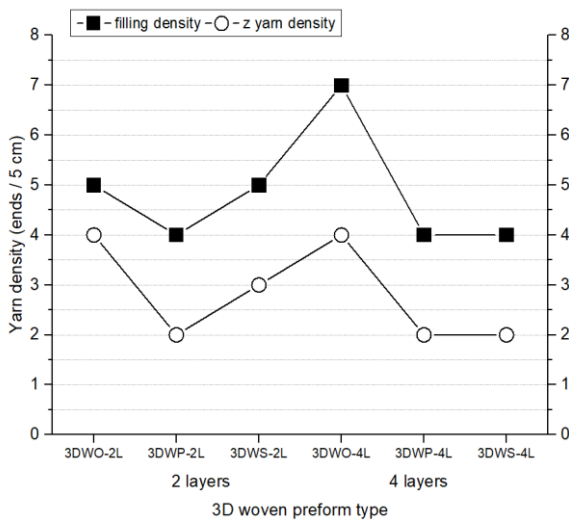


Figure 12. The relation between the fabric type and the filling and z-yarn densities measured on the fabric side (xz-plane).

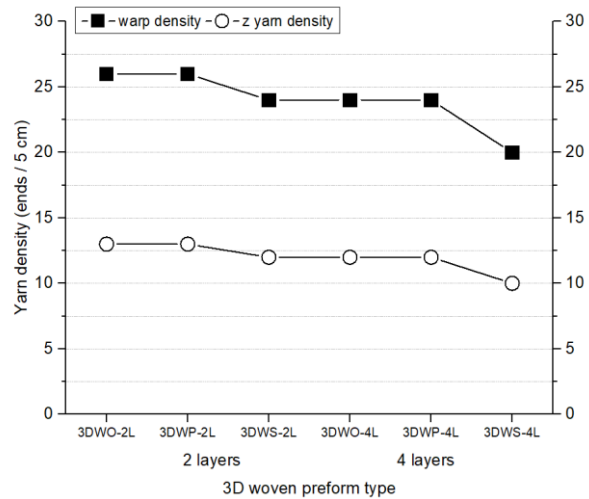


Figure 13. The relation between the fabric type and the warp and z-yarn densities measured on the fabric cross-section (yz-plane).

3.2. Yarn Lengths

Table 2 shows the uncrimped warp yarn length (l_w), filling yarn length (l_f), and z-yarn length (l_z). Figure 14 shows the relation between the fabric types and various yarn lengths. Uncrimped warp and filling yarn lengths were greater in semi-interlaced plain and satin-woven fabrics when compared to non-interlaced structures. In non-interlaced fabric structure, warp and filling yarns run along x and y axes respectively without making any interlacements with other yarn sets and preserving their straight form. However, in semi-interlaced plain and satin fabrics, warp and filling yarns make interlacements with each other according to the weave pattern and become curved. Therefore, the uncrimped warp and filling yarn lengths are greater in semi-interlaced fabrics as expected. Uncrimped z-yarn lengths were found to be greater in plain-woven fabrics compared with satin-weave due possibly to an increased number of yarn interlacements which increase the yarn crimp.

Table 2. The uncrimped warp yarn length (l_w), filling yarn length (l_f), and z-yarn length (l_z) in 3D fabrics.

Sample code	Num of layers	l_w (/20 cm)	l_f (/9 cm)	l_z (cm)
3DWO	2	20.0	9.0	2.1
3DWO	4	20.0	9.0	2.5
3DWP-ZO	2	21.1	9.6	2.3
3DWP-ZO	4	21.3	9.8	3.1
3DWS-ZO	2	21.2	9.5	2.2
3DWS-ZO	4	21.3	9.6	2.7

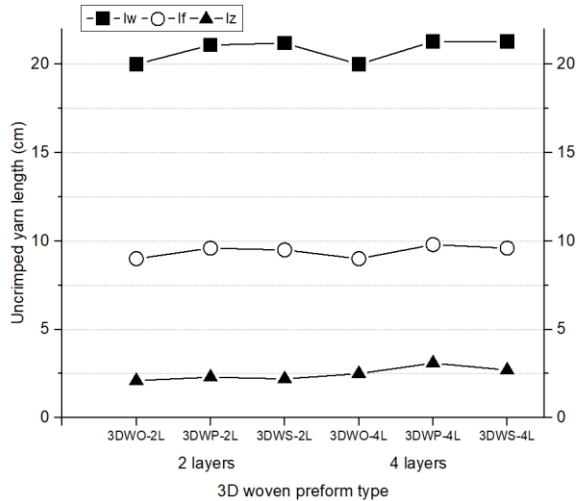


Figure 14. The relation between the fabric types and various yarn lengths.

3.3. Yarn Angles

Figure 15 shows the relation between the fabric type and various yarn angles. $\pm\theta_z$ angle was found to be greater compared with other angles (θ_w and θ_f). θ_z angle was found to be greater in non-interlaced orthogonal fabrics compared with semi-interlaced structures due to the fact that filling-filling and z-z yarn distances are greater in semi-interlaced structures. θ_z angle generally increases as the number of layers is increased. In non-interlaced fabrics, θ_f and θ_w angles are equal to 0° due to the fact that these fabric structures, warp and filling yarns run along x and y axes respectively without making any interlacements with other yarn sets and preserving their straight form. θ_w angle is greater in satin woven fabrics compared with the plain weave. This was attributed to the fact that filling-filling distance measured in xz plane is lower in satin woven fabrics compared with the plain-weave (Figure 10). θ_f angle was found to be greater in 2-layer satin fabrics when compared to 2-layer plain fabrics. However, the θ_f angle was greater in the case of 4-layer plain woven fabrics when compared to satin-weave. This result is also in parallel with yarn distances measured in the yz-plane (Figure 11). Accordingly, θ_f angle increases as the distance between the adjacent warp yarns measured in the yz plane decreases.

It can be concluded that θ_f and θ_w angles are generally affected by weave pattern whereas θ_z angle is generally influenced by weaving operations such as warp let-off, multilayer filling insertion, and beat-up.

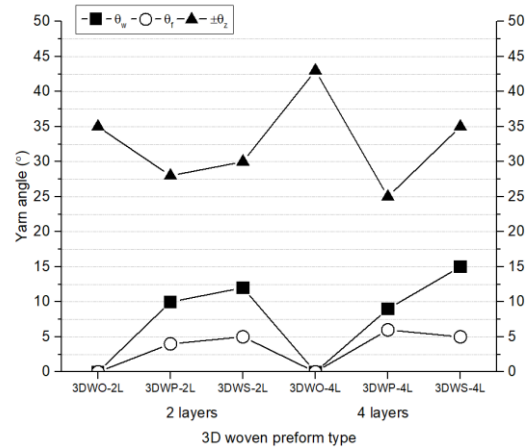


Figure 15. The relation between the fabric type and various yarn angles.

4. Conclusion

Mechanical properties of a composite material are dependent upon the fiber type, matrix type, fiber orientation/architecture, and fiber volume fraction. For 3D textile reinforced composites, the weave pattern, number of layers, yarn angles and other parameters are the main factors determining the fiber orientation and architecture and hence the directional and overall fiber volume fractions. In this study, geometric characterization of 3D woven jute fabrics was carried out. For this purpose, two main types of 3D fabrics were produced such as non-interlaced and semi-interlaced fabrics. The semi-interlaced fabrics were produced using two different weave patterns such as plain and satin weave. Two different numbers of layers i.e. 2 and 4 layers were used for all types of fabrics produced in the study.

Yarn-to-yarn distances and yarn densities: Increasing the number of layers did not have a significant effect on yarn-to-yarn distances. Filling-filling and z-z yarn distances were found to be greater in plain-woven semi-interlaced fabrics when compared to satin-weave semi-interlaced fabrics and non-interlaced orthogonal fabrics due to a large number of interlacements in plain-weave structure. It can be expected that the filling and z-directional fiber volume fractions would be lower in semi-interlaced fabric reinforced composite structures. Yarn density values were also found to be in parallel with the yarn-yarn distance results.

Yarn lengths: The uncrimped warp and filling yarn lengths were greater in semi-interlaced plain and satin fabrics compared with those of non-interlaced structures. Uncrimped z-yarn lengths were greater in plain-woven fabrics when compared to the satin-weave due to larger number of yarn interlacements and hence the yarn curviness in plain-weave.

Yarn angles: z yarn angle was found to be greater than other angles. z yarn angle was greater in non-interlaced fabrics compared with semi-interlaced fabrics due to the fact that filling-filling and z-z yarn distances were greater in semi-interlaced fabrics. z yarn angle increased as the number of layers was increased for all fabric types. Warp yarn angle was greater in satin fabrics compared to plain-woven structures. Filling and warp angles are generally affected by weave pattern whereas z yarn angle is influenced by weaving operations such as warp let-off, multilayer filling insertion, and beat-up. The findings of this study will shed light on the effect of 3D fabric type and geometry on the properties of natural fiber reinforced 3D woven composites.

Author's Contributions

Nesrin Şahbaz Karaduman: Produced the samples, carried out the measurements, performed the experiments and analyzed the results, drafted and wrote the manuscript.

Ethics

There are no ethical issues after the publication of this manuscript.

References

1. Stig, F, Hallström, S. 2012. Spatial modelling of 3D-woven textiles. *Composite Structures*; 94(5): 1495–1502.
2. Ko, F. 3-D textile reinforcements in composite materials. In: Miravete A (ed) 3-D textile reinforcements in composite materials. Woodhead Publishing, Cambridge, 1999, pp 9–42.
3. Mohanty, AK, Misra, M, Drzal, LT. Natural fibers, biopolymers, and biocomposites: An introduction. In: Mohanty A, Misra M, Drzal LT (eds) Natural fiber, biopolymer, and biocomposites. CRC Press, Boca Raton, 2005, pp 1–36.
4. Aziz, SH, Ansell, MP. Optimising the properties of green composites. In: Baillie C (ed) Green composites: Polymer composites and the environment. Woodhead Publishing, Boca Raton, 2004, pp 154–180.
5. Satyanarayana, KG, Arizaga, GGC, Wypych, F. 2009. Biodegradable composites based on lignocellulosic fibers—An overview. *Progress in Polymer Science*; 34(9): 982–1021.
6. Mohanty, AK, Misra, M, Hinrichsen, G. 2000. Biofibres, biodegradable polymers and biocomposites: An overview. *Macromolecular Materials and Engineering*; 276–277(1): 1–24.
7. Bismarck, A, Mishra, S, Lampke, T. Plant fibers as reinforcement for green composites. In: Mohanty A, Misra M, Drzal LT (eds) Natural fibers, biopolymers, and biocomposites. CRC Press, Boca Raton, 2005, pp 37–108.
8. Wambua, P, Ivens, J, Verpoest, I. 2003. Natural fibres: Can they replace glass in fibre reinforced plastics? *Composites Science and Technology*; 63(9): 1259–1264.
9. Joshi, SV, Drzal, LT, Mohanty, AK, Arora, S. 2004. Are natural fiber composites environmentally superior to glass fiber reinforced composites? *Composites Part A: Applied Science and Manufacturing*; 35(3): 371–376.
10. Mehta, G, Mohanty, AK, Thayer, K, Misra, M, Drzal, LT. 2005. Novel biocomposites sheet molding compounds for low cost housing panel applications. *Journal of Polymers and the Environment*; 13: 169–175.
11. Bledzki, AK, Faruk, O, Sperber, VE. Cars from bio-fibres. 2006. *Macromolecular Materials and Engineering*; 291(5): 449–457.
12. Bilisik, K, Karaduman, NS, Bilisik, NE, Bilisik, HE. 2013. Three-dimensional fully interlaced woven preforms for composites. *Textile Research Journal*; 83(19): 2060–2084.
13. Potluri, P, Sharif, T, Jetavat, D. 2008. Robotic approach to textile preforming for composites. *Indian Journal of Fibre & Textile Research*; 33: 333–338.

CFD Modelling of Non-Newtonian Fluid Flow in a Pipe Including Obstacle

Mustafa Murat YAVUZ¹ , Pınar SARI ÇAVDAR^{2*} 

¹İzmir Democracy University, Department of Mechanical Engineering, 35140 İzmir, Turkey

²İzmir Democracy University, Department of Civil Engineering, 35140 İzmir, Turkey

* pınar.cavdar@idu.edu.tr

*0000-0002-1989-4759

Received: 20 January 2021

Accepted: 5 April 2021

DOI: 10.18466/cbayarfbe.865261

Abstract

Pipe flow problems are important in transportation of wastewater, oil lines and supply of water. In this study, a non-Newtonian fluid model is discussed and a CFD solution is presented for flow geometry. The effects on velocity, pressure, dynamic viscosity and cell Reynolds number are discussed for different parameters of flow inside the pipe. Power Law function is considered in the analyses. The velocity profile increased and get more parabolic distribution when flow behaviour index, n was increased. That supports lower pressure profile in the pipe flow. The lowest n value causes to increase the sensitivity for viscous effects. The increased flow consistency index, K causes to increase dynamic viscosity but decreases the Re number. Results are given in different graphs and contours.

Keywords: non-Newtonian fluid, power law, CFD.

1. Introduction

Fluid flow in pipes is used in many areas of mechanical and civil engineering. Heating and cooling applications and fluid distribution networks can be cited as common usage areas for liquid and gas flow. Many fluids, especially liquids, are transported by circular pipes. The reason why circular pipes are used is that they can withstand large pressure differences between inside and outside without deterioration.

Several researchers have analysed the problems of boundary layer flow of non-Newtonian fluids past different geometries in the past. [1-6].

Power-Law fluid model has been carried out by many scientists [7-13]. Gupta [14] carried out a new approximate solution for laminar flux of power-law fluid. Flow model is considered for pipe and straight channels. The results of different methods for pipe and channel flow are compared according to parameters such as pressure, velocity, and length of the boundary layer. Alexandrou et al. [15] have examined the steady state of the non-Newtonian fluid in the Herschel-Bulkley model by considering the expansion of the canal in three dimensions at different rates.

Cebeci et al.[16] and Acrivos et al. [17] have compared laminar boundary layer of non-Newtonian fluid made by approximate solution of the equations by asymptotic method with numerical solution of the equations of power law flux.

Hornbeck [18] worked laminar flow of a compressible fluid in the inlet of a pipe numerically and his numerical technique allows a closer approximation to the basic equations of fluid motion than has been possible in previous investigations. Yapıcı and Albayrak [19] studied the temperature distributions inside the pipe wall and fluid for uniform and non-uniform heat fluxes. Two different mean flow velocities are considered, and the stress distribution is presented inside the pipe wall. Yıldırım et al. [20] examined the wave motion at the interface of two fluids and investigated wavelength, wave number, frequency, amplitude, wave and growth rate in 2D numerical analysis, taking into account the Kelvin-Helmholtz (KH) type instability.

Kırmızıgöl et al. [21] studied both steady-state and time-dependent (transient) computational fluid dynamics (CFD) analysis of the cooling channels and the die cooling system, both in conjugate and solid-only models, performed and compared the pipe flow part of the results with the available experimental data.

Sorgun et al. [22] analysed pipe roughness influences on frictional pressure losses of water with CFD. Batool and Nawaz [23] investigated thermal enhancement of non-Newtonian fluid in micropolar fluid structures. The increased viscosity parameter shifted great vortices to the top wall. Mehryan et al. [24] studied melting process of a non-Newtonian fluid inside a metal foam and determined the effect of power-law index on melting process. Jamshidzadeh et al. [25] studied gas holdup conditions in mixer systems with non-Newtonian fluid. Khan et al. [26] used non-Newtonian Casson fluid to investigate y-shaped fin. Nguyen et al. [27] checked Boltzmann equation to simulate non-Newtonian flow using power law magnetic Reynolds number. Eberhard et al. [28] investigated non-Newtonian fluid in disordered porous structure with local viscosity effects. Studies on non-Newtonian fluids have made great improvements, especially in recent times. Since the working area of these fluids is quite wide. They vary for their characteristics and flow parameters. Studies can be experimental, theoretical or comparative. In this study, a numerical analysing method is used, and the results are compared.

2. Materials and Methods

A circular pipe having a diameter (D) of 0.1 m created. The length of pipe has 15D. A circular 2.5 mm thick obstacle is created 5D far away from the fluid inlet. The obstacle closes partially as a length of 40 mm. Computational fluid dynamics is used in the analyses. The isometric view of geometry is given in Figure 1.

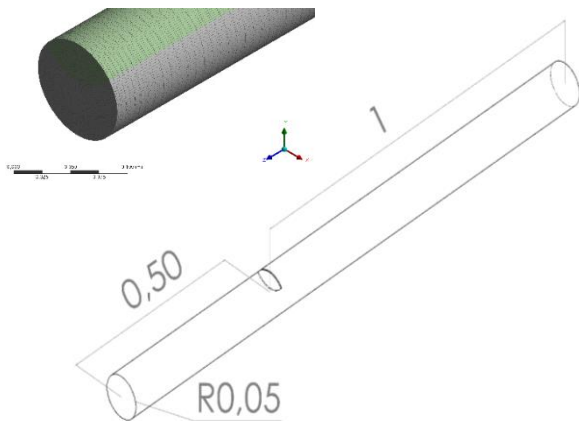


Figure 1. Isometric view of cylinder geometry (all dimensions are in m).

A closer view of the CFD model is also illustrated. The prepared CFD model was checked with mesh independence test for maximum velocity in pipe for $n=2$ and $K=0.1$ power law constants. The coarse and fine mesh variation was found at steady state approximately at 560,000 elements which total mesh quality was detected as 0.79.

2.1. Modelling and Boundary Conditions

Non-Newtonian fluid flow is analysed by considering Power Law function. Viscosity is the critical parameter and can vary with the flow conditions. The basic form of the shear stress (τ) is given in Eq (.2.1).

$$\tau = K \times \left(\frac{du}{dy}\right)^n \quad (2.1)$$

K = flow consistency index
 n =flow behaviour index
 $\frac{du}{dy}$ = shear rate

Effect of n and K is investigated with a constant density of 1000 kg/m^3 . The inlet flow is selected as 0.01 m/s . Inside pipe surfaces are defined as wall. Laminar flow model is used with respect to non-Newtonian parameters and low inlet velocity.

3. Results and Discussion

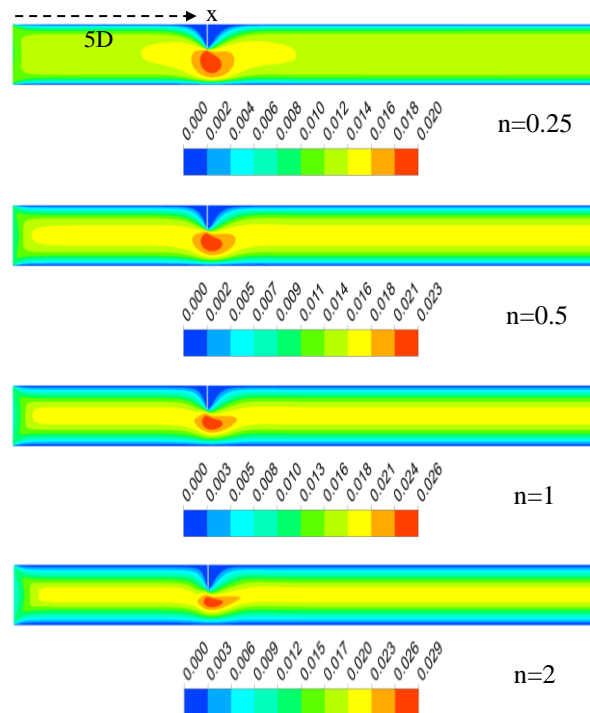


Figure 2. Velocity contours of various “n” values with a constant value of $K=0.1$

In Figure 2, the velocity contours are taken from a vertical section plane at the centre of pipe. The results show that the viscous flow dominantly interacts on the wall. As a result of the increased n coefficient, the low or zero velocity profile interacting with the wall is more common. It was determined that there is a dead flow zone at the front and rear of the obstacle. The dead flow zone is greater behind the obstacle. The flow velocity increases in the transition section due to the narrowing of the cross section. With the increasing number of n , the flow tended to accelerate and showed a more

parabolic high velocity structure in the pipe centre. This situation is also seen at the entrance to the pipe.

In Figure 3, velocity profile is given at 5D. There is no flow or velocity profile at the first 40 mm distance due to obstacle. That obstacle decreases the cross-section area of fluid pass and increases the velocity at the opened section. An asymmetrical velocity distribution profile is formed. Flow velocity profile is formed with a sharper and higher parabolic curve as a result of increasing n coefficient.

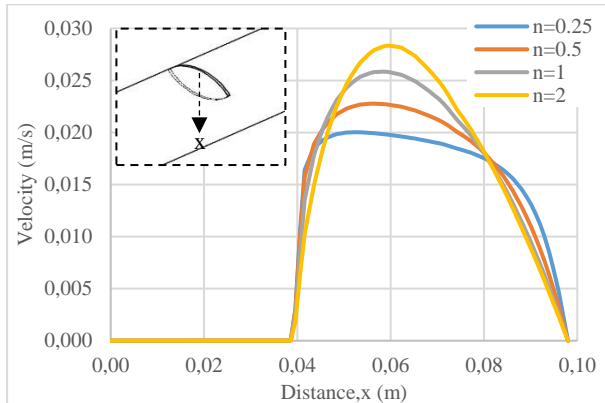


Figure 3. Velocity profiles of various “n” values with a constant K value of 0.1 at 5D.

In Figure 4, velocity profiles are given for $n = 0.25, 0.5, 1, 2$. The flow has stabilized and shows a symmetrical distribution. This situation shows that the flow is not affected by the obstacle effect. As the value of n increases in the non-Newtonian fluid, the maximum velocity increases.

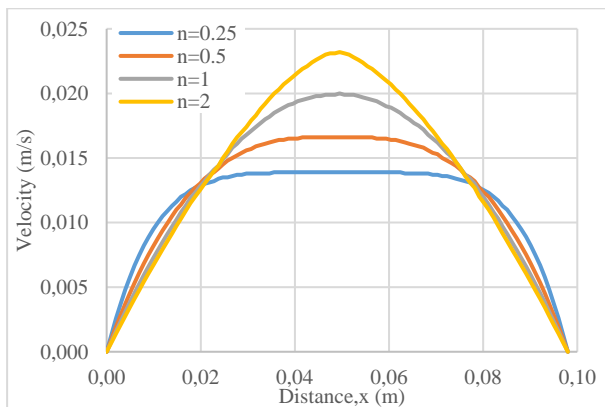


Figure 4. Velocity profiles of various “n” values with a constant K value of 0.1 at 10D.

When the results obtained along the whole channel in Figure 5 are examined, it is seen that the entire flow velocity increased as a result of the increasing n coefficient. There is an instantaneous speed jump at the point where the obstacle flow is located. Considering the results of this instant speed jump, the value of $n = 2$ with the highest velocity and the value of $n = 1$ velocity

reached the same value. The sudden increase in flow velocity has reached its former steady state one diameter ahead of the obstacle.

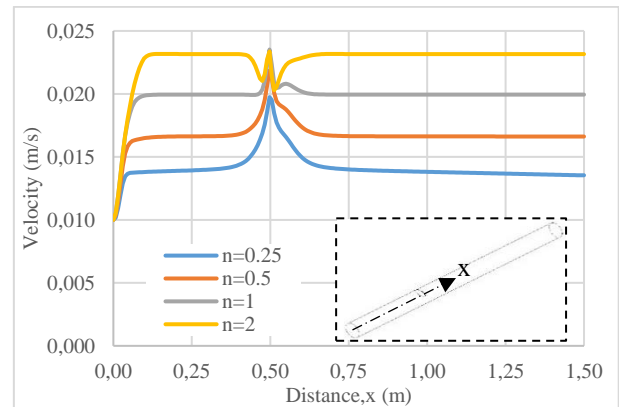


Figure 5. Velocity profiles of various “n” values with a constant K value of 0.1 from inlet to outlet centre.

In Fig. 6 the pressure profile is shown for different n coefficients. It was determined that the pressure decreased due to the increase in flow velocity after the obstacle. The lowest pressure profile is seen at $n = 2$ where the velocity is the highest. There is about 2 times the difference between the highest and low pressures.

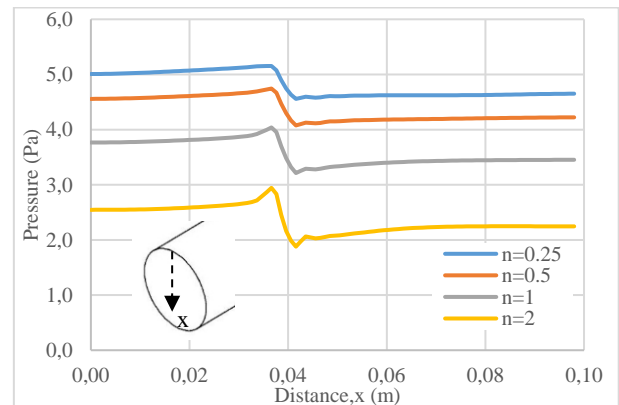


Figure 6. Pressure profiles of various “n” values with a constant K value of 0.1 at 5D.

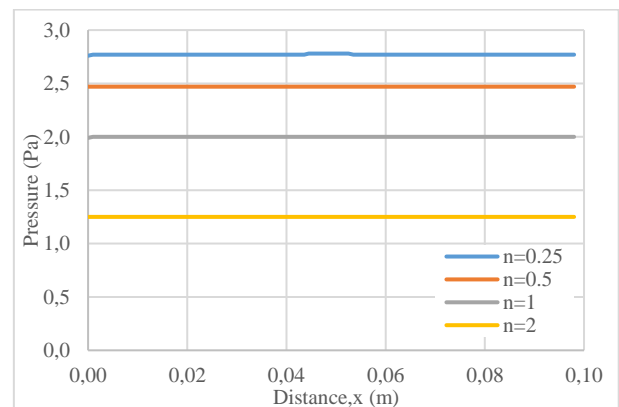


Figure 7. Pressure profiles of various “n” values with a constant K value of 0.1 at 10D.

Figure 8 shows the pressure graph for different n coefficients along the length of the pipe. The graph starting with 3.5 Pa for the $n=2$ value entered the pipe with a pressure 2 times higher for the value $n=0.25$. Pressure drop is observed instantaneously at the point where the obstacle is located. At this point the velocity increased.

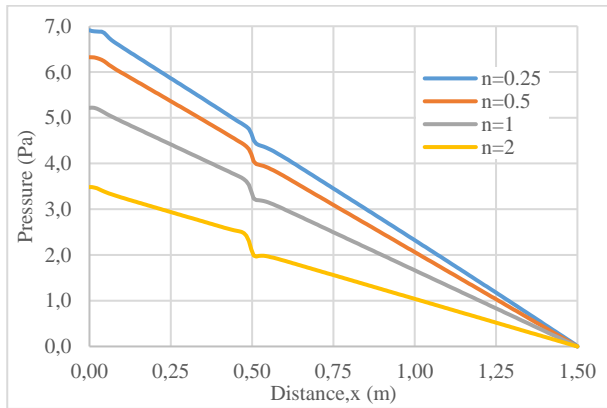


Figure 8. Pressure profiles of various “ n ” values with a constant K value of 0.1 from inlet to outlet centre.

Figure 9 shows the effect of dynamic viscosity. The viscous effect behaved predominantly on the part of the wall with the obstacle. At $n=1$ and $n=2$, the wall interaction with dynamic viscous effect is not seen as dominant.

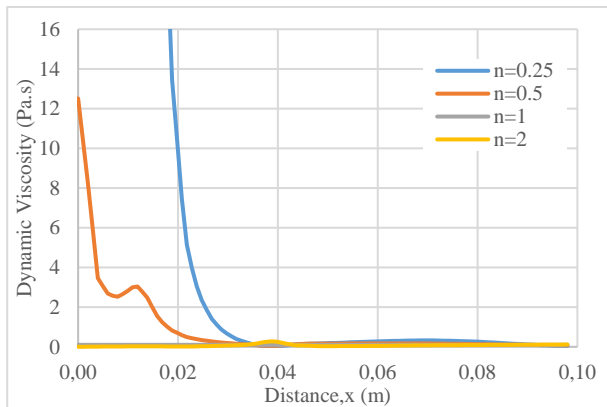


Figure 9. Dynamic viscosity profiles of various “ n ” values with a constant K value of 0.1 at 5D.

In Figure 10, the dynamic viscosity effect is shown at 10D for the condition where the flow develops. For $n = 0.25$ and $n = 0.5$, viscosity is effective. However, the dynamic viscosity value has decreased 3 times in the fluid that travels the distance between 5D and 10D.

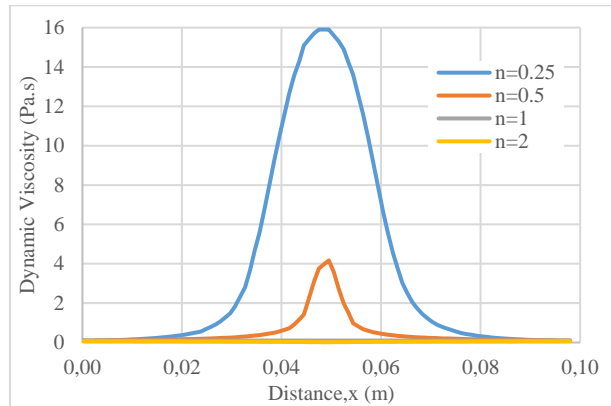


Figure 10. Dynamic viscosity profiles of various “ n ” values with a constant K value of 0.1 at 10D.

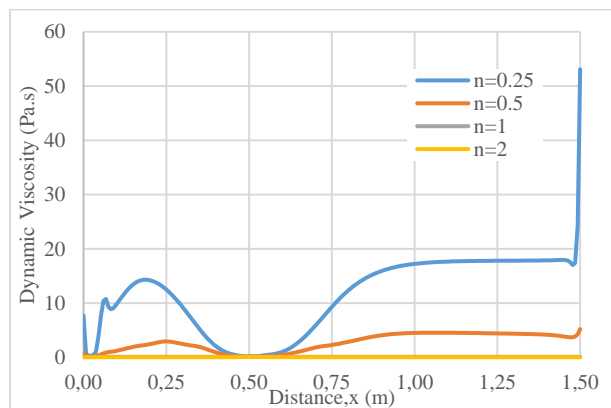


Figure 11. Dynamic viscosity profiles of various “ n ” values with a constant K value of 0.1 from inlet to outlet centre.

Figure 11 shows the dynamic viscosity change along the pipe. The dynamic viscosity effect varies significantly within the pipe for coefficients $n = 0.25$ and 0.5 . Dynamic viscosity of $n=0.25$ behaves more precisely to intra-channel flow conditions.

The cell Reynolds number is shown in Fig. 12. As a result of the effect of increasing speed and low dynamic viscosity, the Reynolds number reached the highest value at $n=2$. At $n=0.25$, it instantly increases the Reynolds number at the corner of the obstacle. It is a factor that the viscosity of $n = 0.25$ is higher than the other values of n coefficients.

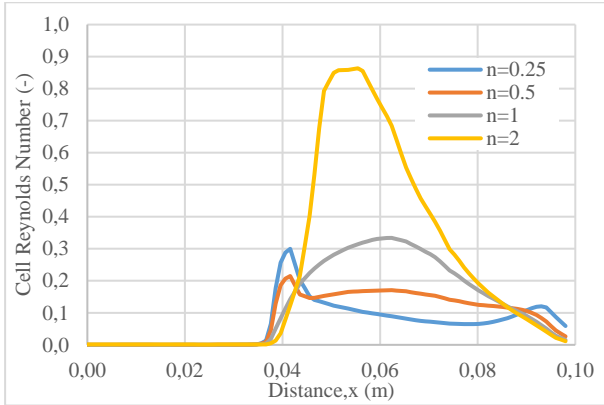


Figure 12. Cell Reynolds number profiles of various “n” values with a constant K value of 0.1 at 5D.

In Figure 13, in 10D, the Reynolds number increased at the centre when $n=1$ and $n=2$ coefficients are used. However, in $n = 0.25$ and $n = 0.5$ results, Re in the centre line decreased.

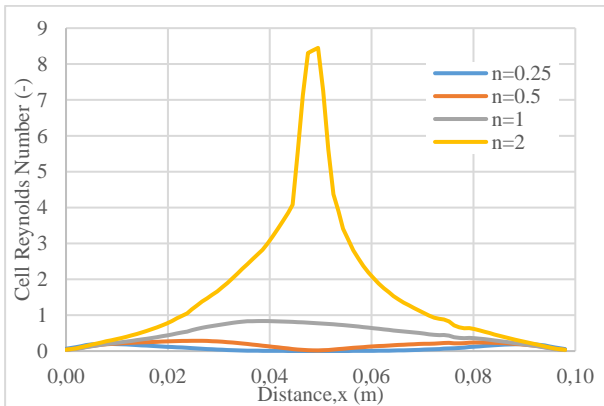


Figure 13. Cell Reynolds number profiles of various “n” values with a constant K value of 0.1 at 10D.

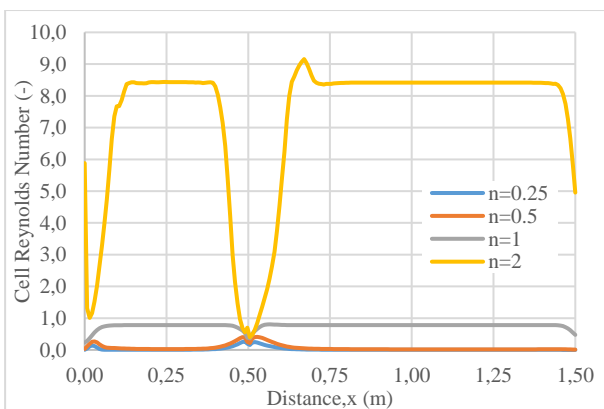


Figure 14. Cell Reynolds number profiles of various “n” values with a constant K value of 0.1 from inlet to outlet centre.

In Fig. 14, it is seen that the Re number is very dominantly high at $n = 0.25$. It was determined that the number of Re was low in the obstacle region. The Re number was more sensitive for $n = 2$.

Effect of K on pressure is given in Fig. 15. Whole various K distributions are similar, only its value changes. It was observed that the pressure increased rapidly with the K coefficient and it was determined that the flow needed higher pressure under these conditions. Velocity profile and magnitude is not affected and same as the first contour profile in Fig. 2.

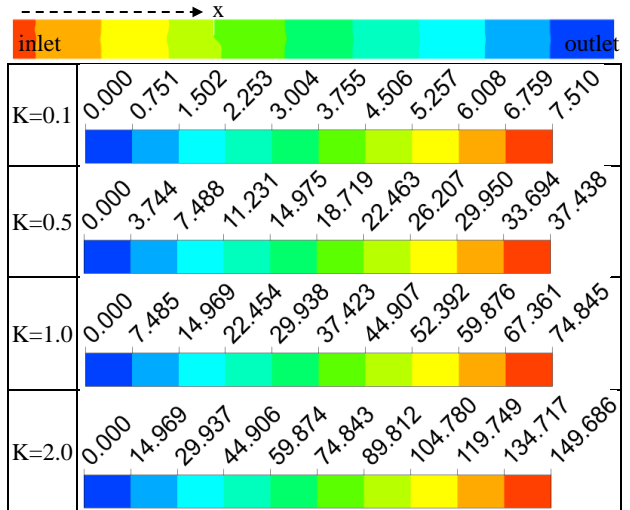


Figure 15. Pressure contours of various “K” values with a constant value of $n=0.25$

In Fig. 16, the effect of K coefficient is shown in the obstacle region. Pressure values increased with the increase of K. The corner of the barrier has a reduction effect.

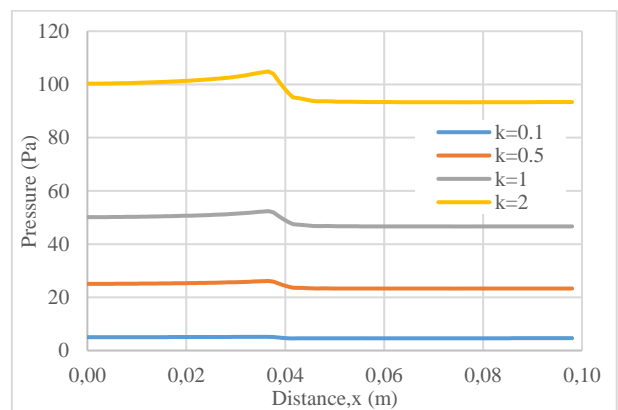


Figure 16. Pressure profiles of various “K” values with a constant n value of 0.25 at 5D.

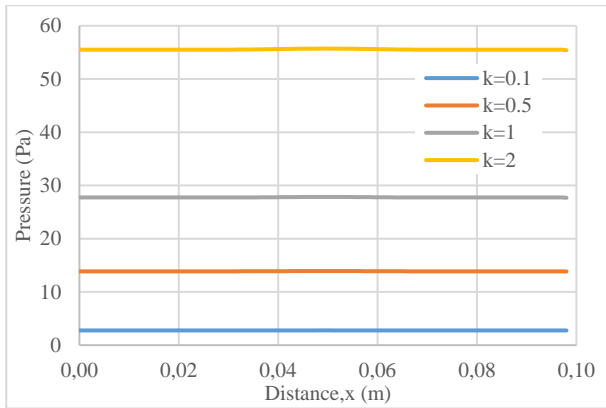


Figure 17. Pressure profiles of various “K” values with a constant n value of 0.25 at 10D.

Figure 17 shows the pressure values at 10D distance. The pressure, which is 56 Pa at $K = 2$, decreases as a result of the increase in the K value.

The results of Fig. 18 show a high-pressure requirement for $K = 2$. The pressure of the flow decreases with the decrease of the K value.

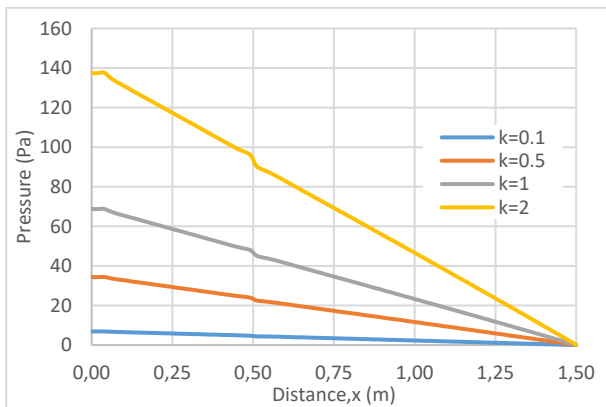


Figure 18. Pressure profiles of various “K” values with a constant n value of 0.25 from inlet to outlet centre.

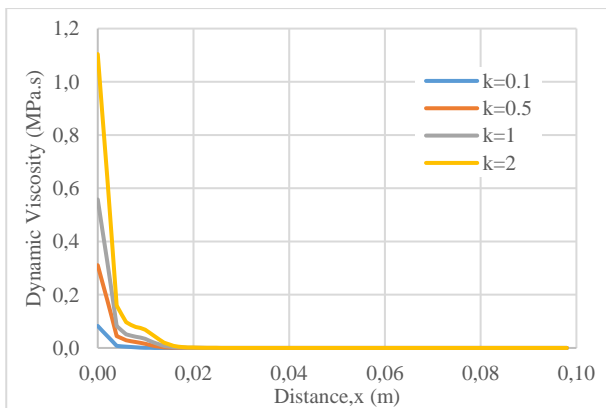


Figure 19. Dynamic viscosity profiles of various “K” values with a constant n value of 0.25 at 5D.

The effect of K coefficient on dynamic viscosity is shown in the obstacle line in Fig. 19. An instantaneous great value was observed at the obstacle-wall corner where there was dead flow. Dynamic viscosity showed an unstable state.

Figure 20 shows the effect of dynamic viscosity in the 10D region. More stable results were obtained in this region where the barrier effect is not dominant. While the dynamic viscosity was above 300 Pa.s for the $K = 2$ value, it decreased to 20 Pa.s for $K = 0.1$.

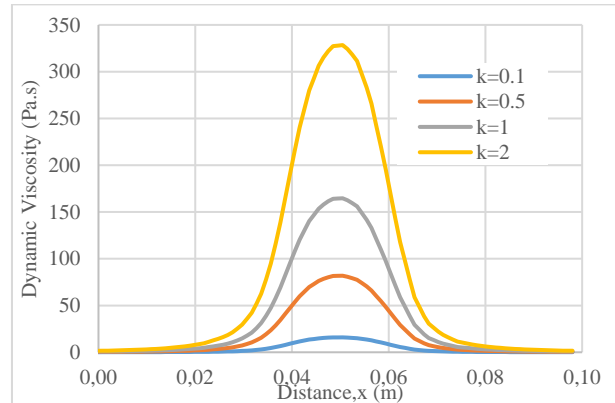


Figure 20. Dynamic viscosity profiles of various “K” values with a constant n value of 0.25 at 10D.

Figure 21 shows the dynamic viscosity effect along the entire pipeline. The dynamic viscosity was reduced in all K coefficient results due to the obstacle. The highest results were obtained at $K = 2$ and the lowest results at $K = 0.1$.

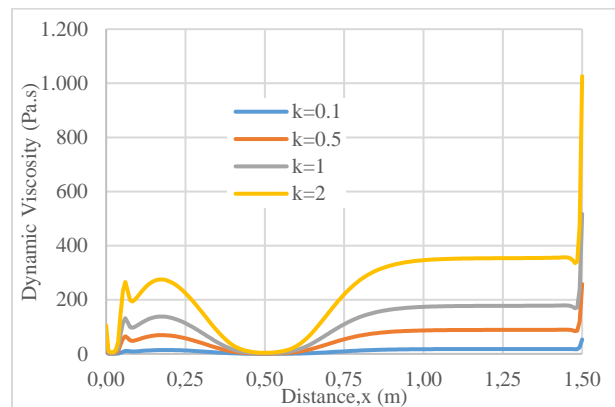


Figure 21. Dynamic viscosity profiles of various “K” values with a constant n value of 0.25 from inlet to outlet centre.

Re number results for different K coefficient are shown in Fig. 22. The highest results were obtained with a value of $K = 0.1$. The lowest result was obtained at $K = 2$.

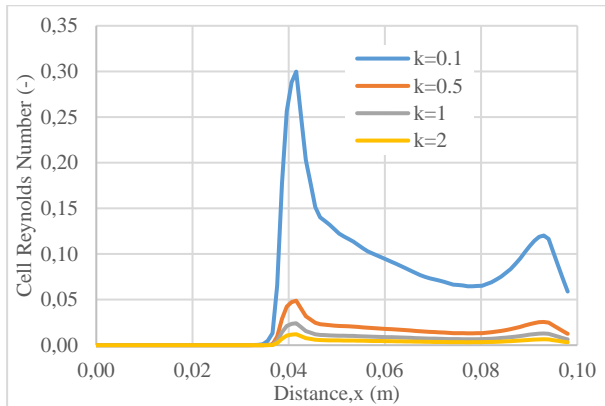


Figure 22. Cell Reynolds number profiles of various “K” values with a constant n value of 0.25 at 5D.

Figure 23 shows the results of the Re number in the region of 10D. The increasing K number decreased the Re number. Results showed a wavy profile. The lowest values were observed in the centre of the pipe. Moderate results are seen near the pipe surface. The highest values were obtained between the wall and the pipe centre.

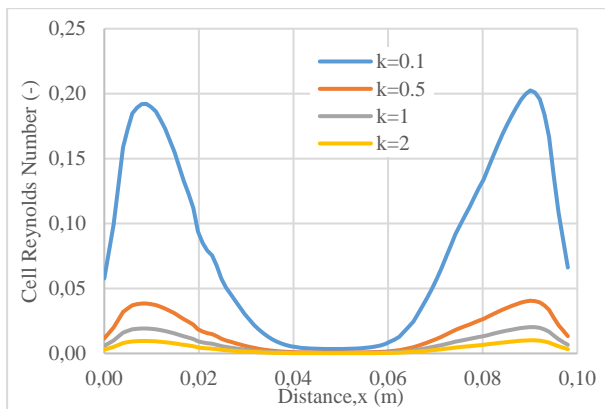


Figure 23. Cell Reynolds number profiles of various “K” values with a constant n value of 0.25 at 10D.

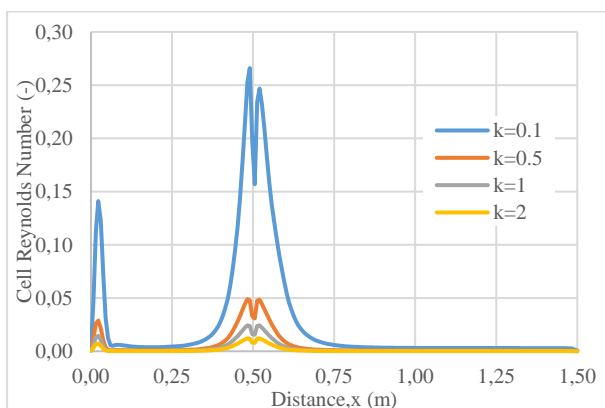


Figure 24. Cell Reynolds number profiles of various “K” values with a constant n value of 0.25 from inlet to outlet centre.

Figure 24 shows the Re number along the entire pipe direction. With the decrease in the K number, there was an increase in the Re number. The Re number is determined as the highest in the front and rear of the obstacle. Some decrease in Re number was observed during the flow passing the obstacle.

4. Conclusion

Non-Newtonian flow analysis was carried out in a pipe with obstructed flow. The effect of different n and K coefficients was examined in the study using numerical analysis method. Results are shown in contours and graphics.

In summary;

While the number of K was constant, increasing the number of n caused the flow velocity to increase.

As a result of the velocity increase, a more parabolic flow velocity profile was formed.

Flow velocity of 0.01 m/s increased up to 0.023 m/s when n=0.25.

At the moment of passing the obstacle, the velocity in front and back of the obstacle instantly decreased at n = 2, and the other n values did not decrease.

As a result of the increasing n value, a lower pressure profile has occurred in the pipe. This shows that flow can be achieved with a lower pressure.

Dynamic viscosity effect was more dominant at n=0.25 and n=0.5 coefficients. However, a lower Re number was obtained.

Different K coefficients were examined for the n = 0.25 coefficient, where the viscous flow exhibits a more sensitive state.

With the increase of the K coefficient, higher-pressure values were obtained in the solutions. It appears that a higher pressure is required for the pipe flow.

When K = 2, dynamic viscosity has the highest value. However, Re number was obtained as the lowest.

While the Re number reached the highest value at the front and rear of the obstacle, a momentary decrease was observed in the area where the flow passed the obstacle.

Throughout a diameter in front and behind the obstacle, this effect continues predominantly.

Author's Contributions

Mustafa Murat Yavuz: Drafted the manuscript, performed the numerical model and result analysis.

Pınar Sarı Çavdar: Performed result interpretation and wrote manuscript preparation.

Ethics

There are no ethical issues after the publication of this manuscript.

References

1. Bird, RB, Stewart, WE., Lightfoot, EM. 1960. Transport phenomena, John Wiley, New York.
2. Hansen, AG., Na, TY. 1968. Similarity solution of laminar, incompressible boundary layer equations of non-Newtonian fluid, *ASME Journal of Basic Engg.* 67: 71-74.
3. Kapur JN, Bhatt BS, Sacheti NC, 1982. Non-Newtonian fluid flows, Pragati Prakashan, Meerut, India.
4. Lee SY, Ames WF, 1996. Similar solutions for non-Newtonian fluids, *AIChE J.* 12: 700-708.
5. Timol MG, Patel M, 2004. On the class of similarity solutions for three dimensional boundary layer flows of non-Newtonian fluids, *J. of Veer Narmad South Gujarat University.* II-B, 103-109.
6. Wells CS, 1964. Unsteady boundary layer flow of a non-Newtonian fluid on a flat plate, *AIAA Journal.* 2(5) :951-952.
7. Bizzell GD, Slatery JC, 1962. Non-Newtonian boundary-layer flow, *Chemical Engineering Science.* 17(10) :777-782.
8. Djukic DjS, 1973. On the use of Crocco's equation for the flow of power-law fluids in a transverse magnetic field, *AIChE Journal.* 19: 1159-1163.
9. Djukic DjS, 1974. Hiemenz magnetic flow of power-law fluids, *Journal of Applied Mechanics, Transaction of the ASME,* 822-823.
10. Na TY, Hansen A, 1967. Radial flow of viscous non-newtonian fluids between disks, *Int. J. Non-Linear Mech.* 2: 261-273.
11. Patel M, Timol MG, 2011. Orthogonal stagnation point flow of a power-law fluid toward a stretching surface, *International Journal of Applied Mechanics and Mathematics (IJAMM).* 7(3): 31-37.
12. Patel M, Patel R, Timol MG, 2012. Group invariance for non-linear pde's: 3-d mhd stagnation point flow of non-newtonian power-law fluids, *International Journal of Mathematics and Scientific Computing (IJMSC).* 2(2):72-80.
13. Patel M, Patel R, Timol MG, 2014. Numerical treatment of MHD Power-law fluid flow using the method of satisfaction of asymptotic boundary conditions (MSABC), *International Journal of Applied Mechanics and Mathematics.* 10(8):61-77.
14. Gupta RC, On developing laminar non-Newtonian flow in pipes and channels, *Nonlinear Analysis: Real World Applications.* 2: 171-193.
15. Alexandrou AN, McGilvray TM, Burgos G, 2001. Steady Herschel-Bulkley fluid flow in three-dimensional expansions, *J. Non-Newtonian Fluid Mech.* 100: 77-96.
16. Cebeci T, Clauss JM, Dyer J, 1969. On the solution of boundary-layer equations for a non-Newtonian power-law fluid, *Chemical Engineering Science.* 24: 1031-1034.
17. Acrivos A, Shah MJ, Petersen EE, 1965. On the solution of the two-dimensional boundary-layer flow equations for a non-Newtonian power law fluid, *Chemical Engineering Science.* 20(2): 101-105.
18. Hornbeck RW, 1964. Laminar flow in the entrance region of a pipe. *Applied Scientific Research, Section A.* 13:224-232.
19. Yapıcı H, Albayrak B, 2004. Numerical solutions of conjugate heat transfer and thermal stresses in a circular pipe externally heated with non-uniform heat flux, *Energy Conversion and Management.* 45(6): 927-937.
20. Yıldırım N, Buchlin J, Benocci C, 2017. Simulation of surface instability at the interface of two fluids. *Celal Bayar University Journal of Science.* 13(2): 365-377.
21. Kırmızıgöl SF, Özyayın O, Acarer S, Armakan E, 2020. Fluid flow and heat transfer simulations of the cooling system in low pressure die casting, *Celal Bayar University Journal of Science.* 16(2):161-168.
22. Sorgun M, Haşıloğlu DG, 2016. Effect of pipe roughness on pressure losses of newtonian fluids in concentric annulus, *Celal Bayar University Journal of Science.* 12(3): 413-417.
23. Batool S, Nawaz M, 2020. Investigation of thermal enhancement in non-Newtonian fluid with hybrid micro-structures in an enclosure, *International Communications in Heat and Mass Transfer.* 117:104777.
24. Mehryan SAM, Heidarshenas MH, Hajjar A, Ghalambaz M, 2020. Numerical study of melting-process of a non-Newtonian fluid inside a metal foam, *Alexandria Engineering Journal.* 59: 191-207
25. Jamshidzadeh M, Ein-Mozaffari F, Lohi A, 2020. Local and overall gas holdup in an aerated coaxial mixing system containing a non-Newtonian fluid, *Transport Phenomena and Fluid Mechanics.* 66: 1-16.
26. Khan ZH, Khan WA, Hamid M, 2021. Non-Newtonian fluid flow around a Y-shaped fin embedded in a square cavity, *Journal of Thermal Analysis and Calorimetry.* 143: 573-585.
27. Nguyen Q, Ghahderijani MJ, Bahrami M, Ahangar EK, D'Orazio A, Bach Q, Karimipour A, 2020. Develop Boltzmann equation to simulate non-Newtonian magneto-hydrodynamic nanofluid flow using power law magnetic Reynolds number, *Math Meth Appl Sci.*, 1-16.
28. Eberhard U, Seybold HJ, Secchi E, Jiménez-Martínez J, Rühls PA, Ofner A, Andrade Jr JS, Holzner M, 2020. Mapping the local viscosity of non-Newtonian fluids flowing through disordered porous structures, *Scientific Reports.* 10, 11733.

Deep Feature Generation for Author Identification

Şükrü Ozan^{1*} , D. Emre Taşar¹ , Umut Özdil¹ 

¹ AdresGezini Inc. Research and Development Center, Folkart Towers B Kule,
Office 3609, PK 35580, Bayraklı, İzmir, Türkiye.

*sukruozan@adresgezini.com

*Orcid: 0000-0002-3227-348X

Received: 24 December 2020

Accepted: 3 May 2021

DOI: 10.18466/cbayarfbe.846016

Abstract

Identifying the authors of a given set of text is a well addressed and complicated task. It requires thorough knowledge of different authors' writing styles and discriminating them. As the main contribution of this paper, we propose to perform this task using machine learning and deep learning methods, state-of-the-art algorithms, and methods used in numerous complex Natural Language Processing (NLP) problems. We used a text corpus of daily newspaper columns written by thirty authors to perform our experiments. The experimental results proved that document embeddings trained via neural network architecture achieve cutting edge accuracy in learning writing styles and identifying authors of given writings even though the dataset has a considerably unbalanced distribution. We represent our experimental results and outsource our codes for interested readers and natural language processing (NLP) enthusiasts as a GitHub repository. They can reproduce and confirm the results and modify them according to their own needs.

Keywords: Natural Language Processing, Document Embeddings, Logistic Regression, Support Vector Machines, Author Identification.

1. Introduction

The rapid increase in the number of digital texts has triggered academic research to identify and verify the authors from a given set of a text corpus. By applying computational learning approaches, authors' writing styles and their thematic interests can be captured with an accuracy comparable with human-level performance (HLP). For a predefined set of given authors, determining the most probable author for the given text is author identification [1] that can be considered as a multi-class text categorization problem from a machine learning (ML) and deep learning (DL) perspective [2]. The author identification is generally performed in a closed domain. However, the numbers of texts from selected authors do not always have to be balanced [3]. ML/DL based author identification can effectively be used in disputed authorship cases [4] and literary analysis studies [5]. Like in any other DL study, the heterogeneous distribution of sample data is a problem for author identification. This problem is addressed thoroughly in [6]. Despite the significant amount of work devoted to author identification of a text, researchers still struggle to deal with cross-domain texts and imbalanced datasets.

One of the fundamental steps in author identifications is stylometry, which refers to discovering the most specific features representing an author's writing characteristics [7]. Earlier approaches focused on generating metrics to describe function word or part-of-speech frequencies to assess the vocabulary's diversity. A detailed review of these approaches is represented in [8] to highlight the importance of extracting features.

In this study, the author identification framework is proposed to generate a text's specific features by combining ML and DL methods commonly used in natural language processing (NLP) literature. The author identification procedure is performed by discovering features, thematic interests, unique characteristics of an author, and writing styles. Most accurate results are achieved with Doc2Vec D-BOW [9,10] model with a C-SVC [11] classifier.

The rest of the paper is organized as follows: Section 2 describes the materials and methods applied for this study. Experiments and results are presented in Section 3. Section 4, as the final section, conclusions and future research suggestions are given.

2. Materials and Methods

2.1 Dataset

A famous Turkish news portal, subsuming more than 50 authors, has been scrutinized to build a corpus. The authors are of different ages, genders. Moreover, their writing themes are from different genres, such as politics, sports, health, and literature. We randomly picked 30 of the authors. Figure 1 shows the number of articles per author, which represents an unbalanced distribution. We intentionally kept the author names hidden and used numbers representing Author IDs. After selecting the authors, we scraped the website and gathered all of their articles labeled with author IDs.

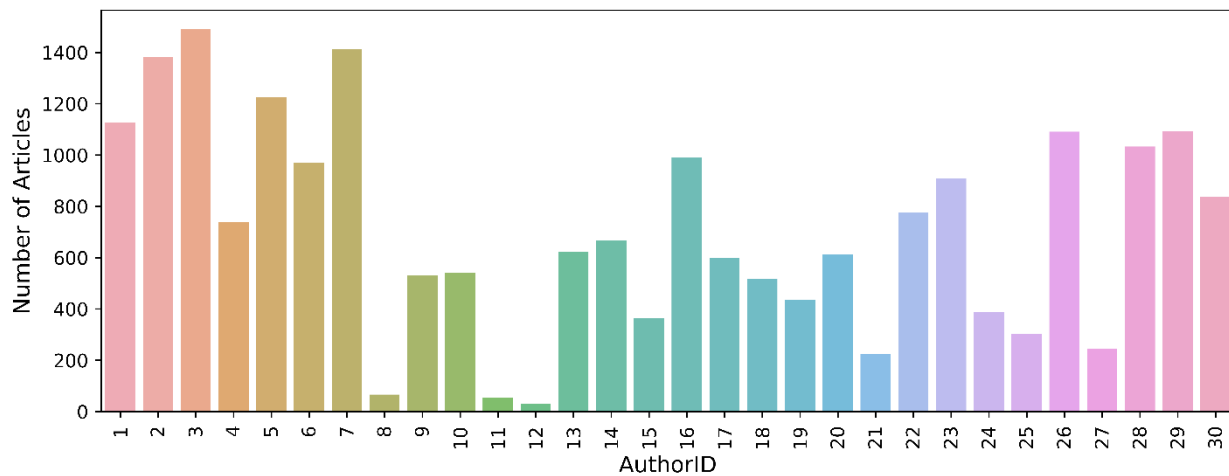


Figure 1. The number of articles per author can be seen in this figure. Authors' names are intentionally hidden and represented as ID numbers.

2.3 Doc2Vec Embeddings

Usage of using Doc2Vec for text classification tasks has gained well-deserved popularity in NLP literature. We used the Gensim [13] implementation of the Doc2Vec method [14]. The method can generate the same embedding sizes for input text with different sizes. The method relies on two main learning models: Distributed Memory (DM) and Distributed Bag of Words (D-BOW). In our experiments, we used both models and compared their performances in the results section.

2.3.1 Distributed Memory (DM)

DM model, depicted in Figure 2a., has a similarity with the Skip-Gram method of Word2Vec [14]. The CBOW

2.2 Data Preprocessing

Data pre-processing is an essential step in NLP methods since it is vital to use clean text data that is free from characters and symbols that may introduce bias and errors during the learning process. The data is scraped directly from the news portal website; hence, it has punctuation symbols and many HTML related tags. There are various text pre-processing methods, including but not limited to converting capital letters to lowercase letters (case folding), clearing symbols, and punctuation marks [12]. We used a 70-30 split scheme for training and validation data sets after the data pre-processing operations.

model can predict a center word based on the context words in a small neighborhood. DM uses a similar approach to randomly sample some context words from an article and predict a word using both the context words and the article ID.

2.3.2 Distributed Bag of Words (D-BOW)

D-BOW model, depicted in Figure 2b., uses the whole article as input and tries to predict consecutive Word chunks from the article having a meaningful context. One advantage of the D-BOW model is that it requires less memory during training time. Activation function weights are enough to be stored for D-BOW to operate.

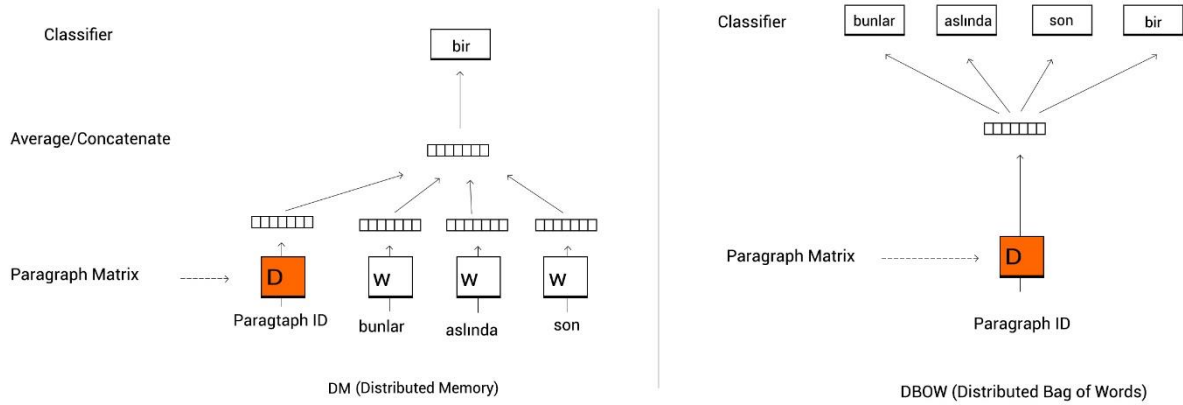


Figure 2. a) Distributed Memory model, where classifier predicts a word as an output parameter and words concatenate as word vectors and paragraph vector. b) Distributed Bag of Words model, where paragraph vector is trained to predict the words inside a small window.

2.4 Classifiers

With either model, DM, and D-BOW, the Doc2Vec method generates a fixed-size embedding vector for each article. These vectors can capture the meaning, syntax, writing style, and other linguistic features of a given text in hyperdimensional space.

Together with the author ID information, the embeddings can be used to train a classifier. In this study, we preferred two different classifiers. Conventionally logistic regression classifier (LRC) is a common choice for the classification of multidimensional data [15]. LRC is proven to be an adequate method, especially for binary classification problems where the number of classes is limited (i.e., $N = 2$). On the other hand, our problem is a multi-class classification problem with 30 classes (i.e., $N > 2$). Multinomial logistic regression classifier MLRC [16] generalizes the binary classification idea of standard LRC to multi-class classification. Once the coefficients are determined after running the MLRC, the probability of predicting an author's class can be done using Equation 2.1, where k is the class number, x is the embedding vector, and β_k is the coefficient vector of class k . Hence, MLRC models the probability of a given data belonging to a class using log-likelihood estimation as given in Equation 2.1.

$$L = \log P(y = k | x_i) \quad \text{where}$$

$$P(y = k | x_i) = \frac{\exp^{\beta^k x}}{1 + \sum_{k=1}^{K-1} \exp^{\beta^k x_k}} \quad (2.1)$$

We used MLRC as our first classifier, and it achieved good accuracies on both training and validation datasets. However, we repeated our experiments also by using support vector machines (SVM) based classifier (C-SVC) [11]. This classifier creates hyperplanes in a

multidimensional space that can be efficient for classification and regression tasks.

It finds the best hyperplane that demonstrates the largest segregation between the two classes. The error of this classifier is correlated with the size of the margin [11]. C-SVC uses kernels with different mathematical models. For this study, we used the linear kernel, in Equation 2.2, where K is the kernel function, D is the decision function, y_i , b , and α_i are indicator vector, equation constant, and dual parameter, respectively. C-SVC classifier achieved even better results than MLRC,

$$K(x_i, x_j) = x_i^T x_j \quad (2.2)$$

$$D = \text{sgn} \cdot \left(\sum_{i=1}^l y_i \alpha_i K(x_i, x) + b \right)$$

2.5 F1 Score as an Accuracy Metric

To better identify the algorithms' classification accuracy, we calculated the F1 Score for each class. F1 Score, which calculates harmonic mean between recall

$$\text{Pr} = \frac{TP}{TP + FP} \quad (2.3)$$

$$\text{Re} = \frac{TP}{TP + FN}$$

$$F1 = 2 * \frac{\text{Pr} * \text{Re}}{\text{Pr} + \text{Re}} \quad (2.4)$$

$$F_{avg} = \frac{2 * P_M * R_M}{P_M + R_M} \quad (2.5)$$

and precision values, can be calculated using Equation 2.4; in this equation, TP, FP, and FN represent true positive, false positive, and false negative values, respectively. Definition of Precision (Pr), Recall (Re) can be calculated using Equation 2.3. The F1-Average score can be calculated using Equation 2.5 for each class. In this equation, macro average values are represented with M . Hence, P_M and R_M represent macro averaged precision and recall values.

3 Results and Discussion

From the NLP perspective, the classification task becomes challenging where the number of classes exceeds 20. Moreover, the data's unbalanced nature makes it even harder for an ML/DL-based algorithm to achieve a good generalization for the whole dataset. In our study, we have both situations.

We started our experiments with hyperparameter tuning of the Doc2Vec model. The parameters, which affect the result most are the embedding size and the number of epochs. By keeping the remaining model parameters constant, we tried different embedding sizes to detect the optimal size. The constant parameters and their default values can be seen in Table 1. We observed the classification accuracy in Table 2 after one epoch of training by trying different embedding sizes.

Table 1. Constant Parameters for Doc2Vec Model

Model Parameters*	Value	Model Parameter	Value
window	10	alpha	0.0061
negative	5	Min_alpha	0.0001
Min_count	1		

* Other model parameters set to default

We used MLRC to calculate the training and validation accuracies. Since the number of classes is considerably high, we achieved the optimum result with a 500-dimensional embedding size. We did not get a significant performance increase after 500. After fixing the embedding size to 500, we tried different epochs and

different classifiers. The results of these experiments are given in Table 3. We further observed that both DM and D-BOW methods start to overfit after a few epochs. Hence, we limited the number of epochs to 10 for each experiment.

As it can be interpreted by looking at Table 3., we achieved the best accuracies for the validation data set for 500-dimensional vector size at the 4th epoch of D-BOW training using the C-SVC classifier. It is also possible to grasp the success of this result by visually examining the embedding vectors. Since the embeddings are in hyperspace, we used the UMAP projection method [17] to visualize them in 2D. Figure 3 shows how the embeddings belonging to seven of the authors are successfully clustered together.

The overall clustering performance of the algorithm can also be shown with a confusion matrix. In Figure 4, the confusion matrix of the classification for 30 authors can be seen. The confusion matrix can also be used to calculate the F1 Score for each of the classes. In Table 4., we listed the calculated F1 Score for each class. For authors 8 and 12, the worst classification results are achieved. These authors have significantly less number of articles compared with the remaining authors. However, we can also see that for another author (author 11) with few articles; high accuracy is achieved. When we closely examine these three authors, we saw that author 11 has a particular subject genre compared with the other authors.

On the other hand, authors 8 and 12 mostly write interview articles where they mostly quote the person being interviewed, making it harder for the algorithm to learn and generalize for these specific authors. If we disregard authors 8 and 12 and only rely on the remaining 28 authors, the training and validation accuracies hit 1.00 and 0.97, respectively. F1 Scores and their weighted averages are found to be 0.98 and 0.97 using Equation 2.3 - 2.5.

Table 2. Train and Validation Accuracies for Vector Sizes

Model Accuracy	D-BOW + MLRC		DM + MLRC	
	Train	Validation	Train	Validation
5	0.7716	0.7453	0.6737	0.6704
25	0.9777	0.9496	0.8602	0.8427
50	0.9904	0.9503	0.9073	0.8823
100	0.9951	0.9516	0.9392	0.9002
300	0.9953	0.9596	0.9646	0.9209
500	0.9936	0.9581	0.9626	0.9225
1000	0.9891	0.9589	0.9555	0.9243



Table 3. This table shows the change in Training and Validation Accuracies for Different Doc2Vec Method and Classifier Combinations for different epoch numbers. All the model combinations tend to overfit the data after a few epochs of training.

Model	D-BOW MLRC		DM MLRC		D-BOW C-SVC		DM C-SVC	
	Train	Validation	Train	Validation	Train	Validation	Train	Validation
Epoch 1	0.9955	0.9601	0.9689	0.9272	0.9685	0.948	0.7968	0.7811
Epoch 2	0.9996	0.9543	0.9966	0.9425	0.9937	0.9654	0.9615	0.9272
Epoch 3	0.9999	0.9486	0.9998	0.9369	0.9967	0.9667	0.9836	0.9433
Epoch 4	1	0.9519	1	0.9373	0.9975	0.9682	0.9894	0.9501
Epoch 5	1	0.948	1	0.938	0.9968	0.9663	0.991	0.9484
Epoch 6	1	0.9501	1	0.9386	0.9956	0.9669	0.9879	0.9507
Epoch 7	1	0.9402	0.9977	0.8573	0.9927	0.9593	0.9555	0.8814
Epoch 8	0.9995	0.9325	0.9651	0.7737	0.9842	0.9427	0.8669	0.7524
Epoch 9	0.6226	0.4788	0.4	0.2454	0.5175	0.4487	0.2689	0.2314
Epoch 10	0.5802	0.4945	0.7323	0.516	0.5367	0.4598	0.5871	0.4838

Table 4. D-BOW + C-SVC Pr, Re, F1 Score Results

Authors	Precision	Recall	F1-Score	#Articles	Authors	Precision	Recall	F1-Score	#Articles
1	0.97	0.99	0.98	514	16	0.91	0.92	0.91	390
2	0.99	0.98	0.98	625	17	1.00	0.99	0.99	247
3	0.98	1.00	0.99	653	18	0.97	0.98	0.97	237
4	0.97	0.96	0.96	281	19	0.97	0.97	0.97	183
5	0.98	1.00	0.99	562	20	0.95	0.95	0.95	293
6	0.97	0.97	0.97	397	21	0.98	0.98	0.98	116
7	0.97	0.97	0.97	645	22	0.99	0.98	0.98	329
8	0.70	0.91	0.79	33	23	0.99	0.99	0.99	361
9	0.98	0.95	0.97	264	24	0.99	0.97	0.98	159
10	1.00	0.98	0.99	243	25	1.00	1.00	1.00	141
11	0.96	0.82	0.89	33	26	0.98	0.98	0.98	462
12	0.68	0.71	0.70	21	27	0.95	0.94	0.94	112
13	0.86	0.92	0.88	226	28	0.95	0.99	0.97	389
14	0.98	0.91	0.94	274	29	0.95	0.95	0.95	415
15	0.98	0.86	0.91	162	30	0.98	0.97	0.97	354
				Accuracy	0.97	0.97	0.97	9121	
				W. Avg	0.97	0.97	0.97	9121	

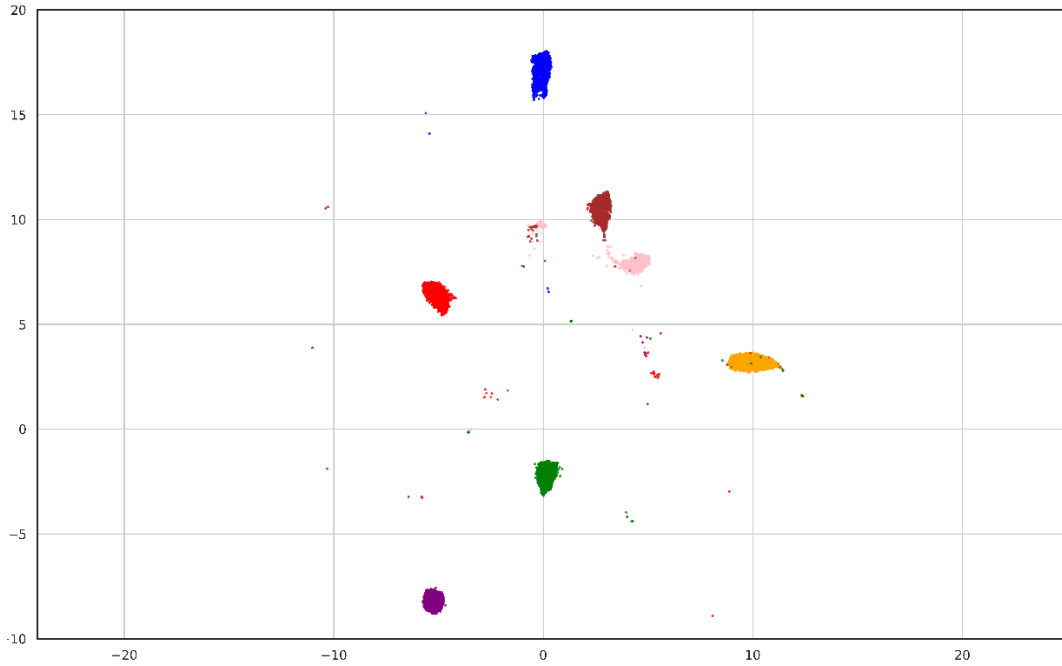


Figure 3. 2D UMAP projection of the training data’s embedding vectors created with the best configuration in Table 3. For display purposes, we zoomed the area where the clusters of seven authors are visible together.

AID	1	2	3	4	5	6	7	8	9	10	11	12	13	14	15	16	17	18	19	20	21	22	23	24	25	26	27	28	29	30					
1	510	0	0	0	0	0	0	0	0	0	0	0	0	1	0	0	0	0	1	0	0	0	0	0	0	0	0	0	0	1					
2	0	612	1	0	0	1	3	0	0	0	0	0	0	1	1	2	0	0	0	0	0	1	0	0	0	0	0	0	1	1	1				
3	0	0	653	0	0	0	0	0	0	0	0	0	0	0	0	0	0	0	0	0	0	0	0	0	0	0	0	0	0	0	0				
4	0	1	0	270	0	1	1	0	1	0	0	0	0	0	0	4	0	0	0	0	0	0	1	0	0	0	0	2	0	0	0				
5	0	0	0	0	560	0	0	0	0	0	0	0	0	0	0	1	0	0	0	0	0	0	0	0	0	0	0	0	0	0	0	0			
6	2	0	0	1	1	384	0	0	1	0	0	0	0	0	0	1	0	0	1	0	0	0	0	0	0	0	0	0	0	1	0	0			
7	0	1	3	1	0	2	626	0	0	0	0	0	0	0	0	2	0	0	0	2	0	0	1	0	0	0	0	4	2	1	0	0			
8	0	0	0	0	0	0	0	30	0	0	0	1	1	0	0	0	0	0	0	0	0	0	0	0	0	1	0	0	0	0	0	0			
9	3	1	0	1	0	0	0	0	0	250	0	0	1	3	0	0	0	2	0	0	0	0	1	0	0	0	0	2	0	0	0	0			
10	0	0	1	1	0	0	0	0	0	0	238	0	0	0	0	0	1	1	0	0	0	0	0	0	0	0	0	1	0	0	0	0			
11	0	0	1	0	0	0	0	0	0	0	0	27	0	0	0	0	0	0	0	5	0	0	0	0	0	0	0	0	0	0	0	0	0		
12	0	0	0	0	0	0	0	4	0	0	0	15	0	0	0	0	0	0	0	0	0	0	0	0	0	1	0	0	0	0	0	0	0		
13	0	0	0	0	0	0	1	3	0	0	0	1	207	0	0	3	0	0	1	0	0	0	0	0	0	0	0	1	9	0	0	0	0		
14	0	2	0	2	2	2	2	1	2	0	0	0	3	249	1	2	0	0	0	0	0	0	0	0	0	0	5	1	0	0	0	0	0		
15	3	0	0	0	2	0	0	1	0	0	0	3	4	0	139	6	0	0	1	0	0	0	0	0	0	0	0	1	2	0	0	0	0		
16	1	2	0	0	1	1	5	1	0	0	0	0	9	0	0	359	0	0	0	1	0	0	1	0	3	0	1	4	1	0	0	0	0		
17	0	0	0	0	0	0	1	0	0	0	0	0	1	0	0	0	245	0	0	0	0	0	0	0	0	0	0	0	0	0	0	0	0	0	
18	0	0	0	1	0	0	0	0	0	0	0	0	0	0	0	0	0	232	1	1	0	1	0	0	0	0	0	1	0	0	0	0	0	0	
19	0	0	0	0	0	0	0	0	0	0	0	0	0	0	0	0	0	0	178	1	0	2	0	0	0	0	0	0	1	0	0	0	0	0	
20	0	1	2	0	0	1	2	1	0	0	1	0	2	1	0	0	0	0	0	0	277	0	0	0	0	1	0	1	1	2	0	0	0	0	
21	0	0	0	0	0	0	0	0	0	0	0	0	1	0	0	0	0	0	1	0	0	114	0	0	0	0	0	0	0	0	0	0	0	0	
22	1	0	0	1	1	1	0	0	0	0	0	0	0	0	0	0	0	1	0	1	0	323	0	0	0	0	0	0	0	0	0	0	0	0	0
23	1	0	0	0	0	0	0	0	0	0	0	0	0	0	0	1	0	0	0	0	0	0	358	0	0	0	0	1	0	0	0	0	0	0	0
24	1	0	0	0	1	0	0	1	0	0	0	0	1	0	0	1	0	0	0	0	0	0	0	154	0	0	0	0	0	0	0	0	0	0	0
25	0	0	0	0	0	0	0	0	0	0	0	0	0	0	0	0	0	0	0	0	0	0	0	0	0	0	0	0	0	0	0	0	0	0	
26	0	0	1	0	0	0	0	1	0	0	0	1	2	0	0	2	0	0	0	0	0	0	0	0	0	0	0	0	453	0	0	2	0	0	
27	2	0	0	0	0	0	0	0	0	0	0	0	1	0	0	1	0	0	0	2	0	0	0	0	0	0	0	1	105	0	0	0	0	0	
28	0	0	2	0	1	1	0	0	0	0	0	0	0	0	0	0	0	0	0	1	0	0	0	0	0	0	0	0	384	0	0	0	0	0	
29	0	0	0	0	0	0	1	0	0	0	0	1	7	0	1	4	1	0	0	0	1	0	0	0	0	3	0	0	396	0	0	0	0	0	
30	0	1	2	1	0	2	0	0	0	0	0	0	0	0	0	3	0	1	0	0	0	0	0	0	0	0	1	1	0	0	342	0	0	0	

Figure 4. Confusion Matrix of classification performed using the best configuration in Table 3 for 30 author classes’ validation data

4 Conclusion

For this study, we scraped 30.403 articles of randomly selected 30 different authors of a popular Turkish news portal. After the pre-processing of raw page source data, we obtained cleaned text for each article. After tagging each article with corresponding author IDs, we obtained our dataset. We used a 70-30 split scheme for training and validation data set. The data set is considerably unbalanced, i.e., the variance in the number of articles is high.

The proposed algorithm mainly relies on the Doc2Vec method, which uses two different learning models: distributed memory and distributed bag of words.

Regardless of the preferred model, this method generates a fixed size embedding vector for given texts of different sizes. We calculated the models’ training and validation accuracy at each training epoch after applying two different classifiers, MLRC and C-SVC. Each of the model and classifier combinations gave good accuracies comparable with HLP. Hence, it is possible to obtain deep features for author classification with the proposed solution methods. The method can detect possible plagiarisms in closed domains, such as a corpus of homework reports submitted by students.

As future work, it is possible to train different convolutional neural networks similar to MGNC-CNN architecture in [18] using these deep feature

embeddings, which may yield good classification accuracies. The deep features can further be used to train recurrent generative adversarial networks [19], generating artificial texts that mimic the corresponding authors' writing styles.

We are outsourcing our code [20] for NLP researchers and enthusiasts to reproduce the reported results and use them in their research.

Acknowledgment

This work is a part of the project supported by the Scientific and Technological Research Council of Turkey (TUBITAK) TEYDEB-1501 program under Project no 3190585, and named "General Purpose Chatbot Application That Can Produce Meaningful Dialog via Machine Learning Algorithms".

Author's Contributions

Şükrü Ozan: Built the algorithms and metric criteria, prepared the web scraping scripts, drafted and wrote the manuscript.

D. Emre Taşar: Supervised the experiments, helped in result interpretation and literature review, assisted in manuscript preparation.

Umut Özdil: Prepared the text pre-processing scripts, assisted in data visualization.

Ethics

The Ethics Committee has ruled that approval was not required for the study.

References

1. Stamatatos, E., Fakotakis, N., Kokkinakis, G.: 2000. Automatic text categorization in terms of genre and author. *Comput. Linguist.* 26(4), 471-495
2. Sebastiani, F. 2002. Machine Learning in Automated Text Categorization. *ACM Computing Surveys*, 34(1): 1-47.
3. Zheng, Rong, et al. 2006. "A framework for authorship identification of online messages: Writing-style features and classification techniques." *Journal of the American society for information science and technology* 57.3 : 378-393.
4. Burrows, J.F. 1987. Word Patterns and Story Shapes: The Statistical Analysis of Narrative Style. *Literary and Linguistic Computing* 2: 61-70.
5. Diederich, J., J. Kindermann, E. Leopold, and G. Paass. 2003.. Authorship Attribution with Support Vector Machines. *Applied Intelligence* 19(1/2): 109-123
6. Luyckx, K., Daelemans 2011, W.: The effect of author set size and data size in authorship attribution. *Literary Linguist. Comput.* 26(1), 35-55
7. Abbasi, Ahmed, and Hsinchun Chen. 2008. "Writeprints: A stylometric approach to identity-level identification and similarity detection in cyberspace." *ACM Transactions on Information Systems (TOIS)* 26.2 : 1-29.
8. Holmes, D. 1998. The Evolution of Stylometry in Humanities Scholarship. *Literary and Linguistic Computing*, 13(3): 111-117.
9. Mikolov, Tomas, et al.2013. "Efficient estimation of word representations in vector space." *arXiv preprint arXiv:1301.3781*.
10. Mikolov, Tomas, et al. 2013. "Distributed representations of words and phrases and their compositionality." *Advances in neural information processing systems*. 26: 3111-3119.
11. Cortes, Corinna, and Vladimir Vapnik.1995. "Support-vector networks." *Machine learning* 20.3: 273-297.
12. Li, J., Huang, G., Fan, C., Sun, Z., & Zhu, H. (2019). Key word extraction for short text via word2vec, doc2vec, and textrank. *Turkish Journal of Electrical Engineering & Computer Sciences*, 27(3), 1794-1805.
13. Rehurek, R., Sojka, P. 2010. Software framework for topic modelling with large corpora. In: *Proceedings of the LREC 2010 Workshop on New Challenges for NLP Frameworks, ELRA*, pp. 45-50.
14. Kim, Donghwa, et al. 2019 "Multi-co-training for document classification using various document representations: TF-IDF, LDA, and Doc2Vec." *Information Sciences* 477 : 15-29.
15. Peng, Chao-Ying Joanne, Kuk Lida Lee, and Gary M. Ingersoll. 2002. "An introduction to logistic regression analysis and reporting." *The journal of educational research* 96.1: 3-14.
16. Kwak, Chanyeong, and Alan Clayton-Matthews.2002 "Multinomial logistic regression." *Nursing research* 51.6: 404-410.
17. Becht, Etienne, et al. 2019. "Dimensionality reduction for visualizing single-cell data using UMAP." *Nature biotechnology* 37.1 : 38-44
18. Zhang, Ye, Stephen Roller, and Byron Wallace. 2016. "MGNC-CNN: A simple approach to exploiting multiple word embeddings for sentence classification." *arXiv preprint arXiv:1603.00968* .
19. Radford, Alec, Luke Metz, and Soumith Chintala. 2015 "Unsupervised representation learning with deep convolutional generative adversarial networks." *arXiv preprint arXiv:1511.06434*
20. "Deep Feature Generation for Author Identification " <https://github.com/adresgezini/DFG4AI/>

Deep Feature Extraction for Detection of Tomato Plant Diseases and Pests based on Leaf Images

Yahya Altuntaş^{1*}, Adnan Fatih Kocamaz²

¹ Apricot Research Institute, Department of Agricultural Machinery and Technologies, 44090 Malatya, Turkey

² Inonu University, Department of Computer Engineering, 44280 Malatya, Turkey

* yahyaaltuntas@gmail.com

*Orcid: 0000-0002-7472-8251

Received: 19 October 2020

Accepted: 30 March 2021

DOI: 10.18466/cbayarfb.812375

Abstract

Plant diseases and pests cause yield and quality losses. It has great importance to detect plant diseases and pests quickly and with high accuracy in terms of preventing yield and quality losses. Plant disease and pest detection performed by plant protection experts through visual observation is a labor-intensive process with a high error rate. Developing effective, fast and highly successful computer-aided disease detection systems has become a necessity in terms of precision agriculture applications. In this study, well-known pre-trained convolutional neural network (CNN) models AlexNet, GoogLeNet and ResNet-50 are used as feature extractors. In addition, a deep learning model that concatenate deep features extracted from 3 CNN models has been proposed. The deep features were used to train the support vector machine classifier. The proposed model was used to classify leaf images of tomato plant diseases and pests, which is a subset of open-access PlantVillage dataset consisting of a total of 18835 images belonging to 10 classes including a healthy one. Accuracy, precision, sensitivity and f-score performance metrics were used with the hold-out validation method in determining model performances. Experimental results show that the detection of tomato plant diseases and pests is possible using concatenated deep features with an overall accuracy rate of 96.99%.

Keywords: convolutional neural networks, deep features extraction, deep learning, image classification, plant diseases and pests detection, precision agriculture.

1. Introduction

Tomato (*Solanum lycopersicum*) is one of the most widely cultivated agricultural products all over the world. As in all other agricultural products, one of the factors that negatively affect tomato cultivation is diseases and pests. Various diseases and pests cause yield and quality losses in crop production [1]. Early and accurate detection of diseases and pests is very important to prevent yield and quality losses. Plant disease and pest detection performed by visual observation by plant protection experts is a labor-intensive process with a high error rate [2]. The development of effective, fast and highly successful computer-aided disease detection systems has become a necessity for precision agriculture applications.

Remarkable progress has been made in plant disease and pest detection with studies based on traditional machine learning methods. Al-Hiary et al. [3] proposed a model for diagnosing 5 diseases that cause symptoms

in leaves in different plant species. They segmented the images using Otsu thresholding and k-means clustering methods and extracted texture features. They used these features to feed artificial neural networks (ANN) classifiers. Dubey and Jalal [4] performed feature extraction from apple images segmented by the k-means clustering method using local binary pattern methods to detect 3 different apple fruit diseases. They classified the obtained features using a support vector machine (SVM). Singh and Misra [5] conducted a study to detect 5 different diseases in 4 different plant species. They obtained the color co-occurrence matrix features from images that were segmented and enhanced with image processing techniques. According to their experimental results, they reported that the best performance was obtained with the SVM classifier. Success in traditional machine learning methods largely depends on the features used. Segmentation is required to extract the features. This situation necessitates that the work carried out with traditional machine learning methods should be under highly controlled conditions and limits the classification success achieved.

Deep learning refers to models that can learn the representations of data through multiple processing layers and thus perform end-to-end learning [6]. Thanks to deep learning, unlike traditional machine learning methods, learning from raw data can be performed without the need for feature extraction. In the literature, many studies have been conducted on the detection of plant diseases and pests based on deep learning [7, 8]. Mohanty et al. [1] retrained AlexNet and GoogLeNet pre-trained convolutional neural network (CNN) models, both from scratch and by fine-tuning. They reported that transfer learning provided faster converge on colored, gray-level and segmented images in their studies. Ferentinos [2] used deep learning methodology to identify plant diseases in his study on an open-access dataset containing 25 plant species and 58 plant-disease combinations. Although there are a limited number of studies on the detection of plant diseases and pests in more than one crop type, many studies have also been conducted on a single crop type such as apple [9], cucumber [10] and rice [11].

Fuentes et al. [12] proposed a deep learning-based approach to detect of tomato diseases and pests. They used a region-based CNN method to detect features on tomato leaf images. Durmuş et al. [13] retrained AlexNet and SqueezeNet pre-trained CNN models from scratch to detect tomato diseases and pests on the open-access PlantVillage dataset. Sardoğan et al. [14] used 500 healthy and infected tomato leaves from the PlantVillage dataset to detect 4 tomato diseases. They classified the features obtained from the fully connected layer of the proposed CNN architecture with the Learning Vector Quantization (LVQ) algorithm. Rangarajan et al. [15] fine-tuned both AlexNet and VGG16 pre-trained CNN models to detect of tomato plant diseases and pests. They analyzed both the role of the number of images and importance of hyperparameters in classification accuracy and execution time. Aversano et al. [16] fine-tuned the VGG19, Xception and ResNet-50 pre-trained CNN models for the detection of tomato diseases and pests.

Agarwal et al. [17] proposed a CNN architecture consisting of 3 convolution and 3 max pooling layers followed by 2 fully connected layers for the detection of tomato diseases and pest. Saeed et al. [18] used tomato, corn and potato leaves images from the PlantVillage dataset to build an automated crop disease recognition system. They selected the deep features extracted from the fully connected layers 6 and 7 of the VGG19 pre-trained CNN model using partial least squares (PLS) regression. They used selected deep features for model estimation using the ensemble baggag tree classifier.

In this study, the effect of using pre-trained CNN models as feature extractors on success in detecting tomato diseases and pests has been investigated. For this purpose, well-known pre-trained CNN models AlexNet, GoogLeNet and ResNet-50 were used as feature extractors. In addition, deep features fusion was performed by concatenating the deep features obtained from 3 CNN models. The obtained deep features were used to train the SVM classifier. According to the results, all CNN models achieved high classification success in detecting tomato diseases and pests by deep feature extraction. Concatenated deep features, on the other hand, achieved the best classification performance with an overall accuracy of 96.99%. The results of the experiments conducted within the scope of the study were compared with each other and with related studies in the literature.

The remaining of the paper is organized as follows: the materials and methods are given in Section 2. The experimental results are presented in Section 3. In Sections 4 and 5 discussion and conclusion remarks are given, respectively.

2. Materials and Methods

2.1. Dataset

In this study, experiments have been carried out on diseased and healthy tomato leaf images, which is a subset of the open-access PlantVillage [19] dataset.



Figure 1. Sample images in the dataset.

Table 1. Details of classes in the dataset

Class Name	Disease Scientific Name	Images (Number)		
		Training	Test	Total
Bacterial spot	Xanthomonas campestris pv. vesicatoria	1703	424	2127
Early blight	Alternaria solani	800	200	1000
Healthy	-	1273	318	1591
Late blight	Phytophthora infestans	1528	381	1909
Leaf mold	Fulvia fulva	800	200	1000
Septoria leaf spot	Septoria lycopersici	1417	354	1771
Spider mites	Tetranychus urticae	1342	334	1676
Target spot	Corynespora cassicola	1124	280	1404
ToMV	Tomato mosaic virus (ToMV)	800	200	1000
TYLCV	Begomovirus (Fam. Geminiviridae)	4287	1070	5357
Total		15074	3761	18835

TYLCV: Tomato yellow leaf curl virus

Since the link reported in the original article has been broken, the version republished by Geetharamani and Pandian [20] has been used. The dataset consists of 18835 images belonging to 10 classes. Images are 256-by-256 pixels resolution and colored. The image format is JPEG. The space occupied by the dataset in the disk is 321 MB.

Sample images from the dataset have been demonstrated in Figure 1. The sample images from left to right in the first row belong to bacterial spot, early blight, healthy, late blight, and leaf mold classes; the sample images in the second row belong to septoria leaf spot, spider mites, target spot, mosaic virus, and yellow leaf curl virus classes.

AlexNet, GoogLeNet and ResNet-50 CNN models take input images with a resolution of 227-by-227, 224-by-224 and 224-by-224 pixels respectively. For this reason, images have been resized to the specified resolutions.

The hold-out validation method has been used to make a one-to-one comparison of the models applied within the scope of the study. For this purpose, the dataset has been divided into training and test groups at a ratio of 4:1. All models have been trained with the same training images and tested with the same testing images. The classes of the dataset, the scientific names of the diseases, the class distribution of the samples, and the number of training and testing images are given in Table 1.

2.2. Convolutional neural networks

CNNs are deep learning models designed to automatically learn representations of data. A CNN architecture consists of two parts. The first part consists of convolution, activation and pooling layers where discriminative features of data is learned, the second

part consists of fully connected layers and softmax layer where the learned features are classified [6].

Thanks to the filters in the convolution layer, the interrelated spatial dependencies of the data are discovered. Filter weights are shared. In this way, it does not affect learning where the same discriminative feature in different locations of the input data [21]. As a result of the convolution process, the weighted sum of inputs is obtained. This layer is followed by an activation layer to get rid of linear dependencies. Although there are different activation functions such as hyperbolic tangent and sigmoid, the most preferred activation function is the Rectified Linear Unit (ReLU). ReLU activation function sets negative values to 0. Feature maps are obtained in this layer. Next comes the pooling layer to shrink in size, without losing valuable information in the data. A maximum or average pooling can be done. Convolution operations are repeated one after another depending on the hyper-parameter values such as input size, filter size, stride and padding. Ultimately, it is transferred to the fully connected layer. The purpose of this layer is to flatten the learned features. Depending on the architecture, there may be one or more fully connected layers. Then the last fully connected layer is passed to a softmax layer. Finally, the model estimation is made by performing class probability calculations of the features learned with the softmax layer. There are as many outputs as the number of classes in the problem addressed in the last fully connected layer.

2.3. Deep feature extraction and proposed model

Deep feature extraction is a transfer learning approach to employ a pre-trained CNN model for a similar task. Deep feature extraction is to use a pre-trained CNN model as a feature extractor. In this approach, the model parameters (weights) are used without fine-tuning [22].

Then a classification algorithm such as SVM is used for the new classification task [23]. In this approach, the pre-trained CNN model is employed as part of the solution of the new task using as a feature extractor.

In the deep feature extraction approach, deep features can be obtained from any layer of a pre-trained CNN model. However, common usage is to extract deep features from the last fully connected layer. In this study, the last fully connected layers of AlexNet, GoogLeNet and ResNet-50 CNN models are used to extract the deep features. In addition, a deep learning model that concatenate deep features obtained from 3 CNN models has been proposed to increase prediction performance. Overall structure of the proposed model is shown in Figure 2.

The pre-trained CNN models used in the study are briefly introduced below. AlexNet [24] is one of the pioneering CNN architecture. AlexNet has a simple architecture that consists of 5 convolution layers, and 3 fully connected layers.

GoogLeNet [25] is a 22 layer CNN architecture that's a variant of the inception network. The most important properties of GoogLeNet architecture is the use of the inception module. The module simply provides a direct link between multiple different layers. This increases network complexity while keeping the computing cost at the same level.

ResNet-50 [26] architecture consists of 50 layers. ResNet-50 is different from other architectures with its micro-architecture module structure. In architecture, it may be preferred to switch to the lower layer by ignoring the change between some layers. In ResNet architecture, the performance rate has been increased by allowing transition operations between blocks with this structure.

2.4. Support vector machines

The deep feature extraction approach requires a classifier method to be trained with the extracted deep features. In this study, SVM proposed by Vapnik [27] was used as a classifier. It has been reported that the SVM classifier shows superior performance in different agricultural image classification problems [28].

The basic principle in solving a classification problem with SVM is to determine a hyperplane that divides samples belonging to two classes optimally from each other. The formula for the output of a linear SVM is given in Equation (2.1), where \vec{w} is the normal vector to the hyperplane and \vec{x} is the input vector. Maximizing margins can be defined as an optimization problem: minimize Equation (2.2) subject to Equation (2.3) where y_i and \vec{x}_i are the correct output of the SVM and the input vector for i^{th} training sample, respectively [29].

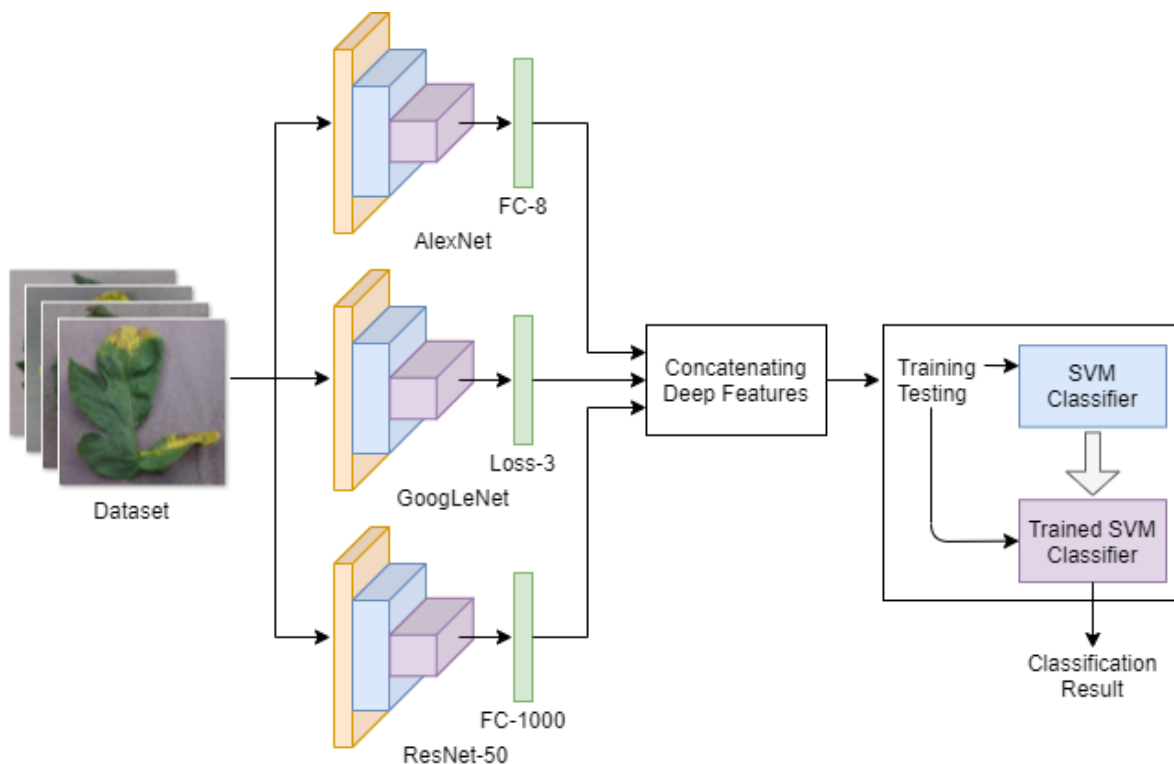


Figure 2. Overall structure of the proposed model

$$u = \vec{w} \cdot \vec{x} - b \quad (2.1)$$

$$\frac{1}{2} \|\vec{w}\|^2 \quad (2.2)$$

$$y_i(\vec{w} \cdot \vec{x}_i - b) \geq 1, \forall i \quad (2.3)$$

$$Pre. = \frac{TN}{TN + FP} \quad (3.2)$$

$$Sen. = \frac{TP}{TP + FN} \quad (3.3)$$

$$F - score = \frac{2TP}{2TP + FP + FN} \quad (3.4)$$

SVM is a binary classifier defined to separate only 2 classes and do not support for multi-class classification problems. One strategy for multi-class classification with SVMs is to create a one-to-one set of classifiers and predict the class chosen by the majority of classifiers [30]. While this enables creating classifiers $K(K-1)/2$ for the classification problem with K classes, the training time of the classifiers may be reduced as the training data set for each classifier will be smaller.

3. Results

In this study, the deep feature extraction method, which is a transfer learning approach employing pre-trained CNN models as feature extractors, was used for the detection of tomato plant diseases and pests. The deep features were obtained from the last fully connected layers of AlexNet, GoogLeNet and ResNet-50 named FC-8, Loss-3 and FC-1000, respectively. In addition, a deep learning model that concatenate 1000 deep features obtained from each of the 3 CNN models proposed to increase predictive performance. Obtained deep features were used to train the SVM classifier. In the configuration of the SVM, all parameters are used in default configurations. Experimental studies were carried out on a computer with i5-8250U CPU, 8 GB RAM, 2 GB GPU, 256 SSD HDD hardware specifications. All experimental studies were implemented in MATLAB 2019b programming environment.

Since there is a sufficient number of images in the dataset, the hold-out validation method was used to make a one-to-one comparison of the models. For this purpose, the dataset was divided into training and test groups at a ratio of 4:1. Accuracy (Acc.), precision (Pre.), sensitivity (Sen.) and f-score performance metrics were calculated for comparison of model performances. These performance metrics are calculated with the indices true positive (TP), false negative (FN), false positive (FP), and true negative (TN) obtained from the confusion matrix. The mathematical equations of performance metrics used in comparing models are as follows:

$$Acc. = \frac{TP + TN}{TP + FN + FP + TN} \quad (3.1)$$

In multi-class classification problems, confusion matrix indices and performance metrics are calculated separately for each class. For the class for which performance metrics are calculated, samples belonging to that class are considered positive and all other samples are considered negative. Then, TP, FN, FP, and TN indices are calculated according to the predictions of the model for the samples treated as positive and negative.

While TP, FN, FP, and TN values are calculated for the Healthy class, samples labeled as Healthy in the dataset are considered positive and all other samples are considered negative. The number of positive samples in the test set, which are predicted as Healthy by the model, gives the TP value. The number of positive samples in the test set that are not predicted as Healthy by the model gives the FN value. The number of negative samples in the test set that are predicted as Healthy by the model gives the FP value. The number of negative samples in the test set that are not predicted as Healthy by the model gives the TN value.

That is, all samples except the class whose confusion matrix indices are calculated are considered negative and are named TN regardless of whether they are correctly predicted in their own class. This situation causes high accuracy and sensitivity values.

In multi-class classification problems, the overall accuracy metric is also used to measure the overall performance of the model. This metric gives us the ratio of the number of correct predictions of the model to the total number of predictions. It is calculated as follows.

$$Overall Acc. = \frac{\sum_{i=1}^N TP_i}{\sum_{i=1}^N (TP_i + FP_i)} \quad (3.5)$$

In the formula, N refers to the number of classes. TP_i and FP_i show the correct and incorrect prediction numbers of the i^{th} class respectively.

The classification results are given in Table 2. The values given in the table are confusion matrix (TP, FN, FP, and TN), Acc., Pre., Sen., F-Score (F-scr), and overall accuracy (Overall Acc.).

Table 2. Classification results

Pre-trained CNN Model	Class	TP	FN	FP	TN	Acc. (%)	Pre.	Sen.	F-Scr	Overall Acc. (%)
AlexNet	Bacterial spot	403	18	21	3319	98.96	0.957	0.993	0.953	92.18
	Early blight	153	50	47	3511	97.42	0.753	0.986	0.759	
	Healthy	304	11	14	3432	99.33	0.965	0.995	0.960	
	Late blight	348	38	33	3342	98.11	0.901	0.990	0.907	
	Leaf mold	168	23	32	3538	98.53	0.879	0.991	0.859	
	Sep. leaf spot	324	39	30	3368	98.16	0.892	0.991	0.903	
	Spider mites	295	39	39	3388	97.92	0.883	0.988	0.883	
	Target spot	242	55	38	3426	97.52	0.814	0.989	0.838	
	ToMV	186	6	14	3555	99.46	0.968	0.996	0.948	
	TYLCV	1044	15	26	2676	98.90	0.985	0.990	0.980	
GoogLeNet	Bacterial spot	390	37	34	3300	98.11	0.913	0.989	0.916	89.31
	Early blight	142	67	58	3494	96.67	0.679	0.983	0.694	
	Healthy	300	16	18	3427	99.09	0.949	0.994	0.946	
	Late blight	329	41	52	3339	97.52	0.889	0.984	0.876	
	Leaf mold	168	29	32	3532	98.37	0.852	0.991	0.846	
	Sep. leaf spot	294	66	60	3341	96.64	0.816	0.982	0.823	
	Spider mites	289	49	45	3378	97.50	0.855	0.986	0.860	
	Target spot	227	57	53	3424	97.07	0.799	0.984	0.804	
	ToMV	181	12	19	3549	99.17	0.937	0.994	0.921	
	TYLCV	1039	28	31	2663	98.43	0.973	0.988	0.972	
ResNet-50	Bacterial spot	414	7	10	3330	99.54	0.983	0.997	0.979	96.96
	Early blight	173	20	27	3541	98.75	0.896	0.992	0.880	
	Healthy	313	3	5	3440	99.78	0.990	0.998	0.987	
	Late blight	368	21	13	3359	99.09	0.946	0.996	0.995	
	Leaf mold	193	6	7	3555	99.65	0.969	0.998	0.967	
	Sep. leaf spot	344	10	10	3397	99.46	0.971	0.997	0.971	
	Spider mites	324	21	10	3406	99.17	0.939	0.997	0.954	
	Target spot	259	18	21	3463	98.96	0.935	0.993	0.929	
	ToMV	194	3	6	3558	99.76	0.984	0.998	0.977	
	TYLCV	1065	5	5	2686	99.73	0.995	0.998	0.995	
Concatenated Deep Features	Bacterial spot	419	4	5	3333	99.76	0.990	0.998	0.989	96.99
	Early blight	175	22	25	3539	98.75	0.888	0.992	0.881	
	Healthy	312	5	6	3438	99.70	0.984	0.998	0.982	
	Late blight	366	15	15	3365	99.20	0.960	0.995	0.960	
	Leaf mold	188	8	12	3553	99.46	0.959	0.996	0.949	
	Sep. leaf spot	345	16	9	3391	99.33	0.955	0.997	0.965	
	Spider mites	326	14	8	3413	99.41	0.958	0.997	0.967	
	Target spot	260	18	20	3463	98.98	0.935	0.994	0.931	
	ToMV	196	6	4	3555	99.73	0.970	0.998	0.975	
	TYLCV	1061	5	9	2686	99.62	0.995	0.996	0.993	

According to the experimental results, the overall accuracy rates obtained by classifying the deep features extracted from the last fully connected layers of AlexNet, GoogLeNet and ResNet-50 pre-trained CNN models with SVM classifier are 92.18%, 89.31% and 96.96%, respectively. According to the experimental results, all CNN models used within the scope of the study showed superior classification performance. However, the best performance has been achieved by using concatenating deep features with an overall accuracy rate of 96.99%. This overall accuracy rate is better than all CNN models individually.

The time taken to extract deep features for 3761 test images and store the resulting deep feature vectors on disk as a separate file was measured as 14 minutes 58 seconds, 20 minutes 19 seconds, and 50 minutes 33 seconds for AlexNet, GoogLeNet and ResNet-50 models, respectively. Experimental results show that deep feature extraction process from CNN models with a high number of layers requires more time.

Table 3. Comparison of the proposed model and the related studies

Related studies	Crops type	Method	Overall Acc. (%)
Fuentes et al., 2017 [12]	Tomato (10 classes)	Region-based CNN	83.60
Durmuş et al., 2017 [13]	Tomato (10 classes)	Retraining a pre-trained CNN model from scratch	95.65
Sardoğan et al., 2018 [14]	Tomato (5 classes)	CNN with LVQ algorithm	86.00
Rangarajan et al., 2018 [15]	Tomato (7 classes)	Fine-tuning a pre-trained CNN model	97.49
Aversano et al., 2020 [16]	Tomato (10 classes)	Fine-tuning a pre-trained CNN model	97.16
Agarwal et al., 2020 [17]	Tomato (10 classes)	CNN	91.20
Saeed et al., 2021 [18]	Tomato (10 classes)	PLS-based deep features selection and ensemble baggage tree classifier	87.11
	Corn (4 classes)		91.67
	Potato (3 classes)		91.67
This study	Tomato (10 classes)	Concatenating deep features and SVM	96.99

4. Discussion

The number of classes dealt with in the related studies is not equal. Sardoğan et al. [14] conducted a study with a total of 5 classes, including 4 diseases and 1 healthy class. Rangarajan et al. [15] conducted a study with a total of 7 classes, including 6 diseases and 1 healthy class. In other related studies, 10 classes, including 9 diseases and 1 healthy class were conducted. Since test samples are not pre-defined in the PlantVillage dataset, the test samples used in related studies are not the same. Also, the number of test samples used is not equal. Sardoğan et al. [14] in their work with a total of 500 images, they used 400 images for training and 100 images for testing. Agarwal et al. [17] in their work with a total of 17500 images, they used 10000 images for training, 7000 images for validation and 500 images for testing. A one-to-one comparison among the related studies is not feasible due to the reasons explained above. Nevertheless, we present a comparison in Table 3 considering several criteria, such as the number of classes, methods, and overall accuracy rates.

5. Conclusion

In this study, the possibilities of detecting tomato plant diseases and pests by deep feature extraction were investigated. For this purpose, well-known pre-trained CNN models AlexNet, GoogLeNet, and ResNet-50 were used as feature extractors. 1000 deep features obtained from the last fully connected layers of CNN models were used to train the SVM classifier. In addition, a deep learning model that concatenate 1000 deep features obtained from each of the 3 CNN models proposed to increase predictive performance. According to the experimental results, while superior classification performance was obtained with deep features extracted from all CNN models, the best result was obtained with the concatenated deep features. The reason for this is considered to be the result of CNN models with different architectures discovering different discriminative features.

In future studies, it is aimed to increase the classification performance with different fusion methods. In addition, the performance of the models to be developed on field condition images will be evaluated.

Author's Contributions

Yahya Altuntaş: Drafted and wrote the manuscript, performed the experiment and result analysis.

Adnan Fatih Kocamaz: Supervised the experiments' progress, result interpretation and helped in manuscript preparation.

Ethics

There are no ethical issues after the publication of this manuscript.

References

1. Mohanty, SP, Hughes, DP, Salathé, M. 2016. Using deep learning for image-based plant disease detection. *Frontiers in plant science*; 7: 1419.
2. Ferentinos, KP. 2018. Deep learning models for plant disease detection and diagnosis. *Computers and Electronics in Agriculture*; 145: 311-318.
3. Al-Hiary, H, Bani-Ahmad, S, Reyalat, M, Braik, M, Alrahmaneh, Z. 2011. Fast and accurate detection and classification of plant diseases. *International Journal of Computer Applications*; 17(1): 31-38.
4. Dubey, SR, Jalal, AS. Detection and classification of apple fruit diseases using complete local binary patterns, proceedings of the 3rd international conference on computer and communication technology, Allahabad, India, 2012, pp 346-351.
5. Singh, V, Misra, AK. 2017. Detection of plant leaf diseases using image segmentation and soft computing techniques. *Information processing in Agriculture*; 4(1): 41-49.
6. LeCun, Y, Bengio, Y, Hinton, G. 2015. Deep learning. *Nature*; 521(7553): 436-444.
7. Ünal, Z. 2020. Smart Farming Becomes Even Smarter With Deep Learning - A Bibliographical Analysis. *IEEE Access*; 8:105587-105609.

8. Kamilaris, A, Prenafeta-Boldú, FX. 2018. Deep learning in agriculture: A survey. *Computers and Electronics in Agriculture*; 147: 70-90.
9. Zhong, Y, Zhao, M. 2020. Research on deep learning in apple leaf disease recognition. *Computers and Electronics in Agriculture*; 168: 105146.
10. Fujita, E, Kawasaki, Y, Uga, H, Kagiwada, S, Iyatomi, H. Basic investigation on a robust and practical plant diagnostic system, proceedings of the 15th IEEE International Conference on Machine Learning and Applications, Anaheim CA, USA, 2016, pp 989-992.
11. Lu, Y, Yi, S, Zeng, N, Liu, Y, Zhang, Y. 2017. Identification of rice diseases using deep convolutional neural networks. *Neurocomputing*; 267: 378-384.
12. Fuentes, A, Yoon, S, Kim, SC, Park, DS. 2017. A robust deep-learning-based detector for real-time tomato plant diseases and pests recognition. *Sensors*; 17(9): 2022.
13. Durmuş, H, Güneş, EO, Kırıcı, M. Disease detection on the leaves of the tomato plants by using deep learning, proceedings of the 6th International Conference on Agro-Geoinformatics, Fairfax VA, USA, 2017, pp 1-5.
14. Sardogan, M, Tuncer, A, Ozen, Y. Plant leaf disease detection and classification based on CNN with LVQ algorithm, proceedings of the 3rd International Conference on Computer Science and Engineering, Sarajevo, Bosnia and Herzegovina, 2018, pp 382-385.
15. Rangarajan, AK, Purushothaman, R, Ramesh, A. 2018. Tomato crop disease classification using pre-trained deep learning algorithm. *Procedia computer science*; 133: 1040-1047.
16. Aversano, L, Bernardi, ML, Cimitile, M, Iammarino, M, Rondinella, S. Tomato diseases Classification Based on VGG and Transfer Learning, proceedings of the IEEE International Workshop on Metrology for Agriculture and Forestry, Virtual Conference, 2020, pp 129-133.
17. Agarwal, M, Singh, A, Arjaria, S, Sinha, A, Gupta, S. 2020. ToLeD: Tomato leaf disease detection using convolution neural network. *Procedia Computer Science*; 167: 293-301.
18. Saeed, F, Khan, MA, Sharif, M, Mittal, M, Goyal, LM, Roy, S. 2021. Deep neural network features fusion and selection based on PLS regression with an application for crops diseases classification. *Applied Soft Computing*; 103: 107164.
19. Hughes, D, Salathé, M. 2015. An open access repository of images on plant health to enable the development of mobile disease diagnostics. *arXiv preprint*; arXiv:1511.08060.
20. Geetharamani, G, Pandian, A. 2019. Identification of plant leaf diseases using a nine-layer deep convolutional neural network. *Computers & Electrical Engineering*; 76: 323-338.
21. Altuntaş, Y, Cömert, Z, Kocamaz, AF. 2019. Identification of haploid and diploid maize seeds using convolutional neural networks and a transfer learning approach. *Computers and Electronics in Agriculture*; 163: 104874.
22. Chatfield, K, Simonyan, K, Vedaldi, A, Zisserman, A. 2014. Return of the devil in the details: Delving deep into convolutional nets. *arXiv preprint*; arXiv:1405.3531.
23. Toğaçar, M, Ergen, B, Cömert, Z. 2020. Classification of flower species by using features extracted from the intersection of feature selection methods in convolutional neural network models. *Measurement*; 158: 107703.
24. Krizhevsky, A, Sutskever, I, Hinton, GE. 2012. Imagenet classification with deep convolutional neural networks. *Advances in neural information processing systems*; 25: 1097-1105.
25. Szegedy, C, Liu, W, Jia, Y, Sermanet, P, Reed, S, Anguelov, D, Rabinovich, A. Going deeper with convolutions, proceedings of the IEEE conference on computer vision and pattern recognition, Boston MA, USA, 2015, pp 1-9.
26. He, K, Zhang, X, Ren, S, Sun, J. Deep residual learning for image recognition, proceedings of the IEEE conference on computer vision and pattern recognition, Las Vegas NV, USA, 2016, pp 770-778.
27. Vapnik, VN. The nature of statistical learning theory; Springer, New York, USA, 2000; pp 313.
28. Altuntaş, Y, Kocamaz, AF. 2019. Renk momentleri ve destek vektör makineleri kullanarak haploid mısır tohumlarının tanımlanmasında renk uzaylarının sınıflandırma performansına etkisinin karşılaştırılması. *Fırat Üniversitesi Mühendislik Bilimleri Dergisi*; 31(2): 551-560.
29. Huang, S, Cai, N, Pacheco, PP, Narrandes, S, Wang, Y, Xu, W. 2018. Applications of support vector machine (SVM) learning in cancer genomics. *Cancer Genomics-Proteomics*; 15(1): 41-51.
30. Bishop, CM. Pattern recognition and machine learning; Springer, New York, USA, 2006; pp 738.

Numerical Solutions of System of First Order Normalized Linear Differential Equations by Using Bernoulli Matrix Method

Kübra ERDEM BİÇER¹ , Mehmet SEZER^{1*} , Mustafa KAZAZ¹ 

¹ Manisa Celal Bayar University Faculty of Art and Science, Manisa, Turkey

*kubra.erdem@cbu.edu.tr

*Orcid: 0000-0002-4998-6531

Received: 23 December 2020

Accepted: 21 May 2021

DOI: 10.18466/cbayarfbe.845017

Abstract

Systems of first order differential equations have been arisen in science and engineering. Specially, the systems of normalized linear differential equations appear in differential geometry and kinematics problems. Since it is difficult to find solutions to these equations analytically, numerical methods are needed for the approximate solutions. In this study, we find the approximate solutions of the Frenet-Like system with variable coefficients upon the initial conditions by means of a matrix method related to the truncated Bernoulli series. This method transforms the mentioned problem into a system of algebraic equations by using the matrix relations and collocation points; so, the required results along with the solutions are obtained and the usability of the method is discussed.

Keywords: Approximate Solutions, Bernoulli polynomials and series, Curves of constant breadth, Matrix Methods, Systems of first order differential equations.

1. Introduction

The systems of differential equations in the normal form usually appear in the concept of differential geometry. For instance, a system of differential equations characterizing E^4 spherical curves can be given as

$$\frac{d\rho}{ds} = \tau f, \quad \frac{df}{ds} = -\tau\rho + \mu g, \quad \frac{dg}{ds} = -\mu f, \quad (1)$$

where s is arc parameter, $\rho(s) = 1/\kappa(s)$ is curvature diameter; κ, τ and μ are curvatures and, $f(s)$ and $g(s)$ are in the class of C^2 [1,2].

The system charactering curves of constant breadth are the same type and can be given as

$$\frac{d\lambda}{d\theta} = \mu, \quad \frac{d\mu}{d\theta} = -\lambda + \rho\tau\delta, \quad \frac{d\delta}{d\theta} = -\rho\tau\mu, \quad (2)$$

where $\theta(s) = \int_0^s \kappa(s) ds$ and $\lambda(\theta)$, $\mu(\theta)$ and $\delta(\theta)$

are the coefficients of the curve [3,4].

Besides, the well known Serret-Frenet Equations

$$\frac{d\vec{t}}{ds} = \kappa\vec{n}, \quad \frac{d\vec{n}}{ds} = -\kappa\vec{t} + \kappa_2\vec{b}, \quad \frac{d\vec{b}}{ds} = -\kappa_2\vec{n},$$

lead us to the system of differential equations [5,6]:

$$\frac{d\varphi_1}{ds} = \kappa\varphi_2, \quad \frac{d\varphi_2}{ds} = -\kappa\varphi_1 + \tau\varphi_3, \quad \frac{d\varphi_3}{ds} = -\tau\varphi_2, \quad (3)$$

where κ_1 and κ_2 are Euclidean curvatures. The solution of this system also gives as a criterion for periodicity of a space curve. Since the normal systems (1), (2) and (3) same type, it is possible to form them as

$$\left. \begin{aligned} \frac{dy_1}{dx} &= a(x)y_2(x) \\ \frac{dy_2}{dx} &= -a(x)y_1(x) + b(x)y_3(x) \\ \frac{dy_3}{dx} &= -b(x)y_2(x) \end{aligned} \right\} \quad (4)$$

Also the normal system is obtained as

$$\left. \begin{aligned} \frac{dT}{ds} &= k_1N_1 + k_2N_2 \\ \frac{dN_1}{ds} &= -k_1T \\ \frac{dN_2}{ds} &= -k_2T \end{aligned} \right\} \quad (5)$$

where

$k_1 = \kappa \cos(\theta)$, $k_2 = \kappa \sin(\theta)$ and $T = T$,
 $N_1 = N \cos \theta - B \sin \theta$, $N_2 = N \sin \theta - B \cos \theta$ for the
 Bishop frame. It can be shown that

$$\kappa(s) = \sqrt{k_1^2 + k_2^2} , \theta(s) = \arctan\left(\frac{k_2}{k_1}\right) \text{ and}$$

$$\tau(s) = -\frac{d\theta(s)}{s} \quad [7].$$

These type systems given in (4) and (5) which are called Frenet-Like system is a class of linear differential equations in normal form

$$\left. \begin{aligned} \frac{dy_1}{ds} &= P_{11}(s)y_1(s) + P_{12}(s)y_2(s) + P_{13}(s)y_3(s) + g_1(s) \\ \frac{dy_2}{ds} &= P_{21}(s)y_1(s) + P_{22}(s)y_2(s) + P_{23}(s)y_3(s) + g_2(s) \\ \frac{dy_3}{ds} &= P_{31}(s)y_1(s) + P_{32}(s)y_2(s) + P_{33}(s)y_3(s) + g_3(s) \end{aligned} \right\} \quad (6)$$

or briefly

$$\frac{dy_j}{ds} = \sum_{k=1}^3 P_{jk}(s)y_k(s) + g_j(s); \quad j = 1, 2, 3$$

where $P_{kj}(s)$ and $g(s)$ are functions on interval $0 \leq a \leq s \leq b$.

In this study, we have developed a method based on Bernoulli polynomials to solve system of linear differential equations. Also this method has been used to solve high-order linear differential-difference equations, linear delay difference equations with variable coefficients and mixed linear Fredholm integro-differential-difference equations, hyperbolic partial differential equations, Helmholtz equations and general functional integro-differential equations with hybrid delays [8-13]. Also many numerical methods have been developed to solve similar equation models [14-20].

We firstly consider the system of differential equations in normal form (6) with the initial conditions

$$y_1(a) = \lambda_1, y_2(a) = \lambda_2, y_3(a) = \lambda_3; 0 \leq a \leq s \leq b. \quad (7)$$

A matrix method is developed to find the approximate solution set in the truncated Bernoulli series form

$$y_j(s) = \sum_{n=0}^N a_{jn} B_n(s); 0 \leq a \leq s \leq b, \quad (8)$$

where a_{jn} , $j = 1, 2, 3$ are unknown Bernoulli coefficients, λ_j , $j = 1, 2, 3$ are the given real constants and $B_n(s)$, $n = 0, 1, \dots, N$. Bernoulli polynomials are defined by [21]

$$\frac{te^{xt}}{e^t - 1} = \sum_{n=0}^{\infty} \frac{B_n(x)}{n!} t^n$$

or

$$B_n(x) = \sum_{r=0}^n \binom{n}{r} b_r x^{n-r}; \quad b_r = B_r(0). \quad (9)$$

Also, an explicit formula for the Bernoulli polynomials is given by

$$B'_n(s) = nB_{n-1}(s), \quad (10)$$

where $B_0(s) = 1$, $B'_0(s) = 1$, $B_1(s) = s - \frac{1}{2}$, $B'_1(s) = 1$

2. Fundamental matrix relations and Bernoulli matrix method

In this section, a new matrix technique is developed by considering Taylor and Bernoulli collocation methods [22-23] to obtain the approximate solution of the system (6) under the condition (7). For this aim, we compose the matrix form of (6), (7) and (8); firstly the matrix form of (6) can be expressed as

$$Y'(s) = P(s)Y(s) + G(s); 0 \leq a \leq s \leq b, \quad (11)$$

where

$$Y'(s) = \begin{bmatrix} y_1'(s) \\ y_2'(s) \\ y_3'(s) \end{bmatrix}, P(s) = \begin{bmatrix} P_{11}(s) & P_{12}(s) & P_{13}(s) \\ P_{21}(s) & P_{22}(s) & P_{23}(s) \\ P_{31}(s) & P_{32}(s) & P_{33}(s) \end{bmatrix},$$

$$Y(s) = \begin{bmatrix} y_1(s) \\ y_2(s) \\ y_3(s) \end{bmatrix}, G(s) = \begin{bmatrix} g_1(s) \\ g_2(s) \\ g_3(s) \end{bmatrix}.$$

Then the matrix form of (8) can be written as

$$y_j(s) = B(s)A_j, \quad (j = 1, 2, 3), \quad (12)$$

where

$$B(s) = [B_0(s) \quad B_1(s) \quad \dots \quad B_N(s)],$$

$$A_j = [a_{j0} \quad a_{j1} \quad a_{j2} \quad \dots \quad a_{jN}(s)]^T.$$

Also by using the expressions (10) and (12), we have the matrix form

$$y_j'(s) = B'(s)A_j = B(s)DA_j; \quad (j = 1, 2, 3), \quad (13)$$

where

$$D = \begin{bmatrix} 0 & 1 & 0 & \dots & 0 \\ 0 & 0 & 2 & \dots & 0 \\ \vdots & \vdots & \vdots & \ddots & \vdots \\ 0 & 0 & 0 & 0 & N \\ 0 & 0 & 0 & 0 & 0 \end{bmatrix}.$$

By using the matrix relations (12) and (13) into the matrices $Y(s)$ and $Y'(s)$, the following matrix forms are obtained as

$$Y(s) = \begin{bmatrix} y_1(s) \\ y_2(s) \\ y_3(s) \end{bmatrix} = \begin{bmatrix} B(s)A_1 \\ B(s)A_2 \\ B(s)A_3 \end{bmatrix} = \bar{B}(s)A, \quad (14)$$

$$Y'(s) = \begin{bmatrix} y_1'(s) \\ y_2'(s) \\ y_3'(s) \end{bmatrix} = \begin{bmatrix} B(s)DA_1 \\ B(s)DA_2 \\ B(s)DA_3 \end{bmatrix} = \overline{B(s)DA},$$

where

$$\bar{B}(s) = \begin{bmatrix} B(s) & 0 & 0 \\ 0 & B(s) & 0 \\ 0 & 0 & B(s) \end{bmatrix},$$

$$\overline{B(s)D} = \begin{bmatrix} B(s)D & 0 & 0 \\ 0 & B(s)D & 0 \\ 0 & 0 & B(s)D \end{bmatrix},$$

$$A = \begin{bmatrix} A_1 \\ A_2 \\ A_3 \end{bmatrix}, \quad A_j = \begin{bmatrix} a_{j0} \\ a_{j1} \\ \vdots \\ a_{jN} \end{bmatrix}, \quad j = 1, 2, 3.$$

By substituting the collocation points defined by

$$s_i = a + \frac{b-a}{N}i, \quad (i = 0, 1, \dots, N),$$

into Eq. (11) along with (14), we gain the system of matrix equations

$$Y'(s_i) = P(s_i)Y(s_i) + G(s_i), \quad (i = 0, 1, \dots, N),$$

or briefly, the fundamental matrix equation

$$Y' = PY + G \Rightarrow (\overline{BD} - \overline{PB})A = G, \quad (15)$$

where

$$P = \begin{bmatrix} P(s_0) & 0 & \dots & 0 \\ 0 & P(s_0) & \dots & 0 \\ \vdots & \vdots & \ddots & \vdots \\ 0 & 0 & \dots & P(s_N) \end{bmatrix}, \quad G = \begin{bmatrix} G(s_0) \\ G(s_1) \\ \vdots \\ G(s_N) \end{bmatrix},$$

$$Y = \begin{bmatrix} Y(s_0) \\ Y(s_1) \\ \vdots \\ Y(s_N) \end{bmatrix} = \begin{bmatrix} \bar{B}(s_0)A \\ \bar{B}(s_1)A \\ \vdots \\ \bar{B}(s_N)A \end{bmatrix} = \bar{B}A,$$

$$Y'(s) = \begin{bmatrix} Y'(s_0) \\ Y'(s_1) \\ \vdots \\ Y'(s_N) \end{bmatrix} = \begin{bmatrix} \overline{B(s_0)DA} \\ \overline{B(s_1)DA} \\ \vdots \\ \overline{B(s_N)DA} \end{bmatrix} = \overline{BDA}.$$

In Eq. (13), the full dimensions of the matrices \overline{BD} , P , \bar{B} , A , and G are $3(N+1) \times 3(N+1)$, $3(N+1) \times 3(N+1)$, $3(N+1) \times 3(N+1)$, $3(N+1) \times 1$ and $3(N+1) \times 1$, respectively.

The fundamental matrix equation (15) corresponding to Eq. (4) can be written in the compact form

$$WA = G \text{ or } [W; G], \quad (16)$$

where

$$W = \overline{BD} - \overline{PB} = [w_{pq}]; \quad p, q = 1, 2, \dots, 3(N+1).$$

The matrix equation (16) corresponds to a system of a linear algebraic equations in $3(N+1)$ unknown Bernoulli coefficients.

By using the initial conditions defined by (7) and the matrix relation $Y(s)$ in (14), we obtain the matrix form for the conditions as

$$\bar{B}(a)A = \lambda \Leftrightarrow [\bar{B}(a); \lambda], \quad (17)$$

where

$$\bar{B}(a) = \begin{bmatrix} B(a) & 0 & 0 \\ 0 & B(a) & 0 \\ 0 & 0 & B(a) \end{bmatrix}, \quad \lambda = \begin{bmatrix} \lambda_1 \\ \lambda_2 \\ \lambda_3 \end{bmatrix}.$$

Consequently, we obtain the new following augmented matrix for the problem (6)-(7) by replacing the row matrices (17) with the rows involving the coefficients a_{10} , a_{20} and a_{30} of the matrix (16):

$$[\tilde{W}; \tilde{G}] \text{ or } \tilde{W}A = \tilde{G}. \quad (18)$$

If rank $\tilde{W} = \text{rank} [\tilde{W}; \tilde{G}] = N+1$, the unknown Bernoulli coefficient matrix can be written as $A = (\tilde{W})^{-1} \tilde{G}$ and the approximate solution in the Bernoulli matrix form is obtained as

$$Y(s) = \bar{B}(s)A,$$

or

$$y_j(s) \cong \sum_{n=0}^N a_{jn} B_n(s).$$

3. Results and Discussion

In this section two examples are given to demonstrate the applicability of this method. These examples have been calculated by using Matlab.

Example 1. Consider the system of first-order linear differential equations

$$\begin{aligned} \frac{dy_1}{dx} &= xy_2(x) - x^2 \\ \frac{dy_2}{dx} &= -xy_1(x) + y_3(x) \\ \frac{dy_3}{dx} &= -y_2(x) + x + 1 \end{aligned} \quad 0 \leq x \leq 1, \quad (19)$$

with the initial conditions $y_1(0) = 1$, $y_2(0) = 0$, $y_3(0) = 1$ which has the exact solution $y_1(x) = 1$, $y_2(x) = x$, $y_3(x) = x + 1$.

The approximate solution is $y_j(s) = \sum_{n=0}^2 a_{jn} B_n(s)$,
 $j=1,2,3$. The collocation points for $N=2$ are
 computed as $\left\{x_1=0, x_2=\frac{1}{2}, x_3=1\right\}$.

The fundamental matrix equation is

$$WA = (\overline{BD} - P\overline{B})A = G,$$

where

$$\overline{BD} = \begin{bmatrix} 0 & 1 & -1 & 0 & 0 & 0 & 0 & 0 & 0 \\ 0 & 0 & 0 & 0 & 1 & -1 & 0 & 0 & 0 \\ 0 & 0 & 0 & 0 & 0 & 0 & 0 & 1 & -1 \\ 0 & 1 & 0 & 0 & 0 & 0 & 0 & 0 & 0 \\ 0 & 0 & 0 & 0 & 1 & 0 & 0 & 0 & 0 \\ 0 & 0 & 0 & 0 & 0 & 0 & 0 & 1 & 0 \\ 0 & 1 & 1 & 0 & 0 & 0 & 0 & 0 & 0 \\ 0 & 0 & 0 & 0 & 1 & 1 & 0 & 0 & 0 \\ 0 & 0 & 0 & 0 & 0 & 0 & 0 & 1 & 1 \end{bmatrix},$$

$$P = \begin{bmatrix} 0 & 0 & 0 & 0 & 0 & 0 & 0 & 0 & 0 \\ 0 & 0 & 1 & 0 & 0 & 0 & 0 & 0 & 0 \\ 0 & -1 & 0 & 0 & 0 & 0 & 0 & 0 & 0 \\ 0 & 0 & 0 & 0 & \frac{1}{2} & 0 & 0 & 0 & 0 \\ 0 & 0 & 0 & -\frac{1}{2} & 0 & 1 & 0 & 0 & 0 \\ 0 & 0 & 0 & 0 & -1 & 0 & 0 & 0 & 0 \\ 0 & 0 & 0 & 0 & 0 & 0 & 0 & 1 & 0 \\ 0 & 0 & 0 & 0 & 0 & 0 & -1 & 0 & 1 \\ 0 & 0 & 0 & 0 & 0 & 0 & 0 & -1 & 0 \end{bmatrix},$$

$$\overline{B} = \begin{bmatrix} 1 & -\frac{1}{2} & \frac{1}{6} & 0 & 0 & 0 & 0 & 0 & 0 \\ 0 & 0 & 0 & 1 & -\frac{1}{2} & \frac{1}{6} & 0 & 0 & 0 \\ 0 & 0 & 0 & 0 & 0 & 0 & 1 & -\frac{1}{2} & \frac{1}{6} \\ 1 & 0 & -\frac{1}{12} & 0 & 0 & 0 & 0 & 0 & 0 \\ 0 & 0 & 0 & 1 & 0 & -\frac{1}{12} & 0 & 0 & 0 \\ 0 & 0 & 0 & 0 & 0 & 0 & 1 & 0 & -\frac{1}{12} \\ 1 & \frac{1}{2} & \frac{1}{6} & 0 & 0 & 0 & 0 & 0 & 0 \\ 0 & 0 & 0 & 1 & \frac{1}{2} & \frac{1}{6} & 0 & 0 & 0 \\ 0 & 0 & 0 & 0 & 0 & 0 & 1 & \frac{1}{2} & \frac{1}{6} \end{bmatrix}.$$

The augmented matrix for this fundamental matrix equation is calculated as

$$[W;G] = \begin{bmatrix} 0 & 1 & -1 & 0 & 0 & 0 & 0 & 0 & 0 & ; & 0 \\ 0 & 0 & 0 & 0 & 1 & -1 & -1 & \frac{1}{2} & -\frac{1}{6} & ; & 0 \\ 0 & 0 & 0 & 1 & -\frac{1}{2} & \frac{1}{6} & 0 & 1 & -1 & ; & 1 \\ 0 & 1 & 0 & -\frac{1}{2} & 0 & \frac{1}{24} & 0 & 0 & 0 & ; & -\frac{1}{4} \\ \frac{1}{2} & 0 & -\frac{1}{24} & 0 & 1 & 0 & -1 & 0 & \frac{1}{12} & ; & 0 \\ 0 & 0 & 0 & 1 & 0 & -\frac{1}{12} & 0 & 1 & 0 & ; & \frac{3}{2} \\ 0 & 1 & 1 & -1 & -\frac{1}{2} & -\frac{1}{6} & 0 & 0 & 0 & ; & -1 \\ 1 & \frac{1}{2} & \frac{1}{6} & 0 & 1 & 1 & -1 & -\frac{1}{2} & -\frac{1}{6} & ; & 0 \\ 0 & 0 & 0 & 1 & \frac{1}{2} & \frac{1}{6} & 0 & 1 & 1 & ; & 2 \end{bmatrix}.$$

From equation (17), we obtain the matrix form of the initial conditions

$$[\overline{B}(0); \lambda] = \begin{bmatrix} 1 & -\frac{1}{2} & \frac{1}{6} & 0 & 0 & 0 & 0 & 0 & 0 & ; & 1 \\ 0 & 0 & 0 & 1 & -\frac{1}{2} & \frac{1}{6} & 0 & 0 & 0 & ; & 0 \\ 0 & 0 & 0 & 0 & 0 & 0 & 1 & -\frac{1}{2} & \frac{1}{6} & ; & 1 \end{bmatrix}.$$

From equation (18), the new augmented matrix based on the conditions is calculated as

$$[\tilde{W}; \tilde{G}] = \begin{bmatrix} 1 & -\frac{1}{2} & \frac{1}{6} & 0 & 0 & 0 & 0 & 0 & 0 & ; & 1 \\ 0 & 0 & 0 & 1 & -\frac{1}{2} & \frac{1}{6} & 0 & 0 & 0 & ; & 0 \\ 0 & 0 & 0 & 0 & 0 & 0 & 1 & -\frac{1}{2} & \frac{1}{6} & ; & 1 \\ 0 & 1 & 0 & -\frac{1}{2} & 0 & \frac{1}{24} & 0 & 0 & 0 & ; & -\frac{1}{4} \\ \frac{1}{2} & 0 & -\frac{1}{24} & 0 & 1 & 0 & -1 & 0 & \frac{1}{12} & ; & 0 \\ 0 & 0 & 0 & 1 & 0 & -\frac{1}{12} & 0 & 1 & 0 & ; & \frac{3}{2} \\ 0 & 1 & 1 & -1 & -\frac{1}{2} & -\frac{1}{6} & 0 & 0 & 0 & ; & -1 \\ 1 & \frac{1}{2} & \frac{1}{6} & 0 & 1 & 1 & -1 & -\frac{1}{2} & -\frac{1}{6} & ; & 0 \\ 0 & 0 & 0 & 1 & \frac{1}{2} & \frac{1}{6} & 0 & 1 & 1 & ; & 2 \end{bmatrix}.$$

Solving this system, the unknown Bernoulli coefficient matrix is obtained as

$$A = \left[1 \ 0 \ 0 \ \frac{1}{2} \ 1 \ 0 \ \frac{3}{2} \ 1 \ 0 \right]^T.$$

By substituting the Bernoulli coefficient matrix into equation (12), we obtain the approximate solution set $y_1(x)=1, y_2(x)=x, y_3(x)=x+1$ which is the exact solution.

Example 2. Consider the curve $\alpha : [0, 2] \rightarrow E_1^3$ given by

$$\alpha(s) = \left(\frac{s^3}{3} + s, \frac{s^3}{3}, \frac{s^2}{\sqrt{2}} \right).$$

The system of differential equations in the normal form corresponding to curve α is as follows [24]

$$\begin{aligned} \lambda_1'(s) &= -\sqrt{2} \cos(\sqrt{2}s) \lambda_2(s) + \sqrt{2} \sin(\sqrt{2}s) \lambda_3(s) \\ \lambda_2'(s) &= -\sqrt{2} \cos(\sqrt{2}s) \lambda_1(s) \\ \lambda_3'(s) &= \sqrt{2} \sin(\sqrt{2}s) \lambda_1(s) \end{aligned} \quad (20)$$

The approximate solution set of this problem is solved using Bernoulli Collocation method with the initial conditions $\lambda_1(0) = 1$, $\lambda_2(0) = 2$ and $\lambda_3(0) = 3$. For initial conditions value of distance d is

$$d = \sqrt{-\lambda_1^2 + \lambda_2^2 + \lambda_3^2} = \sqrt{12} \cong 3.464101615. [16]$$

Solving the problem (20) in the same way as Section 2 for $N = 3$, we get

$$\begin{aligned} \lambda_1(s) &= 11.1592106s^3 - 15.4680213s^2 + \\ & 18.7854967s + 0.999999995 \\ \lambda_2(s) &= 10.77765s^3 - 26.4167678s^2 + \\ & 15.1614944s + 2 \\ \lambda_3(s) &= 10.1776605s^3 - 13.7259918s^2 + \\ & 17.6088868s + 2.99999997. \end{aligned}$$

Hence the value of distance d for obtained approximate solution is

$$d = \sqrt{-\lambda_1^2 + \lambda_2^2 + \lambda_3^2} = \sqrt{12} \cong 3.464101615.$$

Let's briefly summarize the results given in this article as follows:

In section 1, the problem and Bernoulli polynomials have been introduced. In section 2, the matrix relations of the given problem has been obtained and Bernoulli matrix method has been developed. In section 3, two examples have been considered to demonstrate accuracy of the method. In section 4, obtained results have been examined and the advantage of the method have been highlighted.

4. Conclusion

In this study, system of Frenet-Like differential equations which arise in differential geometry as a model for linear equation systems are discussed. To solve this equation system, a numerical method has been developed. This method is based on Bernoulli polynomials and collocations points. To demonstrate the applicability of the present method, two examples have been considered. Obtained results have been showed that the method is suitable for the solutions of

differential equation systems. One of the important advantages of this method is that solutions are obtained very easily and practically by using computer programs. Since linear differential equations are encountered in many physics, chemistry, biology and engineering problems, this method can be extended another models with small modifications, which is another advantage of the method.

Author's Contributions

Kübra Erdem Biçer: Made literature search, performed numerical examples.

Mehmet Sezer: Supervised the manuscript and drafted the manuscript.

Mustafa Kazaz: Helped in results interpretation, performed the analysis.

Ethics

There are no ethical issues after the publication of this manuscript.

References

1. Dannon, V. 1981. Integral Characterizations and Theory of Curves. *Proc. Amer. Math. Soc.*; 4: 600–603.
2. Sezer, M. 1989. Differential Equations and Integral Characterizations for E4- Spherical Curves. *Doga Tr. J. Math.*; 13: 125–131.
3. Köse, Ö. 1986. On Space Curves of Constant Breadth. *Doga Tr. J. Math.*; 10: 11–14.
4. Sezer, M. 1989. Differential Equations Characterizing Space Curves of Constant Breadth and A Criterion for These Curves. *Doga Tr. J. Math.*; 13: 70–78.
5. Do Carmo, MP. *Differential Geometry of Curves and Surfaces.* Prentice Hall, Inc. Englewood Cliffs, 1976.
6. Paşalı Atmaca, S, Akgüller, Ö, Sezer, M. 2013. Integral Characterization of a System of Differential Equations and Applications. *Nonl. Analysis and Differential Equations*; 1(2): 57–66.
7. Çetin, M, Tunçer, Y, Karacan, MK. 2014. Smarandache Curves According to Bishop Frame in Euclidean 3-Space. *Gen. Math. Notes*; 20(2): 50-66.
8. Erdem, K, Yalçınbaş, S. 2012. Numerical approach of linear delay difference equations with variable coefficients in terms of Bernoulli polynomials. *AIP Conf. Proc.*; 1493: 338-344.
9. Erdem, K, Yalçınbaş, S. 2012. Bernoulli Polynomial Approach to High-Order Linear Differential Difference Equations. *AIP Conf. Proc.*; 1479: 360-364.
10. Erdem, K, Yalçınbaş, S, Sezer, M. 2013. A Bernoulli approach with residual correction for solving mixed linear Fredholm integro-differential-difference equation. *Journal of Difference Equations and Applications*; 19(10): 1619-1631.
11. Erdem, K, Yalçınbaş, S. 2016. A matrix approach to solving hyperbolic partial differential equations using Bernoulli polynomials. *Filomat*; 30(4): 993–1000.



12. Erdem, K, Yalçınbaş, S. 2017. Numerical Solutions for Helmholtz Equations using Bernoulli Polynomials. *AIP Conf. Proc.*; 1863: 300021-1–300021-4.
13. Erdem Biçer, K, Sezer, M. 2017. Bernoulli Matrix-Collocation Method for solving General Functional Integro-Differential Equations with Hybrid Delays. *Journal of Inequalities and Special Functions*; 8(3): 85-99.
14. Ahmad H, Khan, TA, Durur, H, İsmail, GM, Yokus, A. 2021. Analytic approximate solutions of diffusion equations arising in oil pollution. *Journal of Ocean Engineering and Science*; 6(1): 62-69.
15. Rasool, G, Zhang, T, Shafiq, A, Durur, H. 2019. Influence of chemical reaction on Marangoni convective flow of nanofluid in the presence of Lorentz forces and thermal radiation: A numerical investigation. *Journal of Advances in Nanotechnology*; 1(1): 32.
16. Ahmad, H, Rafiq, M, Cesarano, C, Durur, H. 2020. Variational iteration algorithm-I with an auxiliary parameter for solving boundary value problems. *Earthline Journal of Mathematical Sciences*; 3(2): 229-247.
17. Yavuz, M, Yokus, A. 2020. Analytical and numerical approaches to nerve impulse model of fractional-order. *Numerical Methods for Partial Differential Equations*; 36(6): 1348-1368.
18. Durur, H, Senol, M, Kurt, A, Tasbozan, O. 2019. Approximate solutions of the time fractional Kadomtsev–Petviashvili equation with conformable derivative. *Erzincan Univ. J. Sci. Technol*; 12(2): 796-806.
19. Yokus, A. 2020. Truncation and convergence dynamics: KdV burgers model in the sense of Caputo derivative. *Boletim da Sociedade Paranaense de Matematica*; doi: 10.5269/bspm.47472.
20. Rasool, G, Shafiq, A, Durur, H. 2020. Darcy-Forchheimer relation in Magnetohydrodynamic Jeffrey nanofluid flow over stretching surface. *Discrete & Continuous Dynamical Systems-S*; doi: 10.3934/dcdss.2020399.
21. Apostol, TM. Introduction to Analytic Number Theory, Springer-Verlag, New York, 1976, pp 264-267.
22. Ates, BY, Çetin, M, Sezer, M. 2015. Taylor polynomial approach for systems of linear differential equations in normal form and residual error estimation. *NTMSCI*; 3: 116-128.
23. Sahiner, B, Sezer, M. 2018. Determining constant breadth curve mate of a curve on a surface via Taylor collocation method. Determining constant breadth curve mate of a curve on a surface via Taylor collocation method. *NTMSCI*; 6(3): 103-115.
24. Cetin, M. Sabit Genişlikli Eğriler Ve Küresel Eğrilerin Diferensiyel Karakterizasyonları. PhD Thesis, Manisa Celal Bayar University, The Institute of Natural and Applied Sciences, 2015.

Comparison of Cellular Autofluorescence Patterns of Two Model Microalgae by Flow Cytometry

Ugur Uzuner^{1*} 

¹Department of Molecular Biology and Genetics, Faculty of Science, Karadeniz Technical University, Trabzon, TURKEY

*uguruzuner@ktu.edu.tr

*Orcid: 0000-0002-5308-3730

Received: 19 November 2020

Accepted: 19 April 2021

DOI: 10.18466/827615

Abstract

Microalgae are widely used in biotechnological research, especially for the production of biochemical compounds, antioxidants, secondary metabolites, pigments, carbohydrates, proteins and lipids. Various analytical methods are needed throughout both experimental and downstream processing of industrial microalgae products. As one of these methods, flow cytometry is an advantageous option for detecting fluorescently labeled recombinant proteins, lipids and metabolic compounds. It is important to take into account the autofluorescent properties of specific compartments of target cells to well establish a distinct labeling protocol during such analytical processes. Because the amount of autofluorescence may interfere with the fluorescent signal detection of specifically labeled protein or lipid content, this can prevent the precise signal detection of labeled molecules. Furthermore, it can lead to an overestimation of the amount of labeled compounds in the cells. In this study, the autofluorescent properties of two freshwater model microalgae *Chlamydomonas reinhardtii* (CC-124) and *Chlorella vulgaris* (CV-898), both of which are predominantly used in industry, were examined by flow cytometry measurements. The experimental findings revealed that fluorescent channel-2 (FL2-H) stands as the most suitable channel to achieve minimal autofluorescence of both CC-124 and CV-898 microalgae strains. The obtained results highlight that one should pay attention to the autofluorescence signals in CC-124 and CV-898 cell lines during the flow cytometry-based detection of biological products when deciding on fluorophore.

Keywords: autofluorescence, cellular morphology, flow cytometry, microalgae

1. Introduction

Microalgae are widely preferred eukaryotic microorganisms in biotechnology as they can produce health promoting lipids, antioxidants, polysaccharides, proteins, secondary metabolites, vitamins and pigments [1]. As the evolutionary ancestors of terrestrial plants, they can be easily cultivated at laboratory conditions in the presence of natural sunlight, atmospheric CO₂, varieties of different low-cost carbon sources and the infinitesimal amounts of trace elements [2]. They currently provide numerous advantages to industrial biotechnology as food and feed supplies with high protein content, feedstocks for different biofuels production processes and sustainable bioremediation agents for municipal and urban wastewaters, all of which make microalgae essential for next generations [3, 4]. As microalgae genome manipulation tools are pretty much

well established, the metabolic engineering efforts on industrially promising microalgae strains

become relatively common [5, 6]. Microalgae are of growing interest towards various mass production systems, particularly for bioenergy, lucrative metabolites, antioxidants, nutraceuticals and pharmaceuticals [7, 8]. In addition, the specific use of photosynthetic microalgae as recombinant production hosts comprises the mass production of value-added compounds, anticarcinogenic and antimicrobial drugs, monoclonal antibodies, pharmaceutical proteins, vaccines, drug additives and various compounds used in cosmetics [9, 10]. On the other hand, it is very important to carry out comprehensive analytical, biochemical and molecular analyzes on newly discovered microalgae strains with reliable analytical methods to reveal their industrial use and commercialization potentials biotechnologically. [11].

During cultivation and downstream processes, the native biological characteristics of microalgae can be disclosed by employing different analytical methods, such as fluorescence and/or electron microscopy, quantitative metric measurements, multi-dimensional single-cell analysis and molecular biology-based diagnostic tools [12]. Recently, different cell sorting mechanisms combined with flow cytometry have been developed and successfully applied to microalgae cultures to eliminate various culture contaminants including bacteria [13]. Electrical microfluidics chips with advanced separation and recognition characteristics were also adapted for microalgae cultures to recognize, label and eventually eliminate culture contaminants [14]. In addition, direct electrical detection of a single bacterium in drinking water could be a highly practical technique for ensuring the contamination-free maintenance and sustainability of open pond microalgae production systems in the future. [15].

Flow cytometry is one of the high-throughput instruments to quantitatively examine the cell size, granularity, heterogeneity of microalgae cells and related culture populations using fluorescence beams [16]. Flow cytometry provides visualization and classification of cells within morphological shapes and analysis of fluorophore-tagged signals of the molecule of interest such as proteins, carbohydrates and lipids. Preparation of cells for analysis by flow cytometry is performed based on immunolabeling approaches. One of the foremost methodological key points during standard flow cytometry analysis is to initially detect the autofluorescence of cells. Autofluorescence is defined as inherent cellular fluorescence derived by the emission of natural compounds within cells, such as chlorophyll and NADH [17]. Such interference of autofluorescence with the specific label was also reported from certain types of mammalian cells [18]. However, to the best of our knowledge, no scientific report has yet been released regarding the natural autofluorescence spectra of the freshwater microalgae strains examined, suggesting the requirement of an optimization step during the flow cytometry-based experimental and analytical processes. This study thus aimed to unravel the cellular autofluorescence spectra of two model microalgae *Chlamydomonas reinhardtii* (CC-124) and *Chlorella vulgaris* Beijerinck (CV-898) cells.

2. Materials and Methods

2.1. Microalgae Culturing and Flow Cytometry Analysis

Chlamydomonas reinhardtii (CC-124: CCALA No: 928) and *Chlorella vulgaris* Beijerinck (CV-898: CCALA No: 898) strains were obtained from Culture Collection of Autotrophic Organisms (CCALA) at Dukelska, Czech Republic. Both strains were immediately enriched in TAP broth or agar plates. 1×10^6 microalgae cells were

then taken and incubated within 100 ml modified TAP (Tris-Acetate-Phosphate) medium on an orbital shaker at room temperature and 120 rpm shaking speed for 5 days. At least 500.000 cells (counted by Countess II FL Automated Cell Counter, Thermofisher), in the presence of over 96% cell viability detected by hemacytometer-based counting, either in the phosphate-buffered saline buffer (1xPBS) or in TAP media were run by flow cytometer, C6 Accuri (from BD Biosciences). Cells were visualized by forward scatter (FSC)-side scatter (SSC) dot plot, and then analyzed by fluorescence channels; FL1-H, FL2-H, FL3-H and FL4-H. Table 1 reveals the excitation and emission values and filters for each channel. 1xPBS and TAP medium alone were also run to understand the background fluorescence of the cell suspensions. Figure 1 represents the wavelengths of each channel. The cell morphology was assessed by FSC (X-axes) and SSC (Y-axes) values (as mean, geometric mean and median), representing the cell size and granularity, respectively. The fluorescence signals of at least 500.000 cells were collected through the employment of a 488 nm laser beam and further analyzed using different filters as shown in Table 1. The autofluorescence patterns of gated cells (P1) were also revealed in the charts by fluorescence channels (FL1-H, FL2-H, FL3-H and FL4-H). Both PBS and TAP medium were also analyzed as blank controls to the cell samples. At least 10.000 events were analyzed for each triplicate experimental run.

Table 1. Excitation and emission of fluorescence channels

	FL1-H	FL2-H	FL3-H	FL4-H
Excitation (nm)	488	488	650	470
Emission (nm)	500-550	550-600	650-700	650
Filter	533/30 (530 BP)	585/40 (585 BP)	670 LP	675/25 (675 BP)

3. Results and Discussion

Recent advances in recombinant DNA technology and genome editing tools have increased R&D initiatives on microalgae strains with renewable, sustainable and economic potentials towards versatile production of various value-added products, secondary metabolites, natural pigments, antioxidants, hydrocarbons, biofuels and derivatives. On the other hand, innovative approaches mostly relying on metabolic engineering and systems biology to develop microalgae strains with improved properties yield abundant recombinants that necessitate extensive screening efforts for targeted product(s). Comparative screening and quantitative analysis of natural and/or recombinantly engineered microalgae cells is of paramount importance for the final selection and full characterization of the most promising strains. In this regard, flow cytometry is a simple

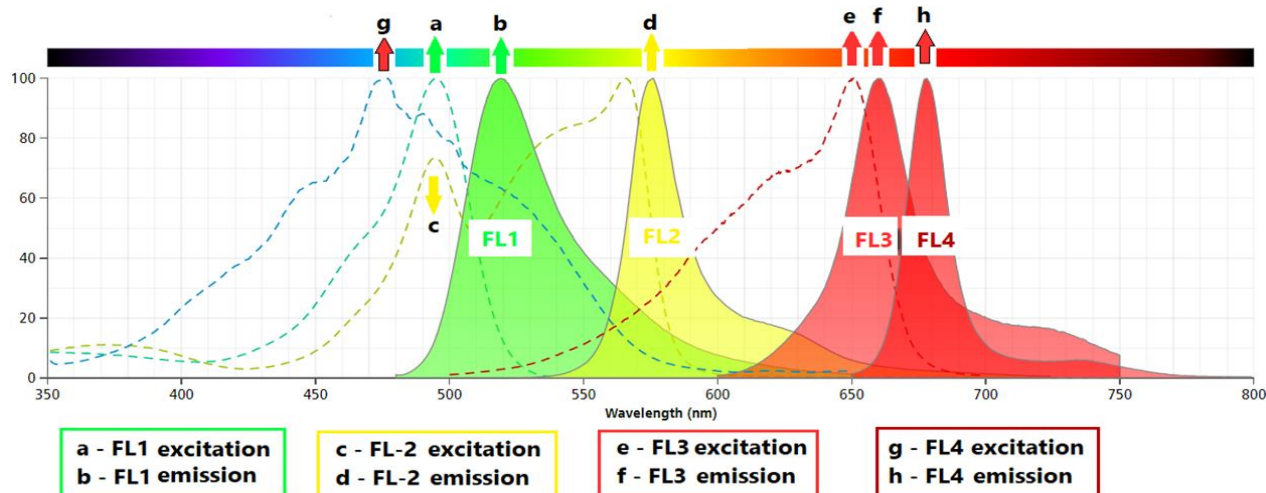


Figure 1. Representative wavelengths for emission and excitation of fluorescence channels 1, 2, 3 and 4 of BD Accuri C6 instrument using FITC, PE, APC and PerCP, respectively (*modified from BD Biosciences's web site*). The spectra can be modified according to dye type.

operational and analytical platform for the quantification of various microalgae cell components and related by-products. To specifically analyze, label and even separate microalgae single cells, numerous high throughput methods with advanced analytical potentials including flow cytometry, electrical flow cytometry, electrical microfluidics chip and fluorescence-activated cell sorting have recently been reported [14, 15, 19, 20]. Among them, flow cytometry allows automatic, low-cost, high-speed and simultaneous analysis of multiple parameters of microalgae cells through qualitative and quantitative measurements of biological and physical characteristics.

Two model microalgae isolates with the adaptation to the cool temperate environments were examined to identify their cellular autofluorescence patterns by flow cytometer, C6 Accuri. The comparative run revealed that CC-124 microalgae cells were larger than CV-898 by the mean of events at FSC axes and the granularity of CC-124 was more intense than CV-898 by the mean of events at SSC axes. The median values were close to the maximum values of means (Figure 2a, b). Cell size was proportional to the granularity. Therefore, because the cell sizes were high, the granularity was also large. Microalgae were also routinely evaluated for cellular dry weight (CDW) to highlight biomass productivity. Therefore, determination of cell granularity seems important for understanding biomass production capacity.

The granularity can change in terms of growth phases such as early and late exponential stages. The cells used in this study were mixed at different growth phases to reveal a general pattern of cell morphology. A study revealed the differences in CDW between some microalgae [1], but to the best of knowledge, there is no study showing the cell size differences through cell granularity by SSC dot plot of flow cytometry analysis.

Some studies use microscopy to understand the sizes of cells [21]. In this scenario, high-resolution microscopy equipped with at least 63X objective might be practical for better visualization of microalgae cells. Therefore, we suggest that microscopies with higher performance could be preferred to perform such comparison comprehensively.

The cellular autofluorescence pattern of the cells was also examined by the implementation of different fluorescence channels. As control, the fluorescence amount of both PBS and microalgae media were firstly detected at a similar range with the cells. We identified that, at FL2-H, PBS is a more suitable environment to run cells in terms of a relatively low level of autofluorescence compared to TAP medium (Figure 3a, b). The lowest fluorescence of both microalgae cells was detected at the FL2-H channel; however, the highest was identified at FL3-H (Figure 3c, d). Experiments need to be adjusted by the subtraction of the mean of fluorescence intensity (MFI) of PBS or TAP medium from the MFI of cells. Image-based [22] or standard flow cytometry [16] are in use to analyze cellular components of microalgae. However, the interference of autofluorescence with the detection of the specific markers of interest was overlooked.

The chlorophyll content of microalgae is one of the main sources of cellular autofluorescence, and fluorescence is used to be measured in cells detected at forward and side scatter plots [23]. As similar, a typical automated cell counter was further optimized for the facilitated quantification of chlorophyll content in microalgae [24]. Nevertheless, our previous work illustrated that although automated cell counter was not favorably effective, flow cytometry-based analysis was revealed as the best analytical instrument to work with microalgae [25], as also commonly stressed by other researchers [26–28].

Flow cytometry is used not only for the detection of fluorescence labeled-components, but also viability detection, biomass estimation, population heterogeneity detection, cell sorting and isolation of axenic algal cultures [29, 30]. Therefore, the elucidation of

autofluorescence patterning in model microalgae is detected by flow cytometry. Recently, the ontological pattern of autofluorescence was also considered to improve spectroscopic methods [31]. In parallel, crucial

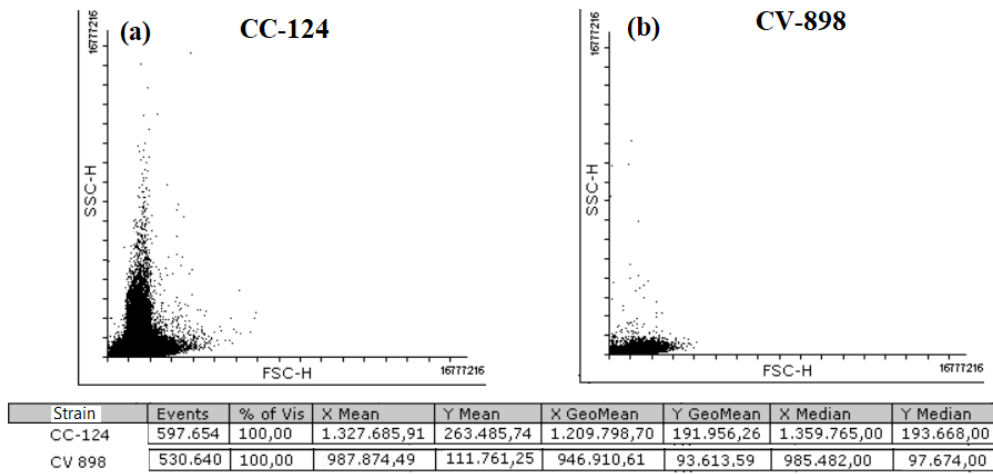


Figure 2. The morphological features of CC-124 (a) and CV-898 (b) by FSC (*forward scatter*) and SSC (*side scatter*) representing cell size and granularity, respectively (X and Y axes were adjusted to 16 million unit).

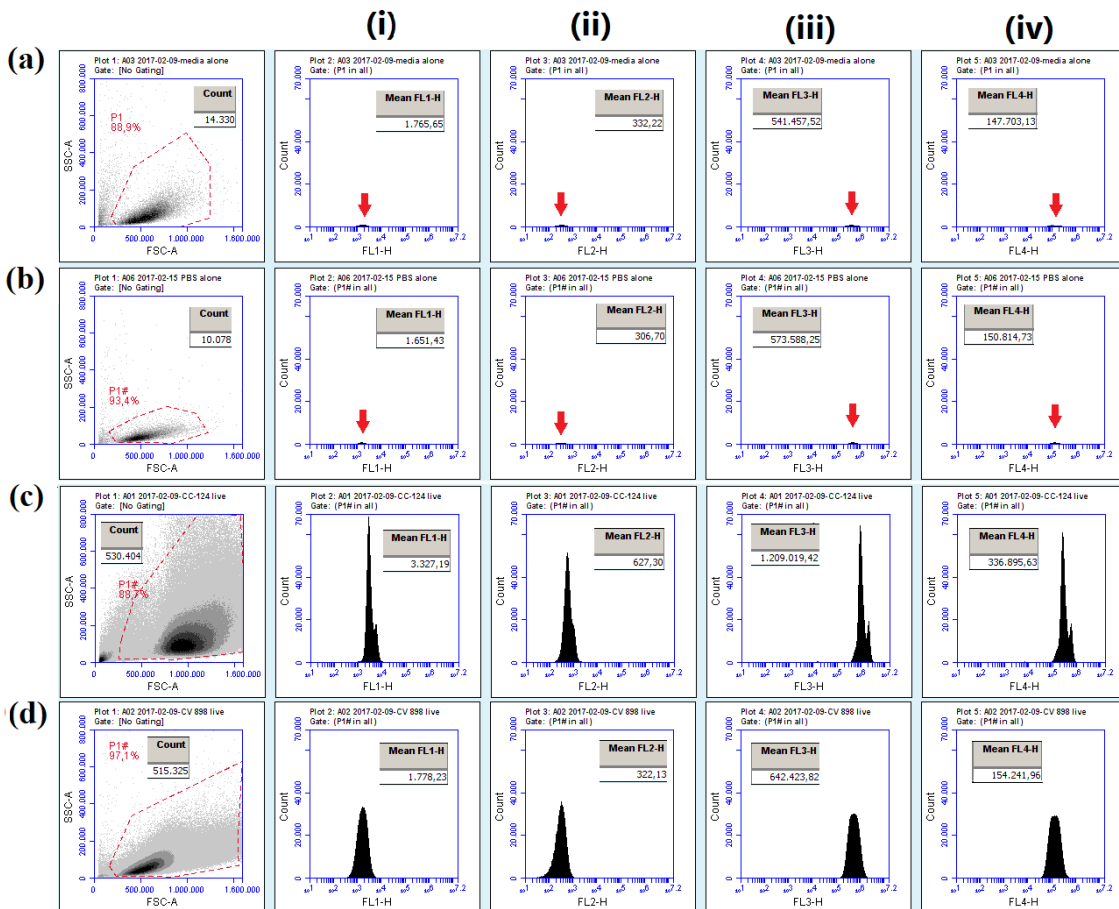


Figure 3. The autofluorescence patterns of TAP medium (a), and PBS buffer (b), CC-124 (c) and CV-898 microalgae cells (d) along with the fluorescence channels (i-iv). (X and Y-axes in cell size (FSC) and granularity (SSC plots) were adjusted to 1.6 million unit).

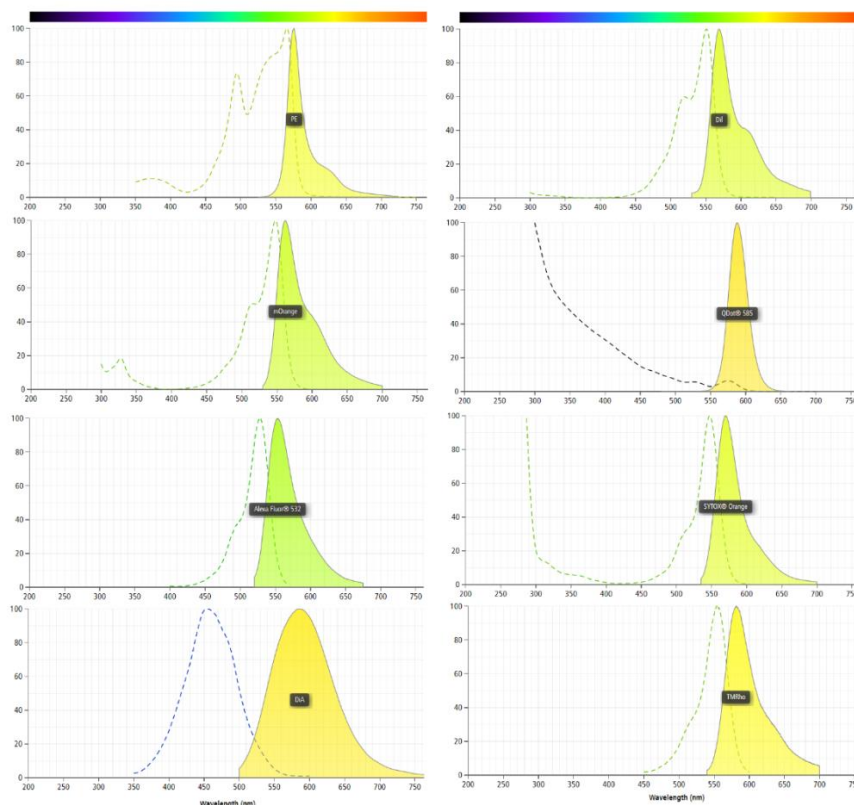


Figure 4. Example wavelengths of some fluorophores given in Table 2.

Table 2. Recommended fluorophores for the signal detection by FL2 channel.

PE	BVU563
mOrange	SYTOX ® Orange
Alexa Fluor ® 532	TMRho
DiA	Kusabira-Orange
Dil	mStrawberry
QDot ® 565	Cy3.5
QDot ® 585	Cy3B
QDot ® 605	Cy3
QDot ® 625	

in terms of the optimization of labeling methods electrophoresis was shown to be a parameter for the investigation of microalgal diversity [32].

Based on the literature, there is no reported study revealing the autofluorescence distributions of microalgae, in particular for both CC-124 and CV-898. These microalgae are of model organisms in industrial biotechnology towards to production of various value-added compounds, proteins, vaccines, biofuels and other bioproducts. Industrially crucial lipids and recombinant proteins as microalgae bioproducts are labeled by fluorophores and flow cytometry can provide cost-effective and handy outputs to disclose these labels and the total amount of bioproducts.

The current findings also suggest that the best strategy to perform any flow cytometry based measurements on both CC-124 and CV-898 model microalgae is to select a fluorophore emitted at fluorescence channel-2. Table 2 exemplifies some of such representative fluorophores. On the other hand, Figure 4 displays the wavelength distributions of some fluorophores given in Table 2, emitting specifically at FL2-H (Figure 4).

4. Conclusion

We found that the minimum fluorescence signal from both model microalgae strains was obtained at only fluorescence channel-2 (FL2-H) of 4 channels. In other words, the obtained results suggest that the most suitable fluorophores for CC-124 and CV-898 cells are the fluorophores emitting at FL2-H. In conclusion, the specific label of interest does not mix with natural signals in both CC-124 and CV-898 cells when the reported results are in consideration. The current knowledge will certainly be practical for the quantitative production of various biomaterials during the versatile biotechnological applications of microalgae.

Acknowledgement

This work was supported by Scientific Research Projects Coordination Unit of Karadeniz Technical University. Project number: FAY-2016-5755. The author thanks to Ramazan ÇAKMAK due to the preparations of microalgae cell cultures and to Prof. Ersan KALAY



allowing to utilize of flow cytometry instrument at the Department of Medical Biology at KTU.

Author's Contributions

Ugur Uzuner: The study was hypothesized, designed, performed and written by Ugur Uzuner.

Ethics

Authors declare that there are no ethical issues related to publication of this manuscript. The performed study is out of scope of any ethical issues.

References

1. Abomohra AE-F, Wagner M, El-Sheekh M, Hanelt D (2013) Lipid and total fatty acid productivity in photoautotrophic fresh water microalgae: screening studies towards biodiesel production. *J Appl Phycol* 25:931–936. <https://doi.org/10.1007/s10811-012-9917-y>
2. Shuba ES, Kifle D (2018) Microalgae to biofuels: 'Promising' alternative and renewable energy, review. *Renewable and Sustainable Energy Reviews* 81:743–755. <https://doi.org/10.1016/j.rser.2017.08.042>
3. Hossain N, Mahlia TMI, Saidur R (2019) Latest development in microalgae-biofuel production with nano-additives. *Biotechnology for Biofuels* 12:125. <https://doi.org/10.1186/s13068-019-1465-0>
4. Torres-Tiji Y, Fields FJ, Mayfield SP (2020) Microalgae as a future food source. *Biotechnology Advances* 41:107536. <https://doi.org/10.1016/j.biotechadv.2020.107536>
5. Fayyaz M, Chew KW, Show PL, et al (2020) Genetic engineering of microalgae for enhanced biorefinery capabilities. *Biotechnology Advances* 43:107554. <https://doi.org/10.1016/j.biotechadv.2020.107554>
6. Kwon YM, Kim KW, Choi T-Y, et al (2018) Manipulation of the microalgal chloroplast by genetic engineering for biotechnological utilization as a green biofactory. *World J Microbiol Biotechnol* 34:183. <https://doi.org/10.1007/s11274-018-2567-8>
7. Yan N, Fan C, Chen Y, Hu Z (2016) The Potential for Microalgae as Bioreactors to Produce Pharmaceuticals. *International Journal of Molecular Sciences* 17:962. <https://doi.org/10.3390/ijms17060962>
8. Jha D, Jain V, Sharma B, et al (2017) Microalgae-based Pharmaceuticals and Nutraceuticals: An Emerging Field with Immense Market Potential. *ChemBioEng Reviews* 4:257–272. <https://doi.org/10.1002/cben.201600023>
9. Szyrka E, Broda D, Oklejewicz B, et al (2020) A Non-Vector Approach to Increase Lipid Levels in the Microalga *Planktochlorella nurekis*. *Molecules* 25: . <https://doi.org/10.3390/molecules25020270>
10. U NM, Mehar JG, Mudliar SN, Shekh AY (2019) Recent Advances in Microalgal Bioactives for Food, Feed, and Healthcare Products: Commercial Potential, Market Space, and Sustainability. *Comprehensive Reviews in Food Science and Food Safety* 18:1882–1897. <https://doi.org/10.1111/1541-4337.12500>
11. Niccolai A, Chini Zittelli G, Rodolfi L, et al (2019) Microalgae of interest as food source: Biochemical composition and digestibility. *Algal Research* 42:101617. <https://doi.org/10.1016/j.algal.2019.101617>
12. Sandmann M, Schafberg M, Lippold M, Rohn S (2018) Analysis of population structures of the microalga *Acutodesmus obliquus* during lipid production using multi-dimensional single-cell analysis. *Scientific Reports* 8:6242. <https://doi.org/10.1038/s41598-018-24638-y>
13. Yuan D, Zhao Q, Yan S, et al (2019) Sheathless separation of microalgae from bacteria using a simple straight channel based on viscoelastic microfluidics. *Lab Chip* 19:2811–2821. <https://doi.org/10.1039/C9LC00482C>
14. Bilican I, Bahadir T, Bilgin K, Guler MT (2020) Alternative screening method for analyzing the water samples through an electrical microfluidics chip with classical microbiological assay comparison of *P. aeruginosa*. *Talanta* 219:121293. <https://doi.org/10.1016/j.talanta.2020.121293>
15. Guler MT, Bilican I (2018) Capacitive detection of single bacterium from drinking water with a detailed investigation of electrical flow cytometry. *Sensors and Actuators A: Physical* 269:454–463. <https://doi.org/10.1016/j.sna.2017.12.008>
16. da Silva TL, Reis A, Medeiros R, et al (2009) Oil production towards biofuel from autotrophic microalgae semicontinuous cultivations monitorized by flow cytometry. *Appl Biochem Biotechnol* 159:568–578. <https://doi.org/10.1007/s12010-008-8443-5>
17. Benson RC, Meyer RA, Zaruba ME, McKhann GM (1979) Cellular autofluorescence--is it due to flavins? *J Histochem Cytochem* 27:44–48. <https://doi.org/10.1177/27.1.438504>
18. Uzuner-Celik S, Peters, L, O'Neill C (2016) Quenching of cellular autofluorescence is necessary for specific detection of DNA methylation by flow cytometry compared to microscopy-based analysis. In: *FEBS Journal*. FEBS PRESS, Kusadasi, TURKEY, pp 249–250
19. Patel A, Antonopoulou I, Enman J, et al (2019) Lipids detection and quantification in oleaginous microorganisms: an overview of the current state of the art. *BMC Chemical Engineering* 1:13. <https://doi.org/10.1186/s42480-019-0013-9>
20. Terashima M, Freeman ES, Jinkerson RE, Jonikas MC (2015) A fluorescence-activated cell sorting-based strategy for rapid isolation of high-lipid *Chlamydomonas* mutants. *Plant J* 81:147–159. <https://doi.org/10.1111/tpj.12682>
21. Nezhad FS, Mansouri H (2019) Induction of Polyploidy by Colchicine on the Green Algae *Dunaliella salina*. *Russian Journal of Marine Biology*. <https://doi.org/10.1134/S1063074019020093>
22. Jeon S-M, Kim JH, Kim T, et al (2015) Morphological, Molecular, and Biochemical Characterization of Monounsaturated Fatty Acids-Rich *Chlamydomonas* sp. KIOST-1 Isolated from Korea. *J Microbiol Biotechnol* 25:723–731. <https://doi.org/10.4014/jmb.1412.12056>
23. Takahashi T (2019) Routine Management of Microalgae Using Autofluorescence from Chlorophyll. *Molecules* 24:4441. <https://doi.org/10.3390/molecules24244441>
24. Takahashi T (2018) Applicability of Automated Cell Counter with a Chlorophyll Detector in Routine Management of Microalgae. *Scientific Reports* 8:4967. <https://doi.org/10.1038/s41598-018-23311-8>
25. Koç E, Çelik-Uzuner S, Uzuner U, Çakmak R (2018) The Detailed Comparison of Cell Death Detected by Annexin V-PI Counterstain Using Fluorescence Microscope, Flow Cytometry and Automated Cell Counter in Mammalian and Microalgae Cells. *Journal*



of *Fluorescence* 28:1393–1404. <https://doi.org/10.1007/s10895-018-2306-4>

26. Sonowal S, Chikkaputtaiah C, Velmurugan N (2019) Role of flow cytometry for the improvement of bioprocessing of oleaginous microorganisms. *Journal of Chemical Technology & Biotechnology* 94:1712–1726. <https://doi.org/10.1002/jctb.5914>
27. Bodénès P, Wang H-Y, Lee T-H, et al (2019) Microfluidic techniques for enhancing biofuel and biorefinery industry based on microalgae. *Biotechnology for Biofuels* 12:33. <https://doi.org/10.1186/s13068-019-1369-z>
28. Markina ZhV (2019) Flow Cytometry as a Method to Study Marine Unicellular Algae: Development, Problems, and Prospects. *Russ J Mar Biol* 45:333–340. <https://doi.org/10.1134/S1063074019050079>
29. Hyka P, Lickova S, Přibyl P, et al (2013) Flow cytometry for the development of biotechnological processes with microalgae. *Biotechnology Advances* 31:2–16. <https://doi.org/10.1016/j.biotechadv.2012.04.007>
30. Reimann R, Zeng B, Jakopec M, et al (2020) Classification of dead and living microalgae *Chlorella vulgaris* by bioimage informatics and machine learning. *Algal Research* 48:101908. <https://doi.org/10.1016/j.algal.2020.101908>
31. Hadady H, Redelman D, Hiibel SR, Geiger EJ (2016) Continuous-flow sorting of microalgae cells based on lipid content by high frequency dielectrophoresis. *AIMS Biophysics* 3:398. <https://doi.org/10.3934/biophy.2016.3.398>
32. Grigoryeva N (2019) Self-Fluorescence of Photosynthetic System: A Powerful Tool for Investigation of Microalgal Biological Diversity. *Microalgae - From Physiology to Application*. <https://doi.org/10.5772/intechopen.88785>

A Novel Donor- π -Acceptor Type Sensitizer for Dye Sensitized Photochemical Hydrogen Generation

Emre Aslan^{1*} 

¹ Selcuk University, Department of Biochemistry, Konya, Turkey

*emreaslan89@gmail.com

*Orcid: 0000-0002-7672-2873

Received: 22 December 2020

Accepted: 19 April 2021

DOI: 10.18466/cbayarfb.844704

Abstract

A novel triphenylamine (TPA) based donor- π -acceptor (D- π -A) dye is synthesized and its structural, optical and electrochemical properties are examined by NMR, UV-Vis absorption spectroscopy and cyclic voltammetry methods, respectively. The synthesized D- π -A dye plays a role as a visible light sensitizer to wide bandgap TiO₂ photocatalyst. Photoelectrochemical and photocatalytic hydrogen evolution reaction (HER) are investigated by using D- π -A dye sensitized TiO₂ (Dye/TiO₂) under visible light irradiation in the aqueous triethanolamine (TEOA) sacrificial electron donor medium. Photoelectrochemical properties of Dye/TiO₂ are investigated by using linear sweep voltammetry (LSV) and chronoamperometry (CA) techniques in the aqueous Na₂SO₄/TEOA solution and its transient photoelectrochemical response is reached 90 $\mu\text{A cm}^{-2}$. In addition, photocatalytic hydrogen evolution rates are found out as 0.52 mmol g⁻¹ h⁻¹ and 1.95 mmol g⁻¹ h⁻¹ by using of Dye/TiO₂ and Dye/TiO₂/Pt, respectively, which are obtained by in situ photoreduction of H₂PtCl₆ on the Dye/TiO₂ photocatalyst. The mechanism of photochemical HER is explained by electrochemical band levels of the D- π -A dye and TiO₂ photocatalyst.

Keywords: dye sensitization, donor- π -acceptor dye, hydrogen evolution reaction, photocatalysis, photoelectrochemical

1. Introduction

The first hydrogen evolution study was performed by using TiO₂ in 1972 with photoelectrochemical method [1]. The development of photocatalytic activity of TiO₂ carried out from that day up to the present. However, there are two big drawbacks of TiO₂, which are high charge recombination rate and absorption only UV light due to the having wide band gap [2]. These disadvantages can be figured out by using co-catalysts to separate charges efficiently and visible light sensitizers to absorb having low energy light. Decreasing of recombination rate and increasing charge separation efficiency are generally utilized on metallic or semiconductor co-catalysts. Although semiconductor co-catalysts are hard to utilize in the photocatalytic reactions because it has to adjust their energy band levels for electron transfer mechanism. Yet, metallic co-catalysts are very useful for easy-to-handle for photocatalytic reactions. It can be clearly seen that Pt is the most used and active co-catalyst for the electrocatalytic, photoelectrochemical and photocatalytic hydrogen evolution reaction (HER) [3]. Wide band gap semiconductor such as TiO₂, ZnO etc.

can be used for water splitting to produce both oxygen and hydrogen under high energy light illumination. However, they are very limited to excite by solar spectrum due to their wide band gap. In order to excite these semiconductors for visible-light-driven water splitting can be modified by doping an ion to narrow the band gap or developing alloys to control the band structure. Another effective approach for harvesting more solar irradiation is the utilization of dye sensitizer. Dye sensitized semiconductor for water splitting by using Ru(bpy)₃²⁺ sensitized Pt/TiO₂/RuO₂ derivatives for the first time [4]. In addition, metal centered porphyrin and phthalocyanine analogues common studied for the photocatalytic reactions due to the high absorption of solar spectrum and adjustable energy levels [5, 6]. Then, metal-free sensitizers have been recently developed for the photocatalytic reactions because of its tunable structure and light absorption region, variety and low-cost. Especially, xanthene dyes and its derivatives have been utilized for photocatalytic hydrogen evolution as the efficient and stable sensitizers [7-9]. Xanthene dyes absorb solar light between 400–600 nm at the 490–560 nm absorption peaks, which is similar to Ru-complex dyes, as alternatives to expensive

Ru-complexes. They found that heavy-halogenated xanthenes have high quantum efficiency for hydrogen evolution, however, they tend to photodehalogenate and instabilities [10]. Due to the increasing photocatalytic activities and stabilities, new class of sensitizers, donor- π -acceptor (D- π -A) dyes developed. They have high intermolecular charge transfer (ICT) ability and configurable absorption, which can be provided high photocatalytic efficiencies and absorption of solar spectrum [11-14]. Recently, donor- π -acceptor (D- π -A) dyes great attention for the both dye sensitized solar cells (DSSC) and photochemical energy conversion reactions because of the mentioned properties above. The high ICT performances of D- π -A dyes reduce the recombination rates [11]. Photocatalytic activities of D- π -A dyes can be changed by different structural properties such as hydrophilicity and steric effect, the amount of dye load, spacer length and the number of anchoring groups of dyes [15-20]. D- π -A dyes consisted of donor groups, π bridge and acceptor groups. Generally, triphenylamine (TPA) based donor moieties have recently been preferred due to prevent aggregations from its non-planar structures by its ease in oxidation of the nitrogen center and own the ability to transport charge carriers via the radical cation species with high stability [21]. Kang research group investigated photocatalytic HER performance by changing chain length in the EDTA solution and reported the dependence on the hydrophilic/hydrophobic character of the binding group to the TPA donor moieties [15, 17]. Tiwari et al. reported that changing π -spacer groups are effectively prevented the aggregation between dye molecules. In addition it provides an well surface protection, which decrease the charge recombination in photocatalytic HER [22]. Li et al. examined by changing of different electronegativities of atom in the π -spacer groups and figured out having high electronegative atoms increased photocatalytic activity [23]. Dessi et al. investigated that photocatalytic HER performances of TPA based D- π -A dyes are improved by increasing donor moieties with the hexyloxy chains attached to the on its terminal TPA group [24]. Moreover, our research group were reported TPA based D- π -A dye sensitized TiO₂ photocatalysts for photocatalytic and photoelectrochemical hydrogen evolution in the triethanolamine (TEOA) sacrificial electron donor media under solar irradiation [25-28]. In these works, firstly, photocatalytic and photoelectrochemical activities on the HER were examined in the absence and presence of extra electron donating two hexyloxy groups on the TPA. Herein, dye without hexyloxy groups displayed more photochemical activity due to its advanced optical absorption and ICT properties [25]. Then, the effect of π -spacer group has investigated in the photocatalytic HER and figured out that adding π -spacer group eventuated higher photocatalytic HER activity [26]. Finally, the very similar TPA based D- π -A dyes were studied by our research group and examined the effect of acceptor and

spacer group on the photocatalytic and photoelectrochemical HER activities. Here, having high electronegativity of an atom in the spacer group increased the photochemical HER activity [27]. In addition, while it suggested that increasing the acceptor strength raise the photocatalytic HER performance, adversely affect the HER activity because it give rise to aggregation of dyes on the TiO₂ photocatalyst [28]. In this study, a novel donor- π -acceptor (D- π -A) dye synthesized for the photochemical hydrogen generation from water splitting. Optical and electrochemical properties of the synthesized D- π -A dye were investigated in order to explain the mechanism of photocatalytic hydrogen evolution. D- π -A dye was used to sensitize TiO₂ photocatalyst. Hydrogen evolution is examined by using photoelectrochemical and photocatalytic methods in the presence of triethanolamine (TEOA) as a sacrificial electron donor under visible light illumination.

2. Materials and Methods

2.1. Materials

All solvents and reagents were purchased as puriss quality. Dichloromethane (CH₂Cl₂), chloroform (CHCl₃), n-hexane, tetrahydrofuran (THF), 1,2-dimethoxyethane (DME), [1,10-bi(diphenylphosphino)ferrocene]dichloro palladium (II) and tetrabutylammonium hexafluorophosphate (Bu₄NPF₆) were supplied from Sigma-Aldrich. Potassium carbonate and potassium hydroxide were purchased from Riedel-de Haen. Column chromatography was carried out by using Merck silica gels (230-400 mesh). Acetonitrile (ACN), tetrahydrofuran (THF), triethanolamine (TEOA), hydrochloric acid (HCl), sodium hydroxyde (NaOH) and sodium sulfate (Na₂SO₄) were obtained by Merck for hydrogen generation experiments.

2.2. Synthesis of D- π -A dye

2.2.1. Synthesis of 4'-{6-[5-(4-{bis[4-(hexyloxy)phenyl]amino}phenyl)-4-(2-ethylhexyl)-2-thienyl]-1,2,4,5-tetrazine-3-yl}-3'-(2-ethylhexyl)-2,2'-bithiophene-5-carbonitrile

4-(5-(6-(5-bromo-4-ethylhexyl)thiophen-2-yl)-1,2,4,5-tetrazin-3-yl)-3-(2-ethylhexyl) thiophene-2-yl)-N, N-bis(4-(hexyloxy) phenyl)aniline (115 mg; 0.116 mmol) and 5-(4,4,5,5-tetramethyl-1,3,2-dioxaborolan-2-yl) thiophene-2-carbonitrile (38 mg; 0.164 mmol) were dissolved in anhydrous DME and K₂CO₃ (54 mg; 0.394 mmol) (in 0.5 mL water) was added. After the solution was saturated with argon gas, Pd(dppf)Cl₂ (5.1 mg; 0.007 mmol) was added. The reaction was stirred for 48h at 90 °C, then cooled to room temperature. The mixture was poured into water (30 mL) and extracted with chloroform and dichloromethane. Organic phases were combined and evaporated by rotary. The product was purified with column chromatography (silica gel, CH₂Cl₂:MeOH 15:0.5).

2.2.2. Synthesis of 4'-{6-[5-(4-{bis[4-(hexyloxy)phenyl]amino}phenyl)-4-(2-ethylhexyl)-2-thienyl]-1,2,4,5-tetrazine-3-yl}-3'-(2-ethylhexyl)-2,2'-bithiophene-5-carboxylic acid (D- π -A dye)

5'-{6-[5-(4-{bis[4-(hexyloxy)phenyl]amino}phenyl)-4-(2-ethylhexyl)-2-thienyl]-1,2,4,5-tetrazine-3-yl}-3'-(2-ethylhexyl)-2,2'-bithiophene-5-carbonitrile (76.4 mg; 0.075 mmol) was dissolved in THF/MeOH (1:1, 10 ml) in the two necked flask. 2 M KOH (0.19 ml) was added into the mixture and refluxed for 48h. The reaction was controlled with TLC and neutralized with HCl. The crude product was extracted with water/CH₂Cl₂ (1:2). The product was purified with a silica gel column chromatography (CH₂Cl₂, CH₂Cl₂/MeOH 15:1) (Figure 1).

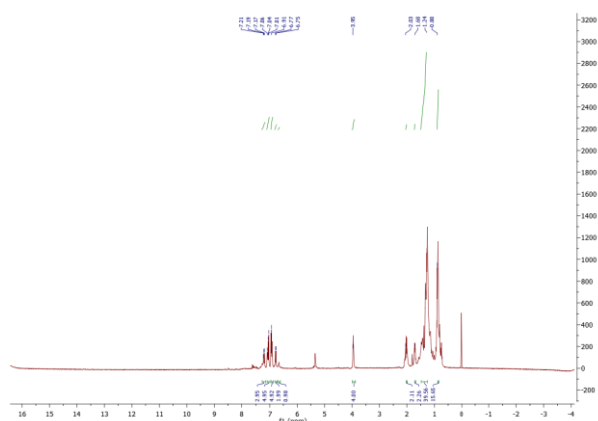


Figure 1. NMR spectrum of synthesized D- π -A dye

2.3. Optical and electrochemical experiments

Optical and electrochemical properties of D- π -A dye have been investigated by Shimadzu UV-1800 UV-Vis absorption spectrophotometer and CH 760D potentiostat, respectively. Absorption spectrum was performed by using 10⁻⁵ M dye solution in tetrahydrofuran (THF). Molar extinction coefficients (ϵ) of dyes have been calculated by using Beer-Lambert law [29]. Electrochemical properties and band diagrams of dye were examined by cyclic voltammetry technique in acetonitrile (ACN) by using 0.1 M tetrabutylammonium hexafluorophosphate (Bu₄NPF₆) solution as supporting electrolyte with standard three electrode setup using glassy carbon electrode (GCE), Pt wire and Ag/AgCl electrodes act as working, counter and reference electrodes, respectively. HOMO and LUMO levels were calculated from oxidation and reduction potentials, respectively.

2.4. Dye sensitization process

TiO₂ coated fluorine doped tin oxide (FTO) glass electrode and powdered TiO₂ are used for the photoelectrochemical and photocatalytic hydrogen evolution reaction (HER), respectively. The dye sensitization process is the same for the both coated

electrode and powdered TiO₂. Firstly, TiO₂ species were calcinated at 450 °C for 45 minutes in order to eliminate adsorbed water and organic impurities on the surface of TiO₂ before the sensitization process. After the calcination, TiO₂ species have been added into the dye solution (10⁻⁵ M in THF). TiO₂ electrode was kept overnight in the dye solution. Powdered TiO₂ stirred with magnetic mixer overnight in the dye solution under dark conditions. Then dye sensitized TiO₂ species were rinsed by THF and ethanol three times to remove unbinding dye molecules. Finally, dye sensitized TiO₂ species were kept under room condition for drying to use in the photoelectrochemical and photocatalytic hydrogen evolution experiments.

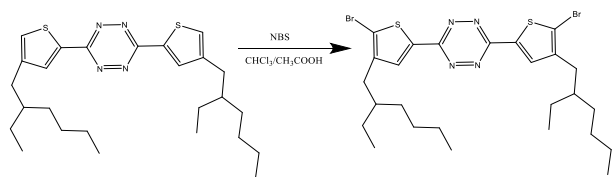
2.5. Photoelectrochemical and photocatalytic HER experiments

Photoelectrochemical properties of dye sensitized TiO₂ electrode were investigated in the 0.1 M Na₂SO₄ and 5% TEOA solution under the LED illumination by on/off cycles. Herein, standard three electrode setup is consisted of dye sensitized TiO₂, Pt plate and Ag/AgCl electrodes act as the photanode working electrode, counter electrode and reference electrode, respectively. Photocatalytic HER experiments were carried out by using powdered TiO₂ sensitized by D- π -A dye in the presence of oxygen-free 5% TEOA solution. This emulsion was prepared in the glove-box and reaction cell is sealed by rubber septum. The sealed reaction cell was put onto solar simulator (Solar Light XPS-300™) and stirring magnetically to occur homogenous photocatalytic reaction. Then, sampling of head space gas taken by gas tight syringe and injected into gas chromatography in order to calculate generated hydrogen amount by using standard calibration curve changing 0.1% and 5% concentration of H₂ in N₂.

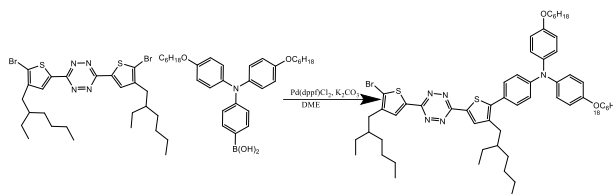
3. Results and Discussion

3.1. Synthesis of D- π -A dye

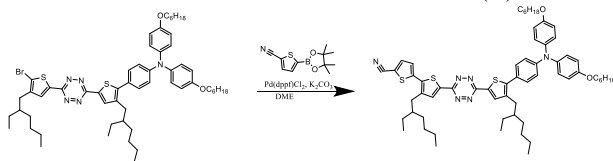
Herein the synthesized D- π -A dye was used as visible light sensitizer. 3,6-bis [4-methylthien-2-yl]-stetrazine (I) was synthesized according to literature [27, 28]. 4'-{6-[5-(4-{bis[4-(hexyloxy)phenyl]amino}phenyl)-4-(2-ethylhexyl)-2-thienyl]-1,2,4,5-tetrazine-3-yl}-3'-(2-ethylhexyl)-2,2'-bithiophene-5-carbonitrile was synthesized between 4-(5-(6-(5-bromo-4-ethylhexyl)thiophen-2-yl)-1,2,4,5-tetrazin-3-yl)-3-(2-ethylhexyl) thiophene-2-yl)-N, N-bis(4-(hexyloxy)phenyl)aniline and 5-(4,4,5,5-tetramethyl-1,3,2-dioxaborolan-2-yl) thiophene-2-carbonitrile by the Suzuki-Miyaura coupling reaction. The intermediate molecule was converted to D- π -A dye by the Knoevenagel condensation reaction.



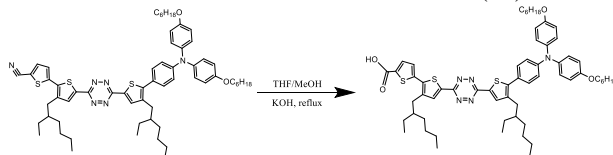
(I)



(II)



(III)



D- π -A dye

Scheme 1. Synthesis procedure and molecular structure of D- π -A dye

3.2. Optical and electrochemical properties of D- π -A dye

Optical properties of D- π -A dye were investigated by UV-Vis absorption spectra. As shown in **figure 2a**, two peaks were observed at the 291 nm and 345 nm originated from localized π - π^* and delocalized π - π^* transitions, respectively, because of intramolecular charge transfer (ICT) properties between donor (triphenylamine) and acceptor (carboxylic acid) groups [30]. Besides, molar absorption coefficient (ϵ) of the sensitizer was calculated as $1800 \text{ M}^{-1} \text{ cm}^{-1}$ (345 nm) by Lambert-Beer Law [29]. Electrochemical properties of sensitizer were investigated by cyclic voltammetry method using glassy carbon electrode (GCE), Pt wire and Ag/AgCl electrodes as working, counter and reference electrodes, respectively, in the 0.1 M tetrabutylammonium hexafluorophosphate (Bu_4NPF_6) solution in acetonitrile (ACN) as a supporting electrolyte. As displayed in **figure 2b**, there is one oxidation peak in the voltammogram at the positive region (0.85 V) because of donor moiety of triphenylamine group. In addition, the peaks at the negative region in the voltammogram are correspond to

π group (-1.00 V and -1.41 V) and acceptor group (-1.85 V, originated from acceptor moieties of carboxylic acid). HOMO and LUMO levels of sensitizer were calculated vs. vacuum level according to equations below [31] from oxidation and reduction potentials, which were found as -5.25 eV and -3.40 eV.

$$E_{\text{LUMO}} = -e(E_{\text{red}} + 4.4) \quad (1)$$

$$E_{\text{HOMO}} = -e(E_{\text{ox}} + 4.4) \quad (2)$$

The electrochemical band gap was figured out as 1.85 eV by subtraction between HOMO and LUMO energy levels. The optical and electrochemical properties of sensitizer in good agreement with before published studies about resemble D- π -A dyes [25-28, 32]. The whole optical and electrochemical parameters of D- π -A dye are given in the **Table 1**.

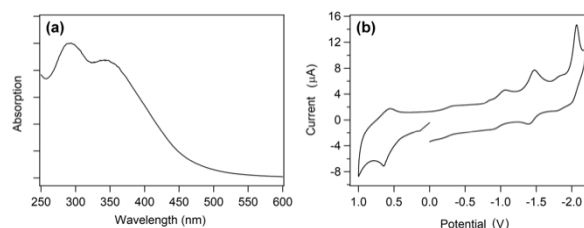


Figure 2. (a) UV-Vis absorption spectra of dye in the THF and (b) cyclic voltammogram of dye by using 0.1 M Bu_4NPF_6 solution in the ACN as supporting electrolyte.

Table 1. Optical and electrochemical parameters of D- π -A dye

	Dye
Absorption Wavelength (λ) / nm	345
Molar Absorption Coefficient (ϵ) / $\text{M}^{-1} \text{ cm}^{-1}$	1800
Oxidation Potential / V	0.85
Reduction Potentials / V	-1.00 / -1.41
HOMO energy level / eV	-5.25
LUMO energy level / eV	-3.40

3.3. Photoelectrochemical and photocatalytic hydrogen evolution

Dye sensitized photochemical water splitting (WS) reactions is named as artificial photosynthesis in the literature studies due to the mimicking the Z-scheme of natural photosynthesis by solar energy into chemical energy [13]. In this study, D- π -A dye has been used as a visible light sensitizer in the both photoelectrochemical and photocatalytic hydrogen evolution reaction from WS. Herein, photochemical reactions have been carried out in the presence of scavenger electron donor triethanolamine (TEOA) in order to increase hydrogen generation by blocking oxygen evolution because it can

be reduced in the presence of generated O_2 and inhibited H_2 generation due to the more positive reduction potential ($E^{O_2/H_2O} = 1.23$ V and $E^{H^+/H_2} = 0.00$ V vs. NHE). In this study, firstly, photoelectrochemical hydrogen evolution experiments have been carried out by linear sweep voltammetry (LSV) and chronoamperometry (CA) techniques by using TiO_2 and D- π -A dye sensitized TiO_2 coated FTO electrodes. Herein, dye sensitized TiO_2 coated FTO, Pt plate and Ag/AgCl electrodes as working, counter and reference electrodes, respectively, under on/off illumination cycles in the oxygen-free aqueous 0.1 M Na_2SO_4 (supporting electrolyte) / 5% TEOA (electron donor) solution. Herein, working electrode utilized as the photoanode because n-type semiconductor electrodes generally participate in photoanode preparation. In the photoelectrochemical system, D- π -A dye excited by light and generated holes and excited electrons. These excited electrons were transferred into Pt plate counter electrode (cathode) to generate hydrogen. Then, the holes in the D- π -A dye on TiO_2 photoanode were refilled by scavenger electron donor TEOA to regenerate the photoelectrochemical system. The hydrogen evolution rates are associated with transient current density and it is directly based on efficiency of intramolecular charge transfer (ICT) properties and absorption of sensitizers on the TiO_2 photoanode [12]. Photoelectrochemical properties of D- π -A dye sensitized TiO_2 electrode was firstly investigated by linear sweep voltammetry (LSV) under visible light illumination with 2 s on/off cycles as shown in **figure 3a**. The D- π -A dye sensitized TiO_2 electrode displayed well-stability between +0.5 V and -0.4 V potential window. After that, CA experiments have been performed in the absence and presence of dye on the TiO_2 electrodes. In the absence of dye, only TiO_2 electrode displays $1 \mu A cm^{-2}$ transient photocurrent density, which was also unstable and inefficient photocurrent character. However, enhancing and stable transient photocurrent density have been monitored by using dye sensitized TiO_2 electrode, which was approximately $90 \mu A cm^{-2}$, during the on/off cycles (**Figure 3a**). These photoactivity and photostability can be originated from absorption of light and intramolecular charge transfer (ICT) properties of D- π -A dye, respectively (*vide supra*). These results are in accordance with the photocatalytic experiment results (*vide infra*).

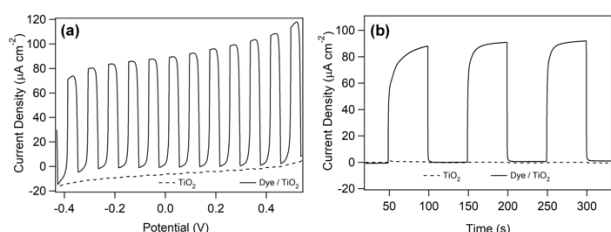


Figure 3. Transient photocurrent response of TiO_2 and D- π -A dye sensitized TiO_2 coated FTO electrodes by using (a) LSV and (b) CA techniques.

Photocatalytic HER properties of D- π -A sensitized TiO_2 have been examined in the aqueous TEOA solution (5%) at pH = 9, which is determined according to our previous studies with very familiar D- π -A dyes [25-28], under solar irradiation ($\lambda \geq 420$ nm) with magnetically stirring for homogenous reaction condition. The amounts of hydrogen generation are shown against time by using Dye/ TiO_2 and Dye/ TiO_2 /Pt, which Pt is occurred by photoreduction of H_2PtCl_6 on the Dye/ TiO_2 photocatalyst, in **figure 4**. The HER rates of Dye/ TiO_2 and Dye/ TiO_2 /Pt were found as 0.52 mmol $g^{-1} h^{-1}$ and 1.95 mmol $g^{-1} h^{-1}$, respectively. After eight hours of photocatalytic reaction 3.00 mmol g^{-1} and 19.23 mmol g^{-1} hydrogen were produced by using Dye/ TiO_2 and Dye/ TiO_2 /Pt, respectively. These results displayed that very stable hydrogen generation rate in the absence and presence of Pt co-catalyst, which can be explained by well intramolecular charge transfer (ICT) of D- π -A type dyes [12].

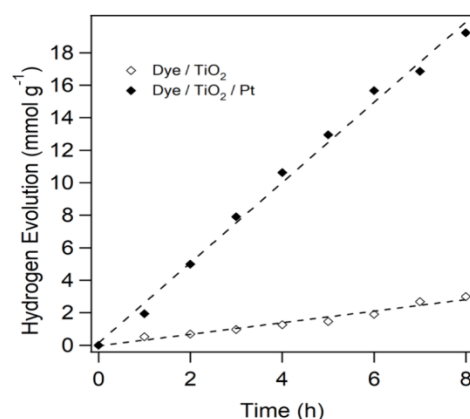


Figure 4. Photocatalytic hydrogen evolution against time by using Dye/ TiO_2 and Dye/ TiO_2 /Pt in the aqueous TEOA (5%) electron donor solution.

The photocatalytic activities of different D- π -A dye sensitized TiO_2 photocatalysts are compared in the same sacrificial media by changing different sensitizers according to our previous studies. These results display that D- π -A dye in this study gives comparable HER rates in the similar conditions.

Table 2. The comparison of HER rates for D- π -A dye with other reported similar structured dye sensitized photocatalytic HER studies

Photocatalysts	HER Rates ($\mu mol g^{-1} h^{-1}$)	References
TiO_2 /MZ-235	531	[25]
TiO_2 /MZ-341	661	
TiO_2 /MC-32	121	[26]
TiO_2 /MZ-048	212	
TiO_2 /MK-3	427	[27]
TiO_2 /MK-4	675	
TiO_2 /MK-2	565	[28]
TiO_2 /MK-8	374	
D- π -A/ TiO_2	520	This work

3.4. Mechanism of HER

The mechanism of dye sensitized hydrogen evolution is figured out by electron transfer mechanism, which generally explained by three main steps. First step is the absorption of light by D- π -A dye and electrons at the HOMO (0.85 V) level are excited to LUMO (-1.00 V) level. Then, the second step are that the photoexcited electrons are injected into conduction band of TiO₂ (-0.5 V). It can be favorable because CB of TiO₂ more positive than LUMO level of dye. The last step is that the excited electrons (e⁻) on the CB of TiO₂ reduced of adsorbed proton onto TiO₂ photocatalyst to generate H₂ gas (or constitute Pt co-catalyst on the TiO₂ in the presence of H₂PtCl₆), also the hole (h⁺) on the HOMO level of dye can be refilled in the same time by giving electrons by electron donor TEOA to regenerate the photocatalytic HER system (Figure 5).

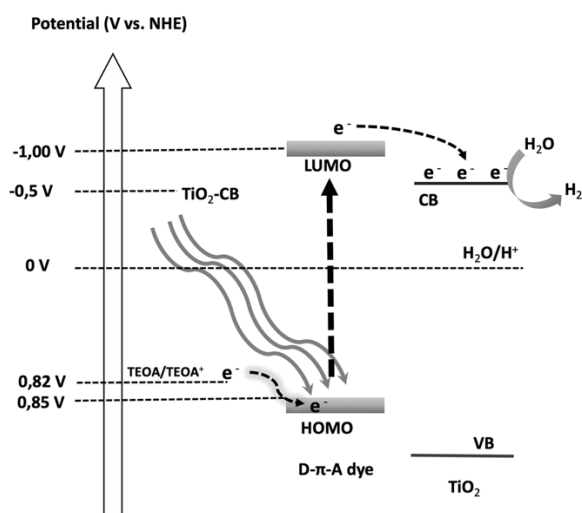
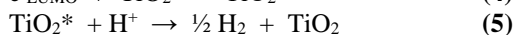
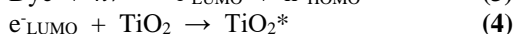
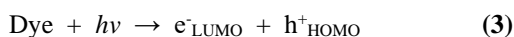


Figure 5. Proposed mechanism of photocatalytic HER by using D- π -A dye sensitized TiO₂

4. Conclusion

A novel D- π -A dye was synthesized and its optical and electrochemical properties were investigated in order to determine light absorption characteristics and electrochemical band levels for explaining reaction mechanism. Photoelectrochemical and photocatalytic HER activities were investigated by D- π -A dye sensitized TiO₂. Herein, advanced photochemical activity of Dye/TiO₂ photocatalyst can be explained by ICT properties of D- π -A dyes for hydrogen evolution. In addition, Dye/TiO₂ the photocatalytic activity of Dye/TiO₂ photocatalyst was dramatically increased adding *in situ* photodeposited co-catalyst Pt. The stabilities of photocatalytic HER were maintained

during the reaction by using both Dye/TiO₂ and Dye/TiO₂/Pt. This study brings on the novel energy application based on light absorption by D- π -A dyes.

Acknowledgement

This work has been done under the umbrella of the Selçuk University Scientific Research Projects (Grant number: 20401033) also accumulation of knowledge from TÜBİTAK-1003 project (Grant number: 215M309). In addition, the author would like to thank to Assoc. Prof. Dr. Mustafa Can from İzmir Katip Çelebi University for the synthesis and characterization of dye molecule, as well as Prof. Dr. Imren Hatay Patir from Selçuk University for the valuable guidance and contributions on the use of laboratory equipment.

Author's Contributions

Emre Aslan: Drafted and wrote the manuscript, performed the experiment and result analysis.

Ethics

There are no ethical issues after the publication of this manuscript.

References

- 1 Fujishima, A. and K. Honda, Electrochemical Photolysis of Water at a Semiconductor Electrode. *Nature*, 1972. **238**(5358): p. 37-38.
- 2 Ma, Y., X. Wang, Y. Jia, X. Chen, H. Han, and C. Li, Titanium Dioxide-Based Nanomaterials for Photocatalytic Fuel Generations. *Chemical Reviews*, 2014. **114**(19): p. 9987-10043.
- 3 Huang, J.-F., Y. Lei, T. Luo, and J.-M. Liu, Photocatalytic H₂ Production from Water by Metal-free Dye-sensitized TiO₂ Semiconductors: The Role and Development Process of Organic Sensitizers. *ChemSusChem*, 2020. **13**(22): p. 5863-5895.
- 4 Borgarello, E., J. Kiwi, E. Pelizzetti, M. Visca, and M. Grätzel, Photochemical cleavage of water by photocatalysis. *Nature*, 1981. **289**: p. 158-160.
- 5 Martín-Gomis, L., F. Fernández-Lázaro, and Á. Sastre-Santos, Advances in phthalocyanine-sensitized solar cells (PeSSCs). *Journal of Materials Chemistry A*, 2014. **2**(38): p. 15672-15682.
- 6 Urbani, M., M. Grätzel, M.K. Nazeeruddin, and T. Torres, Meso-Substituted Porphyrins for Dye-Sensitized Solar Cells. *Chemical Reviews*, 2014. **114**(24): p. 12330-12396.
- 7 Kong, C., S. Min, and G. Lu, Dye-Sensitized NiS_x Catalyst Decorated on Graphene for Highly Efficient Reduction of Water to Hydrogen under Visible Light Irradiation. *ACS Catalysis*, 2014. **4**(8): p. 2763-2769.
- 8 Joseph, K.L.V., J. Lim, A. Anthonysamy, H.-i. Kim, W. Choi, and J.K. Kim, Squaraine-sensitized composite of a reduced graphene oxide/TiO₂ photocatalyst: π - π stacking as a new method of dye anchoring. *Journal of Materials Chemistry A*, 2015. **3**(1): p. 232-239.
- 9 Nada, A.A., H.A. Hamed, M.H. Barakat, N.R. Mohamed, and T.N. Veziroglu, Enhancement of photocatalytic hydrogen production rate using photosensitized TiO₂/RuO₂-MV₂+



- International Journal of Hydrogen Energy*, 2008. **33**(13): p. 3264-3269.
- 10 Shimidzu, T., T. Iyoda, and Y. Koide, An advanced visible-light-induced water reduction with dye-sensitized semiconductor powder catalyst. *Journal of the American Chemical Society*, 1985. **107**(1): p. 35-41.
- 11 Wu, Y. and W. Zhu, Organic sensitizers from D- π -A to D-A- π -A: effect of the internal electron-withdrawing units on molecular absorption, energy levels and photovoltaic performances. *Chemical Society Reviews*, 2013. **42**(5): p. 2039-2058.
- 12 Yu, Z., F. Li, and L. Sun, Recent advances in dye-sensitized photoelectrochemical cells for solar hydrogen production based on molecular components. *Energy & Environmental Science*, 2015. **8**(3): p. 760-775.
- 13 Zhang, X., T. Peng, and S. Song, Recent advances in dye-sensitized semiconductor systems for photocatalytic hydrogen production. *Journal of Materials Chemistry A*, 2016. **4**(7): p. 2365-2402.
- 14 Hardin, B.E., H.J. Snaith, and M.D. McGehee, The renaissance of dye-sensitized solar cells. *Nature Photonics*, 2012. **6**: p. 162.
- 15 Lee, S.-H., Y. Park, K.-R. Wee, H.-J. Son, D.W. Cho, C. Pac, W. Choi, and S.O. Kang, Significance of Hydrophilic Characters of Organic Dyes in Visible-Light Hydrogen Generation Based on TiO₂. *Organic Letters*, 2010. **12**(3): p. 460-463.
- 16 Jae-Hong, K. and A. Kwang-Soon, Tri-Branched Tri-Anchoring Organic Dye for Visible Light-Responsive Dye-Sensitized Photoelectrochemical Water-Splitting Cells. *Japanese Journal of Applied Physics*, 2010. **49**(6R): p. 060219.
- 17 Han, W.-S., K.-R. Wee, H.-Y. Kim, C. Pac, Y. Nabetani, D. Yamamoto, T. Shimada, H. Inoue, H. Choi, K. Cho, and S.O. Kang, Hydrophilicity Control of Visible-Light Hydrogen Evolution and Dynamics of the Charge-Separated State in Dye/TiO₂/Pt Hybrid Systems. *Chemistry – A European Journal*, 2012. **18**(48): p. 15368-15381.
- 18 Choi, S.K., H.S. Yang, J.H. Kim, and H. Park, Organic dye-sensitized TiO₂ as a versatile photocatalyst for solar hydrogen and environmental remediation. *Applied Catalysis B: Environmental*, 2012. **121–122**: p. 206-213.
- 19 Watanabe, M., H. Hagiwara, A. Iribe, Y. Ogata, K. Shiomi, A. Staykov, S. Ida, K. Tanaka, and T. Ishihara, Spacer effects in metal-free organic dyes for visible-light-driven dye-sensitized photocatalytic hydrogen production. *Journal of Materials Chemistry A*, 2014. **2**(32): p. 12952-12961.
- 20 Yu, F.T., S.C. Cui, X. Li, Y.Y. Peng, Y. Yu, K. Yun, S.C. Zhang, J. Li, J.G. Liu, and J.L. Hua, Effect of anchoring groups on N-annulated perylene-based sensitizers for dye-sensitized solar cells and photocatalytic H₂ evolution. *Dyes and Pigments*, 2017. **139**: p. 7-18.
- 21 Thelakkat, M., Star-Shaped, Dendrimeric and Polymeric Triarylamines as Photoconductors and Hole Transport Materials for Electro-Optical Applications. *Macromolecular Materials and Engineering*, 2002. **287**(7): p. 442-461.
- 22 Tiwari, A. and U. Pal, Effect of donor-donor- π -acceptor architecture of triphenylamine-based organic sensitizers over TiO₂ photocatalysts for visible-light-driven hydrogen production. *International Journal of Hydrogen Energy*, 2015. **40**(30): p. 9069-9079.
- 23 Li, X., S. Cui, D. Wang, Y. Zhou, H. Zhou, Y. Hu, J.-g. Liu, Y. Long, W. Wu, J. Hua, and H. Tian, New Organic Donor–Acceptor- π –Acceptor Sensitizers for Efficient Dye-Sensitized Solar Cells and Photocatalytic Hydrogen Evolution under Visible-Light Irradiation. *ChemSusChem*, 2014. **7**(10): p. 2879-2888.
- 24 Dessi, A., M. Monai, M. Bessi, T. Montini, M. Calamante, A. Mordini, G. Reginato, C. Trono, P. Fornasiero, and L. Zani, Towards Sustainable H₂ Production: Rational Design of Hydrophobic Triphenylamine-based Dyes for Sensitized Ethanol Photoreforming. *ChemSusChem*, 2018. **11**(4): p. 793-805.
- 25 Aslan, E., M.K. Gonce, M.Z. Yigit, A. Sarilmaz, E. Stathatos, F. Ozel, M. Can, and I.H. Patir, Photocatalytic H₂ evolution with a Cu₂WS₄ catalyst on a metal free D- π -A organic dye-sensitized TiO₂. *Applied Catalysis B: Environmental*, 2017. **210**: p. 320-327.
- 26 Patir, I.H., E. Aslan, G. Yanalak, M. Karaman, A. Sarilmaz, M. Can, M. Can, and F. Ozel, Donor- π -acceptor dye-sensitized photoelectrochemical and photocatalytic hydrogen evolution by using Cu₂WS₄ co-catalyst. *International Journal of Hydrogen Energy*, 2019. **44**(3): p. 1441-1450.
- 27 Aslan, E., M. Karaman, G. Yanalak, M. Can, F. Ozel, and I.H. Patir, The investigation of novel D- π -A type dyes (MK-3 and MK-4) for visible light driven photochemical hydrogen evolution. *Dyes and Pigments*, 2019. **171**: p. 107710.
- 28 Aslan, E., M. Karaman, G. Yanalak, H. Bilgili, M. Can, F. Ozel, and I.H. Patir, Synthesis of novel tetrazine based D- π -A organic dyes for photoelectrochemical and photocatalytic hydrogen evolution. *Journal of Photochemistry and Photobiology A: Chemistry*, 2020. **390**: p. 112301.
- 29 Swinehart, D.F., The Beer-Lambert Law. *Journal of Chemical Education*, 1962. **39**(7): p. 333.
- 30 Luo, G.-G., H. Lu, Y.-H. Wang, J. Dong, Y. Zhao, and R.-B. Wu, A D- π -A- π -A metal-free organic dye with improved efficiency for the application of solar energy conversion. *Dyes and Pigments*, 2016. **134**: p. 498-505.
- 31 Cardona Claudia, M., W. Li, E. Kaifer Angel, D. Stockdale, and C. Bazan Guillermo, Electrochemical Considerations for Determining Absolute Frontier Orbital Energy Levels of Conjugated Polymers for Solar Cell Applications. *Advanced Materials*, 2011. **23**(20): p. 2367-2371.
- 32 Margalias, A., K. Seintis, M.Z. Yigit, M. Can, D. Sygkridou, V. Giannetas, M. Fakis, and E. Stathatos, The effect of additional electron donating group on the photophysics and photovoltaic performance of two new metal free D- π -A sensitizers. *Dyes and Pigments*, 2015. **121**: p. 316-327.

Fenoxycarb Effects 7th instar *Galleria mellonella* Larvae by Triggering Extra Larval Stages

Esen Poyraz Tınartas^{1*}, Nesrin Ebru Göncü², Kamil Koç¹

¹ Manisa Celal Bayar University, Faculty of Science and Arts, Department of Biology, Manisa, Turkey

² Ege University, Faculty of Science, Department of Biology, İzmir, Turkey

* esen.poyraz@cbu.edu.tr

*Orcid: 0000-0001-7386-2136

Received: 16 November 2020

Accepted: 3 May 2021

DOI: 10.18466/cbayarfb.823562

Abstract

Insect growth regulators are specific chemicals with hormonal effects on insects and these types of chemicals target to reduce the nonspecific effects of pesticides on nature and living things. In this study, we investigated the effects of one of the insect growth regulators, fenoxycarb which mimics the juvenile hormone action, on the growth of a harmful lepidopteran species *Galleria mellonella*, and its some developmental parameters. For this purpose, fenoxycarb was applied on day 0 of 7th instar larvae of the greater wax moth, *Galleria mellonella*. The treatment with 100 ng fenoxycarb had no developmental effect on *Galleria mellonella* larvae. The treatment with relatively high doses of fenoxycarb on day 0 induced the supernumerary larvae formation of 99% and larvae which molted extra larval instar formed healthy pupae in the ratio of 98-99%. Consequently, the effects of fenoxycarb on *Galleria mellonella* larvae occurred in a dose-dependent manner. Although fenoxycarb is a potent insect growth regulator, late *Galleria mellonella* larvae are not susceptible to this chemical, unlike some other Lepidopteran insect species.

Keywords: Development, Fenoxycarb, *Galleria mellonella*, Juvenile hormone.

1. Introduction

Insect growth regulators are produced to develop more specific chemicals against harmful insects that target to reduce the nonspecific effects of pesticides on nature and living things and they show hormonal effects on insects. Most insect growth regulators today are juvenile hormone (JH) analogues, which mimic the mechanism of action of JH. JH provides the continuity of larval characters for holometabolous insects [1]. JH or JH analogues applications disturb the endocrine balance of many insects and finally induces abnormal development [1-4]. No synthetic JH analogue can instantly kill the target organism with a direct toxic effect. Instead, it leads to developmental abnormalities, causing insufficiency in development and reproductive functions [5, 6]. Fenoxycarb, 0-ethyl N-(2-(4-phenoxyphenoxy) ethyl) carbamate, is one of the most effective chemicals among these JH analogues [1].

Galleria mellonella, the greater wax moth, is a harmful lepidopteran species that causes economic losses in the beekeeping industry because its larva feeds on combs, and also their larvae and pupae are one of the oldest

experimental models used in insect physiology [7-10]. Until now, there has been no quantitative report that has examined the responses of the larvae of *Galleria mellonella* to treatments with fenoxycarb. The present study attempted to clarify the response of *Galleria mellonella* to different doses (100 ng to 10 µg) of fenoxycarb during the last larval stage. For this purpose, molting, growth, and some survival parameters after treatments were evaluated and statistical analyses were carried out depending on application doses.

2. Materials and Methods

Galleria mellonella larvae were reared at 30 ± 0.5 °C, $60 \pm 5\%$ relative humidity and constant darkness in the incubator on a diet containing bran (420 g), honeycomb (160 g), honey (150 ml), glycerol (150 ml) and distilled water (30 ml) modified from Bronksill [11].

Eggs were collected every day. During the feeding period, larvae were classified in every 24-hours. The first 24 hours were named as day 0 (Figure 1c- d). At larval-pupal metamorphosis, the classification of larval development was performed according to the

morphology and morphological characteristics of the migration of the pigments from the stemmata [12]. This retraction of pigments occurs in several stages (S1-S5) under hormonal factors [12, 13]. Also, the head capsule width of the larvae was measured by millimeter ocular and was statistically evaluated. After pupal molting, pupae were also classified every 24 hours.

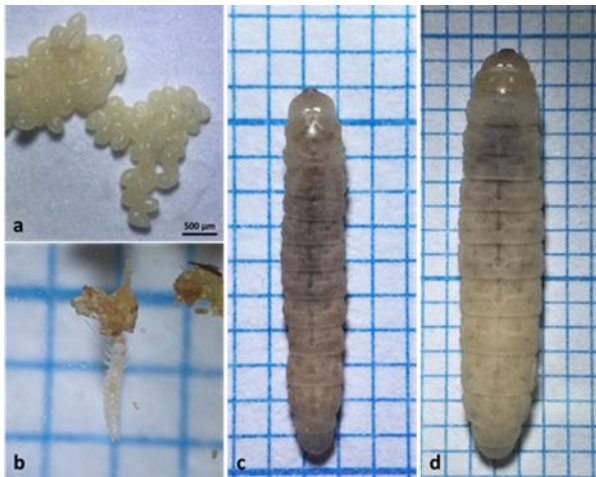


Figure 1. Different developmental stages of *Galleria mellonella* larvae; a) *Galleria mellonella* eggs, b) Feeding early larva of *Galleria mellonella*, c) 6th instar newly ecdysis larva, d) 7th instar newly ecdysis larva.

On day 0 of 7. instar, every ten larvae were topically treated with eight different doses of fenoxycarb (100 ng, 250 ng, 500 ng, 750 ng, 1 µg, 2 µg, 5 µg, and 10 µg) (Fluka, 34343) in 2,5 µl acetone (solvent) with a micropipette along the dorsal midline. Control larvae were treated with an equal amount (2.5 µl) of solvent without fenoxycarb. The groups treated with fenoxycarb were cultured in different incubators and laboratories to prevent any contamination with the control group. The larvae that remained in the 7th instar more than 20 days were defined as “dauer larvae” [1, 14]. Each experimental procedure was performed three times.

Ten randomly selected larvae and/or pupae from groups were weighed from day 0 of the 7th instar to the end of the pupal stage in 24 hours intervals at the same time each day. Analyses of the data were carried out by using SPSS 20.00 software (IBM) ($p < 0.05$ level Mann Whitney’s U-test).

2. Results and Discussion

Hemolymph JH levels are low at the beginning of the last larval stage to provide a pupal commitment of the insect body. Moreover, this period is extremely sensitive to JH applications [3, 15]. In this study, fenoxycarb was applied at the beginning of the last larval stage to evaluate the sensitivity of *Galleria mellonella* to the various levels of JH presence.

Control group larvae were fed for three and a half days (78-84 hours) and then terminate feeding activity and

reached the highest weight values (310 mg) at 78-84 hour period from the beginning of the 7th instar (S1) as similarly reported by Beck [16]. Wandering and cocoon spinning (S1-S5) ranged from 2 and 3 days, 99% of the larvae developed normally to the pupal stage. A gradual decrease in weight was observed until the larval-pupal ecdysis. Increasing silk secretion, degeneration of tissues, and organs such as the silk gland and intestine which occupy large volumes and space in the body should be the main reasons for this decline. The pupal period lasted 7 days.

No appreciable difference was found in insects treated with a dose of 100 ng fenoxycarb per larvae when compared with control larvae. Application of doses among 250-750 ng caused to stop feeding activity resulting in growth deficiency in 5% of larvae, 3% of larvae died in these groups. Extra larval molting occurred in the ratio of between 35-65% (Table 1). 27-47% of larvae showed a prolonged larval stage of 1-2 days and then pupated following a normal course (Figure 2a). Previous studies showed that low and moderate doses of juvenoids caused a significant prolongation of the last larval stages in Holometabola [17] and also *Galleria mellonella* [2]. These differences may be due to differences in the greater wax moth strain used, the rearing conditions, or the chemical factors used because these factors have been shown to influence the actions of JH analogues [1].

The last larval stage of *Galleria mellonella* was sensitive to higher doses of fenoxycarb (1-10 µg) and caused supernumerary molt. 5 µg and 10 µg doses caused extra larval ecdysis occurred synchronously on day 5. Extra larval molting was observed between 95% and 97% (Figure 2b). 8th instar larvae pupated normally in the ratio of 99% and they were morphologically normal. (Table 1). Similarly, early in the last larval instar, the implantation of active corpora allata results in supernumerary larval ecdysis in *Galleria mellonella* [18]. The effect of JH and JH analogues is due to interference with the physiological programming of the secretory functions of the prothoracic glands and the modification of the prothoracic-tropic brain activity [2]. Fenoxycarb treatments may have caused ecdysteroid secretion, so that new larval-larval molting may have been triggered due to high levels of JH and 20-hydroxyecdysone in the hemolymph. The larval-pupal intermediate form was detected in 1-2% of larvae (Figure 2c). After treatments of JH and JH analogues, prolongation of larval stages, larval-pupal intermediate formation, dauer larva formation, and mortality were observed in different ratios in *Epiphyas postvittana* [19], *Ephestia kuehniella* [5], *Bombyx mori* [1, 20]. Extra larval molting was stated in a ratio of 30% in *Ostrinia nubilalis* [21, 22].

Table 1. Effects of fenoxycarb on the development of *Galleria mellonella* larvae

Dosage (in 2.5µl acetone)	Number of treated larvae	Prolongation of last instar	Dauer larvae (%)	Darkened and dead (%)	Poorly development and death (%)	Extra larval molting (%)	Pupation after extra larval molting(%)
Controls	30	-	-	-	-	-	-
100 ng	30	-	-	-	-	-	-
250 ng	30	1-2 days	10	3	5	35	98
500 ng	30	1-2 days	10	3	5	42	98
750 ng	30	1-2 days	-	3	5	65	98
1 µg	30	-	-	2	3	95	99
2 µg	30	-	-	2	3	95	99
5 µg	30	-	-	1	2	97	99
10 µg	30	-	-	1	2	97	99



Figure 2. *Galleria mellonella* larvae and pupae; a) Normally pupated *Galleria mellonella*, b) Supernumerary larvae of *Galleria mellonella*, c) Larval-pupal intermediate pupa formation after 8th instar, d) 9th instar larva molted partially.

The growth rate of larvae is defined during the development period by measuring the head capsule width of the samples taken from the population [8]. We determined that the last larval instar head capsule width is 2000 µm, similarly in Beck [8]. Measurements of 2264.6 µm and 2667.1 µm of head capsule width in different developmental stages (extra larval stages) also proved that fenoxycarb could affect *Galleria mellonella* larvae by molting more than once (Student T-Test, $p < 0.05$) (Figure 3a).

Measuring the body weights of larvae is also an important parameter in determining the growth rate of larvae [8]. Larvae treated with 5 µg of fenoxycarb were fed for the first 4 days and total body weights gradually increased, but this increase was found to be statistically lower than the control group larvae (Mann Whitney's U-test, $p < 0.05$) (Figure 3). Feeding inhibition is a general behavior of insects that comes in contact with various harmful agents [23].

The larvae of the 8th instar were fed for 8 days actively and showed a continuous and significant increase in weight until the 8th day (8-8) (Figure 3c). Sehna [24] reported similarly weight values in super larvae produced by corpora allata implantation. Between days 8 and 11, their feeding activities decreased or stopped, and weight gain slowed statistically (Mann Whitney's U-test, $p < 0.05$). The deceleration in the weight gain is thought to be a result of suppression of nutritional activity with excessive growth in animal size and, also the tracheal system probably does not adapt to these changes [25]. The maximum bodyweight a larva can reach and the weight gain that can be achieved in a single larval stage are species-specific [2, 25] and this value is not affected by JH and JH analogues [2]. These phenomena restrict the growth of insects. Larvae, when they reached 200-300 mg cut off from the feeding in normal development [16], but in some records, this weight could be 590 mg [2, 8], and larval growth is terminated irreversibly [2]. In our study, the ecdysis of the larval-pupal was observed near the known upper limit. The average weight of the 8th instar larvae was 596 mg and the lowest value was 410 mg. All these findings clarify the cause of feeding and growth inhibition and death in the 9th instar.

Pigment migration, which is the main characteristic of the S1- S5 stages, was not observed in S1 and S2 in the 8th larval instar larvae, which is why the distinction between S1 and S2 was not appropriate in this group. Their developmental stages in the graphs were edited every 24 hours up to S3. At the end of day 11, the spinning behavior began following the gut purge and the

total body weight decreased continuously, for the same reason as the control group. The pupal bodyweight of the group treated with fenoxycarb was significantly higher than that of the control group all day (Mann

Whitney's U-test, $p < 0.05$, Figure 3d). Pupal molting occurred within 2-3 days and the pupal stage lasted for 7 days as in the control group.

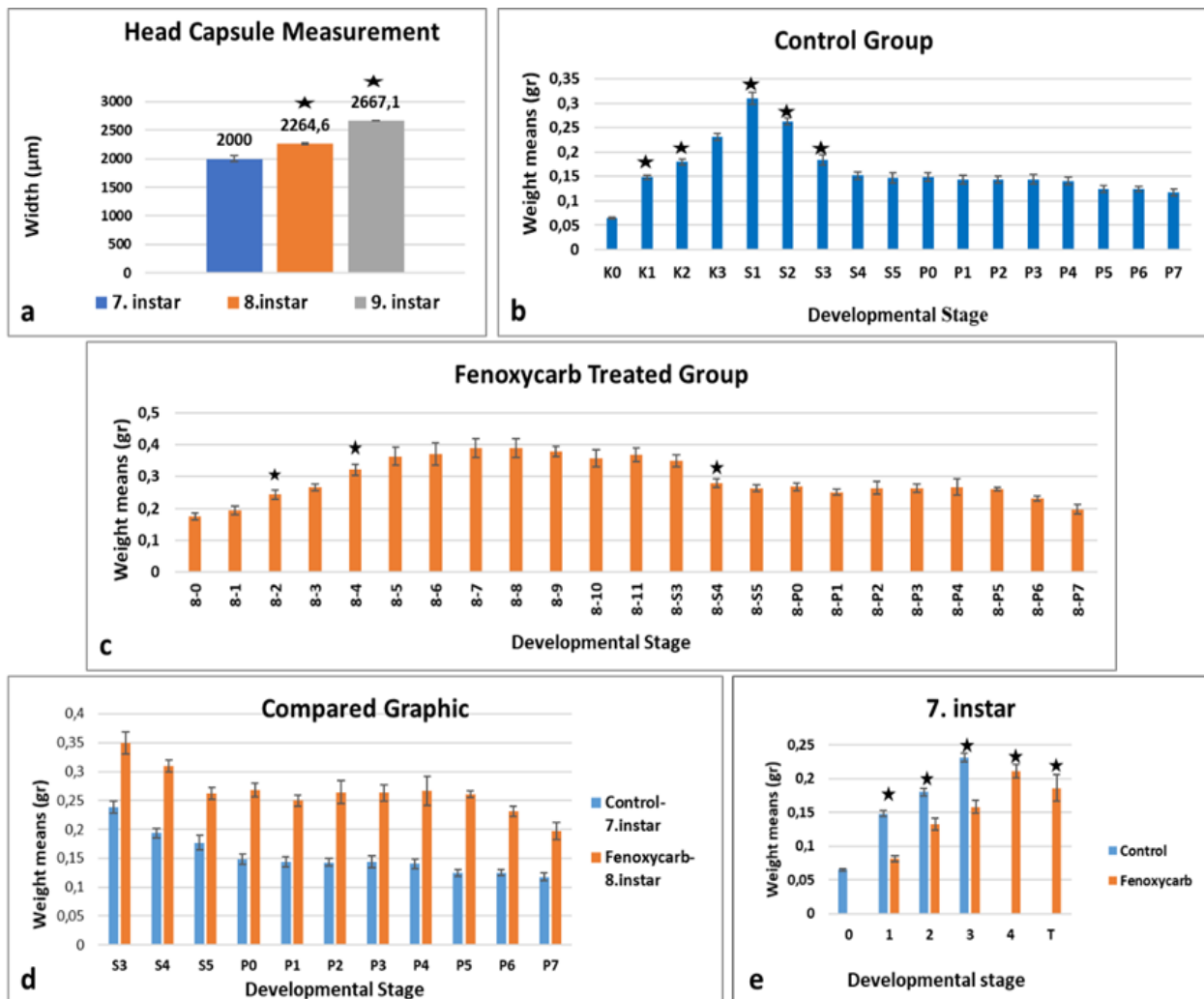


Figure 3. Weight average and head capsule measurement of control and 5 µg fenoxycarb treated groups; a) Head capsule measurements of control and 5 µg fenoxycarb treated group, b) The average of control group weight, c) The weight average of 5µg fenoxycarb treated group, d) Similar developmental stages of the control group and 5 µg fenoxycarb treated group were compared according to their weight changes, e) Comparison of the control group and 5 µg fenoxycarb treated group 7th instar values, T: Transition day from, the bars indicate standard errors. The asterisks indicate the statistically significant differences compared to the previous developmental stage ($p < 0.05$). S1-S5 represents the stages of development based on the retraction of pigments from stemmata, P0-7 represents the pupal days.

3. Conclusion

In comparison to other Lepidopteran species such as *Bombyx mori* and *Ephestia kuehniella* and when applied doses are considered, *Galleria mellonella* is found to be highly resistant to the fenoxycarb at the beginning of the last larval stage. Relatively high doses (5-10 µg) have possibly stimulated the secretion activity of the prothoracic glands and triggered the extra larval ecdysis. However, applications did not affect pupal development and resulted in healthy adults and a new generation

developed from their eggs was also healthy. These results clearly showed that fenoxycarb will be not a suitable agent for the biological control of this insect.

Acknowledgment

We would like to thank the Manisa Celal Bayar University Scientific Research Projects Coordination Unit (BAP) for supporting this study under project number 2014-013. This work was presented at the



Ecology 2018 Symposium (19-23 June 2018, Kastamonu Turkey) as an oral presentation.

Author's Contributions

Esen Poyraz Tınartaş: Drafted and wrote the manuscript, carried out the experiment, and evaluated results.

Nesrin Ebru Göncü: Assisted in analytical analysis on the structure, supervised the experiment's progress, result interpretation, and helped in manuscript preparation.

Kamil Koç: Conceived the presented experiment and supervised the findings of this work.

Ethics

There are no ethical issues after the publication of this manuscript.

References

1. Kamimura, M, Kiuchi, M. 1998. Effects of a juvenile hormone analog, fenoxycarb, on 5th stadium larvae of the silkworm, *Bombyx mori* (Lepidoptera: Bombycidae). *Applied Entomology and Zoology*; 33(2): 333-338.
2. Ciemior, KE, Sehna, F, Schneiderman, HA. 1979. Molting, Growth and Survival of *Galleria mellonella* L. (Lep. Pyralidae) Treated with Juvenoids. *Zeitschrift Fur Angewandte Entomologie-Journal of Applied Entomology*; 88(4): 414-425.
3. Silhacek, DL, Oberlander H. 1975. Time-dosage studies of juvenile hormone action on the development of *Plodia interpunctella*. *Journal of insect physiology*, 21(1), 153-161.
4. Dedos, SG, Szurdoki, F, Székács, A, Shiotsuki, T, Hammock, BD, Shimada, J, Fugo, H. 2002. Fenoxycarb levels and their effects on general and juvenile hormone esterase activity in the hemolymph of the silkworm, *Bombyx mori*. *Pesticide Biochemistry and Physiology*, 73(3): 174-187.
5. Grenier, S, Grenier AM. 1993. Fenoxycarb, a fairly new Insect Growth Regulator: Review of its effects on insects. *Annals of Applied Biology*; 122(2): 369-403.B
6. Beckage, NE, Rechcigl, J, Rechcigl, N. 2000. Insect growth regulators. *Biological and biotechnological control of insect pests*, 123-137.
7. Karlson, P. 1956. Biochemical studies on insect hormones. *Academic Press: In Vitamins & Hormones*; 14: 227-266.
8. Beck, SD. 1960. Growth and Development of The Greater Wax Moth, *Galleria mellonella* (L.) (Lepidoptera: Galleriidae). *Visconsin Academy of Sciences, Arts and Letters*; 49: 137-148.
9. Sehna, F, Meyer, AS. 1968. -Larval-pupal transformation: control by juvenile hormone. *Science*; 159(3818): 981-4.
10. Richman, K, Oberlander, H. 1971. -Effects of fat body on α -ecdysone induced morphogenesis in cultured wing disks of the wax moth, *Galleria mellonella*. *Journal of Insect Physiology*; 17(2): 269-276.
11. Bronskill, JA. 1961. A cage to simplify the rearing of the greater wax moth, *Galleria mellonella* (Lepidoptera: Pyralidae). *Journal the Lepidopterists' Society*; 15: 102-104.
12. Uwo, MF, Ui-Tei, K, Park, P, Takeda, M. 2002. Replacement of midgut epithelium in the greater wax moth, *Galleria mellonella*, during larval-pupal moult. *Cell Tissue Research*; 308(2): 319-31.
13. Jindra, M, Riddiford, LM. 1996. Expression of ecdysteroid-regulated transcripts in the silk gland of the wax moth, *Galleria mellonella*. *Development genes and Evolution*; 206(5): 305-314.
14. Sehna, I F, Janda, V, Nĕmec, V. 1983. Composition, synthetic and cytolytic activities of *Galleria mellonella* silk glands during the last-larval instar under the action of juvenile hormone. *Journal of Insect Physiology*; 29(3): 237-248.
15. Retnakaran, A. 1973. Hormonal induction of supernumerary instars in the spruce budworm, *Choristoneura fumiferana* (Lepidoptera: Tortricidae). *The Canadian Entomologist*; 105(3): 459-461.
16. Beck S. D., 1970. -Neural and Hormonal Control of Pupation in *Galleria mellonella* (Lepidoptera: Galleriidae). *Annals of the Entomological Society of America*. 63(1): 144-149.
17. Sehna, F, Metwall, MM, Elbie, I. 1976. Reactions of immature stages of noctuid moths to juvenoids. *Z. ang. Ent*; 81, 85-102.
18. Sehna, F. 1968. Influence of the corpus allatum on the development of internal organs in *Galleria mellonella* L. *Journal of Insect Physiology*; 14(1), 73-85.
19. Singh, P, Dugdale, J. 1979. Morphogenetic and physiological effects of a juvenile hormone analogue on the light brown apple moth, *Epiphyas postvittana* (Lepidoptera: Tortricidae). *New Zealand Journal of Zoology*; 6: 381-387.
20. Goncu, E, Parlak, O. 2012. The effect of the juvenile hormone analog, fenoxycarb, on ecdysone receptor B1 expression in the midgut of *Bombyx mori* during larval-pupal metamorphosis. *Folia Histochemistry Cytobiology*; 50(1): 52-7.
21. Fujiwara, H, Ogai, S. 2001. Ecdysteroid-induced programmed cell death and cell proliferation during pupal wing development of the silkworm, *Bombyx mori*. *Development Genes & Evolution*; 211(3).
22. Gadenne, C, Grenier, S, Plantevin, G, Mauchamp, B. 1991. Effects of a juvenile hormone mimetic, fenoxycarb, on post-embryonic development of the European corn borer, *Ostrinia nubilalis*. *Hbn. Experientia*; 46(7): 744-747.
23. Leonardi, MG, Cappelozza, S, Ianne, P, Cappelozza, L, Parenti, P, Giordana, B. 1996. Effects of the topical application of an insect growth regulator (fenoxycarb) on some physiological parameters in the fifth instar larvae of the silkworm *Bombyx mori*. *Comparative Biochemistry and Physiology Part B: Biochemistry and Molecular Biology*; 113(2), 361-365.
24. Sehna, F. 1971. Juvenile hormone action and insect growth rate. *Endocrinologia Experimentalis*; 5: 29-33.
25. Callier, V, Nijhout, HF. 2011. Control of body size by oxygen supply reveals size-dependent and size-independent mechanisms of molting and metamorphosis. *Proceedings of the National Academy of Sciences of the United States of America*; 108(35): 14664-14669.

Adhesive Behavior of the Pack-Borided AISI 304L Steel with Microwave Hybrid Heating

Dilek Arslan^{1*} , Recep Onur Uzun² 

^{1*} Graduate School of Applied and Natural Sciences, Department of Mechanical Engineering, Manisa Celal Bayar University, 45140, Manisa, Turkey

² Hasan Ferdi Turgutlu Technology Faculty, Department of Mechanical Engineering, Manisa Celal Bayar University, 45400, Manisa, Turkey

[*da.dilekarlan@gmail.com](mailto:da.dilekarlan@gmail.com)

*Orcid: 0000-0003-0198-0787

Received: 15 November 2020

Accepted: 20 February 2021

DOI: 10.18466/cbayarfbe.826118

Abstract

AISI 304L stainless steel material was pack-borided with microwave hybrid heating method at temperatures of 850, 900 and 950 °C for 2, 4 and 6 hours. The morphology of the boride layer formed on the surface of the samples was examined by an optical microscope. The X-ray diffraction (XRD) analysis showed the presence of the FeB, Fe₂B, Cr₂B and Ni₂B phases on the surface of the borided samples. The Daimler-Benz Rockwell-C adhesion test was carried out to evaluate the adhesive strength of the boride layer to the substrate material. The tests were repeated at least 3 times for each of the samples pack-borided at all process temperatures and times. After the adhesion tests, macro and SEM images of indentation traces were taken. By analysing the indentation craters, it has been determined whether the damages are acceptable or not with reference to the VDI 3198 standard. The indentation craters formed on the surfaces of the samples were pack-borided at 850 °C for all process times, at 900 °C for 2 and 4 hours, and at 950 °C for 2 hours have the best adhesion quality in the HF1 category of the VDI 3198 norm. The pack-boriding treatment with microwave hybrid heating contributed positively to the adhesion strength, but in additions to this, the test results revealed that adhesion decreased with increasing boriding temperature and time.

Keywords: Adhesion test, Daimler-Benz Rockwell-C, microwave hybrid heating, pack-boriding, VDI 3198 norm.

1. Introduction

Boriding changes the microstructure and composition of the material surface by thermochemical diffusion of boron atoms to the material surface; creates a functional surface layer with optimum surface properties. High hardness and low friction coefficient are two important mechanical properties that the boride layer that forms as a result of boriding gives the material surface. Thanks to these features, the major problem that shortens or ends the service life of engineering materials, namely surface wear, is prevented. Morón et al. [1], in their study, reduced the friction coefficient of the AISI H13 steel, which was initially in the range of 0.64-0.71, to 0.10-0.11 values, which they applied pack-boriding at 950 °C for 6 hours, and increased the abrasion resistance by 23 times in the lubricated environment. Kayali et al. [2] achieved a 30-fold reduction in the abrasion rate of the AISI 316L stainless steel alloy that borided with 2 and 6

hours of hold times at 800 and 900 °C. Material surfaces working in contact with each other are connected with micro-welds after a while. With the ongoing relative movement breaking these bonds, the relatively less hard material is transferred to the opposite element, thus creating gaps on the less hard material surface and protrusions on the other surface. This surface wear resulting in material loss is called adhesive wear. Surface hardening is the leading measure to be taken to increase the adhesive strength on the material surface. However, conventional surface hardening methods cannot be applied to austenitic stainless steels. Because they protect their austenitic microstructure from room temperature to high temperatures. For this reason, boriding is widely preferred in order to increase surface hardness due to its easy applicability and economy. In their study, Alias et al. [3] increased the surface hardness of AISI 304 austenitic stainless steel alloy 5 times with the pack-boriding process at 850 °C and for 8

hours. In many studies in the literature, high surface hardness values have been obtained in different types of steels as well as austenitic stainless steels by applying boriding process [4-19]. Thanks to boriding, the surface hardness of the material not only increases; since the chemical reactivity of boron against oxygen is high, a thin oxide film forms on the boride layer. This layer acts as a solid lubricant, reducing the friction coefficient [20, 21]. Boride layer has a low tendency to cold weld so it does not need to be oiled to prevent adhesive wear. Taktak ve Tasgetiren [22] subjected AISI H13 and AISI 304 steels to boriding in a slurry salt bath at 800–950 °C for 3, 5 and 7 hours. The quality of adhesion strength of the boride layers formed on both steel materials borided at 800 °C is in the HF1 and HF2 category and is very high. However, it has been reported that the adhesion quality of the boride layer decreases as the process temperature and time increases. The increase in the quality of adhesion strength between the boride layer and the matrix material increases the adhesion resistance. As the adhesion quality deteriorates, crack formation starts due to internal stresses and progresses, resulting in delaminations on the material surface.

Krelling et al. [23] applied pack-boriding process on AISI 1020 steel with a 4 hour retention time at 1000 °C. After Rockwell C indentation tests, they obtained HF1 quality adhesion strength between the boride layer and the substrate and reported the result that the boriding gave a good adhesion resistance.

This study aimed to increase the adhesion resistance by using a microwave hybrid heating system as a thermal energy source for pack-boriding process. The adhesion strength analysis of the boride layer formed on the surface of AISI 304L stainless steel samples, on which pack boriding was applied for 2, 4 and 6 hours at 850, 900 and 950 °C temperatures with microwave hybrid heating methods, to the matrix material was evaluated by Daimler-Benz Rockwell-C adhesion test.

2. Experimental Procedure

2.1. Pack-boriding process with microwave hybrid heating

The test specimens were manufactured from AISI 304L stainless steel material, whose standard chemical composition is given in Table 1, with a diameter of 20mm and a height of 10 mm. The samples were ground up to 1200 grid and subjected to ultrasonic bath for 30 minutes before the thermochemical treatment. The pack-boriding treatments were carried out in a microwave furnace at 850, 900 ve 950 °C for 2, 4 and 6 h, and the samples were allowed to cool in the open air at the end of the process. Commercial Ekabor-II powder was used as the boriding agent. The samples were placed in AISI 304 stainless steel containers and

covered with boriding powder. The schematic picture of the microwave sintering furnace with the microwave hybrid heating mechanism where the pack-boriding process takes place is given in Figure 1. Heating in the microwave heating system is provided by both microwave radiation and convection heat transfer mechanisms. That's why hybrid heating is in question. Thanks to the microwave absorbing plates around the boriding crucible, which is heated volumetrically by microwave radiation, convection heat transfer accompanies it. This hybrid heating system, which increases thermal diffusion and saves energy with homogeneous heating and homogeneous temperature distribution, is an improvement innovation in the pack-boriding process. The morphology of the boride layer formed on the sample surfaces after the boriding process was examined by optical microscope at x200 magnifications, and the phases formed in the layer were determined by XRD. The samples for microstructural analyses were sanded with SiC abrasive paper up to 1200 grid, polished with 1 µm diamond polishing solution, and etched with Glyceregia solution.

2.2. Adhesion test and characterization

The Daimler-Benz Rockwell-C adhesion test was used to evaluate the adhesion of boride layers. The Rockwell-C indentation test is specified according to the VDI 3198 norm, as a quality test for coated materials. In this test, the plastic deformation that occurs as a result of the penetration of the conical end indenter into the surface of the coated material determines the adhesion quality of the coating. The thickness of the sample must be at least 10 times greater than the indentation depth. The type and volume of damage to the coating gives information about the adhesion of the coating layer at first glance and the fragility secondly. The principle of the method and the quality categories of the adhesion strength of the damage in the coating layer after the test are shown in Figure 2. Grades between HF1-HF4 indicate the presence of sufficient adhesion in the coating layer; the HF5 and HF6 categories indicate insufficient adhesion strength, ie failure of the coating [24, 25]. Indentation processes, BMS 200-RB brand Rockwell hardness measurement device in accordance with VDI 3198 indentation test standards, with 120° conical tip and 150 kg load after repeating 3 times, the craters formed on the sample surfaces were examined using a stereo microscope and SEM (scanning electron microscope). By analyzing the cracks, delaminations and fractures occurring in the boride layer of each sample, it was determined whether the damages were acceptable by referring to the damage categories (HF1-HF6) of the VDI 3198 indentation test standard in Figure 2.

Table 1. AISI 304L stainless steel material chemical composition

Element	C	Mn	P	S	Si	Cr	Ni	N
Wt %	≤ 0.030	≤ 2.00	≤ 0.045	≤ 0.030	≤ 0.75	18-20	8-10	≤ 0,10

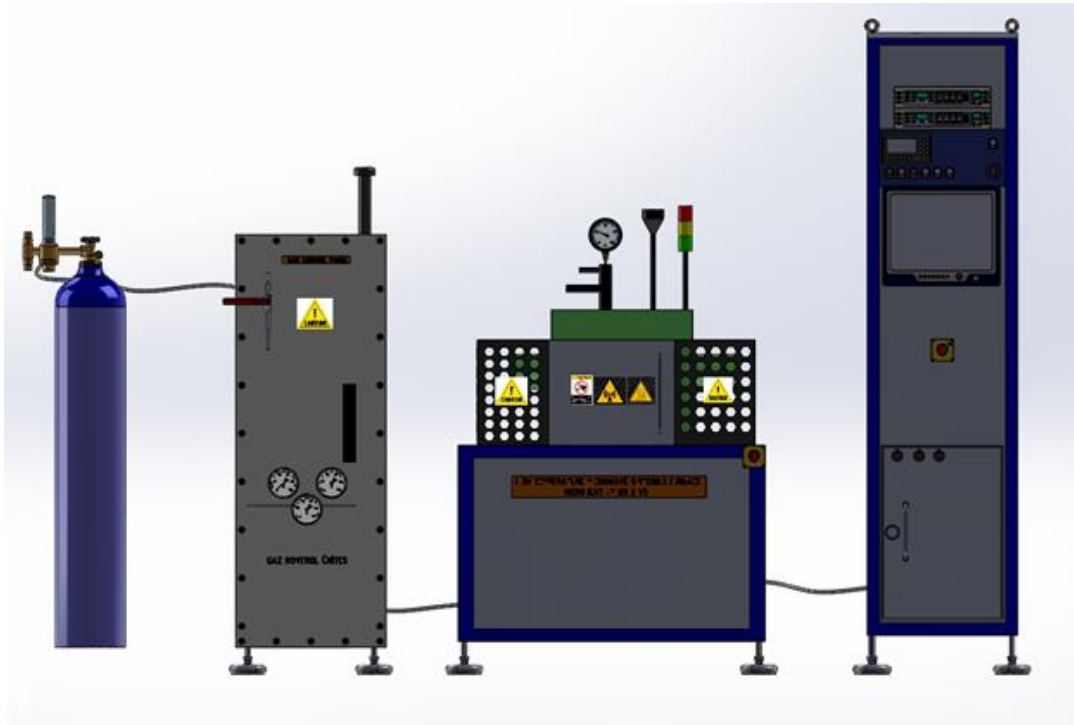


Figure 1. Schematic picture of microwave sintering furnace

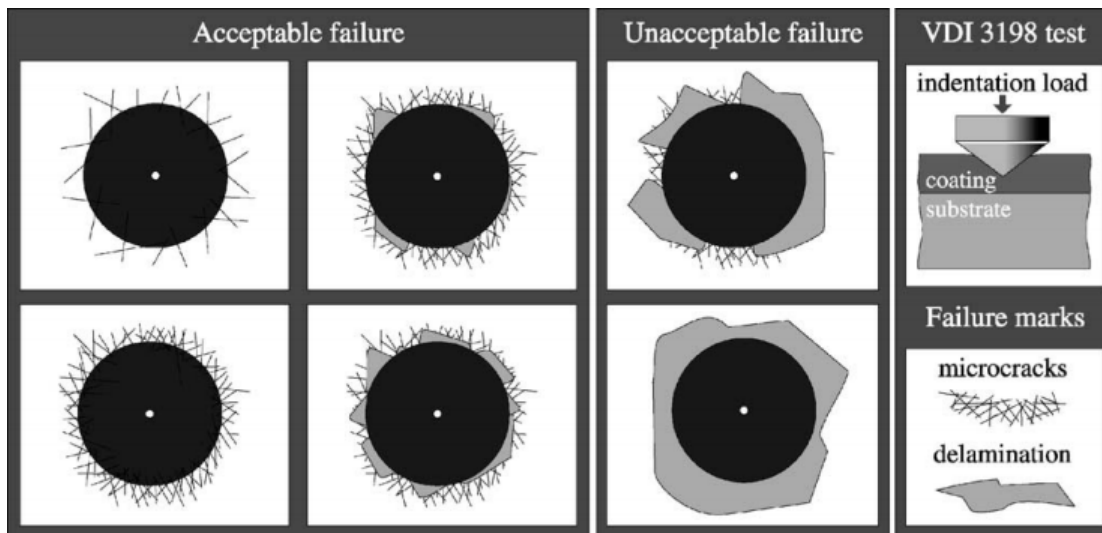


Figure 2. VDI 3198 indentation test adhesion quality classification [24]

3. Results and Discussion

3.1. The Characterization of Boride Layers

In the optical microscope images, the boride layers formed after boriding on the cylindrical samples of AISI 304L stainless steel are bilayer ($Fe_2B + FeB$) and can be clearly distinguished from the base material. As can be seen from Figure 3, the increase in process temperature

and retention time increased the boride layer thickness. Due to the high amount of alloying elements in the structure of AISI 304L stainless steel material, the boride layer formed on its surface has flat and smooth morphology. In Figure 4, XRD analysis showed the presence of Cr_2B and Ni_2B phases in the boride layer besides Fe_2B and FeB phases.

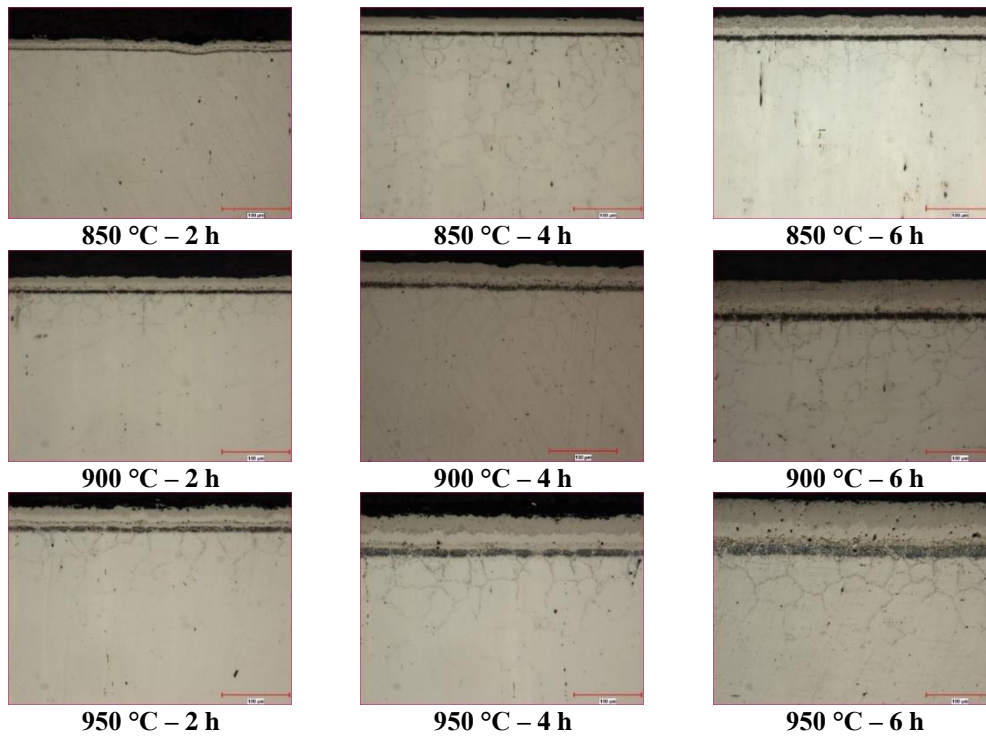


Figure 3. Optical microscope images of AISI 304L samples pack-borided at process temperatures and times with microwave hybrid heating: x200 magnification

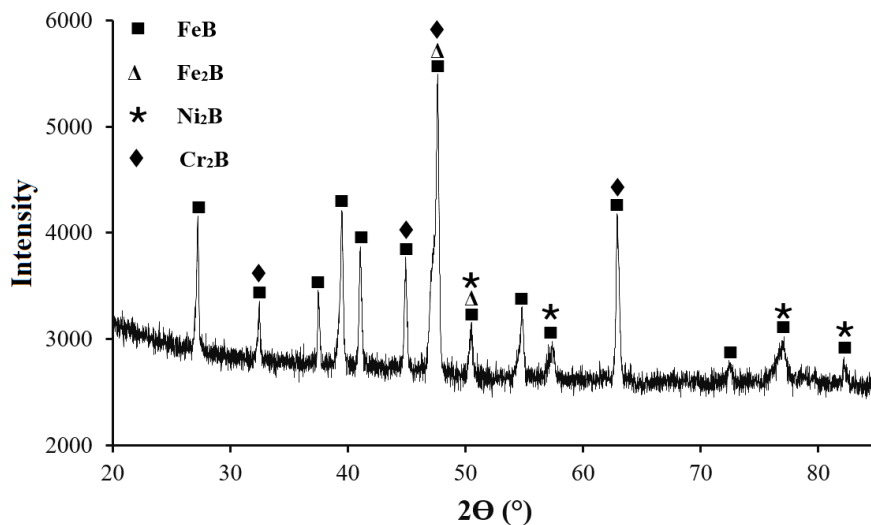


Figure 4. XRD pattern of the pack-borided AISI 304L steel at 900 °C for 6 hours

3.2. The adhesion resistance of boride layer

Macro and SEM images of the indentation traces taken after the adhesion tests on AISI 304L stainless steel samples pack-borided with microwave hybrid heating method are given in Figure 5-18. Whether the appearance of damage occurring in the adhesion test results is acceptable or not was evaluated according to the VDI 3198 norm. In Figure 5, the indentation craters formed on AISI 304L stainless steel sample surfaces, which are pack-borided at 850 °C for all process periods, at 900 °C for 2 and 4 hours, and at 950 °C for 2 hours by microwave hybrid heating method, are as in

the HF1 category of the VDI 3198 and are acceptable. HF1 has the best adhesion quality. Therefore, the adhesion strength of the samples pack-borided at these process temperatures and times is quite good. However, as can be seen in Figure 6, the boride layer on the surface of one of the samples, which was pack-borided at 900 °C for 6 hours, was broken up during the indentation test, and in another there are spillings. A spalling was observed in the boride layer of one of each sample which was pack-borided at 950 °C for 4 and 6 hours. Damages in these samples are of HF5 quality and are unacceptable.

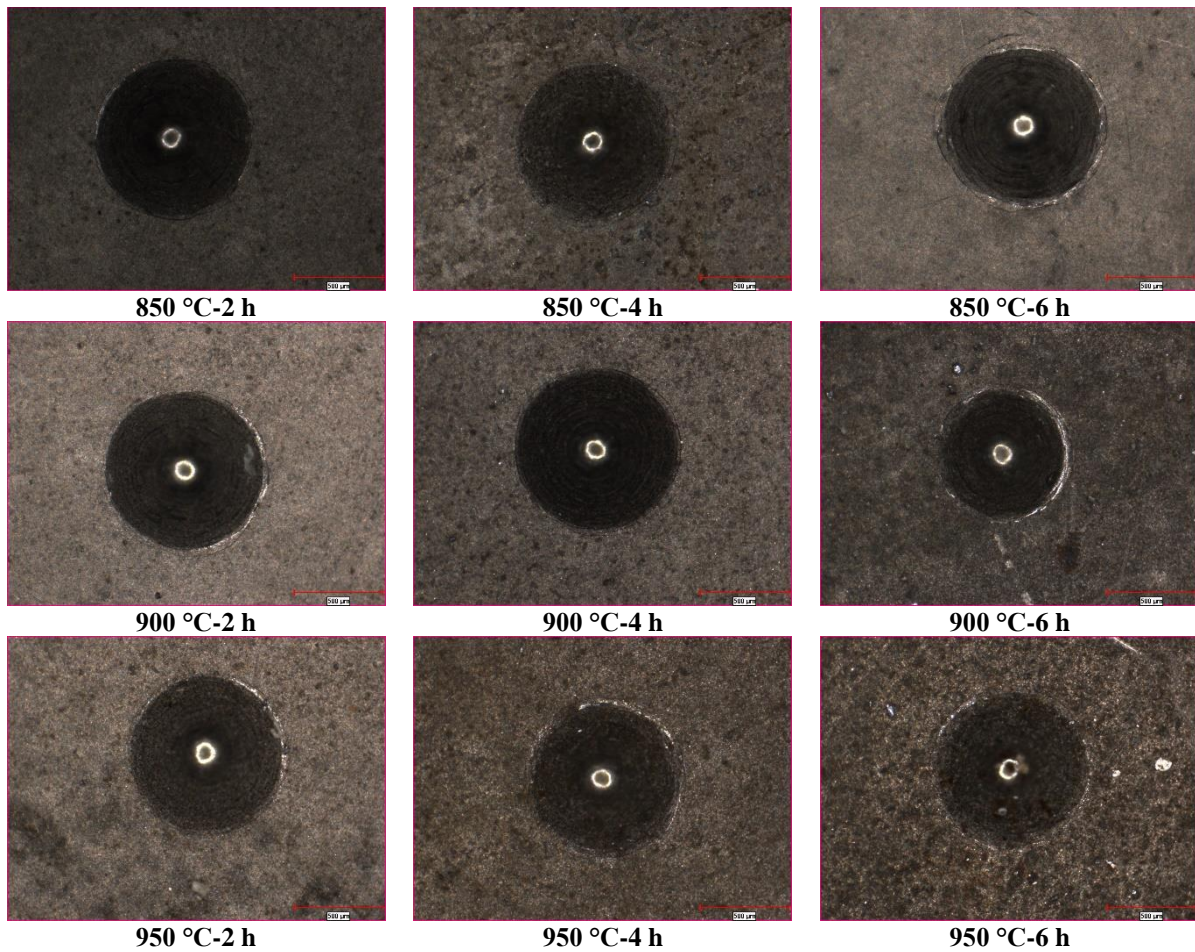


Figure 5. Macro images of the crater formed after the adhesion test on AISI 304L samples pack-borided with microwave hybrid heating



Figure 6. Boride layer removals occurring after the adhesion test in AISI 304L samples pack-borided with microwave hybrid heating

When the SEM images of the indentation traces of the boride layers of AISI 304L stainless steel samples pack-borided with microwave hybrid heating method in Figure 7-11 and Figure 14 are examined, it is more clearly seen that the acceptable damage in these samples

are HF1 quality micro cracks. These micro cracks are in the form of lateral cracks and generally capillary, and belong to the best quality category according to the VDI 3198 norm. Figure 12 shows the SEM image taken after the adhesion test of one of the AISI 304L samples pack-

borided with microwave hybrid heating method at 900 °C with a retention time of 6 hours. It is seen that the adhesion strength quality belongs to the HF3 category due to the curvilinear cracks and occasional spallings in the boride layer on the surface of this sample. The SEM image taken after the adhesion test of another sample pack-borided at the same process temperature and time is given in Figure 13. There are spallation and wear debris in the boride layer of the sample. The adhesion strength of this sample between the boride layer and the base material is HF5 quality and is in unacceptable category.

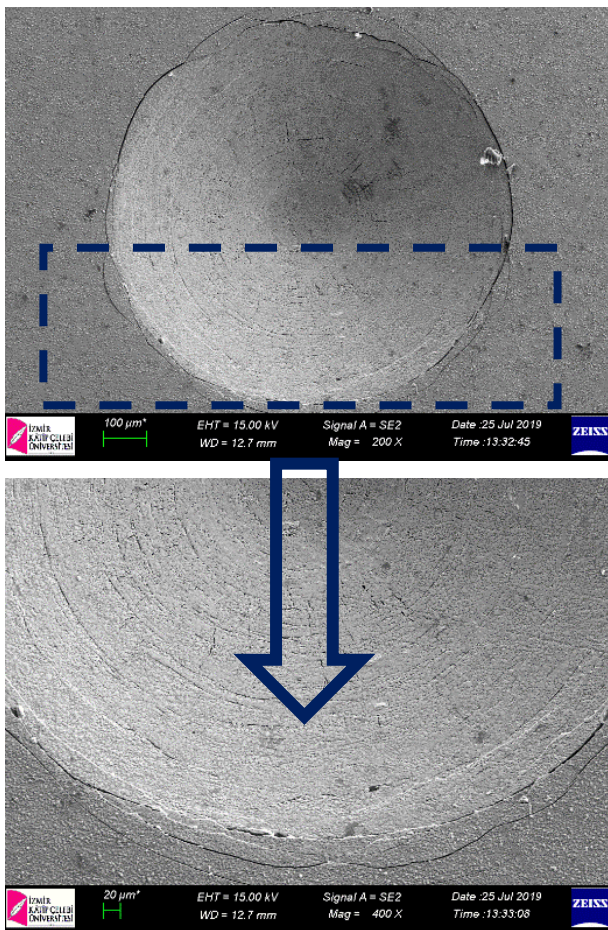


Figure 7. SEM images of the traces and micro cracks formed after the adhesion test on the AISI 304L sample pack-borided at 850 °C for 2 hours with microwave hybrid heating

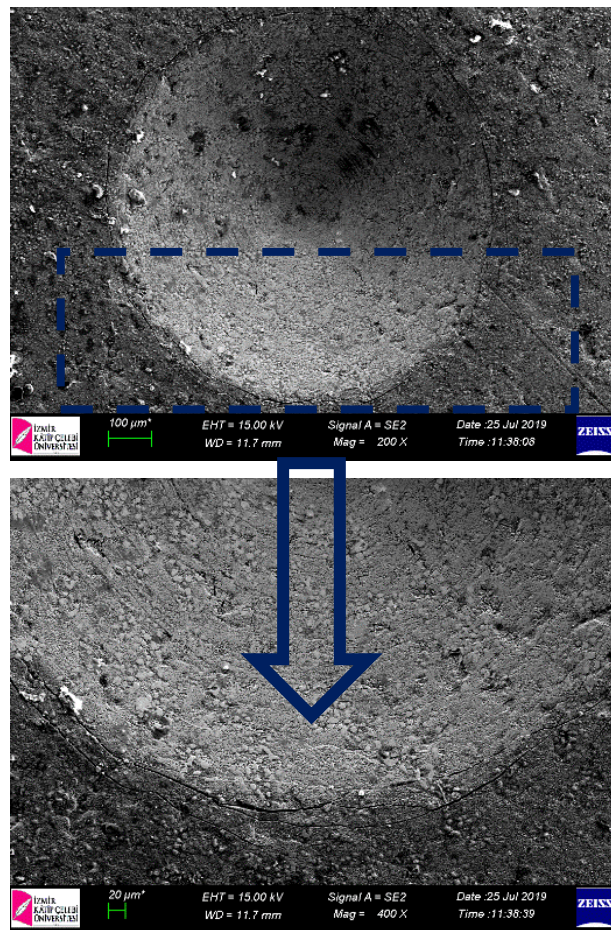


Figure 8. SEM images of the traces and micro cracks formed after the adhesion test in AISI 304L sample pack-borided at 850 °C for 4 hours with microwave hybrid heating

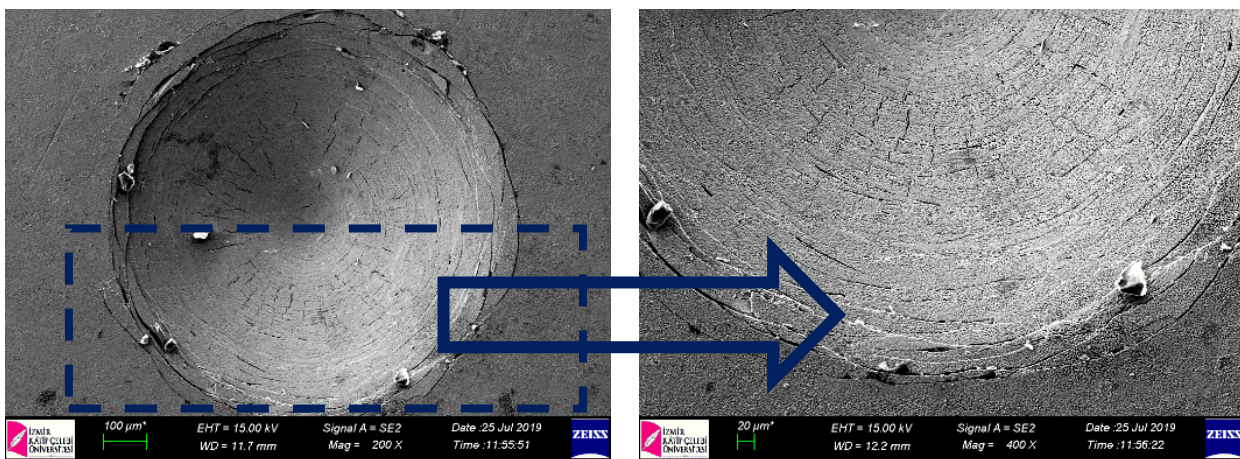


Figure 9. SEM images of the traces and micro cracks formed after the adhesion test on the AISI 304L sample pack-borided at 850 °C for 6 hours with microwave hybrid heating

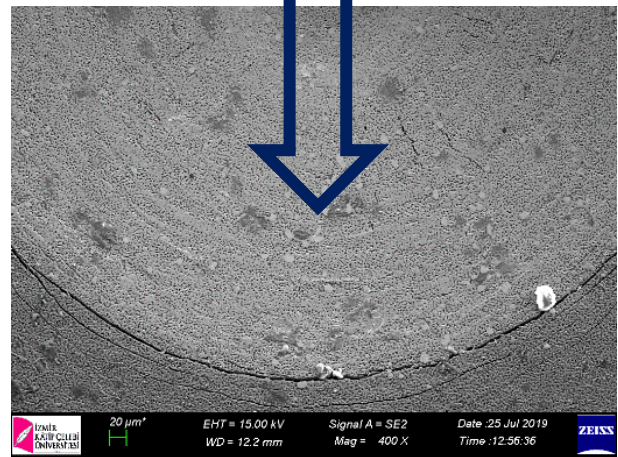
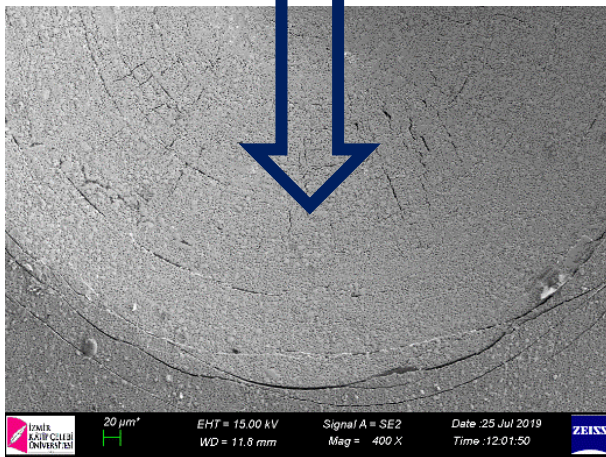
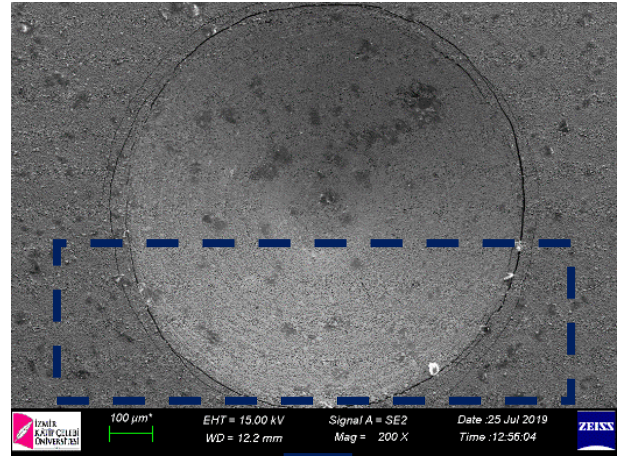
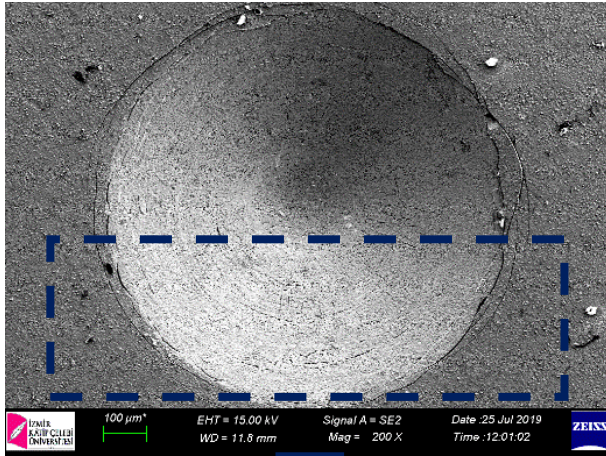


Figure 10. SEM images of the traces and micro cracks formed after the adhesion test in AISI 304L sample pack-borided at 900 °C for 2 hours with microwave hybrid heating

Figure 11. SEM images of the traces and micro cracks formed after the adhesion test in AISI 304L sample pack-borided at 900 °C for 4 hours with microwave hybrid heating

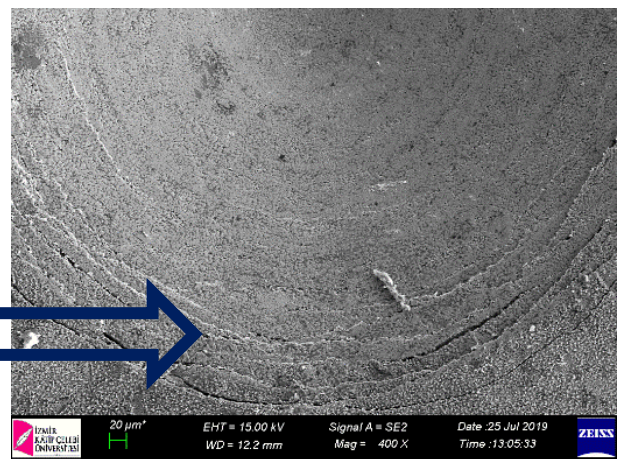
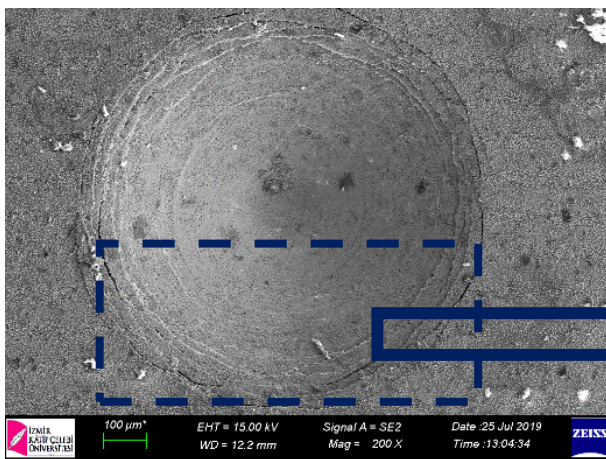


Figure 12. SEM images of the traces and micro cracks formed after the adhesion test on the AISI 304L sample pack-borided at 900 °C for 6 hours with microwave hybrid heating

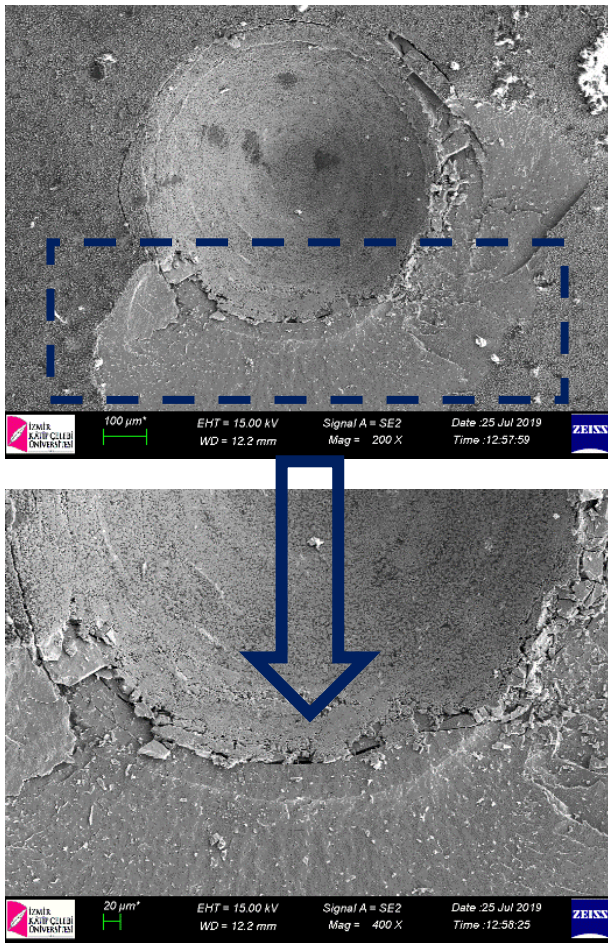


Figure 13. SEM images of the fracture formed after the adhesion test in AISI 304L sample pack-borided for 6 hours at 900 °C with microwave hybrid heating

The indentation craters belonging to one of the pack-borided samples with microwave hybrid heating at 950 °C for 4 hours are shown in Figure 15. There are abrasion scratches and burrs in the boride layer after the adhesion test. This damage is of HF3 type and is acceptable.

The damage appearance after the adhesion test of another sample, which is pack-borided with microwave hybrid heating at 950 °C for 4 hours, is shown in Figure 16. Delaminations occurred in the boride layer of the sample. According to the VDI 3198 indentation test principles, this damage is of the HF5 type and is unacceptable.

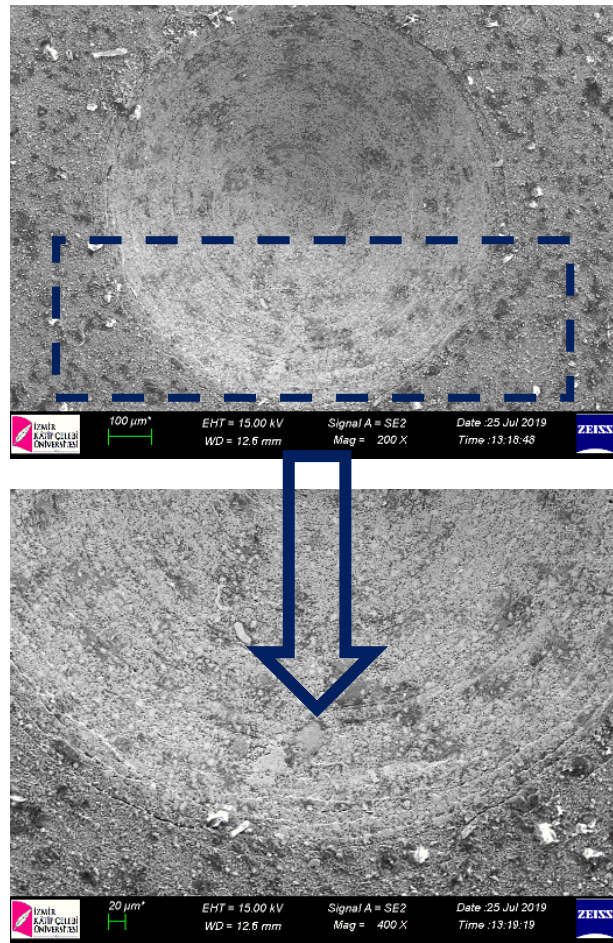


Figure 14. SEM images of the traces and micro cracks formed after the adhesion test of AISI 304L samples pack-borided at 950 °C for 2 hours with microwave hybrid heating

The damage appearance after the indentation test of one of the samples pack-borided with microwave hybrid heating at 950 °C for 6 hours is given in Figure 17. Mosaic cracks and wear lines were formed in the boride layer. This damage is in the HF3 category and is acceptable.

The SEM image showing the damage appearance after the adhesion test of another sample that is pack-borided with microwave hybrid heating at 950 °C for 6 hours is given in Figure 18. Local spallation and delaminations occurred in the boride layer of the sample. According to the VDI 3198 indentation test principles, this damage is of the HF5 type and is unacceptable.

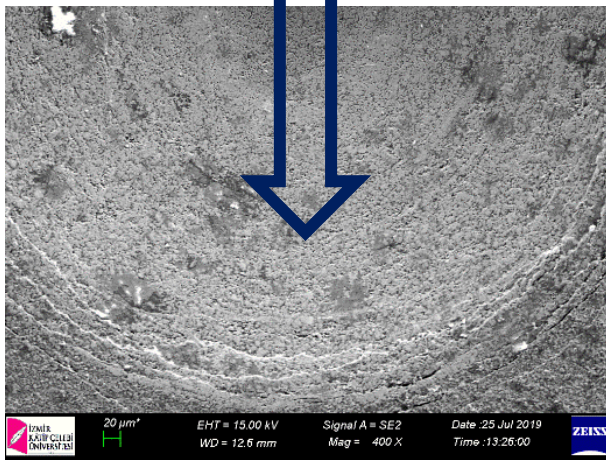
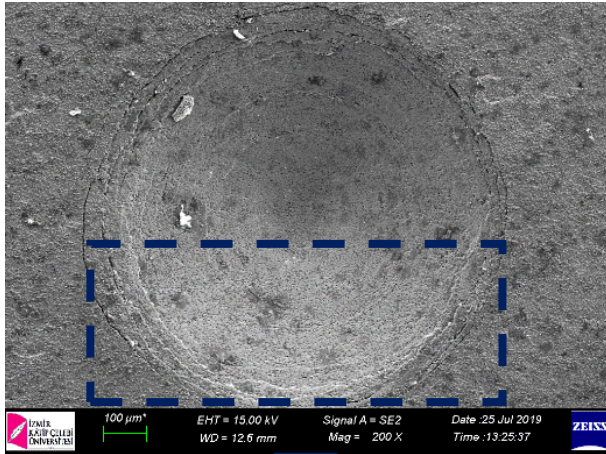


Figure 15. SEM images of the traces and micro cracks formed after the adhesion test of AISI 304L samples pack-borided at 950 °C for 4 hours with microwave hybrid heating

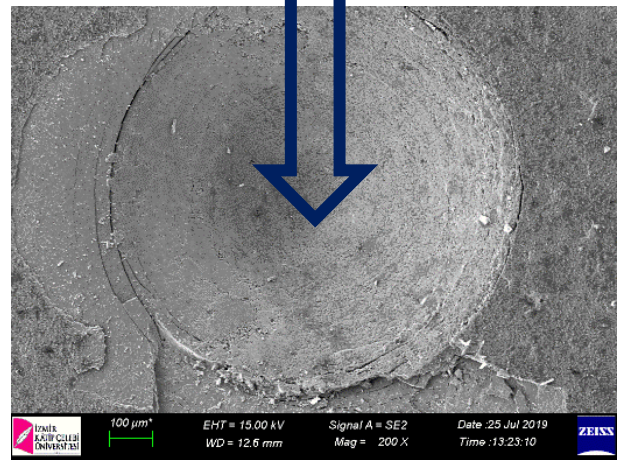
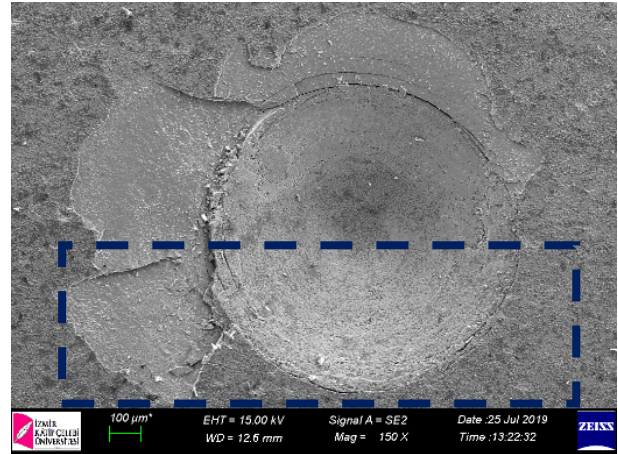


Figure 16. SEM images of the delaminations and cracks formed after the adhesion test of AISI 304L samples pack-borided at 950 °C for 4 hours with microwave hybrid heating

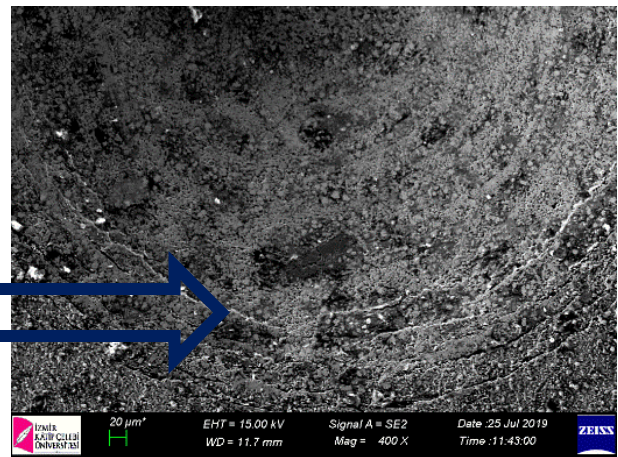
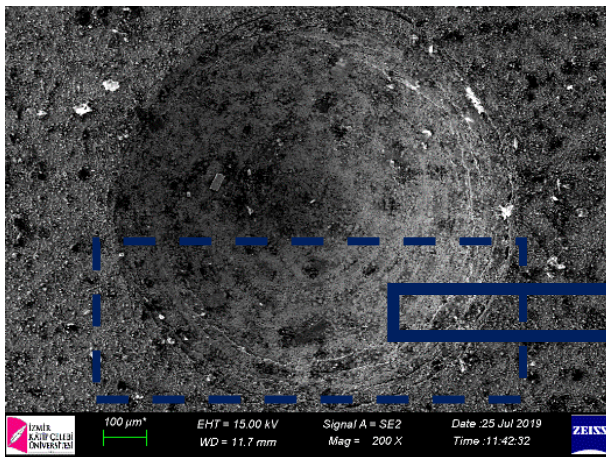


Figure 17. SEM images of the traces and cracks formed after the adhesion test of AISI 304L samples pack-borided at 950 °C for 6 hours with microwave hybrid heating

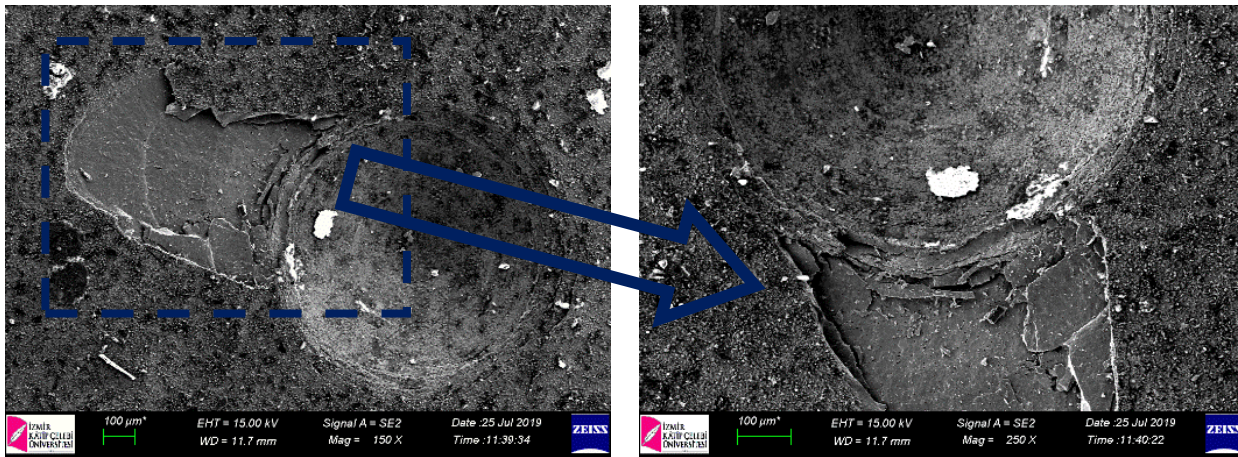


Figure 18. SEM images of the spallation and delaminations formed after the adhesion test of AISI 304L samples pack-borided at 950 °C for 6 hours with microwave hybrid heating

4. Conclusions

Optical microscope examinations showed that both FeB and Fe₂B phase thicknesses increased with the increase of process temperature and retention time in pack-boriding processes performed with microwave hybrid heating method. Uniform and homogeneous boride layers were obtained. However, boride layers formed by the effect of alloying elements are not saw-toothed but flat structure.

XRD pattern analysis showed the presence of FeB, Fe₂B, Cr₂B and Ni₂B phases in the boride layer.

As a result of the Daimler-Benz Rockwell-C adhesion tests carried out, the adhesion strength of the boride layers-substrate of all samples is high, except for the samples that are pack-borided for 6 hours at 900 °C, and at 950 °C for 4 and 6 hours with microwave hybrid heating because the adhesion has decreased with increasing boriding temperature and time. The main reason for the low adhesion strength in these samples is the delamination and spallation of the boride layer as a result of the increase in the thickness of the brittle FeB phase due to the increase in the temperature and retention time of the pack-boriding process.

Author's Contributions

Dilek Arslan: Carried out the experimental processes and examined the results. The manuscript was drafted and written by her.

Recep Onur Uzun: Supervised the experimental procedure and contributed to manuscript preparation.

Ethics

There are no ethical issues after the publication of this manuscript.

References

1. Morón, RC, Hernández-Onofre, I, Contla-Pacheco, AD, Bravo-Bárceñas, D, Campos-Silva, I. 2020. Friction and reciprocating wear behavior of borided AISI H13 steel under dry and lubricated conditions. *Journal of Materials Engineering and Performance*; 29: 4529-4540.
2. Kayali, Y, Büyüksagis, A, Yalcin, Y. 2013. Corrosion and wear behaviors of boronized AISI 316L stainless steel. *Metals and Materials International*; 19(5): 1053-1061.
3. Alias, SK, Abdullah, B, Talari, M, Jumadin, MH, Idham, MF, Ismail, A. 2017. Effect of pack boronizing on microstructure and microhardness of 304 stainless steel. *Key Engineering Materials*; 740: 54-59.
4. Kayali, Y. 2013. Investigation of the diffusion kinetics of borided stainless steels. *The Physics of Metals and Metallography*; 114(12): 1061-1068.
5. Günen, A, Kurt, B, Somunkıran, İ, Kanca, E, Orhan, N. 2015. The effect of process conditions in heat-assisted boronizing treatment on the tensile and bending strength characteristics of the AISI-304 austenitic stainless steel. *The Physics of Metals and Metallography*; 116(9): 896-907.
6. Calik, A, Simsek, M, Karakas, MS, Ucar, N. 2014. Effect of boronizing on microhardness and wear resistance of steel AISI 1050 and chilled cast iron. *Metal Science and Heat Treatment*; 56: 89-92.
7. Yilmaz, SO, Teker, T, Karatas, S. 2016. Wear behavior of iron boride coating on AISI 4140. *Protection of Metals and Physical Chemistry of Surfaces*; 52(1): 119-127.
8. Gunes, I. 2013. Wear behaviour of plasma paste boronized of AISI 8620 steel with borax and B₂O₃ paste mixtures. *Journal of Materials Science & Technology*; 29(7): 662-668.
9. Ulutan, M, Celik, ON, Gasan, H, Er, U. 2010. Effect of different surface treatment methods on the friction and wear behavior of AISI 4140 steel. *Journal of Materials Science & Technology*; 26(3): 251-257.
10. Béjar, MA, Moreno, E. 2006. Abrasive wear resistance of boronized carbon and low-alloy steels. *Journal of Materials Processing Technology*; 173: 352-358.

11. Carrera-Espinoza, R, Figueroa-López, U, Martínez-Trinidad, J, Campos-Silva, I, Hernández-Sánchez, E, Motallebzadeh, A. 2016. Tribological behavior of borided AISI 1018 steel under linear reciprocating sliding conditions. *Wear*; 362-363: 1-7.
12. Tabur, M, Izciler, M, Gul, F, Karacan, I. 2009. Abrasive wear behavior of boronized AISI 8620 steel. *Wear*; 266: 1106-1112.
13. Aichholz, SAC, Meruvia, MS, Júnior, PCS, Torres, RD. 2018. Tribocorrosion behavior of boronized AISI 4140 steel. *Surface and Coatings Technology*; 352: 265-272.
14. Bartkowska, A, Bartkowski, D, Swadźba, R, Przystacki, D, Miklaszewski, A. 2018. Microstructure, chemical composition, wear, and corrosion resistance of FeB-Fe₂B-Fe₃B surface layers produced on Vanadis-6 steel using CO₂ laser. *The International Journal of Advanced Manufacturing Technology*; 95: 1763-1776.
15. Gunes, I, Ulker, S, Taktak, S. 2011. Plasma paste boronizing of AISI 8620, 52100 and 440C steels. *Materials and Design*; 32: 2380-2386.
16. Kayali, Y, Günes, I, Ulu, S. 2012. Diffusion kinetics of borided AISI 52100 and AISI 440C steels. *Vacuum*; 86: 1428-1434.
17. Ozbek, I, Sen, S, Ipek, M, Bindal, C, Zeytin, S, Ucisik, AH. 2004. A mechanical aspect of borides formed on the AISI 440C stainless-steel. *Vacuum*; 73: 643-648.
18. Günen, A, Kanca, E, Demir M, Er, Y, Sağlam, G, Gök, MS. 2017. Micro-abrasion wear behavior of fast borided steel tooth drill bits. *Tribology Transactions*; 60(2): 267-275.
19. Gunes, I, Kanat, S. 2015. Diffusion kinetics and characterization of borided AISI D6 steel. *Protection of Metals and Physical Chemistry of Surfaces*; 51(5): 842-846.
20. Akkaş, M, Islak, S, Özorak, C. 2018. Corrosion and wear properties of Cu-TiC composites produced by hot pressing technique. *Celal Bayar University Journal of Science*; 14(4): 465-469.
21. Kumar, GBV, Rao, CSP, Selvaraj, N. 2011. Mechanical and Tribological Behavior of Particulate Reinforced Aluminum Metal Matrix Composites – a review. *Journal of Minerals & Materials Characterization & Engineering*; 10(1): 59-91.
22. Taktak, S, Tasgetiren S. 2006. Identification of Delamination Failure of Boride Layer on Common Cr-Based Steels. *Journal of Materials Engineering and Performance*; 15(5): 570-574.
23. Krelling, AP, Costa, CE, Milan, JCG, Almeida, EAS. 2017. Micro-abrasive wear mechanisms of borided AISI 1020 steel. *Tribology International*; 111: 234-242.
24. Vidakis, N, Antoniadis, A, Bilalis, N. 2003. The VDI 3198 indentation test evaluation of a reliable qualitative control for layered compounds. *Journal of Materials Processing Technology*; 143-144: 481-485.
25. Verein Deutscher Ingenieure Normen, VDI 3198, *VDI-Verlag*, Dusseldorf, 1991.

Analysis of a Capacitor Modelled with Conformable Fractional Derivative under DC and Sinusoidal Signals

Utku Palaz^{1*}, Reşat Mutlu²

¹Ministry of Education of Republic of Turkey

²Department of Electronics and Telecommunication Engineering, Namık Kemal University, Çorlu, Tekirdağ, Turkey

*utkupalaz@gmail.com

*Orcid: 0000-0003-4579-0424

Received: 25 June 2020

Accepted: 1 June 2021

DOI: 10.18466/cbayarfbe.757813

Abstract

Fractional order circuit elements are successfully used to model circuits and systems in the last few decades. There are different types of fractional derivatives. Recently, another one named “the conformable fractional derivative” (CFD) has been introduced and shown to give good results for modeling supercapacitors. It is imperative to know how circuit elements behave for different current and voltage waveforms in circuit theory so that they can be exploited at their full potential. A CFD capacitor is not a well-known element, and its usage and circuit solutions are rarely addressed in the literature. In this study, it is examined how a CFD capacitor would behave under DC and AC excitations when it is fed by not only a current source but also a voltage source.

Keywords: Fractional Order Derivatives, Circuit Analysis, Circuit Theory, Energy Analysis, Circuit Modeling

1. Introduction

Fractional derivative (FD) is a branch of mathematical analysis [1, 2]. A differential operator can be of any arbitrary order within it. It has first appeared in the 17th century [3]. In the last decades, Fractional Calculus has emerged as a popular research area because of its applicability in many different fields [4-5]. The self-taught Oliver Heaviside has used fractional calculus to find the solution of the telegrapher's equation around 1890 [3]. The fractional-order circuit elements are used to model circuit elements such as capacitors, inductors and memristors [6-10]. Filters, controllers and oscillators which are based on fractional-order circuit elements are made or can be used to model systems [4-5, 8-9, 11-14]. Another FD is suggested in [15]. It is named as “the conformable fractional derivative” (CFD). Its definition is built on the conventional limit definition of the derivative of a function. It casts off the other FD definitions [15]. This makes it simpler and advantageous than the other FDs. The CFD is elaborated in [16]. However, a CFD is actually not an FD: it can be described as a first-order derivative time a power function of the independent variable [15, 16]. This new definition is a broadening of the ordinary derivative. It is also distinct from the other FDs. The CFD is able to accommodate the common features of

FDs. Well-known calculus theorems such as product rule, Rolle's Theorem, Average Value Theorem, partial integration, Taylor series can be easily extended or applied to the CFD. The conformal fractional derivative has a very important property: while the Riemann-Liouville FD of a constant is not zero, the CFD of a constant is zero. Due to these properties, the conformal fractional derivative has become a hot research area. The conformal derivative has also the advantage of being physically interpretable compared to the other types of fractional derivatives [17]. Usage of the FDs in electric circuits has been examined in [18]. Supercapacitors have been modelled using fractional-order models in [19-22]. The oscillation of impulsive conformable fractional differential equations has been inspected in [23]. Electric circuits modelled with FD circuit elements under sinusoidal excitation have been analyzed with the enhanced fractional derivative method, which is called Caputo FD generalizing the differential equations and ordinary integrals are not necessary to describe the fractional-order initial conditions like Riemann-Liouville FD [24-25]. Several electric circuits characterized by CFDs have been solved in [26]. Other circuits modelled with the CFD have been examined in [27]. The conformable fractional derivative has been used to analyze an electric circuit containing a supercapacitor in [28]. Analytical solutions of electrical circuits described by fractional conformable

derivatives in Liouville-Caputo sense is given in [29]. Electric circuits of the CFDs with and without singular kernels have been solved in [30].

It is important to analyze new circuit elements for different current and voltage waveforms so that they can be exploited at full potential. In this paper, the conformal fractional derivative capacitor model for DC and sinusoidal waveforms have been solved. CFD capacitor has been fed with not only voltage sources but also for current sources. The analytical solutions were given with incomplete gamma function for sinusoidal voltage case. The discussions are provided in the conclusion section.

The rest of the paper is structured as follows. The CFD capacitor model is given in the second section. Its analysis for DC and AC signals are given in the third section. Op-amp-based differentiator and integrator circuits with a CFD capacitor are examined in the fourth section. Finally, the paper is concluded in "Conclusions" section.

2. Conformal Fractional Derivative and CFD Capacitor Constitutional Law

The CFD is described in [15] as the follows:

Definition 1. Let $f : [0, +\infty) \rightarrow R$ and $t > 0$. The CFD for $0 < \alpha \leq 1$ is described as

$$D_{\alpha} f(t) = \lim_{p \rightarrow 0} \frac{f(t + p^{(1-\alpha)}) - f(t)}{p} \quad (2.1)$$

For $t > 0$ and the conformable fractional derivative at 0 is defined as $D_{\alpha} f(0) = \lim_{t \rightarrow 0^+} (D_{\alpha} f)(t)$. If it is

differentiable then $D_{\alpha} f(t) = t^{1-\alpha} f'(t)$ (2.2)

Definition 2. Let $\alpha \in (0, 1]$. The conformable fractional integral of a function $f : [0, +\infty) \rightarrow R$ of order α is denoted by $I_{\alpha} f(t)$ and is defined as

$$I_{\alpha} f(t) = \int_0^t s^{(\alpha-1)} f(s) ds \quad (2.3)$$

$$\frac{d^{\alpha} f(t)}{dt^{\alpha}} = f'(t) t^{1-\alpha} = \frac{df(t)}{dt} t^{1-\alpha} \quad (2.4)$$

More information about CFD can be found in [15-17]. If a capacitor can be modelled using CFD [28], its constitutive law can be written as

$$i_c(t) = C_{\alpha} \frac{d^{\alpha} v_c(t)}{dt^{\alpha}} \quad (2.5)$$

Where $i_c(t)$, $v_c(t)$ and C_{α} are CFD capacitor current, CFD capacitor voltage and CFD capacitor coefficient, respectively.

3. The CFD Capacitor Fed by a Current Source

In this section, the solutions of a CFD capacitor is found if it is fed by a current source as shown in Figure 1 for the cases: (a) the current source being constant and (b) it being sinusoidal.

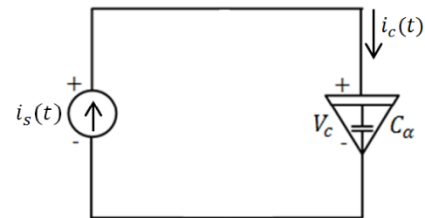


Figure 1: The CFD capacitor fed by a current source

3.1 Constant Current Solution

If the current source has a constant magnitude or the CFD capacitor current is constant;

$$i_s(t) = i_c(t) = I_{dc} = C_{\alpha} \frac{dv_c(t)}{dt} t^{1-\alpha} \quad (3.1)$$

By arranging both sides,

$$\frac{dv_c(t)}{dt} = \frac{I_{dc}}{C_{\alpha} t^{1-\alpha}} \rightarrow dv_c(t) = \frac{I_{dc}}{C_{\alpha} t^{1-\alpha}} dt \quad (3.2)$$

Its voltage can be found as

$$v_c(t) = \int \frac{I_{dc}}{C_{\alpha} t^{1-\alpha}} dt = \frac{I_{dc}}{C_{\alpha}} \int t^{\alpha-1} dt \quad (3.3)$$

$$v_c(t) = \frac{I_{dc} t^{\alpha}}{C_{\alpha} \alpha} + K \quad (3.4)$$

Where K is the integration constant and the capacitor voltage at $t = 0$ is used to find K;

$$v_c(0) = \frac{I_{dc} 0^{\alpha}}{C_{\alpha} \alpha} + K \rightarrow K = v_c(0) \quad (3.5)$$

Using the integration constant, the CFD capacitor current can be obtained as;

$$v_c(t) = \frac{I_{dc} t^{\alpha}}{C_{\alpha} \alpha} + v_c(0) \quad (3.6)$$

3.2 Sinusoidal Current Solution

If a sinusoidal current of $i_s(t) = I_m \cos(\omega t + \varphi)$ is applied to the CFD capacitor, its voltage can be calculated with the following steps:

$$i_s(t) = i_c(t) = I_m \cos(\omega t + \varphi) = C_\alpha \frac{dv_c(t)}{dt} t^{1-\alpha} \quad (3.7)$$

By arranging both sides of the equation, the CFD capacitor voltage is written as

$$\frac{dv_c(t)}{dt} = \frac{I_m \cos(\omega t + \varphi)}{C_\alpha t^{1-\alpha}} \quad (3.8)$$

$$v_c(t) = \frac{I_m}{C_\alpha} \int \cos(\omega t + \varphi) t^{(\alpha-1)} dt \quad (3.9)$$

Using Wolfram Alpha [31], the solution of the integral is found as

$$v_c(t) = \frac{I_m}{C_\alpha} \left(\frac{-t^\alpha (\omega^2 t^2)^{-\alpha}}{2} ((-i\omega t)^\alpha (\cos(\varphi) - i \sin(\varphi)) \Gamma(a, i\omega t) + (i\omega t)^\alpha (\cos(\varphi) + i \sin(\varphi)) \Gamma(a, -i\omega t)) + K \right) \quad (3.10)$$

Using the following identities:

$$e^{i\varphi} = \cos(\varphi) + i \sin(\varphi) \quad (3.11)$$

$$e^{-i\varphi} = \cos(\varphi) - i \sin(\varphi)$$

The capacitor voltage turns into;

$$v_c(t) = \frac{I_m}{C_\alpha} \left(\frac{-t^\alpha (\omega^2 t^2)^{-\alpha}}{2} ((-i\omega t)^\alpha e^{-i\varphi}) \Gamma(a, i\omega t) + (i\omega t)^\alpha e^{i\varphi} \Gamma(a, -i\omega t) \right) + K \quad (3.12)$$

In mathematics, the upper incomplete gamma function is a transcendental function that appears as solutions to diverse problems such as definite integrals.

When splitting the incomplete gamma function at a point $x \geq 0$, two types of the incomplete gamma functions called upper and lower are obtained.

The definition of the upper incomplete gamma function intervals are explained from x to ∞ .

$$\Gamma(s, x) = \int_x^\infty t^{s-1} e^{-t} dt \quad (3.13)$$

If the initial condition is used at $t=0$,

$$v_c(0) = \frac{I_m}{C_\alpha} [0 + K] \rightarrow K = v_c(0) \frac{C_\alpha}{I_m} \quad (3.14)$$

Using the integration constant, the CFD capacitor voltage can be obtained as

$$v_c(t) = -\frac{I_m t^\alpha (\omega^2 t^2)^{-\alpha}}{2C_\alpha} ((-i\omega t)^\alpha e^{-i\varphi}) \Gamma(a, i\omega t) + ((i\omega t)^\alpha e^{i\varphi}) \Gamma(a, -i\omega t) + v_c(0) \quad (3.15)$$

Numerical methods can be used to calculate the CFD capacitor voltage since the solution requires the upper incomplete gamma function which is also evaluated numerically.

4. The CFD Capacitor Fed by a Voltage Source

In this section, the solution of the CFD capacitor fed by a voltage source shown in Figure 2 is found for both of the cases: the voltage source being a constant (a) and a sinusoidal (b).



Figure 2. The CFD capacitor fed by a voltage source

4.1. Constant Voltage Solution

If a step function voltage is applied to the CFD capacitor at time being t_0 :

$$v_C(t) = V_{dc} u(t - t_0) \quad (4.1)$$

The CFD capacitor current becomes

$$i_c(t) = C_\alpha \frac{dv_C(t)}{dt} t^{1-\alpha} = C_\alpha \frac{d(V_{dc} u(t - t_0))}{dt} t^{1-\alpha} \quad (4.2)$$

$$i_c(t) = C_\alpha V_{dc} \delta(t - t_0) t^{1-\alpha} = C_\alpha V_{dc} \delta(t - t_0) t_0^{1-\alpha} \quad (4.3)$$

Where $\delta(t - t_0)$ is the Dirac-delta function [32] shifted to time being t_0 .

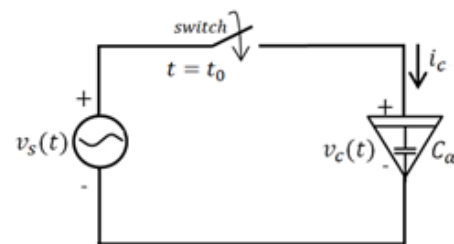


Figure 3. The CFD capacitor fed by a voltage source and depends on the time.

A CFD capacitor without a series resistor withdraws a Dirac pulse as a linear time-invariant resistor does. However, its current magnitude depends on the time the voltage is applied opposite to the case in which an LTI (Linear Time-Invariant) capacitor current pulse

magnitude is constant not depending on the time the step function is applied as shown in Figure 3.

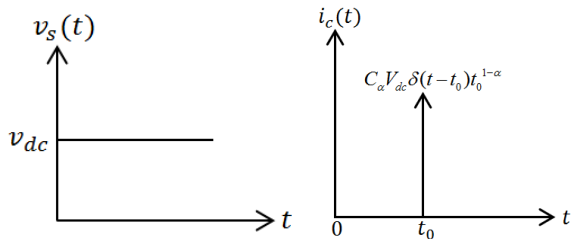


Figure 4. The CFD capacitor voltage and current vs. time when it is fed by a constant voltage

4.2. Sinusoidal Voltage Solution

If a sinusoidal voltage of $v_c(t) = V_m \sin(\omega t + \varphi)u(t - t_0)$ is applied to the CFD capacitor at time being t_0 , its current is found as

$$i_c(t) = C_\alpha \frac{dv_c(t)}{dt} t^{1-\alpha} = C_\alpha \frac{d(V_m \sin(\omega t)u(t - t_0))}{dt} t^{1-\alpha} \quad (4.4)$$

$$i_c(t) = C_\alpha V_m t^{1-\alpha} (\omega \cos(\omega t) + \sin(\omega t) \delta(t - t_0)) \quad (4.5)$$

When the Dirac-delta function rule $f(t)\delta(t - t_0) = f(t_0)\delta(t - t_0)$ is used, the CFD capacitor current can be written as:

$$i_c(t) = C_\alpha V_m \omega \cos(\omega t) t^{1-\alpha} + C_\alpha V_m \sin(\omega t_0) t_0^{1-\alpha} \delta(t - t_0) \quad (4.6)$$

The circuit waveforms are drawn with Matlab™. The CFD capacitor current and voltage for this case is shown in Figure 5 and 6. The CFD capacitor current magnitude is not constant and varies with time due to the term $t^{1-\alpha}$ as shown in Figure 4. When $V_m = 5V$, $\omega = 1 \text{ rad/s}$, $\varphi = 0 \text{ rad/s}$ and $C_\alpha = 1 \text{ F} / \text{s}^{1-\alpha}$ values are used, the CFD capacitor current graph in Figure 6 is sketched for three different alpha values.

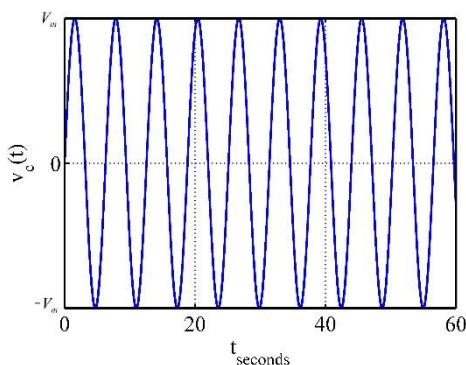


Figure 5. The CFD capacitor voltage vs. time when it is fed by a sinusoidal voltage

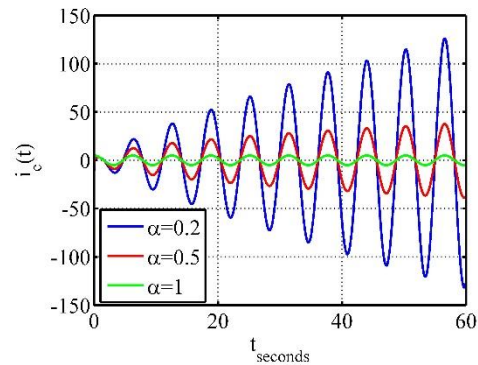


Figure 6. The CFD current vs. time when it is fed by a sinusoidal voltage

All real capacitor models have series and parallel resistors used in their equivalent circuit to model their losses. In this study, the capacitors are assumed to be ideal, ie. without losses and that's why no resistor is used in the analysis. The CFD capacitor current goes to infinity due to the term $t^{1-\alpha}$ as seen in Figure 6 because of this. Such a situation would not appear in a more realistic capacitor model when a series resistor is used.

5. Conclusions

Supercapacitors or ultra-capacitors are becoming more common each day. They cannot be modelled with capacitor constitutive law. Therefore, easier and robust models are needed for their usage and analysis in the circuits. Only then, such capacitors can be fully exploited.

The conformal fractional derivative provides an easier solution than the fractional derivatives such as Caputo and Riemann Liouville. Some capacitors can be modelled using fractional-order derivatives. In this study, the conformal fractional derivative is used to model a capacitor. Every circuit element should be examined for the basic waveforms such as DC and sinusoidal signals. The solutions of the CFD capacitor for the waveforms are given. Only in the case when it is fed by a current source, its voltage is found using a transcendental function the incomplete gamma functions. The solutions can be used in the analysis of the circuits with a CFD capacitor if a supercapacitor is found to be modelled with a good accuracy using experimental data. In comparison to the prior studies, the CFD derivative is more practical and analytical solutions are found to be possible while it has been not possible for other fractional derivatives. The analysis given here can also be used in modelling renewable energy systems or inverters with supercapacitors in the future. This paper can also be used as a tutorial for the researchers who have just been introduced to the research area.

Author's Contributions

Utku Palaz: Made literature search, prepared computer codes for numerical solutions of the sample problems, made simulations, and wrote the manuscript.

Reşat Mutlu: Made literature search, assisted in analytical analysis on the structure, supervised the experiment's progress, result in interpretation, and helped in manuscript preparation.

Ethics

There are no ethical issues after the publication of this manuscript.

References

1. Podlubny, I. (1998). Fractional differential equations: an introduction to fractional derivatives, fractional differential equations, to methods of their solution and some of their applications. Elsevier.
2. Yang, X. J. (2019). General fractional derivatives: theory, methods and applications. Chapman and Hall/CRC.
3. Ross, B. (1977). The development of fractional calculus 1695–1900. *Historia Mathematica*, 4(1), 75-89.
4. Kilbas, A.A.; Srivastava, H.M.; Trujillo, J.J. *Theory and Applications of Fractional Differential Equations*; Elsevier: Amsterdam, The Netherlands, 2006
5. Babiarz, A., Czornik, A., Klamka, J., & Niezabitowski, M. (2017). Theory and applications of non-integer order systems. *Lecture Notes Electrical Engineering*, 407.
6. Moreles, M. A., & Lainez, R. (2016). Mathematical modelling of fractional order circuits. arXiv preprint arXiv:1602.03541.
7. Freeborn, T. J. (2013). A survey of fractional-order circuit models for biology and biomedicine. *IEEE Journal on emerging and selected topics in circuits and systems*, 3(3), 416-424.
8. Adhikary, A., Khanra, M., Pal, J., & Biswas, K. (2017). Realization of fractional order elements. *Inae Letters*, 2(2), 41-47.
9. Tsirimokou, G., Kartci, A., Koton, J., Herencsar, N., & Psychalinos, C. (2018). Comparative study of discrete component realizations of fractional-order capacitor and inductor active emulators. *Journal of Circuits, Systems and Computers*, 27(11), 1850170.
10. Kartci, A., Agambayev, A., Herencsar, N., & Salama, K. N. (2018). Series-, parallel-, and inter-connection of solid-state arbitrary fractional-order capacitors: theoretical study and experimental verification. *IEEE Access*, 6, 10933-10943.
11. Sotner, R., Jerabek, J., Kartci, A., Domansky, O., Herencsar, N., Kledrowetz, V., ... & Yeroglu, C. (2019). Electronically reconfigurable two-path fractional-order PI/D controller employing constant phase blocks based on bilinear segments using CMOS modified current differencing unit. *Microelectronics Journal*, 86, 114-129.
12. Podlubny, I., Petráš, I., Vinagre, B. M., O'leary, P., & Dorčák, L. (2002). Analogue realizations of fractional-order controllers. *Nonlinear dynamics*, 29(1-4), 281-296.
13. Alagoz, B. B., & Alisoy, H. Z. (2014). On the Harmonic Oscillation of High-order Linear Time Invariant Systems. *Scientific Committee*.
14. Alagöz, B. B., & Alisoy, H. Estimation of Reduced Order Equivalent Circuit Model Parameters of Batteries from Noisy Current and Voltage Measurements. *Balkan Journal of Electrical and Computer Engineering*, 6(4), 224-231.
15. Khalil, R.; al Horani, M.; Yousef, A.; Sababheh, M. A new definition of fractional derivative. *J. Comput. Appl. Math.* 2014, 264, 65–70.
16. Abdeljawad, T. (2015). On conformable fractional calculus. *Journal of computational and Applied Mathematics*, 279, 57-66.
17. Zhao, D., & Luo, M. (2017). General conformable fractional derivative and its physical interpretation. *Calcolo*, 54(3), 903-917.
18. Sikora, R. (2017). Fractional derivatives in electrical circuit theory—critical remarks. *Archives of Electrical Engineering*, 66(1), 155-163.
19. Lewandowski, M., & Orzyłowski, M. (2017). Fractional-order models: The case study of the supercapacitor capacitance measurement. *Bulletin of the Polish Academy of Sciences Technical Sciences*, 65(4), 449-457.
20. Kopka, R. (2017). Estimation of supercapacitor energy storage based on fractional differential equations. *Nanoscale research letters*, 12(1), 636.
21. Freeborn, T. J., Elwakil, A. S., & Allagui, A. (2018, May). Supercapacitor fractional-order model discharging from polynomial time-varying currents. In *2018 IEEE International Symposium on Circuits and Systems (ISCAS)* (pp. 1-5). IEEE.
22. Freeborn, T. J., Maundy, B., & Elwakil, A. S. (2013). Measurement of supercapacitor fractional-order model parameters from voltage-excited step response. *IEEE Journal on Emerging and Selected Topics in Circuits and Systems*, 3(3), 367-376.
23. Tariboon, J., & Ntouyas, S. K. (2016). Oscillation of impulsive conformable fractional differential equations. *Open Mathematics*, 14(1), 497-508.
24. Piotrowska, E., & Rogowski, K. (2017, October). Analysis of fractional electrical circuit using Caputo and conformable derivative definitions. In *Conference on Non-integer Order Calculus and Its Applications* (pp. 183-194). Springer, Cham.
25. Piotrowska, Ewa. "Analysis of fractional electrical circuit with sinusoidal input signal using Caputo and conformable derivative definitions." *Poznan University of Technology Academic Journals. Electrical Engineering* (2019).
26. Morales-Delgado, V. F., Gómez-Aguilar, J. F., & Taneco-Hernandez, M. A. (2018). Analytical solutions of electrical circuits described by fractional conformable derivatives in Liouville-Caputo sense. *AEU-International Journal of Electronics and Communications*, 85, 108-117.
27. Martínez, L., Rosales, J. J., Carreño, C. A., & Lozano, J. M. (2018). Electrical circuits described by fractional conformable derivative. *International Journal of Circuit Theory and Applications*, 46(5), 1091-1100.
28. Piotrowska, E. (2018, October). Analysis the conformable fractional derivative and Caputo definitions in the action of an electric circuit containing a supercapacitor. In *Photonics Applications in Astronomy, Communications, Industry, and High-Energy Physics Experiments 2018 (Vol. 10808, p. 108081T)*. International Society for Optics and Photonics.
29. Morales-Delgado, V. F., Gómez-Aguilar, J. F., & Taneco-Hernandez, M. A. (2018). Analytical solutions of electrical circuits described by fractional conformable derivatives in Liouville-Caputo sense. *AEU-International Journal of Electronics and Communications*, 85, 108-117.
30. Gómez-Aguilar, J. F. (2018). Fundamental solutions to electrical circuits of non-integer order via fractional derivatives with and



without singular kernels. The European Physical Journal Plus, 133(5), 197.

31. https://www.wolframalpha.com/input/?i=cos%28omega*t%2Bphi%29*%28t%5E%28a-1%29%29

32. Allen R. L., and Mills D. (2004). Signal analysis: time, frequency, scale, and structure. John Wiley & Sons.

Optimal placement of multiple DGs in radial distribution systems to minimize power loss using BSA

Waleed Fadel^{1*} , Ulaş Kılıç² , Sezai Taşkın³ 

¹Department of Electrical&Electronics, Faculty of Engineering, Girne American University, Mersin 10 – Turkey

²Department of Electrical&Electronics, Faculty of Engineering, Ege University, İzmir – Turkey

³Department of Electrical&Electronics, Faculty of Engineering, Manisa Celal Bayar University, Manisa –Turkey

*waleedfadel@gau.edu.tr

*Orcid: 0000-0002-5061-6474

Received: 18 September 2020

Accepted: 29 March 2021

DOI: 10.18466/cbayarfbe.796140

Abstract

Distributed generation (DG) sources are becoming more important in electrical networks due to the increase of electrical energy demands. However, DG sources can have a profound effect on network power loss. Hence, optimal placement and size of DGs are extremely important. This study presents an efficient heuristic algorithm based on optimal placement and size of multiple DGs within distribution systems in order to reduce power loss. This algorithm is backtracking search algorithm (BSA). Two main DGs, photovoltaic and synchronous compensator, are integrated in two different radial distribution systems (RDS), IEEE 33-bus system and IEEE 69-bus system. To demonstrate the effectiveness of the proposed method, the results obtained by BSA are compared with a genetic algorithm (GA) as well as other results in the literature.

Keywords: BSA, DG placement, DG size, power loss.

1. Introduction

The integration of a solar power plant in distribution network is an important challenge, and it is one of the ways to reduce the environmental pollution that is produced by fossil fuel-based energy generation. Thus, much research has been concentrated on the optimum integration of solar panels in distribution networks in recent years.

Optimal reactive power flow is necessary to maintain power system reliability. It is achieved by minimizing power losses in the transmission line under the constraints of the physical system, using power flow equations. Valuable articles have dealt with this subject for the purpose of reducing power losses. Kansal et al. [1] proposed particle swarm optimization (PSO) to solve for the placement and size of different types of DG's, taking the power loss as an objective function. Kayal et al. [2] presented different types of DG's with different modes, using PSO. Their objective was power loss minimization and voltage stability improvement. Kollu et al. [3] proposed a harmony search algorithm (HSA) for multi-DG placement to reduce power loss, and enhance the voltage profile. García et al. [4] employed

modified teaching–learning based optimization (MTLBO) to solve the problem of placement and sizing of multiple DG's with the single objective of reducing power loss. Injeti et al. [5] used simulated annealing (SA) for a DG placement and size to reduce the power loss, and improve the voltage stability. Manafi et al. [6] presented dynamic PSO for optimal placement of a DG to minimize power loss. Moradi et al. [7] proposed PSO/GA hybrid algorithms as a solution for sizing and placement of a DG to improve voltage regulation, and minimize power loss. Aman et al. [8] employed a PSO algorithm to solve a function with the multiple objectives of maximizing voltage stability and minimizing power losses, and found the optimal DG allocation, weakest link in the network, and the most sensitive voltage bus. Ates et al. [9] examined the impact of hybrid DG on power losses, voltage improvement, and electricity bill in distribution network by using the ETAP. Turan et al. [10] proposed the integration of a solar plant to a PEV parking lot to reduce power consumption and losses considering various operating conditions. Hemeida et al. [11] implemented a new optimization algorithm to the optimal integration of a DG for power loss minimization. Memarzadeh et al. [12] applied a new approach for DG placement in order to improve voltage stability index and

the system reliability. This approach has been tested in various RDS. Kansal et al. [13] proposed a hybrid of heuristic and analytical methods of the PSO (H-PSO) algorithm to determine the optimum places and the best types of DGs.

In this work, we have considered 3 scenarios. In Scenario 1, the tested systems are integrated by active-power DGs (photovoltaic) only, where only one active-power DG can be placed in a given bus. In Scenario 2, one active-power DG and one reactive-power DG (synchronous compensator) are paired and connected together in a bus, where only one pair can be placed in a given bus. In Scenario 3, while in some buses one active-power DG and one reactive-compensator DG are paired and connected as a single pair per bus, in other buses either one active-power DG or one reactive-power DG is placed singly –only one DG per bus. References [2, 5, 6, 7, 8 and 13] dealt only with scenario 1. Ref. [1] dealt with scenarios 1 and 2, but not 3. None of the references used the BSA in their optimizations. In this paper, we applied the BSA on 33-bus as well as 69-bus systems in cases where multiple DGs (up to a total of 16 DGs and 13 buses) are used. As understood from the Ref. [1-8] mentioned above, heuristic algorithms are successfully applied to solve the optimization problem in RDS. In this study, we used the BSA to solve the optimization problem of DG placement and sizing, such as to minimize system power loss in RDS.

This paper is arranged as follows: problem formulation is in Section 2, the proposed algorithm in Section 3, simulation results and discussion in Section 4, and the conclusion in Section 5.

2. Problem formulation

In this paper, active power loss is selected as an objective function. To minimize the objective function, the proposed algorithm is applied in two RDSs under both equality as well as inequality constraints. Minimization of power loss is an optimization problem, mathematical equations of which is well known and is defined as follows,

$$\begin{aligned} &\text{Minimize} && f(x, u) \\ &\text{Such that} && g(x, u) = 0 \\ &&& h(x, u) \leq 0 \end{aligned} \quad (1)$$

where f , g , and h are the fitness function, the equality constraint, and the inequality constraint, respectively. Here, x is the vector of control variables, while u is the vector of state variables. The control variables are the size and the place of DG active power, and of the reactive compensators. The state variables are active and reactive power of the feeder, load, bus voltage, and the line current.

2.1. Objective Function

In this work, power loss is selected as an objective function. The power loss can be demonstrated as equation (2) [14].

$$P_{loss} = P_{feeder} + \sum_{i=1}^{N_{DG}} P_{DG,i} - \sum_{i=1}^N P_{Load,i} \quad i = 1, \dots, N \quad (2)$$

2.2. Equality constraints

Load balancing constraint formulas as follows:

$$CDG_i \cdot P_{DG,i} + CF_i \cdot P_{feeder} = P_{Load,i} + V_i \sum_{j=1}^N V_j (G_{ij} \cos \delta_{ij} + B_{ij} \sin \delta_{ij}) \quad i = 1, \dots, N \quad (3)$$

$$CSC \cdot Q_{sc,i} + CF_i \cdot Q_{feeder} = Q_{Load,i} + V_i \sum_{j=1}^N V_j (G_{ij} \sin \delta_{ij} - B_{ij} \cos \delta_{ij}) \quad i = 1, \dots, N \quad (4)$$

2.3. Inequality constraints

Voltage limits:

The allowable range for all buses is given in equation (5),

$$V_i^{\min} \leq V_i \leq V_i^{\max} \quad i = 1, \dots, N \quad (5)$$

Unit constraints of DGs:

The following constraint is the allowable active power and reactive power sizes of DGs.

$$P_{DG,i}^{\min} \leq P_{DG,i} \leq P_{DG,i}^{\max} \quad i = 1, \dots, N_{DG} \quad (6)$$

$$Q_{sc,i}^{\min} \leq Q_{sc,i} \leq Q_{sc,i}^{\max} \quad i = 1, \dots, N_{SC} \quad (7)$$

Line capacity constraints:

The current limitation of the distribution lines of the system is given by [15].

$$|I_{ij}| \leq |I_{ij}^{\max}| \quad i = 1, \dots, N, \quad j = 1, \dots, N \quad \text{and} \quad i \neq j \quad (8)$$

3. Back-tracking Search Algorithm

BSA is an evolutionary algorithm (EA) introduced by Civicioglu in 2012 [16]. BSA has been applied to solve different optimization problems in various fields such as energy, geophysics, and magnetism [17-19]. The most significant property of BSA that it is not sensitive to the initial values. Selection, mutation, and crossover

operators are used in BSA. The MATLAB® code of BSA can be found in [16]. The basic steps of BSA are outlined as follows [17].

```

Repeat
  Selection-1
  Generation of Trial-Population
  Mutation
  Crossover
  End
  Selection-2
Until stopping conditions are met.
  
```

3.1. Initialization

In the beginning, two different populations (Pop and $oldPop$) are formed as follows:

$$Pop_{i,j} \sim Rand(low_j, up_j) \quad i = 1, \dots, SN \quad j = 1, \dots, D \quad (9)$$

$$oldPop_{i,j} \sim Rand(low_j, up_j) \quad i = 1, \dots, SN \quad j = 1, \dots, D \quad (10)$$

3.2. Selection-I

In this section, the old population ($oldPop$) in the initiation stage is formed using,

$$if \ a < b, \ oldPop := Pop \ end \ | \ a, b \sim Rand(0,1) \quad (11)$$

In equation (11), $:=$ is the update operator. This operator randomly transfers the Pop individuals' variables to $oldPop$ individuals' variables. Then, equation (12) is used to randomly change individuals in the $oldPop$.

$$oldPop := Randshuff(oldPop) \quad (12)$$

where $Randshuff$ is a random mixing function [15].

3.3. Mutation

The mutation process is formed as

$$mutantPop = Pop + W(oldPop - Pop) \quad (13)$$

In equation (13), W controls the amplitude of the search line matrix. $W = 3randn$ is proposed in the Ref.[16]. However, we observed that the performance of 4 is better than that of 3. The function “ $randn$ ” randomly generates numbers between 0 and 1 according to the standard normal distribution [17].

3.4. Crossover

Initialization

In this section, the trial population ($Tpop$) is formed using equation (14). The crossover process consists of two stages. In the first stage, the binary number system is fully valued, and produces $SN * D$ size of a matrix (map). This matrix is used to determine whether or not we have to modify $Tpop$, one row at a time (“individual by individual” in heuristic terms). The second stage, the following equation is obtained from the matrix after its formation.

$$if \ map_{i,j} = 1 \ then \ Tpop_{i,j} = Pop_{i,j} \ else \ Tpop_{i,j} = mutantPop_{i,j} \ end \quad (14)$$

3.5. Selection-II

All the “individual” fitness values produced is calculated in this section. Individuals are sorted according to their fitness values, from best to worst. Then, the SN of them are carried to the next iteration Pop . The remaining ones are omitted. In this way, the best “individuals” among the whole population are transferred to the next generation.

4. Simulation Results and discussion

In this work, two types of DG are integrated in two different RDS. These systems are 33 and 69 bus systems. All nodes integrated of DGs are selected as PQ mode. The results are compared with GA and other recent works.

DG resources are divided into 4 types, determined by ability to deliver active and reactive power. The DG types are:

- Type I: Generating active power (Photovoltaic system).
 - Type II: Generating reactive power (Synchronous compensation).
 - Type III: Generating active and absorbing reactive power (Wind power)
 - Type IV: Generating active and reactive power (Synchronous generator).
- Type I and Type II are performed in our work.

Scenarios and cases

In this study, 3 scenarios and 5 cases are examined. All scenarios are considered under the 5 cases, and the differences between cases, depend on the number of DGs. In the following tables Case1 is base case for IEEE 33- bus system and IEEE 69- bus system.

Scenario1: All DGs are type I, one per bus.

Scenario2: Any pair of DGs (one of type I & one of type II) is connected in the same bus, only one pair per bus.

Scenario3: Some DG pairs (one of type I & one of type II) are connected in the same bus, one pair bus, while single DGs (type-I or type-II) are connected in different buses, one DG per bus.

4.1. IEEE 33-bus system

The IEEE 33-bus system is selected, with a system voltage base of 12.66 kV for all cases, and base apparent power of 100 MVA for all cases. The test system has total active and reactive loads of 3.715 MW and 2.300 MVar, respectively. The data for the line reactance and resistances, and for the loads connected to buses, are given in [20].

Scenario1: In scenario1, 4 cases are constructed considering DG number. One, two, three and four DGs

are integrated in Case2, 3, 4, and 5, respectively, to 33-bus system. In the following tables, all sizes of DGs type I are in (MW), while size of DGs Type II are in (MVar).

The obtained results using BSA for all cases of Scenario1 are given in Table 1. The power loss for Case2, 3, 4, and 5, respectively are 211, 103.966, 87.1669, 72.7878 and 67.67kW. When we compare power loss of all cases, it is concluded that Case2 is better than Case1, Case3 is better than Case2, Case4 is better than Case3, and Case5 is the best for Scenario1.

Power loss reduction (considering Case1) comparison of the proposed algorithm, GA, and other results for all cases of scenario1 are given in Table 2. It is noticed that, the obtained results by the proposed algorithm for all cases are the best among all results.

Table 1. Results by BSA of all cases in Scenario 1 for IEEE 33- bus system

	Case 1	Case 2	Case 3	Case 4	Case 5
Power loss	211	103.966	87.1669	72.7878	67.76
Placement and size of DG Type I	-	2.5753(6)	0.8516(13) 1.1576(30)	0.8000(13) 1.0880(24) 1.0523(30)	0.8400(7) 0.6468 (14) 0.7307(25) 0.8112(31)

Table 2. Comparison of power loss reduction (%) by BSA and others for Scenario 1 of IEEE 33-bus system

Case	Ref. [1]	Ref. [2]	Ref. [5]	Ref. [6]	Ref. [7]	Ref. [11]	Ref. [13]	GA	BSA
2	45.36	-	-	39.73	-	47.37	47.31	45.6	50.73
3	-	-	-	54.54	-	58.68	58.64	58.65	58.69
4	-	27.82	61.12	56.14	-	65.45	65.46	65.31	65.50
5	-	-	-	-	67.68	-	-	67.50	67.89

Scenario 2: The obtained results using BSA for all cases of Scenario2 are given in Table 3. The power loss for Case2, 3, 4, and 5, respectively are 211, 67.739, 28.593, 12.2118 and 8.5364 kW. When we compare power loss of all cases, it is concluded that Case2 is better than Case1, Case3 is better

than Case2, Case4 is better than Case3, and Case5 is the best for Scenario2.

Comparison of power loss reduction of BSA and other for all cases of scenario2 are given in Table 4. It is noticed that the obtained results by BSA for all cases of scenario2 are the best among all results.

Table 3. Results by BSA of all cases in Scenario 2 for IEEE 33- bus system

	Case 1	Case 2	Case 3	Case 4	Case 5
Power loss	211	67.739	28.593	12.2118	8.5364
Placement and size of DG Type I	-	2.5566(6)	0.3964(13) 1.0276(30)	0.8534(13) 0.9229(24) 0.3437(30)	0.4350 (7) 0.7180(14) 1.0174(24) 1.0151(30)
Placement	-		0.7537(13)	0.3676(13)	0.5289(7)

and size of DG Type II		1.7580(6)	0.9009(30)	0.4642(24) 0.1949(30)	0.2477 14) 0.5040(24) 0.8370(30)
------------------------	--	-----------	------------	--------------------------	--

Table 4. Comparison of power loss reduction (%) by BSA and others for Scenario 2 of IEEE 33-bus system

Case	Ref. [1]	GA	BSA
2	67.79	67.89	67.89
3	-	86.44	86.45
4	-	93.00	94.21
5	-	95.56	95.95

Scenario 3: The obtained results by BSA for all cases of Scenario3 are given in Table 5. The power loss for Case2, 3, 4, and 5, respectively are 211, 29.8235, 13.8957, 8.7463 and 7.4533kW. When we compare power loss of all cases, it is concluded that Case2 is better than Case1, Case3 is better than Case2, Case4 is better than Case3, and Case5 is the best among all cases in Scenario3.

Table 5. Results by BSA of all cases in Scenario 3 for IEEE 33-bus system

	Case 1	Case 2	Case 3	Case 4	Case 5
Power loss	211	29.8235	13.8957	8.7463	7.4533
Placement and size of DG Type I	-	0.6247(29) 0.6755(14)	1.0070(24) 0.6972(30) 0.7833(13) 0.3295(30)	0.5724 (3) 0.4820(12) 0.4270(27) 0.3781(13) 0.9094(24) 0.7673(30)	0.2647(25) 0.3866(26) 0.3918(31) 0.7962(13) 0.1000(21) 0.6283(24) 0.2068(28) 0.1734(31)
Placement and size of DG Type II	-	0.1000(30) 0.3781(14)	0.2393 (8) 0.1261(14) 0.2076(13) 0.9685(30)	0.3194(4) 0.1321(10) 0.3987(31) 0.1000(13) 0.3871(24) 0.6595(30)	0.3439(23) 0.4105(27) 0.5653(30) 0.2732(13) 0.1393(21) 0.1000(24) 0.2093(28) 0.1000(31)

4.2. IEEE 69- bus system

The IEEE 33-bus system is selected, with system voltage base of 12.66 kV for all cases, and base apparent power of 100 MVA for all cases. The test system has total active and reactive loads of 3.802 MW and 2.694 MVar, respectively. The data for the line reactance and resistances, and for the loads connected to nodes, are given in [20].

Scenario 1: The obtained results using BSA for all cases of Scenario1 are given in Table 7. The power loss for Case2, 3, 4, and 5, respectively are 225, 83.0704, 71.567, 69.3767 and 67.84 kW. When we compare

In Table 5, all values in bold font indicate that DG pairs (one of type I & one of type II) are connected in the same bus, while others are connected in different buses. Power loss reduction of BSA and GA results for all cases of scenario3 are given in Table 6. It is noticed that the obtained results by the proposed algorithm for all cases are better than GA results.

Table 6. Comparison of power loss reduction (%) by BSA and others for Scenario 3 of IEEE 33-bus system

Case	GA	BSA
2	83.28	85.87
3	93.00	93.41
4	94.51	95.86
5	95.67	96.47

power loss of all cases, it is concluded that Case2 is better than Case1, Case3 is better than Case2, Case4 is better than Case3,

and Case5 is the best for Scenario1. Comparison of power loss reduction of BSA and other for all cases of scenario1 are given in Table 8. It is noticed that, the obtained results by BSA for all cases of scenario1 are the best among all results.

Table 7. Results by BSA of all cases in Scenario 1 for IEEE 69-bus system

	Case 1	Case 2	Case 3	Case 4	Case 5
Power loss	225	83.0704	71.567	69.3767	67.84
Placement and size of DG Type I	-	1.8710 (61)	0.5291 (17) 1.7820 (61)	0.5885 (11) 0.3445 (20) 1.7338 (61)	0.5448 (11) 0.3572 (20) 0.7188 (50) 1.7181 (61)

5.7156 and 2.0784 kW. When we compare power loss of all cases, it is found that Case2 is better than Case1, Case3 is better than Case2, Case4 is better than Case3, and Case5 is the best for Scenario2.

Power loss reduction comparison of the proposed algorithm, GA, and other results for all cases of the scenario2 are given in Table 10. It is noticed that, the obtained results by BSA for all cases are the best among all results.

Scenario 2: The obtained results by BSA for all cases of Scenario2 are given in Table 9. The power loss for Case2, 3, 4, and 5, respectively are 225, 23.133, 7.7836,

Table 8. Comparison of power loss reduction (%) by BSA and others for Scenario 1 of IEEE 69-bus system

Case	Ref. [1]	Ref. [5]	Ref. [11]	Ref. [12]	Ref. [13]	GA	BSA
2	62.94	-	63.01	63.02	62.95	63.08	63.08
3	-	-	68.14	-	68.09	68.19	68.19
4	-	65,68	69.14	-	69.09	69.07	69.17
5	-	-	-	-	-	69.80	69.85

Table 9. Results by BSA of all cases in Scenario 2 for IEEE 69-bus system

	Case 1	Case 2	Case 3	Case 4	Case 5
Power loss	225	23.133	7.7836	5.7156	2.0784
Placement and size of DG Type I	-	2.0275(61)	0.5280(15) 1.7266(61)	0.3037(19) 1.6533(61) 0.1501(66)	0.2774(11) 0.2575(18) 0.5289(49) 1.1995(61)
Placement and size of DG Type II	-	1.4447(61)	0.4654(15) 1.2207(61)	0.2203(19) 1.1344(61) 0.3391(66)	0.5206(11) 0.3569(18) 0.7771(49) 1.6666(61)

Table 10. Comparison of power loss reduction (%) by BSA and others for Scenario 2 of IEEE 69-bus system

Case	Ref. [1]	GA	BSA
2	89.01	89.72	89.72
3	-	96.23	96.54
4	-	96.48	97.46
5	-	97.37	99.08

the same bus, while others are connected in different buses.

In Table 12, comparison of power loss reduction of the proposed algorithm and GA for cases of scenario3 is given. It is noticed that the obtained results by BSA for all cases of scenario3 are better than GA results.

Table 12. Comparison of power loss reduction (%) by BSA and others for Scenario 3 of IEEE 69-bus system

Case	GA	BSA
2	96.64	96.75
3	97.63	98.14
4	97.94	98.36
5	99.01	99.16

Scenario 3: The obtained results by proposed algorithm for all cases of Scenario3 are given in Table 11. The power loss for Case2, 3, 4, and 5, respectively are 225, 7.3167, 4.1776, 3.6989 and 1.8875kW. When we compare power loss of all cases, it is noticed that Case2 is better than Case1, Case3 is better than Case2, Case4 is better than Case3, and Case5 is the best for Scenario3. In Table 11, all values in bold font indicate that DG pairs (one of type I & one of type II) are connected in

Table 11. Results by BSA of all cases in Scenario 3 for IEEE 69-bus system

	Case 1	Case 2	Case 3	Case 4	Case 5
Power loss	225	7.3167	4.1776	3.6989	1.8875
Placement and size of DG Type I	-	0.5126(17)	0.4080(17)	0.6224(8)	0.2696(4)
		1.7805(61)	1.8000(61)	0.2630(21)	0.3414(19)
		0.3387(66)	0.7848(61)	0.8759(62)	0.2383(53)
		0.1000(61)	1.2000(62)	0.3674(64)	0.3477 (12)
Placement and size of DG Type II	-	0.3400(16)	0.1000(15)	0.3180(12)	0.2734(2)
		1.2483(61)	1.1792(61)	0.1000(21)	0.1314(15)
		0.4645(66)	0.2400(61)	0.8745(62)	0.1757(49)
		0.3094(61)	0.5464(62)	0.3532(64)	0.3036(12)

Variation of fitness function versus iteration number of IEEE 33- and 69-bus system for Scenario-3 are shown in Fig.1 and 2, respectively. In Fig.1, the value of fitness nearly at 62nd, 50th, 45th and 52nd iteration for Case2, 3, 4, and 5, respectively; in Fig.2, the value of fitness nearly at 74nd, 46th, 52th and 53th iteration for Case2, 3,

4, and 5, respectively are approached to the optimal solution.

It can be seen from the figures that all fitness values are reached the optimal solution before 75th iteration and there is no change after that.

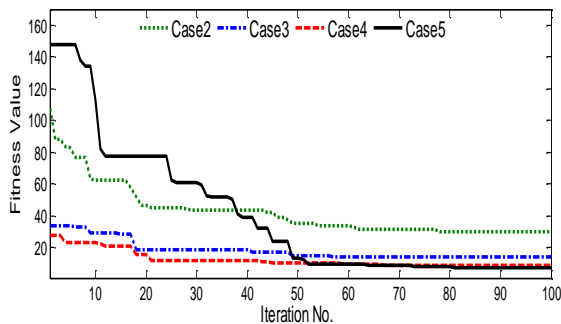


Figure 1. Fitness variation with iteration number for 33 bus system with scenario3

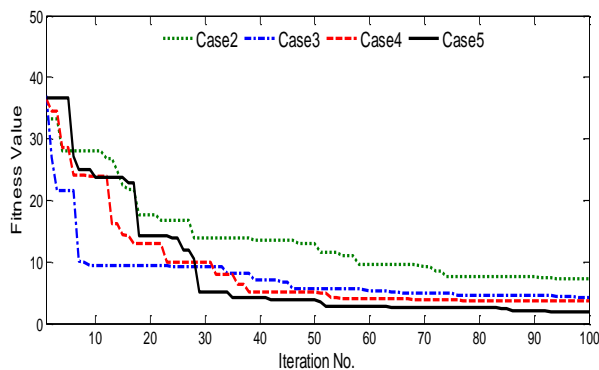


Figure 2. Fitness variation with iteration number for 69 bus system with scenario 3

Summary: According to the obtained results by BSA for all scenarios and cases of both test systems, it is noted that power loss reduction gradually increases as the number of DGs is increased, as well as by changing the DG type, as shown in Fig. 3 and 4. It is clearly observed that the results of Case 5 of each scenarios offer the greatest power loss reduction for both the IEEE 33- and 69-bus system. The noticeable increase in power loss reduction under Scenario-3 is better than those in other scenarios. So, it is better to integrate some DGs, as in Scenario-3, in order to increase the power loss reduction. The location, size, type, and the number of DGs are the basic steps for planning improvements in system performance, especially the system power loss.

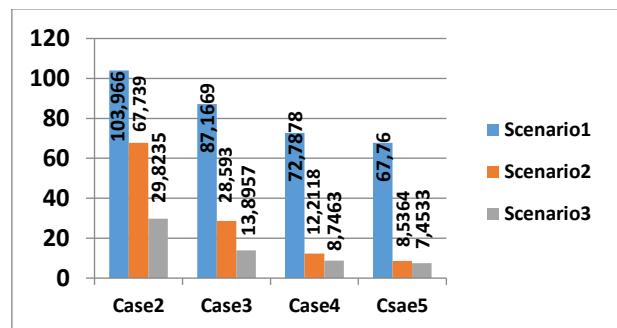


Figure 3. Demonstrate power loss (kW) in each scenario with their different cases for 33 bus system

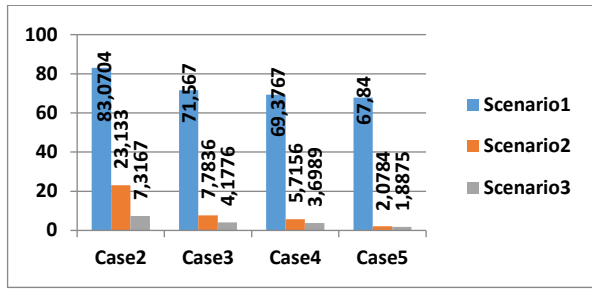


Figure 4. Demonstrate power loss (kW) in each scenario with their different cases for 69 bus system

5. Conclusion

In this work, the BSA is successfully applied in RDS to find optimal size, number, type, and location of DGs. These DGs are connected to the test systems and minimized their power loss. The DGs are integrated under 3 scenarios and 5 cases in each scenario. Under Scenario-3 (Case5), power loss is reduced by 99.16%, 96.47%, respectively for 33 and 69 bus systems. It's noticed that it is better to select suitable DG type to minimize power loss to a considerable amount. But the best way is to put DG type, and number in consideration.

It is concluded that an optimal size, type, number of DG with suitable location can reduce the power losses by considerable amounts.

In future work, Type III: Generating active and absorbing reactive power (wind power) and Type IV: Generating active and reactive power (synchronous generator) will considered by using the BSA.

Nomenclature

DG	Distributed generation
f	Fitness function
g	Equality constraint
h	Inequality constraint
x	Control variables
u	State variables
P_{loss}	Total power loss
P_{feeder}	Feeder active power
Q_{feeder}	Feeder reactive power
$P_{DG,i}$	DG active power output at i^{th} bus
$P_{Load,i}$	Active load at i^{th} bus
$Q_{Load,i}$	Reactive load at i^{th} bus
N	Total bus number
N_{DG}	Total number of DG
N_{SC}	Total number of SC

CF_i	Status (on/off) of the feeder
CDG_i	Status (on/off) of the distributed generation at i^{th} bus
CSC_i	Status (on/off) of the synchronous compensator at i^{th} bus
V_i	Voltage magnitude at i^{th} bus
δ_{ij}	The voltage angle difference between buses i and j
$Q_{sc,i}$	SC reactive power output at i^{th} bus
G_{ij}	Transfer conductance between buses i and j
SC	Synchronous compensator
SN	Number of population size
D	the number of optimization parameters
$Randshuff$	random mixing function
$Rand(low, up)$	produce a random number between low and up
Pop	Population
$oldPop$	Old population
\sim	Produce
$Tpop$	Trial population
$P_{DG,i}^{min}$	Minimum DG active power output at i^{th} bus
$P_{DG,i}^{max}$	Maximum DG active power output at i^{th} bus
I_{ij}	Current magnitude at branch ij
I_{ij}^{max}	Allowable maximum current magnitude at branch ij
a, b	$Rand(0,1)$
$:=$	Update operator
$mutantPop$	Population of mutation
W	Value
$randn$	Generates numbers between 0 , 1
map	Matrix ($SN * D$)
$Q_{sc,i}^{min}$	Minimum SC reactive power output at i^{th} bus
$Q_{sc,i}^{max}$	Maximum SC reactive power output at i^{th} bus
B_{ij}	Transfer susceptance between buses i and j

Author's Contributions

Waleed Fadel: Methodology, Software.

Ulas Kilic: Visualization, Investigation, Supervision.

Sezai Taskin: Investigation, Supervision, Writing.

Ethics

There are no ethical issues after the publication of this manuscript.

6. References

1. Kansal, S., Kumar, V. and Tyagi, B., 2013. Optimal placement of different type of DG sources in distribution networks. *International Journal of Electrical Power & Energy Systems*, 53, pp.752-760.
2. Kayal, P. and Chanda, C.K., 2013. Placement of wind and solar based DGs in distribution system for power loss minimization and voltage stability improvement. *International Journal of Electrical Power & Energy Systems*, 53, pp.795-809.
3. Kollu, R., Rayapudi, S.R. and Sadhu, V.L.N., 2014. A novel method for optimal placement of distributed generation in distribution systems using HSDO. *International Transactions on Electrical Energy Systems*, 24(4), pp.547-561.
4. García, J.A.M. and Mena, A.J.G., 2013. Optimal distributed generation location and size using a modified teaching-learning based optimization algorithm. *International journal of electrical power & energy systems*, 50, pp.65-75.
5. Injeti, S.K. and Kumar, N.P., 2013. A novel approach to identify optimal access point and capacity of multiple DGs in a small, medium and large scale radial distribution systems. *International Journal of Electrical Power & Energy Systems*, 45(1), pp.142-151.
6. Manafi, H., Ghadimi, N., Ojaroudi, M. and Farhadi, P., 2013. Optimal placement of distributed generations in radial distribution systems using various PSO and DE algorithms. *Elektronika ir Elektrotechnika*, 19(10), pp.53-57.
7. Moradi, M.H. and Abedini, M., 2012. A combination of genetic algorithm and particle swarm optimization for optimal DG location and sizing in distribution systems. *International Journal of Electrical Power & Energy Systems*, 34(1), pp.66-74.
8. Aman, M.M., Jasmon, G.B., Bakar, A.H.A. and Mokhlis, H., 2013. A new approach for optimum DG placement and sizing based on voltage stability maximization and minimization of power losses. *Energy Conversion and Management*, 70, pp.202-210.
9. Ates, Y., Gokcek, T. and Arabul A. Y., 2020, Impact of hybrid power generation on voltage, losses, and electricity cost in distribution networks. *Turkish Journal of Electrical Engineering & Computer Sciences*, 1-16.
10. Turan, M.T., Ates, Y., Erdinc, O., Gokalp, E. and Catalão, J.P., 2019. Effect of electric vehicle parking lots equipped with roof mounted photovoltaic panels on the distribution network. *International Journal of Electrical Power & Energy Systems*, 109, pp.283-289.
11. Hemeida, M.G., Ibrahim, A.A., Mohamed, A.A.A., Alkhalaf, S. and El-Dine, A.M.B., 2020. Optimal allocation of distributed generators DG based Manta Ray Foraging Optimization algorithm (MRFO). *Ain Shams Engineering Journal*.
12. Memarzadeh, G. and Keynia, F., 2020. A new index-based method for optimal DG placement in distribution networks. *Engineering Reports*, 2(10), p.e12243.
13. Kayal, P. and Chanda, C.K., 2013. Placement of wind and solar based DGs in distribution system for power loss minimization and voltage stability improvement. *International Journal of Electrical Power & Energy Systems*, 53, pp.795-809.
14. Kansal, S., Kumar, V. and Tyagi, B., 2016. Hybrid approach for optimal placement of multiple DGs of multiple types in distribution networks. *International Journal of Electrical Power & Energy Systems*, 75, pp.226-235.
15. Fadel, W., Kilic, U. and Taskin, S., 2017. Placement of Dg, Cb, and Tesc in radial distribution system for power loss minimization using back-tracking search algorithm. *Electrical Engineering*, 99(3), pp.791-802.
16. Aman, M.M., Jasmon, G.B., Bakar, A.H.A. and Mokhlis, H., 2014. A new approach for optimum simultaneous multi-DG distributed generation Units placement and sizing based on maximization of system loadability using HPSO (hybrid particle swarm optimization) algorithm. *Energy*, 66, pp.202-215.
17. Civicioglu, P., 2013. Backtracking search optimization algorithm for numerical optimization problems. *Applied Mathematics and Computation*, 219(15), pp.8121-8144.
18. Kılıç, U., 2015. Backtracking search algorithm-based optimal power flow with valve point effect and prohibited zones. *Electrical Engineering*, 97(2), pp.101-110.
19. Song, X., Zhang, X., Zhao, S. and Li, L., 2015. Backtracking search algorithm for effective and efficient surface wave analysis. *Journal of Applied Geophysics*, 114, pp.19-31.
20. Duan, H. and Luo, Q., 2014. Adaptive backtracking search algorithm for induction magnetometer optimization. *IEEE Transactions on Magnetics*, 50(12), pp.1-6.
21. Moradi, M.H., Zeinalzadeh, A., Mohammadi, Y. and Abedini, M., 2014. An efficient hybrid method for solving the optimal siting and sizing problem of DG and shunt capacitor banks simultaneously based on imperialist competitive algorithm and genetic algorithm. *International Journal of Electrical Power & Energy Systems*, 54, pp.101-111.

Frame Detection with Deep Learning

Mete Yildirim^{1*}, Radosveta Ivanova Sokullu¹

¹ Department of Electrical and Electronics Engineering, Ege University, 35030, Bornova, İzmir, Turkey

*mete.yildirim@mail.ege.edu.tr

*Orcid: 0000-0001-6335-4752

Received: 25 February 2020

Accepted: 21 May 2021

DOI: 10.18466/cbayarfbe.693942

Abstract

Deep learning has become a way of solution for the realization of complex computations. As electronic communication starts to use more complex channels, the systems need to handle tough computations. For this reason, research on the use of deep learning in communication has increased recently. These researchers aim to realize many applications used in communication with deep learning. Frame detection is one of the first things a receiver must handle, and it may require a lot of hard computations. Deep learning-based frame detection can be an alternative approach. This study aims to build models that perform frame detection with deep learning. The proposed models provide the performance of correlation-based frame receivers commonly used for frame detection. The mean square root error of the prediction deviation is used as an evaluation metric to compare the proposed model to classic systems.

Keywords: Communication, correlator, deep learning, frame detection, neural network

1. Introduction

Many modern communication systems transmit information in the form of a packet or frame in order to share the transmission medium. Frame structure usually contains information that determines its start and endpoint. The receiver must detect these points correctly. This process is called frame detection [1–2].

Frame detection is vital to the performance of the system. The error to be made in frame detection can cause a lot of other synchronization problems in the system such as symbol, frequency, and etc. which in turn reduces the performance of the system.

Mostly, the good frame detection depends on the algorithm used and the structure of the frame. A well-designed frame should not increase the overhead information while facilitating frame detection, nor should it be in a format that costs more processing time and energy.

The use of neural networks, which is the most primitive version of the deep learning model, is not new. [3] and the references within summarize these studies. These studies cover many important topics for communication systems such as modulation, demodulation, detection, synchronization, coding. These studies have not produced very successful results. However, the deep learning models obtained with multi-layered neural

networks succeeded in producing successful results in communication systems. [4–6] are some of the review papers examine many excellent applications of deep learning to electronic communication. [7–14] show very successful machine learning-based communication. [9] combines all communication blocks in one entity and put forward a different approach for digital communication. [7] implements deep learning-based communication with software defined radio on AWGN channels. Generally, these papers try to optimize overall performance of the digital systems and do not let us know if deep learning can handle some very important receiver tasks such as frame detection individually and how good it is in these tasks. This motivates us to examine a deep learning-based frame detection. In this study, we will consider received signals that contains a frame in various noise levels. The proposed models detect frame beginning for various size of preamble information in various level of signal to noise ratio and the performance of the models compared to the correlation-based detector.

2. Deep Learning Foundation

Deep learning is performed with deep neural network (DNN) that is very similar the shallow neural network (NN) in structure. Unlike NN, DNN generally have many layers. The connection between these layers may differ from NN and can be very complicated. DNN has

different approaches than NN that help to create many successful applications to the various field. The calculation in NN is done by a neuron. Being the most basic unit of NN, a neuron does a simple calculation on the given input given as $z = w^T x + b$. The output is estimated with an activation function $a = g(z)$ [15-17]. The activation function, $g(\cdot)$, is generally non-linear. Some of them are named as “relu, tanh, sigmoid” etc. These non-linear function gives power to the model for non-linear output estimation. The structure that combines many neurons named layer. The neurons in a layer do not have inner connection and works independently.

The machine learning generally subcategorized in two. They are supervised and unsupervised learning. In this study we only consider supervised learning. The supervised learning is performed based on known input and output. The model sets the inner parameters by itself to get desired outputs for the given inputs. This is done on many samples that is known as training samples. The best inner parameters are saved and used for validation data that is used to understand the model training mood. If the model is not undertrained nor over trained, it becomes ready to use for prediction on new datasets. For satisfactory result, the network must be provided enough training examples $(x(i), y(i))$. The samples can be applied the model on vector based known feature vector. The computation of a neuron for the input features vector x is given as $z = w^T x + b$, where w is weighting vector and b is constant, hence a layer output given as is $Z = W^T x + b$, where W is a matrix, b is a constant vector. After calculation nonlinear output of neurons with the one of mentioned activation functions, the output is applied to next layer. In this calculation, W and b are randomly initialized to small numbers. That calculation goes on until the last layer. The last layer of model must have neurons as many as the number of classes in classification problem. In other words, each class is represented with a neuron on last layer where the calculated values are converted to probability by using softmax function etc. In general, a NN is mapping of N_i dimension of input to N_o dimension of output given as $f(x; W, b): R^{N_i} \rightarrow R^{N_o}$. The difference between real output and model output is calculated with a cost function.

$$\sum_{i=1}^m (y^{(i)} \log a^{[L](i)} + (1 - y^{(i)}) \log (1 - a^{[L](i)})) \quad (2.1)$$

The cost function is chosen according to the need. (2.1) shows a cost function for binary classification named as logistic regression log likelihood [18].

The cost function can be maximized using gradient decent that is called the training of network. The more on deep learning, such as multinomial classification, softmax and etc. can be found in [19].

3. Frame Detection Model

A frame is generally a joint structure of the preamble and an information message. A preamble known as marker is mostly a predesigned sequence of bits while the information message is a random sequence of symbols from the used alphabet. Sometimes the preamble itself can be made from the message to be transmitted for reducing waste of resources as given in [20]. Frame detection can be examined in two basic categories without loss of generality. These are correlation-based receiver (CBR) and maximum likelihood-based receiver (MLR)[2]. In the CBR, the received sequence is correlated with the local preamble and the correlation peak is used to determine starting position of the frame. The weaknesses of CBR can be considered as long processing time, saving a copy of preamble locally and sensitivity to frequency variation. The MLR shows better performance in the case of frequency deviation but considered as a costly way of handling frame detection.

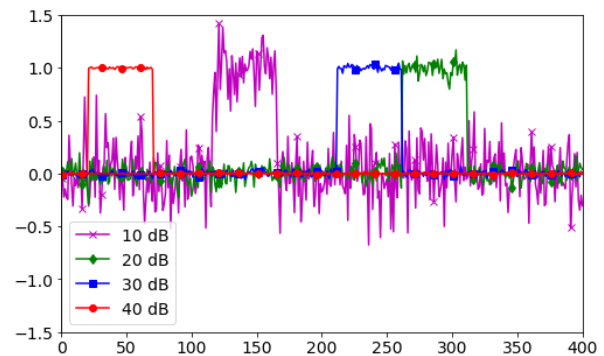


Figure 1. The samples of received signals.

In this study, we consider the frame detection with deep learning and examine the different models and compare their performance to the basic correlator-based detector. The two are compared in terms of the deviation from the actual frame starting position by evaluating the deviation as a mean squared estimation error. The received signal is corrupted by the noise that reduces signal-to-noise ratio. The Fig.1 shows four signals received by a receiver at different time with various signal to noise ratio. This information could be considered a preamble to actual message signal to be transmitted. Since the message is a sequence of random symbols, it is preferred not to show in the figure for the sake of better visualization clarity. The receiver has to find where the frame starts. We consider the correlation-based frame detector against the deep learning-based frame detector. While the deep learning-based receiver does not need to know what kind of preamble is sent, the correlation-based receiver needs to know the exact preamble. Therefore, the preamble between the receiver and the transmitter must be agreed beforehand which can be considered handicap of correlated-based receiver. Further, the CBR may require long processing

time. For the deep learning, it only requires a good training before it is used.

The CBR correlates the received information with locally saved one and used the peak point as the starting position of the frame. The proposed DL model uses a softmax layer at the output and calculates the probability of every possible position for the preamble in the received corrupted sequence and choses the highest probability as the starting position of the frame. The input to model is the received sequence. As it could be possible to consider real and imaginary part separately, only the real part is considered in this study which turns out to provide satisfactory results.

The proposed deep learning-based receiver uses fully connected layers. It has 6 hidden layers, dropout=0.2, number of neurons per layer 512, training size between 100000-150000. While it is possible to provide deeper and larger NN, to have moderate training time, parameters are used. First, we provide the figures that shows the model neither overfits nor underfits. The overfitting and underfitting are two important issues in the training process of a NN model. The loss and the accuracy for the validation and the training datasets are considered to decide a well-fitting model. In Fig.1 accuracy and loss graphs are given for various signal to noise ratio against number of the epochs. It is clearly seen that different signal to noise ratio requires different number of epochs. For example, 5 epochs are enough for -10dB while it becomes 30 epochs for 5dB. Generally, it requires more epochs around 0-10dB.

The expected outcome for the model to generalize well is that the accuracy should be on the rise while for the loss is getting smaller and the gap between the validation and the training set should be moderately

close for both as the number of the epochs increase. It is understood from the graphs on Fig.2 that around 15 epochs are enough for well generalized model. The proposed model is trained for various SNR and preamble size. The Fig.3 shows DL model prediction versus CBR prediction error in terms of mean squared deviation. The two compared for the various preamble size in the range of 5 to 40 symbol for the signal to noise ration from -15dB to 10dB. It is seen from the figure; DL model can put so close performance to CBR with even a simple model given above. Both receivers give zero deviation error above 10dB.

Deep learning model can be in various forms. Some forms show better performance than others. The wisdom behind it cannot be explained mathematically. Hence, developing a good deep learning model is achieved through trial and error. The number of neurons used in model is considered part of parameters used in a model. Apart from the total number of neurons, their distribution can be matter. In the study the distribution of neurons to the hidden layers are considered as one of the parameters to adjust. Hence, we try to find out the best distribution to the hidden layers. Several distribution approaches are tested with various size of preamble. After many trainings of these models, we have seen that even distribution is the best choice in term of classification accuracy. The even distribution means that all the hidden layers have same number of neurons. The output of the proposed model is shown in Fig.4 that is tested for two different preamble sizes in the range of -15dB to 15dB signal to noise ratio. The Fig.4 shows the performance of the model with even and uneven distribution of neurons to the hidden layers for preamble size 5 and 10. The model with the even distribution generally shows better performance

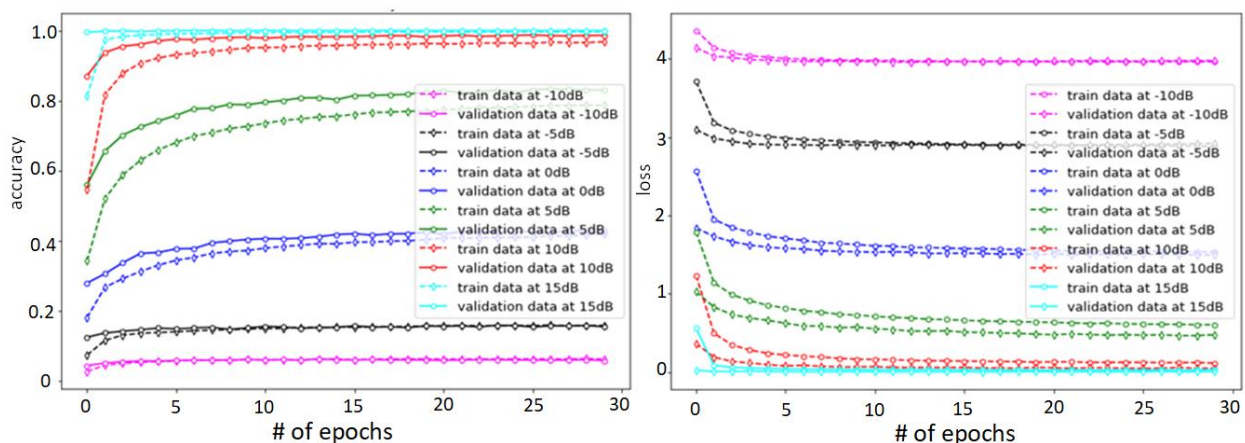


Figure 2. The loss and the accuracy of deep learning-based receiver.

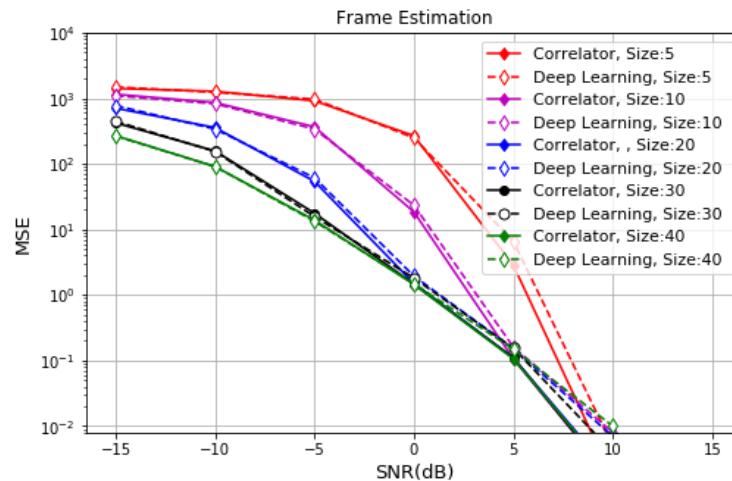


Figure 3. The Deep Learning-based and the correlator-based detector performance.

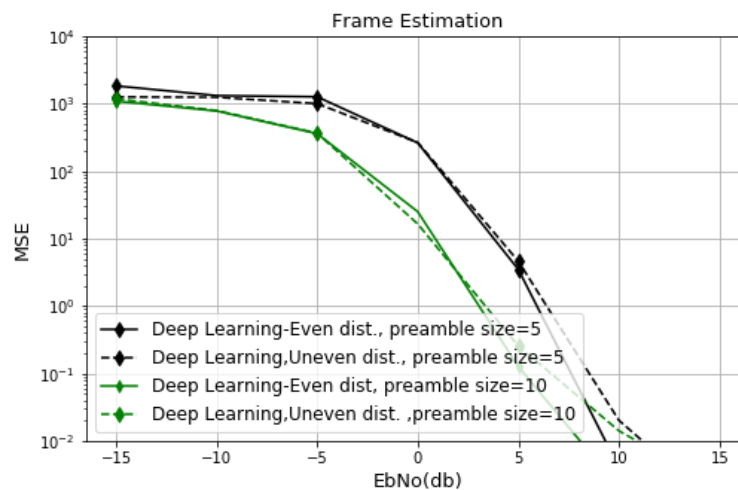


Figure 4. Distribution of neurons

4. Conclusion

A deep learning model is designed to make frame detection. This model has been shown to be well-fitting. For this purpose, loss and accuracy graphs in validation and training datasets are given by simulation. Then, frame detection performances of these models were compared with correlation-based system. The mean square error of deviation is used as comparison metric. Then, some parameters of the model are adjusted and the best performing model for frame detection is formed. The model is observed to be successful in comparison to correlator-based detector. The deep learning-based detector is considered to superior to correlator-based detector since the second must have the preamble beforehand for detection while the first does not need to know it. This is considered as one of the proposed model superiorities to the correlator-based detector. The second superiority is that the correlator-

based detector has to do heavy correlation calculations for every detection while the deep learning-based detector needs only offline training. This helps to reduce processing time and memory requirements seriously, requires less computing power and less power consumption at the receiver. These advantages come from the fact that DL based model just need to save weighted parameters that is used in some simple mathematical calculation to estimate the frame position. Observing the contribution of deep learning-based model frame detection, the conclusion we arrive is that the future communication systems must consider to use the DL based technologies.

Acknowledgement

This study was carried out in the Department of Electrical and Electronics Engineering of Ege University within the scope of the project supported by TUBITAK 2218.



Author's Contributions

Mete Yıldırım: Conceptualization, Methodology, Validation, Simulation, Formal analysis, Investigation, Writing - original draft, Writing - review, and editing.
Radosveta Ivanova Sokullu: Conceptualization, Methodology, Validation, Formal analysis, Investigation, Writing - review & editing, Supervision.

Ethics

There are no ethical issues after the publication of this manuscript.

References

1. Massey, J. 1972. Optimum frame synchronization. *IEEE transactions on communications*; 20(2): 115–119.
2. Scholtz, R. 1980. Frame synchronization techniques. *IEEE transactions on communications*; 28(8): 1204–1213.
3. Ibnkahla, M. 2000. Applications of neural networks to digital communications—a survey. *Signal processing*; 80(7): 1185–1215.
4. Qin Z, Ye H, Li G, Juang F. 1972. Deep learning in physical layer communications. *ArXiv*: 1807.11713
5. Simeone, O. 2018. A very brief introduction to machine learning with applications to communication systems. *IEEE Transactions on Cognitive Communications and Networking*; 4(4): 648–664.
6. Wang T, Wen CK, Wang H, Gao F, Jiang T. 2017. Deep learning for wireless physical layer: Opportunities and challenges. *China Communications*; 14(11): 92–111.
7. Dörner S, Cammerer S, Hoydis J, Brink S. 2017. Deep learning based communication over the air. *IEEE Journal of Selected Topics in Signal Processing*; 12(1): 132–143.
8. O'Shea T, Hoydis J. 2017. An introduction to deep learning for the physical layer. *IEEE Transactions on Cognitive Communications and Networking*; 3(4): 563–575.
9. O'Shea T J, Karra K, Clancy T C. 2016. Learning to communicate: Channel auto-encoders, domain specific regularizers, and attention. *arXiv*: 1608.06409.
10. TO'Shea T J, Roy T, West N, Hilburn B C. 2018. Physical Layer Communications System Design Over-the-Air Using Adversarial Networks. *ArXiv*: 1803.03145.
11. O'Shea T J, Hoydis J. 2017. An introduction to machine learning communications systems. *ArXiv*: 1702.
12. O'Shea T J, Erpek T, Clancy T.C. 2017. Deep learning based MIMO communications. *arXiv*:1707.07980.
13. TO'Shea T J, Roy T, West N, Hilburn B C. 2018. Physical Layer Communications System Design Over-the-Air Using Adversarial Networks. *ArXiv*: 1803.03145.
14. O'Shea T J, Hoydis J. 2017. An introduction to machine learning communications systems. *ArXiv*: 1702.
15. Ramachandran, P., Zoph, B. and Le, Q.V., 2017. Searching for activation functions. *arXiv preprint arXiv:1710.05941*.
16. Nwankpa, C., Ijomah, W., Gachagan, A., & Marshall, S. 2018. Activation functions: Comparison of trends in practice and research for deep learning. *arXiv preprint arXiv:1811.03378*.
17. Agostinelli, F., Hoffman, M., Sadowski, P., & Baldi, P. 2014. Learning activation functions to improve deep neural networks. *arXiv preprint arXiv:1412.6830*.
18. Nie, F., Hu, Z., & Li, X. 2018. An investigation for loss functions widely used in machine learning. *Communications in Information and Systems*, 18(1), 37-52.
19. LeCun Y, Bengio Y, Hinton G. 2015. Deep learning. *Nature*; 521(7553): 4362
20. Schmidl T M, Cox D C. 1997. Robust frequency and timing synchronization for OFDM. *IEEE transactions on communications*; 45(12): 1613–1621.

Anatomy of *Carlina corymbosa* L., *Carthamus dentatus* Vahl. and *Picnomon acarna* (L.) Cass. (Asteraceae)

Ummahan Öz^{1*} 

¹Department of Plant and Animal Production, Alaşehir Vocational School, Manisa Celal Bayar University, Manisa Turkey

*ummahanoz48@gmail.com

*Orcid: 0000-0002-0281-1048

Received: 25 August 2020

Accepted: 19 April 2021

DOI: 10.18466/cbayarfbe.785328

Abstract

Species of *Carlina corymbosa* L., *Carthamus dentatus* Vahl. and *Picnomon acarna* (L.) Cass. are belonging to Asteraceae family. The purpose of the study is to determine the anatomical structures of these species in the same tribe and to compare the features. Samples of root, stem and leaf of each species were collected, fixed and examined using a light microscope. In addition, some anatomical features were measured. Secondary growth was observed in the root cross section of each species. Secretory ducts were determined in all species. While the pith is filled with xylem elements in *C. corymbosa* and *C. dentatus*, the pith of *P. acarna* consists of different shaped parenchyma cells. Periderm was observed in the stem in all species. All species contain bicollateral vascular bundles in stem. In all species, glandular and non-glandular trichomes were observed on the leaf cross section, on the surface of the adaxial and abaxial epidermis. While *C. corymbosa* has dorsiventral mesophyll, unifacial mesophyll is observed in other species. There is bicollateral vascular bundle in *C. corymbosa* whereas collateral vascular bundle was identified in *C. dentatus* and *P. acarna*. Also, *C. corymbosa* and *C. dentatus* have only one vascular bundle in the midrib but *P. acarna* has three vascular bundles.

Keywords: Anatomy, bicollateral, collateral, dorsiventral, secretory duct, unifacial.

1. Introduction

Carlina corymbosa L., *Carthamus dentatus* Vahl. and *Picnomon acarna* (L.) Cass. are member of Asterales order, Asteraceae family, Carduoideae subfamily and Cardueae tribe [1].

The Asteraceae family is represented in the world with about 1911 genera and 32913 species [2]. In Turkey, there are 133 genera and 1156 species belonging to this family and tribe of Cardueae includes 39 genera and approximately 500 taxa [3-4].

The taxa belonging to Cardueae have morphological similarity features and these similarities cause problems in classification. In taxonomic studies, it is seen that only the use of morphological characters is insufficient and therefore, the necessity of anatomical, cytological, molecular, palynological studies etc. is revealed [5].

There are anatomical differences in the species belonging to Asteraceae family. In this family, the secretory structures (cavities, idioblast, ducts and

trichomes etc.) are important anatomical characters and these structures are used for identification the species. For example, the micromorphology of trichome is a feature that can be used in the systematics of the Asteraceae [6]. Glandular and non-glandular trichomes are used as distinguished [7].

The aim of this research is to determine the anatomical features of *Carlina corymbosa* L., *Carthamus dentatus* Vahl. and *Picnomon acarna* (L.) Cass., which are members of the Cardueae tribe.

2. Material and Methods

2.1 Study areas and selected species

Carlina corymbosa L., *Carthamus dentatus* Vahl. and *Picnomon acarna* (L.) Cass. were collected in August 2018 from natural environments in Milas, Muğla (Figure 1). Their collection localities were as follows: *Carlina corymbosa* and *Picnomon acarna*, N 37°21'52.503", E 27°48'11.386" 62 m.; *Carthamus dentatus*, N 37°19'49.851", E 27°45'39.420" 80 m. The taxonomic descriptions of all species were made according the Flora of Turkey [1].

2.2 Sampling

Root, stem and leaves of species were fixed in 70% ethanol for the anatomical studies. Cross sections were taken from each plant material by using razor blade and sections were stained with hematoxylin.

Well-stained sections were examined with BAB Image Analysing Systems Microscope (BAB-95) and photographed with BAB Microscope Camera. Anatomical structures were measured using BAB measurement program.



Figure 1. a) *Carlina corymbosa*, b) *Carthamus dentatus*, c) *Picnomon acarna*

3. Results and Discussion

3.1 *Carlina corymbosa*

In root cross section, secondary growth was observed. On the outermost, there is thick and multi-layered periderm. There are secretory ducts in the secondary cortex. The cambium cells, which between phloem and xylem, and the sclerenchyma tissues are clearly distinguished. Pith rays consist of distinct and 2-4 layered cells. Pith is filled with metaxylem (Figure 2).

The stem of *C. corymbosa* is almost circular. Uniseriate epidermis, consisting of rectangular-shaped cells surrounded by thick cuticle, is observed in cross section of the stem. The periderm layer consist of different sized and shaped cells. Endodermis and vascular bundles can be clearly distinguished. Sclerenchyma consists of 4-8 layered cells and the cambium is not very distinguishable. Phloem and xylem are well developed. The stem contains bicollateral vascular

bundles. The pith is filled by oval and different sized parenchyma cells. In addition, calcium oxalate crystals are found in pith (Figure 3).

In cross section of *C. corymbosa* leaf, there is a uniseriate epidermis with thin cuticle on adaxial and abaxial surfaces. Surface of both epidermis are covered with trichomes. Glandular and non-glandular trichome types are present. Uniseriate filiform trichome with elongated apical cells and capitate stalked trichomes are observed. Another trichome (bulbiferous flagellate trichome) feature of the observed was as follows: stalk 2-celled, the length of the cells more than the width, second stalk cell swollen; apical cells long, flagellate. Dorsiventral mesophyll and bicollateral vascular bundles are observed in leaf. The midrib has only one vascular bundle. The adaxial parenchyma cells are 3-4 layered and abaxial parenchyma cells are 1-2 layered in midrib (Figure 4).

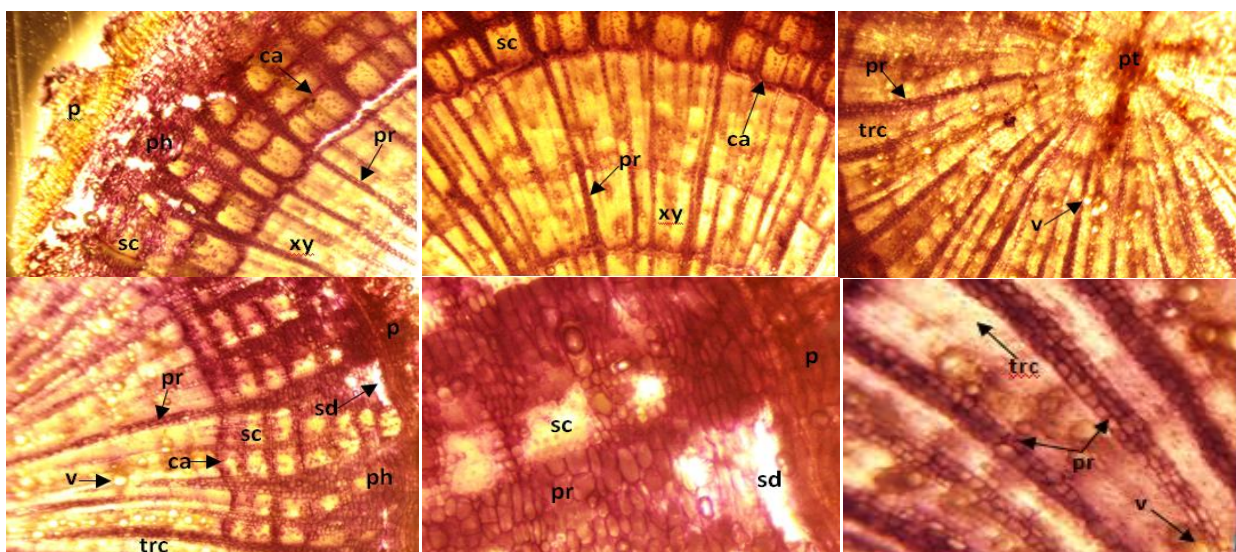


Figure 2. Root anatomy of *C. corymbosa* (ca: cambium; p: periderm; ph: phloem; pr: pith ray; pt: pith; sc: sclerenchyma; sd: secretory duct; trc: tracheid; v: vessel; xy: xylem)

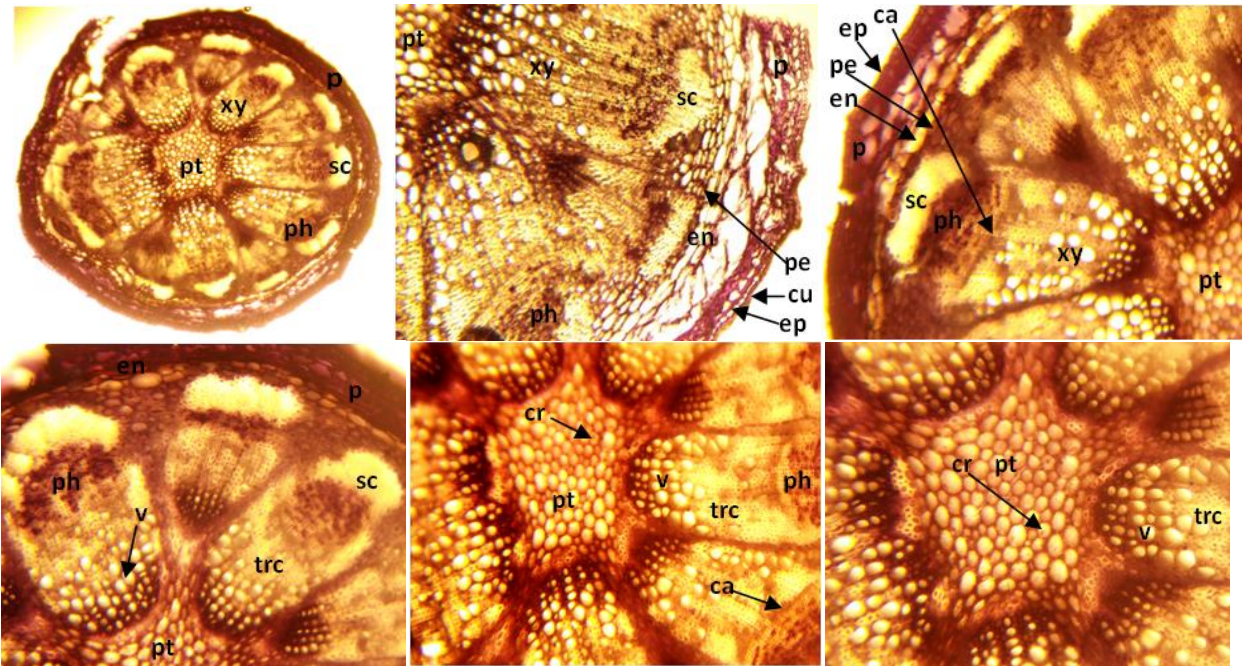


Figure 3. Stem anatomy of *C. corymbosa* (ca: cambium; cr: calcium oxalate crystals; cu: cuticle; ep: epidermis; en: endodermis; p: periderm; pe: pericycle; ph: phloem; pt: pith; sc: sclerenchyma; sd: secretory duct; trc: tracheid; v: vessel; xy: xylem)

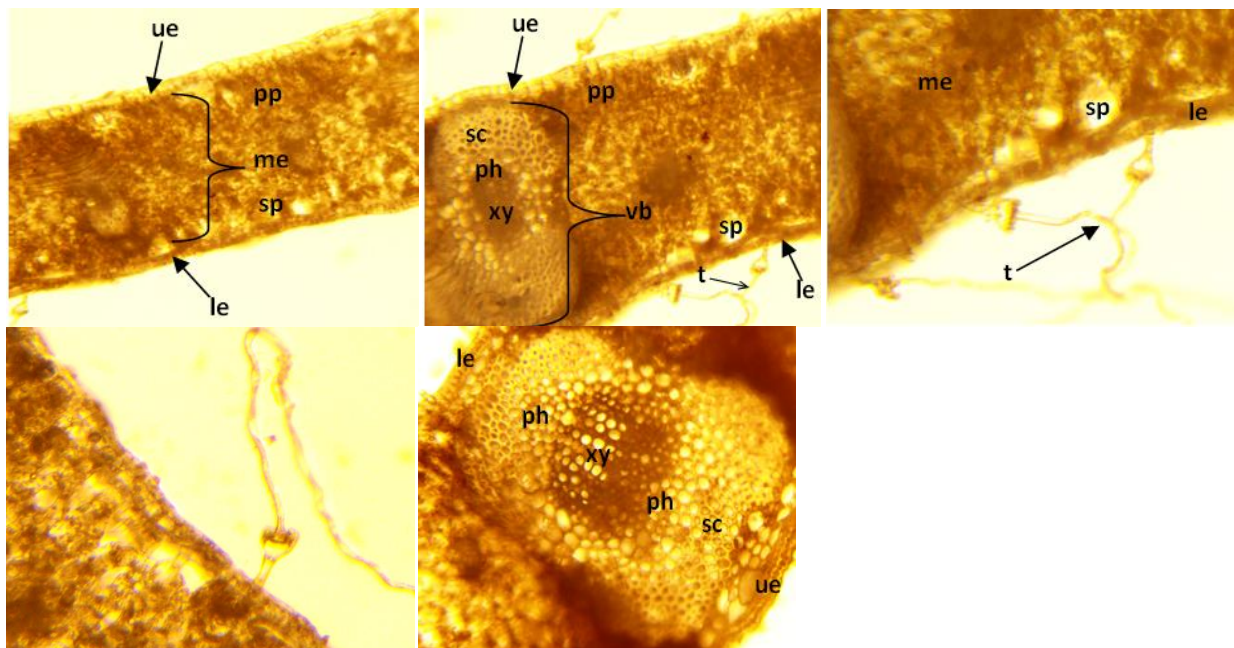


Figure 4. Leaf anatomy of *C. corymbosa* (le: lower epidermis; me: mesophyll; ph: phloem; pp: palisade parenchyma; sc: sclerenchyma; sp: spongy parenchyma; t: trichome; ue: upper epidermis; vb: vascular bundle; xy: xylem)

3.2 *Carthamus dentatus*

Periderm and partially crushed epidermis are observed in the outermost part of the root cross section obtained from *C. dentatus*. There are secretory ducts in cortex and it is observed multi-layered sclerenchyma above the

phloem. The cambium is clearly distinguished. Xylem is well developed and there are 2-5 layered pith rays. In addition to this, the pith is filled by xylem elements (Figure 5).

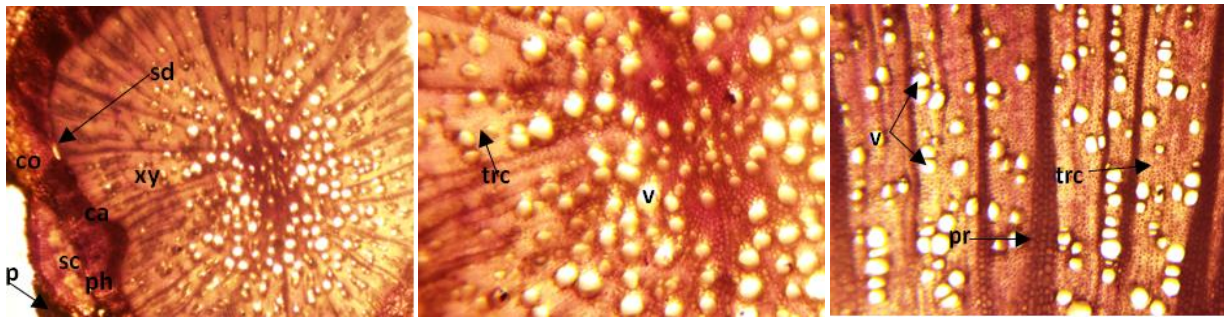


Figure 5. Root anatomy of *C. dentatus* (ca: cambium; co: cortex; p: periderm; ph: phloem; pr: pith ray; sc: sclerenchyma; trc: tracheid; v: vessel; xy: xylem)

In the stem cross section taken by *C. dentatus*, the epidermis is determined as monolayered which is composed of rectangular or oval cells. The epidermis contains multicellular non-glandular unbranched and multicellular glandular trichomes. The periderm, consisting of different sized and shaped cells, is located underneath the epidermis. The cortex cells are observed flattened in a narrow region. There are resin ducts in the

cortex and also cambium is distinguishable between phloem and xylem. Sclerenchyma which between cortex and vascular bundles, consists of 4-10 layered cells. Vascular bundles are bicollateral. Pith rays consist of 1-2 layered oval and rectangular cells. The pith is filled with by hexagonal and oval parenchyma cells. Calcium oxalate crystals are present in pith (Figure 6).

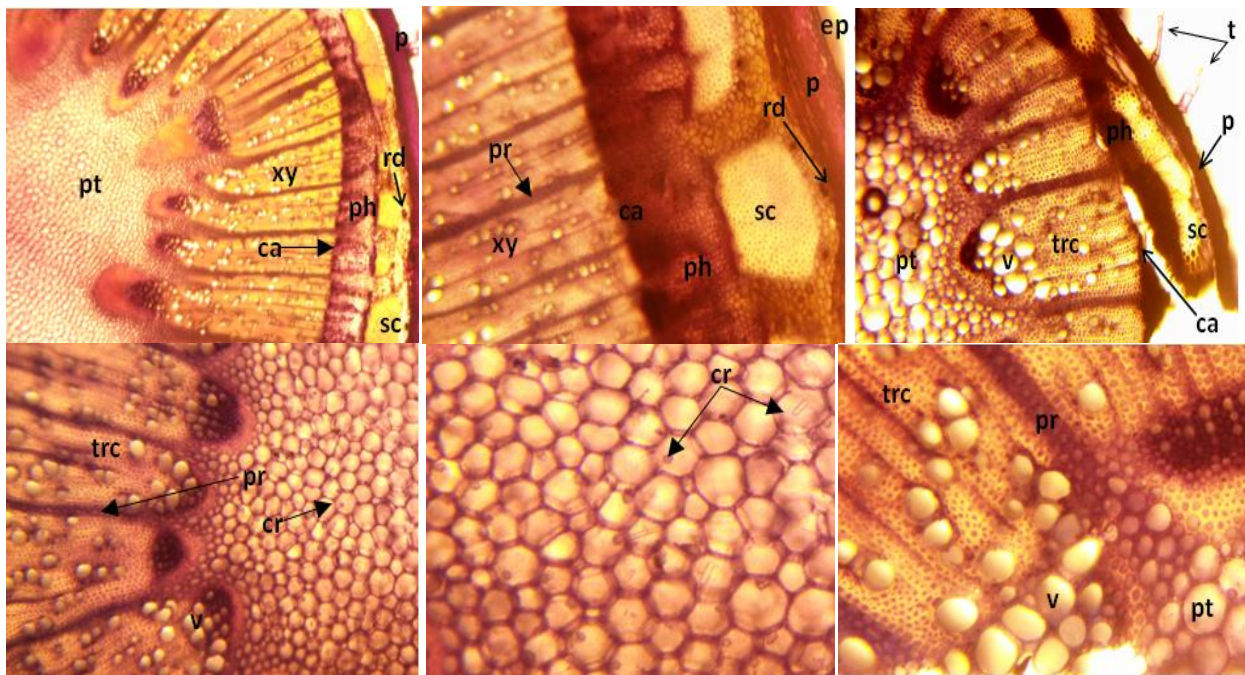


Figure 6. Stem anatomy of *C. dentatus* (ca: cambium; cr: calcium oxalate crystals; ep: epidermis; p: periderm; ph: phloem; pr: pith ray; pt: pith; rd: resin duct; sc: sclerenchyma; trc: tracheid; v: vessel; xy: xylem)

In the cross section of leaf, there is a uniseriate epidermis with thin cuticle on adaxial and abaxial surfaces. Surface of both epidermis are covered with multicellular eglandular and multicellular glandular trichomes. Many different types of trichomes were identified in the leaf cross section. The trichomes were multicellular nonglandular unbranched and multicellular glandular. Trichomes are observed as uniseriate and biseriate. The trichomes observed are as follows: long

stalked capitate, one cell shriveled multicellular non glandular, conical, biseriate pedunculata glandular, biseriate vesicular glandular, short stalked capitate, sessile two-celled glandular, uniseriate multicellular non-glandular trichome. Collateral vascular bundles are observed in unifacial leaf. The midrib has only one vascular bundle and vascular bundle is surrounded by a sheath of sclerenchyma. Small collateral vascular bundles are observed in the mesophyll (Figure 7)

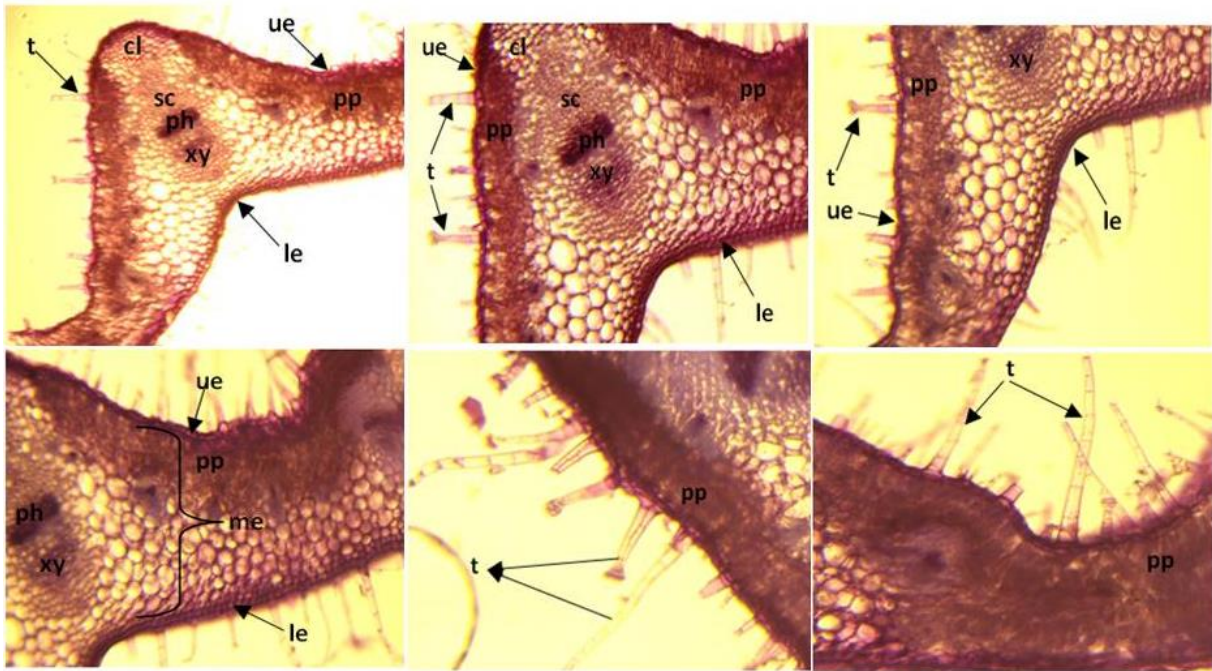


Figure 7. Leaf anatomy of *C. dentatus* (cl: collenchyma; le: lower epidermis; me: mesophyll; ph: phloem; pp: palisade parenchyma; sc: sclerenchyma; t: trichome; ue: upper epidermis; xy: xylem)

3.3. *Picnomon acarna*

In the root cross section, periderm layer consisting of multi-layered, irregularly shaped cells are observed on the outermost and the partially crushed epidermis is identified. Secretory ducts are observed in the cortex.

The endodermis appears as a thin line and is not easily distinguishable. Cambium cells located between phloem and xylem are distinct. The pith consists of differently shaped parenchyma cells (Figure 8).

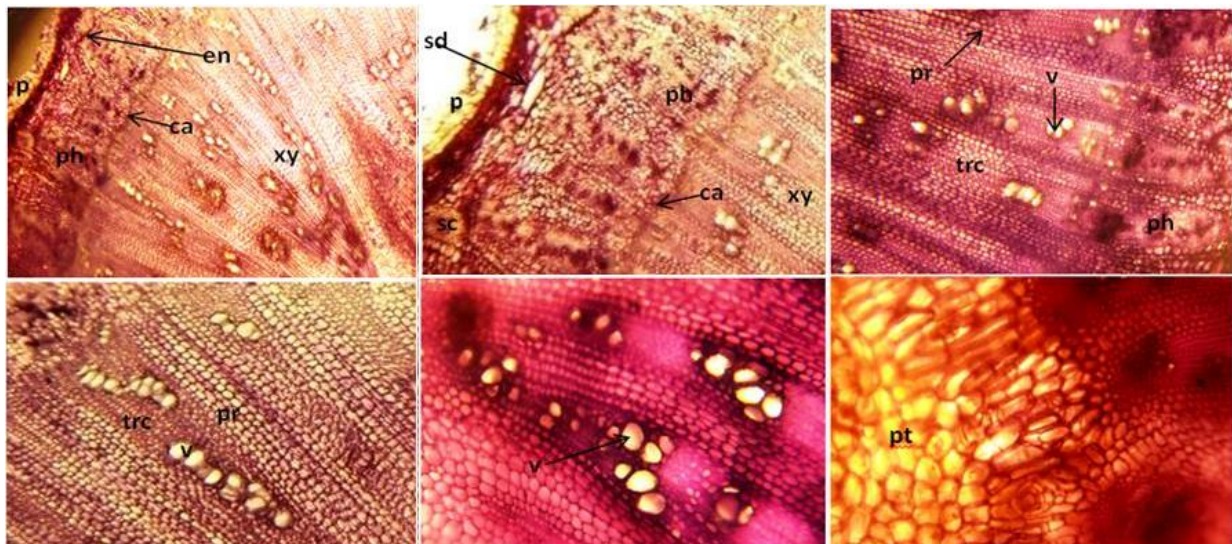


Figure 8. Root anatomy of *P. acarna* (ca: cambium; en: endodermis; p: periderm; ph: phloem; pr: pith ray; pt: pith; sc: sclerenchyma; sd: secretory duct; trc: tracheid; v: vessel; xy: xylem)

There is a thick periderm layer, consisting of different sized and shaped cells, on the outermost surface of the stem. A narrow cortex is observed in the cross section and secretory ducts in cortex are present. The central cylinder is surrounded by an endodermis and pericycle

is clearly distinguishable. Multi-layered pith ray are observed between bicollateral vascular bundles. The cambium is distinguishable between phloem and xylem. Sclerenchyma consists of 3-10 layered cells. The pith contains large polygonal and hexagonal parenchymatous cells (Figure 9).

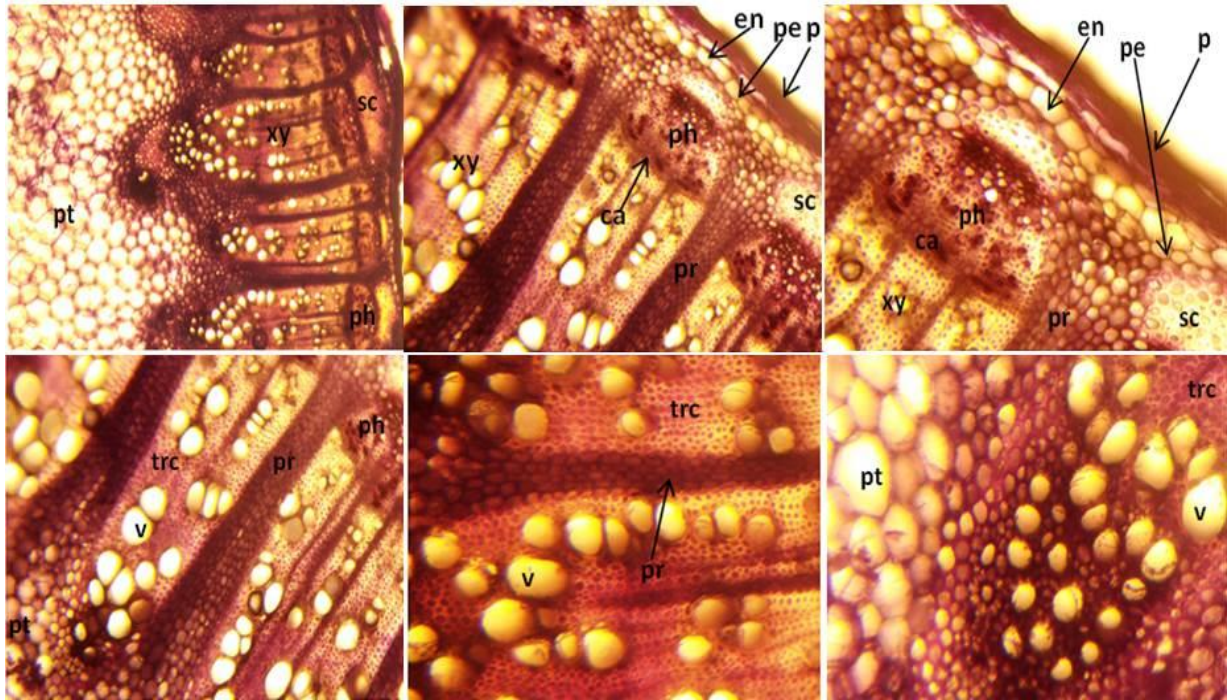


Figure 9. Stem anatomy of *P. acarna* (ca: cambium; en: endodermis; p: periderm; pe: pericycle; ph: phloem; pt: pith; pr:pith ray; sc: sclerenchyma; trc: tracheid; v: vessel; xy: xylem)

In the cross section of leaf, there is a uniseriate epidermis with thin cuticle on adaxial and abaxial surfaces. Epidermis cells are observed square or rectangular. Surface of both epidermis are covered with whip-like and flagellate-filiform trichomes. Unifacial

mesophyll are observed in leaf. Vascular bundles are observed in the middle part of parenchyma tissue in the mesophyll. The midrib has three collateral vascular bundles. The upper and lower parts of the vascular bundles are surrounded by sclerenchyma (Figure 10).

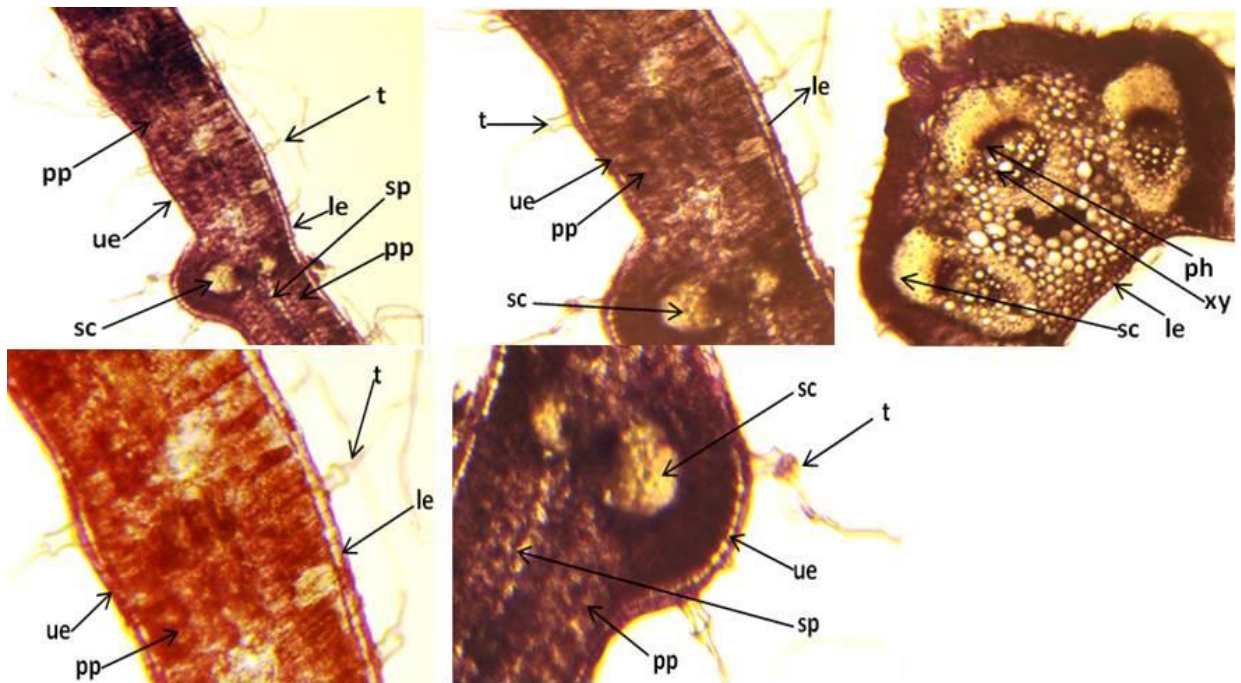


Figure 10. Leaf anatomy of *P. acarna* (le: lower epidermis; ph: phloem; pp: palisade parenchyma; sc: sclerenchyma; sp: spongy parenchyma; t: trichome; ue: upper epidermis; xy: xylem)

Table 1. Measurements of anatomical structures of species

Cross section of plants	<i>Carlina corymbosa</i>	<i>Carthamus dentatus</i>	<i>Picnomon acarna</i>
Root			
Root diameter (µm)	5753.75±400.52	2880.76±327.65	6919.89±1453.54
Periderm thickness (µm)	300.06±62.41	120.22±25.83	230.36±71.22
Phloem thickness (µm)	125.56±23.57	162.61±10.50	373.10±45.99
Xylem thickness (µm)	1847.16±157.75	832.06±99.93	1561.37±186.44
Vessel diameter (µm)	39.38±13.81	42.83±12.48	38.30±8.91
Stem			
Vascular bundles number	12	23-24	26-27
Periderm thickness (µm)	106.14±21.75	70.16±22.72	69.72±14.00
Thickness of sclerenchyma (µm)	95.56±15.63	72.51±12.17	147.63±38.99
Phloem thickness (µm)	163.81±18.58	200.85±36.84	198.64±42.36
Xylem thickness (µm)	471.77±52.14	963.90±204.43	909.24±145.92
Vessel diameter (µm)	29.58±6.75	35.94±10.42	51.61±14.65
Pith diameter (µm)	429.20±52.86	1145.85±88.75	1727.55±277.26
Leaf			
Adaxial epidermis thickness (µm)	18.75±2.61	16.92±2.45	13.94±1.80
Abaxial epidermis thickness (µm)	21.08±2.54	16.39±3.20	12.15±2.02
Mesophyll thickness (µm)	412.19±34.99	311.73±61.67	188.69±19.55
Midrib thickness (µm)	668.65±14.91	757.07±115.87	652.31±32.99
Number of vascular bundles in midrib	1	1	3

µm: micrometer

The root, stem and leaf anatomical features of all species are given as above. In addition, some anatomical characters of these species were measured and indicated Table 1

The species belonging to the Asteraceae family have different anatomical structures [8]. Trichomes are important characteristic in phylogenetic studies related to the Asteraceae family [9-11]. In a study investigating the anatomy of the *C. dentatus* [12], it was stated that this species has glandular and non-glandular trichome, but the trichome types are not mentioned in detail. Long stalked capitate, one cell shriveled multicellular non glandular, conical, biseriate pedunculata glandular, biseriate vesicular glandular, short stalked capitate, sessile two-celled glandular, uniseriate multicellular non-glandular trichomes has been identified in this research. *C. corymbosa* contains uniseriate filiform, capitate stalked and bulbiferous flagellate trichomes whereas *P. acarna* has whip-like and flagellate-filiform trichomes. One of the distinguishing features of Asteraceae is the presence of secretory ducts [13-14]. The secretory ducts are observed in all species used in the research.

Similar results were obtained when these species belonging to the same tribus were examined. In the root cross sections, the best secondary growth was observed in the *C. corymbosa* and periderm was thicker than others. However, in the root section of *P. acarna*, the pith was filled with parenchyma cells as different from the others and root diameter is highest in the this species. In the Asteraceae family, the vascular bundles and leaf midrib differences are also valuable anatomical features [15-19]. The maximum number of vascular

bundle in the stem was determined in *P. acarna*. Bicollateral vascular bundle was observed in the stem of all species used in the study. While collateral vascular bundle was determined in the leaf cross sections of *C. dentatus* and *P. acarna*, bicollateral vascular bundle was detected in the *C. corymbosa*. Also, *C. corymbosa* and *C. dentatus* have only one vascular bundle in the midrib but *P. acarna* has three vascular bundles.

There are calcium oxalate crystals in the tribe Cardueae. In a study of Cardueae [20], it was stated that *C. dentatus* contains prismatic and styloid crystals. Likewise, calcium oxalate crystals were observed in the pith of stem in all species in this study.

4. Conclusion

This study gives information about the anatomical features of the root, stem and leaf sections of *Carlina corymbosa*, *Carthamus dentatus* and *Picnomon acarna*. In the study, it was determined trichomes with different characteristics and this trichome diversity will contribute to the trichome micromorphology of Asteraceae. In addition, the results obtained from the study will constitute resource for the another research related to the anatomy of the Cardueae.

Author's Contributions

Ummahan Öz: Responsible of all processes; planning the research, obtaining and analyzing data, drafting and writing the article.

Ethics

There is no ethical issues after the publication of this article.

References

1. Davis, P. Flora of Turkey and the East Aegean Islands, Vol.5; Edinburgh University Press: Edinburgh, 1975.
2. El-Gazzar ,A, El-Husseini, N, Khafagi ,A, Mostafa, N. 2019. Computer-generated Keys to the Egypt.9.The Spiny Taxa of Asteraceae. *Egyptian Journal of Botany*; 59 (1): 107-138.
3. Seçmen, Ö, Gemici, Y, Görk, G, Bekat, L, Leblebici, E. Tohumlu Bitkiler Sistematigi; Ege Üniversitesi Yayınları, Fen Fakültesi Kitapları Serisi No: 116, İzmir, Turkey, 2011.
4. Kurt, A, Ozcan , M, Colak, N, Ozogul, Y, Glew, R, Ozogul, F, Ayaz, FA. 2019. Fatty Acids of Oil and Antioxidant Capacity of Phenolics from Fruits of 11 Cardueae (Carduoideae, Asteraceae) Taxa From Northeast Anatolia (Turkey). *Botanica Serbica*; 43(1): 31-45.
5. Ozcan, M, Akinci, N.2019. Micromorpho-anatomical Fruit Characteristics and Pappus Features of Representative Cardueae(Asteraceae) Taxa: Their Systematic Significance. *Flora*; 256: 16-35.
6. Dere, S, Aktas Akcin, T. 2017. Anatomical and Micromorphological Properties of Some *Tanacetum* L. (Asteraceae) Taxa from Turkey and their Systematic Implications. *Acta Botanica Croatica*; 76(2): 138-145.
7. Haratym, W, Weryszko-Chmielewska, E, Konarska, A. 2020. Microstructural and Histochemical Analysis of Aboveground Organs of *Centaurea cyanus* Used in Herbal Medicine. *Protoplasma*; 257: 285-298.
8. Karahan, F. 2020. Morphology, Anatomy, Palynology and Achene Micromorphology of *Bellis* L. (Asteraceae) Species from Turkey. *Acta Botanica Croatica*; 79(1): 59-67.
9. Makbul, S, Coskuncelebi , K, Beyazoğlu, O. 2011. Notes on the Stem Anatomy of *Scorzonera* (Asteraceae) Taxa from Northeast Turkey. *Phytologia Balcanica*; 17(1): 113-121.
10. Muravnik, L, Kostina, O, Shavarda, Alexey. 2016. Glandular trichomes of *Tussilago farfara* (Senecioneae, Asteraceae). *Planta*; 244: 737-752.
11. Muravnik, L, Kostina, O, Mosina, A. 2019. Glandular trichomes of the leaves in three *Doronicum* species (Senecioneae, Asteraceae): morphology, histochemistry and ultrastructure. *Protoplasma*; 256: 789-803.
12. Yağci Tuzun, C, Tarikahya, Hacıoglu, B, Bulbul, AS, Arslan, Y, Subasi, I. 2019. Comparative Anatomical Studies on Some Species of *Carthamus* L. in Turkey. *Fresenius Environmental Bulletin*; 28(5): 4072-4079
13. Zuccolotto, T, Bressan, J, Lourenço, A, Bruginski, E, Veiga, A, Marinho, J, Raeski, P, Heiden, G, Salvador, M, Murakami, F, Budel, J, Campos, F. 2019. Chemical, Antioxidant, and Antimicrobial Evaluation of Essential oils and an Anatomical Study of the Aerial Parts from *Baccharis* Species (Asteraceae). *Chemistry & Biodiversity*; 16(4).
14. Gavrilovic, Milan, Rancic, D, Garcia-Jacas, N, Susanna, A, Djacic-Stevanovic, Z, Marin, P, Javackovic, P. 2020. Anatomy of Balkan *Amphicarpus* Vis. (Cardueae, Asteraceae) taxa. *Biologia*; 75: 209-222.
15. Inceer, H, Ozcan, M. 2011. Leaf anatomy as an additional taxonomy tool for 18 taxa of *Matricaria* L. and *Tripleurospermum* Sch. Bip. (Anthemideae- Asteraceae) in Turkey. *Plant Systematics and Evolution*; 296:205-215.
16. Aydin, Ö, Coşkunçelebi, K, Güzel, ME. 2013. A contribution to taxonomy of *Centaurea* including *Psephellus* (Asteraceae) based on anatomical and molecular data. *Turkish Journal of Botany*. 37: 419-427.
17. Ozcan, M, Unver, M, Eminagaoglu, O. 2014. Comparative anatomical and ecological investigations on some *Centaurea* (Asteraceae) taxa from Turkey and their taxonomic significance. *Pakistan Journal of Botany*. 46(6): 1287-1301.
18. Ekeke ,C, Mensah, SI. 2015. Comparative Anatomy of Midrib and Its Significance in the Taxonomy of the Family Asteraceae from Nigeria. *Journal of Plant Sciences*; 10(5): 200-205.
19. Ozcan, M, Demiralay, M, Kahriman, A. 2015. Leaf anatomical notes on *Cirsium* Miller (Asteraceae, Carduoideae) from Turkey. *Plant Systematics and Evolution*; 301: 1995-2012.
20. Kartal, C. 2016. Calcium Oxalate Crystals in Some Species of the Tribe Cardueae (Asteraceae). *Botanical Sciences*; 94(1): 107-119.

Positioning of Cubic Shaped Particles with Different Edge Structures in Nematic Medium

Aslı Karausta¹, Emre Büküşoğlu^{1*}

¹ Department of Chemical Engineering, Middle East Technical University, Dumlupınar Bulvarı,
Çankaya, Ankara, Turkey

* emrebuk@metu.edu.tr

*Orcid: 0000-0002-3128-059X

Received: 9 November 2020

Accepted: 24 May 2021

DOI: 10.18466/cbayarfbe.835483

Abstract

Liquid crystals (LC) are phases of matter that possess long range orientational order while maintaining fluidic properties. LCs have been shown to provide a medium that result in self-assembly of the colloidal particles through elastic interactions. One parameter that affects the positioning of the particles in LC medium is the edge sharpness of the particles. Simulation studies in the literature suggests that the edge sharpness of the particles directly affect the LC director profile at the vicinity of the particles, and playing a critical role in the formation and the shapes of the topological defects. This article presents a systematic study to show the effects of the edge sharpness on the orientation and the defect structure around the cubic shaped particles. The particles were shown to orient with their diagonal preferably parallel to the direction of the far field nematic director when the particles mediate planar anchoring. Whereas the particles with homeotropic anchoring did not exhibit strong preference in their orientation. We also showed defect structures to form around the particles with homeotropic surface anchoring. The defect structure around the particles with round edges were ring shaped, whereas the defects with S-shapes were formed around sharp-edged or truncated particles. The findings herein were found to be consistent with the simulations present in literature. The findings would find use in next generation materials for optics, photonics and responsive systems.

Keywords: *Alignment, Colloids, Defects, Liquid Crystals.*

1. Introduction

Liquid crystals (LCs) are the phases of matter that exhibit both fluidic properties and molecular ordering which are currently being developed for emerging applications.[1–3] In the nematic phases, the molecules exhibit orientational order along a unique direction called the director.[1] When colloidal particles are dispersed in a LC medium, the director profile is affected due to the interfacial interactions, which leads to useful observations that are unique to LCs.[4, 5, 14–16, 6–13] These interfacial phenomena can be described using three generalized concepts, which can be classified as surface anchoring, elasticity and the formation of the defects.[2] When a LC medium is in contact with a surface, the interaction of the mesogenic molecules at the interface results in a preferred orientation of the LCs, called the easy axis, which is the outcome of the maintained minimum energy state. This orientation can then be shifted due to the external fields, which is penalized with a surface anchoring energy. The

long-range orientation of the LCs underlies the existence of the elastic properties of the LCs. When the natural orientation of the LC medium is affected by a geometric constraint, for example the presence of the colloids or surfaces, the director is strained that results in an energetic penalty. When LCs cannot satisfy the present surface anchoring in its medium via just elastic deformations, topological defects occur, which are defined as the local regions of low orientational ordering, or singularity. These three concepts were used in the current literature to define the positioning of the colloidal species dispersed in LC medium.

Studies in the literature showed that the surface anchoring and the director field around a particle is critically important in their positioning, and their interaction with the colloidal particles in a LC media.[4, 7, 11] For example, Poulin and Weitz demonstrated that the chaining of the spherical particles, which mediate planar anchoring of LCs on their surfaces, in a direction that is around an angle of 30° from the far-field

director.[7] Musevic and collaborators showed that spherical particles with homeotropic surface alignment which causes the formation of a satellite point or a Saturn ring to maintain straight chain or as kinked chains, respectively.[17] These different symmetries of the aggregates can be explained by the minimization of the elastic energy free energy.

The effect of particle shape on particle organization in LCs has not yet fully been studied in the literature.[5, 8, 9, 11, 18, 19] Recently, the experimental studies of Lapointe and his collaborators and the simulation studies of Hung and Bale demonstrated that the interaction of the particles that have different shapes (cube, triangle and pentagonal prism) is strongly related to the orientation of these particles towards each other.[9, 20] This effect varies depending on the orientation of the particles with respect to the far field director and the strain of the LC ordering at the vicinity of the particles. As a result, the organization of the particle in LC media is strongly affected. Lapointe and his collaborators also showed that these particles can form assemblies as the multiple (double and triple) organizations, with their shapes to critically effect the symmetry of the interactions. Thus, the studies presented in the literature highlights the critical importance of the particle shapes on their individual orientation and their interaction symmetry. Although the studies showed the importance of the particle shapes on their positioning, the experimental studies are currently limited to the particles with planar surface anchoring.[9] A recent simulation study by Beller et al. showed that the colloidal particles with homeotropic anchoring to mediate defect structures that are critically dependent on the shapes and sharpness of the particles.[21] For example, the cubic shaped particles maintain minimum energy state with their surface normal orientation of 45° with respect to the far field nematic director. In addition, the particles with curved edges maintain a ring-shaped defect, where increasing the sharpness of the edges resulted in the formation of the S-shaped defects that follow the sharp edges of the particles. The studies followed in this article would also be considered as an experimental that mimics a similar system to these simulation studies.

In this study, we experimentally investigated the positioning of the cubic shaped particles in nematic LC medium. We determined the effect of surface anchoring and the edge sharpness of the particles on their alignment in LC medium. In addition, we characterized the shapes of the defects formed around the colloidal particles dispersed in nematic medium. The study highlights the importance of the details of the particle geometry on their positioning in LC medium and suggests routes for the design of the self-assembled colloidal particles in LCs.

2. Materials and Methods

2.1. Materials

A room temperature nematic liquid crystal 4-cyano-4'-pentylbiphenyl (5CB) was purchased from HCCH Jiangsu Hecheng Chemical Materials Co., Ltd. (Nanjing, China). Dimethyloctadecyl [3-(trimethoxysilyl) propyl] ammonium chloride (DMOAP), polyvinyl alcohol (PVA), and anhydrous ethanol were obtained from Sigma-Aldrich Co. Ltd. (St. Louis, USA) and used without further purification. Glass slides were obtained from Marienfeld GmbH (Lauda-Königshofen, Germany). The cubic shaped zeolite A particles were obtained from Prof. Halil Kalıpçılar and Prof. Berna Topuz.

2.2. Methods

2.2.1. DMOAP Functionalization of the Particles

Approximately 2% wt particle (zeolite 4A) in 1 mL deionized water was prepared and placed into ultrasonic bath for 10 minutes to disperse the particles. Then, 100 μ l of DMOAP was added and the solution was kept in ultrasonic bath for another 10 minutes. The particles were then rinsed three times with deionized water and water was substituted with ethanol.

2.2.2. Functionalization of the Glass Surfaces

PVA coated surfaces were used for planar anchoring. Glass surfaces were coated with 5% wt PVA in water using a spincoater (5000 rpm for 2 minutes) and then rubbed with a velvet cloth to maintain unidirectional surface anchoring of LCs. DMOAP functionalization was used for the homeotropic anchoring. Before functionalization of the glass surfaces, O_2 plasma etching was applied to the glass slides using a Diener Electronics, Zepto Plasma Unit. Then, DMOAP was deposited on the glass surfaces from 10 minutes incubation in its 1% wt aqueous solution. The glass slides were finally rinsed with water and dried with nitrogen stream.

2.2.3. Preparation of the Liquid Crystal-Microparticle Suspensions

The particles (about 1 g/L) were dispersed in 5CB using a vortex mixer. 5CB, the particles and anhydrous ethanol was mixed in the isotropic phase until homogenous suspension is maintained. Then, ethanol was evaporated under vacuum to obtain a nematic suspension at room temperature. The suspension is then filled between two glass slides in the nematic phase and equilibrated for about an hour before the imaging.

2.2.4. Optical Microscopy

Optical characterizations of the films were performed using Olympus BX50 and BX53 microscopes (Olympus

Inc., Japan) equipped with a polarizer and an analyzer filter. Three independent samples were prepared to determine angle distribution of the particles. An average of around 100 images were collected from each sample. The images were analyzed using angle analysis of Fiji imagej, an open source image processing software.

2.2.5. Scanning Electron Microscopy

Quanta 400F Field Emission series scanning electron microscope was used to characterize the shapes of the particles at higher resolution.

3. Results and Discussion

We used cubic shaped particles to study the effect of the edge sharpness on the alignment and the LC director profiles around the particles. For the systematic studies, we obtained cubic shaped zeolite 4A particles with round, truncated and sharp edges as shown in the scanning electron micrographs in Figure 1. As shown, the sizes of the particles were in the range of 1 μm to 6 μm . This range is important and useful when considering the range 1 μm to 10 μm , where the interplay of the elasticity and the surface anchoring usually occur.[2] Although the sizes of the particles are within a range of interest in the field, the particles used in this study is not common in studying such interactions. Thus, we first performed studies to understand the surface anchoring of LCs on bare and functionalized particles in the first section below. Then, the next two sections are dedicated to the alignment and positioning of the particles in LCs and the investigation of the defect structures around the particles, respectively.

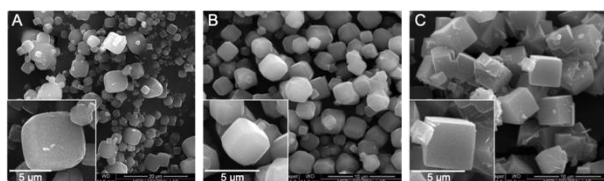


Figure 1. Scanning electron micrographs of zeolite 4A with (A) rounded edge, (B) truncated edge, (C) sharp edges. Insets showing the magnified images of the representative particles.

3.1. Determination of Surface Anchoring of LCs on the Surfaces of the Microparticles

The anchoring condition on the surface of the particles is one of the important parameters affecting the alignment of the particles in liquid crystalline media. Thus, we first analyzed the anchoring of the LCs on the surfaces of these particles since the anchoring of 5CB on the surfaces of the zeolite particles was not readily available in the literature. For this purpose, we dispersed zeolite 4A into 5CB in its nematic phase and collected images of the particles within the range of 2-6 μm using

a polarized microscope equipped with crossed polarizers and a first order retardation plate (FOP). As seen in Figure 2A, the far field director of the nematic 5CB was in the direction of one of the polarizers (shown as *R*, far from the particles), thus, dark appearance was observed under polarized light. However, the distortion of the nematic director around the particles due to the anchoring condition at the surface of the particle resulted in a bright transmitted light as shown by white arrows in the polarized micrographs of Figure 2A-*ii*. Also, when FOP was inserted into the light path, red and blue colors were observed (shown by blue and red arrows in Figure 2A-*iii*).[22] This coloring was consistent with the planar alignment of LCs at the sides of the particles. Using this characterization, the LC anchoring on particle surface was determined as planar and a sketch of the ordering profile of the LCs at the vicinity of the particles was shown in the right panel of Figure 2A-*iv*. Here we note that we observed ~80% of the zeolite 4A particles exhibited planar anchoring of the LCs on their surfaces.

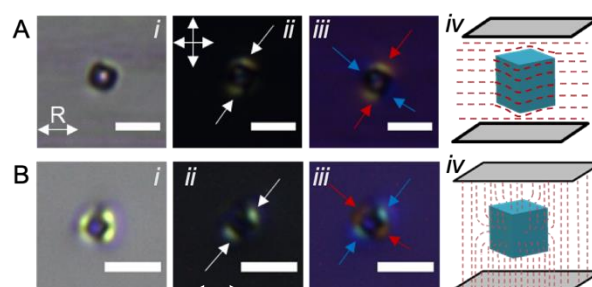


Figure 2. Optical characterizations of the (A) bare and (B) DMOAP functionalized zeolite particles. Brightfield (*i*), polarized light (*ii*) and polarized with first order retardation plate (*iii*) micrographs of single particles dispersed in nematic 5CB). The sketch in the right panel shows the schematic representation of the LC director profile around the particles determined from the micrographs. Double headed arrow indicates the rubbing direction of the two glass slides, R indicates the far field nematic director. Scale bars: 5 μm .

We then modified the LC surface anchoring of the particles with dimethyloctadecyl[3-(trimethoxysilyl)propyl] ammonium chloride (DMOAP) for the expectation of a homeotropic surface anchoring. After functionalization, we checked the anchoring from polarized light micrographs as shown in Figure 2B. The far field director in the images shown in Figure 2B-*ii* is perpendicular to the imaging plane (in-plane), so dark appearance was observed under polarized light. However, the distortion of the nematic director around the particles due to the anchoring condition at the surface of the particle resulted in a bright appearance as indicated by white arrows in the polarized micrographs of Figure 2B-*ii*. Also, when FOP was inserted (Figure 2B-*iii*), which is with a different symmetry compared with that of the planar

particles. When we compared the FOP micrographs of DMOAP coated particles and bare particles, it was seen that the red and blue colors around the particles were located at different sides that pointed out the difference in the anchoring conditions on the surface of the particles. This coloring suggested a homeotropic anchoring of LCs at the surfaces of particles, which would appear dark if particle surface mediated planar anchoring. Using this characterization, the LC anchoring on particle surface was determined as homeotropic and a sketch of the ordering profile of the LCs at the vicinity of the particles was shown in the right panel of Figure 2B-iv. We note that we observed ~90% of the zeolite 4A particles exhibited homeotropic anchoring of the LCs on their surfaces.

3.2. Particle Alignment in Nematic Liquid Crystals

After characterizing the surface anchoring of LCs on the surfaces of bare and DMOAP functionalized zeolite 4A particles, we next characterized the orientation of particles in nematic 5CB. For the analysis, orientations of the single zeolite 4A particles were examined by measuring the angles that the particles maintain in 5CB. When we analyzed bare zeolite 4A particles with sharp edges in planar and homeotropic cells, we evidenced the particles to maintain a position with an angle of 0° in planar medium whereas there was no significant tendency in the case of particles in homeotropic cells as shown in Figure 3.

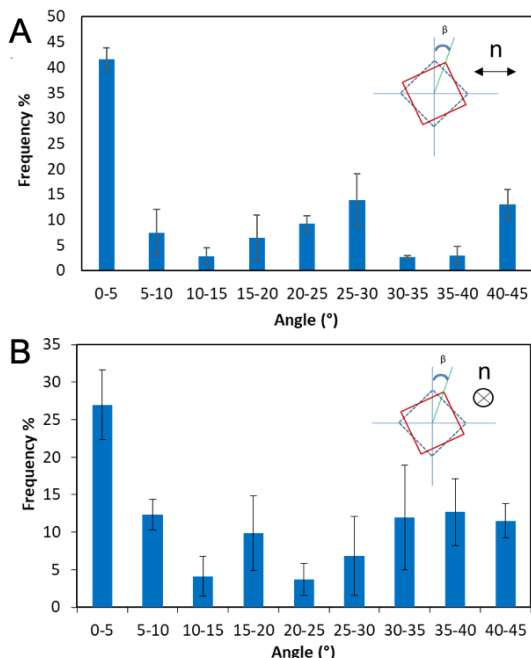


Figure 3. Angle distribution of the bare single zeolite 4A particles with sharp edges in a) planar cell b) homeotropic cell and schematic representation of orientations of the particles. β indicates the angle that the particle oriented in LC media.

As shown in Figure 3, the particles exhibited a preferred orientation along the nematic director, which was expected due to the elastic effects of the LC medium. However, that elastic anisotropy is missing in the direction orthogonal to the nematic director due to the lack of the elastic force anisotropy. Consistent with this, we also observed the same trend in the relative orientation of the DMOAP coated particles with respect to the far field nematic director.

In order to investigate the effect of the edge sharpness of the particles on their orientation in nematic medium, zeolite 4A with rounded and truncated edges were also used. When we analyzed the orientation of the single bare zeolite 4A with truncated edges (Figure 4, red data) and round edges (Figure 4, green data), we observed that the single particles dispersed in planar medium to generally maintain an orientation with an angle around 0° with respect to the far field nematic director, consistent with the observations described above for the particles with sharp edges. However, when compared among the three types of the particles, the frequency of the round-edged particles to maintain an angle of 0° is significantly lower than that of the other two particle shapes. This is expected when considering the loss of the shape anisotropy with the rounding of the edges of a cubic particle.

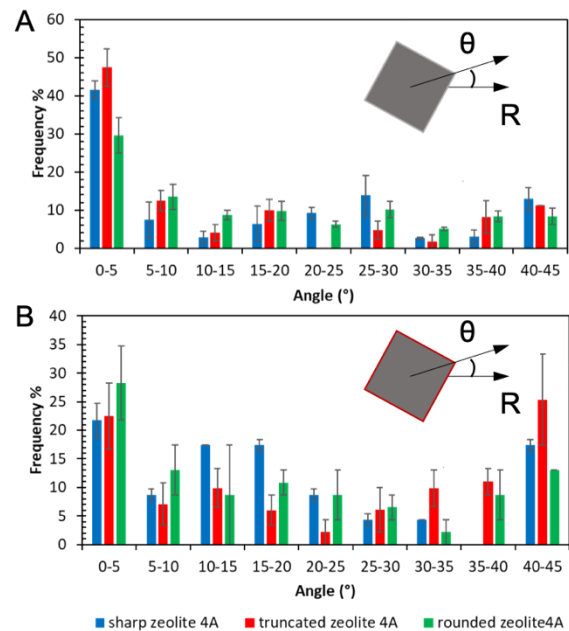


Figure 4. Angle distribution of (A) the bare and (B) the DMOAP coated single zeolite 4A particles with sharp, truncated and rounded edges in planar LC medium. The schematic representation of orientations of the particles are shown as insets where β indicates the angle that the particle oriented in LC media.

When the orientation of the DMOAP functionalized particles were quantified in nematic 5CB, we did not observe a significantly pronounced orientation of the particles with respect to the far field nematic director, independent of the particle shapes. As shown in Figure 4B, the particles maintaining an average orientation of 0 to 5° with respect to the nematic director were almost half of those observed in particles with planar surface anchoring. We reasoned that this significant difference in the distribution of the orientation of the particles would be due to the formation of defects around the particles with surfaces mediating homeotropic orientation, which we detailed below.

3.3. Defect Structures Around Cubic Particles Suspended in Nematic Medium

The literature suggested a range of defect shapes that could form around the cubic shaped particles.[21] Interestingly, simulation studies suggested that at the vicinity of the cubic particles mediating homeotropic orientations, defect loops form that wraps the particles.[21] When the sharpness of the particles at their edges are increased, they have found that the ring shapes of the defects were deformed and maintained shapes that follows the edges of the particles. Herein, we collected images of the three types of the DMOAP coated particles under the microscope to provide evidence of whether or not there are defects present, and whether or not their shapes are affected by the sharpness of the cubic particles.

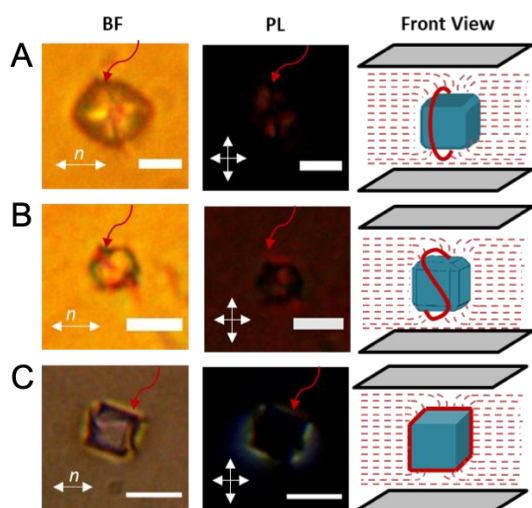


Figure 5. Brightfield (BF) and polarized light (PL) micrographs of DMOAP-coated zeolite 4A particles with (A) rounded, (B) truncated and (C) sharp edges and the corresponding schematic illustrations of the nematic director field and the shapes of the defects around the particles in nematic planar cell. Red arrows in micrographs indicate the defects around the particles. Dashed and solid red lines in schematic illustrations represent the director field and defects, respectively. Scale bars: $5 \mu\text{m}$

Figure 5A-B demonstrates the representative micrographs of the particles with round, truncated and sharp edges, respectively. Evidently, defect structures around DMOAP coated particles with rounded edges were in the shape of a ring (Figure 5A). Defects with S-shapes were formed around DMOAP coated, truncated particles (Figure 5B). As the sharpness of the particles is high (Figure 5C), the shapes of the disclinations (indicated with solid red lines) are deformed and maintained a shape that wrapped the edges of the particles. These observations of the sharpness-dependent shapes of the defects formed around the cubic particles provides the first experimental evidence to the findings of the simulations.[21]

After finding the evidence of the formation of the defects around particles mediating homeotropic surface anchoring, we revisited the alignment of the particles in nematic medium shown in Figure 4. When we compared the distributions of the alignments of the DMOAP coated particles, we did not observe a significant difference in their alignment with respect to the defect structures. However, when the alignment of the particles mediating homeotropic orientation were compared with that of the particles mediating planar anchoring, we found that the particles with homeotropic anchoring not to exhibit a strong preference in the alignment with respect to the far field nematic director. There exists a slight preference of the angles close to 0° and 45° , which is consistent with the literature.[21] However, it does not appear to be strong when compared with the planar particles.

4. Conclusion

We have investigated the positioning of the cubic shaped microparticles with different edge sharpness in nematic liquid crystals. Our results of this study are two-folds. First, we found a relationship between the edge sharpness and the alignment of the particles with respect to the far field director. Specifically, the planar particles with sharp edges to preferentially align with their diagonal parallel to the far field nematic director, which was lowered with the rounding of the particle edges. Second, from the imaging of the particles with homeotropic surface anchoring in the nematic LCs, we found that the defect structure around the particles to be affected by the edge sharpness of the particles. The defect structures observed around the rounded particles were close to a ring shapes, whereas the defects around the cubic particles with sharp edges to maintain a deformed ring with line defects following the proximity of the edges. The observations reached in this study is consistent with the simulations performed on similar systems in literature. The findings would find use in next generation materials for optics, photonics and responsive systems.

Acknowledgement

The authors thank the financial support provided by Scientific and Technological Research Council of Turkey (TÜBİTAK) under award number 116C093.

Author's Contributions

Aslı Karausta: Performed the experiment and result analysis.

Emre Bukusoglu: Assisted in analytical analysis on the structure, supervised the experiment's progress, result interpretation and helped in manuscript preparation.

Ethics

There are no ethical issues after the publication of this manuscript.

References

1. de Gennes, P. G., Prost, J., The Physics of Liquid Crystals; Second Edi, Oxford, New York, 1993.
2. Bukusoglu, E., Bedolla-Pantoja, M. A., Mushenheim, P. C., Wang, X., Abbott, N. L. 2016. Design of responsive and active (Soft) materials using liquid crystals. *Annual Review of Chemical and Biomolecular Engineering*; 7: 163–196.
3. Bai, Y., Abbott, N. L. 2011. Recent advances in colloidal and interfacial phenomena involving liquid crystals. *Langmuir*; 7: 5719–5738.
4. Loudet, J. C., Barois, P., Poulin, P. 2000. Colloidal ordering from phase separation in a liquid-crystalline continuous phase. *Nature*; 407: 611–613.
5. Mondiot, F., Chandran, S. P., Mondain-Monval, O., Loudet, J. C. 2009. Shape-induced dispersion of colloids in anisotropic fluids. *Physical Review Letters*; 103: 1–4.
6. Prathap Chandran, S., Mondiot, F., Mondain-Monval, O., Loudet, J. C. 2011. Photonic control of surface anchoring on solid colloids dispersed in liquid crystals. *Langmuir*; 27: 15185–15198.
7. Poulin, P., Weitz, D. A. 1998. Inverted and multiple nematic emulsions. *Physical Review E*; 57: 626–637.
8. Yuan, Y., Martinez, A., Senyuk, B., Tasinkevych, M., Smalyukh, I. I. 2018. Chiral liquid crystal colloids. *Nature Materials*; 17: 71–78.
9. Lapointe, C. P., Mason, T. G., Smalyukh, I. I. 2009. Shape-controlled colloidal interactions in nematic liquid crystals. *Science*; 326: 1083–1086.
10. Senyuk, B., Liu, Q., Bililign, E., Nystrom, P. D., Smalyukh, I. I. 2015. Geometry-guided colloidal interactions and self-tiling of elastic dipoles formed by truncated pyramid particles in liquid crystals. *Physical Review E*; 91: 1–8.
11. Yuan, Y., Liu, Q., Senyuk, B., Smalyukh, I. I. 2019. Elastic colloidal monopoles and reconfigurable self-assembly in liquid crystals *Nature*; 570: 214–218.
12. Wood, T. A., Lintuvuori, J. S., Schofield, A. B., Marenduzzo, D., Poon, W. C. K. 2014. A Self-Quenched Defect Glass in a Colloid-Nematic Liquid Crystal Composite. *Science*; 79: 79–83.
13. Koenig, G. M., de Pablo, J. J., Abbott, N. L. 2009. Characterization of the reversible interaction of pairs of nanoparticles dispersed in nematic liquid crystals. *Langmuir*; 25: 13318–13321.
14. Rahimi, M., Roberts, T. F., Armas-Pérez, J. C., Wang, X., Bukusoglu, E., Abbott, N. L., de Pablo, J. J. 2015. Nanoparticle self-assembly at the interface of liquid crystal droplets. *Proceedings of the National Academy of the Sciences of the U. S. A.*; 112: 5297–5302.
15. Wang, X., Miller, D. S., de Pablo, J. J., Abbott, N. L. 2014. Organized assemblies of colloids formed at the poles of micrometer-sized droplets of liquid crystal. *Soft Matter*; 10: 8821–8.
16. Wang, X., Miller, D. S., De Pablo, J. J., Abbott, N. L. 2014. Reversible switching of liquid crystalline order permits synthesis of homogeneous populations of dipolar patchy microparticles. *Advanced Functional Materials*; 24: 6219–6226.
17. Muševič, I., Škarabot, M., Tkalec, U., Ravnik, M., Žumer, S. 2006. Two-dimensional nematic colloidal crystals self-assembled by topological defects. *Science*; 313: 954–958.
18. Lapointe, C. P., Mayoral, K., Mason, T. G. 2013. Star colloids in nematic liquid crystals. *Soft Matter*; 9: 7843.
19. Lapointe, C., Hultgren, A., Silevitch, D. M., Felton, E. J., Reich, D. H., Leheny, R. L. 2004. Elastic Torque and the Levitation of Metal Wires by a Nematic Liquid Crystal. *Science*; 303: 652–655.
20. Hung, F. R., Bale, S. 2009. Faceted nanoparticles in a nematic liquid crystal: defect structures and potentials of mean force. *Molecular Simulation*; 35: 822–834.
21. Beller, D. A., Gharbi, A., Liu, I. B. 2015. Shape-controlled orientation and assembly of colloids with sharp edges in nematic liquid crystals. *Soft Matter*; 11: 1078–1086.
22. Miller, D. S., Carlton, R. J., Mushenheim, P. C., Abbott, N. L. 2013. Introduction to optical methods for characterizing liquid crystals at interfaces. *Langmuir*; 29: 3154–3169.

Geometric Characterization of Three-Dimensional (3D) Woven Jute Fiber Preforms for Composites

Nesrin Şahbaz Karaduman¹*

¹ Department of Textile, Footwear and Leather, Akdagmadeni Vocational High School, Yozgat Bozok University, 66300, Yozgat, Turkey
[*nesrin38@gmail.com](mailto:nesrin38@gmail.com)

*Orcid: 0000-0001-9555-7044

Received: 15 November 2020

Accepted: 30 March 2021

DOI: 10.18466/cbayarfbe.826090

Abstract

Fiber-reinforced composite materials have many advantages in various engineering applications when compared to traditional materials such as glass, metals, ceramics, and unreinforced plastics. Recently, textile-reinforced composites are increasingly used in various industries including aerospace, construction, and automotive. This study aims to investigate the geometric characteristics of three-dimensional (3D) woven preforms which are used as reinforcement materials in composites. To this end, 3D woven preforms with three different weave types were produced namely 3D orthogonal, 3D plain z-orthogonal, and 3D satin z-orthogonal. The effect of weave pattern and the number of layers on the geometric characteristics of the produced fabrics was investigated. For this purpose, yarn-yarn distances and density, yarn lengths, and yarn angles were measured. The effect of the number of layers on the geometric parameters was limited. Yarn-to-yarn distances in plain-weave fabrics were found to be greater when compared to other types of fabrics whereas the yarn density decreased in plain woven fabrics due to a large number of interlacements. This shows that in composite form, the fiber volume fraction in the filling and z-directions will be lower in the semi-interlaced fabrics when compared to the non-interlaced orthogonal structures. It was also shown that filling and warp angles are a function of weave type while z yarn angle is associated with the weaving operations such as beat-up, multi-layer filling insertion, and warp yarn let off.

Keywords: Geometric characterization, Jute fiber, Natural fiber composites, Three dimensional (3D) woven preform.

1. Introduction

Fiber-reinforced composites have many advantages over traditional materials such as metals, glass, ceramics, and plastics. These advantages include high strength and stiffness, low weight, tailorability, fracture toughness, and corrosion resistance. Fibers are the main load-bearing element in a composite system due to their high strength and stiffness whereas the matrix determines the final shape of the composite and protects the fibers against harmful environments. The matrix phase is also responsible for homogenously dispersing applied loads to reinforcing fibers. Fiber and matrix type, fiber orientation/architecture, and fiber volume fraction determine the mechanical properties of a composite material.

Textile-reinforced composites are a group of materials that use a textile form as reinforcement such as yarns, woven, knitted, braided, nonwoven, and multiaxial fabrics. Textile fabrics can be manufactured in two-dimensional (2D) and three-dimensional (3D) forms. The main difference between the two is the use of through-the-thickness or z-yarns in the latter. The type and parameters of textile structure determine the fiber architecture and orientation as well as fiber volume fraction in composite materials.

The first application of textile fabrics was in the aerospace industry where carbon-carbon composites were produced using layered 2D textile fabrics. These composites were produced by simply stacking 2D woven fabrics one on top of the other and impregnating with the resin using one of the composite manufacturing methods. These composite structures were prone to

delamination and showed poor damage tolerance due to a lack of through-the-thickness reinforcement (z-yarns). The solution to these problems of layered structures was the development of 3D fabric manufacturing processes which incorporated z-yarns in the thickness direction to bind the fabric layers and create a compact 3D structure which has good interlaminar strength and damage tolerance [1]. Moreover, 3D fabrics eliminate the labor-intensive layering step in composite processing reducing the overall cost and allow net-shape manufacturing. For all these reasons, 3D textile-reinforced composite structures have been used in the aerospace industry since the 1960s. Nowadays 3D textile composites are used in various industries including aerospace, civil engineering, automotive, and sports [2].

In recent years, natural fibers have attracted considerable attention as composite reinforcement due to increased environmental concerns such as global warming and environmental pollution as well as economic reasons such as rising petroleum prices and depletion of fossil fuels. Natural bast fibers such as jute, hemp, flax, and kenaf are increasingly being used as reinforcement materials due to their low density and high strength/stiffness. Natural fibers are environmentally friendly, sustainable, renewable, and biodegradable [3-7]. Owing to these distinct advantages, natural fibers can compete with glass fibers in various composite applications [8-11].

A literature survey showed that the number of studies on the geometric parameters of 3D woven natural fiber fabrics is limited. This study aims to investigate the geometric characteristics of 3D woven jute preforms as a potential candidate as reinforcement in composites. For this purpose, non-interlaced and semi-interlaced 3D woven preforms with three different weave types were produced namely 3D orthogonal, 3D plain z-orthogonal, and 3D satin z-orthogonal. The effect of weave pattern and the number of layers on the geometric characteristics of the produced fabrics was investigated. For this purpose, yarn-yarn distances and density, yarn lengths, and yarn angles were measured. The results were evaluated taking into account the corresponding composite properties.

2. Materials and Methods

2.1. Materials Used

3D weaving requires three yarn sets such as warp, filling and, z-yarns (through-the-thickness yarns). In this study jute yarns with a linear density of 250 tex were used as warp, filling and z-yarns to make 3D woven preforms. Jute yarns were provided by Erkollar Ltd. (Gaziantep, Turkey).

2.2. 3D Woven Fabric Production

An in-house developed 3D weaving apparatus was used to produce the 3D woven jute fabrics. Two main groups of fabrics were produced such as a) Non-interlaced orthogonal and b) Semi-interlaced orthogonal fabrics. In non-interlaced fabrics, warp, filling, and z-yarns run along the length (x-axis), width (y-axis) and thickness (z-axis) of the fabric respectively without making interlacements with other yarn sets (Figure 1(a) and 2(a)). The production of this fabric requires six distinct steps such as warp let-off, 2D shedding, multilayer filling insertion, z-yarn insertion, beating, and fabric take-up [12]. Figure 3 shows 3D orthogonal weaving principle schematically. The second group of 3D fabrics produced in this study i.e. semi-interlaced fabrics were produced using two distinct weave patterns such as plain-weave and satin-weave. These patterns were chosen due to the fact that plain-weave fabrics contain a large number of interlacements when compared to satin-weave making it easier to observe the effect of any geometrical differences on fabric properties. In these fabrics, warp and filling yarns make interlacements according to 1/1 plain (Figure 1(b), 2(b)) and 1/4 satin (Figure 1(c), 2(c)) weave patterns while z-yarns run along the thickness of the fabrics between adjacent warp yarns without making any interlacements with other two yarn sets. Fabric production started with warp let-off. Then, z-yarns are divided into two groups, such that an odd number of yarns are laid in the +z direction while an even number of yarns are laid in -z direction. Then the filling yarn makes interlacements with warp yarns according to the weave pattern in every layer. Then z-yarns move in alternate directions to their first position such that an odd number of yarns are laid in the -z direction while an even number of yarns are laid in +z direction. This cycle of movements was repeated to make preforms. Two different number of layers such as 2 and 4 layers were used for the production of all the fabrics in this study. Table 1 lists the produced 3D fabric samples together with their sample codes.

Table 1. Produced 3D fabric samples.

Fabric Type	Number of Layers	Sample Code	
Orthogonal	2	3DWO	
	4		
Semi-interlaced	Plain	2	3DWP-ZO
		4	
	Satin	2	3DWS-ZO
		4	

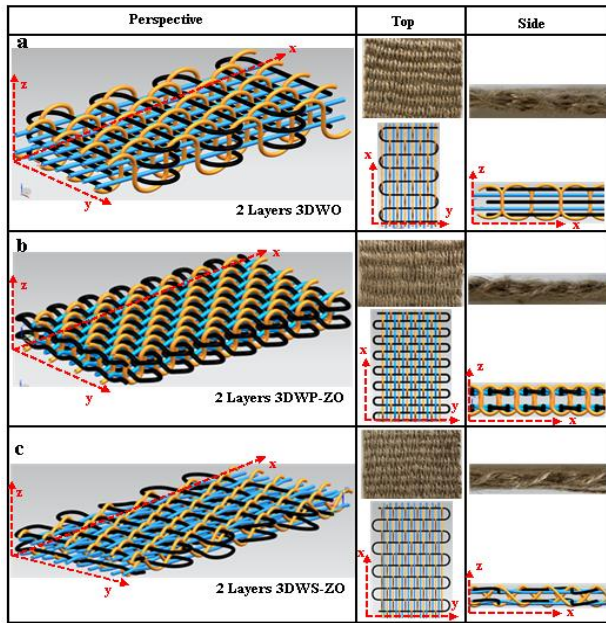


Figure 1. Two-layer fabric samples and their computer drawings (a) 3D orthogonal fabric; (b) 3D plain-weave z-orthogonal fabric; (c) 3D satin-weave z-orthogonal fabric.

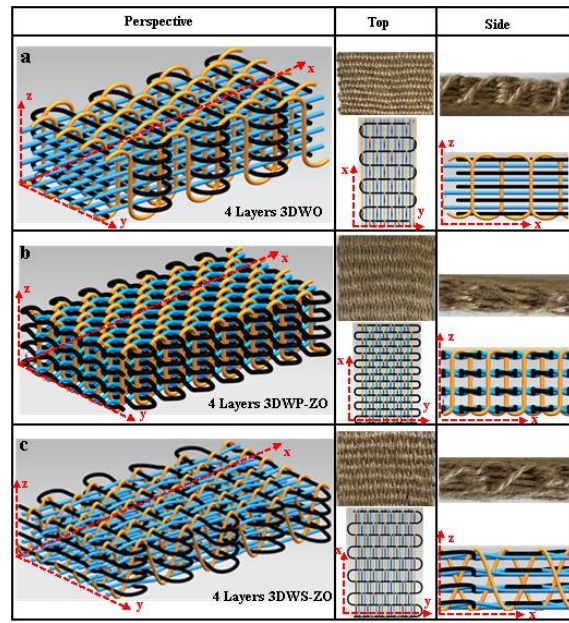


Figure 2. Four-layer fabric samples and their computer drawings (a) 3D orthogonal fabric; (b) 3D plain-weave z-orthogonal fabric; (c) 3D satin-weave z-orthogonal fabric.

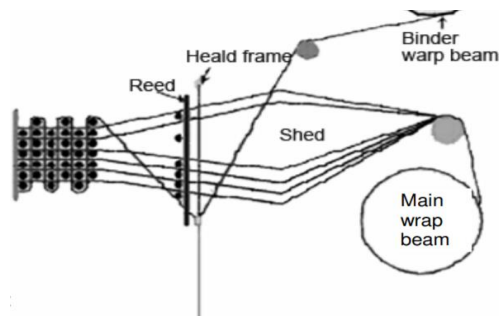


Figure 3. 3D orthogonal weaving principle [13].

2.3. Computer Modeling

The produced fabric samples were modeled using NX-Unigraphics 7.5 software to clearly demonstrate the yarn paths and interlacements in 3D structures and for future analysis.

2.4. Determination of Fabric Dimensions

In 3D woven fabrics, fabric length (Sl), width (Sw), and thickness (St) were measured. The fabric length was limited to 20 cm in all the fabrics. Figure 4 shows the fabric dimensions and yarn sets on actual fabric and computer model.

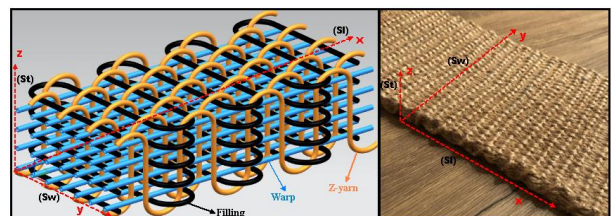


Figure 4. Demonstration of the fabric dimensions and yarn sets on computer model and actual fabric sample.

2.5. Determination of Yarn-to-Yarn Distances and Yarn Density

Yarn-to-yarn distances of adjacent yarns were measured on the 3D woven fabric samples. Warp-warp (w-w), filling-filling (f-f), and z-yarn-z-yarn (z-z) distances were measured on top side (x-y plane), side (x-z plane), and cross-section (y-z plane). Figure 5 highlights the yarn-to-yarn distances and other related parameters for measurements.

Yarn density measurements were carried out for warp, filling, and z-yarns on top, side, and cross-section planes of the fabrics. The number of yarns in 5 cm was considered for yarn density measurements.

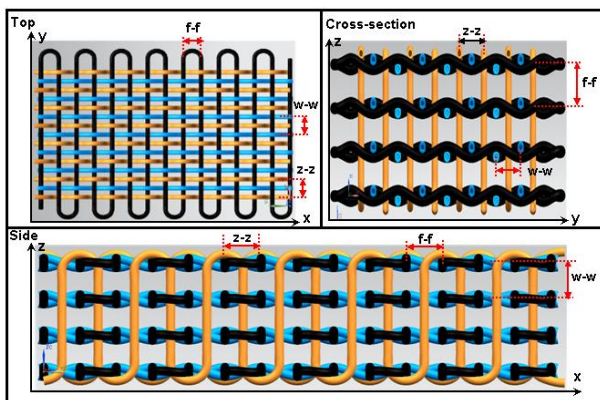


Figure 5. The illustration of the parameters considered in yarn-to-yarn distance measurements.

2.6. Determination of the Yarn Lengths

Uncrimped yarn lengths were measured in 3D woven fabrics. In fabric structure, especially at the interlacement points, warp, filling, and z-yarns follow curved paths and the yarns become curved. This is referred to as the “yarn crimp”. The length of the path that warp, filling, and z-yarns follow in the fabric structure is hence called the “uncrimped yarn length”. In this study, guide yarns were used in order to be able to measure the uncrimped yarn lengths. First, the guide yarn was inserted in the structure following the exact same yarn path as the yarn (i.e. warp, filling or z-yarn) whose uncrimped length is to be measured. Then the ends of this guide yarn were marked before it is withdrawn from the structure.

The distance between the markings on the straightened guide yarn gives the uncrimped yarn length. Uncrimped warp yarn length (l_w), uncrimped filling yarn length (l_f), and uncrimped z-yarn length (l_z) were measured for all fabric types (Figure 6).

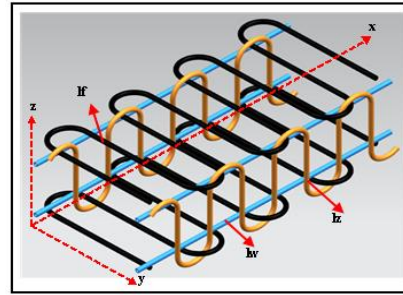


Figure 6. Illustration of uncrimped warp, filling, and z-yarn length on the computer model.

2.7. Determination of the Yarn Angles

The following yarn angle measurements were carried out in 3D woven fabric structures:

- The filling angle between the filling yarn and warp yarn in the fabric width direction (y-axis) (θ_f) (Figure 7(a))
- The filling trajectory angle between the filling yarn and z- yarn in the fabric thickness direction (z-axis) (θ_{fz}) (Figure 7(a))
- The warp angle between the warp yarn and filling yarn in the fabric length direction (x-axis) (θ_w) (Figure 7(b))
- The warp trajectory angle between the warp yarn and z- yarn in the fabric thickness direction (z-axis) (θ_{wz}) (Figure 7(b))
- The z-yarn angle between the z-yarn and warp yarn in the fabric length direction (x-axis) (θ_z) (Figure 8)
- The z-yarn trajectory angle between z-yarn and warp yarn in the thickness direction (z-axis) (θ_{zw}) (Figure 8)

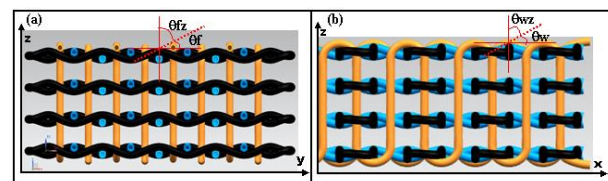


Figure 7. Demonstration of (a) θ_f and θ_{fz} angles (b) θ_w and θ_{wz} angles.

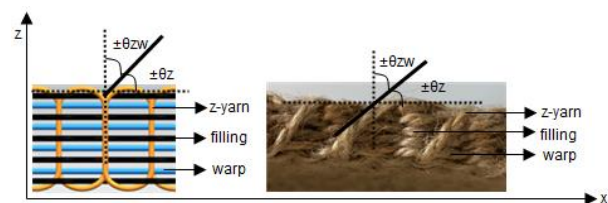


Figure 8. Demonstration of θ_z and θ_{zw} angles.

3. Results and Discussion

In the current study, the geometric characterization of 3D woven jute fabrics was carried out for their possible application in fiber-reinforced composites. For this purpose, 3D orthogonal, 3D plain z-orthogonal, and 3D satin z-orthogonal woven fabrics were produced (Figure 9).

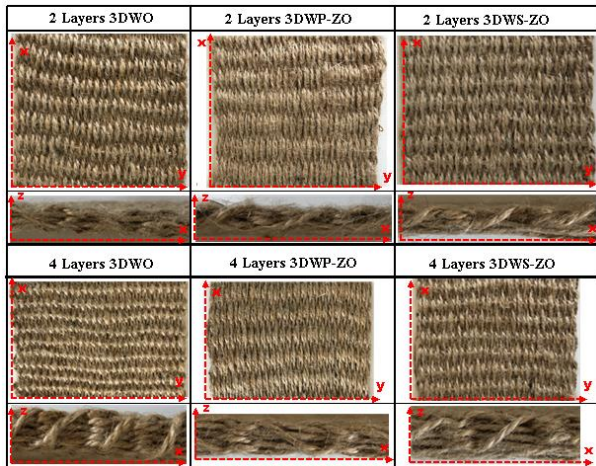


Figure 9. Fabric types produced in the current study.

3.1. Yarn-to-Yarn Distances and Yarn Density

Figure 10 shows the relation between the fabric type and the yarn-to-yarn distances measured on the fabric side (xz-plane). Filling-filling and z-yarn-z-yarn distances were found to be the same with each other and greater than the warp-warp distance. The number of layers did not have a significant effect on the yarn-to-yarn distances. When the semi-interlaced fabrics were compared with the non-interlaced structures, filling-filling and z-z yarn distances were found to be similar in satin-weave and non-interlaced orthogonal fabrics. In plain-weave fabrics, however, filling-filling and z-z yarn distances were found to be greater than other types of fabrics. This was attributed to relatively large number of warp-filling interlacements in plain-woven fabrics which prevent the adjacent filling yarns from approaching each other during the beat-up action. The same can be stated for the z-yarns. This effect was limited in satin-woven fabrics due to a smaller number of interlacement points in satin fabrics. Hence filling-filling and z-z distances were similar to those of the non-interlaced fabrics. When composite properties are considered, directional fiber volume fractions in filling and z directions will be lower in semi-interlaced structures when compared to non-interlaced fabric composites.

Figure 11 shows the relation between the fabric type and the yarn-to-yarn distances measured on the fabric cross section (yz-plane). Filling-filling, warp-warp and z-z distances measured on fabric cross section plane

were in a narrow range of 0.2 to 0.6 cm. As the number of layers was increased, warp-warp distance was found to decrease. Warp-warp and filling-filling distances (distances between the adjacent layers) were lower in semi-interlaced structures due to the more compact nature of the fabrics resulting from a large number of interlacements. z-z distance increased as the number of layers was increased. On the other hand, z-z distances were greater in semi-interlaced structures. In these structures, warp-filling interlacement points prevent the adjacent z-yarns from approaching each other, thus increasing the z-z yarn distances.

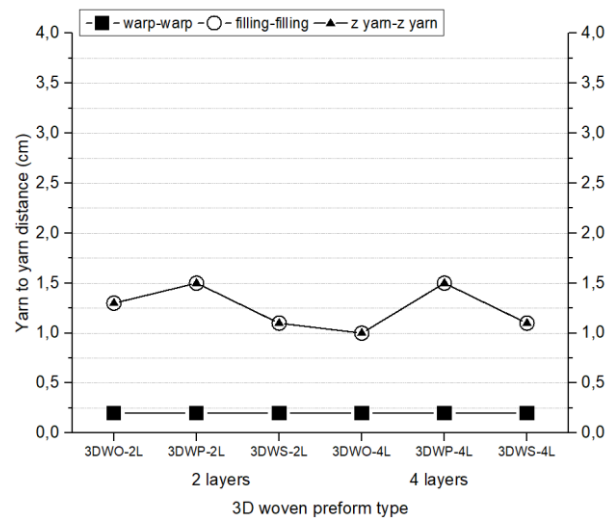


Figure 10. The relation between the fabric type and the yarn-to-yarn distances measured on the fabric side (xz-plane).

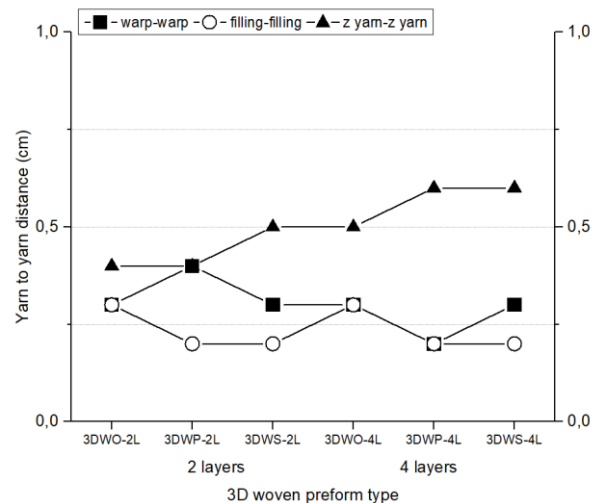


Figure 11. The relation between the fabric type and the yarn-to-yarn distances measured on the fabric cross section (yz-plane).

Figure 12 shows the relation between the fabric type and the filling and z-yarn densities measured on the

fabric side (xz-plane). It was observed that the filling and z-yarn density values are very similar to each other. (Figure 12). Filling-filling and z-z yarn densities were lower in plain-weave semi-interlaced fabrics in line with the increment observed in filling-filling and z-z yarn distances in these structures. As explained above, warp-filling interlacement points in plain-weave semi-interlaced fabrics prevent the adjacent filling yarns from approaching each other, thus increasing the yarn-to-yarn distances and lowering the yarn density values. However, the effect of warp-filling interlacements was minimized in satin-weave semi-interlaced fabrics due to a lower number of warp-filling interlacements in satin structure. Accordingly, yarn density values were similar to those of the non-interlaced fabrics and higher than those of the plain-weave fabric samples.

Figure 13 shows the relation between the fabric type and the warp and z-yarn densities measured on the fabric cross-section (yz-plane). Warp yarn density values were found to be twice as higher as the z-yarn densities (Figure 13). This is an expected result because one z yarn is placed between two adjacent warp yarns when producing 3D fabric structures. The measured yarn densities are indicative of a successful 3D fabric weaving operation which resulted in uniform fabric structures. In semi-interlaced fabrics, z-yarn densities were lower due to increasing z-z distance. z-directional fiber volume fraction in these structures should be expected to be lower.

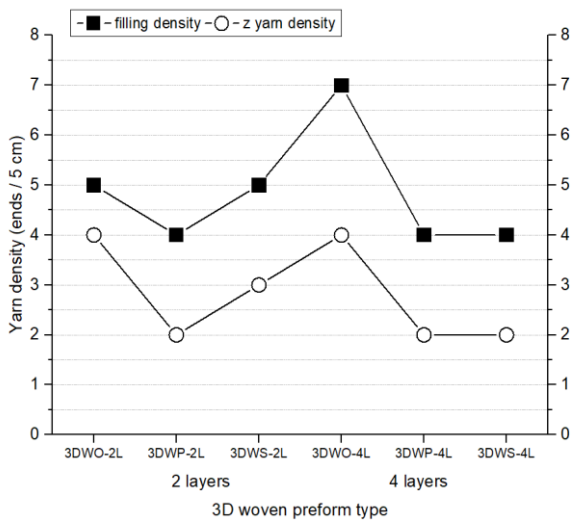


Figure 12. The relation between the fabric type and the filling and z-yarn densities measured on the fabric side (xz-plane).

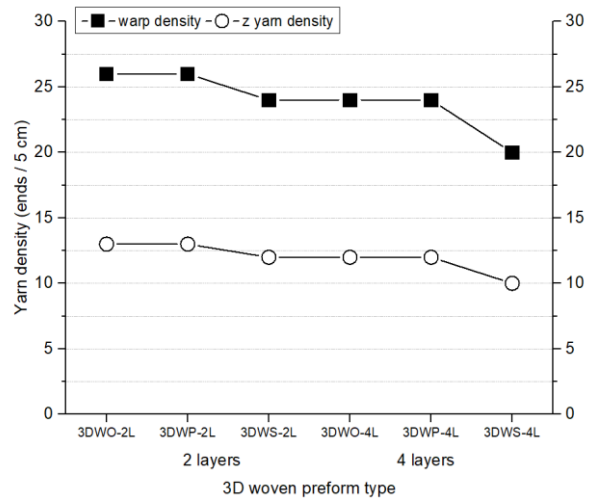


Figure 13. The relation between the fabric type and the warp and z-yarn densities measured on the fabric cross-section (yz-plane).

3.2. Yarn Lengths

Table 2 shows the uncrimped warp yarn length (l_w), filling yarn length (l_f), and z-yarn length (l_z). Figure 14 shows the relation between the fabric types and various yarn lengths. Uncrimped warp and filling yarn lengths were greater in semi-interlaced plain and satin-woven fabrics when compared to non-interlaced structures. In non-interlaced fabric structure, warp and filling yarns run along x and y axes respectively without making any interlacements with other yarn sets and preserving their straight form. However, in semi-interlaced plain and satin fabrics, warp and filling yarns make interlacements with each other according to the weave pattern and become curved. Therefore, the uncrimped warp and filling yarn lengths are greater in semi-interlaced fabrics as expected. Uncrimped z-yarn lengths were found to be greater in plain-woven fabrics compared with satin-weave due possibly to an increased number of yarn interlacements which increase the yarn crimp.

Table 2. The uncrimped warp yarn length (l_w), filling yarn length (l_f), and z-yarn length (l_z) in 3D fabrics.

Sample code	Num of layers	l_w (/20 cm)	l_f (/9 cm)	l_z (cm)
3DWO	2	20.0	9.0	2.1
3DWO	4	20.0	9.0	2.5
3DWP-ZO	2	21.1	9.6	2.3
3DWP-ZO	4	21.3	9.8	3.1
3DWS-ZO	2	21.2	9.5	2.2
3DWS-ZO	4	21.3	9.6	2.7

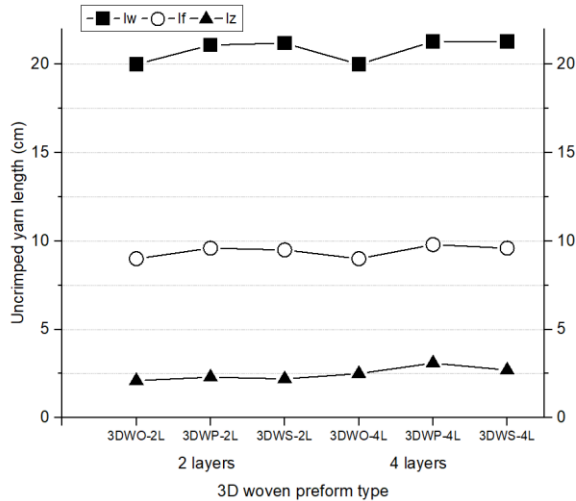


Figure 14. The relation between the fabric types and various yarn lengths.

3.3. Yarn Angles

Figure 15 shows the relation between the fabric type and various yarn angles. $\pm\theta_z$ angle was found to be greater compared with other angles (θ_w and θ_f). θ_z angle was found to be greater in non-interlaced orthogonal fabrics compared with semi-interlaced structures due to the fact that filling-filling and z-z yarn distances are greater in semi-interlaced structures. θ_z angle generally increases as the number of layers is increased. In non-interlaced fabrics, θ_f and θ_w angles are equal to 0° due to the fact that these fabric structures, warp and filling yarns run along x and y axes respectively without making any interlacements with other yarn sets and preserving their straight form. θ_w angle is greater in satin woven fabrics compared with the plain weave. This was attributed to the fact that filling-filling distance measured in xz plane is lower in satin woven fabrics compared with the plain-weave (Figure 10). θ_f angle was found to be greater in 2-layer satin fabrics when compared to 2-layer plain fabrics. However, the θ_f angle was greater in the case of 4-layer plain woven fabrics when compared to satin-weave. This result is also in parallel with yarn distances measured in the yz-plane (Figure 11). Accordingly, θ_f angle increases as the distance between the adjacent warp yarns measured in the yz plane decreases.

It can be concluded that θ_f and θ_w angles are generally affected by weave pattern whereas θ_z angle is generally influenced by weaving operations such as warp let-off, multilayer filling insertion, and beat-up.

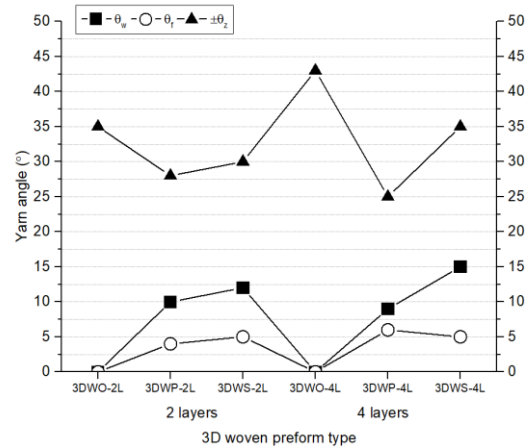


Figure 15. The relation between the fabric type and various yarn angles.

4. Conclusion

Mechanical properties of a composite material are dependent upon the fiber type, matrix type, fiber orientation/architecture, and fiber volume fraction. For 3D textile reinforced composites, the weave pattern, number of layers, yarn angles and other parameters are the main factors determining the fiber orientation and architecture and hence the directional and overall fiber volume fractions. In this study, geometric characterization of 3D woven jute fabrics was carried out. For this purpose, two main types of 3D fabrics were produced such as non-interlaced and semi-interlaced fabrics. The semi-interlaced fabrics were produced using two different weave patterns such as plain and satin weave. Two different numbers of layers i.e. 2 and 4 layers were used for all types of fabrics produced in the study.

Yarn-to-yarn distances and yarn densities: Increasing the number of layers did not have a significant effect on yarn-to-yarn distances. Filling-filling and z-z yarn distances were found to be greater in plain-woven semi-interlaced fabrics when compared to satin-weave semi-interlaced fabrics and non-interlaced orthogonal fabrics due to a large number of interlacements in plain-weave structure. It can be expected that the filling and z-directional fiber volume fractions would be lower in semi-interlaced fabric reinforced composite structures. Yarn density values were also found to be in parallel with the yarn-yarn distance results.

Yarn lengths: The uncrimped warp and filling yarn lengths were greater in semi-interlaced plain and satin fabrics compared with those of non-interlaced structures. Uncrimped z-yarn lengths were greater in plain-woven fabrics when compared to the satin-weave due to larger number of yarn interlacements and hence the yarn curviness in plain-weave.

Yarn angles: z yarn angle was found to be greater than other angles. z yarn angle was greater in non-interlaced fabrics compared with semi-interlaced fabrics due to the fact that filling-filling and z-z yarn distances were greater in semi-interlaced fabrics. z yarn angle increased as the number of layers was increased for all fabric types. Warp yarn angle was greater in satin fabrics compared to plain-woven structures. Filling and warp angles are generally affected by weave pattern whereas z yarn angle is influenced by weaving operations such as warp let-off, multilayer filling insertion, and beat-up. The findings of this study will shed light on the effect of 3D fabric type and geometry on the properties of natural fiber reinforced 3D woven composites.

Author's Contributions

Nesrin Şahbaz Karaduman: Produced the samples, carried out the measurements, performed the experiments and analyzed the results, drafted and wrote the manuscript.

Ethics

There are no ethical issues after the publication of this manuscript.

References

1. Stig, F, Hallström, S. 2012. Spatial modelling of 3D-woven textiles. *Composite Structures*; 94(5): 1495–1502.
2. Ko, F. 3-D textile reinforcements in composite materials. In: Miravete A (ed) 3-D textile reinforcements in composite materials. Woodhead Publishing, Cambridge, 1999, pp 9–42.
3. Mohanty, AK, Misra, M, Drzal, LT. Natural fibers, biopolymers, and biocomposites: An introduction. In: Mohanty A, Misra M, Drzal LT (eds) Natural fiber, biopolymer, and biocomposites. CRC Press, Boca Raton, 2005, pp 1–36.
4. Aziz, SH, Ansell, MP. Optimising the properties of green composites. In: Baillie C (ed) Green composites: Polymer composites and the environment. Woodhead Publishing, Boca Raton, 2004, pp 154–180.
5. Satyanarayana, KG, Arizaga, GGC, Wypych, F. 2009. Biodegradable composites based on lignocellulosic fibers—An overview. *Progress in Polymer Science*; 34(9): 982–1021.
6. Mohanty, AK, Misra, M, Hinrichsen, G. 2000. Biofibres, biodegradable polymers and biocomposites: An overview. *Macromolecular Materials and Engineering*; 276–277(1): 1–24.
7. Bismarck, A, Mishra, S, Lampke, T. Plant fibers as reinforcement for green composites. In: Mohanty A, Misra M, Drzal LT (eds) Natural fibers, biopolymers, and biocomposites. CRC Press, Boca Raton, 2005, pp 37–108.
8. Wambua, P, Ivens, J, Verpoest, I. 2003. Natural fibres: Can they replace glass in fibre reinforced plastics? *Composites Science and Technology*; 63(9): 1259–1264.
9. Joshi, SV, Drzal, LT, Mohanty, AK, Arora, S. 2004. Are natural fiber composites environmentally superior to glass fiber reinforced composites? *Composites Part A: Applied Science and Manufacturing*; 35(3): 371–376.
10. Mehta, G, Mohanty, AK, Thayer, K, Misra, M, Drzal, LT. 2005. Novel biocomposites sheet molding compounds for low cost housing panel applications. *Journal of Polymers and the Environment*; 13: 169–175.
11. Bledzki, AK, Faruk, O, Sperber, VE. Cars from bio-fibres. 2006. *Macromolecular Materials and Engineering*; 291(5): 449–457.
12. Bilisik, K, Karaduman, NS, Bilisik, NE, Bilisik, HE. 2013. Three-dimensional fully interlaced woven preforms for composites. *Textile Research Journal*; 83(19): 2060–2084.
13. Potluri, P, Sharif, T, Jetavat, D. 2008. Robotic approach to textile preforming for composites. *Indian Journal of Fibre & Textile Research*; 33: 333–338.

CFD Modelling of Non-Newtonian Fluid Flow in a Pipe Including Obstacle

Mustafa Murat YAVUZ¹ , Pınar SARI ÇAVDAR^{2*} 

¹İzmir Democracy University, Department of Mechanical Engineering, 35140 İzmir, Turkey

²İzmir Democracy University, Department of Civil Engineering, 35140 İzmir, Turkey

* pınar.cavdar@idu.edu.tr

*0000-0002-1989-4759

Received: 20 January 2021

Accepted: 5 April 2021

DOI: 10.18466/cbayarfbe.865261

Abstract

Pipe flow problems are important in transportation of wastewater, oil lines and supply of water. In this study, a non-Newtonian fluid model is discussed and a CFD solution is presented for flow geometry. The effects on velocity, pressure, dynamic viscosity and cell Reynolds number are discussed for different parameters of flow inside the pipe. Power Law function is considered in the analyses. The velocity profile increased and get more parabolic distribution when flow behaviour index, n was increased. That supports lower pressure profile in the pipe flow. The lowest n value causes to increase the sensitivity for viscous effects. The increased flow consistency index, K causes to increase dynamic viscosity but decreases the Re number. Results are given in different graphs and contours.

Keywords: non-Newtonian fluid, power law, CFD.

1. Introduction

Fluid flow in pipes is used in many areas of mechanical and civil engineering. Heating and cooling applications and fluid distribution networks can be cited as common usage areas for liquid and gas flow. Many fluids, especially liquids, are transported by circular pipes. The reason why circular pipes are used is that they can withstand large pressure differences between inside and outside without deterioration.

Several researchers have analysed the problems of boundary layer flow of non-Newtonian fluids past different geometries in the past. [1-6].

Power-Law fluid model has been carried out by many scientists [7-13]. Gupta [14] carried out a new approximate solution for laminar flux of power-law fluid. Flow model is considered for pipe and straight channels. The results of different methods for pipe and channel flow are compared according to parameters such as pressure, velocity, and length of the boundary layer. Alexandrou et al. [15] have examined the steady state of the non-Newtonian fluid in the Herschel-Bulkley model by considering the expansion of the canal in three dimensions at different rates.

Cebeci et al.[16] and Acrivos et al. [17] have compared laminar boundary layer of non-Newtonian fluid made by approximate solution of the equations by asymptotic method with numerical solution of the equations of power law flux.

Hornbeck [18] worked laminar flow of a compressible fluid in the inlet of a pipe numerically and his numerical technique allows a closer approximation to the basic equations of fluid motion than has been possible in previous investigations. Yapıcı and Albayrak [19] studied the temperature distributions inside the pipe wall and fluid for uniform and non-uniform heat fluxes. Two different mean flow velocities are considered, and the stress distribution is presented inside the pipe wall. Yıldırım et al. [20] examined the wave motion at the interface of two fluids and investigated wavelength, wave number, frequency, amplitude, wave and growth rate in 2D numerical analysis, taking into account the Kelvin-Helmholtz (KH) type instability.

Kırmızıgöl et al. [21] studied both steady-state and time-dependent (transient) computational fluid dynamics (CFD) analysis of the cooling channels and the die cooling system, both in conjugate and solid-only models, performed and compared the pipe flow part of the results with the available experimental data.

Sorgun et al. [22] analysed pipe roughness influences on frictional pressure losses of water with CFD. Batool and Nawaz [23] investigated thermal enhancement of non-Newtonian fluid in micropolar fluid structures. The increased viscosity parameter shifted great vortices to the top wall. Mehryan et al. [24] studied melting process of a non-Newtonian fluid inside a metal foam and determined the effect of power-law index on melting process. Jamshidzadeh et al. [25] studied gas holdup conditions in mixer systems with non-Newtonian fluid. Khan et al. [26] used non-Newtonian Casson fluid to investigate y-shaped fin. Nguyen et al. [27] checked Boltzmann equation to simulate non-Newtonian flow using power law magnetic Reynolds number. Eberhard et al. [28] investigated non-Newtonian fluid in disordered porous structure with local viscosity effects. Studies on non-Newtonian fluids have made great improvements, especially in recent times. Since the working area of these fluids is quite wide. They vary for their characteristics and flow parameters. Studies can be experimental, theoretical or comparative. In this study, a numerical analysing method is used, and the results are compared.

2. Materials and Methods

A circular pipe having a diameter (D) of 0.1 m created. The length of pipe has 15D. A circular 2.5 mm thick obstacle is created 5D far away from the fluid inlet. The obstacle closes partially as a length of 40 mm. Computational fluid dynamics is used in the analyses. The isometric view of geometry is given in Figure 1.

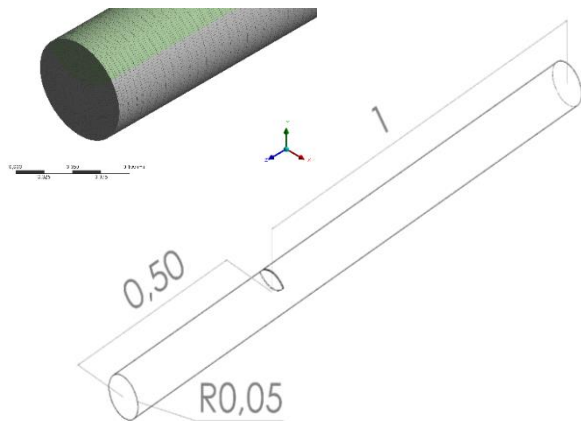


Figure 1. Isometric view of cylinder geometry (all dimensions are in m).

A closer view of the CFD model is also illustrated. The prepared CFD model was checked with mesh independence test for maximum velocity in pipe for $n=2$ and $K=0.1$ power law constants. The coarse and fine mesh variation was found at steady state approximately at 560,000 elements which total mesh quality was detected as 0.79.

2.1. Modelling and Boundary Conditions

Non-Newtonian fluid flow is analysed by considering Power Law function. Viscosity is the critical parameter and can vary with the flow conditions. The basic form of the shear stress (τ) is given in Eq (.2.1).

$$\tau = K \times \left(\frac{du}{dy}\right)^n \quad (2.1)$$

K = flow consistency index
 n =flow behaviour index
 $\frac{du}{dy}$ = shear rate

Effect of n and K is investigated with a constant density of 1000 kg/m^3 . The inlet flow is selected as 0.01 m/s . Inside pipe surfaces are defined as wall. Laminar flow model is used with respect to non-Newtonian parameters and low inlet velocity.

3. Results and Discussion

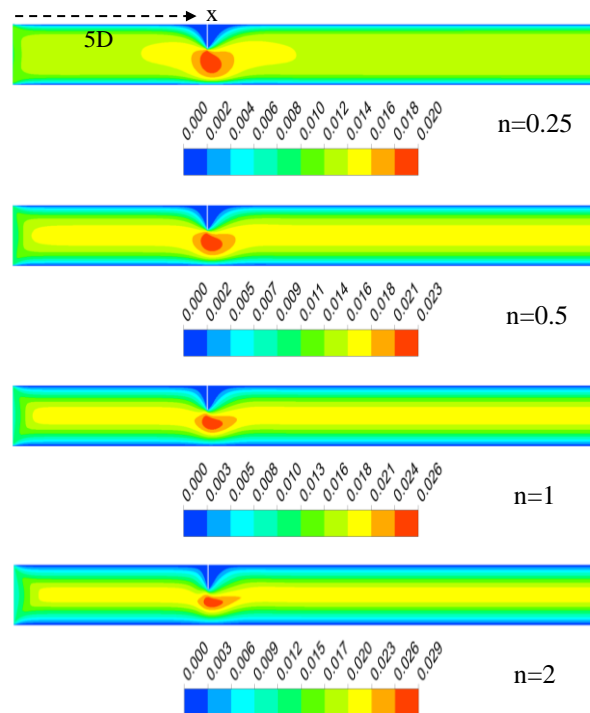


Figure 2. Velocity contours of various “n” values with a constant value of $K=0.1$

In Figure 2, the velocity contours are taken from a vertical section plane at the centre of pipe. The results show that the viscous flow dominantly interacts on the wall. As a result of the increased n coefficient, the low or zero velocity profile interacting with the wall is more common. It was determined that there is a dead flow zone at the front and rear of the obstacle. The dead flow zone is greater behind the obstacle. The flow velocity increases in the transition section due to the narrowing of the cross section. With the increasing number of n , the flow tended to accelerate and showed a more

parabolic high velocity structure in the pipe centre. This situation is also seen at the entrance to the pipe.

In Figure 3, velocity profile is given at 5D. There is no flow or velocity profile at the first 40 mm distance due to obstacle. That obstacle decreases the cross-section area of fluid pass and increases the velocity at the opened section. An asymmetrical velocity distribution profile is formed. Flow velocity profile is formed with a sharper and higher parabolic curve as a result of increasing n coefficient.

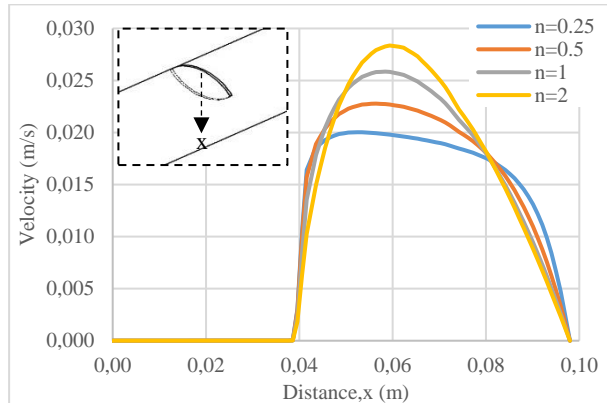


Figure 3. Velocity profiles of various “n” values with a constant K value of 0.1 at 5D.

In Figure 4, velocity profiles are given for $n = 0.25, 0.5, 1, 2$. The flow has stabilized and shows a symmetrical distribution. This situation shows that the flow is not affected by the obstacle effect. As the value of n increases in the non-Newtonian fluid, the maximum velocity increases.

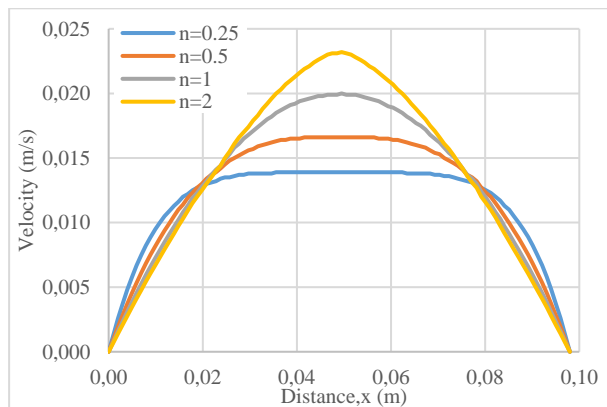


Figure 4. Velocity profiles of various “n” values with a constant K value of 0.1 at 10D.

When the results obtained along the whole channel in Figure 5 are examined, it is seen that the entire flow velocity increased as a result of the increasing n coefficient. There is an instantaneous speed jump at the point where the obstacle flow is located. Considering the results of this instant speed jump, the value of $n = 2$ with the highest velocity and the value of $n = 1$ velocity

reached the same value. The sudden increase in flow velocity has reached its former steady state one diameter ahead of the obstacle.

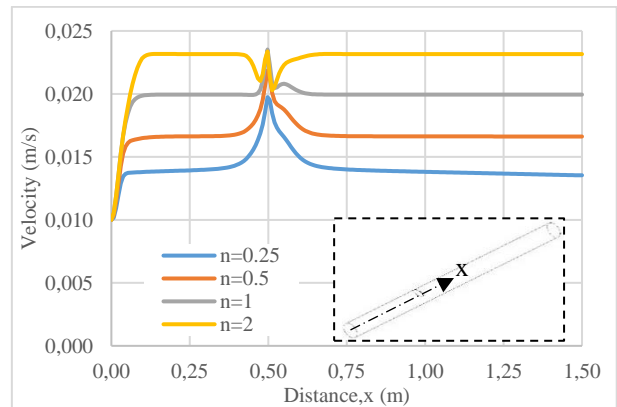


Figure 5. Velocity profiles of various “n” values with a constant K value of 0.1 from inlet to outlet centre.

In Fig. 6 the pressure profile is shown for different n coefficients. It was determined that the pressure decreased due to the increase in flow velocity after the obstacle. The lowest pressure profile is seen at $n = 2$ where the velocity is the highest. There is about 2 times the difference between the highest and low pressures.

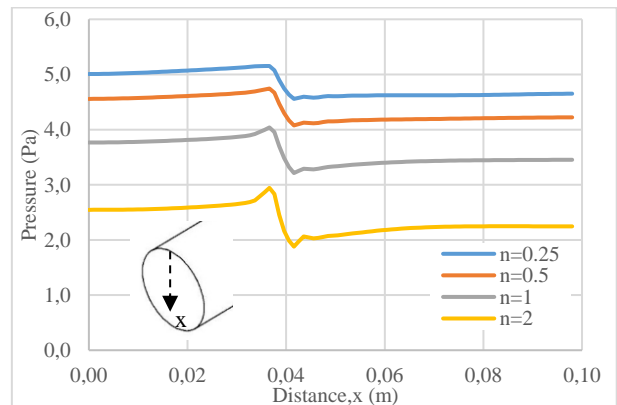


Figure 6. Pressure profiles of various “n” values with a constant K value of 0.1 at 5D.

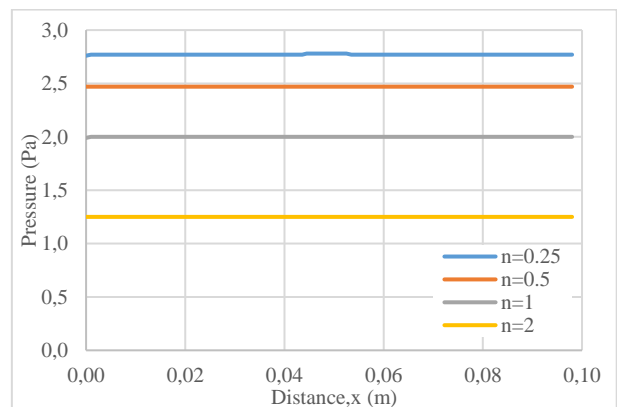


Figure 7. Pressure profiles of various “n” values with a constant K value of 0.1 at 10D.

Figure 8 shows the pressure graph for different n coefficients along the length of the pipe. The graph starting with 3.5 Pa for the $n=2$ value entered the pipe with a pressure 2 times higher for the value $n=0.25$. Pressure drop is observed instantaneously at the point where the obstacle is located. At this point the velocity increased.

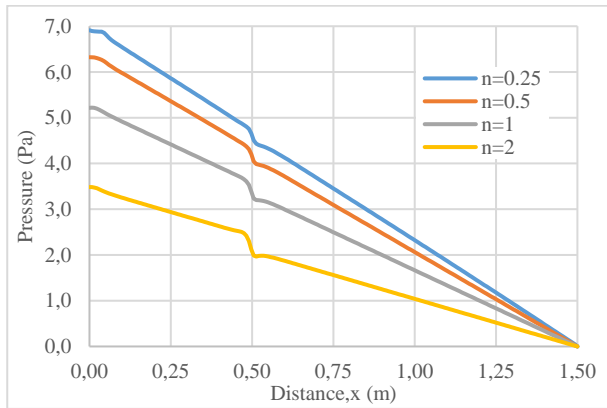


Figure 8. Pressure profiles of various “ n ” values with a constant K value of 0.1 from inlet to outlet centre.

Figure 9 shows the effect of dynamic viscosity. The viscous effect behaved predominantly on the part of the wall with the obstacle. At $n=1$ and $n=2$, the wall interaction with dynamic viscous effect is not seen as dominant.

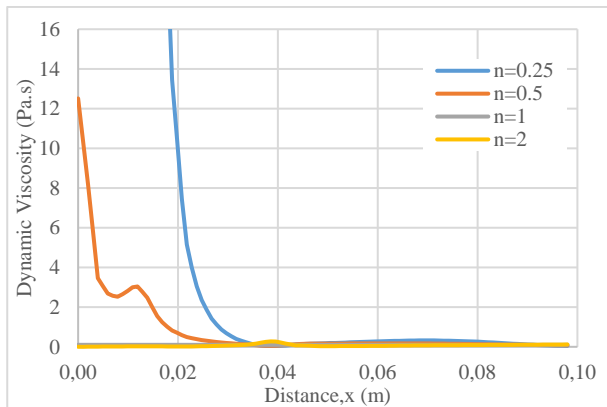


Figure 9. Dynamic viscosity profiles of various “ n ” values with a constant K value of 0.1 at 5D.

In Figure 10, the dynamic viscosity effect is shown at 10D for the condition where the flow develops. For $n = 0.25$ and $n = 0.5$, viscosity is effective. However, the dynamic viscosity value has decreased 3 times in the fluid that travels the distance between 5D and 10D.

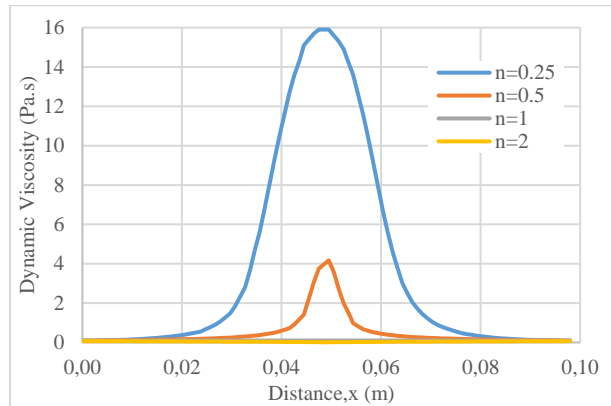


Figure 10. Dynamic viscosity profiles of various “ n ” values with a constant K value of 0.1 at 10D.

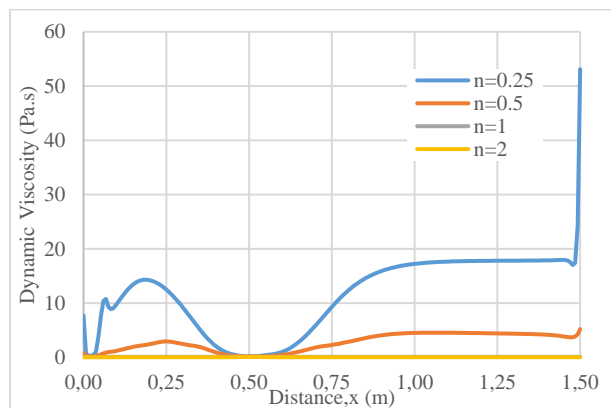


Figure 11. Dynamic viscosity profiles of various “ n ” values with a constant K value of 0.1 from inlet to outlet centre.

Figure 11 shows the dynamic viscosity change along the pipe. The dynamic viscosity effect varies significantly within the pipe for coefficients $n = 0.25$ and 0.5 . Dynamic viscosity of $n=0.25$ behaves more precisely to intra-channel flow conditions.

The cell Reynolds number is shown in Fig. 12. As a result of the effect of increasing speed and low dynamic viscosity, the Reynolds number reached the highest value at $n=2$. At $n=0.25$, it instantly increases the Reynolds number at the corner of the obstacle. It is a factor that the viscosity of $n = 0.25$ is higher than the other values of n coefficients.

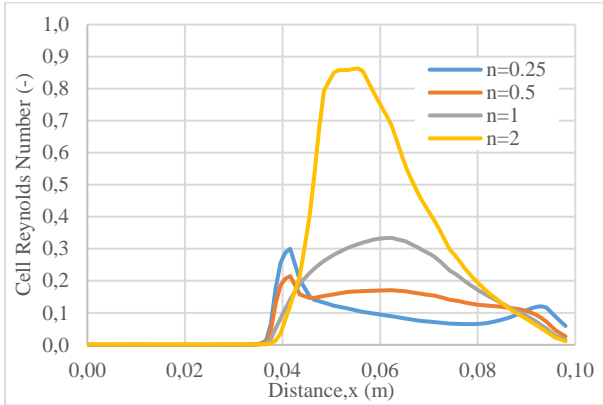


Figure 12. Cell Reynolds number profiles of various “n” values with a constant K value of 0.1 at 5D.

In Figure 13, in 10D, the Reynolds number increased at the centre when $n=1$ and $n=2$ coefficients are used. However, in $n = 0.25$ and $n = 0.5$ results, Re in the centre line decreased.

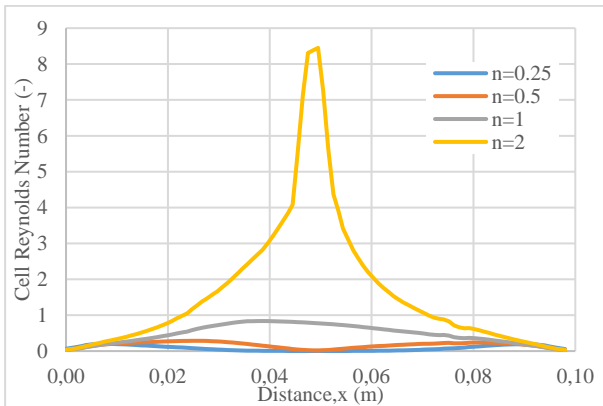


Figure 13. Cell Reynolds number profiles of various “n” values with a constant K value of 0.1 at 10D.

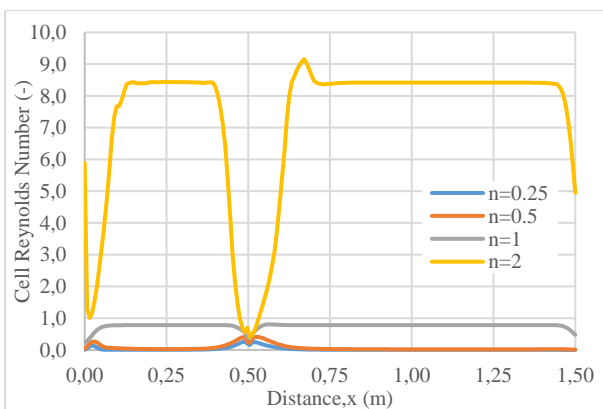


Figure 14. Cell Reynolds number profiles of various “n” values with a constant K value of 0.1 from inlet to outlet centre.

In Fig. 14, it is seen that the Re number is very dominantly high at $n = 0.25$. It was determined that the number of Re was low in the obstacle region. The Re number was more sensitive for $n = 2$.

Effect of K on pressure is given in Fig. 15. Whole various K distributions are similar, only its value changes. It was observed that the pressure increased rapidly with the K coefficient and it was determined that the flow needed higher pressure under these conditions. Velocity profile and magnitude is not affected and same as the first contour profile in Fig. 2.

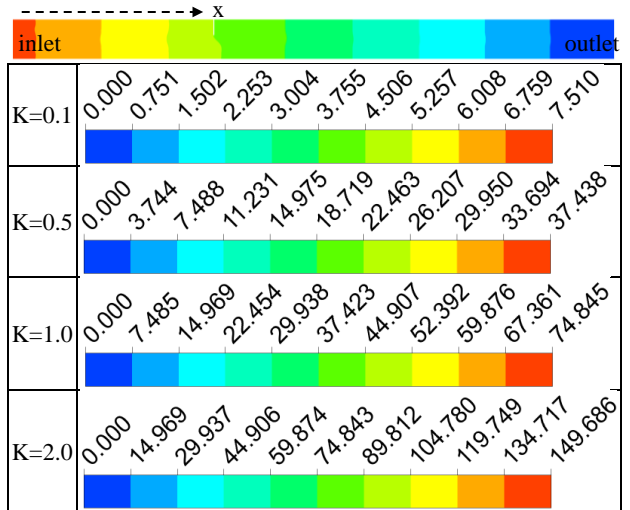


Figure 15. Pressure contours of various “K” values with a constant value of $n=0.25$

In Fig. 16, the effect of K coefficient is shown in the obstacle region. Pressure values increased with the increase of K. The corner of the barrier has a reduction effect.

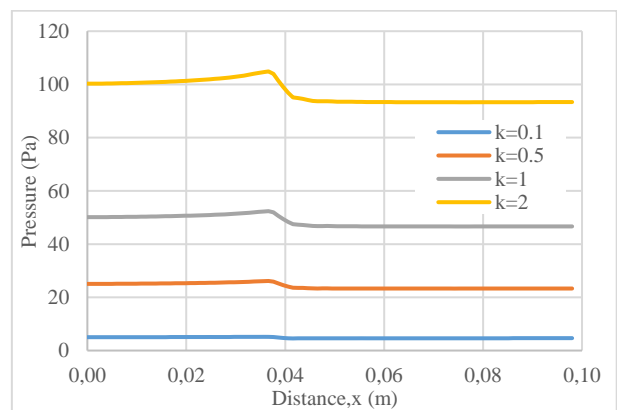


Figure 16. Pressure profiles of various “K” values with a constant n value of 0.25 at 5D.

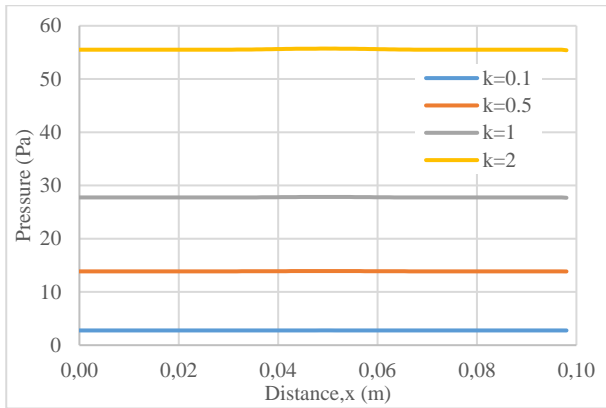


Figure 17. Pressure profiles of various “K” values with a constant n value of 0.25 at 10D.

Figure 17 shows the pressure values at 10D distance. The pressure, which is 56 Pa at $K = 2$, decreases as a result of the increase in the K value.

The results of Fig. 18 show a high-pressure requirement for $K = 2$. The pressure of the flow decreases with the decrease of the K value.

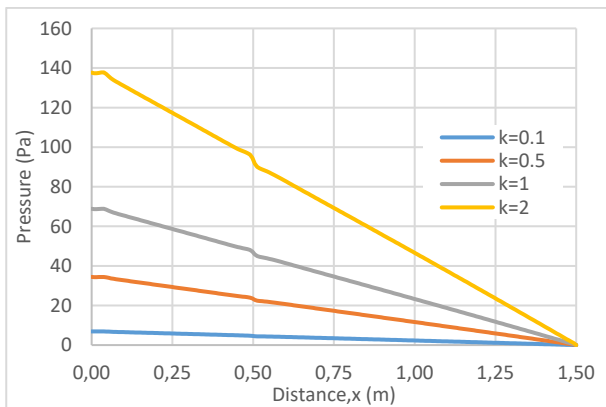


Figure 18. Pressure profiles of various “K” values with a constant n value of 0.25 from inlet to outlet centre.

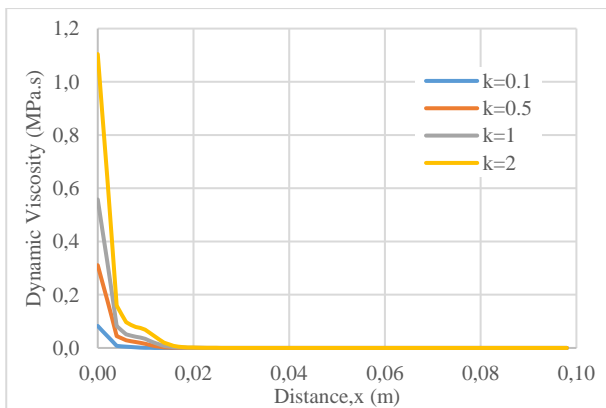


Figure 19. Dynamic viscosity profiles of various “K” values with a constant n value of 0.25 at 5D.

The effect of K coefficient on dynamic viscosity is shown in the obstacle line in Fig. 19. An instantaneous great value was observed at the obstacle-wall corner where there was dead flow. Dynamic viscosity showed an unstable state.

Figure 20 shows the effect of dynamic viscosity in the 10D region. More stable results were obtained in this region where the barrier effect is not dominant. While the dynamic viscosity was above 300 Pa.s for the $K = 2$ value, it decreased to 20 Pa.s for $K = 0.1$.

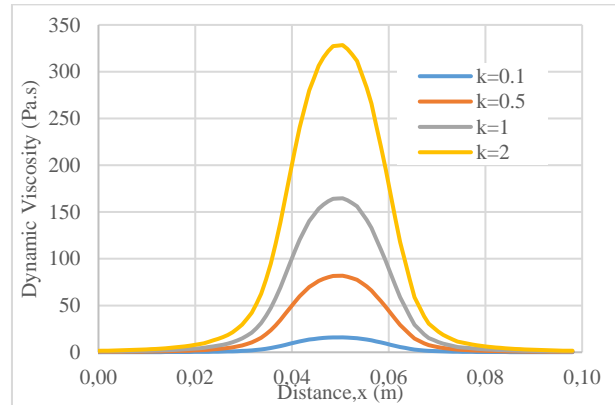


Figure 20. Dynamic viscosity profiles of various “K” values with a constant n value of 0.25 at 10D.

Figure 21 shows the dynamic viscosity effect along the entire pipeline. The dynamic viscosity was reduced in all K coefficient results due to the obstacle. The highest results were obtained at $K = 2$ and the lowest results at $K = 0.1$.

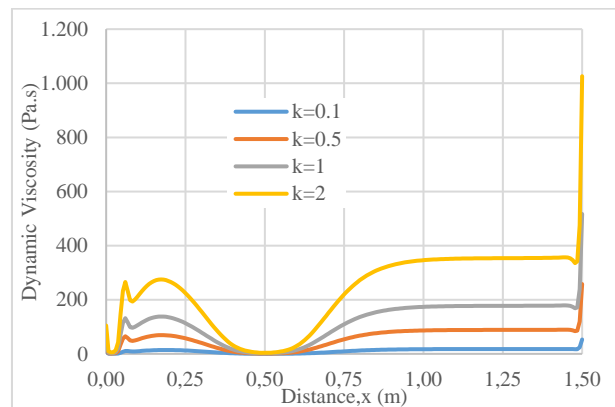


Figure 21. Dynamic viscosity profiles of various “K” values with a constant n value of 0.25 from inlet to outlet centre.

Re number results for different K coefficient are shown in Fig. 22. The highest results were obtained with a value of $K = 0.1$. The lowest result was obtained at $K = 2$.

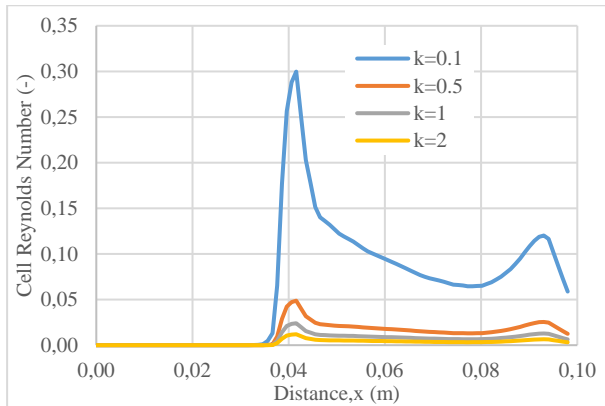


Figure 22. Cell Reynolds number profiles of various “K” values with a constant n value of 0.25 at 5D.

Figure 23 shows the results of the Re number in the region of 10D. The increasing K number decreased the Re number. Results showed a wavy profile. The lowest values were observed in the centre of the pipe. Moderate results are seen near the pipe surface. The highest values were obtained between the wall and the pipe centre.

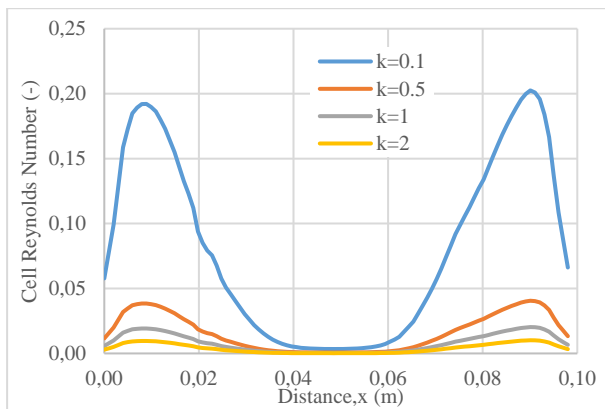


Figure 23. Cell Reynolds number profiles of various “K” values with a constant n value of 0.25 at 10D.

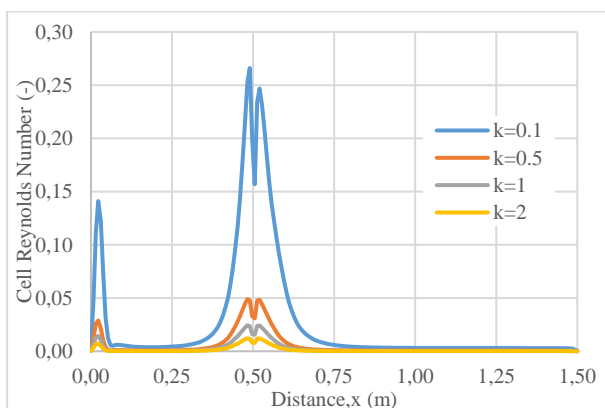


Figure 24. Cell Reynolds number profiles of various “K” values with a constant n value of 0.25 from inlet to outlet centre.

Figure 24 shows the Re number along the entire pipe direction. With the decrease in the K number, there was an increase in the Re number. The Re number is determined as the highest in the front and rear of the obstacle. Some decrease in Re number was observed during the flow passing the obstacle.

4. Conclusion

Non-Newtonian flow analysis was carried out in a pipe with obstructed flow. The effect of different n and K coefficients was examined in the study using numerical analysis method. Results are shown in contours and graphics.

In summary;

While the number of K was constant, increasing the number of n caused the flow velocity to increase.

As a result of the velocity increase, a more parabolic flow velocity profile was formed.

Flow velocity of 0.01 m/s increased up to 0.023 m/s when n=0.25.

At the moment of passing the obstacle, the velocity in front and back of the obstacle instantly decreased at n = 2, and the other n values did not decrease.

As a result of the increasing n value, a lower pressure profile has occurred in the pipe. This shows that flow can be achieved with a lower pressure.

Dynamic viscosity effect was more dominant at n=0.25 and n=0.5 coefficients. However, a lower Re number was obtained.

Different K coefficients were examined for the n = 0.25 coefficient, where the viscous flow exhibits a more sensitive state.

With the increase of the K coefficient, higher-pressure values were obtained in the solutions. It appears that a higher pressure is required for the pipe flow.

When K = 2, dynamic viscosity has the highest value. However, Re number was obtained as the lowest.

While the Re number reached the highest value at the front and rear of the obstacle, a momentary decrease was observed in the area where the flow passed the obstacle.

Throughout a diameter in front and behind the obstacle, this effect continues predominantly.

Author’s Contributions

Mustafa Murat Yavuz: Drafted the manuscript, performed the numerical model and result analysis.

Pınar Sarı Çavdar: Performed result interpretation and wrote manuscript preparation.

Ethics

There are no ethical issues after the publication of this manuscript.

References

1. Bird, RB, Stewart, WE., Lightfoot, EM. 1960. Transport phenomena, John Wiley, New York.
2. Hansen, AG., Na, TY. 1968. Similarity solution of laminar, incompressible boundary layer equations of non-Newtonian fluid, *ASME Journal of Basic Engg.* 67: 71-74.
3. Kapur JN, Bhatt BS, Sacheti NC, 1982. Non-Newtonian fluid flows, Pragati Prakashan, Meerut, India.
4. Lee SY, Ames WF, 1996. Similar solutions for non-Newtonian fluids, *AIChE J.* 12: 700-708.
5. Timol MG, Patel M, 2004. On the class of similarity solutions for three dimensional boundary layer flows of non-Newtonian fluids, *J. of Veer Narmad South Gujarat University.* II-B, 103-109.
6. Wells CS, 1964. Unsteady boundary layer flow of a non-Newtonian fluid on a flat plate, *AIAA Journal.* 2(5) :951-952.
7. Bizzell GD, Slattery JC, 1962. Non-Newtonian boundary-layer flow, *Chemical Engineering Science.* 17(10) :777-782.
8. Djukic DjS, 1973. On the use of Crocco's equation for the flow of power-law fluids in a transverse magnetic field, *AIChE Journal.* 19: 1159-1163.
9. Djukic DjS, 1974. Hiemenz magnetic flow of power-law fluids, *Journal of Applied Mechanics, Transaction of the ASME,* 822-823.
10. Na TY, Hansen A, 1967. Radial flow of viscous non-newtonian fluids between disks, *Int. J. Non-Linear Mech.* 2: 261-273.
11. Patel M, Timol MG, 2011. Orthogonal stagnation point flow of a power-law fluid toward a stretching surface, *International Journal of Applied Mechanics and Mathematics (IJAMM).* 7(3): 31-37.
12. Patel M, Patel R, Timol MG, 2012. Group invariance for non-linear pde's: 3-d mhd stagnation point flow of non-newtonian power-law fluids, *International Journal of Mathematics and Scientific Computing (IJMSC).* 2(2):72-80.
13. Patel M, Patel R, Timol MG, 2014. Numerical treatment of MHD Power-law fluid flow using the method of satisfaction of asymptotic boundary conditions (MSABC), *International Journal of Applied Mechanics and Mathematics.* 10(8):61-77.
14. Gupta RC, On developing laminar non-Newtonian flow in pipes and channels, *Nonlinear Analysis: Real World Applications.* 2: 171-193.
15. Alexandrou AN, McGilvrey TM, Burgos G, 2001. Steady Herschel-Bulkley fluid flow in three-dimensional expansions, *J. Non-Newtonian Fluid Mech.* 100: 77-96.
16. Cebeci T, Clauss JM, Dyer J, 1969. On the solution of boundary-layer equations for a non-Newtonian power-law fluid, *Chemical Engineering Science.* 24: 1031-1034.
17. Acrivos A, Shah MJ, Petersen EE, 1965. On the solution of the two-dimensional boundary-layer flow equations for a non-Newtonian power law fluid, *Chemical Engineering Science.* 20(2): 101-105.
18. Hornbeck RW, 1964. Laminar flow in the entrance region of a pipe. *Applied Scientific Research, Section A.* 13:224-232.
19. Yapıcı H, Albayrak B, 2004. Numerical solutions of conjugate heat transfer and thermal stresses in a circular pipe externally heated with non-uniform heat flux, *Energy Conversion and Management.* 45(6): 927-937.
20. Yıldırım N, Buchlin J, Benocci C, 2017. Simulation of surface instability at the interface of two fluids. *Celal Bayar University Journal of Science.* 13(2): 365-377.
21. Kırmızıgöl SF, Özeydin O, Acarer S, Armakan E, 2020. Fluid flow and heat transfer simulations of the cooling system in low pressure die casting, *Celal Bayar University Journal of Science.* 16(2):161-168.
22. Sorgun M, Haşıloğlu DG, 2016. Effect of pipe roughness on pressure losses of newtonian fluids in concentric annulus, *Celal Bayar University Journal of Science.* 12(3): 413-417.
23. Batool S, Nawaz M, 2020. Investigation of thermal enhancement in non-Newtonian fluid with hybrid micro-structures in an enclosure, *International Communications in Heat and Mass Transfer.* 117:104777.
24. Mehryan SAM, Heidarshenas MH, Hajjar A, Ghalambaz M, 2020. Numerical study of melting-process of a non-Newtonian fluid inside a metal foam, *Alexandria Engineering Journal.* 59: 191-207
25. Jamshidzadeh M, Ein-Mozaffari F, Lohi A, 2020. Local and overall gas holdup in an aerated coaxial mixing system containing a non-Newtonian fluid, *Transport Phenomena and Fluid Mechanics.* 66: 1-16.
26. Khan ZH, Khan WA, Hamid M, 2021. Non-Newtonian fluid flow around a Y-shaped fin embedded in a square cavity, *Journal of Thermal Analysis and Calorimetry.* 143: 573-585.
27. Nguyen Q, Ghahderijani MJ, Bahrami M, Ahangar EK, D'Orazio A, Bach Q, Karimipour A, 2020. Develop Boltzmann equation to simulate non-Newtonian magneto-hydrodynamic nanofluid flow using power law magnetic Reynolds number, *Math Meth Appl Sci.*, 1-16.
28. Eberhard U, Seybold HJ, Secchi E, Jiménez-Martínez J, Rühls PA, Ofner A, Andrade Jr JS, Holzner M, 2020. Mapping the local viscosity of non-Newtonian fluids flowing through disordered porous structures, *Scientific Reports.* 10, 11733.

Deep Feature Generation for Author Identification

Şükrü Ozan^{1*} , D. Emre Taşar¹ , Umut Özdil¹ 

¹ AdresGezini Inc. Research and Development Center, Folkart Towers B Kule,
Office 3609, PK 35580, Bayraklı, İzmir, Türkiye.

*sukruozan@adresgezini.com

*Orcid: 0000-0002-3227-348X

Received: 24 December 2020

Accepted: 3 May 2021

DOI: 10.18466/cbayarfbe.846016

Abstract

Identifying the authors of a given set of text is a well addressed and complicated task. It requires thorough knowledge of different authors' writing styles and discriminating them. As the main contribution of this paper, we propose to perform this task using machine learning and deep learning methods, state-of-the-art algorithms, and methods used in numerous complex Natural Language Processing (NLP) problems. We used a text corpus of daily newspaper columns written by thirty authors to perform our experiments. The experimental results proved that document embeddings trained via neural network architecture achieve cutting edge accuracy in learning writing styles and identifying authors of given writings even though the dataset has a considerably unbalanced distribution. We represent our experimental results and outsource our codes for interested readers and natural language processing (NLP) enthusiasts as a GitHub repository. They can reproduce and confirm the results and modify them according to their own needs.

Keywords: Natural Language Processing, Document Embeddings, Logistic Regression, Support Vector Machines, Author Identification.

1. Introduction

The rapid increase in the number of digital texts has triggered academic research to identify and verify the authors from a given set of a text corpus. By applying computational learning approaches, authors' writing styles and their thematic interests can be captured with an accuracy comparable with human-level performance (HLP). For a predefined set of given authors, determining the most probable author for the given text is author identification [1] that can be considered as a multi-class text categorization problem from a machine learning (ML) and deep learning (DL) perspective [2]. The author identification is generally performed in a closed domain. However, the numbers of texts from selected authors do not always have to be balanced [3]. ML/DL based author identification can effectively be used in disputed authorship cases [4] and literary analysis studies [5]. Like in any other DL study, the heterogeneous distribution of sample data is a problem for author identification. This problem is addressed thoroughly in [6]. Despite the significant amount of work devoted to author identification of a text, researchers still struggle to deal with cross-domain texts and imbalanced datasets.

One of the fundamental steps in author identifications is stylometry, which refers to discovering the most specific features representing an author's writing characteristics [7]. Earlier approaches focused on generating metrics to describe function word or part-of-speech frequencies to assess the vocabulary's diversity. A detailed review of these approaches is represented in [8] to highlight the importance of extracting features.

In this study, the author identification framework is proposed to generate a text's specific features by combining ML and DL methods commonly used in natural language processing (NLP) literature. The author identification procedure is performed by discovering features, thematic interests, unique characteristics of an author, and writing styles. Most accurate results are achieved with Doc2Vec D-BOW [9,10] model with a C-SVC [11] classifier.

The rest of the paper is organized as follows: Section 2 describes the materials and methods applied for this study. Experiments and results are presented in Section 3. Section 4, as the final section, conclusions and future research suggestions are given.

2. Materials and Methods

2.1 Dataset

A famous Turkish news portal, subsuming more than 50 authors, has been scrutinized to build a corpus. The authors are of different ages, genders. Moreover, their writing themes are from different genres, such as politics, sports, health, and literature. We randomly picked 30 of the authors. Figure 1 shows the number of articles per author, which represents an unbalanced distribution. We intentionally kept the author names hidden and used numbers representing Author IDs. After selecting the authors, we scraped the website and gathered all of their articles labeled with author IDs.

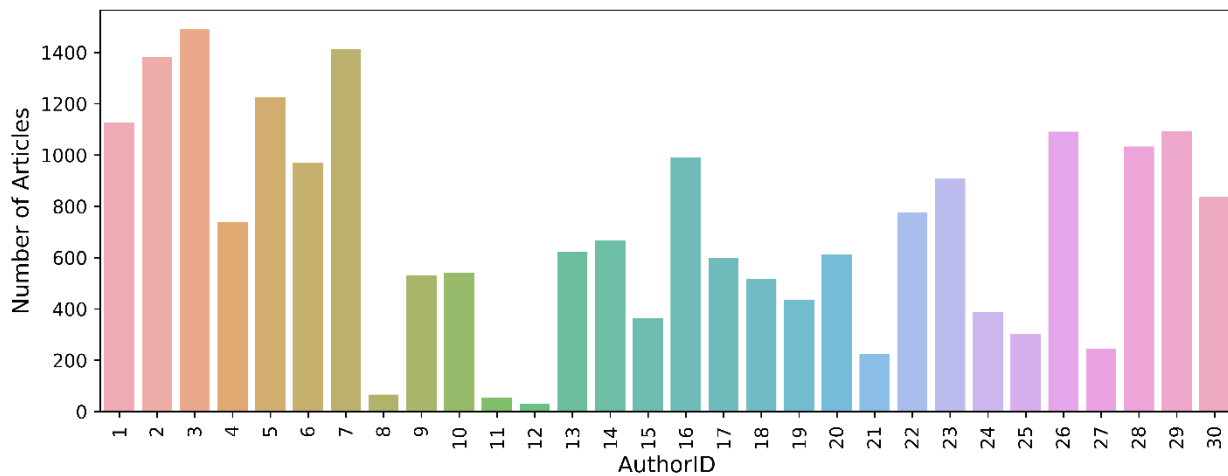


Figure 1. The number of articles per author can be seen in this figure. Authors' names are intentionally hidden and represented as ID numbers.

2.3 Doc2Vec Embeddings

Usage of using Doc2Vec for text classification tasks has gained well-deserved popularity in NLP literature. We used the Gensim [13] implementation of the Doc2Vec method [14]. The method can generate the same embedding sizes for input text with different sizes. The method relies on two main learning models: Distributed Memory (DM) and Distributed Bag of Words (D-BOW). In our experiments, we used both models and compared their performances in the results section.

2.3.1 Distributed Memory (DM)

DM model, depicted in Figure 2a., has a similarity with the Skip-Gram method of Word2Vec [14]. The CBOW

2.2 Data Preprocessing

Data pre-processing is an essential step in NLP methods since it is vital to use clean text data that is free from characters and symbols that may introduce bias and errors during the learning process. The data is scraped directly from the news portal website; hence, it has punctuation symbols and many HTML related tags. There are various text pre-processing methods, including but not limited to converting capital letters to lowercase letters (case folding), clearing symbols, and punctuation marks [12]. We used a 70-30 split scheme for training and validation data sets after the data pre-processing operations.

model can predict a center word based on the context words in a small neighborhood. DM uses a similar approach to randomly sample some context words from an article and predict a word using both the context words and the article ID.

2.3.2 Distributed Bag of Words (D-BOW)

D-BOW model, depicted in Figure 2b., uses the whole article as input and tries to predict consecutive Word chunks from the article having a meaningful context. One advantage of the D-BOW model is that it requires less memory during training time. Activation function weights are enough to be stored for D-BOW to operate.

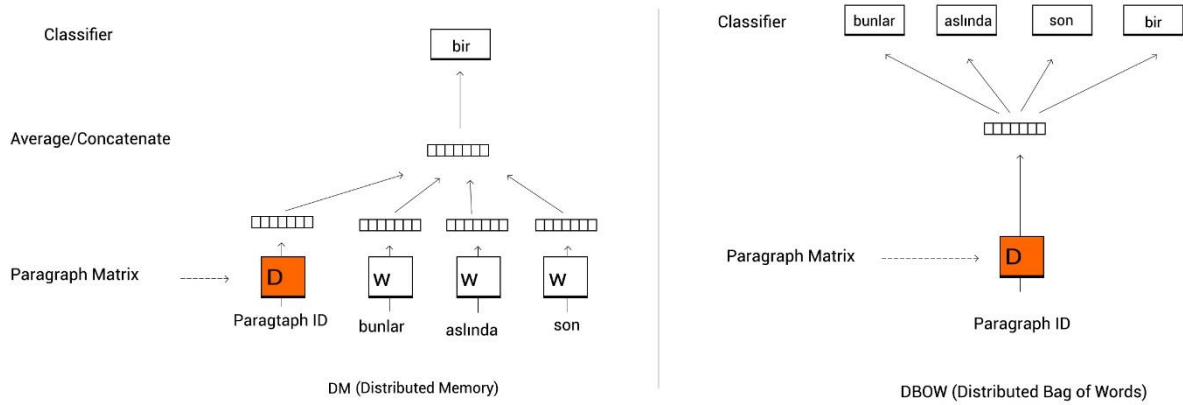


Figure 2. a) Distributed Memory model, where classifier predicts a word as an output parameter and words concatenate as word vectors and paragraph vector. b) Distributed Bag of Words model, where paragraph vector is trained to predict the words inside a small window.

2.4 Classifiers

With either model, DM, and D-BOW, the Doc2Vec method generates a fixed-size embedding vector for each article. These vectors can capture the meaning, syntax, writing style, and other linguistic features of a given text in hyperdimensional space.

Together with the author ID information, the embeddings can be used to train a classifier. In this study, we preferred two different classifiers. Conventionally logistic regression classifier (LRC) is a common choice for the classification of multidimensional data [15]. LRC is proven to be an adequate method, especially for binary classification problems where the number of classes is limited (i.e. $N = 2$). On the other hand, our problem is a multi-class classification problem with 30 classes (i.e., $N > 2$). Multinomial logistic regression classifier MLRC [16] generalizes the binary classification idea of standard LRC to multi-class classification. Once the coefficients are determined after running the MLRC, the probability of predicting an author's class can be done using Equation 2.1, where k is the class number, x is the embedding vector, and β_k is the coefficient vector of class k . Hence, MLRC models the probability of a given data belonging to a class using log-likelihood estimation as given in Equation 2.1.

$$L = \log P(y = k | x_i) \quad \text{where}$$

$$P(y = k | x_i) = \frac{\exp^{\beta^k x}}{1 + \sum_{k=1}^{K-1} \exp^{\beta^k x_k}} \quad (2.1)$$

We used MLRC as our first classifier, and it achieved good accuracies on both training and validation datasets. However, we repeated our experiments also by using support vector machines (SVM) based classifier (C-SVC) [11]. This classifier creates hyperplanes in a

multidimensional space that can be efficient for classification and regression tasks.

It finds the best hyperplane that demonstrates the largest segregation between the two classes. The error of this classifier is correlated with the size of the margin [11]. C-SVC uses kernels with different mathematical models. For this study, we used the linear kernel, in Equation 2.2, where K is the kernel function, D is the decision function, y_i , b , and α_i are indicator vector, equation constant, and dual parameter, respectively. C-SVC classifier achieved even better results than MLRC,

$$K(x_i, x_j) = x_i^T x_j \quad (2.2)$$

$$D = \text{sgn} \cdot \left(\sum_{i=1}^l y_i \alpha_i K(x_i, x) + b \right)$$

2.5 F1 Score as an Accuracy Metric

To better identify the algorithms' classification accuracy, we calculated the F1 Score for each class. F1 Score, which calculates harmonic mean between recall

$$\text{Pr} = \frac{TP}{TP + FP} \quad (2.3)$$

$$\text{Re} = \frac{TP}{TP + FN}$$

$$F1 = 2 * \frac{\text{Pr} * \text{Re}}{\text{Pr} + \text{Re}} \quad (2.4)$$

$$F_{avg} = \frac{2 * P_M * R_M}{P_M + R_M} \quad (2.5)$$

and precision values, can be calculated using Equation 2.4; in this equation, TP, FP, and FN represent true positive, false positive, and false negative values, respectively. Definition of Precision (Pr), Recall (Re) can be calculated using Equation 2.3. The F1-Average score can be calculated using Equation 2.5 for each class. In this equation, macro average values are represented with M . Hence, P_M and R_M represent macro averaged precision and recall values.

3 Results and Discussion

From the NLP perspective, the classification task becomes challenging where the number of classes exceeds 20. Moreover, the data's unbalanced nature makes it even harder for an ML/DL-based algorithm to achieve a good generalization for the whole dataset. In our study, we have both situations.

We started our experiments with hyperparameter tuning of the Doc2Vec model. The parameters, which affect the result most are the embedding size and the number of epochs. By keeping the remaining model parameters constant, we tried different embedding sizes to detect the optimal size. The constant parameters and their default values can be seen in Table 1. We observed the classification accuracy in Table 2 after one epoch of training by trying different embedding sizes.

Table 1. Constant Parameters for Doc2Vec Model

Model Parameters*	Value	Model Parameter	Value
window	10	alpha	0.0061
negative	5	Min_alpha	0.0001
Min_count	1		

* Other model parameters set to default

We used MLRC to calculate the training and validation accuracies. Since the number of classes is considerably high, we achieved the optimum result with a 500-dimensional embedding size. We did not get a significant performance increase after 500. After fixing the embedding size to 500, we tried different epochs and

different classifiers. The results of these experiments are given in Table 3. We further observed that both DM and D-BOW methods start to overfit after a few epochs. Hence, we limited the number of epochs to 10 for each experiment.

As it can be interpreted by looking at Table 3., we achieved the best accuracies for the validation data set for 500-dimensional vector size at the 4th epoch of D-BOW training using the C-SVC classifier. It is also possible to grasp the success of this result by visually examining the embedding vectors. Since the embeddings are in hyperspace, we used the UMAP projection method [17] to visualize them in 2D. Figure 3 shows how the embeddings belonging to seven of the authors are successfully clustered together.

The overall clustering performance of the algorithm can also be shown with a confusion matrix. In Figure 4, the confusion matrix of the classification for 30 authors can be seen. The confusion matrix can also be used to calculate the F1 Score for each of the classes. In Table 4., we listed the calculated F1 Score for each class. For authors 8 and 12, the worst classification results are achieved. These authors have significantly less number of articles compared with the remaining authors. However, we can also see that for another author (author 11) with few articles; high accuracy is achieved. When we closely examine these three authors, we saw that author 11 has a particular subject genre compared with the other authors.

On the other hand, authors 8 and 12 mostly write interview articles where they mostly quote the person being interviewed, making it harder for the algorithm to learn and generalize for these specific authors. If we disregard authors 8 and 12 and only rely on the remaining 28 authors, the training and validation accuracies hit 1.00 and 0.97, respectively. F1 Scores and their weighted averages are found to be 0.98 and 0.97 using Equation 2.3 - 2.5.

Table 2. Train and Validation Accuracies for Vector Sizes

Model Accuracy	D-BOW + MLRC		DM + MLRC	
	Train	Validation	Train	Validation
5	0.7716	0.7453	0.6737	0.6704
25	0.9777	0.9496	0.8602	0.8427
50	0.9904	0.9503	0.9073	0.8823
100	0.9951	0.9516	0.9392	0.9002
300	0.9953	0.9596	0.9646	0.9209
500	0.9936	0.9581	0.9626	0.9225
1000	0.9891	0.9589	0.9555	0.9243



Table 3. This table shows the change in Training and Validation Accuracies for Different Doc2Vec Method and Classifier Combinations for different epoch numbers. All the model combinations tend to overfit the data after a few epochs of training.

Model	D-BOW MLRC		DM MLRC		D-BOW C-SVC		DM C-SVC	
	Train	Validation	Train	Validation	Train	Validation	Train	Validation
Epoch 1	0.9955	0.9601	0.9689	0.9272	0.9685	0.948	0.7968	0.7811
Epoch 2	0.9996	0.9543	0.9966	0.9425	0.9937	0.9654	0.9615	0.9272
Epoch 3	0.9999	0.9486	0.9998	0.9369	0.9967	0.9667	0.9836	0.9433
Epoch 4	1	0.9519	1	0.9373	0.9975	0.9682	0.9894	0.9501
Epoch 5	1	0.948	1	0.938	0.9968	0.9663	0.991	0.9484
Epoch 6	1	0.9501	1	0.9386	0.9956	0.9669	0.9879	0.9507
Epoch 7	1	0.9402	0.9977	0.8573	0.9927	0.9593	0.9555	0.8814
Epoch 8	0.9995	0.9325	0.9651	0.7737	0.9842	0.9427	0.8669	0.7524
Epoch 9	0.6226	0.4788	0.4	0.2454	0.5175	0.4487	0.2689	0.2314
Epoch 10	0.5802	0.4945	0.7323	0.516	0.5367	0.4598	0.5871	0.4838

Table 4. D-BOW + C-SVC Pr, Re, F1 Score Results

Authors	Precision	Recall	F1-Score	#Articles	Authors	Precision	Recall	F1-Score	#Articles
1	0.97	0.99	0.98	514	16	0.91	0.92	0.91	390
2	0.99	0.98	0.98	625	17	1.00	0.99	0.99	247
3	0.98	1.00	0.99	653	18	0.97	0.98	0.97	237
4	0.97	0.96	0.96	281	19	0.97	0.97	0.97	183
5	0.98	1.00	0.99	562	20	0.95	0.95	0.95	293
6	0.97	0.97	0.97	397	21	0.98	0.98	0.98	116
7	0.97	0.97	0.97	645	22	0.99	0.98	0.98	329
8	0.70	0.91	0.79	33	23	0.99	0.99	0.99	361
9	0.98	0.95	0.97	264	24	0.99	0.97	0.98	159
10	1.00	0.98	0.99	243	25	1.00	1.00	1.00	141
11	0.96	0.82	0.89	33	26	0.98	0.98	0.98	462
12	0.68	0.71	0.70	21	27	0.95	0.94	0.94	112
13	0.86	0.92	0.88	226	28	0.95	0.99	0.97	389
14	0.98	0.91	0.94	274	29	0.95	0.95	0.95	415
15	0.98	0.86	0.91	162	30	0.98	0.97	0.97	354
				Accuracy	0.97	0.97	0.97	9121	
				W. Avg	0.97	0.97	0.97	9121	

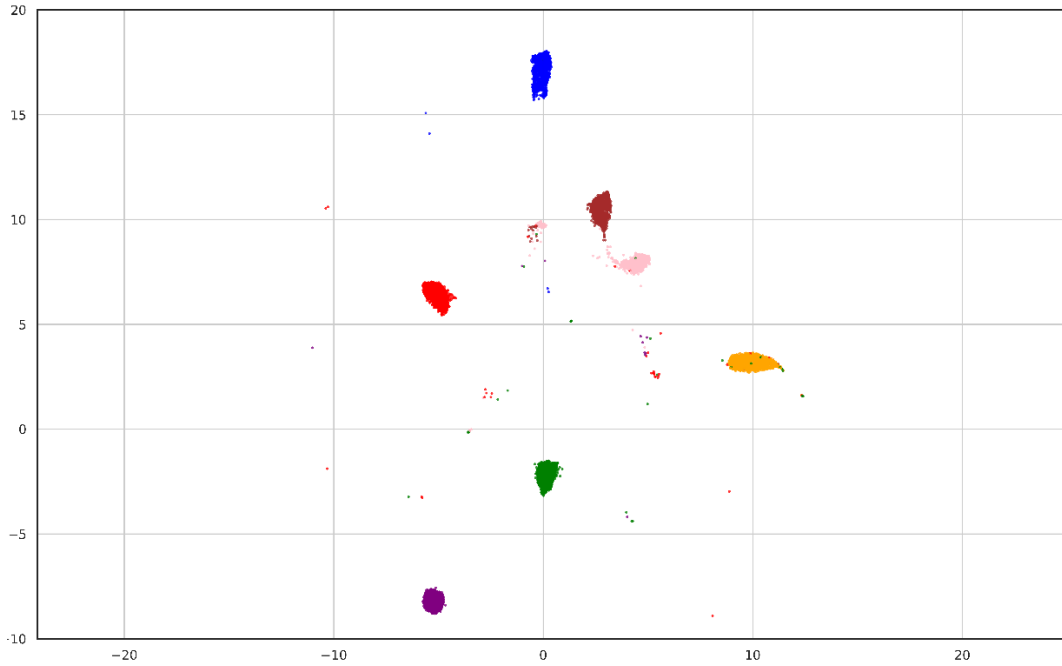


Figure 3. 2D UMAP projection of the training data’s embedding vectors created with the best configuration in Table 3. For display purposes, we zoomed the area where the clusters of seven authors are visible together.

AID	1	2	3	4	5	6	7	8	9	10	11	12	13	14	15	16	17	18	19	20	21	22	23	24	25	26	27	28	29	30	
1	510	0	0	0	0	0	0	0	0	0	0	0	0	1	0	0	1	0	0	1	0	0	0	0	0	0	0	0	0	1	
2	0	612	1	0	0	1	3	0	0	0	0	0	0	1	1	2	0	0	0	0	0	1	0	0	0	0	0	1	1	1	
3	0	0	653	0	0	0	0	0	0	0	0	0	0	0	0	0	0	0	0	0	0	0	0	0	0	0	0	0	0	0	
4	0	1	0	270	0	1	1	0	1	0	0	0	0	0	0	4	0	0	0	0	0	0	1	0	0	0	0	2	0	0	
5	0	0	0	0	560	0	0	0	0	0	0	0	0	0	0	1	0	0	0	0	0	0	0	0	0	0	0	0	0	0	
6	2	0	0	1	1	384	0	0	1	0	0	0	0	0	0	1	0	0	1	0	0	0	0	0	0	0	0	1	0	0	
7	0	1	3	1	0	2	626	0	0	0	0	0	0	0	0	2	0	0	0	2	0	0	1	0	0	0	0	4	2	1	
8	0	0	0	0	0	0	0	30	0	0	0	1	1	0	0	0	0	0	0	0	0	0	0	0	0	1	0	0	0	0	
9	3	1	0	1	0	0	0	0	250	0	0	0	1	3	0	0	0	2	0	0	0	0	1	0	0	0	0	2	0	0	
10	0	0	1	1	0	0	0	0	0	238	0	0	0	0	0	0	1	1	0	0	0	0	0	0	0	0	1	0	0	0	
11	0	0	1	0	0	0	0	0	0	0	27	0	0	0	0	0	0	0	0	5	0	0	0	0	0	0	0	0	0	0	
12	0	0	0	0	0	0	0	4	0	0	0	15	0	0	0	0	0	0	0	0	0	0	0	0	1	0	0	0	1	0	
13	0	0	0	0	0	0	1	3	0	0	0	1	207	0	0	3	0	0	1	0	0	0	0	0	0	0	1	9	0	0	
14	0	2	0	2	2	2	2	1	2	0	0	0	3	249	1	2	0	0	0	0	0	0	0	0	0	5	1	0	0		
15	3	0	0	0	2	0	0	1	0	0	0	3	4	0	139	6	0	0	1	0	0	0	0	0	0	0	1	2	0	0	
16	1	2	0	0	1	1	5	1	0	0	0	0	9	0	0	359	0	0	0	1	0	0	1	0	3	0	1	4	1	1	
17	0	0	0	0	0	0	1	0	0	0	0	0	1	0	0	0	245	0	0	0	0	0	0	0	0	0	0	0	0	0	
18	0	0	0	1	0	0	0	0	0	0	0	0	0	0	0	0	0	232	1	1	0	1	0	0	0	0	0	1	0	0	
19	0	0	0	0	0	0	0	0	0	0	0	0	0	0	0	0	0	0	178	1	0	2	0	0	0	0	0	0	1	0	0
20	0	1	2	0	0	1	2	1	0	0	1	0	2	1	0	0	0	0	0	0	277	0	0	0	0	1	1	1	2	0	
21	0	0	0	0	0	0	0	0	0	0	0	0	1	0	0	0	0	1	0	0	0	114	0	0	0	0	0	0	0	0	
22	1	0	0	1	1	1	0	0	0	0	0	0	0	0	0	0	1	0	0	1	0	323	0	0	0	0	0	0	0	0	
23	1	0	0	0	0	0	0	0	0	0	0	0	0	0	0	1	0	0	0	0	0	0	358	0	0	0	0	1	0	0	
24	1	0	0	0	1	0	0	1	0	0	0	0	1	0	0	1	0	0	0	0	0	0	0	154	0	0	0	0	0	0	
25	0	0	0	0	0	0	0	0	0	0	0	0	0	0	0	0	0	0	0	0	0	0	0	0	141	0	0	0	0	0	
26	0	0	1	0	0	0	0	1	0	0	0	1	2	0	0	2	0	0	0	0	0	0	0	0	0	453	0	0	2	0	
27	2	0	0	0	0	0	0	0	0	0	0	0	1	0	0	1	0	0	0	2	0	0	0	0	0	1	105	0	0	0	
28	0	0	2	0	1	1	0	0	0	0	0	0	0	0	0	0	0	0	0	1	0	0	0	0	0	0	0	384	0	0	
29	0	0	0	0	0	0	1	0	0	0	0	1	7	0	1	4	1	0	0	0	1	0	0	0	0	3	0	0	396	0	
30	0	1	2	1	0	2	0	0	0	0	0	0	0	0	0	3	0	1	0	0	0	0	0	0	0	0	1	1	0	342	

Figure 4. Confusion Matrix of classification performed using the best configuration in Table 3 for 30 author classes’ validation data

4 Conclusion

For this study, we scraped 30.403 articles of randomly selected 30 different authors of a popular Turkish news portal. After the pre-processing of raw page source data, we obtained cleaned text for each article. After tagging each article with corresponding author IDs, we obtained our dataset. We used a 70-30 split scheme for training and validation data set. The data set is considerably unbalanced, i.e., the variance in the number of articles is high.

The proposed algorithm mainly relies on the Doc2Vec method, which uses two different learning models: distributed memory and distributed bag of words.

Regardless of the preferred model, this method generates a fixed size embedding vector for given texts of different sizes. We calculated the models’ training and validation accuracy at each training epoch after applying two different classifiers, MLRC and C-SVC. Each of the model and classifier combinations gave good accuracies comparable with HLP. Hence, it is possible to obtain deep features for author classification with the proposed solution methods. The method can detect possible plagiarisms in closed domains, such as a corpus of homework reports submitted by students.

As future work, it is possible to train different convolutional neural networks similar to MGNC-CNN architecture in [18] using these deep feature

embeddings, which may yield good classification accuracies. The deep features can further be used to train recurrent generative adversarial networks [19], generating artificial texts that mimic the corresponding authors' writing styles.

We are outsourcing our code [20] for NLP researchers and enthusiasts to reproduce the reported results and use them in their research.

Acknowledgment

This work is a part of the project supported by the Scientific and Technological Research Council of Turkey (TUBITAK) TEYDEB-1501 program under Project no 3190585, and named "General Purpose Chatbot Application That Can Produce Meaningful Dialog via Machine Learning Algorithms".

Author's Contributions

Şükrü Ozan: Built the algorithms and metric criteria, prepared the web scraping scripts, drafted and wrote the manuscript.

D. Emre Taşar: Supervised the experiments, helped in result interpretation and literature review, assisted in manuscript preparation.

Umut Özdil: Prepared the text pre-processing scripts, assisted in data visualization.

Ethics

The Ethics Committee has ruled that approval was not required for the study.

References

1. Stamatatos, E., Fakotakis, N., Kokkinakis, G.: 2000. Automatic text categorization in terms of genre and author. *Comput. Linguist.* 26(4), 471-495
2. Sebastiani, F. 2002. Machine Learning in Automated Text Categorization. *ACM Computing Surveys*, 34(1): 1-47.
3. Zheng, Rong, et al. 2006. "A framework for authorship identification of online messages: Writing-style features and classification techniques." *Journal of the American society for information science and technology* 57.3 : 378-393.
4. Burrows, J.F. 1987. Word Patterns and Story Shapes: The Statistical Analysis of Narrative Style. *Literary and Linguistic Computing* 2: 61-70.
5. Diederich, J., J. Kindermann, E. Leopold, and G. Paass. 2003.. Authorship Attribution with Support Vector Machines. *Applied Intelligence* 19(1/2): 109-123
6. Luyckx, K., Daelemans 2011, W.: The effect of author set size and data size in authorship attribution. *Literary Linguist. Comput.* 26(1), 35-55
7. Abbasi, Ahmed, and Hsinchun Chen. 2008. "Writeprints: A stylometric approach to identity-level identification and similarity detection in cyberspace." *ACM Transactions on Information Systems (TOIS)* 26.2 : 1-29.
8. Holmes, D. 1998. The Evolution of Stylometry in Humanities Scholarship. *Literary and Linguistic Computing*, 13(3): 111-117.
9. Mikolov, Tomas, et al.2013. "Efficient estimation of word representations in vector space." *arXiv preprint arXiv:1301.3781*.
10. Mikolov, Tomas, et al. 2013. "Distributed representations of words and phrases and their compositionality." *Advances in neural information processing systems*. 26: 3111-3119.
11. Cortes, Corinna, and Vladimir Vapnik.1995. "Support-vector networks." *Machine learning* 20.3: 273-297.
12. Li, J., Huang, G., Fan, C., Sun, Z., & Zhu, H. (2019). Key word extraction for short text via word2vec, doc2vec, and textrank. *Turkish Journal of Electrical Engineering & Computer Sciences*, 27(3), 1794-1805.
13. Rehurek, R., Sojka, P. 2010. Software framework for topic modelling with large corpora. In: *Proceedings of the LREC 2010 Workshop on New Challenges for NLP Frameworks, ELRA*, pp. 45-50.
14. Kim, Donghwa, et al. 2019 "Multi-co-training for document classification using various document representations: TF-IDF, LDA, and Doc2Vec." *Information Sciences* 477 : 15-29.
15. Peng, Chao-Ying Joanne, Kuk Lida Lee, and Gary M. Ingersoll. 2002. "An introduction to logistic regression analysis and reporting." *The journal of educational research* 96.1: 3-14.
16. Kwak, Chanyeong, and Alan Clayton-Matthews.2002 "Multinomial logistic regression." *Nursing research* 51.6: 404-410.
17. Becht, Etienne, et al. 2019. "Dimensionality reduction for visualizing single-cell data using UMAP." *Nature biotechnology* 37.1 : 38-44
18. Zhang, Ye, Stephen Roller, and Byron Wallace. 2016. "MGNC-CNN: A simple approach to exploiting multiple word embeddings for sentence classification." *arXiv preprint arXiv:1603.00968* .
19. Radford, Alec, Luke Metz, and Soumith Chintala. 2015 "Unsupervised representation learning with deep convolutional generative adversarial networks." *arXiv preprint arXiv:1511.06434*
20. "Deep Feature Generation for Author Identification " <https://github.com/adresgezini/DFG4AI/>

Deep Feature Extraction for Detection of Tomato Plant Diseases and Pests based on Leaf Images

Yahya Altuntaş^{1*}, Adnan Fatih Kocamaz²

¹ Apricot Research Institute, Department of Agricultural Machinery and Technologies, 44090 Malatya, Turkey

² Inonu University, Department of Computer Engineering, 44280 Malatya, Turkey

* yahyaaltuntas@gmail.com

*Orcid: 0000-0002-7472-8251

Received: 19 October 2020

Accepted: 30 March 2021

DOI: 10.18466/cbayarfb.812375

Abstract

Plant diseases and pests cause yield and quality losses. It has great importance to detect plant diseases and pests quickly and with high accuracy in terms of preventing yield and quality losses. Plant disease and pest detection performed by plant protection experts through visual observation is a labor-intensive process with a high error rate. Developing effective, fast and highly successful computer-aided disease detection systems has become a necessity in terms of precision agriculture applications. In this study, well-known pre-trained convolutional neural network (CNN) models AlexNet, GoogLeNet and ResNet-50 are used as feature extractors. In addition, a deep learning model that concatenate deep features extracted from 3 CNN models has been proposed. The deep features were used to train the support vector machine classifier. The proposed model was used to classify leaf images of tomato plant diseases and pests, which is a subset of open-access PlantVillage dataset consisting of a total of 18835 images belonging to 10 classes including a healthy one. Accuracy, precision, sensitivity and f-score performance metrics were used with the hold-out validation method in determining model performances. Experimental results show that the detection of tomato plant diseases and pests is possible using concatenated deep features with an overall accuracy rate of 96.99%.

Keywords: convolutional neural networks, deep features extraction, deep learning, image classification, plant diseases and pests detection, precision agriculture.

1. Introduction

Tomato (*Solanum lycopersicum*) is one of the most widely cultivated agricultural products all over the world. As in all other agricultural products, one of the factors that negatively affect tomato cultivation is diseases and pests. Various diseases and pests cause yield and quality losses in crop production [1]. Early and accurate detection of diseases and pests is very important to prevent yield and quality losses. Plant disease and pest detection performed by visual observation by plant protection experts is a labor-intensive process with a high error rate [2]. The development of effective, fast and highly successful computer-aided disease detection systems has become a necessity for precision agriculture applications.

Remarkable progress has been made in plant disease and pest detection with studies based on traditional machine learning methods. Al-Hiary et al. [3] proposed a model for diagnosing 5 diseases that cause symptoms

in leaves in different plant species. They segmented the images using Otsu thresholding and k-means clustering methods and extracted texture features. They used these features to feed artificial neural networks (ANN) classifiers. Dubey and Jalal [4] performed feature extraction from apple images segmented by the k-means clustering method using local binary pattern methods to detect 3 different apple fruit diseases. They classified the obtained features using a support vector machine (SVM). Singh and Misra [5] conducted a study to detect 5 different diseases in 4 different plant species. They obtained the color co-occurrence matrix features from images that were segmented and enhanced with image processing techniques. According to their experimental results, they reported that the best performance was obtained with the SVM classifier. Success in traditional machine learning methods largely depends on the features used. Segmentation is required to extract the features. This situation necessitates that the work carried out with traditional machine learning methods should be under highly controlled conditions and limits the classification success achieved.

Deep learning refers to models that can learn the representations of data through multiple processing layers and thus perform end-to-end learning [6]. Thanks to deep learning, unlike traditional machine learning methods, learning from raw data can be performed without the need for feature extraction. In the literature, many studies have been conducted on the detection of plant diseases and pests based on deep learning [7, 8]. Mohanty et al. [1] retrained AlexNet and GoogLeNet pre-trained convolutional neural network (CNN) models, both from scratch and by fine-tuning. They reported that transfer learning provided faster converge on colored, gray-level and segmented images in their studies. Ferentinos [2] used deep learning methodology to identify plant diseases in his study on an open-access dataset containing 25 plant species and 58 plant-disease combinations. Although there are a limited number of studies on the detection of plant diseases and pests in more than one crop type, many studies have also been conducted on a single crop type such as apple [9], cucumber [10] and rice [11].

Fuentes et al. [12] proposed a deep learning-based approach to detect of tomato diseases and pests. They used a region-based CNN method to detect features on tomato leaf images. Durmuş et al. [13] retrained AlexNet and SqueezeNet pre-trained CNN models from scratch to detect tomato diseases and pests on the open-access PlantVillage dataset. Sardoğan et al. [14] used 500 healthy and infected tomato leaves from the PlantVillage dataset to detect 4 tomato diseases. They classified the features obtained from the fully connected layer of the proposed CNN architecture with the Learning Vector Quantization (LVQ) algorithm. Rangarajan et al. [15] fine-tuned both AlexNet and VGG16 pre-trained CNN models to detect of tomato plant diseases and pests. They analyzed both the role of the number of images and importance of hyperparameters in classification accuracy and execution time. Aversano et al. [16] fine-tuned the VGG19, Xception and ResNet-50 pre-trained CNN models for the detection of tomato diseases and pests.

Agarwal et al. [17] proposed a CNN architecture consisting of 3 convolution and 3 max pooling layers followed by 2 fully connected layers for the detection of tomato diseases and pest. Saeed et al. [18] used tomato, corn and potato leaves images from the PlantVillage dataset to build an automated crop disease recognition system. They selected the deep features extracted from the fully connected layers 6 and 7 of the VGG19 pre-trained CNN model using partial least squares (PLS) regression. They used selected deep features for model estimation using the ensemble baggag tree classifier.

In this study, the effect of using pre-trained CNN models as feature extractors on success in detecting tomato diseases and pests has been investigated. For this purpose, well-known pre-trained CNN models AlexNet, GoogLeNet and ResNet-50 were used as feature extractors. In addition, deep features fusion was performed by concatenating the deep features obtained from 3 CNN models. The obtained deep features were used to train the SVM classifier. According to the results, all CNN models achieved high classification success in detecting tomato diseases and pests by deep feature extraction. Concatenated deep features, on the other hand, achieved the best classification performance with an overall accuracy of 96.99%. The results of the experiments conducted within the scope of the study were compared with each other and with related studies in the literature.

The remaining of the paper is organized as follows: the materials and methods are given in Section 2. The experimental results are presented in Section 3. In Sections 4 and 5 discussion and conclusion remarks are given, respectively.

2. Materials and Methods

2.1. Dataset

In this study, experiments have been carried out on diseased and healthy tomato leaf images, which is a subset of the open-access PlantVillage [19] dataset.



Figure 1. Sample images in the dataset.

Table 1. Details of classes in the dataset

Class Name	Disease Scientific Name	Images (Number)		
		Training	Test	Total
Bacterial spot	Xanthomonas campestris pv. vesicatoria	1703	424	2127
Early blight	Alternaria solani	800	200	1000
Healthy	-	1273	318	1591
Late blight	Phytophthora infestans	1528	381	1909
Leaf mold	Fulvia fulva	800	200	1000
Septoria leaf spot	Septoria lycopersici	1417	354	1771
Spider mites	Tetranychus urticae	1342	334	1676
Target spot	Corynespora cassicola	1124	280	1404
ToMV	Tomato mosaic virus (ToMV)	800	200	1000
TYLCV	Begomovirus (Fam. Geminiviridae)	4287	1070	5357
Total		15074	3761	18835

TYLCV: Tomato yellow leaf curl virus

Since the link reported in the original article has been broken, the version republished by Geetharamani and Pandian [20] has been used. The dataset consists of 18835 images belonging to 10 classes. Images are 256-by-256 pixels resolution and colored. The image format is JPEG. The space occupied by the dataset in the disk is 321 MB.

Sample images from the dataset have been demonstrated in Figure 1. The sample images from left to right in the first row belong to bacterial spot, early blight, healthy, late blight, and leaf mold classes; the sample images in the second row belong to septoria leaf spot, spider mites, target spot, mosaic virus, and yellow leaf curl virus classes.

AlexNet, GoogLeNet and ResNet-50 CNN models take input images with a resolution of 227-by-227, 224-by-224 and 224-by-224 pixels respectively. For this reason, images have been resized to the specified resolutions.

The hold-out validation method has been used to make a one-to-one comparison of the models applied within the scope of the study. For this purpose, the dataset has been divided into training and test groups at a ratio of 4:1. All models have been trained with the same training images and tested with the same testing images. The classes of the dataset, the scientific names of the diseases, the class distribution of the samples, and the number of training and testing images are given in Table 1.

2.2. Convolutional neural networks

CNNs are deep learning models designed to automatically learn representations of data. A CNN architecture consists of two parts. The first part consists of convolution, activation and pooling layers where discriminative features of data is learned, the second

part consists of fully connected layers and softmax layer where the learned features are classified [6].

Thanks to the filters in the convolution layer, the interrelated spatial dependencies of the data are discovered. Filter weights are shared. In this way, it does not affect learning where the same discriminative feature in different locations of the input data [21]. As a result of the convolution process, the weighted sum of inputs is obtained. This layer is followed by an activation layer to get rid of linear dependencies. Although there are different activation functions such as hyperbolic tangent and sigmoid, the most preferred activation function is the Rectified Linear Unit (ReLU). ReLU activation function sets negative values to 0. Feature maps are obtained in this layer. Next comes the pooling layer to shrink in size, without losing valuable information in the data. A maximum or average pooling can be done. Convolution operations are repeated one after another depending on the hyper-parameter values such as input size, filter size, stride and padding. Ultimately, it is transferred to the fully connected layer. The purpose of this layer is to flatten the learned features. Depending on the architecture, there may be one or more fully connected layers. Then the last fully connected layer is passed to a softmax layer. Finally, the model estimation is made by performing class probability calculations of the features learned with the softmax layer. There are as many outputs as the number of classes in the problem addressed in the last fully connected layer.

2.3. Deep feature extraction and proposed model

Deep feature extraction is a transfer learning approach to employ a pre-trained CNN model for a similar task. Deep feature extraction is to use a pre-trained CNN model as a feature extractor. In this approach, the model parameters (weights) are used without fine-tuning [22].

Then a classification algorithm such as SVM is used for the new classification task [23]. In this approach, the pre-trained CNN model is employed as part of the solution of the new task using as a feature extractor.

In the deep feature extraction approach, deep features can be obtained from any layer of a pre-trained CNN model. However, common usage is to extract deep features from the last fully connected layer. In this study, the last fully connected layers of AlexNet, GoogLeNet and ResNet-50 CNN models are used to extract the deep features. In addition, a deep learning model that concatenate deep features obtained from 3 CNN models has been proposed to increase prediction performance. Overall structure of the proposed model is shown in Figure 2.

The pre-trained CNN models used in the study are briefly introduced below. AlexNet [24] is one of the pioneering CNN architecture. AlexNet has a simple architecture that consists of 5 convolution layers, and 3 fully connected layers.

GoogLeNet [25] is a 22 layer CNN architecture that's a variant of the inception network. The most important properties of GoogLeNet architecture is the use of the inception module. The module simply provides a direct link between multiple different layers. This increases network complexity while keeping the computing cost at the same level.

ResNet-50 [26] architecture consists of 50 layers. ResNet-50 is different from other architectures with its micro-architecture module structure. In architecture, it may be preferred to switch to the lower layer by ignoring the change between some layers. In ResNet architecture, the performance rate has been increased by allowing transition operations between blocks with this structure.

2.4. Support vector machines

The deep feature extraction approach requires a classifier method to be trained with the extracted deep features. In this study, SVM proposed by Vapnik [27] was used as a classifier. It has been reported that the SVM classifier shows superior performance in different agricultural image classification problems [28].

The basic principle in solving a classification problem with SVM is to determine a hyperplane that divides samples belonging to two classes optimally from each other. The formula for the output of a linear SVM is given in Equation (2.1), where \vec{w} is the normal vector to the hyperplane and \vec{x} is the input vector. Maximizing margins can be defined as an optimization problem: minimize Equation (2.2) subject to Equation (2.3) where y_i and \vec{x}_i are the correct output of the SVM and the input vector for i^{th} training sample, respectively [29].

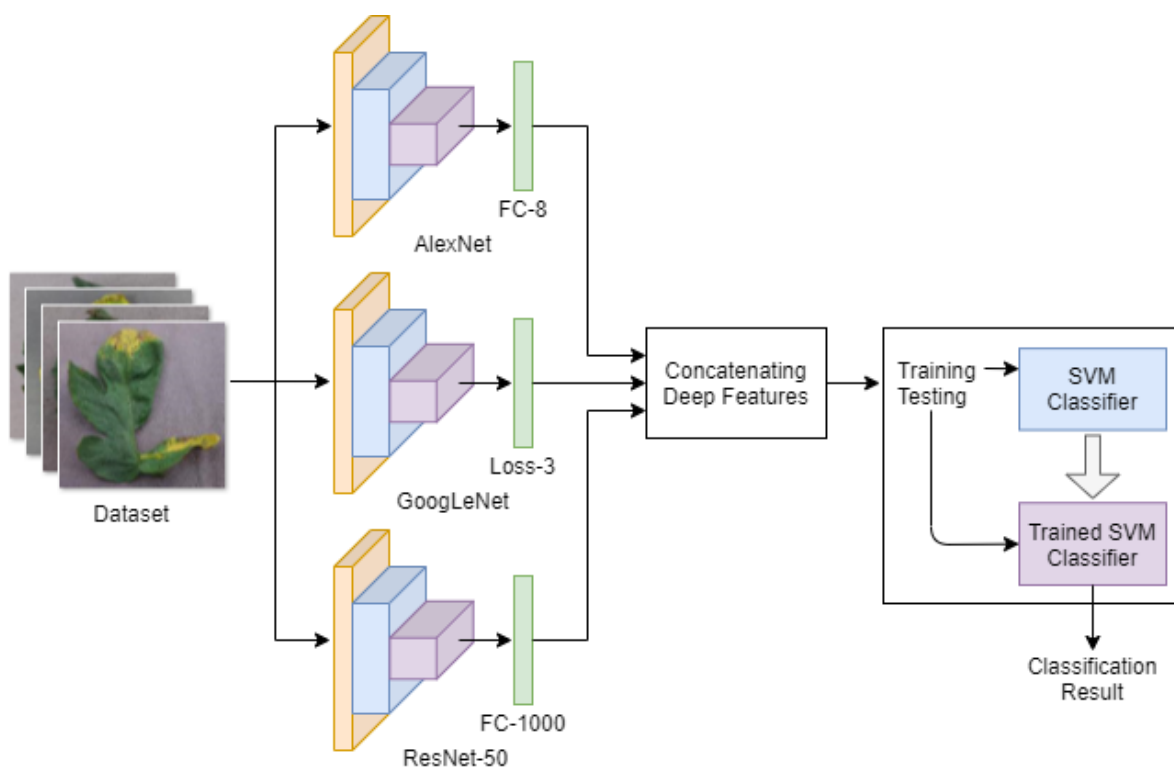


Figure 2. Overall structure of the proposed model

$$u = \vec{w} \cdot \vec{x} - b \quad (2.1)$$

$$\frac{1}{2} \|\vec{w}\|^2 \quad (2.2)$$

$$y_i(\vec{w} \cdot \vec{x}_i - b) \geq 1, \forall i \quad (2.3)$$

$$Pre. = \frac{TN}{TN + FP} \quad (3.2)$$

$$Sen. = \frac{TP}{TP + FN} \quad (3.3)$$

$$F - score = \frac{2TP}{2TP + FP + FN} \quad (3.4)$$

SVM is a binary classifier defined to separate only 2 classes and do not support for multi-class classification problems. One strategy for multi-class classification with SVMs is to create a one-to-one set of classifiers and predict the class chosen by the majority of classifiers [30]. While this enables creating classifiers $K(K-1)/2$ for the classification problem with K classes, the training time of the classifiers may be reduced as the training data set for each classifier will be smaller.

3. Results

In this study, the deep feature extraction method, which is a transfer learning approach employing pre-trained CNN models as feature extractors, was used for the detection of tomato plant diseases and pests. The deep features were obtained from the last fully connected layers of AlexNet, GoogLeNet and ResNet-50 named FC-8, Loss-3 and FC-1000, respectively. In addition, a deep learning model that concatenate 1000 deep features obtained from each of the 3 CNN models proposed to increase predictive performance. Obtained deep features were used to train the SVM classifier. In the configuration of the SVM, all parameters are used in default configurations. Experimental studies were carried out on a computer with i5-8250U CPU, 8 GB RAM, 2 GB GPU, 256 SSD HDD hardware specifications. All experimental studies were implemented in MATLAB 2019b programming environment.

Since there is a sufficient number of images in the dataset, the hold-out validation method was used to make a one-to-one comparison of the models. For this purpose, the dataset was divided into training and test groups at a ratio of 4:1. Accuracy (Acc.), precision (Pre.), sensitivity (Sen.) and f-score performance metrics were calculated for comparison of model performances. These performance metrics are calculated with the indices true positive (TP), false negative (FN), false positive (FP), and true negative (TN) obtained from the confusion matrix. The mathematical equations of performance metrics used in comparing models are as follows:

$$Acc. = \frac{TP + TN}{TP + FN + FP + TN} \quad (3.1)$$

In multi-class classification problems, confusion matrix indices and performance metrics are calculated separately for each class. For the class for which performance metrics are calculated, samples belonging to that class are considered positive and all other samples are considered negative. Then, TP, FN, FP, and TN indices are calculated according to the predictions of the model for the samples treated as positive and negative.

While TP, FN, FP, and TN values are calculated for the Healthy class, samples labeled as Healthy in the dataset are considered positive and all other samples are considered negative. The number of positive samples in the test set, which are predicted as Healthy by the model, gives the TP value. The number of positive samples in the test set that are not predicted as Healthy by the model gives the FN value. The number of negative samples in the test set that are predicted as Healthy by the model gives the FP value. The number of negative samples in the test set that are not predicted as Healthy by the model gives the TN value.

That is, all samples except the class whose confusion matrix indices are calculated are considered negative and are named TN regardless of whether they are correctly predicted in their own class. This situation causes high accuracy and sensitivity values.

In multi-class classification problems, the overall accuracy metric is also used to measure the overall performance of the model. This metric gives us the ratio of the number of correct predictions of the model to the total number of predictions. It is calculated as follows.

$$Overall Acc. = \frac{\sum_{i=1}^N TP_i}{\sum_{i=1}^N (TP_i + FP_i)} \quad (3.5)$$

In the formula, N refers to the number of classes. TP_i and FP_i show the correct and incorrect prediction numbers of the i^{th} class respectively.

The classification results are given in Table 2. The values given in the table are confusion matrix (TP, FN, FP, and TN), Acc., Pre., Sen., F-Score (F-scr), and overall accuracy (Overall Acc.).

Table 2. Classification results

Pre-trained CNN Model	Class	TP	FN	FP	TN	Acc. (%)	Pre.	Sen.	F-Scr	Overall Acc. (%)
AlexNet	Bacterial spot	403	18	21	3319	98.96	0.957	0.993	0.953	92.18
	Early blight	153	50	47	3511	97.42	0.753	0.986	0.759	
	Healthy	304	11	14	3432	99.33	0.965	0.995	0.960	
	Late blight	348	38	33	3342	98.11	0.901	0.990	0.907	
	Leaf mold	168	23	32	3538	98.53	0.879	0.991	0.859	
	Sep. leaf spot	324	39	30	3368	98.16	0.892	0.991	0.903	
	Spider mites	295	39	39	3388	97.92	0.883	0.988	0.883	
	Target spot	242	55	38	3426	97.52	0.814	0.989	0.838	
	ToMV	186	6	14	3555	99.46	0.968	0.996	0.948	
	TYLCV	1044	15	26	2676	98.90	0.985	0.990	0.980	
GoogLeNet	Bacterial spot	390	37	34	3300	98.11	0.913	0.989	0.916	89.31
	Early blight	142	67	58	3494	96.67	0.679	0.983	0.694	
	Healthy	300	16	18	3427	99.09	0.949	0.994	0.946	
	Late blight	329	41	52	3339	97.52	0.889	0.984	0.876	
	Leaf mold	168	29	32	3532	98.37	0.852	0.991	0.846	
	Sep. leaf spot	294	66	60	3341	96.64	0.816	0.982	0.823	
	Spider mites	289	49	45	3378	97.50	0.855	0.986	0.860	
	Target spot	227	57	53	3424	97.07	0.799	0.984	0.804	
	ToMV	181	12	19	3549	99.17	0.937	0.994	0.921	
	TYLCV	1039	28	31	2663	98.43	0.973	0.988	0.972	
ResNet-50	Bacterial spot	414	7	10	3330	99.54	0.983	0.997	0.979	96.96
	Early blight	173	20	27	3541	98.75	0.896	0.992	0.880	
	Healthy	313	3	5	3440	99.78	0.990	0.998	0.987	
	Late blight	368	21	13	3359	99.09	0.946	0.996	0.995	
	Leaf mold	193	6	7	3555	99.65	0.969	0.998	0.967	
	Sep. leaf spot	344	10	10	3397	99.46	0.971	0.997	0.971	
	Spider mites	324	21	10	3406	99.17	0.939	0.997	0.954	
	Target spot	259	18	21	3463	98.96	0.935	0.993	0.929	
	ToMV	194	3	6	3558	99.76	0.984	0.998	0.977	
	TYLCV	1065	5	5	2686	99.73	0.995	0.998	0.995	
Concatenated Deep Features	Bacterial spot	419	4	5	3333	99.76	0.990	0.998	0.989	96.99
	Early blight	175	22	25	3539	98.75	0.888	0.992	0.881	
	Healthy	312	5	6	3438	99.70	0.984	0.998	0.982	
	Late blight	366	15	15	3365	99.20	0.960	0.995	0.960	
	Leaf mold	188	8	12	3553	99.46	0.959	0.996	0.949	
	Sep. leaf spot	345	16	9	3391	99.33	0.955	0.997	0.965	
	Spider mites	326	14	8	3413	99.41	0.958	0.997	0.967	
	Target spot	260	18	20	3463	98.98	0.935	0.994	0.931	
	ToMV	196	6	4	3555	99.73	0.970	0.998	0.975	
	TYLCV	1061	5	9	2686	99.62	0.995	0.996	0.993	

According to the experimental results, the overall accuracy rates obtained by classifying the deep features extracted from the last fully connected layers of AlexNet, GoogLeNet and ResNet-50 pre-trained CNN models with SVM classifier are 92.18%, 89.31% and 96.96%, respectively. According to the experimental results, all CNN models used within the scope of the study showed superior classification performance. However, the best performance has been achieved by using concatenating deep features with an overall accuracy rate of 96.99%. This overall accuracy rate is better than all CNN models individually.

The time taken to extract deep features for 3761 test images and store the resulting deep feature vectors on disk as a separate file was measured as 14 minutes 58 seconds, 20 minutes 19 seconds, and 50 minutes 33 seconds for AlexNet, GoogLeNet and ResNet-50 models, respectively. Experimental results show that deep feature extraction process from CNN models with a high number of layers requires more time.

Table 3. Comparison of the proposed model and the related studies

Related studies	Crops type	Method	Overall Acc. (%)
Fuentes et al., 2017 [12]	Tomato (10 classes)	Region-based CNN	83.60
Durmuş et al., 2017 [13]	Tomato (10 classes)	Retraining a pre-trained CNN model from scratch	95.65
Sardoğan et al., 2018 [14]	Tomato (5 classes)	CNN with LVQ algorithm	86.00
Rangarajan et al., 2018 [15]	Tomato (7 classes)	Fine-tuning a pre-trained CNN model	97.49
Aversano et al., 2020 [16]	Tomato (10 classes)	Fine-tuning a pre-trained CNN model	97.16
Agarwal et al., 2020 [17]	Tomato (10 classes)	CNN	91.20
Saeed et al., 2021 [18]	Tomato (10 classes)	PLS-based deep features selection and ensemble baggage tree classifier	87.11
	Corn (4 classes)		91.67
	Potato (3 classes)		91.67
This study	Tomato (10 classes)	Concatenating deep features and SVM	96.99

4. Discussion

The number of classes dealt with in the related studies is not equal. Sardoğan et al. [14] conducted a study with a total of 5 classes, including 4 diseases and 1 healthy class. Rangarajan et al. [15] conducted a study with a total of 7 classes, including 6 diseases and 1 healthy class. In other related studies, 10 classes, including 9 diseases and 1 healthy class were conducted. Since test samples are not pre-defined in the PlantVillage dataset, the test samples used in related studies are not the same. Also, the number of test samples used is not equal. Sardoğan et al. [14] in their work with a total of 500 images, they used 400 images for training and 100 images for testing. Agarwal et al. [17] in their work with a total of 17500 images, they used 10000 images for training, 7000 images for validation and 500 images for testing. A one-to-one comparison among the related studies is not feasible due to the reasons explained above. Nevertheless, we present a comparison in Table 3 considering several criteria, such as the number of classes, methods, and overall accuracy rates.

5. Conclusion

In this study, the possibilities of detecting tomato plant diseases and pests by deep feature extraction were investigated. For this purpose, well-known pre-trained CNN models AlexNet, GoogLeNet, and ResNet-50 were used as feature extractors. 1000 deep features obtained from the last fully connected layers of CNN models were used to train the SVM classifier. In addition, a deep learning model that concatenate 1000 deep features obtained from each of the 3 CNN models proposed to increase predictive performance. According to the experimental results, while superior classification performance was obtained with deep features extracted from all CNN models, the best result was obtained with the concatenated deep features. The reason for this is considered to be the result of CNN models with different architectures discovering different discriminative features.

In future studies, it is aimed to increase the classification performance with different fusion methods. In addition, the performance of the models to be developed on field condition images will be evaluated.

Author's Contributions

Yahya Altuntaş: Drafted and wrote the manuscript, performed the experiment and result analysis.

Adnan Fatih Kocamaz: Supervised the experiments' progress, result interpretation and helped in manuscript preparation.

Ethics

There are no ethical issues after the publication of this manuscript.

References

1. Mohanty, SP, Hughes, DP, Salathé, M. 2016. Using deep learning for image-based plant disease detection. *Frontiers in plant science*; 7: 1419.
2. Ferentinos, KP. 2018. Deep learning models for plant disease detection and diagnosis. *Computers and Electronics in Agriculture*; 145: 311-318.
3. Al-Hiary, H, Bani-Ahmad, S, Reyalat, M, Braik, M, Alrahmaneh, Z. 2011. Fast and accurate detection and classification of plant diseases. *International Journal of Computer Applications*; 17(1): 31-38.
4. Dubey, SR, Jalal, AS. Detection and classification of apple fruit diseases using complete local binary patterns, proceedings of the 3rd international conference on computer and communication technology, Allahabad, India, 2012, pp 346-351.
5. Singh, V, Misra, AK. 2017. Detection of plant leaf diseases using image segmentation and soft computing techniques. *Information processing in Agriculture*; 4(1): 41-49.
6. LeCun, Y, Bengio, Y, Hinton, G. 2015. Deep learning. *Nature*; 521(7553): 436-444.
7. Ünal, Z. 2020. Smart Farming Becomes Even Smarter With Deep Learning - A Bibliographical Analysis. *IEEE Access*; 8:105587-105609.

8. Kamilaris, A, Prenafeta-Boldú, FX. 2018. Deep learning in agriculture: A survey. *Computers and Electronics in Agriculture*; 147: 70-90.
9. Zhong, Y, Zhao, M. 2020. Research on deep learning in apple leaf disease recognition. *Computers and Electronics in Agriculture*; 168: 105146.
10. Fujita, E, Kawasaki, Y, Uga, H, Kagiwada, S, Iyatomi, H. Basic investigation on a robust and practical plant diagnostic system, proceedings of the 15th IEEE International Conference on Machine Learning and Applications, Anaheim CA, USA, 2016, pp 989-992.
11. Lu, Y, Yi, S, Zeng, N, Liu, Y, Zhang, Y. 2017. Identification of rice diseases using deep convolutional neural networks. *Neurocomputing*; 267: 378-384.
12. Fuentes, A, Yoon, S, Kim, SC, Park, DS. 2017. A robust deep-learning-based detector for real-time tomato plant diseases and pests recognition. *Sensors*; 17(9): 2022.
13. Durmuş, H, Güneş, EO, Kırıcı, M. Disease detection on the leaves of the tomato plants by using deep learning, proceedings of the 6th International Conference on Agro-Geoinformatics, Fairfax VA, USA, 2017, pp 1-5.
14. Sardogan, M, Tuncer, A, Ozen, Y. Plant leaf disease detection and classification based on CNN with LVQ algorithm, proceedings of the 3rd International Conference on Computer Science and Engineering, Sarajevo, Bosnia and Herzegovina, 2018, pp 382-385.
15. Rangarajan, AK, Purushothaman, R, Ramesh, A. 2018. Tomato crop disease classification using pre-trained deep learning algorithm. *Procedia computer science*; 133: 1040-1047.
16. Aversano, L, Bernardi, ML, Cimitile, M, Iammarino, M, Rondinella, S. Tomato diseases Classification Based on VGG and Transfer Learning, proceedings of the IEEE International Workshop on Metrology for Agriculture and Forestry, Virtual Conference, 2020, pp 129-133.
17. Agarwal, M, Singh, A, Arjaria, S, Sinha, A, Gupta, S. 2020. ToLeD: Tomato leaf disease detection using convolution neural network. *Procedia Computer Science*; 167: 293-301.
18. Saeed, F, Khan, MA, Sharif, M, Mittal, M, Goyal, LM, Roy, S. 2021. Deep neural network features fusion and selection based on PLS regression with an application for crops diseases classification. *Applied Soft Computing*; 103: 107164.
19. Hughes, D, Salathé, M. 2015. An open access repository of images on plant health to enable the development of mobile disease diagnostics. *arXiv preprint*; arXiv:1511.08060.
20. Geetharamani, G, Pandian, A. 2019. Identification of plant leaf diseases using a nine-layer deep convolutional neural network. *Computers & Electrical Engineering*; 76: 323-338.
21. Altuntaş, Y, Cömert, Z, Kocamaz, AF. 2019. Identification of haploid and diploid maize seeds using convolutional neural networks and a transfer learning approach. *Computers and Electronics in Agriculture*; 163: 104874.
22. Chatfield, K, Simonyan, K, Vedaldi, A, Zisserman, A. 2014. Return of the devil in the details: Delving deep into convolutional nets. *arXiv preprint*; arXiv:1405.3531.
23. Toğaçar, M, Ergen, B, Cömert, Z. 2020. Classification of flower species by using features extracted from the intersection of feature selection methods in convolutional neural network models. *Measurement*; 158: 107703.
24. Krizhevsky, A, Sutskever, I, Hinton, GE. 2012. Imagenet classification with deep convolutional neural networks. *Advances in neural information processing systems*; 25: 1097-1105.
25. Szegedy, C, Liu, W, Jia, Y, Sermanet, P, Reed, S, Anguelov, D, Rabinovich, A. Going deeper with convolutions, proceedings of the IEEE conference on computer vision and pattern recognition, Boston MA, USA, 2015, pp 1-9.
26. He, K, Zhang, X, Ren, S, Sun, J. Deep residual learning for image recognition, proceedings of the IEEE conference on computer vision and pattern recognition, Las Vegas NV, USA, 2016, pp 770-778.
27. Vapnik, VN. The nature of statistical learning theory; Springer, New York, USA, 2000; pp 313.
28. Altuntaş, Y, Kocamaz, AF. 2019. Renk momentleri ve destek vektör makineleri kullanarak haploid mısır tohumlarının tanımlanmasında renk uzaylarının sınıflandırma performansına etkisinin karşılaştırılması. *Fırat Üniversitesi Mühendislik Bilimleri Dergisi*; 31(2): 551-560.
29. Huang, S, Cai, N, Pacheco, PP, Narrandes, S, Wang, Y, Xu, W. 2018. Applications of support vector machine (SVM) learning in cancer genomics. *Cancer Genomics-Proteomics*; 15(1): 41-51.
30. Bishop, CM. Pattern recognition and machine learning; Springer, New York, USA, 2006; pp 738.

Numerical Solutions of System of First Order Normalized Linear Differential Equations by Using Bernoulli Matrix Method

Kübra ERDEM BİÇER¹ , Mehmet SEZER^{1*} , Mustafa KAZAZ¹ 

¹ Manisa Celal Bayar University Faculty of Art and Science, Manisa, Turkey

*kubra.erdem@cbu.edu.tr

*Orcid: 0000-0002-4998-6531

Received: 23 December 2020

Accepted: 21 May 2021

DOI: 10.18466/cbayarfbe.845017

Abstract

Systems of first order differential equations have been arisen in science and engineering. Specially, the systems of normalized linear differential equations appear in differential geometry and kinematics problems. Since it is difficult to find solutions to these equations analytically, numerical methods are needed for the approximate solutions. In this study, we find the approximate solutions of the Frenet-Like system with variable coefficients upon the initial conditions by means of a matrix method related to the truncated Bernoulli series. This method transforms the mentioned problem into a system of algebraic equations by using the matrix relations and collocation points; so, the required results along with the solutions are obtained and the usability of the method is discussed.

Keywords: Approximate Solutions, Bernoulli polynomials and series, Curves of constant breadth, Matrix Methods, Systems of first order differential equations.

1. Introduction

The systems of differential equations in the normal form usually appear in the concept of differential geometry. For instance, a system of differential equations characterizing E^4 spherical curves can be given as

$$\frac{d\rho}{ds} = \tau f, \quad \frac{df}{ds} = -\tau\rho + \mu g, \quad \frac{dg}{ds} = -\mu f, \quad (1)$$

where s is arc parameter, $\rho(s) = 1/\kappa(s)$ is curvature diameter; κ, τ and μ are curvatures and, $f(s)$ and $g(s)$ are in the class of C^2 [1,2].

The system charactering curves of constant breadth are the same type and can be given as

$$\frac{d\lambda}{d\theta} = \mu, \quad \frac{d\mu}{d\theta} = -\lambda + \rho\tau\delta, \quad \frac{d\delta}{d\theta} = -\rho\tau\mu, \quad (2)$$

where $\theta(s) = \int_0^s \kappa(s) ds$ and $\lambda(\theta)$, $\mu(\theta)$ and $\delta(\theta)$

are the coefficients of the curve [3,4].

Besides, the well known Serret-Frenet Equations

$$\frac{d\vec{t}}{ds} = \kappa\vec{n}, \quad \frac{d\vec{n}}{ds} = -\kappa\vec{t} + \kappa_2\vec{b}, \quad \frac{d\vec{b}}{ds} = -\kappa_2\vec{n},$$

lead us to the system of differential equations [5,6]:

$$\frac{d\varphi_1}{ds} = \kappa\varphi_2, \quad \frac{d\varphi_2}{ds} = -\kappa\varphi_1 + \tau\varphi_3, \quad \frac{d\varphi_3}{ds} = -\tau\varphi_2, \quad (3)$$

where κ_1 and κ_2 are Euclidean curvatures. The solution of this system also gives as a criterion for periodicity of a space curve. Since the normal systems (1), (2) and (3) same type, it is possible to form them as

$$\left. \begin{aligned} \frac{dy_1}{dx} &= a(x)y_2(x) \\ \frac{dy_2}{dx} &= -a(x)y_1(x) + b(x)y_3(x) \\ \frac{dy_3}{dx} &= -b(x)y_2(x) \end{aligned} \right\} \quad (4)$$

Also the normal system is obtained as

$$\left. \begin{aligned} \frac{dT}{ds} &= k_1N_1 + k_2N_2 \\ \frac{dN_1}{ds} &= -k_1T \\ \frac{dN_2}{ds} &= -k_2T \end{aligned} \right\} \quad (5)$$

where

$k_1 = \kappa \cos(\theta)$, $k_2 = \kappa \sin(\theta)$ and $T = T$,
 $N_1 = N \cos \theta - B \sin \theta$, $N_2 = N \sin \theta - B \cos \theta$ for the
 Bishop frame. It can be shown that

$$\kappa(s) = \sqrt{k_1^2 + k_2^2} , \theta(s) = \arctan\left(\frac{k_2}{k_1}\right) \text{ and}$$

$$\tau(s) = -\frac{d\theta(s)}{s} \quad [7].$$

These type systems given in (4) and (5) which are called Frenet-Like system is a class of linear differential equations in normal form

$$\left. \begin{aligned} \frac{dy_1}{ds} &= P_{11}(s)y_1(s) + P_{12}(s)y_2(s) + P_{13}(s)y_3(s) + g_1(s) \\ \frac{dy_2}{ds} &= P_{21}(s)y_1(s) + P_{22}(s)y_2(s) + P_{23}(s)y_3(s) + g_2(s) \\ \frac{dy_3}{ds} &= P_{31}(s)y_1(s) + P_{32}(s)y_2(s) + P_{33}(s)y_3(s) + g_3(s) \end{aligned} \right\} \quad (6)$$

or briefly

$$\frac{dy_j}{ds} = \sum_{k=1}^3 P_{jk}(s)y_k(s) + g_j(s); \quad j = 1, 2, 3$$

where $P_{kj}(s)$ and $g(s)$ are functions on interval $0 \leq a \leq s \leq b$.

In this study, we have developed a method based on Bernoulli polynomials to solve system of linear differential equations. Also this method has been used to solve high-order linear differential-difference equations, linear delay difference equations with variable coefficients and mixed linear Fredholm integro-differential-difference equations, hyperbolic partial differential equations, Helmholtz equations and general functional integro-differential equations with hybrid delays [8-13]. Also many numerical methods have been developed to solve similar equation models [14-20].

We firstly consider the system of differential equations in normal form (6) with the initial conditions

$$y_1(a) = \lambda_1, y_2(a) = \lambda_2, y_3(a) = \lambda_3; 0 \leq a \leq s \leq b. \quad (7)$$

A matrix method is developed to find the approximate solution set in the truncated Bernoulli series form

$$y_j(s) = \sum_{n=0}^N a_{jn} B_n(s); 0 \leq a \leq s \leq b, \quad (8)$$

where a_{jn} , $j = 1, 2, 3$ are unknown Bernoulli coefficients, λ_j , $j = 1, 2, 3$ are the given real constants and $B_n(s)$, $n = 0, 1, \dots, N$. Bernoulli polynomials are defined by [21]

$$\frac{te^{xt}}{e^t - 1} = \sum_{n=0}^{\infty} \frac{B_n(x)}{n!} t^n$$

or

$$B_n(x) = \sum_{r=0}^n \binom{n}{r} b_r x^{n-r}; \quad b_r = B_r(0). \quad (9)$$

Also, an explicit formula for the Bernoulli polynomials is given by

$$B'_n(s) = nB_{n-1}(s), \quad (10)$$

where $B_0(s) = 1$, $B'_0(s) = 1$, $B_1(s) = s - \frac{1}{2}$, $B'_1(s) = 1$

2. Fundamental matrix relations and Bernoulli matrix method

In this section, a new matrix technique is developed by considering Taylor and Bernoulli collocation methods [22-23] to obtain the approximate solution of the system (6) under the condition (7). For this aim, we compose the matrix form of (6), (7) and (8); firstly the matrix form of (6) can be expressed as

$$Y'(s) = P(s)Y(s) + G(s); 0 \leq a \leq s \leq b, \quad (11)$$

where

$$Y'(s) = \begin{bmatrix} y_1'(s) \\ y_2'(s) \\ y_3'(s) \end{bmatrix}, P(s) = \begin{bmatrix} P_{11}(s) & P_{12}(s) & P_{13}(s) \\ P_{21}(s) & P_{22}(s) & P_{23}(s) \\ P_{31}(s) & P_{32}(s) & P_{33}(s) \end{bmatrix},$$

$$Y(s) = \begin{bmatrix} y_1(s) \\ y_2(s) \\ y_3(s) \end{bmatrix}, G(s) = \begin{bmatrix} g_1(s) \\ g_2(s) \\ g_3(s) \end{bmatrix}.$$

Then the matrix form of (8) can be written as

$$y_j(s) = B(s)A_j, \quad (j = 1, 2, 3), \quad (12)$$

where

$$B(s) = [B_0(s) \quad B_1(s) \quad \dots \quad B_N(s)],$$

$$A_j = [a_{j0} \quad a_{j1} \quad a_{j2} \quad \dots \quad a_{jN}(s)]^T.$$

Also by using the expressions (10) and (12), we have the matrix form

$$y_j'(s) = B'(s)A_j = B(s)DA_j; \quad (j = 1, 2, 3), \quad (13)$$

where

$$D = \begin{bmatrix} 0 & 1 & 0 & \dots & 0 \\ 0 & 0 & 2 & \dots & 0 \\ \vdots & \vdots & \vdots & \ddots & \vdots \\ 0 & 0 & 0 & 0 & N \\ 0 & 0 & 0 & 0 & 0 \end{bmatrix}.$$

By using the matrix relations (12) and (13) into the matrices $Y(s)$ and $Y'(s)$, the following matrix forms are obtained as

$$\begin{aligned}
 Y(s) &= \begin{bmatrix} y_1(s) \\ y_2(s) \\ y_3(s) \end{bmatrix} = \begin{bmatrix} B(s)A_1 \\ B(s)A_2 \\ B(s)A_3 \end{bmatrix} = \bar{B}(s)A, \\
 Y'(s) &= \begin{bmatrix} y_1'(s) \\ y_2'(s) \\ y_3'(s) \end{bmatrix} = \begin{bmatrix} B(s)DA_1 \\ B(s)DA_2 \\ B(s)DA_3 \end{bmatrix} = \overline{B(s)DA},
 \end{aligned} \tag{14}$$

where

$$\begin{aligned}
 \bar{B}(s) &= \begin{bmatrix} B(s) & 0 & 0 \\ 0 & B(s) & 0 \\ 0 & 0 & B(s) \end{bmatrix}, \\
 \overline{B(s)D} &= \begin{bmatrix} B(s)D & 0 & 0 \\ 0 & B(s)D & 0 \\ 0 & 0 & B(s)D \end{bmatrix}, \\
 A &= \begin{bmatrix} A_1 \\ A_2 \\ A_3 \end{bmatrix}, \quad A_j = \begin{bmatrix} a_{j0} \\ a_{j1} \\ \vdots \\ a_{jN} \end{bmatrix}, \quad j = 1, 2, 3.
 \end{aligned}$$

By substituting the collocation points defined by

$$s_i = a + \frac{b-a}{N}i, \quad (i = 0, 1, \dots, N),$$

into Eq. (11) along with (14), we gain the system of matrix equations

$$Y'(s_i) = P(s_i)Y(s_i) + G(s_i), \quad (i = 0, 1, \dots, N),$$

or briefly, the fundamental matrix equation

$$Y' = PY + G \Rightarrow (\overline{BD} - \overline{PB})A = G, \tag{15}$$

where

$$P = \begin{bmatrix} P(s_0) & 0 & \dots & 0 \\ 0 & P(s_0) & \dots & 0 \\ \vdots & \vdots & \ddots & \vdots \\ 0 & 0 & \dots & P(s_N) \end{bmatrix}, \quad G = \begin{bmatrix} G(s_0) \\ G(s_1) \\ \vdots \\ G(s_N) \end{bmatrix},$$

$$Y = \begin{bmatrix} Y(s_0) \\ Y(s_1) \\ \vdots \\ Y(s_N) \end{bmatrix} = \begin{bmatrix} \bar{B}(s_0)A \\ \bar{B}(s_1)A \\ \vdots \\ \bar{B}(s_N)A \end{bmatrix} = \bar{B}A,$$

$$Y'(s) = \begin{bmatrix} Y'(s_0) \\ Y'(s_1) \\ \vdots \\ Y'(s_N) \end{bmatrix} = \begin{bmatrix} \overline{B(s_0)DA} \\ \overline{B(s_1)DA} \\ \vdots \\ \overline{B(s_N)DA} \end{bmatrix} = \overline{BDA}.$$

In Eq. (13), the full dimensions of the matrices \overline{BD} , P , \bar{B} , A , and G are $3(N+1) \times 3(N+1)$, $3(N+1) \times 3(N+1)$, $3(N+1) \times 3(N+1)$, $3(N+1) \times 1$ and $3(N+1) \times 1$, respectively.

The fundamental matrix equation (15) corresponding to Eq. (4) can be written in the compact form

$$WA = G \text{ or } [W; G], \tag{16}$$

where

$$W = \overline{BD} - \overline{PB} = [w_{pq}]; \quad p, q = 1, 2, \dots, 3(N+1).$$

The matrix equation (16) corresponds to a system of a linear algebraic equations in $3(N+1)$ unknown Bernoulli coefficients.

By using the initial conditions defined by (7) and the matrix relation $Y(s)$ in (14), we obtain the matrix form for the conditions as

$$\bar{B}(a)A = \lambda \Leftrightarrow [\bar{B}(a); \lambda], \tag{17}$$

where

$$\bar{B}(a) = \begin{bmatrix} B(a) & 0 & 0 \\ 0 & B(a) & 0 \\ 0 & 0 & B(a) \end{bmatrix}, \quad \lambda = \begin{bmatrix} \lambda_1 \\ \lambda_2 \\ \lambda_3 \end{bmatrix}.$$

Consequently, we obtain the new following augmented matrix for the problem (6)-(7) by replacing the row matrices (17) with the rows involving the coefficients a_{10}, a_{20} and a_{30} of the matrix (16):

$$[\tilde{W}; \tilde{G}] \text{ or } \tilde{W}A = \tilde{G}. \tag{18}$$

If $\text{rank } \tilde{W} = \text{rank } [\tilde{W}; \tilde{G}] = N+1$, the unknown Bernoulli coefficient matrix can be written as $A = (\tilde{W})^{-1} \tilde{G}$ and the approximate solution in the Bernoulli matrix form is obtained as

$$Y(s) = \bar{B}(s)A,$$

or

$$y_j(s) \cong \sum_{n=0}^N a_{jn} B_n(s).$$

3. Results and Discussion

In this section two examples are given to demonstrate the applicability of this method. These examples have been calculated by using Matlab.

Example 1. Consider the system of first-order linear differential equations

$$\begin{aligned}
 \frac{dy_1}{dx} &= xy_2(x) - x^2 \\
 \frac{dy_2}{dx} &= -xy_1(x) + y_3(x) \\
 \frac{dy_3}{dx} &= -y_2(x) + x + 1
 \end{aligned} \quad 0 \leq x \leq 1, \tag{19}$$

with the initial conditions $y_1(0) = 1, y_2(0) = 0, y_3(0) = 1$ which has the exact solution $y_1(x) = 1, y_2(x) = x, y_3(x) = x + 1$.

The approximate solution is $y_j(s) = \sum_{n=0}^2 a_{jn} B_n(s)$,
 $j=1,2,3$. The collocation points for $N=2$ are
 computed as $\left\{x_1=0, x_2=\frac{1}{2}, x_3=1\right\}$.

The fundamental matrix equation is

$$WA = (\overline{BD} - P\overline{B})A = G,$$

where

$$\overline{BD} = \begin{bmatrix} 0 & 1 & -1 & 0 & 0 & 0 & 0 & 0 & 0 \\ 0 & 0 & 0 & 0 & 1 & -1 & 0 & 0 & 0 \\ 0 & 0 & 0 & 0 & 0 & 0 & 0 & 1 & -1 \\ 0 & 1 & 0 & 0 & 0 & 0 & 0 & 0 & 0 \\ 0 & 0 & 0 & 0 & 1 & 0 & 0 & 0 & 0 \\ 0 & 0 & 0 & 0 & 0 & 0 & 0 & 1 & 0 \\ 0 & 1 & 1 & 0 & 0 & 0 & 0 & 0 & 0 \\ 0 & 0 & 0 & 0 & 1 & 1 & 0 & 0 & 0 \\ 0 & 0 & 0 & 0 & 0 & 0 & 0 & 1 & 1 \end{bmatrix},$$

$$P = \begin{bmatrix} 0 & 0 & 0 & 0 & 0 & 0 & 0 & 0 & 0 \\ 0 & 0 & 1 & 0 & 0 & 0 & 0 & 0 & 0 \\ 0 & -1 & 0 & 0 & 0 & 0 & 0 & 0 & 0 \\ 0 & 0 & 0 & 0 & \frac{1}{2} & 0 & 0 & 0 & 0 \\ 0 & 0 & 0 & -\frac{1}{2} & 0 & 1 & 0 & 0 & 0 \\ 0 & 0 & 0 & 0 & -1 & 0 & 0 & 0 & 0 \\ 0 & 0 & 0 & 0 & 0 & 0 & 0 & 1 & 0 \\ 0 & 0 & 0 & 0 & 0 & 0 & -1 & 0 & 1 \\ 0 & 0 & 0 & 0 & 0 & 0 & 0 & -1 & 0 \end{bmatrix},$$

$$\overline{B} = \begin{bmatrix} 1 & -\frac{1}{2} & \frac{1}{6} & 0 & 0 & 0 & 0 & 0 & 0 \\ 0 & 0 & 0 & 1 & -\frac{1}{2} & \frac{1}{6} & 0 & 0 & 0 \\ 0 & 0 & 0 & 0 & 0 & 0 & 1 & -\frac{1}{2} & \frac{1}{6} \\ 1 & 0 & -\frac{1}{12} & 0 & 0 & 0 & 0 & 0 & 0 \\ 0 & 0 & 0 & 1 & 0 & -\frac{1}{12} & 0 & 0 & 0 \\ 0 & 0 & 0 & 0 & 0 & 0 & 1 & 0 & -\frac{1}{12} \\ 1 & \frac{1}{2} & \frac{1}{6} & 0 & 0 & 0 & 0 & 0 & 0 \\ 0 & 0 & 0 & 1 & \frac{1}{2} & \frac{1}{6} & 0 & 0 & 0 \\ 0 & 0 & 0 & 0 & 0 & 0 & 1 & \frac{1}{2} & \frac{1}{6} \end{bmatrix}.$$

The augmented matrix for this fundamental matrix equation is calculated as

$$[W;G] = \begin{bmatrix} 0 & 1 & -1 & 0 & 0 & 0 & 0 & 0 & 0 & ; & 0 \\ 0 & 0 & 0 & 0 & 1 & -1 & -1 & \frac{1}{2} & -\frac{1}{6} & ; & 0 \\ 0 & 0 & 0 & 1 & -\frac{1}{2} & \frac{1}{6} & 0 & 1 & -1 & ; & 1 \\ 0 & 1 & 0 & -\frac{1}{2} & 0 & \frac{1}{24} & 0 & 0 & 0 & ; & -\frac{1}{4} \\ \frac{1}{2} & 0 & -\frac{1}{24} & 0 & 1 & 0 & -1 & 0 & \frac{1}{12} & ; & 0 \\ 0 & 0 & 0 & 1 & 0 & -\frac{1}{12} & 0 & 1 & 0 & ; & \frac{3}{2} \\ 0 & 1 & 1 & -1 & -\frac{1}{2} & -\frac{1}{6} & 0 & 0 & 0 & ; & -1 \\ 1 & \frac{1}{2} & \frac{1}{6} & 0 & 1 & 1 & -1 & -\frac{1}{2} & -\frac{1}{6} & ; & 0 \\ 0 & 0 & 0 & 1 & \frac{1}{2} & \frac{1}{6} & 0 & 1 & 1 & ; & 2 \end{bmatrix}.$$

From equation (17), we obtain the matrix form of the initial conditions

$$[\overline{B}(0); \lambda] = \begin{bmatrix} 1 & -\frac{1}{2} & \frac{1}{6} & 0 & 0 & 0 & 0 & 0 & 0 & ; & 1 \\ 0 & 0 & 0 & 1 & -\frac{1}{2} & \frac{1}{6} & 0 & 0 & 0 & ; & 0 \\ 0 & 0 & 0 & 0 & 0 & 0 & 1 & -\frac{1}{2} & \frac{1}{6} & ; & 1 \end{bmatrix}.$$

From equation (18), the new augmented matrix based on the conditions is calculated as

$$[\tilde{W}; \tilde{G}] = \begin{bmatrix} 1 & -\frac{1}{2} & \frac{1}{6} & 0 & 0 & 0 & 0 & 0 & 0 & ; & 1 \\ 0 & 0 & 0 & 1 & -\frac{1}{2} & \frac{1}{6} & 0 & 0 & 0 & ; & 0 \\ 0 & 0 & 0 & 0 & 0 & 0 & 1 & -\frac{1}{2} & \frac{1}{6} & ; & 1 \\ 0 & 1 & 0 & -\frac{1}{2} & 0 & \frac{1}{24} & 0 & 0 & 0 & ; & -\frac{1}{4} \\ \frac{1}{2} & 0 & -\frac{1}{24} & 0 & 1 & 0 & -1 & 0 & \frac{1}{12} & ; & 0 \\ 0 & 0 & 0 & 1 & 0 & -\frac{1}{12} & 0 & 1 & 0 & ; & \frac{3}{2} \\ 0 & 1 & 1 & -1 & -\frac{1}{2} & -\frac{1}{6} & 0 & 0 & 0 & ; & -1 \\ 1 & \frac{1}{2} & \frac{1}{6} & 0 & 1 & 1 & -1 & -\frac{1}{2} & -\frac{1}{6} & ; & 0 \\ 0 & 0 & 0 & 1 & \frac{1}{2} & \frac{1}{6} & 0 & 1 & 1 & ; & 2 \end{bmatrix}.$$

Solving this system, the unknown Bernoulli coefficient matrix is obtained as

$$A = \left[1 \ 0 \ 0 \ \frac{1}{2} \ 1 \ 0 \ \frac{3}{2} \ 1 \ 0 \right]^T.$$

By substituting the Bernoulli coefficient matrix into equation (12), we obtain the approximate solution set $y_1(x)=1, y_2(x)=x, y_3(x)=x+1$ which is the exact solution.

Example 2. Consider the curve $\alpha : [0, 2] \rightarrow E_1^3$ given by

$$\alpha(s) = \left(\frac{s^3}{3} + s, \frac{s^3}{3}, \frac{s^2}{\sqrt{2}} \right).$$

The system of differential equations in the normal form corresponding to curve α is as follows [24]

$$\begin{aligned} \lambda_1'(s) &= -\sqrt{2} \cos(\sqrt{2}s) \lambda_2(s) + \sqrt{2} \sin(\sqrt{2}s) \lambda_3(s) \\ \lambda_2'(s) &= -\sqrt{2} \cos(\sqrt{2}s) \lambda_1(s) \\ \lambda_3'(s) &= \sqrt{2} \sin(\sqrt{2}s) \lambda_1(s) \end{aligned} \quad (20)$$

The approximate solution set of this problem is solved using Bernoulli Collocation method with the initial conditions $\lambda_1(0) = 1$, $\lambda_2(0) = 2$ and $\lambda_3(0) = 3$. For initial conditions value of distance d is

$$d = \sqrt{-\lambda_1^2 + \lambda_2^2 + \lambda_3^2} = \sqrt{12} \cong 3.464101615. [16]$$

Solving the problem (20) in the same way as Section 2 for $N = 3$, we get

$$\begin{aligned} \lambda_1(s) &= 11.1592106s^3 - 15.4680213s^2 + \\ &18.7854967s + 0.999999995 \\ \lambda_2(s) &= 10.77765s^3 - 26.4167678s^2 + \\ &15.1614944s + 2 \\ \lambda_3(s) &= 10.1776605s^3 - 13.7259918s^2 + \\ &17.6088868s + 2.99999997. \end{aligned}$$

Hence the value of distance d for obtained approximate solution is

$$d = \sqrt{-\lambda_1^2 + \lambda_2^2 + \lambda_3^2} = \sqrt{12} \cong 3.464101615 .$$

Let's briefly summarize the results given in this article as follows:

In section 1, the problem and Bernoulli polynomials have been introduced. In section 2, the matrix relations of the given problem has been obtained and Bernoulli matrix method has been developed. In section 3, two examples have been considered to demonstrate accuracy of the method. In section 4, obtained results have been examined and the advantage of the method have been highlighted.

4. Conclusion

In this study, system of Frenet-Like differential equations which arise in differential geometry as a model for linear equation systems are discussed. To solve this equation system, a numerical method has been developed. This method is based on Bernoulli polynomials and collocations points. To demonstrate the applicability of the present method, two examples have been considered. Obtained results have been showed that the method is suitable for the solutions of

differential equation systems. One of the important advantages of this method is that solutions are obtained very easily and practically by using computer programs. Since linear differential equations are encountered in many physics, chemistry, biology and engineering problems, this method can be extended another models with small modifications, which is another advantage of the method.

Author's Contributions

Kübra Erdem Biçer: Made literature search, performed numerical examples.

Mehmet Sezer: Supervised the manuscript and drafted the manuscript.

Mustafa Kazaz: Helped in results interpretation, performed the analysis.

Ethics

There are no ethical issues after the publication of this manuscript.

References

1. Dannon, V. 1981. Integral Characterizations and Theory of Curves. *Proc. Amer. Math. Soc.*; 4: 600–603.
2. Sezer, M. 1989. Differential Equations and Integral Characterizations for E4- Spherical Curves. *Doga Tr. J. Math.*; 13: 125–131.
3. Köse, Ö. 1986. On Space Curves of Constant Breadth. *Doga Tr. J. Math.*; 10: 11–14.
4. Sezer, M. 1989. Differential Equations Characterizing Space Curves of Constant Breadth and A Criterion for These Curves. *Doga Tr. J. Math.*; 13: 70–78.
5. Do Carmo, MP. *Differential Geometry of Curves and Surfaces.* Prentice Hall, Inc. Englewood Cliffs, 1976.
6. Paşalı Atmaca, S, Akgüller, Ö, Sezer, M. 2013. Integral Characterization of a System of Differential Equations and Applications. *Nonl. Analysis and Differential Equations*; 1(2): 57-66.
7. Çetin, M, Tunçer, Y, Karacan, MK. 2014. Smarandache Curves According to Bishop Frame in Euclidean 3-Space. *Gen. Math. Notes*; 20(2): 50-66.
8. Erdem, K, Yalçınbaş, S. 2012. Numerical approach of linear delay difference equations with variable coefficients in terms of Bernoulli polynomials. *AIP Conf. Proc.*; 1493: 338-344.
9. Erdem, K, Yalçınbaş, S. 2012. Bernoulli Polynomial Approach to High-Order Linear Differential Difference Equations. *AIP Conf. Proc.*; 1479: 360-364.
10. Erdem, K, Yalçınbaş, S, Sezer, M. 2013. A Bernoulli approach with residual correction for solving mixed linear Fredholm integro-differential-difference equation. *Journal of Difference Equations and Applications*; 19(10): 1619-1631.
11. Erdem, K, Yalçınbaş, S. 2016. A matrix approach to solving hyperbolic partial differential equations using Bernoulli polynomials. *Filomat*; 30(4): 993–1000.

12. Erdem, K, Yalçınbaş, S. 2017. Numerical Solutions for Helmholtz Equations using Bernoulli Polynomials. *AIP Conf. Proc.*; 1863: 300021-1–300021-4.
13. Erdem Biçer, K, Sezer, M. 2017. Bernoulli Matrix-Collocation Method for solving General Functional Integro-Differential Equations with Hybrid Delays. *Journal of Inequalities and Special Functions*; 8(3): 85-99.
14. Ahmad H, Khan, TA, Durur, H, İsmail, GM, Yokus, A. 2021. Analytic approximate solutions of diffusion equations arising in oil pollution. *Journal of Ocean Engineering and Science*; 6(1): 62-69.
15. Rasool, G, Zhang, T, Shafiq, A, Durur, H. 2019. Influence of chemical reaction on Marangoni convective flow of nanofluid in the presence of Lorentz forces and thermal radiation: A numerical investigation. *Journal of Advances in Nanotechnology*; 1(1): 32.
16. Ahmad, H, Rafiq, M, Cesarano, C, Durur, H. 2020. Variational iteration algorithm-I with an auxiliary parameter for solving boundary value problems. *Earthline Journal of Mathematical Sciences*; 3(2): 229-247.
17. Yavuz, M, Yokus, A. 2020. Analytical and numerical approaches to nerve impulse model of fractional-order. *Numerical Methods for Partial Differential Equations*; 36(6): 1348-1368.
18. Durur, H, Senol, M, Kurt, A, Tasbozan, O. 2019. Approximate solutions of the time fractional Kadomtsev–Petviashvili equation with conformable derivative. *Erzincan Univ. J. Sci. Technol*; 12(2): 796-806.
19. Yokus, A. 2020. Truncation and convergence dynamics: KdV burgers model in the sense of Caputo derivative. *Boletim da Sociedade Paranaense de Matematica*; doi: 10.5269/bspm.47472.
20. Rasool, G, Shafiq, A, Durur, H. 2020. Darcy-Forchheimer relation in Magnetohydrodynamic Jeffrey nanofluid flow over stretching surface. *Discrete & Continuous Dynamical Systems-S*; doi: 10.3934/dcdss.2020399.
21. Apostol, TM. Introduction to Analytic Number Theory, Springer-Verlag, New York, 1976, pp 264-267.
22. Ates, BY, Çetin, M, Sezer, M. 2015. Taylor polynomial approach for systems of linear differential equations in normal form and residual error estimation. *NTMSCI*; 3: 116-128.
23. Sahiner, B, Sezer, M. 2018. Determining constant breadth curve mate of a curve on a surface via Taylor collocation method. Determining constant breadth curve mate of a curve on a surface via Taylor collocation method. *NTMSCI*; 6(3): 103-115.
24. Cetin, M. Sabit Genişlikli Eğriler Ve Küresel Eğrilerin Diferensiyel Karakterizasyonları. PhD Thesis, Manisa Celal Bayar University, The Institute of Natural and Applied Sciences, 2015.

Comparison of Cellular Autofluorescence Patterns of Two Model Microalgae by Flow Cytometry

Ugur Uzuner^{1*} 

¹Department of Molecular Biology and Genetics, Faculty of Science, Karadeniz Technical University, Trabzon, TURKEY

*uguruzuner@ktu.edu.tr

*Orcid: 0000-0002-5308-3730

Received: 19 November 2020

Accepted: 19 April 2021

DOI: 10.18466/827615

Abstract

Microalgae are widely used in biotechnological research, especially for the production of biochemical compounds, antioxidants, secondary metabolites, pigments, carbohydrates, proteins and lipids. Various analytical methods are needed throughout both experimental and downstream processing of industrial microalgae products. As one of these methods, flow cytometry is an advantageous option for detecting fluorescently labeled recombinant proteins, lipids and metabolic compounds. It is important to take into account the autofluorescent properties of specific compartments of target cells to well establish a distinct labeling protocol during such analytical processes. Because the amount of autofluorescence may interfere with the fluorescent signal detection of specifically labeled protein or lipid content, this can prevent the precise signal detection of labeled molecules. Furthermore, it can lead to an overestimation of the amount of labeled compounds in the cells. In this study, the autofluorescent properties of two freshwater model microalgae *Chlamydomonas reinhardtii* (CC-124) and *Chlorella vulgaris* (CV-898), both of which are predominantly used in industry, were examined by flow cytometry measurements. The experimental findings revealed that fluorescent channel-2 (FL2-H) stands as the most suitable channel to achieve minimal autofluorescence of both CC-124 and CV-898 microalgae strains. The obtained results highlight that one should pay attention to the autofluorescence signals in CC-124 and CV-898 cell lines during the flow cytometry-based detection of biological products when deciding on fluorophore.

Keywords: autofluorescence, cellular morphology, flow cytometry, microalgae

1. Introduction

Microalgae are widely preferred eukaryotic microorganisms in biotechnology as they can produce health promoting lipids, antioxidants, polysaccharides, proteins, secondary metabolites, vitamins and pigments [1]. As the evolutionary ancestors of terrestrial plants, they can be easily cultivated at laboratory conditions in the presence of natural sunlight, atmospheric CO₂, varieties of different low-cost carbon sources and the infinitesimal amounts of trace elements [2]. They currently provide numerous advantages to industrial biotechnology as food and feed supplies with high protein content, feedstocks for different biofuels production processes and sustainable bioremediation agents for municipal and urban wastewaters, all of which make microalgae essential for next generations [3, 4]. As microalgae genome manipulation tools are pretty much

well established, the metabolic engineering efforts on industrially promising microalgae strains

become relatively common [5, 6]. Microalgae are of growing interest towards various mass production systems, particularly for bioenergy, lucrative metabolites, antioxidants, nutraceuticals and pharmaceuticals [7, 8]. In addition, the specific use of photosynthetic microalgae as recombinant production hosts comprises the mass production of value-added compounds, anticarcinogenic and antimicrobial drugs, monoclonal antibodies, pharmaceutical proteins, vaccines, drug additives and various compounds used in cosmetics [9, 10]. On the other hand, it is very important to carry out comprehensive analytical, biochemical and molecular analyzes on newly discovered microalgae strains with reliable analytical methods to reveal their industrial use and commercialization potentials biotechnologically. [11].

During cultivation and downstream processes, the native biological characteristics of microalgae can be disclosed by employing different analytical methods, such as fluorescence and/or electron microscopy, quantitative metric measurements, multi-dimensional single-cell analysis and molecular biology-based diagnostic tools [12]. Recently, different cell sorting mechanisms combined with flow cytometry have been developed and successfully applied to microalgae cultures to eliminate various culture contaminants including bacteria [13]. Electrical microfluidics chips with advanced separation and recognition characteristics were also adapted for microalgae cultures to recognize, label and eventually eliminate culture contaminants [14]. In addition, direct electrical detection of a single bacterium in drinking water could be a highly practical technique for ensuring the contamination-free maintenance and sustainability of open pond microalgae production systems in the future. [15].

Flow cytometry is one of the high-throughput instruments to quantitatively examine the cell size, granularity, heterogeneity of microalgae cells and related culture populations using fluorescence beams [16]. Flow cytometry provides visualization and classification of cells within morphological shapes and analysis of fluorophore-tagged signals of the molecule of interest such as proteins, carbohydrates and lipids. Preparation of cells for analysis by flow cytometry is performed based on immunolabeling approaches. One of the foremost methodological key points during standard flow cytometry analysis is to initially detect the autofluorescence of cells. Autofluorescence is defined as inherent cellular fluorescence derived by the emission of natural compounds within cells, such as chlorophyll and NADH [17]. Such interference of autofluorescence with the specific label was also reported from certain types of mammalian cells [18]. However, to the best of our knowledge, no scientific report has yet been released regarding the natural autofluorescence spectra of the freshwater microalgae strains examined, suggesting the requirement of an optimization step during the flow cytometry-based experimental and analytical processes. This study thus aimed to unravel the cellular autofluorescence spectra of two model microalgae *Chlamydomonas reinhardtii* (CC-124) and *Chlorella vulgaris* Beijerinck (CV-898) cells.

2. Materials and Methods

2.1. Microalgae Culturing and Flow Cytometry Analysis

Chlamydomonas reinhardtii (CC-124: CCALA No: 928) and *Chlorella vulgaris* Beijerinck (CV-898: CCALA No: 898) strains were obtained from Culture Collection of Autotrophic Organisms (CCALA) at Dukelska, Czech Republic. Both strains were immediately enriched in TAP broth or agar plates. 1×10^6 microalgae cells were

then taken and incubated within 100 ml modified TAP (Tris-Acetate-Phosphate) medium on an orbital shaker at room temperature and 120 rpm shaking speed for 5 days. At least 500.000 cells (counted by Countess II FL Automated Cell Counter, Thermofisher), in the presence of over 96% cell viability detected by hemacytometer-based counting, either in the phosphate-buffered saline buffer (1xPBS) or in TAP media were run by flow cytometer, C6 Accuri (from BD Biosciences). Cells were visualized by forward scatter (FSC)-side scatter (SSC) dot plot, and then analyzed by fluorescence channels; FL1-H, FL2-H, FL3-H and FL4-H. Table 1 reveals the excitation and emission values and filters for each channel. 1xPBS and TAP medium alone were also run to understand the background fluorescence of the cell suspensions. Figure 1 represents the wavelengths of each channel. The cell morphology was assessed by FSC (X-axes) and SSC (Y-axes) values (as mean, geometric mean and median), representing the cell size and granularity, respectively. The fluorescence signals of at least 500.000 cells were collected through the employment of a 488 nm laser beam and further analyzed using different filters as shown in Table 1. The autofluorescence patterns of gated cells (P1) were also revealed in the charts by fluorescence channels (FL1-H, FL2-H, FL3-H and FL4-H). Both PBS and TAP medium were also analyzed as blank controls to the cell samples. At least 10.000 events were analyzed for each triplicate experimental run.

Table 1. Excitation and emission of fluorescence channels

	FL1-H	FL2-H	FL3-H	FL4-H
Excitation (nm)	488	488	650	470
Emission (nm)	500-550	550-600	650-700	650
Filter	533/30 (530 BP)	585/40 (585 BP)	670 LP	675/25 (675 BP)

3. Results and Discussion

Recent advances in recombinant DNA technology and genome editing tools have increased R&D initiatives on microalgae strains with renewable, sustainable and economic potentials towards versatile production of various value-added products, secondary metabolites, natural pigments, antioxidants, hydrocarbons, biofuels and derivatives. On the other hand, innovative approaches mostly relying on metabolic engineering and systems biology to develop microalgae strains with improved properties yield abundant recombinants that necessitate extensive screening efforts for targeted product(s). Comparative screening and quantitative analysis of natural and/or recombinantly engineered microalgae cells is of paramount importance for the final selection and full characterization of the most promising strains. In this regard, flow cytometry is a simple

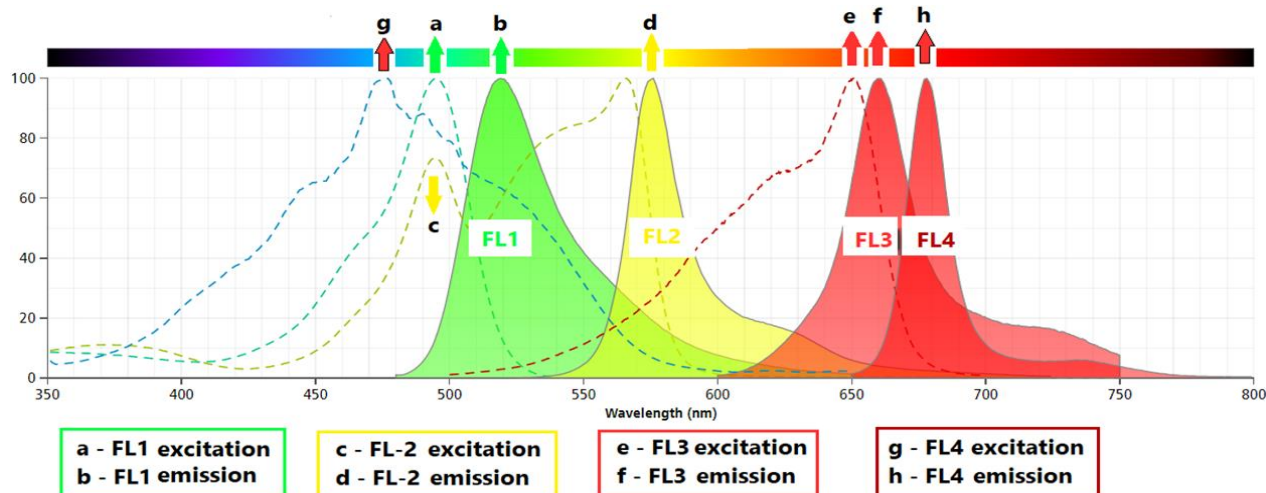


Figure 1. Representative wavelengths for emission and excitation of fluorescence channels 1, 2, 3 and 4 of BD Accuri C6 instrument using FITC, PE, APC and PerCP, respectively (*modified from BD Biosciences's web site*). The spectra can be modified according to dye type.

operational and analytical platform for the quantification of various microalgae cell components and related by-products. To specifically analyze, label and even separate microalgae single cells, numerous high throughput methods with advanced analytical potentials including flow cytometry, electrical flow cytometry, electrical microfluidics chip and fluorescence-activated cell sorting have recently been reported [14, 15, 19, 20]. Among them, flow cytometry allows automatic, low-cost, high-speed and simultaneous analysis of multiple parameters of microalgae cells through qualitative and quantitative measurements of biological and physical characteristics.

Two model microalgae isolates with the adaptation to the cool temperate environments were examined to identify their cellular autofluorescence patterns by flow cytometer, C6 Accuri. The comparative run revealed that CC-124 microalgae cells were larger than CV-898 by the mean of events at FSC axes and the granularity of CC-124 was more intense than CV-898 by the mean of events at SSC axes. The median values were close to the maximum values of means (Figure 2a, b). Cell size was proportional to the granularity. Therefore, because the cell sizes were high, the granularity was also large. Microalgae were also routinely evaluated for cellular dry weight (CDW) to highlight biomass productivity. Therefore, determination of cell granularity seems important for understanding biomass production capacity.

The granularity can change in terms of growth phases such as early and late exponential stages. The cells used in this study were mixed at different growth phases to reveal a general pattern of cell morphology. A study revealed the differences in CDW between some microalgae [1], but to the best of knowledge, there is no study showing the cell size differences through cell granularity by SSC dot plot of flow cytometry analysis.

Some studies use microscopy to understand the sizes of cells [21]. In this scenario, high-resolution microscopy equipped with at least 63X objective might be practical for better visualization of microalgae cells. Therefore, we suggest that microscopies with higher performance could be preferred to perform such comparison comprehensively.

The cellular autofluorescence pattern of the cells was also examined by the implementation of different fluorescence channels. As control, the fluorescence amount of both PBS and microalgae media were firstly detected at a similar range with the cells. We identified that, at FL2-H, PBS is a more suitable environment to run cells in terms of a relatively low level of autofluorescence compared to TAP medium (Figure 3a, b). The lowest fluorescence of both microalgae cells was detected at the FL2-H channel; however, the highest was identified at FL3-H (Figure 3c, d). Experiments need to be adjusted by the subtraction of the mean of fluorescence intensity (MFI) of PBS or TAP medium from the MFI of cells. Image-based [22] or standard flow cytometry [16] are in use to analyze cellular components of microalgae. However, the interference of autofluorescence with the detection of the specific markers of interest was overlooked.

The chlorophyll content of microalgae is one of the main sources of cellular autofluorescence, and fluorescence is used to be measured in cells detected at forward and side scatter plots [23]. As similar, a typical automated cell counter was further optimized for the facilitated quantification of chlorophyll content in microalgae [24]. Nevertheless, our previous work illustrated that although automated cell counter was not favorably effective, flow cytometry-based analysis was revealed as the best analytical instrument to work with microalgae [25], as also commonly stressed by other researchers [26–28].

Flow cytometry is used not only for the detection of fluorescence labeled-components, but also viability detection, biomass estimation, population heterogeneity detection, cell sorting and isolation of axenic algal cultures [29, 30]. Therefore, the elucidation of

autofluorescence patterning in model microalgae is detected by flow cytometry. Recently, the ontological pattern of autofluorescence was also considered to improve spectroscopic methods [31]. In parallel, crucial

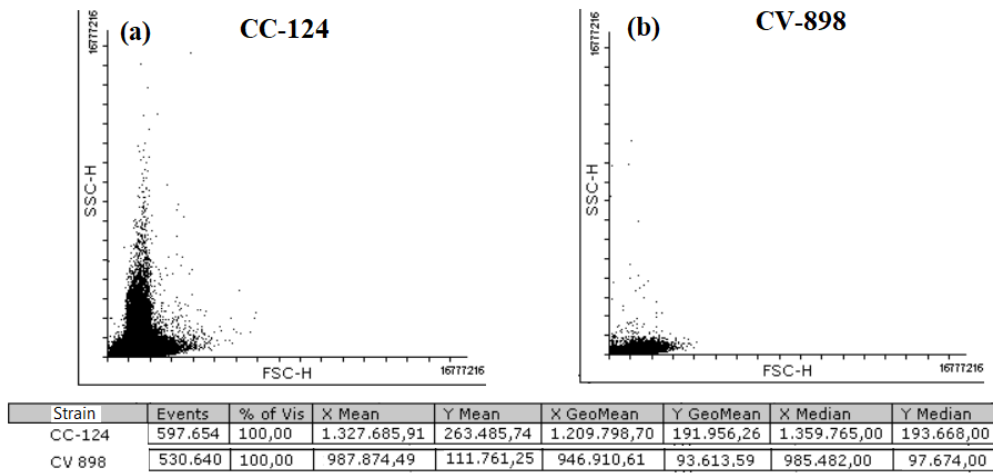


Figure 2. The morphological features of CC-124 (a) and CV-898 (b) by FSC (*forward scatter*) and SSC (*side scatter*) representing cell size and granularity, respectively (X and Y axes were adjusted to 16 million unit).

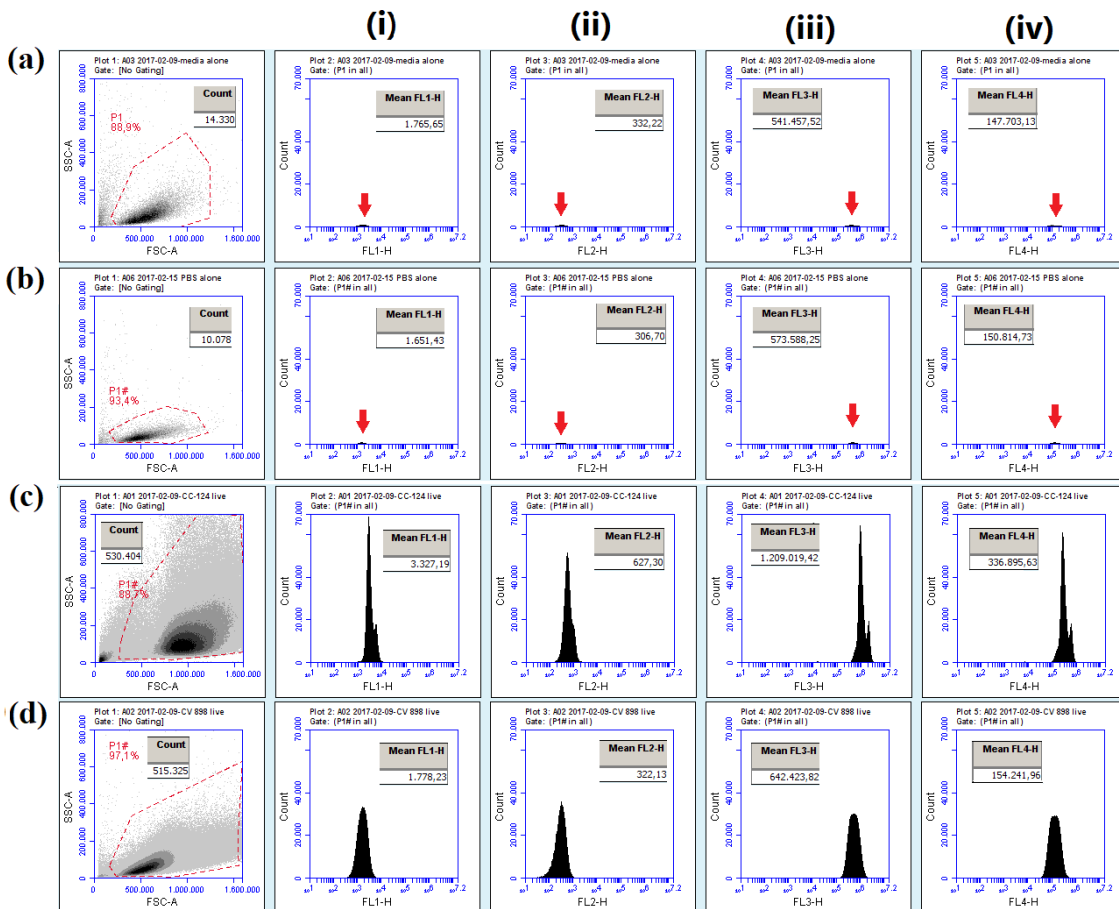


Figure 3. The autofluorescence patterns of TAP medium (a), and PBS buffer (b), CC-124 (c) and CV-898 microalgae cells (d) along with the fluorescence channels (i-iv). (X and Y-axes in cell size (FSC) and granularity (SSC plots) were adjusted to 1.6 million unit).

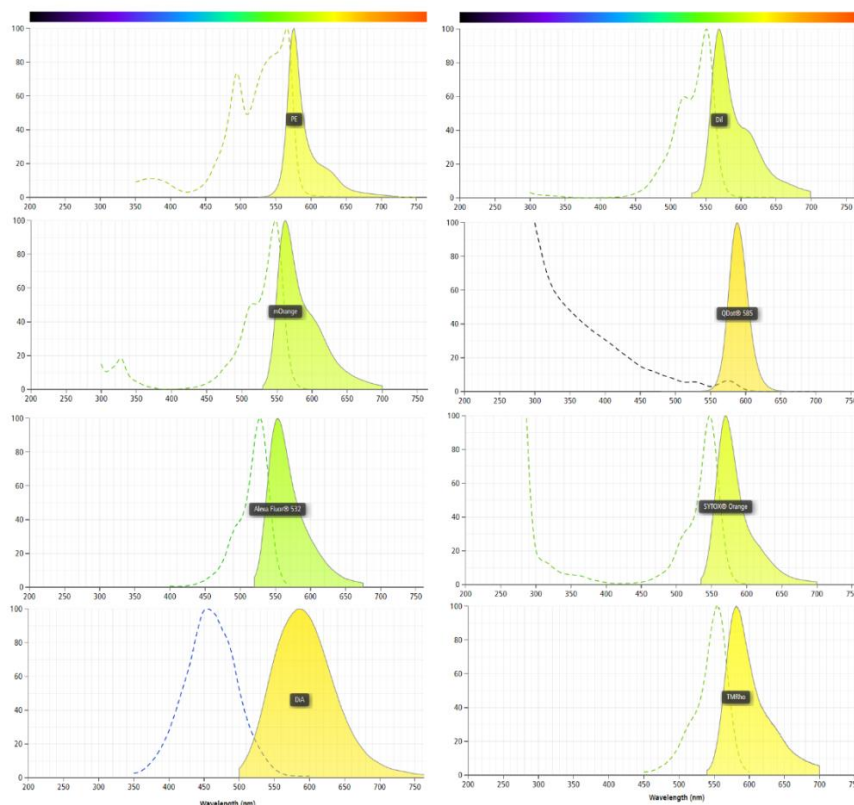


Figure 4. Example wavelengths of some fluorophores given in Table 2.

Table 2. Recommended fluorophores for the signal detection by FL2 channel.

PE	BVU563
mOrange	SYTOX ® Orange
Alexa Fluor ® 532	TMRho
DiA	Kusabira-Orange
Dil	mStrawberry
QDot ® 565	Cy3.5
QDot ® 585	Cy3B
QDot ® 605	Cy3
QDot ® 625	

in terms of the optimization of labeling methods electrophoresis was shown to be a parameter for the investigation of microalgal diversity [32].

Based on the literature, there is no reported study revealing the autofluorescence distributions of microalgae, in particular for both CC-124 and CV-898. These microalgae are of model organisms in industrial biotechnology towards to production of various value-added compounds, proteins, vaccines, biofuels and other bioproducts. Industrially crucial lipids and recombinant proteins as microalgae bioproducts are labeled by fluorophores and flow cytometry can provide cost-effective and handy outputs to disclose these labels and the total amount of bioproducts.

The current findings also suggest that the best strategy to perform any flow cytometry based measurements on both CC-124 and CV-898 model microalgae is to select a fluorophore emitted at fluorescence channel-2. Table 2 exemplifies some of such representative fluorophores. On the other hand, Figure 4 displays the wavelength distributions of some fluorophores given in Table 2, emitting specifically at FL2-H (Figure 4).

4. Conclusion

We found that the minimum fluorescence signal from both model microalgae strains was obtained at only fluorescence channel-2 (FL2-H) of 4 channels. In other words, the obtained results suggest that the most suitable fluorophores for CC-124 and CV-898 cells are the fluorophores emitting at FL2-H. In conclusion, the specific label of interest does not mix with natural signals in both CC-124 and CV-898 cells when the reported results are in consideration. The current knowledge will certainly be practical for the quantitative production of various biomaterials during the versatile biotechnological applications of microalgae.

Acknowledgement

This work was supported by Scientific Research Projects Coordination Unit of Karadeniz Technical University. Project number: FAY-2016-5755. The author thanks to Ramazan ÇAKMAK due to the preparations of microalgae cell cultures and to Prof. Ersan KALAY



allowing to utilize of flow cytometry instrument at the Department of Medical Biology at KTU.

Author's Contributions

Ugur Uzuner: The study was hypothesized, designed, performed and written by Ugur Uzuner.

Ethics

Authors declare that there are no ethical issues related to publication of this manuscript. The performed study is out of scope of any ethical issues.

References

1. Abomohra AE-F, Wagner M, El-Sheekh M, Hanelt D (2013) Lipid and total fatty acid productivity in photoautotrophic fresh water microalgae: screening studies towards biodiesel production. *J Appl Phycol* 25:931–936. <https://doi.org/10.1007/s10811-012-9917-y>
2. Shuba ES, Kifle D (2018) Microalgae to biofuels: 'Promising' alternative and renewable energy, review. *Renewable and Sustainable Energy Reviews* 81:743–755. <https://doi.org/10.1016/j.rser.2017.08.042>
3. Hossain N, Mahlia TMI, Saidur R (2019) Latest development in microalgae-biofuel production with nano-additives. *Biotechnology for Biofuels* 12:125. <https://doi.org/10.1186/s13068-019-1465-0>
4. Torres-Tiji Y, Fields FJ, Mayfield SP (2020) Microalgae as a future food source. *Biotechnology Advances* 41:107536. <https://doi.org/10.1016/j.biotechadv.2020.107536>
5. Fayyaz M, Chew KW, Show PL, et al (2020) Genetic engineering of microalgae for enhanced biorefinery capabilities. *Biotechnology Advances* 43:107554. <https://doi.org/10.1016/j.biotechadv.2020.107554>
6. Kwon YM, Kim KW, Choi T-Y, et al (2018) Manipulation of the microalgal chloroplast by genetic engineering for biotechnological utilization as a green biofactory. *World J Microbiol Biotechnol* 34:183. <https://doi.org/10.1007/s11274-018-2567-8>
7. Yan N, Fan C, Chen Y, Hu Z (2016) The Potential for Microalgae as Bioreactors to Produce Pharmaceuticals. *International Journal of Molecular Sciences* 17:962. <https://doi.org/10.3390/ijms17060962>
8. Jha D, Jain V, Sharma B, et al (2017) Microalgae-based Pharmaceuticals and Nutraceuticals: An Emerging Field with Immense Market Potential. *ChemBioEng Reviews* 4:257–272. <https://doi.org/10.1002/cben.201600023>
9. Szyrka E, Broda D, Oklejewicz B, et al (2020) A Non-Vector Approach to Increase Lipid Levels in the Microalga *Planktochlorella nurekis*. *Molecules* 25: . <https://doi.org/10.3390/molecules25020270>
10. U NM, Mehar JG, Mudliar SN, Shekh AY (2019) Recent Advances in Microalgal Bioactives for Food, Feed, and Healthcare Products: Commercial Potential, Market Space, and Sustainability. *Comprehensive Reviews in Food Science and Food Safety* 18:1882–1897. <https://doi.org/10.1111/1541-4337.12500>
11. Niccolai A, Chini Zittelli G, Rodolfi L, et al (2019) Microalgae of interest as food source: Biochemical composition and digestibility. *Algal Research* 42:101617. <https://doi.org/10.1016/j.algal.2019.101617>
12. Sandmann M, Schafberg M, Lippold M, Rohn S (2018) Analysis of population structures of the microalga *Acutodesmus obliquus* during lipid production using multi-dimensional single-cell analysis. *Scientific Reports* 8:6242. <https://doi.org/10.1038/s41598-018-24638-y>
13. Yuan D, Zhao Q, Yan S, et al (2019) Sheathless separation of microalgae from bacteria using a simple straight channel based on viscoelastic microfluidics. *Lab Chip* 19:2811–2821. <https://doi.org/10.1039/C9LC00482C>
14. Bilican I, Bahadir T, Bilgin K, Guler MT (2020) Alternative screening method for analyzing the water samples through an electrical microfluidics chip with classical microbiological assay comparison of *P. aeruginosa*. *Talanta* 219:121293. <https://doi.org/10.1016/j.talanta.2020.121293>
15. Guler MT, Bilican I (2018) Capacitive detection of single bacterium from drinking water with a detailed investigation of electrical flow cytometry. *Sensors and Actuators A: Physical* 269:454–463. <https://doi.org/10.1016/j.sna.2017.12.008>
16. da Silva TL, Reis A, Medeiros R, et al (2009) Oil production towards biofuel from autotrophic microalgae semicontinuous cultivations monitored by flow cytometry. *Appl Biochem Biotechnol* 159:568–578. <https://doi.org/10.1007/s12010-008-8443-5>
17. Benson RC, Meyer RA, Zaruba ME, McKhann GM (1979) Cellular autofluorescence--is it due to flavins? *J Histochem Cytochem* 27:44–48. <https://doi.org/10.1177/27.1.438504>
18. Uzuner-Celik S, Peters, L, O'Neill C (2016) Quenching of cellular autofluorescence is necessary for specific detection of DNA methylation by flow cytometry compared to microscopy-based analysis. In: *FEBS Journal*. FEBS PRESS, Kusadasi, TURKEY, pp 249–250
19. Patel A, Antonopoulou I, Enman J, et al (2019) Lipids detection and quantification in oleaginous microorganisms: an overview of the current state of the art. *BMC Chemical Engineering* 1:13. <https://doi.org/10.1186/s42480-019-0013-9>
20. Terashima M, Freeman ES, Jinkerson RE, Jonikas MC (2015) A fluorescence-activated cell sorting-based strategy for rapid isolation of high-lipid *Chlamydomonas* mutants. *Plant J* 81:147–159. <https://doi.org/10.1111/tpj.12682>
21. Nezhad FS, Mansouri H (2019) Induction of Polyploidy by Colchicine on the Green Algae *Dunaliella salina*. *Russian Journal of Marine Biology*. <https://doi.org/10.1134/S1063074019020093>
22. Jeon S-M, Kim JH, Kim T, et al (2015) Morphological, Molecular, and Biochemical Characterization of Monounsaturated Fatty Acids-Rich *Chlamydomonas* sp. KIOST-1 Isolated from Korea. *J Microbiol Biotechnol* 25:723–731. <https://doi.org/10.4014/jmb.1412.12056>
23. Takahashi T (2019) Routine Management of Microalgae Using Autofluorescence from Chlorophyll. *Molecules* 24:4441. <https://doi.org/10.3390/molecules24244441>
24. Takahashi T (2018) Applicability of Automated Cell Counter with a Chlorophyll Detector in Routine Management of Microalgae. *Scientific Reports* 8:4967. <https://doi.org/10.1038/s41598-018-23311-8>
25. Koç E, Çelik-Uzuner S, Uzuner U, Çakmak R (2018) The Detailed Comparison of Cell Death Detected by Annexin V-PI Counterstain Using Fluorescence Microscope, Flow Cytometry and Automated Cell Counter in Mammalian and Microalgae Cells. *Journal*



of *Fluorescence* 28:1393–1404. <https://doi.org/10.1007/s10895-018-2306-4>

26. Sonowal S, Chikkaputtaiah C, Velmurugan N (2019) Role of flow cytometry for the improvement of bioprocessing of oleaginous microorganisms. *Journal of Chemical Technology & Biotechnology* 94:1712–1726. <https://doi.org/10.1002/jctb.5914>
27. Bodénès P, Wang H-Y, Lee T-H, et al (2019) Microfluidic techniques for enhancing biofuel and biorefinery industry based on microalgae. *Biotechnology for Biofuels* 12:33. <https://doi.org/10.1186/s13068-019-1369-z>
28. Markina ZhV (2019) Flow Cytometry as a Method to Study Marine Unicellular Algae: Development, Problems, and Prospects. *Russ J Mar Biol* 45:333–340. <https://doi.org/10.1134/S1063074019050079>
29. Hyka P, Lickova S, Přibyl P, et al (2013) Flow cytometry for the development of biotechnological processes with microalgae. *Biotechnology Advances* 31:2–16. <https://doi.org/10.1016/j.biotechadv.2012.04.007>
30. Reimann R, Zeng B, Jakopec M, et al (2020) Classification of dead and living microalgae *Chlorella vulgaris* by bioimage informatics and machine learning. *Algal Research* 48:101908. <https://doi.org/10.1016/j.algal.2020.101908>
31. Hadady H, Redelman D, Hiibel SR, Geiger EJ (2016) Continuous-flow sorting of microalgae cells based on lipid content by high frequency dielectrophoresis. *AIMS Biophysics* 3:398. <https://doi.org/10.3934/biophy.2016.3.398>
32. Grigoryeva N (2019) Self-Fluorescence of Photosynthetic System: A Powerful Tool for Investigation of Microalgal Biological Diversity. *Microalgae - From Physiology to Application*. <https://doi.org/10.5772/intechopen.88785>

A Novel Donor- π -Acceptor Type Sensitizer for Dye Sensitized Photochemical Hydrogen Generation

Emre Aslan^{1*} 

¹ Selcuk University, Department of Biochemistry, Konya, Turkey

*emreaslan89@gmail.com

*Orcid: 0000-0002-7672-2873

Received: 22 December 2020

Accepted: 19 April 2021

DOI: 10.18466/cbayarfb.844704

Abstract

A novel triphenylamine (TPA) based donor- π -acceptor (D- π -A) dye is synthesized and its structural, optical and electrochemical properties are examined by NMR, UV-Vis absorption spectroscopy and cyclic voltammetry methods, respectively. The synthesized D- π -A dye plays a role as a visible light sensitizer to wide bandgap TiO₂ photocatalyst. Photoelectrochemical and photocatalytic hydrogen evolution reaction (HER) are investigated by using D- π -A dye sensitized TiO₂ (Dye/TiO₂) under visible light irradiation in the aqueous triethanolamine (TEOA) sacrificial electron donor medium. Photoelectrochemical properties of Dye/TiO₂ are investigated by using linear sweep voltammetry (LSV) and chronoamperometry (CA) techniques in the aqueous Na₂SO₄/TEOA solution and its transient photoelectrochemical response is reached 90 $\mu\text{A cm}^{-2}$. In addition, photocatalytic hydrogen evolution rates are found out as 0.52 mmol g⁻¹ h⁻¹ and 1.95 mmol g⁻¹ h⁻¹ by using of Dye/TiO₂ and Dye/TiO₂/Pt, respectively, which are obtained by in situ photoreduction of H₂PtCl₆ on the Dye/TiO₂ photocatalyst. The mechanism of photochemical HER is explained by electrochemical band levels of the D- π -A dye and TiO₂ photocatalyst.

Keywords: dye sensitization, donor- π -acceptor dye, hydrogen evolution reaction, photocatalysis, photoelectrochemical

1. Introduction

The first hydrogen evolution study was performed by using TiO₂ in 1972 with photoelectrochemical method [1]. The development of photocatalytic activity of TiO₂ carried out from that day up to the present. However, there are two big drawbacks of TiO₂, which are high charge recombination rate and absorption only UV light due to the having wide band gap [2]. These disadvantages can be figured out by using co-catalysts to separate charges efficiently and visible light sensitizers to absorb having low energy light. Decreasing of recombination rate and increasing charge separation efficiency are generally utilized on metallic or semiconductor co-catalysts. Although semiconductor co-catalysts are hard to utilize in the photocatalytic reactions because it has to adjust their energy band levels for electron transfer mechanism. Yet, metallic co-catalysts are very useful for easy-to-handle for photocatalytic reactions. It can be clearly seen that Pt is the most used and active co-catalyst for the electrocatalytic, photoelectrochemical and photocatalytic hydrogen evolution reaction (HER) [3]. Wide band gap semiconductor such as TiO₂, ZnO etc.

can be used for water splitting to produce both oxygen and hydrogen under high energy light illumination. However, they are very limited to excite by solar spectrum due to their wide band gap. In order to excite these semiconductors for visible-light-driven water splitting can be modified by doping an ion to narrow the band gap or developing alloys to control the band structure. Another effective approach for harvesting more solar irradiation is the utilization of dye sensitizer. Dye sensitized semiconductor for water splitting by using Ru(bpy)₃²⁺ sensitized Pt/TiO₂/RuO₂ derivatives for the first time [4]. In addition, metal centered porphyrin and phthalocyanine analogues common studied for the photocatalytic reactions due to the high absorption of solar spectrum and adjustable energy levels [5, 6]. Then, metal-free sensitizers have been recently developed for the photocatalytic reactions because of its tunable structure and light absorption region, variety and low-cost. Especially, xanthene dyes and its derivatives have been utilized for photocatalytic hydrogen evolution as the efficient and stable sensitizers [7-9]. Xanthene dyes absorb solar light between 400–600 nm at the 490–560 nm absorption peaks, which is similar to Ru-complex dyes, as alternatives to expensive

Ru-complexes. They found that heavy-halogenated xanthenes have high quantum efficiency for hydrogen evolution, however, they tend to photodehalogenate and instabilities [10]. Due to the increasing photocatalytic activities and stabilities, new class of sensitizers, donor- π -acceptor (D- π -A) dyes developed. They have high intermolecular charge transfer (ICT) ability and configurable absorption, which can be provided high photocatalytic efficiencies and absorption of solar spectrum [11-14]. Recently, donor- π -acceptor (D- π -A) dyes great attention for the both dye sensitized solar cells (DSSC) and photochemical energy conversion reactions because of the mentioned properties above. The high ICT performances of D- π -A dyes reduce the recombination rates [11]. Photocatalytic activities of D- π -A dyes can be changed by different structural properties such as hydrophilicity and steric effect, the amount of dye load, spacer length and the number of anchoring groups of dyes [15-20]. D- π -A dyes consisted of donor groups, π bridge and acceptor groups. Generally, triphenylamine (TPA) based donor moieties have recently been preferred due to prevent aggregations from its non-planar structures by its ease in oxidation of the nitrogen center and own the ability to transport charge carriers via the radical cation species with high stability [21]. Kang research group investigated photocatalytic HER performance by changing chain length in the EDTA solution and reported the dependence on the hydrophilic/hydrophobic character of the binding group to the TPA donor moieties [15, 17]. Tiwari et al. reported that changing π -spacer groups are effectively prevented the aggregation between dye molecules. In addition it provides an well surface protection, which decrease the charge recombination in photocatalytic HER [22]. Li et al. examined by changing of different electronegativities of atom in the π -spacer groups and figured out having high electronegative atoms increased photocatalytic activity [23]. Dessi et al. investigated that photocatalytic HER performances of TPA based D- π -A dyes are improved by increasing donor moieties with the hexyloxy chains attached to the on its terminal TPA group [24]. Moreover, our research group were reported TPA based D- π -A dye sensitized TiO₂ photocatalysts for photocatalytic and photoelectrochemical hydrogen evolution in the triethanolamine (TEOA) sacrificial electron donor media under solar irradiation [25-28]. In these works, firstly, photocatalytic and photoelectrochemical activities on the HER were examined in the absence and presence of extra electron donating two hexyloxy groups on the TPA. Herein, dye without hexyloxy groups displayed more photochemical activity due to its advanced optical absorption and ICT properties [25]. Then, the effect of π -spacer group has investigated in the photocatalytic HER and figured out that adding π -spacer group eventuated higher photocatalytic HER activity [26]. Finally, the very similar TPA based D- π -A dyes were studied by our research group and examined the effect of acceptor and

spacer group on the photocatalytic and photoelectrochemical HER activities. Here, having high electronegativity of an atom in the spacer group increased the photochemical HER activity [27]. In addition, while it suggested that increasing the acceptor strength raise the photocatalytic HER performance, adversely affect the HER activity because it give rise to aggregation of dyes on the TiO₂ photocatalyst [28]. In this study, a novel donor- π -acceptor (D- π -A) dye synthesized for the photochemical hydrogen generation from water splitting. Optical and electrochemical properties of the synthesized D- π -A dye were investigated in order to explain the mechanism of photocatalytic hydrogen evolution. D- π -A dye was used to sensitize TiO₂ photocatalyst. Hydrogen evolution is examined by using photoelectrochemical and photocatalytic methods in the presence of triethanolamine (TEOA) as a sacrificial electron donor under visible light illumination.

2. Materials and Methods

2.1. Materials

All solvents and reagents were purchased as puriss quality. Dichloromethane (CH₂Cl₂), chloroform (CHCl₃), n-hexane, tetrahydrofuran (THF), 1,2-dimethoxyethane (DME), [1,10-bi(diphenylphosphino)ferrocene]dichloro palladium (II) and tetrabutylammonium hexafluorophosphate (Bu₄NPF₆) were supplied from Sigma-Aldrich. Potassium carbonate and potassium hydroxide were purchased from Riedel-de Haen. Column chromatography was carried out by using Merck silica gels (230–400 mesh). Acetonitrile (ACN), tetrahydrofuran (THF), triethanolamine (TEOA), hydrochloric acid (HCl), sodium hydroxide (NaOH) and sodium sulfate (Na₂SO₄) were obtained by Merck for hydrogen generation experiments.

2.2. Synthesis of D- π -A dye

2.2.1. Synthesis of 4'-{6-[5-(4-{bis[4-(hexyloxy)phenyl]amino}phenyl)-4-(2-ethylhexyl)-2-thienyl]-1,2,4,5-tetrazine-3-yl}-3'-(2-ethylhexyl)-2,2'-bithiophene-5-carbonitrile

4-(5-(6-(5-bromo-4-ethylhexyl)thiophen-2-yl)-1,2,4,5-tetrazin-3-yl)-3-(2-ethylhexyl) thiophene-2-yl)-N, N-bis(4-(hexyloxy) phenyl)aniline (115 mg; 0.116 mmol) and 5-(4,4,5,5-tetramethyl-1,3,2-dioxaborolan-2-yl) thiophene-2-carbonitrile (38 mg; 0.164 mmol) were dissolved in anhydrous DME and K₂CO₃ (54 mg; 0.394 mmol) (in 0.5 mL water) was added. After the solution was saturated with argon gas, Pd(dppf)Cl₂ (5.1 mg; 0.007 mmol) was added. The reaction was stirred for 48h at 90 °C, then cooled to room temperature. The mixture was poured into water (30 mL) and extracted with chloroform and dichloromethane. Organic phases were combined and evaporated by rotary. The product was purified with column chromatography (silica gel, CH₂Cl₂:MeOH 15:0.5).

2.2.2. Synthesis of 4'-{6-[5-(4-{bis[4-(hexyloxy)phenyl]amino}phenyl)-4-(2-ethylhexyl)-2-thienyl]-1,2,4,5-tetrazine-3-yl}-3'-(2-ethylhexyl)-2,2'-bithiophene-5-carboxylic acid (D- π -A dye)

5'-{6-[5-(4-{bis[4-(hexyloxy)phenyl]amino}phenyl)-4-(2-ethylhexyl)-2-thienyl]-1,2,4,5-tetrazine-3-yl}-3'-(2-ethylhexyl)-2,2'-bithiophene-5-carbonitrile (76.4 mg; 0.075 mmol) was dissolved in THF/MeOH (1:1, 10 ml) in the two necked flask. 2 M KOH (0.19 ml) was added into the mixture and refluxed for 48h. The reaction was controlled with TLC and neutralized with HCl. The crude product was extracted with water/CH₂Cl₂ (1:2). The product was purified with a silica gel column chromatography (CH₂Cl₂, CH₂Cl₂/MeOH 15:1) (Figure 1).

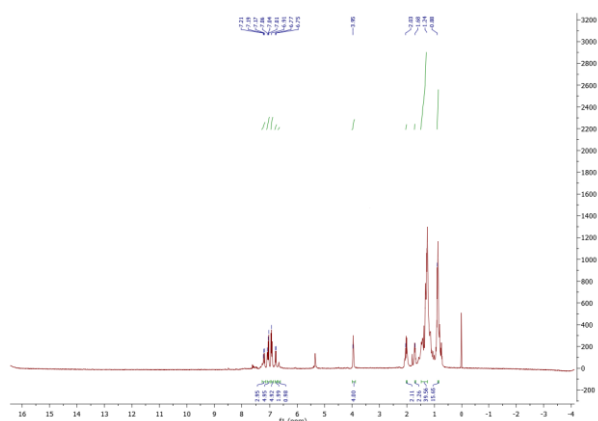


Figure 1. NMR spectrum of synthesized D- π -A dye

2.3. Optical and electrochemical experiments

Optical and electrochemical properties of D- π -A dye have been investigated by Shimadzu UV-1800 UV-Vis absorption spectrophotometer and CH 760D potentiostat, respectively. Absorption spectrum was performed by using 10⁻⁵ M dye solution in tetrahydrofuran (THF). Molar extinction coefficients (ϵ) of dyes have been calculated by using Beer-Lambert law [29]. Electrochemical properties and band diagrams of dye were examined by cyclic voltammetry technique in acetonitrile (ACN) by using 0.1 M tetrabutylammonium hexafluorophosphate (Bu₄NPF₆) solution as supporting electrolyte with standard three electrode setup using glassy carbon electrode (GCE), Pt wire and Ag/AgCl electrodes act as working, counter and reference electrodes, respectively. HOMO and LUMO levels were calculated from oxidation and reduction potentials, respectively.

2.4. Dye sensitization process

TiO₂ coated fluorine doped tin oxide (FTO) glass electrode and powdered TiO₂ are used for the photoelectrochemical and photocatalytic hydrogen evolution reaction (HER), respectively. The dye sensitization process is the same for the both coated

electrode and powdered TiO₂. Firstly, TiO₂ species were calcinated at 450 °C for 45 minutes in order to eliminate adsorbed water and organic impurities on the surface of TiO₂ before the sensitization process. After the calcination, TiO₂ species have been added into the dye solution (10⁻⁵ M in THF). TiO₂ electrode was kept overnight in the dye solution. Powdered TiO₂ stirred with magnetic mixer overnight in the dye solution under dark conditions. Then dye sensitized TiO₂ species were rinsed by THF and ethanol three times to remove unbinding dye molecules. Finally, dye sensitized TiO₂ species were kept under room condition for drying to use in the photoelectrochemical and photocatalytic hydrogen evolution experiments.

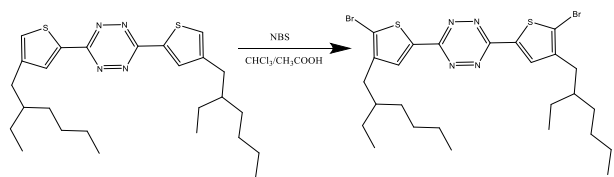
2.5. Photoelectrochemical and photocatalytic HER experiments

Photoelectrochemical properties of dye sensitized TiO₂ electrode were investigated in the 0.1 M Na₂SO₄ and 5% TEOA solution under the LED illumination by on/off cycles. Herein, standard three electrode setup is consisted of dye sensitized TiO₂, Pt plate and Ag/AgCl electrodes act as the photanode working electrode, counter electrode and reference electrode, respectively. Photocatalytic HER experiments were carried out by using powdered TiO₂ sensitized by D- π -A dye in the presence of oxygen-free 5% TEOA solution. This emulsion was prepared in the glove-box and reaction cell is sealed by rubber septum. The sealed reaction cell was put onto solar simulator (Solar Light XPS-300™) and stirring magnetically to occur homogenous photocatalytic reaction. Then, sampling of head space gas taken by gas tight syringe and injected into gas chromatography in order to calculate generated hydrogen amount by using standard calibration curve changing 0.1% and 5% concentration of H₂ in N₂.

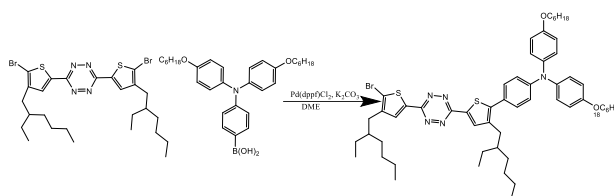
3. Results and Discussion

3.1. Synthesis of D- π -A dye

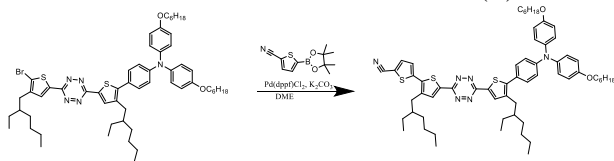
Herein the synthesized D- π -A dye was used as visible light sensitizer. 3,6-bis [4-methylthien-2-yl]-stetrazine (I) was synthesized according to literature [27, 28]. 4'-{6-[5-(4-{bis[4-(hexyloxy)phenyl]amino}phenyl)-4-(2-ethylhexyl)-2-thienyl]-1,2,4,5-tetrazine-3-yl}-3'-(2-ethylhexyl)-2,2'-bithiophene-5-carbonitrile was synthesized between 4-(5-(6-(5-bromo-4-ethylhexyl)thiophen-2-yl)-1,2,4,5-tetrazin-3-yl)-3-(2-ethylhexyl) thiophene-2-yl)-N, N-bis(4-(hexyloxy)phenyl)aniline and 5-(4,4,5,5-tetramethyl-1,3,2-dioxaborolan-2-yl) thiophene-2-carbonitrile by the Suzuki-Miyaura coupling reaction. The intermediate molecule was converted to D- π -A dye by the Knoevenagel condensation reaction.



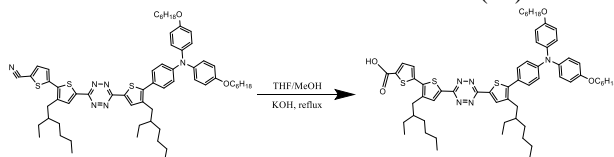
(I)



(II)



(III)



D- π -A dye

Scheme 1. Synthesis procedure and molecular structure of D- π -A dye

3.2. Optical and electrochemical properties of D- π -A dye

Optical properties of D- π -A dye were investigated by UV-Vis absorption spectra. As shown in **figure 2a**, two peaks were observed at the 291 nm and 345 nm originated from localized π - π^* and delocalized π - π^* transitions, respectively, because of intramolecular charge transfer (ICT) properties between donor (triphenylamine) and acceptor (carboxylic acid) groups [30]. Besides, molar absorption coefficient (ϵ) of the sensitizer was calculated as $1800 \text{ M}^{-1} \text{ cm}^{-1}$ (345 nm) by Lambert-Beer Law [29]. Electrochemical properties of sensitizer were investigated by cyclic voltammetry method using glassy carbon electrode (GCE), Pt wire and Ag/AgCl electrodes as working, counter and reference electrodes, respectively, in the 0.1 M tetrabutylammonium hexafluorophosphate (Bu_4NPF_6) solution in acetonitrile (ACN) as a supporting electrolyte. As displayed in **figure 2b**, there is one oxidation peak in the voltammogram at the positive region (0.85 V) because of donor moiety of triphenylamine group. In addition, the peaks at the negative region in the voltammogram are correspond to

π group (-1.00 V and -1.41 V) and acceptor group (-1.85 V, originated from acceptor moieties of carboxylic acid). HOMO and LUMO levels of sensitizer were calculated vs. vacuum level according to equations below [31] from oxidation and reduction potentials, which were found as -5.25 eV and -3.40 eV.

$$E_{\text{LUMO}} = -e(E_{\text{red}} + 4.4) \quad (1)$$

$$E_{\text{HOMO}} = -e(E_{\text{ox}} + 4.4) \quad (2)$$

The electrochemical band gap was figured out as 1.85 eV by subtraction between HOMO and LUMO energy levels. The optical and electrochemical properties of sensitizer in good agreement with before published studies about resemble D- π -A dyes [25-28, 32]. The whole optical and electrochemical parameters of D- π -A dye are given in the **Table 1**.

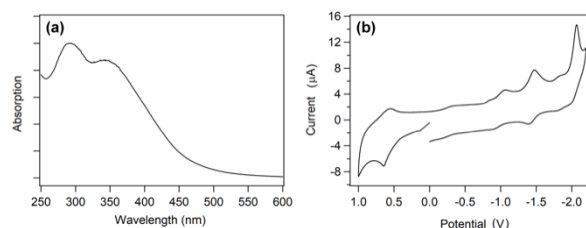


Figure 2. (a) UV-Vis absorption spectra of dye in the THF and (b) cyclic voltammogram of dye by using 0.1 M Bu_4NPF_6 solution in the ACN as supporting electrolyte.

Table 1. Optical and electrochemical parameters of D- π -A dye

	Dye
Absorption Wavelength (λ) / nm	345
Molar Absorption Coefficient (ϵ) / $\text{M}^{-1} \text{ cm}^{-1}$	1800
Oxidation Potential / V	0.85
Reduction Potentials / V	-1.00 / -1.41
HOMO energy level / eV	-5.25
LUMO energy level / eV	-3.40

3.3. Photoelectrochemical and photocatalytic hydrogen evolution

Dye sensitized photochemical water splitting (WS) reactions is named as artificial photosynthesis in the literature studies due to the mimicking the Z-scheme of natural photosynthesis by solar energy into chemical energy [13]. In this study, D- π -A dye has been used as a visible light sensitizer in the both photoelectrochemical and photocatalytic hydrogen evolution reaction from WS. Herein, photochemical reactions have been carried out in the presence of scavenger electron donor triethanolamine (TEOA) in order to increase hydrogen generation by blocking oxygen evolution because it can

be reduced in the presence of generated O_2 and inhibited H_2 generation due to the more positive reduction potential ($E^{O_2/H_2O} = 1.23$ V and $E^{H^+/H_2} = 0.00$ V vs. NHE). In this study, firstly, photoelectrochemical hydrogen evolution experiments have been carried out by linear sweep voltammetry (LSV) and chronoamperometry (CA) techniques by using TiO_2 and D- π -A dye sensitized TiO_2 coated FTO electrodes. Herein, dye sensitized TiO_2 coated FTO, Pt plate and Ag/AgCl electrodes as working, counter and reference electrodes, respectively, under on/off illumination cycles in the oxygen-free aqueous 0.1 M Na_2SO_4 (supporting electrolyte) / 5% TEOA (electron donor) solution. Herein, working electrode utilized as the photoanode because n-type semiconductor electrodes generally participate in photoanode preparation. In the photoelectrochemical system, D- π -A dye excited by light and generated holes and excited electrons. These excited electrons were transferred into Pt plate counter electrode (cathode) to generate hydrogen. Then, the holes in the D- π -A dye on TiO_2 photoanode were refilled by scavenger electron donor TEOA to regenerate the photoelectrochemical system. The hydrogen evolution rates are associated with transient current density and it is directly based on efficiency of intramolecular charge transfer (ICT) properties and absorption of sensitizers on the TiO_2 photoanode [12]. Photoelectrochemical properties of D- π -A dye sensitized TiO_2 electrode was firstly investigated by linear sweep voltammetry (LSV) under visible light illumination with 2 s on/off cycles as shown in **figure 3a**. The D- π -A dye sensitized TiO_2 electrode displayed well-stability between +0.5 V and -0.4 V potential window. After that, CA experiments have been performed in the absence and presence of dye on the TiO_2 electrodes. In the absence of dye, only TiO_2 electrode displays $1 \mu A cm^{-2}$ transient photocurrent density, which was also unstable and inefficient photocurrent character. However, enhancing and stable transient photocurrent density have been monitored by using dye sensitized TiO_2 electrode, which was approximately $90 \mu A cm^{-2}$, during the on/off cycles (**Figure 3a**). These photoactivity and photostability can be originated from absorption of light and intramolecular charge transfer (ICT) properties of D- π -A dye, respectively (*vide supra*). These results are in accordance with the photocatalytic experiment results (*vide infra*).

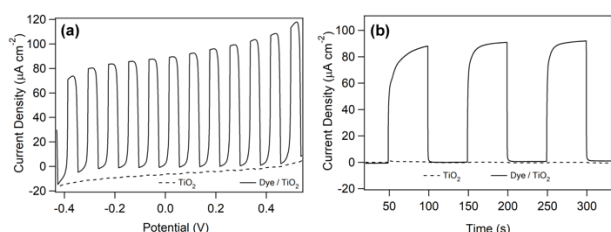


Figure 3. Transient photocurrent response of TiO_2 and D- π -A dye sensitized TiO_2 coated FTO electrodes by using (a) LSV and (b) CA techniques.

Photocatalytic HER properties of D- π -A sensitized TiO_2 have been examined in the aqueous TEOA solution (5%) at pH = 9, which is determined according to our previous studies with very familiar D- π -A dyes [25-28], under solar irradiation ($\lambda \geq 420$ nm) with magnetically stirring for homogenous reaction condition. The amounts of hydrogen generation are shown against time by using Dye/ TiO_2 and Dye/ TiO_2 /Pt, which Pt is occurred by photoreduction of H_2PtCl_6 on the Dye/ TiO_2 photocatalyst, in **figure 4**. The HER rates of Dye/ TiO_2 and Dye/ TiO_2 /Pt were found as 0.52 mmol $g^{-1} h^{-1}$ and 1.95 mmol $g^{-1} h^{-1}$, respectively. After eight hours of photocatalytic reaction 3.00 mmol g^{-1} and 19.23 mmol g^{-1} hydrogen were produced by using Dye/ TiO_2 and Dye/ TiO_2 /Pt, respectively. These results displayed that very stable hydrogen generation rate in the absence and presence of Pt co-catalyst, which can be explained by well intramolecular charge transfer (ICT) of D- π -A type dyes [12].

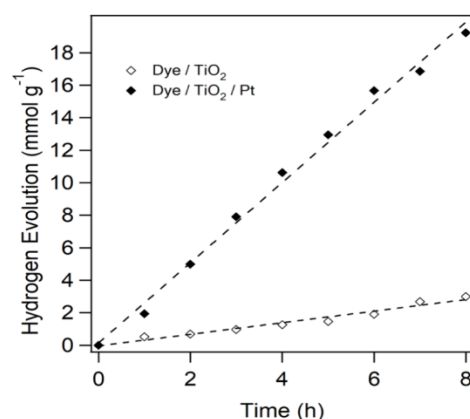


Figure 4. Photocatalytic hydrogen evolution against time by using Dye/ TiO_2 and Dye/ TiO_2 /Pt in the aqueous TEOA (5%) electron donor solution.

The photocatalytic activities of different D- π -A dye sensitized TiO_2 photocatalysts are compared in the same sacrificial media by changing different sensitizers according to our previous studies. These results display that D- π -A dye in this study gives comparable HER rates in the similar conditions.

Table 2. The comparison of HER rates for D- π -A dye with other reported similar structured dye sensitized photocatalytic HER studies

Photocatalysts	HER Rates ($\mu mol g^{-1} h^{-1}$)	References
TiO_2 /MZ-235	531	[25]
TiO_2 /MZ-341	661	
TiO_2 /MC-32	121	[26]
TiO_2 /MZ-048	212	
TiO_2 /MK-3	427	[27]
TiO_2 /MK-4	675	
TiO_2 /MK-2	565	[28]
TiO_2 /MK-8	374	
D-π-A/TiO_2	520	This work

3.4. Mechanism of HER

The mechanism of dye sensitized hydrogen evolution is figured out by electron transfer mechanism, which generally explained by three main steps. First step is the absorption of light by D- π -A dye and electrons at the HOMO (0.85 V) level are excited to LUMO (-1.00 V) level. Then, the second step are that the photoexcited electrons are injected into conduction band of TiO₂ (-0.5 V). It can be favorable because CB of TiO₂ more positive than LUMO level of dye. The last step is that the excited electrons (e⁻) on the CB of TiO₂ reduced of adsorbed proton onto TiO₂ photocatalyst to generate H₂ gas (or constitute Pt co-catalyst on the TiO₂ in the presence of H₂PtCl₆), also the hole (h⁺) on the HOMO level of dye can be refilled in the same time by giving electrons by electron donor TEOA to regenerate the photocatalytic HER system (Figure 5).

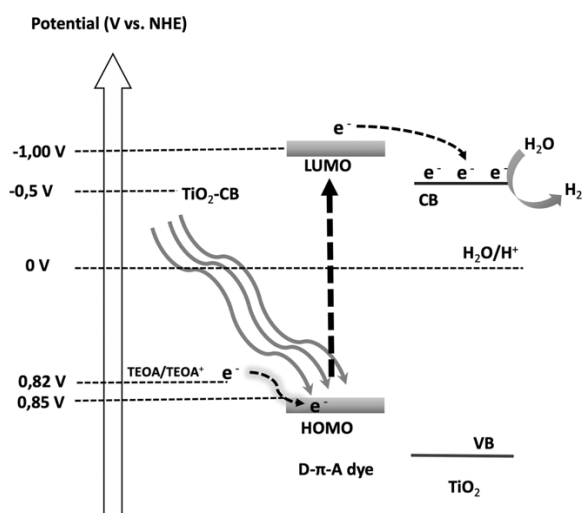
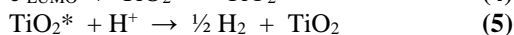
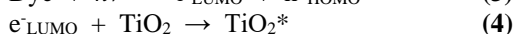
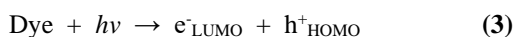


Figure 5. Proposed mechanism of photocatalytic HER by using D- π -A dye sensitized TiO₂

4. Conclusion

A novel D- π -A dye was synthesized and its optical and electrochemical properties were investigated in order to determine light absorption characteristics and electrochemical band levels for explaining reaction mechanism. Photoelectrochemical and photocatalytic HER activities were investigated by D- π -A dye sensitized TiO₂. Herein, advanced photochemical activity of Dye/TiO₂ photocatalyst can be explained by ICT properties of D- π -A dyes for hydrogen evolution. In addition, Dye/TiO₂ the photocatalytic activity of Dye/TiO₂ photocatalyst was dramatically increased adding *in situ* photodeposited co-catalyst Pt. The stabilities of photocatalytic HER were maintained

during the reaction by using both Dye/TiO₂ and Dye/TiO₂/Pt. This study brings on the novel energy application based on light absorption by D- π -A dyes.

Acknowledgement

This work has been done under the umbrella of the Selçuk University Scientific Research Projects (Grant number: 20401033) also accumulation of knowledge from TÜBİTAK-1003 project (Grant number: 215M309). In addition, the author would like to thank to Assoc. Prof. Dr. Mustafa Can from İzmir Katip Çelebi University for the synthesis and characterization of dye molecule, as well as Prof. Dr. Imren Hatay Patir from Selçuk University for the valuable guidance and contributions on the use of laboratory equipment.

Author's Contributions

Emre Aslan: Drafted and wrote the manuscript, performed the experiment and result analysis.

Ethics

There are no ethical issues after the publication of this manuscript.

References

- 1 Fujishima, A. and K. Honda, Electrochemical Photolysis of Water at a Semiconductor Electrode. *Nature*, 1972. **238**(5358): p. 37-38.
- 2 Ma, Y., X. Wang, Y. Jia, X. Chen, H. Han, and C. Li, Titanium Dioxide-Based Nanomaterials for Photocatalytic Fuel Generations. *Chemical Reviews*, 2014. **114**(19): p. 9987-10043.
- 3 Huang, J.-F., Y. Lei, T. Luo, and J.-M. Liu, Photocatalytic H₂ Production from Water by Metal-free Dye-sensitized TiO₂ Semiconductors: The Role and Development Process of Organic Sensitizers. *ChemSusChem*, 2020. **13**(22): p. 5863-5895.
- 4 Borgarello, E., J. Kiwi, E. Pelizzetti, M. Visca, and M. Grätzel, Photochemical cleavage of water by photocatalysis. *Nature*, 1981. **289**: p. 158-160.
- 5 Martín-Gomis, L., F. Fernández-Lázaro, and Á. Sastre-Santos, Advances in phthalocyanine-sensitized solar cells (PeSSCs). *Journal of Materials Chemistry A*, 2014. **2**(38): p. 15672-15682.
- 6 Urbani, M., M. Grätzel, M.K. Nazeeruddin, and T. Torres, Meso-Substituted Porphyrins for Dye-Sensitized Solar Cells. *Chemical Reviews*, 2014. **114**(24): p. 12330-12396.
- 7 Kong, C., S. Min, and G. Lu, Dye-Sensitized NiS_x Catalyst Decorated on Graphene for Highly Efficient Reduction of Water to Hydrogen under Visible Light Irradiation. *ACS Catalysis*, 2014. **4**(8): p. 2763-2769.
- 8 Joseph, K.L.V., J. Lim, A. Anthonysamy, H.-i. Kim, W. Choi, and J.K. Kim, Squaraine-sensitized composite of a reduced graphene oxide/TiO₂ photocatalyst: π - π stacking as a new method of dye anchoring. *Journal of Materials Chemistry A*, 2015. **3**(1): p. 232-239.
- 9 Nada, A.A., H.A. Hamed, M.H. Barakat, N.R. Mohamed, and T.N. Veziroglu, Enhancement of photocatalytic hydrogen production rate using photosensitized TiO₂/RuO₂-MV²⁺.



- International Journal of Hydrogen Energy*, 2008. **33**(13): p. 3264-3269.
- 10 Shimidzu, T., T. Iyoda, and Y. Koide, An advanced visible-light-induced water reduction with dye-sensitized semiconductor powder catalyst. *Journal of the American Chemical Society*, 1985. **107**(1): p. 35-41.
- 11 Wu, Y. and W. Zhu, Organic sensitizers from D- π -A to D-A- π -A: effect of the internal electron-withdrawing units on molecular absorption, energy levels and photovoltaic performances. *Chemical Society Reviews*, 2013. **42**(5): p. 2039-2058.
- 12 Yu, Z., F. Li, and L. Sun, Recent advances in dye-sensitized photoelectrochemical cells for solar hydrogen production based on molecular components. *Energy & Environmental Science*, 2015. **8**(3): p. 760-775.
- 13 Zhang, X., T. Peng, and S. Song, Recent advances in dye-sensitized semiconductor systems for photocatalytic hydrogen production. *Journal of Materials Chemistry A*, 2016. **4**(7): p. 2365-2402.
- 14 Hardin, B.E., H.J. Snaith, and M.D. McGehee, The renaissance of dye-sensitized solar cells. *Nature Photonics*, 2012. **6**: p. 162.
- 15 Lee, S.-H., Y. Park, K.-R. Wee, H.-J. Son, D.W. Cho, C. Pac, W. Choi, and S.O. Kang, Significance of Hydrophilic Characters of Organic Dyes in Visible-Light Hydrogen Generation Based on TiO₂. *Organic Letters*, 2010. **12**(3): p. 460-463.
- 16 Jae-Hong, K. and A. Kwang-Soon, Tri-Branched Tri-Anchoring Organic Dye for Visible Light-Responsive Dye-Sensitized Photoelectrochemical Water-Splitting Cells. *Japanese Journal of Applied Physics*, 2010. **49**(6R): p. 060219.
- 17 Han, W.-S., K.-R. Wee, H.-Y. Kim, C. Pac, Y. Nabetani, D. Yamamoto, T. Shimada, H. Inoue, H. Choi, K. Cho, and S.O. Kang, Hydrophilicity Control of Visible-Light Hydrogen Evolution and Dynamics of the Charge-Separated State in Dye/TiO₂/Pt Hybrid Systems. *Chemistry – A European Journal*, 2012. **18**(48): p. 15368-15381.
- 18 Choi, S.K., H.S. Yang, J.H. Kim, and H. Park, Organic dye-sensitized TiO₂ as a versatile photocatalyst for solar hydrogen and environmental remediation. *Applied Catalysis B: Environmental*, 2012. **121–122**: p. 206-213.
- 19 Watanabe, M., H. Hagiwara, A. Iribe, Y. Ogata, K. Shiomi, A. Staykov, S. Ida, K. Tanaka, and T. Ishihara, Spacer effects in metal-free organic dyes for visible-light-driven dye-sensitized photocatalytic hydrogen production. *Journal of Materials Chemistry A*, 2014. **2**(32): p. 12952-12961.
- 20 Yu, F.T., S.C. Cui, X. Li, Y.Y. Peng, Y. Yu, K. Yun, S.C. Zhang, J. Li, J.G. Liu, and J.L. Hua, Effect of anchoring groups on N-annulated perylene-based sensitizers for dye-sensitized solar cells and photocatalytic H₂ evolution. *Dyes and Pigments*, 2017. **139**: p. 7-18.
- 21 Thelakkat, M., Star-Shaped, Dendrimeric and Polymeric Triarylamines as Photoconductors and Hole Transport Materials for Electro-Optical Applications. *Macromolecular Materials and Engineering*, 2002. **287**(7): p. 442-461.
- 22 Tiwari, A. and U. Pal, Effect of donor-donor- π -acceptor architecture of triphenylamine-based organic sensitizers over TiO₂ photocatalysts for visible-light-driven hydrogen production. *International Journal of Hydrogen Energy*, 2015. **40**(30): p. 9069-9079.
- 23 Li, X., S. Cui, D. Wang, Y. Zhou, H. Zhou, Y. Hu, J.-g. Liu, Y. Long, W. Wu, J. Hua, and H. Tian, New Organic Donor–Acceptor- π –Acceptor Sensitizers for Efficient Dye-Sensitized Solar Cells and Photocatalytic Hydrogen Evolution under Visible-Light Irradiation. *ChemSusChem*, 2014. **7**(10): p. 2879-2888.
- 24 Dessi, A., M. Monai, M. Bessi, T. Montini, M. Calamante, A. Mordini, G. Reginato, C. Trono, P. Fornasiero, and L. Zani, Towards Sustainable H₂ Production: Rational Design of Hydrophobic Triphenylamine-based Dyes for Sensitized Ethanol Photoreforming. *ChemSusChem*, 2018. **11**(4): p. 793-805.
- 25 Aslan, E., M.K. Gonce, M.Z. Yigit, A. Sarilmaz, E. Stathatos, F. Ozel, M. Can, and I.H. Patir, Photocatalytic H₂ evolution with a Cu₂WS₄ catalyst on a metal free D- π -A organic dye-sensitized TiO₂. *Applied Catalysis B: Environmental*, 2017. **210**: p. 320-327.
- 26 Patir, I.H., E. Aslan, G. Yanalak, M. Karaman, A. Sarilmaz, M. Can, M. Can, and F. Ozel, Donor- π -acceptor dye-sensitized photoelectrochemical and photocatalytic hydrogen evolution by using Cu₂WS₄ co-catalyst. *International Journal of Hydrogen Energy*, 2019. **44**(3): p. 1441-1450.
- 27 Aslan, E., M. Karaman, G. Yanalak, M. Can, F. Ozel, and I.H. Patir, The investigation of novel D- π -A type dyes (MK-3 and MK-4) for visible light driven photochemical hydrogen evolution. *Dyes and Pigments*, 2019. **171**: p. 107710.
- 28 Aslan, E., M. Karaman, G. Yanalak, H. Bilgili, M. Can, F. Ozel, and I.H. Patir, Synthesis of novel tetrazine based D- π -A organic dyes for photoelectrochemical and photocatalytic hydrogen evolution. *Journal of Photochemistry and Photobiology A: Chemistry*, 2020. **390**: p. 112301.
- 29 Swinehart, D.F., The Beer-Lambert Law. *Journal of Chemical Education*, 1962. **39**(7): p. 333.
- 30 Luo, G.-G., H. Lu, Y.-H. Wang, J. Dong, Y. Zhao, and R.-B. Wu, A D- π -A- π -A metal-free organic dye with improved efficiency for the application of solar energy conversion. *Dyes and Pigments*, 2016. **134**: p. 498-505.
- 31 Cardona Claudia, M., W. Li, E. Kaifer Angel, D. Stockdale, and C. Bazan Guillermo, Electrochemical Considerations for Determining Absolute Frontier Orbital Energy Levels of Conjugated Polymers for Solar Cell Applications. *Advanced Materials*, 2011. **23**(20): p. 2367-2371.
- 32 Margalias, A., K. Seintis, M.Z. Yigit, M. Can, D. Sygkridou, V. Giannetas, M. Fakis, and E. Stathatos, The effect of additional electron donating group on the photophysics and photovoltaic performance of two new metal free D- π -A sensitizers. *Dyes and Pigments*, 2015. **121**: p. 316-327.

Fenoxycarb Effects 7th instar *Galleria mellonella* Larvae by Triggering Extra Larval Stages

Esen Poyraz Tınartas^{1*}, Nesrin Ebru Göncü², Kamil Koç¹

¹ Manisa Celal Bayar University, Faculty of Science and Arts, Department of Biology, Manisa, Turkey

² Ege University, Faculty of Science, Department of Biology, İzmir, Turkey

* esen.poyraz@cbu.edu.tr

*Orcid: 0000-0001-7386-2136

Received: 16 November 2020

Accepted: 3 May 2021

DOI: 10.18466/cbayarfb.823562

Abstract

Insect growth regulators are specific chemicals with hormonal effects on insects and these types of chemicals target to reduce the nonspecific effects of pesticides on nature and living things. In this study, we investigated the effects of one of the insect growth regulators, fenoxycarb which mimics the juvenile hormone action, on the growth of a harmful lepidopteran species *Galleria mellonella*, and its some developmental parameters. For this purpose, fenoxycarb was applied on day 0 of 7th instar larvae of the greater wax moth, *Galleria mellonella*. The treatment with 100 ng fenoxycarb had no developmental effect on *Galleria mellonella* larvae. The treatment with relatively high doses of fenoxycarb on day 0 induced the supernumerary larvae formation of 99% and larvae which molted extra larval instar formed healthy pupae in the ratio of 98-99%. Consequently, the effects of fenoxycarb on *Galleria mellonella* larvae occurred in a dose-dependent manner. Although fenoxycarb is a potent insect growth regulator, late *Galleria mellonella* larvae are not susceptible to this chemical, unlike some other Lepidopteran insect species.

Keywords: Development, Fenoxycarb, *Galleria mellonella*, Juvenile hormone.

1. Introduction

Insect growth regulators are produced to develop more specific chemicals against harmful insects that target to reduce the nonspecific effects of pesticides on nature and living things and they show hormonal effects on insects. Most insect growth regulators today are juvenile hormone (JH) analogues, which mimic the mechanism of action of JH. JH provides the continuity of larval characters for holometabolous insects [1]. JH or JH analogues applications disturb the endocrine balance of many insects and finally induces abnormal development [1-4]. No synthetic JH analogue can instantly kill the target organism with a direct toxic effect. Instead, it leads to developmental abnormalities, causing insufficiency in development and reproductive functions [5, 6]. Fenoxycarb, 0-ethyl N-(2-(4-phenoxyphenoxy) ethyl) carbamate, is one of the most effective chemicals among these JH analogues [1].

Galleria mellonella, the greater wax moth, is a harmful lepidopteran species that causes economic losses in the beekeeping industry because its larva feeds on combs, and also their larvae and pupae are one of the oldest

experimental models used in insect physiology [7-10]. Until now, there has been no quantitative report that has examined the responses of the larvae of *Galleria mellonella* to treatments with fenoxycarb. The present study attempted to clarify the response of *Galleria mellonella* to different doses (100 ng to 10 µg) of fenoxycarb during the last larval stage. For this purpose, molting, growth, and some survival parameters after treatments were evaluated and statistical analyses were carried out depending on application doses.

2. Materials and Methods

Galleria mellonella larvae were reared at 30 ± 0.5 °C, $60 \pm 5\%$ relative humidity and constant darkness in the incubator on a diet containing bran (420 g), honeycomb (160 g), honey (150 ml), glycerol (150 ml) and distilled water (30 ml) modified from Bronksill [11].

Eggs were collected every day. During the feeding period, larvae were classified in every 24-hours. The first 24 hours were named as day 0 (Figure 1c- d). At larval-pupal metamorphosis, the classification of larval development was performed according to the

morphology and morphological characteristics of the migration of the pigments from the stemmata [12]. This retraction of pigments occurs in several stages (S1-S5) under hormonal factors [12, 13]. Also, the head capsule width of the larvae was measured by millimeter ocular and was statistically evaluated. After pupal molting, pupae were also classified every 24 hours.

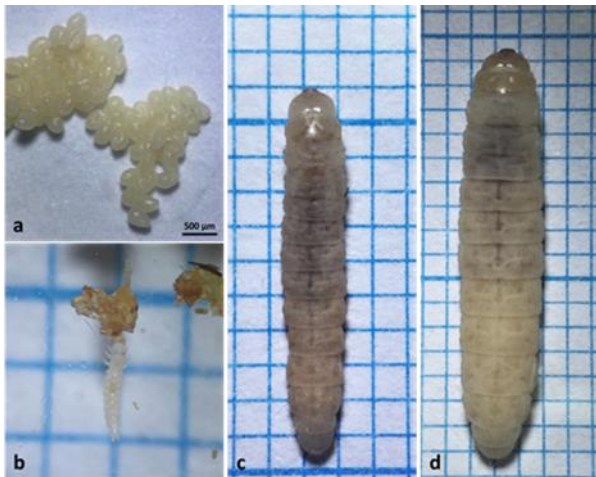


Figure 1. Different developmental stages of *Galleria mellonella* larvae; a) *Galleria mellonella* eggs, b) Feeding early larva of *Galleria mellonella*, c) 6th instar newly ecdysis larva, d) 7th instar newly ecdysis larva.

On day 0 of 7. instar, every ten larvae were topically treated with eight different doses of fenoxycarb (100 ng, 250 ng, 500 ng, 750 ng, 1 µg, 2 µg, 5 µg, and 10 µg) (Fluka, 34343) in 2,5 µl acetone (solvent) with a micropipette along the dorsal midline. Control larvae were treated with an equal amount (2.5 µl) of solvent without fenoxycarb. The groups treated with fenoxycarb were cultured in different incubators and laboratories to prevent any contamination with the control group. The larvae that remained in the 7th instar more than 20 days were defined as “dauer larvae” [1, 14]. Each experimental procedure was performed three times.

Ten randomly selected larvae and/or pupae from groups were weighed from day 0 of the 7th instar to the end of the pupal stage in 24 hours intervals at the same time each day. Analyses of the data were carried out by using SPSS 20.00 software (IBM) ($p < 0.05$ level Mann Whitney’s U-test).

2. Results and Discussion

Hemolymph JH levels are low at the beginning of the last larval stage to provide a pupal commitment of the insect body. Moreover, this period is extremely sensitive to JH applications [3, 15]. In this study, fenoxycarb was applied at the beginning of the last larval stage to evaluate the sensitivity of *Galleria mellonella* to the various levels of JH presence.

Control group larvae were fed for three and a half days (78-84 hours) and then terminate feeding activity and

reached the highest weight values (310 mg) at 78-84 hour period from the beginning of the 7th instar (S1) as similarly reported by Beck [16]. Wandering and cocoon spinning (S1-S5) ranged from 2 and 3 days, 99% of the larvae developed normally to the pupal stage. A gradual decrease in weight was observed until the larval-pupal ecdysis. Increasing silk secretion, degeneration of tissues, and organs such as the silk gland and intestine which occupy large volumes and space in the body should be the main reasons for this decline. The pupal period lasted 7 days.

No appreciable difference was found in insects treated with a dose of 100 ng fenoxycarb per larvae when compared with control larvae. Application of doses among 250-750 ng caused to stop feeding activity resulting in growth deficiency in 5% of larvae, 3% of larvae died in these groups. Extra larval molting occurred in the ratio of between 35-65% (Table 1). 27-47% of larvae showed a prolonged larval stage of 1-2 days and then pupated following a normal course (Figure 2a). Previous studies showed that low and moderate doses of juvenoids caused a significant prolongation of the last larval stages in Holometabola [17] and also *Galleria mellonella* [2]. These differences may be due to differences in the greater wax moth strain used, the rearing conditions, or the chemical factors used because these factors have been shown to influence the actions of JH analogues [1].

The last larval stage of *Galleria mellonella* was sensitive to higher doses of fenoxycarb (1-10 µg) and caused supernumerary molt. 5 µg and 10 µg doses caused extra larval ecdysis occurred synchronously on day 5. Extra larval molting was observed between 95% and 97% (Figure 2b). 8th instar larvae pupated normally in the ratio of 99% and they were morphologically normal. (Table 1). Similarly, early in the last larval instar, the implantation of active corpora allata results in supernumerary larval ecdysis in *Galleria mellonella* [18]. The effect of JH and JH analogues is due to interference with the physiological programming of the secretory functions of the prothoracic glands and the modification of the prothoracic-tropic brain activity [2]. Fenoxycarb treatments may have caused ecdysteroid secretion, so that new larval-larval molting may have been triggered due to high levels of JH and 20-hydroxyecdysone in the hemolymph. The larval-pupal intermediate form was detected in 1-2% of larvae (Figure 2c). After treatments of JH and JH analogues, prolongation of larval stages, larval-pupal intermediate formation, dauer larva formation, and mortality were observed in different ratios in *Epiphyas postvittana* [19], *Ephestia kuehniella* [5], *Bombyx mori* [1, 20]. Extra larval molting was stated in a ratio of 30% in *Ostrinia nubilalis* [21, 22].

Table 1. Effects of fenoxycarb on the development of *Galleria mellonella* larvae

Dosage (in 2.5µl acetone)	Number of treated larvae	Prolongation of last instar	Dauer larvae (%)	Darkened and dead (%)	Poorly development and death (%)	Extra larval molting (%)	Pupation after extra larval molting(%)
Controls	30	-	-	-	-	-	-
100 ng	30	-	-	-	-	-	-
250 ng	30	1-2 days	10	3	5	35	98
500 ng	30	1-2 days	10	3	5	42	98
750 ng	30	1-2 days	-	3	5	65	98
1 µg	30	-	-	2	3	95	99
2 µg	30	-	-	2	3	95	99
5 µg	30	-	-	1	2	97	99
10 µg	30	-	-	1	2	97	99



Figure 2. *Galleria mellonella* larvae and pupae; a) Normally pupated *Galleria mellonella*, b) Supernumerary larvae of *Galleria mellonella*, c) Larval-pupal intermediate pupa formation after 8th instar, d) 9th instar larva molted partially.

The growth rate of larvae is defined during the development period by measuring the head capsule width of the samples taken from the population [8]. We determined that the last larval instar head capsule width is 2000 µm, similarly in Beck [8]. Measurements of 2264.6 µm and 2667.1 µm of head capsule width in different developmental stages (extra larval stages) also proved that fenoxycarb could affect *Galleria mellonella* larvae by molting more than once (Student T-Test, $p < 0.05$) (Figure 3a).

Measuring the body weights of larvae is also an important parameter in determining the growth rate of larvae [8]. Larvae treated with 5 µg of fenoxycarb were fed for the first 4 days and total body weights gradually increased, but this increase was found to be statistically lower than the control group larvae (Mann Whitney's U-test, $p < 0.05$) (Figure 3). Feeding inhibition is a general behavior of insects that comes in contact with various harmful agents [23].

The larvae of the 8th instar were fed for 8 days actively and showed a continuous and significant increase in weight until the 8th day (8-8) (Figure 3c). Sehna [24] reported similarly weight values in super larvae produced by corpora allata implantation. Between days 8 and 11, their feeding activities decreased or stopped, and weight gain slowed statistically (Mann Whitney's U-test, $p < 0.05$). The deceleration in the weight gain is thought to be a result of suppression of nutritional activity with excessive growth in animal size and, also the tracheal system probably does not adapt to these changes [25]. The maximum bodyweight a larva can reach and the weight gain that can be achieved in a single larval stage are species-specific [2, 25] and this value is not affected by JH and JH analogues [2]. These phenomena restrict the growth of insects. Larvae, when they reached 200-300 mg cut off from the feeding in normal development [16], but in some records, this weight could be 590 mg [2, 8], and larval growth is terminated irreversibly [2]. In our study, the ecdysis of the larval-pupal was observed near the known upper limit. The average weight of the 8th instar larvae was 596 mg and the lowest value was 410 mg. All these findings clarify the cause of feeding and growth inhibition and death in the 9th instar.

Pigment migration, which is the main characteristic of the S1- S5 stages, was not observed in S1 and S2 in the 8th larval instar larvae, which is why the distinction between S1 and S2 was not appropriate in this group. Their developmental stages in the graphs were edited every 24 hours up to S3. At the end of day 11, the spinning behavior began following the gut purge and the

total body weight decreased continuously, for the same reason as the control group. The pupal bodyweight of the group treated with fenoxycarb was significantly higher than that of the control group all day (Mann

Whitney's U-test, $p < 0.05$, Figure 3d). Pupal molting occurred within 2-3 days and the pupal stage lasted for 7 days as in the control group.

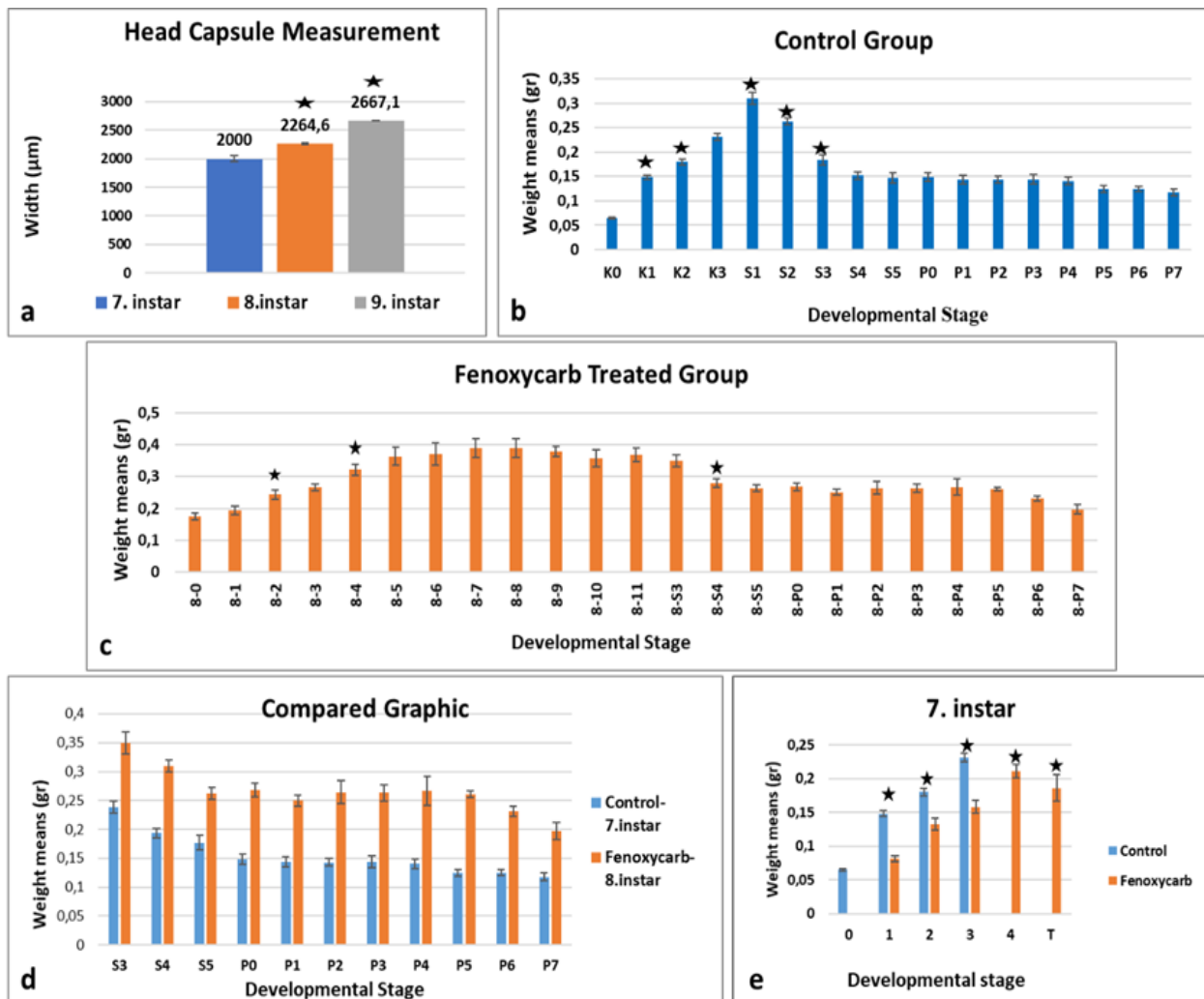


Figure 3. Weight average and head capsule measurement of control and 5 µg fenoxycarb treated groups; a) Head capsule measurements of control and 5 µg fenoxycarb treated group, b) The average of control group weight, c) The weight average of 5µg fenoxycarb treated group, d) Similar developmental stages of the control group and 5 µg fenoxycarb treated group were compared according to their weight changes, e) Comparison of the control group and 5 µg fenoxycarb treated group 7th instar values, T: Transition day from, the bars indicate standard errors. The asterisks indicate the statistically significant differences compared to the previous developmental stage ($p < 0.05$). S1-S5 represents the stages of development based on the retraction of pigments from stemmata, P0-7 represents the pupal days.

3. Conclusion

In comparison to other Lepidopteran species such as *Bombyx mori* and *Ephestia kuehniella* and when applied doses are considered, *Galleria mellonella* is found to be highly resistant to the fenoxycarb at the beginning of the last larval stage. Relatively high doses (5-10 µg) have possibly stimulated the secretion activity of the prothoracic glands and triggered the extra larval ecdysis. However, applications did not affect pupal development and resulted in healthy adults and a new generation

developed from their eggs was also healthy. These results clearly showed that fenoxycarb will be not a suitable agent for the biological control of this insect.

Acknowledgment

We would like to thank the Manisa Celal Bayar University Scientific Research Projects Coordination Unit (BAP) for supporting this study under project number 2014-013. This work was presented at the



Ecology 2018 Symposium (19-23 June 2018, Kastamonu Turkey) as an oral presentation.

Author's Contributions

Esen Poyraz Tınartaş: Drafted and wrote the manuscript, carried out the experiment, and evaluated results.

Nesrin Ebru Göncü: Assisted in analytical analysis on the structure, supervised the experiment's progress, result interpretation, and helped in manuscript preparation.

Kamil Koç: Conceived the presented experiment and supervised the findings of this work.

Ethics

There are no ethical issues after the publication of this manuscript.

References

1. Kamimura, M, Kiuchi, M. 1998. Effects of a juvenile hormone analog, fenoxycarb, on 5th stadium larvae of the silkworm, *Bombyx mori* (Lepidoptera: Bombycidae). *Applied Entomology and Zoology*; 33(2): 333-338.
2. Ciemior, KE, Sehna, F, Schneiderman, HA. 1979. Molting, Growth and Survival of *Galleria mellonella* L. (Lep. Pyralidae) Treated with Juvenoids. *Zeitschrift Fur Angewandte Entomologie-Journal of Applied Entomology*; 88(4): 414-425.
3. Silhacek, DL, Oberlander H. 1975. Time-dosage studies of juvenile hormone action on the development of *Plodia interpunctella*. *Journal of insect physiology*, 21(1), 153-161.
4. Dedos, SG, Szurdoki, F, Székács, A, Shiotsuki, T, Hammock, BD, Shimada, J, Fugo, H. 2002. Fenoxycarb levels and their effects on general and juvenile hormone esterase activity in the hemolymph of the silkworm, *Bombyx mori*. *Pesticide Biochemistry and Physiology*, 73(3): 174-187.
5. Grenier, S, Grenier AM. 1993. Fenoxycarb, a fairly new Insect Growth Regulator: Review of its effects on insects. *Annals of Applied Biology*; 122(2): 369-403.B
6. Beckage, NE, Rechcigl, J, Rechcigl, N. 2000. Insect growth regulators. *Biological and biotechnological control of insect pests*, 123-137.
7. Karlson, P. 1956. Biochemical studies on insect hormones. *Academic Press: In Vitamins & Hormones*; 14: 227-266.
8. Beck, SD. 1960. Growth and Development of The Greater Wax Moth, *Galleria mellonella* (L.) (Lepidoptera: Galleriidae). *Visconsin Academy of Sciences, Arts and Letters*; 49: 137-148.
9. Sehna, F, Meyer, AS. 1968. -Larval-pupal transformation: control by juvenile hormone. *Science*; 159(3818): 981-4.
10. Richman, K, Oberlander, H. 1971. -Effects of fat body on α -ecdysone induced morphogenesis in cultured wing disks of the wax moth, *Galleria mellonella*. *Journal of Insect Physiology*; 17(2): 269-276.
11. Bronskill, JA. 1961. A cage to simplify the rearing of the greater wax moth, *Galleria mellonella* (Lepidoptera: Pyralidae). *Journal the Lepidopterists' Society*; 15: 102-104.
12. Uwo, MF, Ui-Tei, K, Park, P, Takeda, M. 2002. Replacement of midgut epithelium in the greater wax moth, *Galleria mellonella*, during larval-pupal moult. *Cell Tissue Research*; 308(2): 319-31.
13. Jindra, M, Riddiford, LM. 1996. Expression of ecdysteroid-regulated transcripts in the silk gland of the wax moth, *Galleria mellonella*. *Development genes and Evolution*; 206(5): 305-314.
14. Sehna, I F, Janda, V, Nĕmec, V. 1983. Composition, synthetic and cytolytic activities of *Galleria mellonella* silk glands during the last-larval instar under the action of juvenile hormone. *Journal of Insect Physiology*; 29(3): 237-248.
15. Retnakaran, A. 1973. Hormonal induction of supernumerary instars in the spruce budworm, *Choristoneura fumiferana* (Lepidoptera: Tortricidae). *The Canadian Entomologist*; 105(3): 459-461.
16. Beck S. D., 1970. -Neural and Hormonal Control of Pupation in *Galleria mellonella* (Lepidoptera: Galleriidae). *Annals of the Entomological Society of America*. 63(1): 144-149.
17. Sehna, F, Metwall, MM, Elbie, I. 1976. Reactions of immature stages of noctuid moths to juvenoids. *Z. ang. Ent*; 81, 85-102.
18. Sehna, F. 1968. Influence of the corpus allatum on the development of internal organs in *Galleria mellonella* L. *Journal of Insect Physiology*; 14(1), 73-85.
19. Singh, P, Dugdale, J. 1979. Morphogenetic and physiological effects of a juvenile hormone analogue on the light brown apple moth, *Epiphyas postvittana* (Lepidoptera: Tortricidae). *New Zealand Journal of Zoology*; 6: 381-387.
20. Goncu, E, Parlak, O. 2012. The effect of the juvenile hormone analog, fenoxycarb, on ecdysone receptor B1 expression in the midgut of *Bombyx mori* during larval-pupal metamorphosis. *Folia Histochemistry Cytobiology*; 50(1): 52-7.
21. Fujiwara, H, Ogai, S. 2001. Ecdysteroid-induced programmed cell death and cell proliferation during pupal wing development of the silkworm, *Bombyx mori*. *Development Genes & Evolution*; 211(3).
22. Gadenne, C, Grenier, S, Plantevin, G, Mauchamp, B. 1991. Effects of a juvenile hormone mimetic, fenoxycarb, on post-embryonic development of the European corn borer, *Ostrinia nubilalis*. *Hbn. Experientia*; 46(7): 744-747.
23. Leonardi, MG, Cappelozza, S, Ianne, P, Cappelozza, L, Parenti, P, Giordana, B. 1996. Effects of the topical application of an insect growth regulator (fenoxycarb) on some physiological parameters in the fifth instar larvae of the silkworm *Bombyx mori*. *Comparative Biochemistry and Physiology Part B: Biochemistry and Molecular Biology*; 113(2), 361-365.
24. Sehna, F. 1971. Juvenile hormone action and insect growth rate. *Endocrinologia Experimentalis*; 5: 29-33.
25. Callier, V, Nijhout, HF. 2011. Control of body size by oxygen supply reveals size-dependent and size-independent mechanisms of molting and metamorphosis. *Proceedings of the National Academy of Sciences of the United States of America*; 108(35): 14664-14669.

Adhesive Behavior of the Pack-Borided AISI 304L Steel with Microwave Hybrid Heating

Dilek Arslan^{1*} , Recep Onur Uzun² 

^{1*} Graduate School of Applied and Natural Sciences, Department of Mechanical Engineering, Manisa Celal Bayar University, 45140, Manisa, Turkey

² Hasan Ferdi Turgutlu Technology Faculty, Department of Mechanical Engineering, Manisa Celal Bayar University, 45400, Manisa, Turkey

[*da.dilekarlan@gmail.com](mailto:da.dilekarlan@gmail.com)

*Orcid: 0000-0003-0198-0787

Received: 15 November 2020

Accepted: 20 February 2021

DOI: 10.18466/cbayarfbe.826118

Abstract

AISI 304L stainless steel material was pack-borided with microwave hybrid heating method at temperatures of 850, 900 and 950 °C for 2, 4 and 6 hours. The morphology of the boride layer formed on the surface of the samples was examined by an optical microscope. The X-ray diffraction (XRD) analysis showed the presence of the FeB, Fe₂B, Cr₂B and Ni₂B phases on the surface of the borided samples. The Daimler-Benz Rockwell-C adhesion test was carried out to evaluate the adhesive strength of the boride layer to the substrate material. The tests were repeated at least 3 times for each of the samples pack-borided at all process temperatures and times. After the adhesion tests, macro and SEM images of indentation traces were taken. By analysing the indentation craters, it has been determined whether the damages are acceptable or not with reference to the VDI 3198 standard. The indentation craters formed on the surfaces of the samples were pack-borided at 850 °C for all process times, at 900 °C for 2 and 4 hours, and at 950 °C for 2 hours have the best adhesion quality in the HF1 category of the VDI 3198 norm. The pack-boriding treatment with microwave hybrid heating contributed positively to the adhesion strength, but in additions to this, the test results revealed that adhesion decreased with increasing boriding temperature and time.

Keywords: Adhesion test, Daimler-Benz Rockwell-C, microwave hybrid heating, pack-boriding, VDI 3198 norm.

1. Introduction

Boriding changes the microstructure and composition of the material surface by thermochemical diffusion of boron atoms to the material surface; creates a functional surface layer with optimum surface properties. High hardness and low friction coefficient are two important mechanical properties that the boride layer that forms as a result of boriding gives the material surface. Thanks to these features, the major problem that shortens or ends the service life of engineering materials, namely surface wear, is prevented. Morón et al. [1], in their study, reduced the friction coefficient of the AISI H13 steel, which was initially in the range of 0.64-0.71, to 0.10-0.11 values, which they applied pack-boriding at 950 °C for 6 hours, and increased the abrasion resistance by 23 times in the lubricated environment. Kayali et al. [2] achieved a 30-fold reduction in the abrasion rate of the AISI 316L stainless steel alloy that borided with 2 and 6

hours of hold times at 800 and 900 °C. Material surfaces working in contact with each other are connected with micro-welds after a while. With the ongoing relative movement breaking these bonds, the relatively less hard material is transferred to the opposite element, thus creating gaps on the less hard material surface and protrusions on the other surface. This surface wear resulting in material loss is called adhesive wear. Surface hardening is the leading measure to be taken to increase the adhesive strength on the material surface. However, conventional surface hardening methods cannot be applied to austenitic stainless steels. Because they protect their austenitic microstructure from room temperature to high temperatures. For this reason, boriding is widely preferred in order to increase surface hardness due to its easy applicability and economy. In their study, Alias et al. [3] increased the surface hardness of AISI 304 austenitic stainless steel alloy 5 times with the pack-boriding process at 850 °C and for 8

hours. In many studies in the literature, high surface hardness values have been obtained in different types of steels as well as austenitic stainless steels by applying boriding process [4-19]. Thanks to boriding, the surface hardness of the material not only increases; since the chemical reactivity of boron against oxygen is high, a thin oxide film forms on the boride layer. This layer acts as a solid lubricant, reducing the friction coefficient [20, 21]. Boride layer has a low tendency to cold weld so it does not need to be oiled to prevent adhesive wear. Taktak ve Tasgetiren [22] subjected AISI H13 and AISI 304 steels to boriding in a slurry salt bath at 800–950 °C for 3, 5 and 7 hours. The quality of adhesion strength of the boride layers formed on both steel materials borided at 800 °C is in the HF1 and HF2 category and is very high. However, it has been reported that the adhesion quality of the boride layer decreases as the process temperature and time increases. The increase in the quality of adhesion strength between the boride layer and the matrix material increases the adhesion resistance. As the adhesion quality deteriorates, crack formation starts due to internal stresses and progresses, resulting in delaminations on the material surface.

Krelling et al. [23] applied pack-boriding process on AISI 1020 steel with a 4 hour retention time at 1000 °C. After Rockwell C indentation tests, they obtained HF1 quality adhesion strength between the boride layer and the substrate and reported the result that the boriding gave a good adhesion resistance.

This study aimed to increase the adhesion resistance by using a microwave hybrid heating system as a thermal energy source for pack-boriding process. The adhesion strength analysis of the boride layer formed on the surface of AISI 304L stainless steel samples, on which pack boriding was applied for 2, 4 and 6 hours at 850, 900 and 950 °C temperatures with microwave hybrid heating methods, to the matrix material was evaluated by Daimler-Benz Rockwell-C adhesion test.

2. Experimental Procedure

2.1. Pack-boriding process with microwave hybrid heating

The test specimens were manufactured from AISI 304L stainless steel material, whose standard chemical composition is given in Table 1, with a diameter of 20mm and a height of 10 mm. The samples were ground up to 1200 grid and subjected to ultrasonic bath for 30 minutes before the thermochemical treatment. The pack-boriding treatments were carried out in a microwave furnace at 850, 900 ve 950 °C for 2, 4 and 6 h, and the samples were allowed to cool in the open air at the end of the process. Commercial Ekabor-II powder was used as the boriding agent. The samples were placed in AISI 304 stainless steel containers and

covered with boriding powder. The schematic picture of the microwave sintering furnace with the microwave hybrid heating mechanism where the pack-boriding process takes place is given in Figure 1. Heating in the microwave heating system is provided by both microwave radiation and convection heat transfer mechanisms. That's why hybrid heating is in question. Thanks to the microwave absorbing plates around the boriding crucible, which is heated volumetrically by microwave radiation, convection heat transfer accompanies it. This hybrid heating system, which increases thermal diffusion and saves energy with homogeneous heating and homogeneous temperature distribution, is an improvement innovation in the pack-boriding process. The morphology of the boride layer formed on the sample surfaces after the boriding process was examined by optical microscope at x200 magnifications, and the phases formed in the layer were determined by XRD. The samples for microstructural analyses were sanded with SiC abrasive paper up to 1200 grid, polished with 1 µm diamond polishing solution, and etched with Glyceregia solution.

2.2. Adhesion test and characterization

The Daimler-Benz Rockwell-C adhesion test was used to evaluate the adhesion of boride layers. The Rockwell-C indentation test is specified according to the VDI 3198 norm, as a quality test for coated materials. In this test, the plastic deformation that occurs as a result of the penetration of the conical end indenter into the surface of the coated material determines the adhesion quality of the coating. The thickness of the sample must be at least 10 times greater than the indentation depth. The type and volume of damage to the coating gives information about the adhesion of the coating layer at first glance and the fragility secondly. The principle of the method and the quality categories of the adhesion strength of the damage in the coating layer after the test are shown in Figure 2. Grades between HF1-HF4 indicate the presence of sufficient adhesion in the coating layer; the HF5 and HF6 categories indicate insufficient adhesion strength, ie failure of the coating [24, 25]. Indentation processes, BMS 200-RB brand Rockwell hardness measurement device in accordance with VDI 3198 indentation test standards, with 120° conical tip and 150 kg load after repeating 3 times, the craters formed on the sample surfaces were examined using a stereo microscope and SEM (scanning electron microscope). By analyzing the cracks, delaminations and fractures occurring in the boride layer of each sample, it was determined whether the damages were acceptable by referring to the damage categories (HF1-HF6) of the VDI 3198 indentation test standard in Figure 2.

Table 1. AISI 304L stainless steel material chemical composition

Element	C	Mn	P	S	Si	Cr	Ni	N
Wt %	≤ 0.030	≤ 2.00	≤ 0.045	≤ 0.030	≤ 0.75	18-20	8-10	≤ 0,10

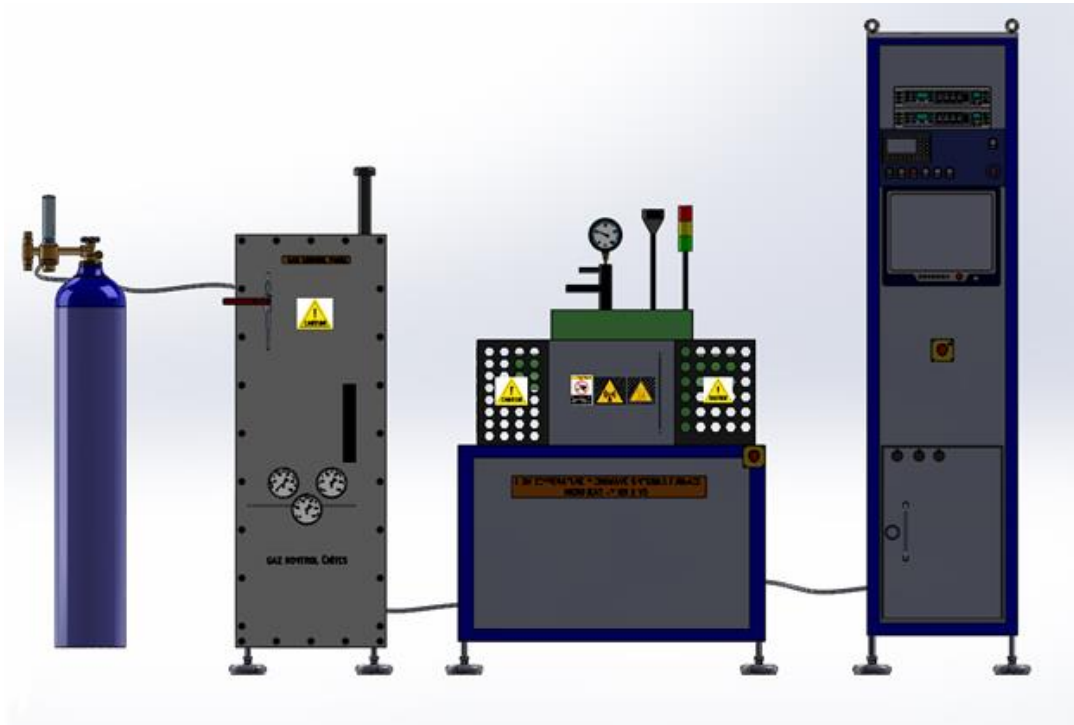


Figure 1. Schematic picture of microwave sintering furnace

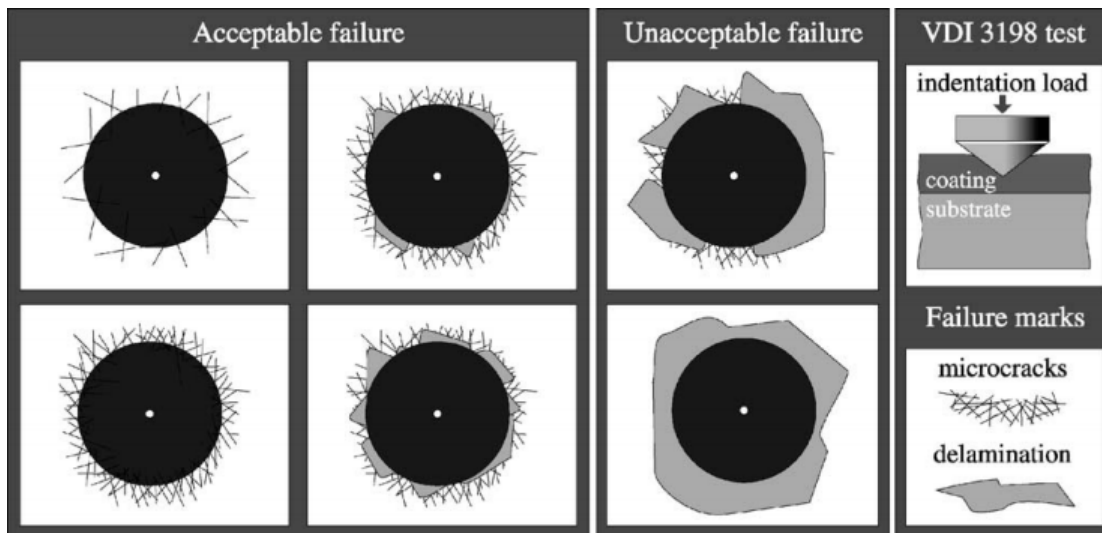


Figure 2. VDI 3198 indentation test adhesion quality classification [24]

3. Results and Discussion

3.1. The Characterization of Boride Layers

In the optical microscope images, the boride layers formed after boriding on the cylindrical samples of AISI 304L stainless steel are bilayer ($Fe_2B + FeB$) and can be clearly distinguished from the base material. As can be seen from Figure 3, the increase in process temperature

and retention time increased the boride layer thickness. Due to the high amount of alloying elements in the structure of AISI 304L stainless steel material, the boride layer formed on its surface has flat and smooth morphology. In Figure 4, XRD analysis showed the presence of Cr_2B and Ni_2B phases in the boride layer besides Fe_2B and FeB phases.

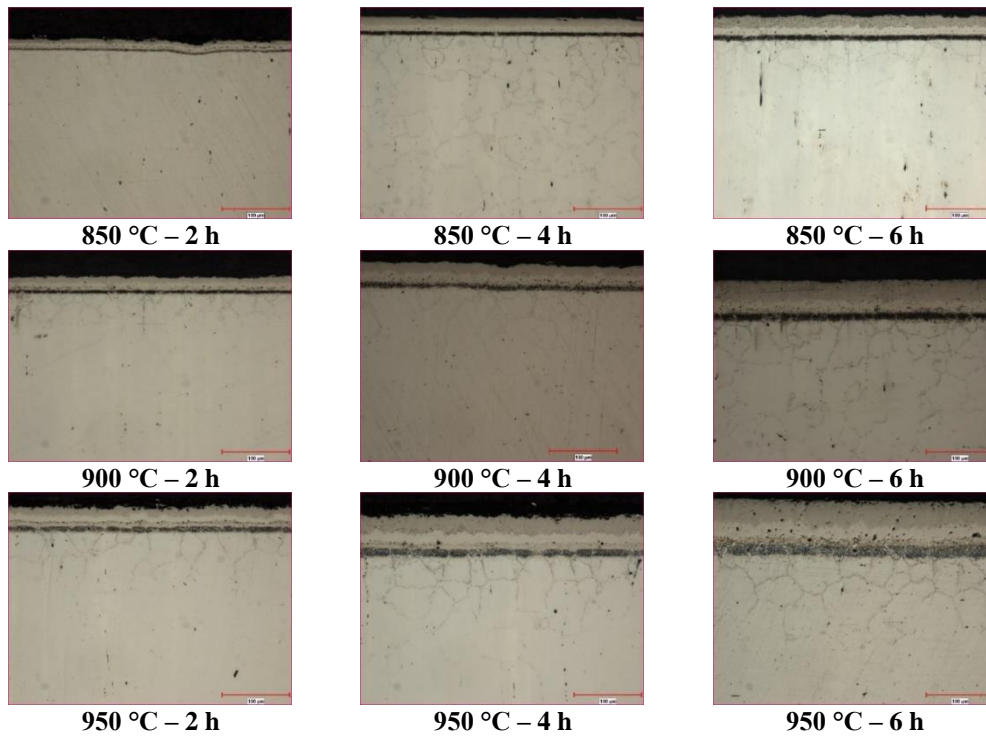


Figure 3. Optical microscope images of AISI 304L samples pack-borided at process temperatures and times with microwave hybrid heating: x200 magnification

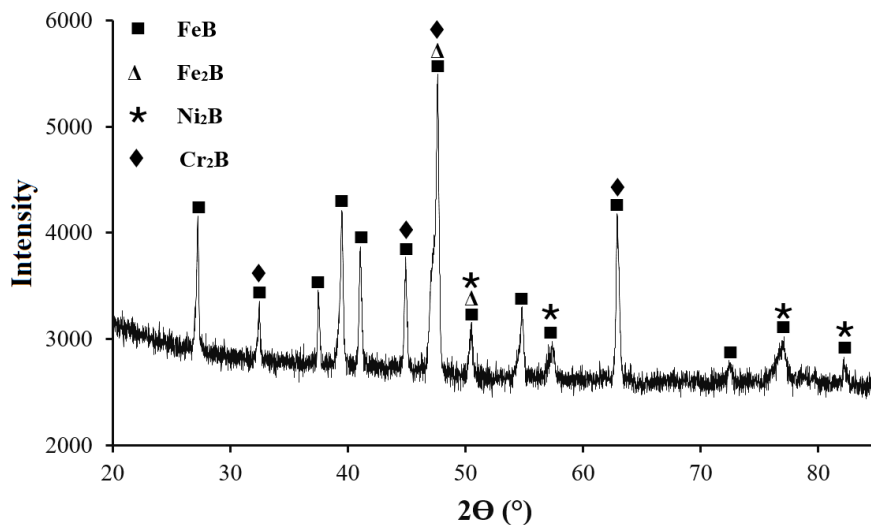


Figure 4. XRD pattern of the pack-borided AISI 304L steel at 900 °C for 6 hours

3.2. The adhesion resistance of boride layer

Macro and SEM images of the indentation traces taken after the adhesion tests on AISI 304L stainless steel samples pack-borided with microwave hybrid heating method are given in Figure 5-18. Whether the appearance of damage occurring in the adhesion test results is acceptable or not was evaluated according to the VDI 3198 norm. In Figure 5, the indentation craters formed on AISI 304L stainless steel sample surfaces, which are pack-borided at 850 °C for all process periods, at 900 °C for 2 and 4 hours, and at 950 °C for 2 hours by microwave hybrid heating method, are as in

the HF1 category of the VDI 3198 and are acceptable. HF1 has the best adhesion quality. Therefore, the adhesion strength of the samples pack-borided at these process temperatures and times is quite good. However, as can be seen in Figure 6, the boride layer on the surface of one of the samples, which was pack-borided at 900 °C for 6 hours, was broken up during the indentation test, and in another there are spillings. A spalling was observed in the boride layer of one of each sample which was pack-borided at 950 °C for 4 and 6 hours. Damages in these samples are of HF5 quality and are unacceptable.

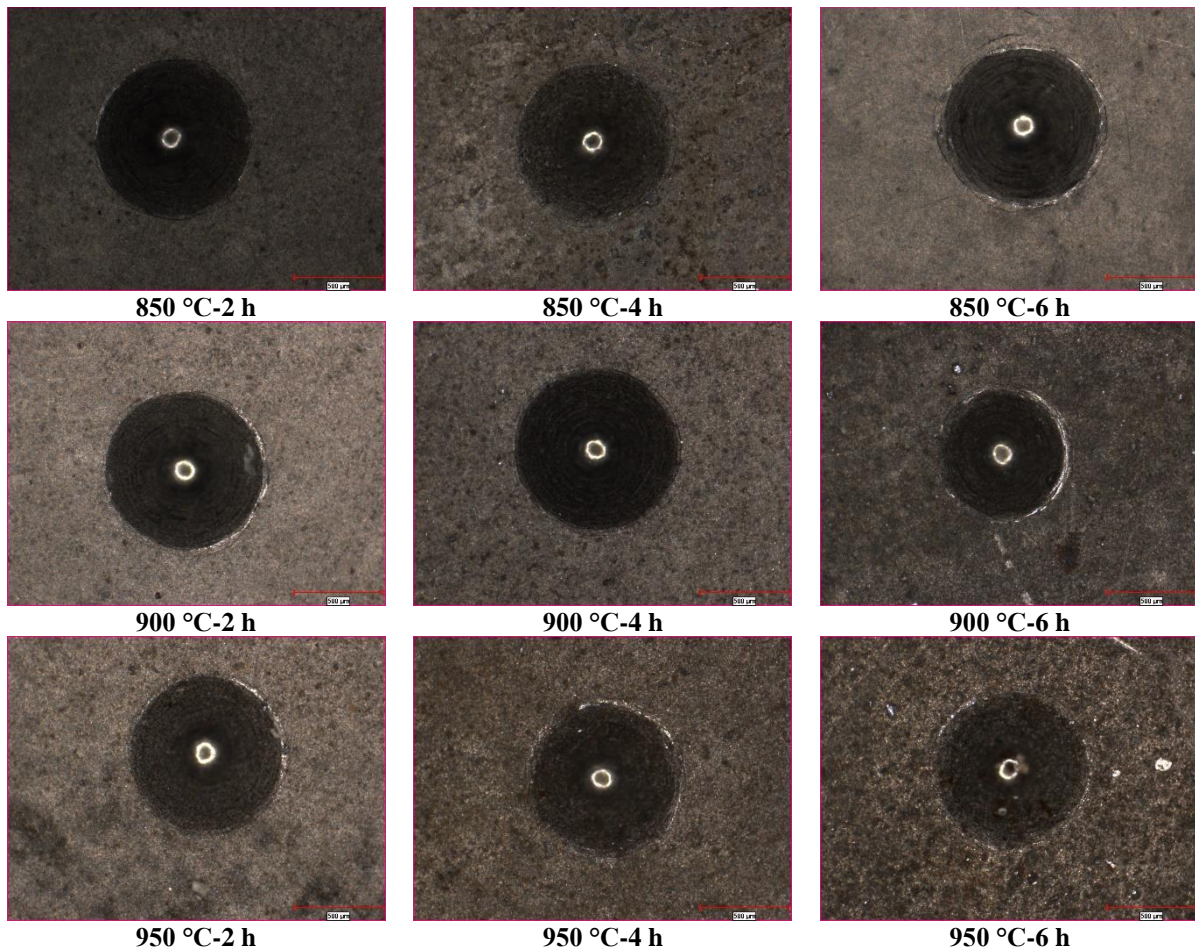


Figure 5. Macro images of the crater formed after the adhesion test on AISI 304L samples pack-borided with microwave hybrid heating



Figure 6. Boride layer removals occurring after the adhesion test in AISI 304L samples pack-borided with microwave hybrid heating

When the SEM images of the indentation traces of the boride layers of AISI 304L stainless steel samples pack-borided with microwave hybrid heating method in Figure 7-11 and Figure 14 are examined, it is more clearly seen that the acceptable damage in these samples

are HF1 quality micro cracks. These micro cracks are in the form of lateral cracks and generally capillary, and belong to the best quality category according to the VDI 3198 norm. Figure 12 shows the SEM image taken after the adhesion test of one of the AISI 304L samples pack-

borided with microwave hybrid heating method at 900 °C with a retention time of 6 hours. It is seen that the adhesion strength quality belongs to the HF3 category due to the curvilinear cracks and occasional spallings in the boride layer on the surface of this sample. The SEM image taken after the adhesion test of another sample pack-borided at the same process temperature and time is given in Figure 13. There are spallation and wear debris in the boride layer of the sample. The adhesion strength of this sample between the boride layer and the base material is HF5 quality and is in unacceptable category.

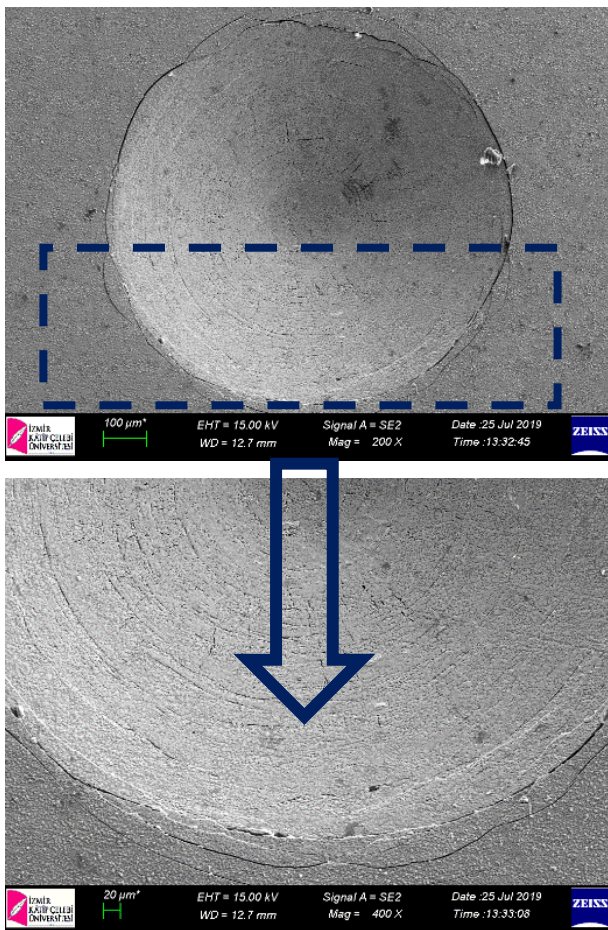


Figure 7. SEM images of the traces and micro cracks formed after the adhesion test on the AISI 304L sample pack-borided at 850 °C for 2 hours with microwave hybrid heating

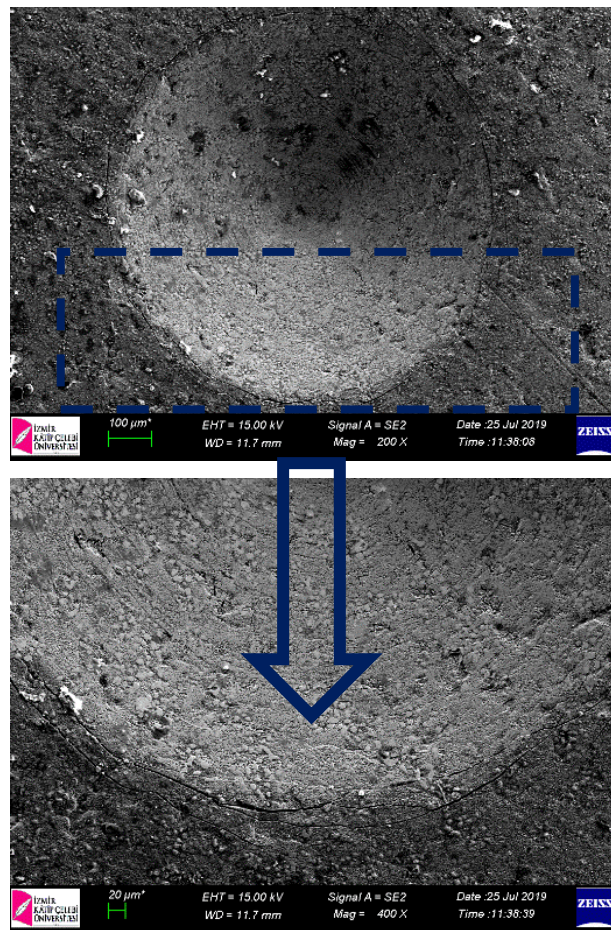


Figure 8. SEM images of the traces and micro cracks formed after the adhesion test in AISI 304L sample pack-borided at 850 °C for 4 hours with microwave hybrid heating

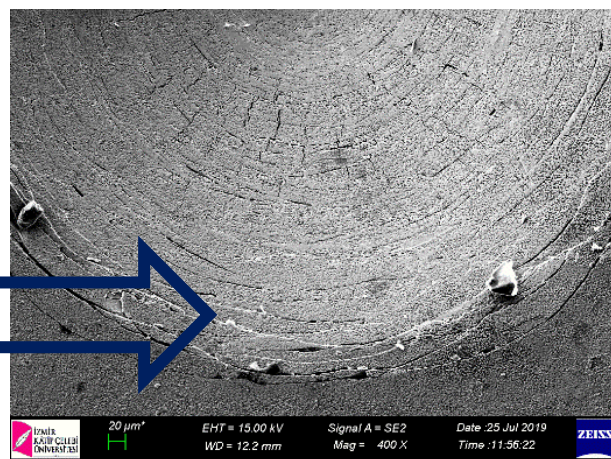
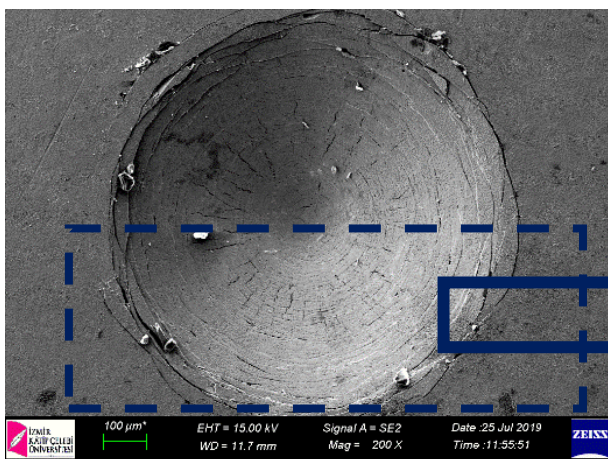


Figure 9. SEM images of the traces and micro cracks formed after the adhesion test on the AISI 304L sample pack-borided at 850 °C for 6 hours with microwave hybrid heating

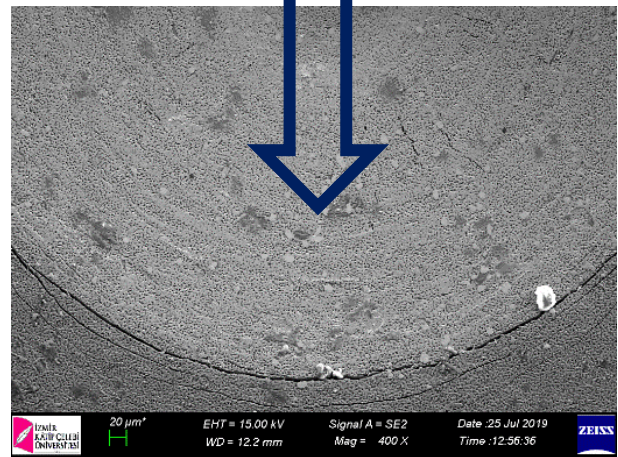
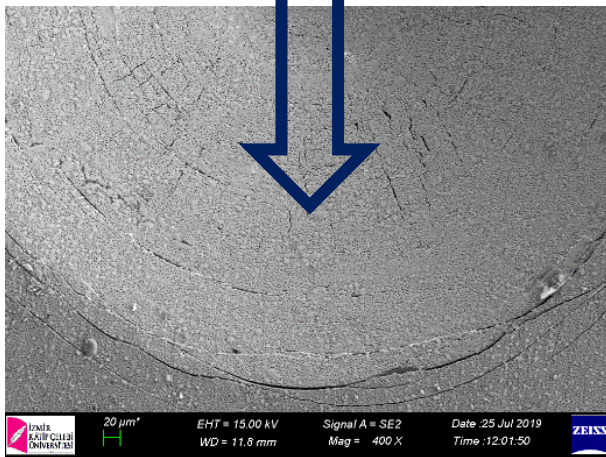
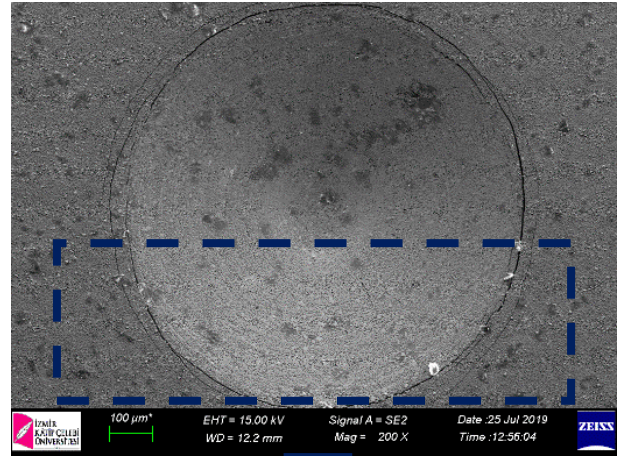
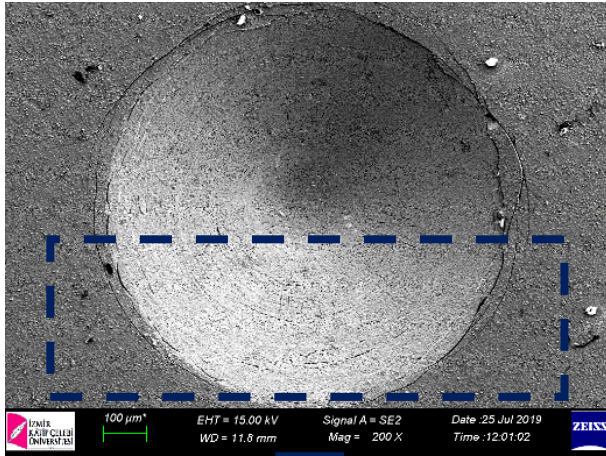


Figure 10. SEM images of the traces and micro cracks formed after the adhesion test in AISI 304L sample pack-borided at 900 °C for 2 hours with microwave hybrid heating

Figure 11. SEM images of the traces and micro cracks formed after the adhesion test in AISI 304L sample pack-borided at 900 °C for 4 hours with microwave hybrid heating

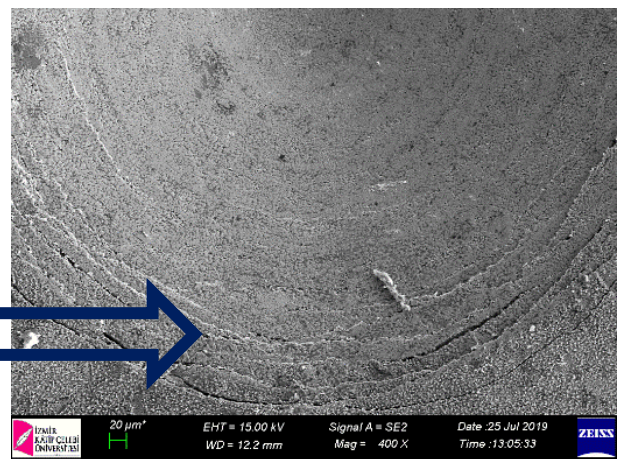
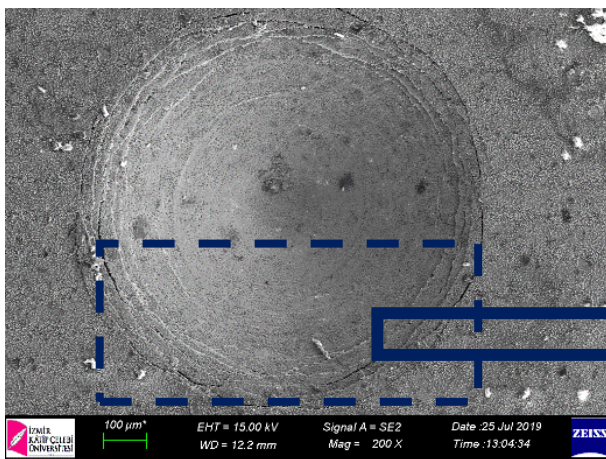


Figure 12. SEM images of the traces and micro cracks formed after the adhesion test on the AISI 304L sample pack-borided at 900 °C for 6 hours with microwave hybrid heating

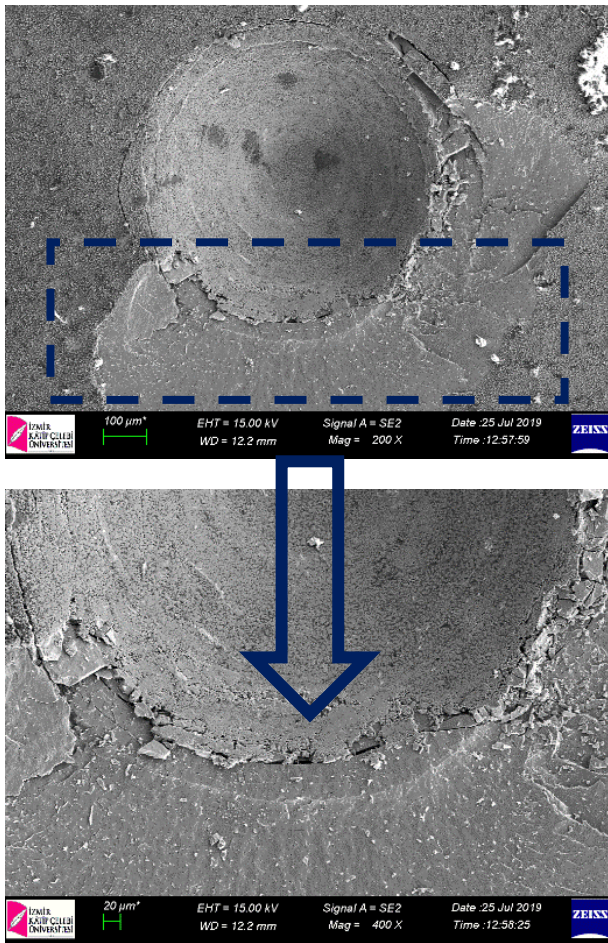


Figure 13. SEM images of the fracture formed after the adhesion test in AISI 304L sample pack-borided for 6 hours at 900 °C with microwave hybrid heating

The indentation craters belonging to one of the pack-borided samples with microwave hybrid heating at 950 °C for 4 hours are shown in Figure 15. There are abrasion scratches and burrs in the boride layer after the adhesion test. This damage is of HF3 type and is acceptable.

The damage appearance after the adhesion test of another sample, which is pack-borided with microwave hybrid heating at 950 °C for 4 hours, is shown in Figure 16. Delaminations occurred in the boride layer of the sample. According to the VDI 3198 indentation test principles, this damage is of the HF5 type and is unacceptable.

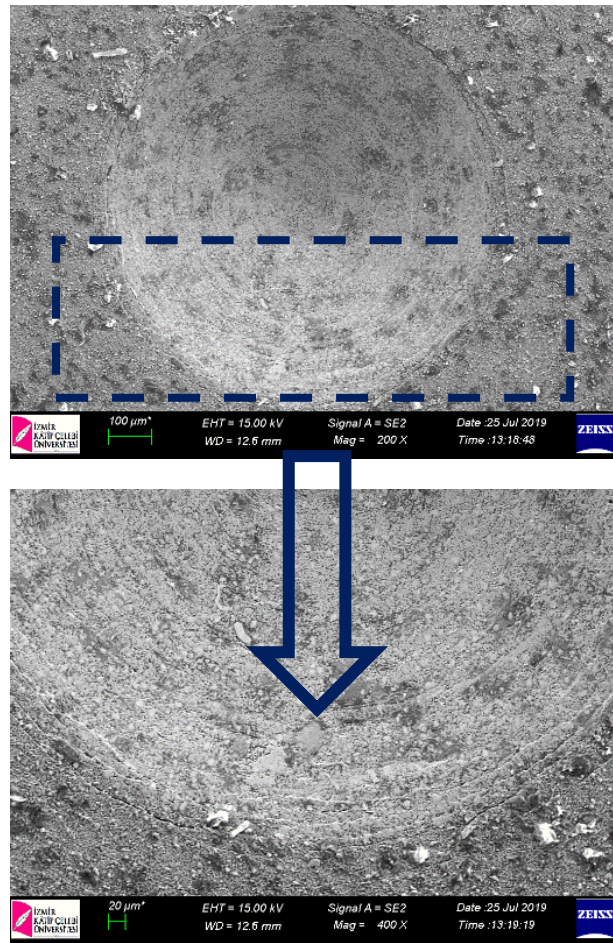


Figure 14. SEM images of the traces and micro cracks formed after the adhesion test of AISI 304L samples pack-borided at 950 °C for 2 hours with microwave hybrid heating

The damage appearance after the indentation test of one of the samples pack-borided with microwave hybrid heating at 950 °C for 6 hours is given in Figure 17. Mosaic cracks and wear lines were formed in the boride layer. This damage is in the HF3 category and is acceptable.

The SEM image showing the damage appearance after the adhesion test of another sample that is pack-borided with microwave hybrid heating at 950 °C for 6 hours is given in Figure 18. Local spallation and delaminations occurred in the boride layer of the sample. According to the VDI 3198 indentation test principles, this damage is of the HF5 type and is unacceptable.

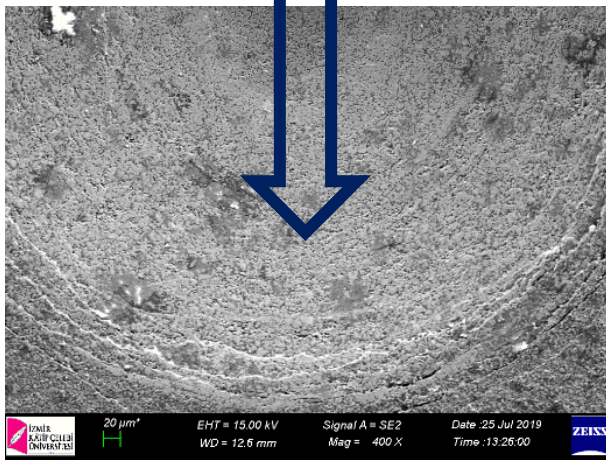
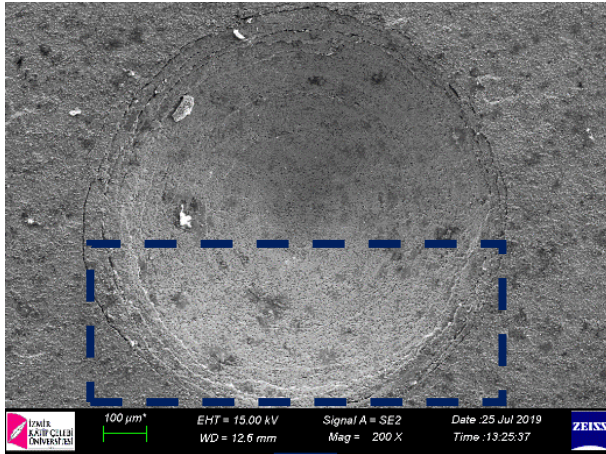


Figure 15. SEM images of the traces and micro cracks formed after the adhesion test of AISI 304L samples pack-borided at 950 °C for 4 hours with microwave hybrid heating

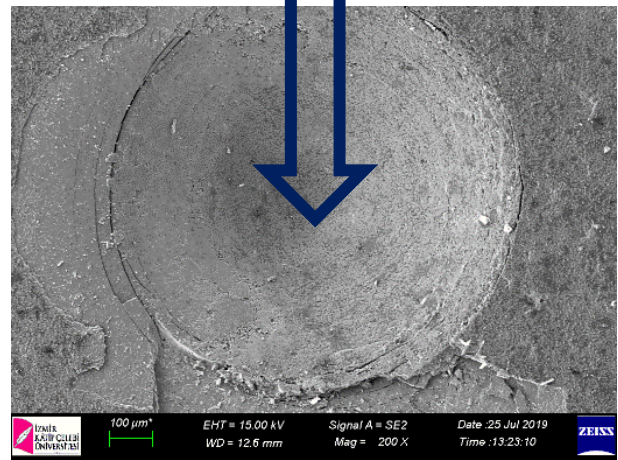
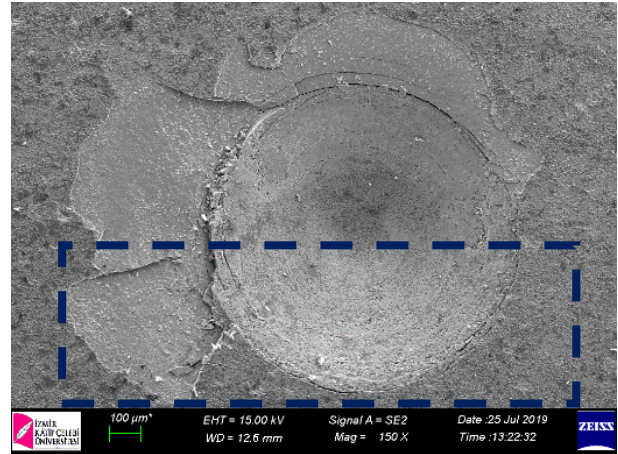


Figure 16. SEM images of the delaminations and cracks formed after the adhesion test of AISI 304L samples pack-borided at 950 °C for 4 hours with microwave hybrid heating

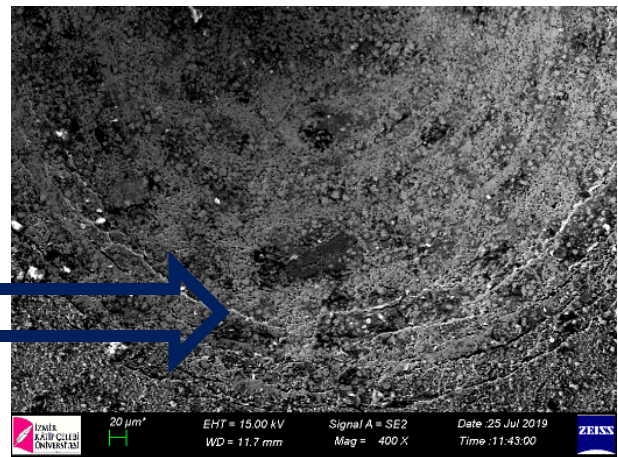
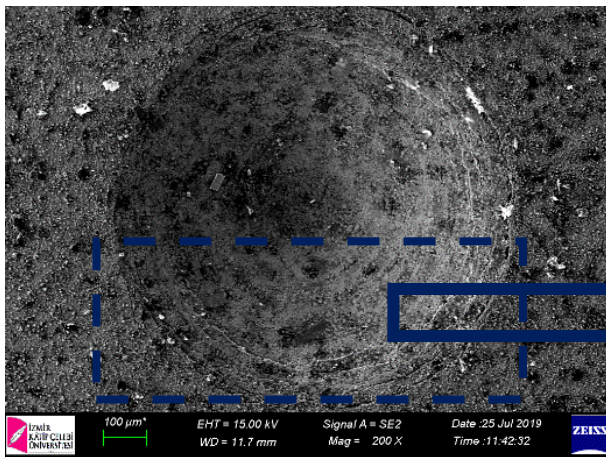


Figure 17. SEM images of the traces and cracks formed after the adhesion test of AISI 304L samples pack-borided at 950 °C for 6 hours with microwave hybrid heating

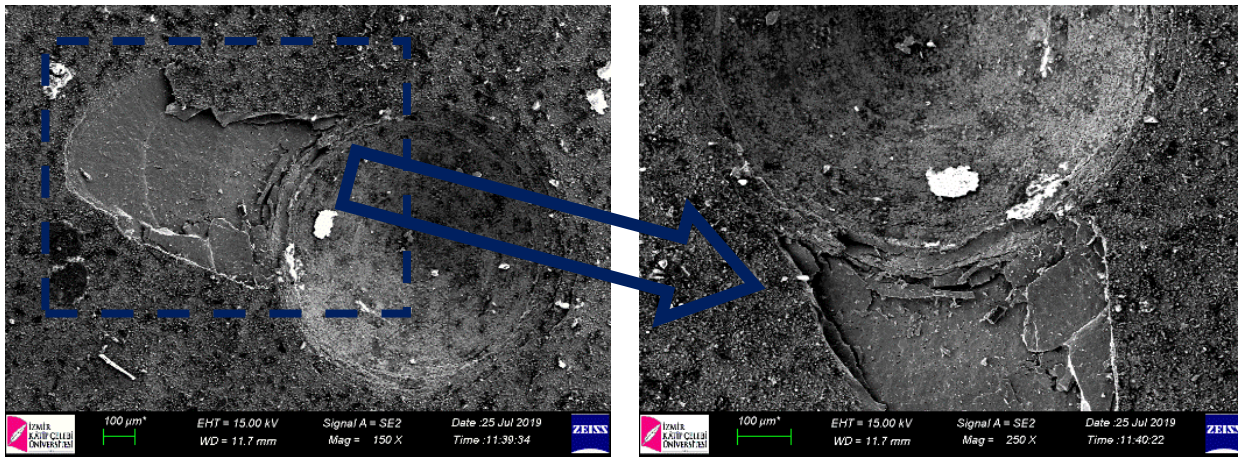


Figure 18. SEM images of the spallation and delaminations formed after the adhesion test of AISI 304L samples pack-borided at 950 °C for 6 hours with microwave hybrid heating

4. Conclusions

Optical microscope examinations showed that both FeB and Fe₂B phase thicknesses increased with the increase of process temperature and retention time in pack-boriding processes performed with microwave hybrid heating method. Uniform and homogeneous boride layers were obtained. However, boride layers formed by the effect of alloying elements are not saw-toothed but flat structure.

XRD pattern analysis showed the presence of FeB, Fe₂B, Cr₂B and Ni₂B phases in the boride layer.

As a result of the Daimler-Benz Rockwell-C adhesion tests carried out, the adhesion strength of the boride layers-substrate of all samples is high, except for the samples that are pack-borided for 6 hours at 900 °C, and at 950 °C for 4 and 6 hours with microwave hybrid heating because the adhesion has decreased with increasing boriding temperature and time. The main reason for the low adhesion strength in these samples is the delamination and spallation of the boride layer as a result of the increase in the thickness of the brittle FeB phase due to the increase in the temperature and retention time of the pack-boriding process.

Author's Contributions

Dilek Arslan: Carried out the experimental processes and examined the results. The manuscript was drafted and written by her.

Recep Onur Uzun: Supervised the experimental procedure and contributed to manuscript preparation.

Ethics

There are no ethical issues after the publication of this manuscript.

References

1. Morón, RC, Hernández-Onofre, I, Contla-Pacheco, AD, Bravo-Bárceñas, D, Campos-Silva, I. 2020. Friction and reciprocating wear behavior of borided AISI H13 steel under dry and lubricated conditions. *Journal of Materials Engineering and Performance*; 29: 4529-4540.
2. Kayali, Y, Büyüksagis, A, Yalcin, Y. 2013. Corrosion and wear behaviors of boronized AISI 316L stainless steel. *Metals and Materials International*; 19(5): 1053-1061.
3. Alias, SK, Abdullah, B, Talari, M, Jumadin, MH, Idham, MF, Ismail, A. 2017. Effect of pack boronizing on microstructure and microhardness of 304 stainless steel. *Key Engineering Materials*; 740: 54-59.
4. Kayali, Y. 2013. Investigation of the diffusion kinetics of borided stainless steels. *The Physics of Metals and Metallography*; 114(12): 1061-1068.
5. Günen, A, Kurt, B, Somunkıran, İ, Kanca, E, Orhan, N. 2015. The effect of process conditions in heat-assisted boronizing treatment on the tensile and bending strength characteristics of the AISI-304 austenitic stainless steel. *The Physics of Metals and Metallography*; 116(9): 896-907.
6. Calik, A, Simsek, M, Karakas, MS, Ucar, N. 2014. Effect of boronizing on microhardness and wear resistance of steel AISI 1050 and chilled cast iron. *Metal Science and Heat Treatment*; 56: 89-92.
7. Yilmaz, SO, Teker, T, Karatas, S. 2016. Wear behavior of iron boride coating on AISI 4140. *Protection of Metals and Physical Chemistry of Surfaces*; 52(1): 119-127.
8. Gunes, I. 2013. Wear behaviour of plasma paste boronized of AISI 8620 steel with borax and B₂O₃ paste mixtures. *Journal of Materials Science & Technology*; 29(7): 662-668.
9. Ulutan, M, Celik, ON, Gasan, H, Er, U. 2010. Effect of different surface treatment methods on the friction and wear behavior of AISI 4140 steel. *Journal of Materials Science & Technology*; 26(3): 251-257.
10. Béjar, MA, Moreno, E. 2006. Abrasive wear resistance of boronized carbon and low-alloy steels. *Journal of Materials Processing Technology*; 173: 352-358.



11. Carrera-Espinoza, R, Figueroa-López, U, Martínez-Trinidad, J, Campos-Silva, I, Hernández-Sánchez, E, Motallebzadeh, A. 2016. Tribological behavior of borided AISI 1018 steel under linear reciprocating sliding conditions. *Wear*; 362-363: 1-7.
12. Tabur, M, Izciler, M, Gul, F, Karacan, I. 2009. Abrasive wear behavior of boronized AISI 8620 steel. *Wear*; 266: 1106-1112.
13. Aichholz, SAC, Meruvia, MS, Júnior, PCS, Torres, RD. 2018. Tribocorrosion behavior of boronized AISI 4140 steel. *Surface and Coatings Technology*; 352: 265-272.
14. Bartkowska, A, Bartkowski, D, Swadźba, R, Przystacki, D, Miklaszewski, A. 2018. Microstructure, chemical composition, wear, and corrosion resistance of FeB-Fe₂B-Fe₃B surface layers produced on Vanadis-6 steel using CO₂ laser. *The International Journal of Advanced Manufacturing Technology*; 95: 1763-1776.
15. Gunes, I, Ulker, S, Taktak, S. 2011. Plasma paste boronizing of AISI 8620, 52100 and 440C steels. *Materials and Design*; 32: 2380-2386.
16. Kayali, Y, Günes, I, Ulu, S. 2012. Diffusion kinetics of borided AISI 52100 and AISI 440C steels. *Vacuum*; 86: 1428-1434.
17. Ozbek, I, Sen, S, Ipek, M, Bindal, C, Zeytin, S, Ucisik, AH. 2004. A mechanical aspect of borides formed on the AISI 440C stainless-steel. *Vacuum*; 73: 643-648.
18. Günen, A, Kanca, E, Demir M, Er, Y, Sağlam, G, Gök, MS. 2017. Micro-abrasion wear behavior of fast borided steel tooth drill bits. *Tribology Transactions*; 60(2): 267-275.
19. Gunes, I, Kanat, S. 2015. Diffusion kinetics and characterization of borided AISI D6 steel. *Protection of Metals and Physical Chemistry of Surfaces*; 51(5): 842-846.
20. Akkaş, M, Islak, S, Özorak, C. 2018. Corrosion and wear properties of Cu-TiC composites produced by hot pressing technique. *Celal Bayar University Journal of Science*; 14(4): 465-469.
21. Kumar, GBV, Rao, CSP, Selvaraj, N. 2011. Mechanical and Tribological Behavior of Particulate Reinforced Aluminum Metal Matrix Composites – a review. *Journal of Minerals & Materials Characterization & Engineering*; 10(1): 59-91.
22. Taktak, S, Tasgetiren S. 2006. Identification of Delamination Failure of Boride Layer on Common Cr-Based Steels. *Journal of Materials Engineering and Performance*; 15(5): 570-574.
23. Krelling, AP, Costa, CE, Milan, JCG, Almeida, EAS. 2017. Micro-abrasive wear mechanisms of borided AISI 1020 steel. *Tribology International*; 111: 234-242.
24. Vidakis, N, Antoniadis, A, Bilalis, N. 2003. The VDI 3198 indentation test evaluation of a reliable qualitative control for layered compounds. *Journal of Materials Processing Technology*; 143-144: 481-485.
25. Verein Deutscher Ingenieure Normen, VDI 3198, *VDI-Verlag*, Dusseldorf, 1991.

Analysis of a Capacitor Modelled with Conformable Fractional Derivative under DC and Sinusoidal Signals

Utku Palaz^{1*}, Reşat Mutlu²

¹Ministry of Education of Republic of Turkey

²Department of Electronics and Telecommunication Engineering, Namık Kemal University, Çorlu, Tekirdağ, Turkey

*utkupalaz@gmail.com

*Orcid: 0000-0003-4579-0424

Received: 25 June 2020

Accepted: 1 June 2021

DOI: 10.18466/cbayarfbe.757813

Abstract

Fractional order circuit elements are successfully used to model circuits and systems in the last few decades. There are different types of fractional derivatives. Recently, another one named “the conformable fractional derivative” (CFD) has been introduced and shown to give good results for modeling supercapacitors. It is imperative to know how circuit elements behave for different current and voltage waveforms in circuit theory so that they can be exploited at their full potential. A CFD capacitor is not a well-known element, and its usage and circuit solutions are rarely addressed in the literature. In this study, it is examined how a CFD capacitor would behave under DC and AC excitations when it is fed by not only a current source but also a voltage source.

Keywords: Fractional Order Derivatives, Circuit Analysis, Circuit Theory, Energy Analysis, Circuit Modeling

1. Introduction

Fractional derivative (FD) is a branch of mathematical analysis [1, 2]. A differential operator can be of any arbitrary order within it. It has first appeared in the 17th century [3]. In the last decades, Fractional Calculus has emerged as a popular research area because of its applicability in many different fields [4-5]. The self-taught Oliver Heaviside has used fractional calculus to find the solution of the telegrapher's equation around 1890 [3]. The fractional-order circuit elements are used to model circuit elements such as capacitors, inductors and memristors [6-10]. Filters, controllers and oscillators which are based on fractional-order circuit elements are made or can be used to model systems [4-5, 8-9, 11-14]. Another FD is suggested in [15]. It is named as “the conformable fractional derivative” (CFD). Its definition is built on the conventional limit definition of the derivative of a function. It casts off the other FD definitions [15]. This makes it simpler and advantageous than the other FDs. The CFD is elaborated in [16]. However, a CFD is actually not an FD: it can be described as a first-order derivative time a power function of the independent variable [15, 16]. This new definition is a broadening of the ordinary derivative. It is also distinct from the other FDs. The CFD is able to accommodate the common features of

FDs. Well-known calculus theorems such as product rule, Rolle's Theorem, Average Value Theorem, partial integration, Taylor series can be easily extended or applied to the CFD. The conformal fractional derivative has a very important property: while the Riemann-Liouville FD of a constant is not zero, the CFD of a constant is zero. Due to these properties, the conformal fractional derivative has become a hot research area. The conformal derivative has also the advantage of being physically interpretable compared to the other types of fractional derivatives [17]. Usage of the FDs in electric circuits has been examined in [18]. Supercapacitors have been modelled using fractional-order models in [19-22]. The oscillation of impulsive conformable fractional differential equations has been inspected in [23]. Electric circuits modelled with FD circuit elements under sinusoidal excitation have been analyzed with the enhanced fractional derivative method, which is called Caputo FD generalizing the differential equations and ordinary integrals are not necessary to describe the fractional-order initial conditions like Riemann-Liouville FD [24-25]. Several electric circuits characterized by CFDs have been solved in [26]. Other circuits modelled with the CFD have been examined in [27]. The conformable fractional derivative has been used to analyze an electric circuit containing a supercapacitor in [28]. Analytical solutions of electrical circuits described by fractional conformable

derivatives in Liouville-Caputo sense is given in [29]. Electric circuits of the CFDs with and without singular kernels have been solved in [30].

It is important to analyze new circuit elements for different current and voltage waveforms so that they can be exploited at full potential. In this paper, the conformal fractional derivative capacitor model for DC and sinusoidal waveforms have been solved. CFD capacitor has been fed with not only voltage sources but also for current sources. The analytical solutions were given with incomplete gamma function for sinusoidal voltage case. The discussions are provided in the conclusion section.

The rest of the paper is structured as follows. The CFD capacitor model is given in the second section. Its analysis for DC and AC signals are given in the third section. Op-amp-based differentiator and integrator circuits with a CFD capacitor are examined in the fourth section. Finally, the paper is concluded in "Conclusions" section.

2. Conformal Fractional Derivative and CFD Capacitor Constitutional Law

The CFD is described in [15] as the follows:

Definition 1. Let $f : [0, +\infty) \rightarrow R$ and $t > 0$. The CFD for $0 < \alpha \leq 1$ is described as

$$D_{\alpha} f(t) = \lim_{p \rightarrow 0} \frac{f(t + p^{(1-\alpha)}) - f(t)}{p} \quad (2.1)$$

For $t > 0$ and the conformable fractional derivative at 0 is defined as $D_{\alpha} f(0) = \lim_{t \rightarrow 0^+} (D_{\alpha} f)(t)$. If it is

differentiable then $D_{\alpha} f(t) = t^{1-\alpha} f'(t)$ (2.2)

Definition 2. Let $\alpha \in (0, 1]$. The conformable fractional integral of a function $f : [0, +\infty) \rightarrow R$ of order α is denoted by $I_{\alpha} f(t)$ and is defined as

$$I_{\alpha} f(t) = \int_0^t s^{(\alpha-1)} f(s) ds \quad (2.3)$$

$$\frac{d^{\alpha} f(t)}{dt^{\alpha}} = f'(t) t^{1-\alpha} = \frac{df(t)}{dt} t^{1-\alpha} \quad (2.4)$$

More information about CFD can be found in [15-17]. If a capacitor can be modelled using CFD [28], its constitutive law can be written as

$$i_c(t) = C_{\alpha} \frac{d^{\alpha} v_c(t)}{dt^{\alpha}} \quad (2.5)$$

Where $i_c(t)$, $v_c(t)$ and C_{α} are CFD capacitor current, CFD capacitor voltage and CFD capacitor coefficient, respectively.

3. The CFD Capacitor Fed by a Current Source

In this section, the solutions of a CFD capacitor is found if it is fed by a current source as shown in Figure 1 for the cases: (a) the current source being constant and (b) it being sinusoidal.

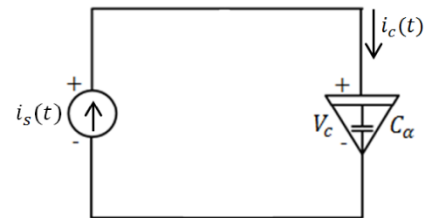


Figure 1: The CFD capacitor fed by a current source

3.1 Constant Current Solution

If the current source has a constant magnitude or the CFD capacitor current is constant;

$$i_s(t) = i_c(t) = I_{dc} = C_{\alpha} \frac{dv_c(t)}{dt} t^{1-\alpha} \quad (3.1)$$

By arranging both sides,

$$\frac{dv_c(t)}{dt} = \frac{I_{dc}}{C_{\alpha} t^{1-\alpha}} \rightarrow dv_c(t) = \frac{I_{dc}}{C_{\alpha} t^{1-\alpha}} dt \quad (3.2)$$

Its voltage can be found as

$$v_c(t) = \int \frac{I_{dc}}{C_{\alpha} t^{1-\alpha}} dt = \frac{I_{dc}}{C_{\alpha}} \int t^{\alpha-1} dt \quad (3.3)$$

$$v_c(t) = \frac{I_{dc} t^{\alpha}}{C_{\alpha} \alpha} + K \quad (3.4)$$

Where K is the integration constant and the capacitor voltage at $t = 0$ is used to find K;

$$v_c(0) = \frac{I_{dc} 0^{\alpha}}{C_{\alpha} \alpha} + K \rightarrow K = v_c(0) \quad (3.5)$$

Using the integration constant, the CFD capacitor current can be obtained as;

$$v_c(t) = \frac{I_{dc} t^{\alpha}}{C_{\alpha} \alpha} + v_c(0) \quad (3.6)$$

3.2 Sinusoidal Current Solution

If a sinusoidal current of $i_s(t) = I_m \cos(\omega t + \varphi)$ is applied to the CFD capacitor, its voltage can be calculated with the following steps:

$$i_s(t) = i_c(t) = I_m \cos(\omega t + \varphi) = C_\alpha \frac{dv_c(t)}{dt} t^{1-\alpha} \quad (3.7)$$

By arranging both sides of the equation, the CFD capacitor voltage is written as

$$\frac{dv_c(t)}{dt} = \frac{I_m \cos(\omega t + \varphi)}{C_\alpha t^{1-\alpha}} \quad (3.8)$$

$$v_c(t) = \frac{I_m}{C_\alpha} \int \cos(\omega t + \varphi) t^{(\alpha-1)} dt \quad (3.9)$$

Using Wolfram Alpha [31], the solution of the integral is found as

$$v_c(t) = \frac{I_m}{C_\alpha} \left(\frac{-t^\alpha (\omega^2 t^2)^{-\alpha}}{2} ((-i\omega t)^\alpha (\cos(\varphi) - i \sin(\varphi)) \Gamma(a, i\omega t) + (i\omega t)^\alpha (\cos(\varphi) + i \sin(\varphi)) \Gamma(a, -i\omega t)) + K \right) \quad (3.10)$$

Using the following identities:

$$e^{i\varphi} = \cos(\varphi) + i \sin(\varphi) \quad (3.11)$$

$$e^{-i\varphi} = \cos(\varphi) - i \sin(\varphi)$$

The capacitor voltage turns into;

$$v_c(t) = \frac{I_m}{C_\alpha} \left(\frac{-t^\alpha (\omega^2 t^2)^{-\alpha}}{2} ((-i\omega t)^\alpha e^{-i\varphi}) \Gamma(a, i\omega t) + (i\omega t)^\alpha e^{i\varphi} \Gamma(a, -i\omega t) + K \right) \quad (3.12)$$

In mathematics, the upper incomplete gamma function is a transcendental function that appears as solutions to diverse problems such as definite integrals.

When splitting the incomplete gamma function at a point $x \geq 0$, two types of the incomplete gamma functions called upper and lower are obtained.

The definition of the upper incomplete gamma function intervals are explained from x to ∞ .

$$\Gamma(s, x) = \int_x^\infty t^{s-1} e^{-t} dt \quad (3.13)$$

If the initial condition is used at $t=0$,

$$v_c(0) = \frac{I_m}{C_\alpha} [0 + K] \rightarrow K = v_c(0) \frac{C_\alpha}{I_m} \quad (3.14)$$

Using the integration constant, the CFD capacitor voltage can be obtained as

$$v_c(t) = -\frac{I_m t^\alpha (\omega^2 t^2)^{-\alpha}}{2C_\alpha} ((-i\omega t)^\alpha e^{-i\varphi}) \Gamma(a, i\omega t) + ((i\omega t)^\alpha e^{i\varphi}) \Gamma(a, -i\omega t) + v_c(0) \quad (3.15)$$

Numerical methods can be used to calculate the CFD capacitor voltage since the solution requires the upper incomplete gamma function which is also evaluated numerically.

4. The CFD Capacitor Fed by a Voltage Source

In this section, the solution of the CFD capacitor fed by a voltage source shown in Figure 2 is found for both of the cases: the voltage source being a constant (a) and a sinusoidal (b).



Figure 2. The CFD capacitor fed by a voltage source

4.1. Constant Voltage Solution

If a step function voltage is applied to the CFD capacitor at time being t_0 :

$$v_C(t) = V_{dc} u(t - t_0) \quad (4.1)$$

The CFD capacitor current becomes

$$i_c(t) = C_\alpha \frac{dv_C(t)}{dt} t^{1-\alpha} = C_\alpha \frac{d(V_{dc} u(t - t_0))}{dt} t^{1-\alpha} \quad (4.2)$$

$$i_c(t) = C_\alpha V_{dc} \delta(t - t_0) t^{1-\alpha} = C_\alpha V_{dc} \delta(t - t_0) t_0^{1-\alpha} \quad (4.3)$$

Where $\delta(t - t_0)$ is the Dirac-delta function [32] shifted to time being t_0 .

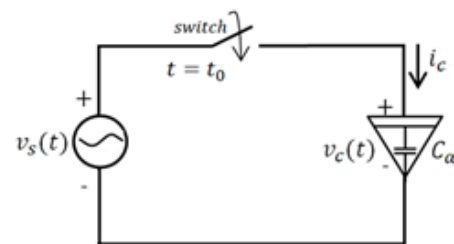


Figure 3. The CFD capacitor fed by a voltage source and depends on the time.

A CFD capacitor without a series resistor withdraws a Dirac pulse as a linear time-invariant resistor does. However, its current magnitude depends on the time the voltage is applied opposite to the case in which an LTI (Linear Time-Invariant) capacitor current pulse

magnitude is constant not depending on the time the step function is applied as shown in Figure 3.

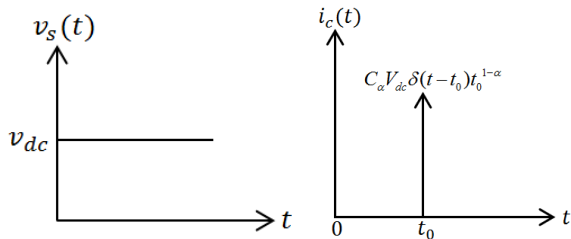


Figure 4. The CFD capacitor voltage and current vs. time when it is fed by a constant voltage

4.2. Sinusoidal Voltage Solution

If a sinusoidal voltage of $v_c(t) = V_m \sin(\omega t + \varphi)u(t - t_0)$ is applied to the CFD capacitor at time being t_0 , its current is found as

$$i_c(t) = C_\alpha \frac{dv_c(t)}{dt} t^{1-\alpha} = C_\alpha \frac{d(V_m \sin(\omega t)u(t - t_0))}{dt} t^{1-\alpha} \quad (4.4)$$

$$i_c(t) = C_\alpha V_m t^{1-\alpha} (\omega \cos(\omega t) + \sin(\omega t) \delta(t - t_0)) \quad (4.5)$$

When the Dirac-delta function rule $f(t)\delta(t - t_0) = f(t_0)\delta(t - t_0)$ is used, the CFD capacitor current can be written as:

$$i_c(t) = C_\alpha V_m \omega \cos(\omega t) t^{1-\alpha} + C_\alpha V_m \sin(\omega t_0) t_0^{1-\alpha} \delta(t - t_0) \quad (4.6)$$

The circuit waveforms are drawn with Matlab™. The CFD capacitor current and voltage for this case is shown in Figure 5 and 6. The CFD capacitor current magnitude is not constant and varies with time due to the term $t^{1-\alpha}$ as shown in Figure 4. When $V_m = 5V$, $\omega = 1 \text{ rad/s}$, $\varphi = 0 \text{ rad/s}$ and $C_\alpha = 1 \text{ F} / \text{s}^{1-\alpha}$ values are used, the CFD capacitor current graph in Figure 6 is sketched for three different alpha values.

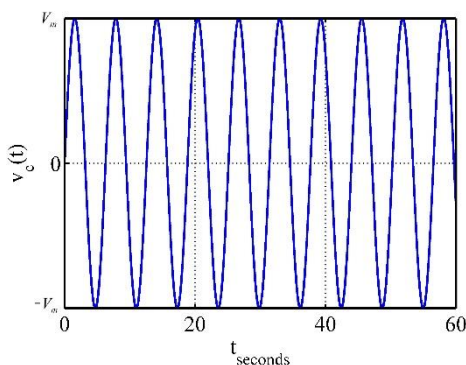


Figure 5. The CFD capacitor voltage vs. time when it is fed by a sinusoidal voltage

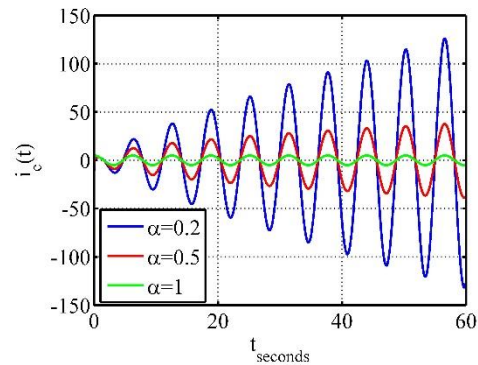


Figure 6. The CFD current vs. time when it is fed by a sinusoidal voltage

All real capacitor models have series and parallel resistors used in their equivalent circuit to model their losses. In this study, the capacitors are assumed to be ideal, ie. without losses and that's why no resistor is used in the analysis. The CFD capacitor current goes to infinity due to the term $t^{1-\alpha}$ as seen in Figure 6 because of this. Such a situation would not appear in a more realistic capacitor model when a series resistor is used.

5. Conclusions

Supercapacitors or ultra-capacitors are becoming more common each day. They cannot be modelled with capacitor constitutive law. Therefore, easier and robust models are needed for their usage and analysis in the circuits. Only then, such capacitors can be fully exploited.

The conformal fractional derivative provides an easier solution than the fractional derivatives such as Caputo and Riemann Liouville. Some capacitors can be modelled using fractional-order derivatives. In this study, the conformal fractional derivative is used to model a capacitor. Every circuit element should be examined for the basic waveforms such as DC and sinusoidal signals. The solutions of the CFD capacitor for the waveforms are given. Only in the case when it is fed by a current source, its voltage is found using a transcendental function the incomplete gamma functions. The solutions can be used in the analysis of the circuits with a CFD capacitor if a supercapacitor is found to be modelled with a good accuracy using experimental data. In comparison to the prior studies, the CFD derivative is more practical and analytical solutions are found to be possible while it has been not possible for other fractional derivatives. The analysis given here can also be used in modelling renewable energy systems or inverters with supercapacitors in the future. This paper can also be used as a tutorial for the researchers who have just been introduced to the research area.

Author's Contributions

Utku Palaz: Made literature search, prepared computer codes for numerical solutions of the sample problems, made simulations, and wrote the manuscript.

Reşat Mutlu: Made literature search, assisted in analytical analysis on the structure, supervised the experiment's progress, result in interpretation, and helped in manuscript preparation.

Ethics

There are no ethical issues after the publication of this manuscript.

References

1. Podlubny, I. (1998). Fractional differential equations: an introduction to fractional derivatives, fractional differential equations, to methods of their solution and some of their applications. Elsevier.
2. Yang, X. J. (2019). General fractional derivatives: theory, methods and applications. Chapman and Hall/CRC.
3. Ross, B. (1977). The development of fractional calculus 1695–1900. *Historia Mathematica*, 4(1), 75-89.
4. Kilbas, A.A.; Srivastava, H.M.; Trujillo, J.J. *Theory and Applications of Fractional Differential Equations*; Elsevier: Amsterdam, The Netherlands, 2006
5. Babiarz, A., Czornik, A., Klamka, J., & Niezabitowski, M. (2017). Theory and applications of non-integer order systems. *Lecture Notes Electrical Engineering*, 407.
6. Moreles, M. A., & Lainez, R. (2016). Mathematical modelling of fractional order circuits. arXiv preprint arXiv:1602.03541.
7. Freeborn, T. J. (2013). A survey of fractional-order circuit models for biology and biomedicine. *IEEE Journal on emerging and selected topics in circuits and systems*, 3(3), 416-424.
8. Adhikary, A., Khanra, M., Pal, J., & Biswas, K. (2017). Realization of fractional order elements. *Inae Letters*, 2(2), 41-47.
9. Tsimokou, G., Kartci, A., Koton, J., Herencsar, N., & Psychalinos, C. (2018). Comparative study of discrete component realizations of fractional-order capacitor and inductor active emulators. *Journal of Circuits, Systems and Computers*, 27(11), 1850170.
10. Kartci, A., Agambayev, A., Herencsar, N., & Salama, K. N. (2018). Series-, parallel-, and inter-connection of solid-state arbitrary fractional-order capacitors: theoretical study and experimental verification. *IEEE Access*, 6, 10933-10943.
11. Sotner, R., Jerabek, J., Kartci, A., Domansky, O., Herencsar, N., Kledrowetz, V., ... & Yeroglu, C. (2019). Electronically reconfigurable two-path fractional-order PI/D controller employing constant phase blocks based on bilinear segments using CMOS modified current differencing unit. *Microelectronics Journal*, 86, 114-129.
12. Podlubny, I., Petráš, I., Vinagre, B. M., O'leary, P., & Dorčák, L. (2002). Analogue realizations of fractional-order controllers. *Nonlinear dynamics*, 29(1-4), 281-296.
13. Alagoz, B. B., & Alisoy, H. Z. (2014). On the Harmonic Oscillation of High-order Linear Time Invariant Systems. *Scientific Committee*.
14. Alagöz, B. B., & Alisoy, H. Estimation of Reduced Order Equivalent Circuit Model Parameters of Batteries from Noisy Current and Voltage Measurements. *Balkan Journal of Electrical and Computer Engineering*, 6(4), 224-231.
15. Khalil, R.; al Horani, M.; Yousef, A.; Sababheh, M. A new definition of fractional derivative. *J. Comput. Appl. Math.* 2014, 264, 65–70.
16. Abdeljawad, T. (2015). On conformable fractional calculus. *Journal of computational and Applied Mathematics*, 279, 57-66.
17. Zhao, D., & Luo, M. (2017). General conformable fractional derivative and its physical interpretation. *Calcolo*, 54(3), 903-917.
18. Sikora, R. (2017). Fractional derivatives in electrical circuit theory—critical remarks. *Archives of Electrical Engineering*, 66(1), 155-163.
19. Lewandowski, M., & Orzyłowski, M. (2017). Fractional-order models: The case study of the supercapacitor capacitance measurement. *Bulletin of the Polish Academy of Sciences Technical Sciences*, 65(4), 449-457.
20. Kopka, R. (2017). Estimation of supercapacitor energy storage based on fractional differential equations. *Nanoscale research letters*, 12(1), 636.
21. Freeborn, T. J., Elwakil, A. S., & Allagui, A. (2018, May). Supercapacitor fractional-order model discharging from polynomial time-varying currents. In *2018 IEEE International Symposium on Circuits and Systems (ISCAS)* (pp. 1-5). IEEE.
22. Freeborn, T. J., Maundy, B., & Elwakil, A. S. (2013). Measurement of supercapacitor fractional-order model parameters from voltage-excited step response. *IEEE Journal on Emerging and Selected Topics in Circuits and Systems*, 3(3), 367-376.
23. Tariboon, J., & Ntouyas, S. K. (2016). Oscillation of impulsive conformable fractional differential equations. *Open Mathematics*, 14(1), 497-508.
24. Piotrowska, E., & Rogowski, K. (2017, October). Analysis of fractional electrical circuit using Caputo and conformable derivative definitions. In *Conference on Non-integer Order Calculus and Its Applications* (pp. 183-194). Springer, Cham.
25. Piotrowska, Ewa. "Analysis of fractional electrical circuit with sinusoidal input signal using Caputo and conformable derivative definitions." *Poznan University of Technology Academic Journals. Electrical Engineering* (2019).
26. Morales-Delgado, V. F., Gómez-Aguilar, J. F., & Taneco-Hernandez, M. A. (2018). Analytical solutions of electrical circuits described by fractional conformable derivatives in Liouville-Caputo sense. *AEU-International Journal of Electronics and Communications*, 85, 108-117.
27. Martínez, L., Rosales, J. J., Carreño, C. A., & Lozano, J. M. (2018). Electrical circuits described by fractional conformable derivative. *International Journal of Circuit Theory and Applications*, 46(5), 1091-1100.
28. Piotrowska, E. (2018, October). Analysis the conformable fractional derivative and Caputo definitions in the action of an electric circuit containing a supercapacitor. In *Photonics Applications in Astronomy, Communications, Industry, and High-Energy Physics Experiments 2018 (Vol. 10808, p. 108081T)*. International Society for Optics and Photonics.
29. Morales-Delgado, V. F., Gómez-Aguilar, J. F., & Taneco-Hernandez, M. A. (2018). Analytical solutions of electrical circuits described by fractional conformable derivatives in Liouville-Caputo sense. *AEU-International Journal of Electronics and Communications*, 85, 108-117.
30. Gómez-Aguilar, J. F. (2018). Fundamental solutions to electrical circuits of non-integer order via fractional derivatives with and



without singular kernels. The European Physical Journal Plus, 133(5), 197.

31. https://www.wolframalpha.com/input/?i=cos%28omega*t%2Bphi%29*%28t%5E%28a-1%29%29

32. Allen R. L., and Mills D. (2004). Signal analysis: time, frequency, scale, and structure. John Wiley & Sons.

Optimal placement of multiple DGs in radial distribution systems to minimize power loss using BSA

Waleed Fadel^{1*} , Ulaş Kılıç² , Sezai Taşkın³ 

¹Department of Electrical&Electronics, Faculty of Engineering, Girne American University, Mersin 10 – Turkey

²Department of Electrical&Electronics, Faculty of Engineering, Ege University, İzmir – Turkey

³Department of Electrical&Electronics, Faculty of Engineering, Manisa Celal Bayar University, Manisa –Turkey

*waleedfadel@gau.edu.tr

*Orcid: 0000-0002-5061-6474

Received: 18 September 2020

Accepted: 29 March 2021

DOI: 10.18466/cbayarfbe.796140

Abstract

Distributed generation (DG) sources are becoming more important in electrical networks due to the increase of electrical energy demands. However, DG sources can have a profound effect on network power loss. Hence, optimal placement and size of DGs are extremely important. This study presents an efficient heuristic algorithm based on optimal placement and size of multiple DGs within distribution systems in order to reduce power loss. This algorithm is backtracking search algorithm (BSA). Two main DGs, photovoltaic and synchronous compensator, are integrated in two different radial distribution systems (RDS), IEEE 33-bus system and IEEE 69-bus system. To demonstrate the effectiveness of the proposed method, the results obtained by BSA are compared with a genetic algorithm (GA) as well as other results in the literature.

Keywords: BSA, DG placement, DG size, power loss.

1. Introduction

The integration of a solar power plant in distribution network is an important challenge, and it is one of the ways to reduce the environmental pollution that is produced by fossil fuel-based energy generation. Thus, much research has been concentrated on the optimum integration of solar panels in distribution networks in recent years.

Optimal reactive power flow is necessary to maintain power system reliability. It is achieved by minimizing power losses in the transmission line under the constraints of the physical system, using power flow equations. Valuable articles have dealt with this subject for the purpose of reducing power losses. Kansal et al. [1] proposed particle swarm optimization (PSO) to solve for the placement and size of different types of DG's, taking the power loss as an objective function. Kayal et al. [2] presented different types of DG's with different modes, using PSO. Their objective was power loss minimization and voltage stability improvement. Kollu et al. [3] proposed a harmony search algorithm (HSA) for multi-DG placement to reduce power loss, and enhance the voltage profile. García et al. [4] employed

modified teaching–learning based optimization (MTLBO) to solve the problem of placement and sizing of multiple DG's with the single objective of reducing power loss. Injeti et al. [5] used simulated annealing (SA) for a DG placement and size to reduce the power loss, and improve the voltage stability. Manafi et al. [6] presented dynamic PSO for optimal placement of a DG to minimize power loss. Moradi et al. [7] proposed PSO/GA hybrid algorithms as a solution for sizing and placement of a DG to improve voltage regulation, and minimize power loss. Aman et al. [8] employed a PSO algorithm to solve a function with the multiple objectives of maximizing voltage stability and minimizing power losses, and found the optimal DG allocation, weakest link in the network, and the most sensitive voltage bus. Ates et al. [9] examined the impact of hybrid DG on power losses, voltage improvement, and electricity bill in distribution network by using the ETAP. Turan et al. [10] proposed the integration of a solar plant to a PEV parking lot to reduce power consumption and losses considering various operating conditions. Hemeida et al. [11] implemented a new optimization algorithm to the optimal integration of a DG for power loss minimization. Memarzadeh et al. [12] applied a new approach for DG placement in order to improve voltage stability index and

the system reliability. This approach has been tested in various RDS. Kansal et al. [13] proposed a hybrid of heuristic and analytical methods of the PSO (H-PSO) algorithm to determine the optimum places and the best types of DGs.

In this work, we have considered 3 scenarios. In Scenario 1, the tested systems are integrated by active-power DGs (photovoltaic) only, where only one active-power DG can be placed in a given bus. In Scenario 2, one active-power DG and one reactive-power DG (synchronous compensator) are paired and connected together in a bus, where only one pair can be placed in a given bus. In Scenario 3, while in some buses one active-power DG and one reactive-compensator DG are paired and connected as a single pair per bus, in other buses either one active-power DG or one reactive-power DG is placed singly –only one DG per bus. References [2, 5, 6, 7, 8 and 13] dealt only with scenario 1. Ref. [1] dealt with scenarios 1 and 2, but not 3. None of the references used the BSA in their optimizations. In this paper, we applied the BSA on 33-bus as well as 69-bus systems in cases where multiple DGs (up to a total of 16 DGs and 13 buses) are used. As understood from the Ref. [1-8] mentioned above, heuristic algorithms are successfully applied to solve the optimization problem in RDS. In this study, we used the BSA to solve the optimization problem of DG placement and sizing, such as to minimize system power loss in RDS.

This paper is arranged as follows: problem formulation is in Section 2, the proposed algorithm in Section 3, simulation results and discussion in Section 4, and the conclusion in Section 5.

2. Problem formulation

In this paper, active power loss is selected as an objective function. To minimize the objective function, the proposed algorithm is applied in two RDSs under both equality as well as inequality constraints. Minimization of power loss is an optimization problem, mathematical equations of which is well known and is defined as follows,

$$\begin{aligned} &\text{Minimize} && f(x, u) \\ &\text{Such that} && g(x, u) = 0 \\ &&& h(x, u) \leq 0 \end{aligned} \quad (1)$$

where f , g , and h are the fitness function, the equality constraint, and the inequality constraint, respectively. Here, x is the vector of control variables, while u is the vector of state variables. The control variables are the size and the place of DG active power, and of the reactive compensators. The state variables are active and reactive power of the feeder, load, bus voltage, and the line current.

2.1. Objective Function

In this work, power loss is selected as an objective function. The power loss can be demonstrated as equation (2) [14].

$$P_{loss} = P_{feeder} + \sum_{i=1}^{N_{DG}} P_{DG,i} - \sum_{i=1}^N P_{Load,i} \quad i = 1, \dots, N \quad (2)$$

2.2. Equality constraints

Load balancing constraint formulas as follows:

$$CDG_i \cdot P_{DG,i} + CF_i \cdot P_{feeder} = P_{Load,i} + V_i \sum_{j=1}^N V_j (G_{ij} \cos \delta_{ij} + B_{ij} \sin \delta_{ij}) \quad i = 1, \dots, N \quad (3)$$

$$CSC \cdot Q_{sc,i} + CF_i \cdot Q_{feeder} = Q_{Load,i} + V_i \sum_{j=1}^N V_j (G_{ij} \sin \delta_{ij} - B_{ij} \cos \delta_{ij}) \quad i = 1, \dots, N \quad (4)$$

2.3. Inequality constraints

Voltage limits:

The allowable range for all buses is given in equation (5),

$$V_i^{\min} \leq V_i \leq V_i^{\max} \quad i = 1, \dots, N \quad (5)$$

Unit constraints of DGs:

The following constraint is the allowable active power and reactive power sizes of DGs.

$$P_{DG,i}^{\min} \leq P_{DG,i} \leq P_{DG,i}^{\max} \quad i = 1, \dots, N_{DG} \quad (6)$$

$$Q_{sc,i}^{\min} \leq Q_{sc,i} \leq Q_{sc,i}^{\max} \quad i = 1, \dots, N_{SC} \quad (7)$$

Line capacity constraints:

The current limitation of the distribution lines of the system is given by [15].

$$|I_{ij}| \leq |I_{ij}^{\max}| \quad i = 1, \dots, N, \quad j = 1, \dots, N \quad \text{and} \quad i \neq j \quad (8)$$

3. Back-tracking Search Algorithm

BSA is an evolutionary algorithm (EA) introduced by Civicioglu in 2012 [16]. BSA has been applied to solve different optimization problems in various fields such as energy, geophysics, and magnetism [17-19]. The most significant property of BSA that it is not sensitive to the initial values. Selection, mutation, and crossover

operators are used in BSA. The MATLAB® code of BSA can be found in [16]. The basic steps of BSA are outlined as follows [17].

```

Repeat
  Selection-1
  Generation of Trial-Population
  Mutation
  Crossover
  End
  Selection-2
Until stopping conditions are met.
  
```

3.1. Initialization

In the beginning, two different populations (Pop and $oldPop$) are formed as follows:

$$Pop_{i,j} \sim Rand(low_j, up_j) \quad i = 1, \dots, SN \quad j = 1, \dots, D \quad (9)$$

$$oldPop_{i,j} \sim Rand(low_j, up_j) \quad i = 1, \dots, SN \quad j = 1, \dots, D \quad (10)$$

3.2. Selection-I

In this section, the old population ($oldPop$) in the initiation stage is formed using,

$$if \ a < b, \ oldPop := Pop \ end \ | \ a, b \sim Rand(0,1) \quad (11)$$

In equation (11), $:=$ is the update operator. This operator randomly transfers the Pop individuals' variables to $oldPop$ individuals' variables. Then, equation (12) is used to randomly change individuals in the $oldPop$.

$$oldPop := Randshuff(oldPop) \quad (12)$$

where $Randshuff$ is a random mixing function [15].

3.3. Mutation

The mutation process is formed as

$$mutantPop = Pop + W(oldPop - Pop) \quad (13)$$

In equation (13), W controls the amplitude of the search line matrix. $W = 3randn$ is proposed in the Ref.[16]. However, we observed that the performance of 4 is better than that of 3. The function “ $randn$ ” randomly generates numbers between 0 and 1 according to the standard normal distribution [17].

3.4. Crossover

Initialization

In this section, the trial population ($Tpop$) is formed using equation (14). The crossover process consists of two stages. In the first stage, the binary number system is fully valued, and produces $SN * D$ size of a matrix (map). This matrix is used to determine whether or not we have to modify $Tpop$, one row at a time (“*individual by individual*” in heuristic terms). The second stage, the following equation is obtained from the matrix after its formation.

$$if \ map_{i,j} = 1 \ then \ Tpop_{i,j} = Pop_{i,j} \ else \ Tpop_{i,j} = mutantPop_{i,j} \ end \quad (14)$$

3.5. Selection-II

All the “individual” fitness values produced is calculated in this section. Individuals are sorted according to their fitness values, from best to worst. Then, the SN of them are carried to the next iteration Pop . The remaining ones are omitted. In this way, the best “individuals” among the whole population are transferred to the next generation.

4. Simulation Results and discussion

In this work, two types of DG are integrated in two different RDS. These systems are 33 and 69 bus systems. All nodes integrated of DGs are selected as PQ mode. The results are compared with GA and other recent works.

DG resources are divided into 4 types, determined by ability to deliver active and reactive power. The DG types are:

- Type I: Generating active power (Photovoltaic system).
 - Type II: Generating reactive power (Synchronous compensation).
 - Type III: Generating active and absorbing reactive power (Wind power)
 - Type IV: Generating active and reactive power (Synchronous generator).
- Type I and Type II are performed in our work.

Scenarios and cases

In this study, 3 scenarios and 5 cases are examined. All scenarios are considered under the 5 cases, and the differences between cases, depend on the number of DGs. In the following tables Case1 is base case for IEEE 33- bus system and IEEE 69- bus system.

Scenario1: All DGs are type I, one per bus.

Scenario2: Any pair of DGs (one of type I & one of type II) is connected in the same bus, only one pair per bus.

Scenario3: Some DG pairs (one of type I & one of type II) are connected in the same bus, one pair bus, while single DGs (type-I or type-II) are connected in different buses, one DG per bus.

4.1. IEEE 33-bus system

The IEEE 33-bus system is selected, with a system voltage base of 12.66 kV for all cases, and base apparent power of 100 MVA for all cases. The test system has total active and reactive loads of 3.715 MW and 2.300 MVar, respectively. The data for the line reactance and resistances, and for the loads connected to buses, are given in [20].

Scenario1: In scenario1, 4 cases are constructed considering DG number. One, two, three and four DGs

are integrated in Case2, 3, 4, and 5, respectively, to 33-bus system. In the following tables, all sizes of DGs type I are in (MW), while size of DGs Type II are in (MVar).

The obtained results using BSA for all cases of Scenario1 are given in Table 1. The power loss for Case2, 3, 4, and 5, respectively are 211, 103.966, 87.1669, 72.7878 and 67.67kW. When we compare power loss of all cases, it is concluded that Case2 is better than Case1, Case3 is better than Case2, Case4 is better than Case3, and Case5 is the best for Scenario1.

Power loss reduction (considering Case1) comparison of the proposed algorithm, GA, and other results for all cases of scenario1 are given in Table 2. It is noticed that, the obtained results by the proposed algorithm for all cases are the best among all results.

Table 1. Results by BSA of all cases in Scenario 1 for IEEE 33- bus system

	Case 1	Case 2	Case 3	Case 4	Case 5
Power loss	211	103.966	87.1669	72.7878	67.76
Placement and size of DG Type I	-	2.5753(6)	0.8516(13) 1.1576(30)	0.8000(13) 1.0880(24) 1.0523(30)	0.8400(7) 0.6468 (14) 0.7307(25) 0.8112(31)

Table 2. Comparison of power loss reduction (%) by BSA and others for Scenario 1 of IEEE 33-bus system

Case	Ref. [1]	Ref. [2]	Ref. [5]	Ref. [6]	Ref. [7]	Ref. [11]	Ref. [13]	GA	BSA
2	45.36	-	-	39.73	-	47.37	47.31	45.6	50.73
3	-	-	-	54.54	-	58.68	58.64	58.65	58.69
4	-	27.82	61.12	56.14	-	65.45	65.46	65.31	65.50
5	-	-	-	-	67.68	-	-	67.50	67.89

Scenario 2: The obtained results using BSA for all cases of Scenario2 are given in Table 3. The power loss for Case2, 3, 4, and 5, respectively are 211, 67.739, 28.593, 12.2118 and 8.5364 kW. When we compare power loss of all cases, it is concluded that Case2 is better than Case1, Case3 is better

than Case2, Case4 is better than Case3, and Case5 is the best for Scenario2.

Comparison of power loss reduction of BSA and other for all cases of scenario2 are given in Table 4. It is noticed that the obtained results by BSA for all cases of scenario2 are the best among all results.

Table 3. Results by BSA of all cases in Scenario 2 for IEEE 33- bus system

	Case 1	Case 2	Case 3	Case 4	Case 5
Power loss	211	67.739	28.593	12.2118	8.5364
Placement and size of DG Type I	-	2.5566(6)	0.3964(13) 1.0276(30)	0.8534(13) 0.9229(24) 0.3437(30)	0.4350 (7) 0.7180(14) 1.0174(24) 1.0151(30)
Placement	-		0.7537(13)	0.3676(13)	0.5289(7)

and size of DG Type II		1.7580(6)	0.9009(30)	0.4642(24) 0.1949(30)	0.2477 14) 0.5040(24) 0.8370(30)
------------------------	--	-----------	------------	--------------------------	--

Table 4. Comparison of power loss reduction (%) by BSA and others for Scenario 2 of IEEE 33-bus system

Case	Ref. [1]	GA	BSA
2	67.79	67.89	67.89
3	-	86.44	86.45
4	-	93.00	94.21
5	-	95.56	95.95

Scenario 3: The obtained results by BSA for all cases of Scenario3 are given in Table 5. The power loss for Case2, 3, 4, and 5, respectively are 211, 29.8235, 13.8957, 8.7463 and 7.4533kW. When we compare power loss of all cases, it is concluded that Case2 is better than Case1, Case3 is better than Case2, Case4 is better than Case3, and Case5 is the best among all cases in Scenario3.

Table 5. Results by BSA of all cases in Scenario 3 for IEEE 33-bus system

	Case 1	Case 2	Case 3	Case 4	Case 5
Power loss	211	29.8235	13.8957	8.7463	7.4533
Placement and size of DG Type I	-	0.6247(29) 0.6755(14)	1.0070(24) 0.6972(30) 0.7833(13) 0.3295(30)	0.5724 (3) 0.4820(12) 0.4270(27) 0.3781(13) 0.9094(24) 0.7673(30)	0.2647(25) 0.3866(26) 0.3918(31) 0.7962(13) 0.1000(21) 0.6283(24) 0.2068(28) 0.1734(31)
Placement and size of DG Type II	-	0.1000(30) 0.3781(14)	0.2393 (8) 0.1261(14) 0.2076(13) 0.9685(30)	0.3194(4) 0.1321(10) 0.3987(31) 0.1000(13) 0.3871(24) 0.6595(30)	0.3439(23) 0.4105(27) 0.5653(30) 0.2732(13) 0.1393(21) 0.1000(24) 0.2093(28) 0.1000(31)

4.2. IEEE 69- bus system

The IEEE 33-bus system is selected, with system voltage base of 12.66 kV for all cases, and base apparent power of 100 MVA for all cases. The test system has total active and reactive loads of 3.802 MW and 2.694 MVar, respectively. The data for the line reactance and resistances, and for the loads connected to nodes, are given in [20].

Scenario 1: The obtained results using BSA for all cases of Scenario1 are given in Table 7. The power loss for Case2, 3, 4, and 5, respectively are 225, 83.0704, 71.567, 69.3767 and 67.84 kW. When we compare

In Table 5, all values in bold font indicate that DG pairs (one of type I & one of type II) are connected in the same bus, while others are connected in different buses. Power loss reduction of BSA and GA results for all cases of scenario3 are given in Table 6. It is noticed that the obtained results by the proposed algorithm for all cases are better than GA results.

Table 6. Comparison of power loss reduction (%) by BSA and others for Scenario 3 of IEEE 33-bus system

Case	GA	BSA
2	83.28	85.87
3	93.00	93.41
4	94.51	95.86
5	95.67	96.47

power loss of all cases, it is concluded that Case2 is better than Case1, Case3 is better than Case2, Case4 is better than Case3,

and Case5 is the best for Scenario1. Comparison of power loss reduction of BSA and other for all cases of scenario1 are given in Table 8. It is noticed that, the obtained results by BSA for all cases of scenario1 are the best among all results.

Table 7. Results by BSA of all cases in Scenario 1 for IEEE 69-bus system

	Case 1	Case 2	Case 3	Case 4	Case 5
Power loss	225	83.0704	71.567	69.3767	67.84
Placement and size of DG Type I	-	1.8710 (61)	0.5291 (17) 1.7820 (61)	0.5885 (11) 0.3445 (20) 1.7338 (61)	0.5448 (11) 0.3572 (20) 0.7188 (50) 1.7181 (61)

5.7156 and 2.0784 kW. When we compare power loss of all cases, it is found that Case2 is better than Case1, Case3 is better than Case2, Case4 is better than Case3, and Case5 is the best for Scenario2.

Power loss reduction comparison of the proposed algorithm, GA, and other results for all cases of the scenario2 are given in Table 10. It is noticed that, the obtained results by BSA for all cases are the best among all results.

Scenario 2: The obtained results by BSA for all cases of Scenario2 are given in Table 9. The power loss for Case2, 3, 4, and 5, respectively are 225, 23.133, 7.7836,

Table 8. Comparison of power loss reduction (%) by BSA and others for Scenario 1 of IEEE 69-bus system

Case	Ref. [1]	Ref. [5]	Ref. [11]	Ref. [12]	Ref. [13]	GA	BSA
2	62.94	-	63.01	63.02	62.95	63.08	63.08
3	-	-	68.14	-	68.09	68.19	68.19
4	-	65,68	69.14	-	69.09	69.07	69.17
5	-	-	-	-	-	69.80	69.85

Table 9. Results by BSA of all cases in Scenario 2 for IEEE 69-bus system

	Case 1	Case 2	Case 3	Case 4	Case 5
Power loss	225	23.133	7.7836	5.7156	2.0784
Placement and size of DG Type I	-	2.0275(61)	0.5280(15) 1.7266(61)	0.3037(19) 1.6533(61) 0.1501(66)	0.2774(11) 0.2575(18) 0.5289(49) 1.1995(61)
Placement and size of DG Type II	-	1.4447(61)	0.4654(15) 1.2207(61)	0.2203(19) 1.1344(61) 0.3391(66)	0.5206(11) 0.3569(18) 0.7771(49) 1.6666(61)

Table 10. Comparison of power loss reduction (%) by BSA and others for Scenario 2 of IEEE 69-bus system

Case	Ref. [1]	GA	BSA
2	89.01	89.72	89.72
3	-	96.23	96.54
4	-	96.48	97.46
5	-	97.37	99.08

Scenario 3: The obtained results by proposed algorithm for all cases of Scenario3 are given in Table 11. The power loss for Case2, 3, 4, and 5, respectively are 225, 7.3167, 4.1776, 3.6989 and 1.8875kW. When we compare power loss of all cases, it is noticed that Case2 is better than Case1, Case3 is better than Case2, Case4 is better than Case3, and Case5 is the best for Scenario3. In Table 11, all values in bold font indicate that DG pairs (one of type I & one of type II) are connected in

the same bus, while others are connected in different buses.

In Table 12, comparison of power loss reduction of the proposed algorithm and GA for cases of scenario3 is given. It is noticed that the obtained results by BSA for all cases of scenario3 are better than GA results.

Table 12. Comparison of power loss reduction (%) by BSA and others for Scenario 3 of IEEE 69-bus system

Case	GA	BSA
2	96.64	96.75
3	97.63	98.14
4	97.94	98.36
5	99.01	99.16

Table 11. Results by BSA of all cases in Scenario 3 for IEEE 69-bus system

	Case 1	Case 2	Case 3	Case 4	Case 5
Power loss	225	7.3167	4.1776	3.6989	1.8875
Placement and size of DG Type I	-	0.5126(17)	0.4080(17)	0.6224(8)	0.2696(4)
		1.7805(61)	1.8000(61)	0.2630(21)	0.5359 (50)
		0.3387(66)	0.7848(61)	0.8759(62)	0.1000(61)
					1.2000(62)
Placement and size of DG Type II	-	0.3400(16)	0.1000(15)	0.3180(12)	0.2734(2)
		1.2483(61)	1.1792(61)	0.1000(21)	0.3654(50)
		0.4645(66)	0.4645(66)	0.2400(61)	0.3094(61)
				0.8745(62)	0.5464(62)
				0.3532(64)	

Variation of fitness function versus iteration number of IEEE 33- and 69-bus system for Scenario-3 are shown in Fig.1 and 2, respectively. In Fig.1, the value of fitness nearly at 62nd, 50th, 45th and 52nd iteration for Case2, 3, 4, and 5, respectively; in Fig.2, the value of fitness nearly at 74nd, 46th, 52th and 53th iteration for Case2, 3,

4, and 5, respectively are approached to the optimal solution.

It can be seen from the figures that all fitness values are reached the optimal solution before 75th iteration and there is no change after that.

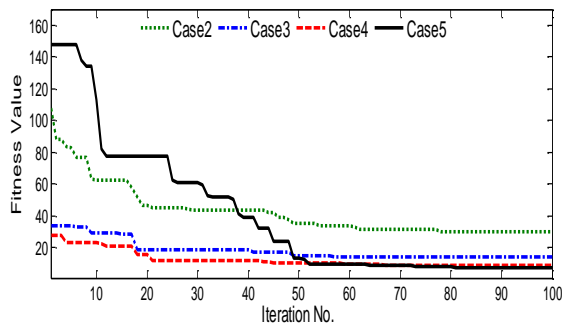


Figure 1. Fitness variation with iteration number for 33 bus system with scenario3

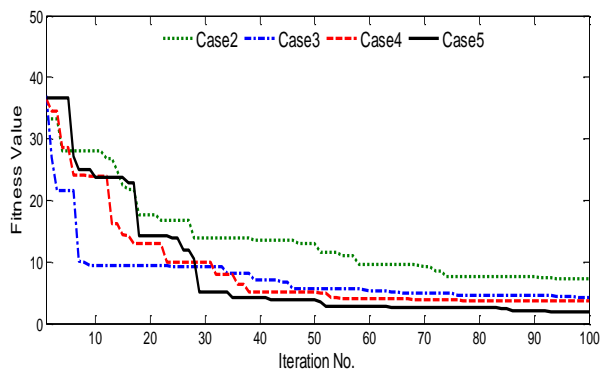


Figure 2. Fitness variation with iteration number for 69 bus system with scenario 3

Summary: According to the obtained results by BSA for all scenarios and cases of both test systems, it is noted that power loss reduction gradually increases as the number of DGs is increased, as well as by changing the DG type, as shown in Fig. 3 and 4. It is clearly observed that the results of Case 5 of each scenarios offer the greatest power loss reduction for both the IEEE 33- and 69-bus system. The noticeable increase in power loss reduction under Scenario-3 is better than those in other scenarios. So, it is better to integrate some DGs, as in Scenario-3, in order to increase the power loss reduction. The location, size, type, and the number of DGs are the basic steps for planning improvements in system performance, especially the system power loss.

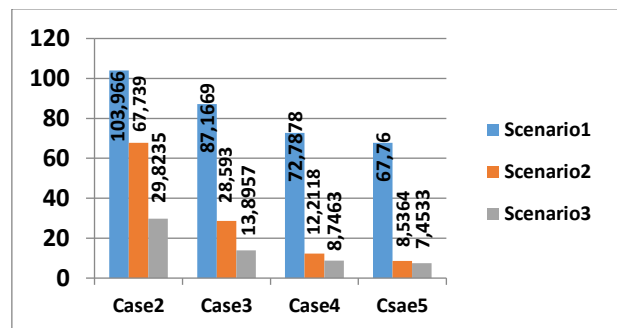


Figure 3. Demonstrate power loss (kW) in each scenario with their different cases for 33 bus system

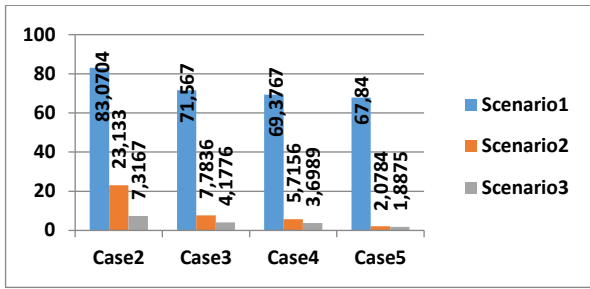


Figure 4. Demonstrate power loss (kW) in each scenario with their different cases for 69 bus system

5. Conclusion

In this work, the BSA is successfully applied in RDS to find optimal size, number, type, and location of DGs. These DGs are connected to the test systems and minimized their power loss. The DGs are integrated under 3 scenarios and 5 cases in each scenario. Under Scenario-3 (Case5), power loss is reduced by 99.16%, 96.47%, respectively for 33 and 69 bus systems. It's noticed that it is better to select suitable DG type to minimize power loss to a considerable amount. But the best way is to put DG type, and number in consideration.

It is concluded that an optimal size, type, number of DG with suitable location can reduce the power losses by considerable amounts.

In future work, Type III: Generating active and absorbing reactive power (wind power) and Type IV: Generating active and reactive power (synchronous generator) will considered by using the BSA.

Nomenclature

DG	Distributed generation
f	Fitness function
g	Equality constraint
h	Inequality constraint
x	Control variables
u	State variables
P_{loss}	Total power loss
P_{feeder}	Feeder active power
Q_{feeder}	Feeder reactive power
$P_{DG,i}$	DG active power output at i^{th} bus
$P_{Load,i}$	Active load at i^{th} bus
$Q_{Load,i}$	Reactive load at i^{th} bus
N	Total bus number
N_{DG}	Total number of DG
N_{SC}	Total number of SC

CF_i	Status (on/off) of the feeder
CDG_i	Status (on/off) of the distributed generation at i^{th} bus
CSC_i	Status (on/off) of the synchronous compensator at i^{th} bus
V_i	Voltage magnitude at i^{th} bus
δ_{ij}	The voltage angle difference between buses i and j
$Q_{sc,i}$	SC reactive power output at i^{th} bus
G_{ij}	Transfer conductance between buses i and j
SC	Synchronous compensator
SN	Number of population size
D	the number of optimization parameters
$Randshuff$	random mixing function
$Rand(low, up)$	produce a random number between low and up
Pop	Population
$oldPop$	Old population
\sim	Produce
$Tpop$	Trial population
$P_{DG,i}^{min}$	Minimum DG active power output at i^{th} bus
$P_{DG,i}^{max}$	Maximum DG active power output at i^{th} bus
I_{ij}	Current magnitude at branch ij
I_{ij}^{max}	Allowable maximum current magnitude at branch ij
a, b	$Rand(0,1)$
$:=$	Update operator
$mutantPop$	Population of mutation
W	Value
$randn$	Generates numbers between 0 , 1
map	Matrix ($SN * D$)
$Q_{sc,i}^{min}$	Minimum SC reactive power output at i^{th} bus
$Q_{sc,i}^{max}$	Maximum SC reactive power output at i^{th} bus
B_{ij}	Transfer susceptance between buses i and j

Author's Contributions

Waleed Fadel: Methodology, Software.

Ulas Kilic: Visualization, Investigation, Supervision.

Sezai Taskin: Investigation, Supervision, Writing.

Ethics

There are no ethical issues after the publication of this manuscript.

6. References

1. Kansal, S., Kumar, V. and Tyagi, B., 2013. Optimal placement of different type of DG sources in distribution networks. *International Journal of Electrical Power & Energy Systems*, 53, pp.752-760.
2. Kayal, P. and Chanda, C.K., 2013. Placement of wind and solar based DGs in distribution system for power loss minimization and voltage stability improvement. *International Journal of Electrical Power & Energy Systems*, 53, pp.795-809.
3. Kollu, R., Rayapudi, S.R. and Sadhu, V.L.N., 2014. A novel method for optimal placement of distributed generation in distribution systems using HSDO. *International Transactions on Electrical Energy Systems*, 24(4), pp.547-561.
4. García, J.A.M. and Mena, A.J.G., 2013. Optimal distributed generation location and size using a modified teaching-learning based optimization algorithm. *International journal of electrical power & energy systems*, 50, pp.65-75.
5. Injeti, S.K. and Kumar, N.P., 2013. A novel approach to identify optimal access point and capacity of multiple DGs in a small, medium and large scale radial distribution systems. *International Journal of Electrical Power & Energy Systems*, 45(1), pp.142-151.
6. Manafi, H., Ghadimi, N., Ojaroudi, M. and Farhadi, P., 2013. Optimal placement of distributed generations in radial distribution systems using various PSO and DE algorithms. *Elektronika ir Elektrotechnika*, 19(10), pp.53-57.
7. Moradi, M.H. and Abedini, M., 2012. A combination of genetic algorithm and particle swarm optimization for optimal DG location and sizing in distribution systems. *International Journal of Electrical Power & Energy Systems*, 34(1), pp.66-74.
8. Aman, M.M., Jasmon, G.B., Bakar, A.H.A. and Mokhlis, H., 2013. A new approach for optimum DG placement and sizing based on voltage stability maximization and minimization of power losses. *Energy Conversion and Management*, 70, pp.202-210.
9. Ates, Y., Gokcek, T. and Arabul A. Y., 2020, Impact of hybrid power generation on voltage, losses, and electricity cost in distribution networks. *Turkish Journal of Electrical Engineering & Computer Sciences*, 1-16.
10. Turan, M.T., Ates, Y., Erdinc, O., Gokalp, E. and Catalão, J.P., 2019. Effect of electric vehicle parking lots equipped with roof mounted photovoltaic panels on the distribution network. *International Journal of Electrical Power & Energy Systems*, 109, pp.283-289.
11. Hemeida, M.G., Ibrahim, A.A., Mohamed, A.A.A., Alkhalaf, S. and El-Dine, A.M.B., 2020. Optimal allocation of distributed generators DG based Manta Ray Foraging Optimization algorithm (MRFO). *Ain Shams Engineering Journal*.
12. Memarzadeh, G. and Keynia, F., 2020. A new index-based method for optimal DG placement in distribution networks. *Engineering Reports*, 2(10), p.e12243.
13. Kayal, P. and Chanda, C.K., 2013. Placement of wind and solar based DGs in distribution system for power loss minimization and voltage stability improvement. *International Journal of Electrical Power & Energy Systems*, 53, pp.795-809.
14. Kansal, S., Kumar, V. and Tyagi, B., 2016. Hybrid approach for optimal placement of multiple DGs of multiple types in distribution networks. *International Journal of Electrical Power & Energy Systems*, 75, pp.226-235.
15. Fadel, W., Kilic, U. and Taskin, S., 2017. Placement of Dg, Cb, and Tesc in radial distribution system for power loss minimization using back-tracking search algorithm. *Electrical Engineering*, 99(3), pp.791-802.
16. Aman, M.M., Jasmon, G.B., Bakar, A.H.A. and Mokhlis, H., 2014. A new approach for optimum simultaneous multi-DG distributed generation Units placement and sizing based on maximization of system loadability using HPSO (hybrid particle swarm optimization) algorithm. *Energy*, 66, pp.202-215.
17. Civicioglu, P., 2013. Backtracking search optimization algorithm for numerical optimization problems. *Applied Mathematics and Computation*, 219(15), pp.8121-8144.
18. Kılıç, U., 2015. Backtracking search algorithm-based optimal power flow with valve point effect and prohibited zones. *Electrical Engineering*, 97(2), pp.101-110.
19. Song, X., Zhang, X., Zhao, S. and Li, L., 2015. Backtracking search algorithm for effective and efficient surface wave analysis. *Journal of Applied Geophysics*, 114, pp.19-31.
20. Duan, H. and Luo, Q., 2014. Adaptive backtracking search algorithm for induction magnetometer optimization. *IEEE Transactions on Magnetics*, 50(12), pp.1-6.
21. Moradi, M.H., Zeinalzadeh, A., Mohammadi, Y. and Abedini, M., 2014. An efficient hybrid method for solving the optimal siting and sizing problem of DG and shunt capacitor banks simultaneously based on imperialist competitive algorithm and genetic algorithm. *International Journal of Electrical Power & Energy Systems*, 54, pp.101-111.

Frame Detection with Deep Learning

Mete Yildirim^{1*}, Radosveta Ivanova Sokullu¹

¹ Department of Electrical and Electronics Engineering, Ege University, 35030, Bornova, İzmir, Turkey

*mete.yildirim@mail.ege.edu.tr

*Orcid: 0000-0001-6335-4752

Received: 25 February 2020

Accepted: 21 May 2021

DOI: 10.18466/cbayarfbe.693942

Abstract

Deep learning has become a way of solution for the realization of complex computations. As electronic communication starts to use more complex channels, the systems need to handle tough computations. For this reason, research on the use of deep learning in communication has increased recently. These researchers aim to realize many applications used in communication with deep learning. Frame detection is one of the first things a receiver must handle, and it may require a lot of hard computations. Deep learning-based frame detection can be an alternative approach. This study aims to build models that perform frame detection with deep learning. The proposed models provide the performance of correlation-based frame receivers commonly used for frame detection. The mean square root error of the prediction deviation is used as an evaluation metric to compare the proposed model to classic systems.

Keywords: Communication, correlator, deep learning, frame detection, neural network

1. Introduction

Many modern communication systems transmit information in the form of a packet or frame in order to share the transmission medium. Frame structure usually contains information that determines its start and endpoint. The receiver must detect these points correctly. This process is called frame detection [1–2].

Frame detection is vital to the performance of the system. The error to be made in frame detection can cause a lot of other synchronization problems in the system such as symbol, frequency, and etc. which in turn reduces the performance of the system.

Mostly, the good frame detection depends on the algorithm used and the structure of the frame. A well-designed frame should not increase the overhead information while facilitating frame detection, nor should it be in a format that costs more processing time and energy.

The use of neural networks, which is the most primitive version of the deep learning model, is not new. [3] and the references within summarize these studies. These studies cover many important topics for communication systems such as modulation, demodulation, detection, synchronization, coding. These studies have not produced very successful results. However, the deep learning models obtained with multi-layered neural

networks succeeded in producing successful results in communication systems. [4–6] are some of the review papers examine many excellent applications of deep learning to electronic communication. [7–14] show very successful machine learning-based communication. [9] combines all communication blocks in one entity and put forward a different approach for digital communication. [7] implements deep learning-based communication with software defined radio on AWGN channels. Generally, these papers try to optimize overall performance of the digital systems and do not let us know if deep learning can handle some very important receiver tasks such as frame detection individually and how good it is in these tasks. This motivates us to examine a deep learning-based frame detection. In this study, we will consider received signals that contains a frame in various noise levels. The proposed models detect frame beginning for various size of preamble information in various level of signal to noise ratio and the performance of the models compared to the correlation-based detector.

2. Deep Learning Foundation

Deep learning is performed with deep neural network (DNN) that is very similar the shallow neural network (NN) in structure. Unlike NN, DNN generally have many layers. The connection between these layers may differ from NN and can be very complicated. DNN has

different approaches than NN that help to create many successful applications to the various field. The calculation in NN is done by a neuron. Being the most basic unit of NN, a neuron does a simple calculation on the given input given as $z = w^T x + b$. The output is estimated with an activation function $a = g(z)$ [15-17]. The activation function, $g(\cdot)$, is generally non-linear. Some of them are named as “relu, tanh, sigmoid” etc. These non-linear function gives power to the model for non-linear output estimation. The structure that combines many neurons named layer. The neurons in a layer do not have inner connection and works independently.

The machine learning generally subcategorized in two. They are supervised and unsupervised learning. In this study we only consider supervised learning. The supervised learning is performed based on known input and output. The model sets the inner parameters by itself to get desired outputs for the given inputs. This is done on many samples that is known as training samples. The best inner parameters are saved and used for validation data that is used to understand the model training mood. If the model is not undertrained nor over trained, it becomes ready to use for prediction on new datasets. For satisfactory result, the network must be provided enough training examples $(x(i), y(i))$. The samples can be applied the model on vector based known feature vector. The computation of a neuron for the input features vector x is given as $z = w^T x + b$, where w is weighting vector and b is constant, hence a layer output given as is $Z = W^T x + b$, where W is a matrix, b is a constant vector. After calculation nonlinear output of neurons with the one of mentioned activation functions, the output is applied to next layer. In this calculation, W and b are randomly initialized to small numbers. That calculation goes on until the last layer. The last layer of model must have neurons as many as the number of classes in classification problem. In other words, each class is represented with a neuron on last layer where the calculated values are converted to probability by using softmax function etc. In general, a NN is mapping of N_i dimension of input to N_o dimension of output given as $f(x; W, b): R^{N_i} \rightarrow R^{N_o}$. The difference between real output and model output is calculated with a cost function.

$$\sum_{i=1}^m (y^{(i)} \log a^{[L](i)} + (1 - y^{(i)}) \log (1 - a^{[L](i)})) \quad (2.1)$$

The cost function is chosen according to the need. (2.1) shows a cost function for binary classification named as logistic regression log likelihood [18].

The cost function can be maximized using gradient decent that is called the training of network. The more on deep learning, such as multinomial classification, softmax and etc. can be found in [19].

3. Frame Detection Model

A frame is generally a joint structure of the preamble and an information message. A preamble known as marker is mostly a predesigned sequence of bits while the information message is a random sequence of symbols from the used alphabet. Sometimes the preamble itself can be made from the message to be transmitted for reducing waste of resources as given in [20]. Frame detection can be examined in two basic categories without loss of generality. These are correlation-based receiver (CBR) and maximum likelihood-based receiver (MLR)[2]. In the CBR, the received sequence is correlated with the local preamble and the correlation peak is used to determine starting position of the frame. The weaknesses of CBR can be considered as long processing time, saving a copy of preamble locally and sensitivity to frequency variation. The MLR shows better performance in the case of frequency deviation but considered as a costly way of handling frame detection.

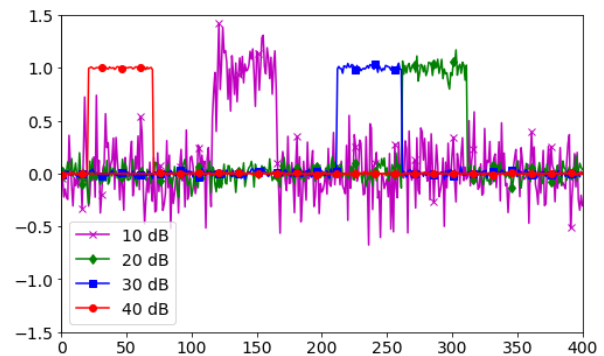


Figure 1. The samples of received signals.

In this study, we consider the frame detection with deep learning and examine the different models and compare their performance to the basic correlator-based detector. The two are compared in terms of the deviation from the actual frame starting position by evaluating the deviation as a mean squared estimation error. The received signal is corrupted by the noise that reduces signal-to-noise ratio. The Fig.1 shows four signals received by a receiver at different time with various signal to noise ratio. This information could be considered a preamble to actual message signal to be transmitted. Since the message is a sequence of random symbols, it is preferred not to show in the figure for the sake of better visualization clarity. The receiver has to find where the frame starts. We consider the correlation-based frame detector against the deep learning-based frame detector. While the deep learning-based receiver does not need to know what kind of preamble is sent, the correlation-based receiver needs to know the exact preamble. Therefore, the preamble between the receiver and the transmitter must be agreed beforehand which can be considered handicap of correlated-based receiver. Further, the CBR may require long processing

time. For the deep learning, it only requires a good training before it is used.

The CBR correlates the received information with locally saved one and used the peak point as the starting position of the frame. The proposed DL model uses a softmax layer at the output and calculates the probability of every possible position for the preamble in the received corrupted sequence and choses the highest probability as the starting position of the frame. The input to model is the received sequence. As it could be possible to consider real and imaginary part separately, only the real part is considered in this study which turns out to provide satisfactory results.

The proposed deep learning-based receiver uses fully connected layers. It has 6 hidden layers, dropout=0.2, number of neurons per layer 512, training size between 100000-150000. While it is possible to provide deeper and larger NN, to have moderate training time, parameters are used. First, we provide the figures that shows the model neither overfits nor underfits. The overfitting and underfitting are two important issues in the training process of a NN model. The loss and the accuracy for the validation and the training datasets are considered to decide a well-fitting model. In Fig.1 accuracy and loss graphs are given for various signal to noise ratio against number of the epochs. It is clearly seen that different signal to noise ratio requires different number of epochs. For example, 5 epochs are enough for -10dB while it becomes 30 epochs for 5dB. Generally, it requires more epochs around 0-10dB.

The expected outcome for the model to generalize well is that the accuracy should be on the rise while for the loss is getting smaller and the gap between the validation and the training set should be moderately

close for both as the number of the epochs increase. It is understood from the graphs on Fig.2 that around 15 epochs are enough for well generalized model. The proposed model is trained for various SNR and preamble size. The Fig.3 shows DL model prediction versus CBR prediction error in terms of mean squared deviation. The two compared for the various preamble size in the range of 5 to 40 symbol for the signal to noise ration from -15dB to 10dB. It is seen from the figure; DL model can put so close performance to CBR with even a simple model given above. Both receivers give zero deviation error above 10dB.

Deep learning model can be in various forms. Some forms show better performance than others. The wisdom behind it cannot be explained mathematically. Hence, developing a good deep learning model is achieved through trial and error. The number of neurons used in model is considered part of parameters used in a model. Apart from the total number of neurons, their distribution can be matter. In the study the distribution of neurons to the hidden layers are considered as one of the parameters to adjust. Hence, we try to find out the best distribution to the hidden layers. Several distribution approaches are tested with various size of preamble. After many trainings of these models, we have seen that even distribution is the best choice in term of classification accuracy. The even distribution means that all the hidden layers have same number of neurons. The output of the proposed model is shown in Fig.4 that is tested for two different preamble sizes in the range of -15dB to 15dB signal to noise ratio. The Fig.4 shows the performance of the model with even and uneven distribution of neurons to the hidden layers for preamble size 5 and 10. The model with the even distribution generally shows better performance

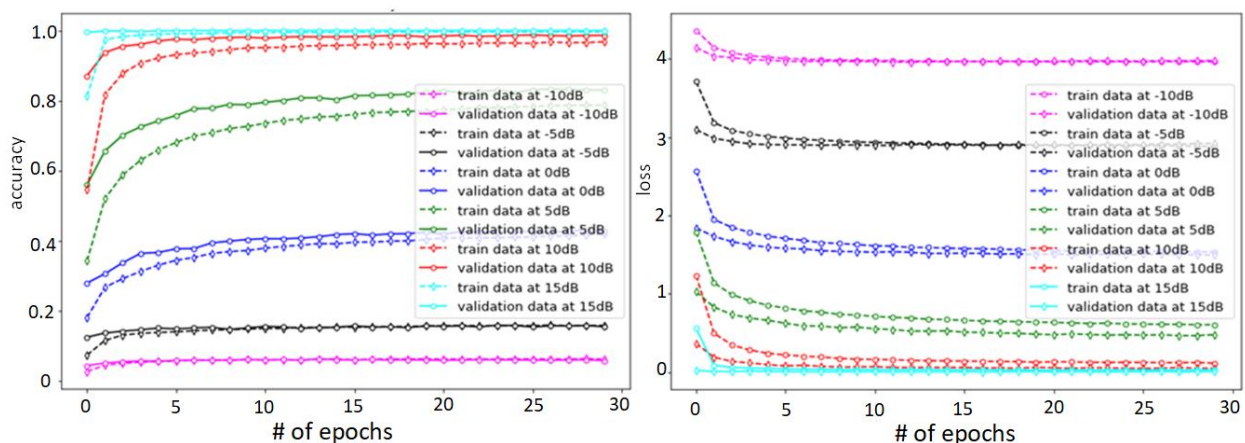


Figure 2. The loss and the accuracy of deep learning-based receiver.

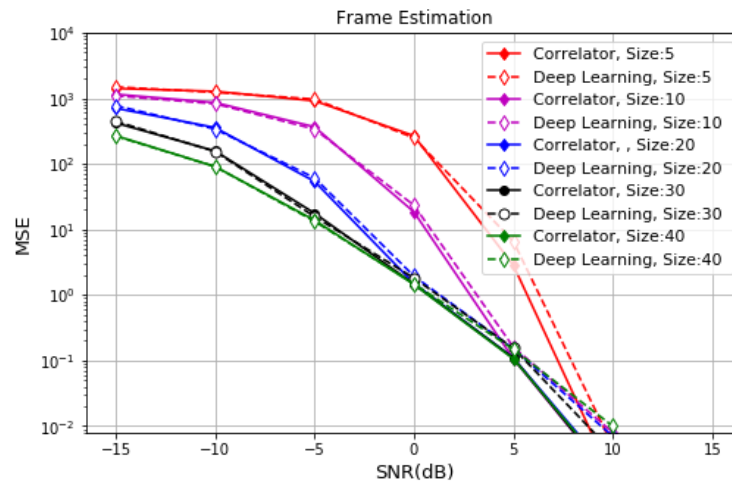


Figure 3. The Deep Learning-based and the correlator-based detector performance.

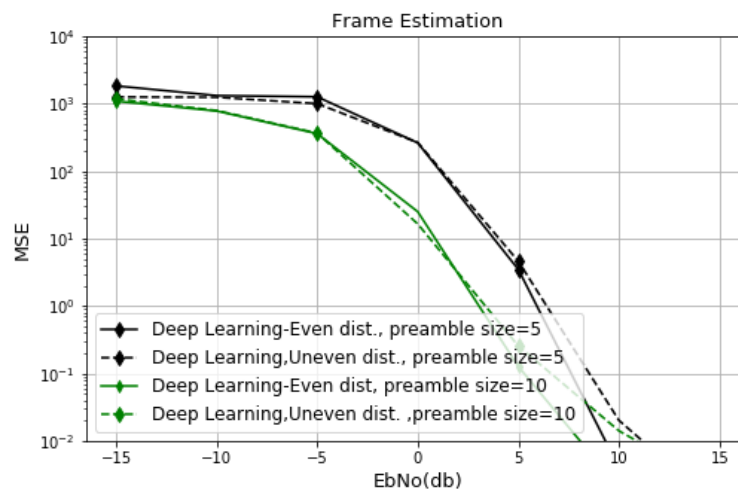


Figure 4. Distribution of neurons

4. Conclusion

A deep learning model is designed to make frame detection. This model has been shown to be well-fitting. For this purpose, loss and accuracy graphs in validation and training datasets are given by simulation. Then, frame detection performances of these models were compared with correlation-based system. The mean square error of deviation is used as comparison metric. Then, some parameters of the model are adjusted and the best performing model for frame detection is formed. The model is observed to be successful in comparison to correlator-based detector. The deep learning-based detector is considered to superior to correlator-based detector since the second must have the preamble beforehand for detection while the first does not need to know it. This is considered as one of the proposed model superiorities to the correlator-based detector. The second superiority is that the correlator-

based detector has to do heavy correlation calculations for every detection while the deep learning-based detector needs only offline training. This helps to reduce processing time and memory requirements seriously, requires less computing power and less power consumption at the receiver. These advantages come from the fact that DL based model just need to save weighted parameters that is used in some simple mathematical calculation to estimate the frame position. Observing the contribution of deep learning-based model frame detection, the conclusion we arrive is that the future communication systems must consider to use the DL based technologies.

Acknowledgement

This study was carried out in the Department of Electrical and Electronics Engineering of Ege University within the scope of the project supported by TUBITAK 2218.



Author's Contributions

Mete Yıldırım: Conceptualization, Methodology, Validation, Simulation, Formal analysis, Investigation, Writing - original draft, Writing - review, and editing.
Radosveta Ivanova Sokullu: Conceptualization, Methodology, Validation, Formal analysis, Investigation, Writing - review & editing, Supervision.

Ethics

There are no ethical issues after the publication of this manuscript.

References

1. Massey, J. 1972. Optimum frame synchronization. *IEEE transactions on communications*; 20(2): 115–119.
2. Scholtz, R. 1980. Frame synchronization techniques. *IEEE transactions on communications*; 28(8): 1204–1213.
3. Ibnkahla, M. 2000. Applications of neural networks to digital communications—a survey. *Signal processing*; 80(7): 1185–1215.
4. Qin Z, Ye H, Li G, Juang F. 1972. Deep learning in physical layer communications. *ArXiv*: 1807.11713
5. Simeone, O. 2018. A very brief introduction to machine learning with applications to communication systems. *IEEE Transactions on Cognitive Communications and Networking*; 4(4): 648–664.
6. Wang T, Wen CK, Wang H, Gao F, Jiang T. 2017. Deep learning for wireless physical layer: Opportunities and challenges. *China Communications*; 14(11): 92–111.
7. Dörner S, Cammerer S, Hoydis J, Brink S. 2017. Deep learning based communication over the air. *IEEE Journal of Selected Topics in Signal Processing*; 12(1): 132–143.
8. O'Shea T, Hoydis J. 2017. An introduction to deep learning for the physical layer. *IEEE Transactions on Cognitive Communications and Networking*; 3(4): 563–575.
9. O'Shea T J, Karra K, Clancy T C. 2016. Learning to communicate: Channel auto-encoders, domain specific regularizers, and attention. *arXiv*: 1608.06409.
10. TO'Shea T J, Roy T, West N, Hilburn B C. 2018. Physical Layer Communications System Design Over-the-Air Using Adversarial Networks. *ArXiv*: 1803.03145.
11. O'Shea T J, Hoydis J. 2017. An introduction to machine learning communications systems. *ArXiv*: 1702.
12. O'Shea T J, Erpek T, Clancy T.C. 2017. Deep learning based MIMO communications. *arXiv*:1707.07980.
13. TO'Shea T J, Roy T, West N, Hilburn B C. 2018. Physical Layer Communications System Design Over-the-Air Using Adversarial Networks. *ArXiv*: 1803.03145.
14. O'Shea T J, Hoydis J. 2017. An introduction to machine learning communications systems. *ArXiv*: 1702.
15. Ramachandran, P., Zoph, B. and Le, Q.V., 2017. Searching for activation functions. *arXiv preprint arXiv:1710.05941*.
16. Nwankpa, C., Ijomah, W., Gachagan, A., & Marshall, S. 2018. Activation functions: Comparison of trends in practice and research for deep learning. *arXiv preprint arXiv:1811.03378*.
17. Agostinelli, F., Hoffman, M., Sadowski, P., & Baldi, P. 2014. Learning activation functions to improve deep neural networks. *arXiv preprint arXiv:1412.6830*.
18. Nie, F., Hu, Z., & Li, X. 2018. An investigation for loss functions widely used in machine learning. *Communications in Information and Systems*, 18(1), 37-52.
19. LeCun Y, Bengio Y, Hinton G. 2015. Deep learning. *Nature*; 521(7553): 4362
20. Schmidl T M, Cox D C. 1997. Robust frequency and timing synchronization for OFDM. *IEEE transactions on communications*; 45(12): 1613–1621.

Anatomy of *Carlina corymbosa* L., *Carthamus dentatus* Vahl. and *Picnomon acarna* (L.) Cass. (Asteraceae)

Ummahan Öz^{1*} 

¹Department of Plant and Animal Production, Alaşehir Vocational School, Manisa Celal Bayar University, Manisa Turkey

*ummahanoz48@gmail.com

*Orcid: 0000-0002-0281-1048

Received: 25 August 2020

Accepted: 19 April 2021

DOI: 10.18466/cbayarfbe.785328

Abstract

Species of *Carlina corymbosa* L., *Carthamus dentatus* Vahl. and *Picnomon acarna* (L.) Cass. are belonging to Asteraceae family. The purpose of the study is to determine the anatomical structures of these species in the same tribe and to compare the features. Samples of root, stem and leaf of each species were collected, fixed and examined using a light microscope. In addition, some anatomical features were measured. Secondary growth was observed in the root cross section of each species. Secretory ducts were determined in all species. While the pith is filled with xylem elements in *C. corymbosa* and *C. dentatus*, the pith of *P. acarna* consists of different shaped parenchyma cells. Periderm was observed in the stem in all species. All species contain bicollateral vascular bundles in stem. In all species, glandular and non-glandular trichomes were observed on the leaf cross section, on the surface of the adaxial and abaxial epidermis. While *C. corymbosa* has dorsiventral mesophyll, unifacial mesophyll is observed in other species. There is bicollateral vascular bundle in *C. corymbosa* whereas collateral vascular bundle was identified in *C. dentatus* and *P. acarna*. Also, *C. corymbosa* and *C. dentatus* have only one vascular bundle in the midrib but *P. acarna* has three vascular bundles.

Keywords: Anatomy, bicollateral, collateral, dorsiventral, secretory duct, unifacial.

1. Introduction

Carlina corymbosa L., *Carthamus dentatus* Vahl. and *Picnomon acarna* (L.) Cass. are member of Asterales order, Asteraceae family, Carduoideae subfamily and Cardueae tribe [1].

The Asteraceae family is represented in the world with about 1911 genera and 32913 species [2]. In Turkey, there are 133 genera and 1156 species belonging to this family and tribe of Cardueae includes 39 genera and approximately 500 taxa [3-4].

The taxa belonging to Cardueae have morphological similarity features and these similarities cause problems in classification. In taxonomic studies, it is seen that only the use of morphological characters is insufficient and therefore, the necessity of anatomical, cytological, molecular, palynological studies etc. is revealed [5].

There are anatomical differences in the species belonging to Asteraceae family. In this family, the secretory structures (cavities, idioblast, ducts and

trichomes etc.) are important anatomical characters and these structures are used for identification the species. For example, the micromorphology of trichome is a feature that can be used in the systematics of the Asteraceae [6]. Glandular and non-glandular trichomes are used as distinguished [7].

The aim of this research is to determine the anatomical features of *Carlina corymbosa* L., *Carthamus dentatus* Vahl. and *Picnomon acarna* (L.) Cass., which are members of the Cardueae tribe.

2. Material and Methods

2.1 Study areas and selected species

Carlina corymbosa L., *Carthamus dentatus* Vahl. and *Picnomon acarna* (L.) Cass. were collected in August 2018 from natural environments in Milas, Muğla (Figure 1). Their collection localities were as follows: *Carlina corymbosa* and *Picnomon acarna*, N 37°21'52.503", E 27°48'11.386" 62 m.; *Carthamus dentatus*, N 37°19'49.851", E 27°45'39.420" 80 m. The taxonomic descriptions of all species were made according the Flora of Turkey [1].

2.2 Sampling

Root, stem and leaves of species were fixed in 70% ethanol for the anatomical studies. Cross sections were taken from each plant material by using razor blade and sections were stained with hematoxylin.

Well-stained sections were examined with BAB Image Analysing Systems Microscope (BAB-95) and photographed with BAB Microscope Camera. Anatomical structures were measured using BAB measurement program.



Figure 1. a) *Carlina corymbosa*, b) *Carthamus dentatus*, c) *Picnomon acarna*

3. Results and Discussion

3.1 *Carlina corymbosa*

In root cross section, secondary growth was observed. On the outermost, there is thick and multi-layered periderm. There are secretory ducts in the secondary cortex. The cambium cells, which between phloem and xylem, and the sclerenchyma tissues are clearly distinguished. Pith rays consist of distinct and 2-4 layered cells. Pith is filled with metaxylem (Figure 2).

The stem of *C. corymbosa* is almost circular. Uniseriate epidermis, consisting of rectangular-shaped cells surrounded by thick cuticle, is observed in cross section of the stem. The periderm layer consist of different sized and shaped cells. Endodermis and vascular bundles can be clearly distinguished. Sclerenchyma consists of 4-8 layered cells and the cambium is not very distinguishable. Phloem and xylem are well developed. The stem contains bicollateral vascular

bundles. The pith is filled by oval and different sized parenchyma cells. In addition, calcium oxalate crystals are found in pith (Figure 3).

In cross section of *C. corymbosa* leaf, there is a uniseriate epidermis with thin cuticle on adaxial and abaxial surfaces. Surface of both epidermis are covered with trichomes. Glandular and non-glandular trichome types are present. Uniseriate filiform trichome with elongated apical cells and capitate stalked trichomes are observed. Another trichome (bulbiferous flagellate trichome) feature of the observed was as follows: stalk 2-celled, the length of the cells more than the width, second stalk cell swollen; apical cells long, flagellate. Dorsiventral mesophyll and bicollateral vascular bundles are observed in leaf. The midrib has only one vascular bundle. The adaxial parenchyma cells are 3-4 layered and abaxial parenchyma cells are 1-2 layered in midrib (Figure 4).

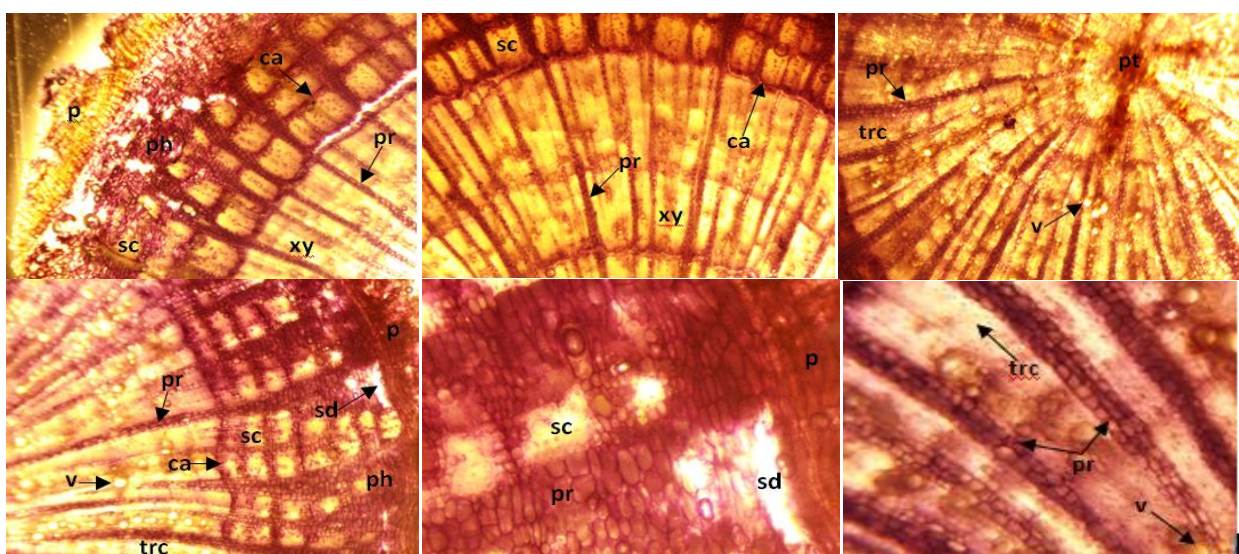


Figure 2. Root anatomy of *C. corymbosa* (ca: cambium; p: periderm; ph: phloem; pr: pith ray; pt: pith; sc: sclerenchyma; sd: secretory duct; trc: tracheid; v: vessel; xy: xylem)

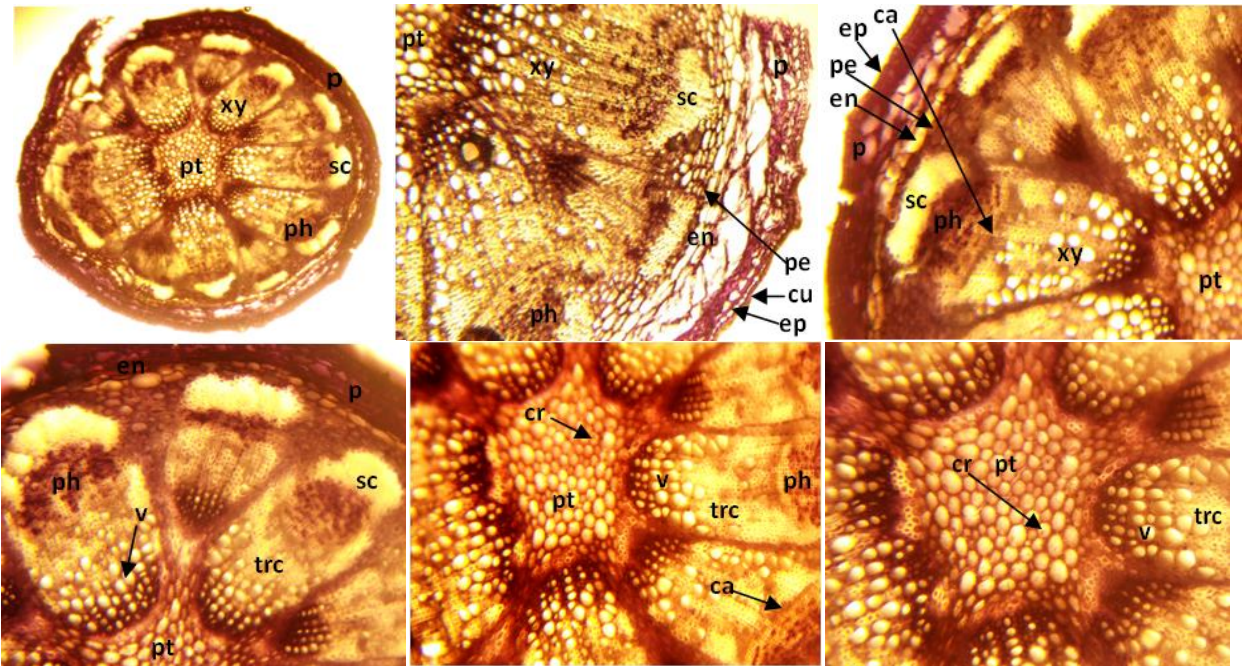


Figure 3. Stem anatomy of *C. corymbosa* (ca: cambium; cr: calcium oxalate crystals; cu: cuticle; ep: epidermis; en: endodermis; p: periderm; pe: pericycle; ph: phloem; pt: pith; sc: sclerenchyma; sd: secretory duct; trc: tracheid; v: vessel; xy: xylem)

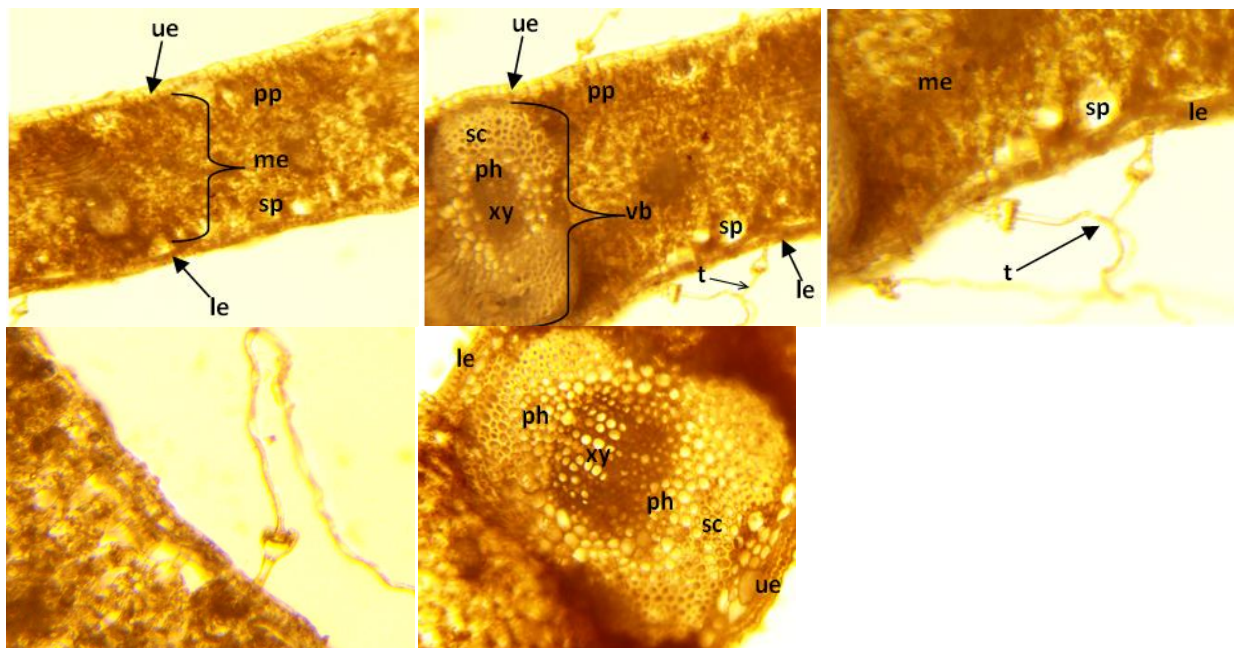


Figure 4. Leaf anatomy of *C. corymbosa* (le: lower epidermis; me: mesophyll; ph: phloem; pp: palisade parenchyma; sc: sclerenchyma; sp: spongy parenchyma; t: trichome; ue: upper epidermis; vb: vascular bundle; xy: xylem)

3.2 *Carthamus dentatus*

Periderm and partially crushed epidermis are observed in the outermost part of the root cross section obtained from *C. dentatus*. There are secretory ducts in cortex and it is observed multi-layered sclerenchyma above the

phloem. The cambium is clearly distinguished. Xylem is well developed and there are 2-5 layered pith rays. In addition to this, the pith is filled by xylem elements (Figure 5).

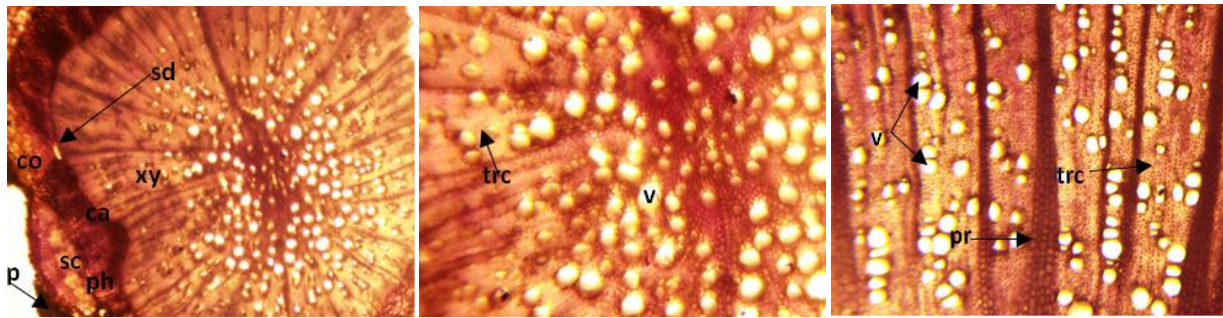


Figure 5. Root anatomy of *C. dentatus* (ca: cambium; co: cortex; p: periderm; ph: phloem; pr: pith ray; sc: sclerenchyma; trc: tracheid; v: vessel; xy: xylem)

In the stem cross section taken by *C. dentatus*, the epidermis is determined as monolayered which is composed of rectangular or oval cells. The epidermis contains multicellular non-glandular unbranched and multicellular glandular trichomes. The periderm, consisting of different sized and shaped cells, is located underneath the epidermis. The cortex cells are observed flattened in a narrow region. There are resin ducts in the

cortex and also cambium is distinguishable between phloem and xylem. Sclerenchyma which between cortex and vascular bundles, consists of 4-10 layered cells. Vascular bundles are bicollateral. Pith rays consist of 1-2 layered oval and rectangular cells. The pith is filled with by hexagonal and oval parenchyma cells. Calcium oxalate crystals are present in pith (Figure 6).

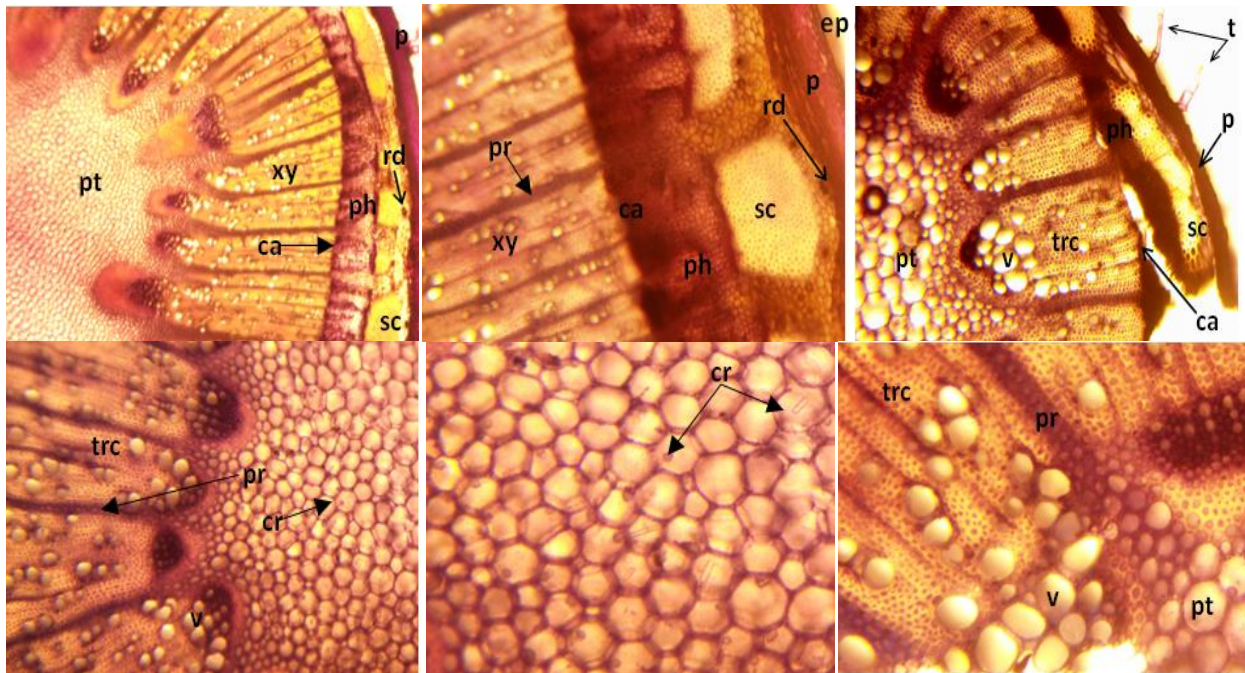


Figure 6. Stem anatomy of *C. dentatus* (ca: cambium; cr: calcium oxalate crystals; ep: epidermis; p: periderm; ph: phloem; pr: pith ray; pt: pith; rd: resin duct; sc: sclerenchyma; trc: tracheid; v: vessel; xy: xylem)

In the cross section of leaf, there is a uniseriate epidermis with thin cuticle on adaxial and abaxial surfaces. Surface of both epidermis are covered with multicellular eglandular and multicellular glandular trichomes. Many different types of trichomes were identified in the leaf cross section. The trichomes were multicellular nonglandular unbranched and multicellular glandular. Trichomes are observed as uniseriate and biseriate. The trichomes observed are as follows: long

stalked capitate, one cell shriveled multicellular non glandular, conical, biseriate pedunculata glandular, biseriate vesicular glandular, short stalked capitate, sessile two-celled glandular, uniseriate multicellular non-glandular trichome. Collateral vascular bundles are observed in unifacial leaf. The midrib has only one vascular bundle and vascular bundle is surrounded by a sheath of sclerenchyma. Small collateral vascular bundles are observed in the mesophyll (Figure 7)

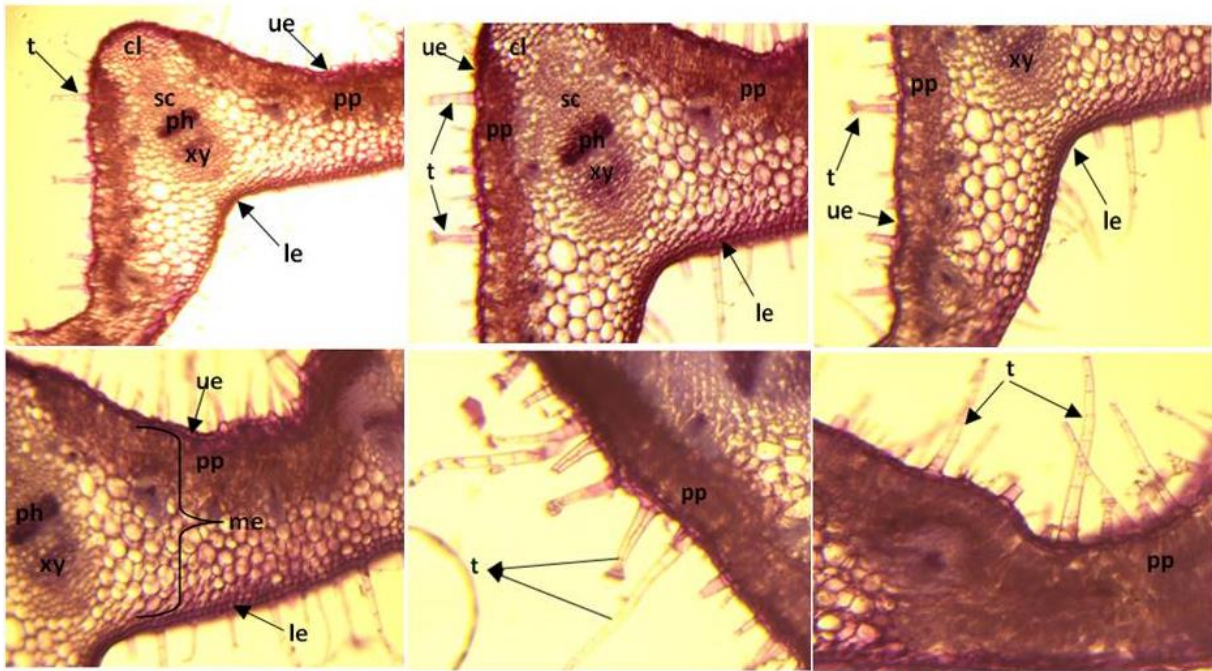


Figure 7. Leaf anatomy of *C. dentatus* (cl: collenchyma; le: lower epidermis; me: mesophyll; ph: phloem; pp: palisade parenchyma; sc: sclerenchyma; t: trichome; ue: upper epidermis; xy: xylem)

3.3. *Picnomon acarna*

In the root cross section, periderm layer consisting of multi-layered, irregularly shaped cells are observed on the outermost and the partially crushed epidermis is identified. Secretory ducts are observed in the cortex.

The endodermis appears as a thin line and is not easily distinguishable. Cambium cells located between phloem and xylem are distinct. The pith consists of differently shaped parenchyma cells (Figure 8).

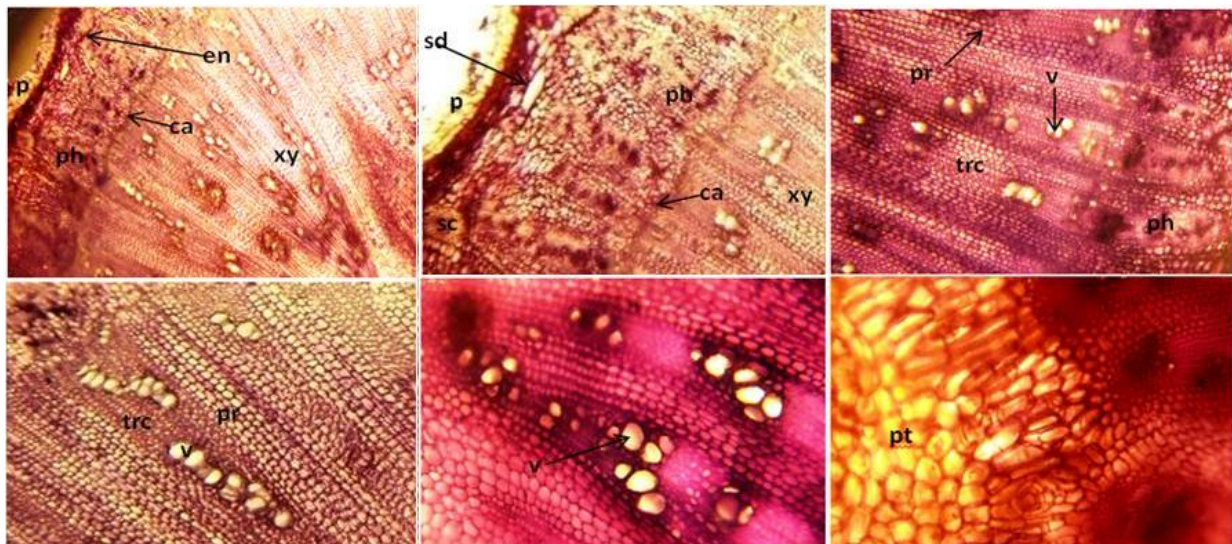


Figure 8. Root anatomy of *P. acarna* (ca: cambium; en: endodermis; p: periderm; ph: phloem; pr: pith ray; pt: pith; sc: sclerenchyma; sd: secretory duct; trc: tracheid; v: vessel; xy: xylem)

There is a thick periderm layer, consisting of different sized and shaped cells, on the outermost surface of the stem. A narrow cortex is observed in the cross section and secretory ducts in cortex are present. The central cylinder is surrounded by an endodermis and pericycle

is clearly distinguishable. Multi-layered pith ray are observed between bicollateral vascular bundles. The cambium is distinguishable between phloem and xylem. Sclerenchyma consists of 3-10 layered cells. The pith contains large polygonal and hexagonal parenchymatous cells (Figure 9).

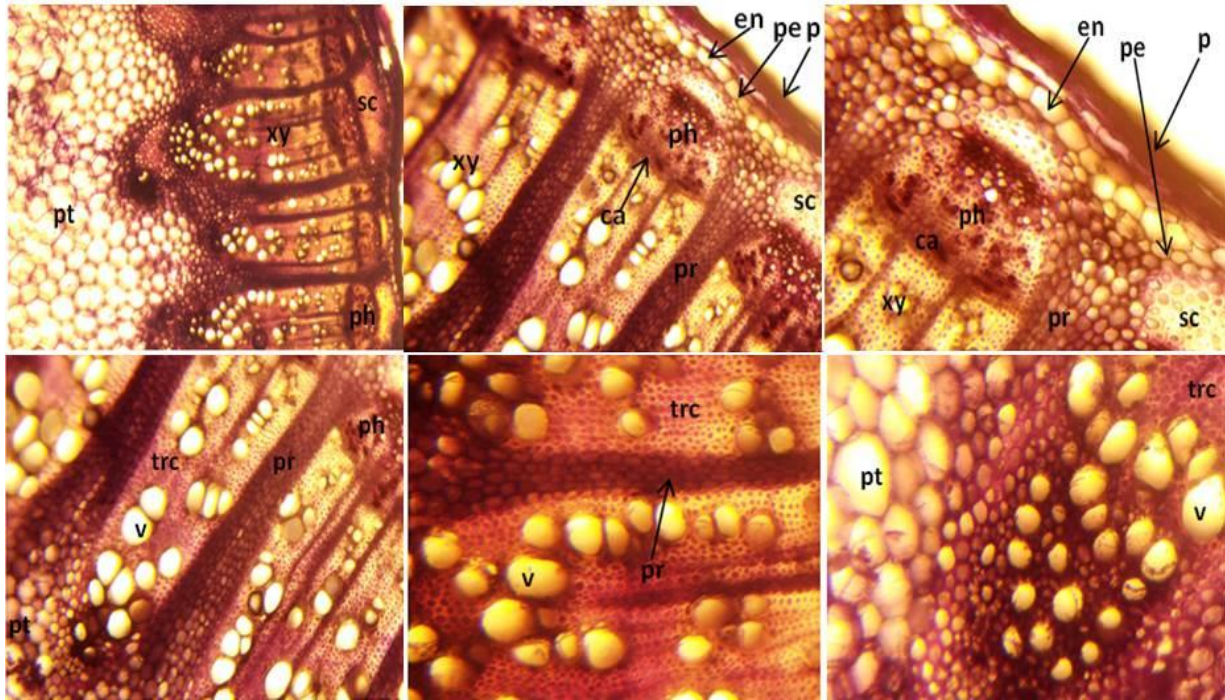


Figure 9. Stem anatomy of *P. acarna* (ca: cambium; en: endodermis; p: periderm; pe: pericycle; ph: phloem; pt: pith; pr:pith ray; sc: sclerenchyma; trc: tracheid; v: vessel; xy: xylem)

In the cross section of leaf, there is a uniseriate epidermis with thin cuticle on adaxial and abaxial surfaces. Epidermis cells are observed square or rectangular. Surface of both epidermis are covered with whip-like and flagellate-filiform trichomes. Unifacial

mesophyll are observed in leaf. Vascular bundles are observed in the middle part of parenchyma tissue in the mesophyll. The midrib has three collateral vascular bundles. The upper and lower parts of the vascular bundles are surrounded by sclerenchyma (Figure 10).

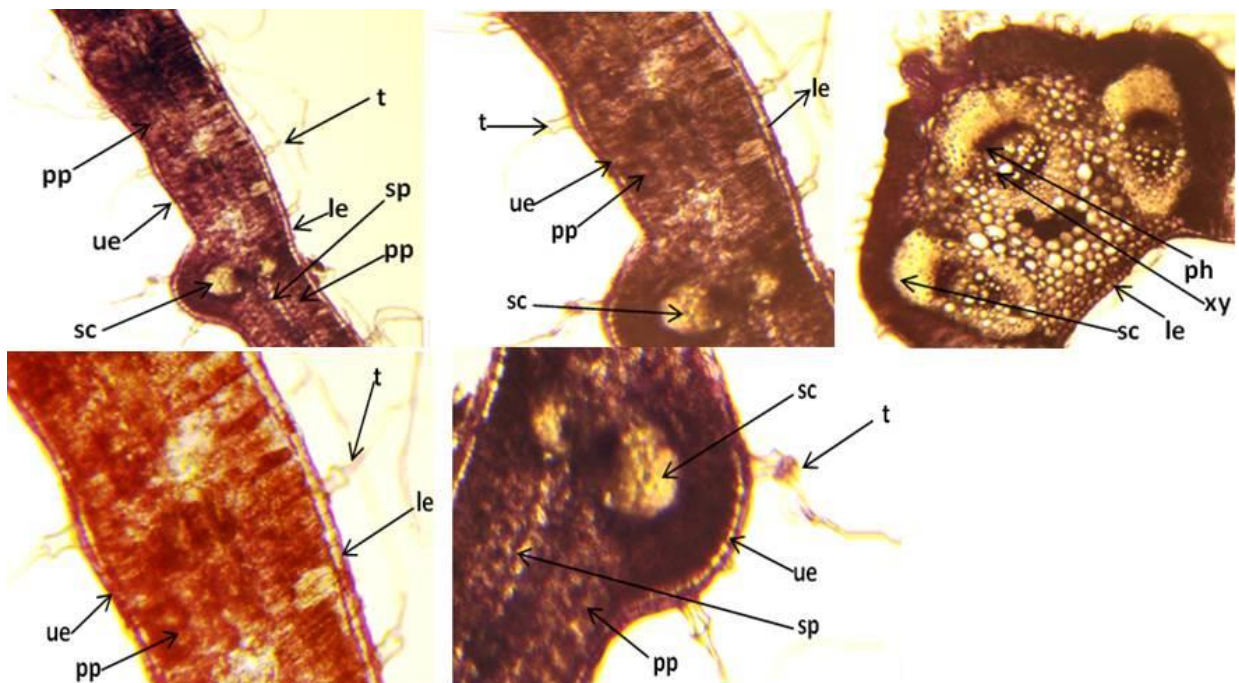


Figure 10. Leaf anatomy of *P. acarna* (le: lower epidermis; ph: phloem; pp: palisade parenchyma; sc: sclerenchyma; sp: spongy parenchyma; t: trichome; ue: upper epidermis; xy: xylem)

Table 1. Measurements of anatomical structures of species

Cross section of plants	<i>Carlina corymbosa</i>	<i>Carthamus dentatus</i>	<i>Picnomon acarna</i>
Root			
Root diameter (µm)	5753.75±400.52	2880.76±327.65	6919.89±1453.54
Periderm thickness (µm)	300.06±62.41	120.22±25.83	230.36±71.22
Phloem thickness (µm)	125.56±23.57	162.61±10.50	373.10±45.99
Xylem thickness (µm)	1847.16±157.75	832.06±99.93	1561.37±186.44
Vessel diameter (µm)	39.38±13.81	42.83±12.48	38.30±8.91
Stem			
Vascular bundles number	12	23-24	26-27
Periderm thickness (µm)	106.14±21.75	70.16±22.72	69.72±14.00
Thickness of sclerenchyma (µm)	95.56±15.63	72.51±12.17	147.63±38.99
Phloem thickness (µm)	163.81±18.58	200.85±36.84	198.64±42.36
Xylem thickness (µm)	471.77±52.14	963.90±204.43	909.24±145.92
Vessel diameter (µm)	29.58±6.75	35.94±10.42	51.61±14.65
Pith diameter (µm)	429.20±52.86	1145.85±88.75	1727.55±277.26
Leaf			
Adaxial epidermis thickness (µm)	18.75±2.61	16.92±2.45	13.94±1.80
Abaxial epidermis thickness (µm)	21.08±2.54	16.39±3.20	12.15±2.02
Mesophyll thickness (µm)	412.19±34.99	311.73±61.67	188.69±19.55
Midrib thickness (µm)	668.65±14.91	757.07±115.87	652.31±32.99
Number of vascular bundles in midrib	1	1	3

µm: micrometer

The root, stem and leaf anatomical features of all species are given as above. In addition, some anatomical characters of these species were measured and indicated Table 1.

The species belonging to the Asteraceae family have different anatomical structures [8]. Trichomes are important characteristic in phylogenetic studies related to the Asteraceae family [9-11]. In a study investigating the anatomy of the *C. dentatus* [12], it was stated that this species has glandular and non-glandular trichome, but the trichome types are not mentioned in detail. Long stalked capitate, one cell shriveled multicellular non glandular, conical, biseriate pedunculata glandular, biseriate vesicular glandular, short stalked capitate, sessile two-celled glandular, uniseriate multicellular non-glandular trichomes has been identified in this research. *C. corymbosa* contains uniseriate filiform, capitate stalked and bulbiferous flagellate trichomes whereas *P. acarna* has whip-like and flagellate-filiform trichomes. One of the distinguishing features of Asteraceae is the presence of secretory ducts [13-14]. The secretory ducts are observed in all species used in the research.

Similar results were obtained when these species belonging to the same tribus were examined. In the root cross sections, the best secondary growth was observed in the *C. corymbosa* and periderm was thicker than others. However, in the root section of *P. acarna*, the pith was filled with parenchyma cells as different from the others and root diameter is highest in the this species. In the Asteraceae family, the vascular bundles and leaf midrib differences are also valuable anatomical features [15-19]. The maximum number of vascular

bundle in the stem was determined in *P. acarna*. Bicollateral vascular bundle was observed in the stem of all species used in the study. While collateral vascular bundle was determined in the leaf cross sections of *C. dentatus* and *P. acarna*, bicollateral vascular bundle was detected in the *C. corymbosa*. Also, *C. corymbosa* and *C. dentatus* have only one vascular bundle in the midrib but *P. acarna* has three vascular bundles.

There are calcium oxalate crystals in the tribe Cardueae. In a study of Cardueae [20], it was stated that *C. dentatus* contains prismatic and styloid crystals. Likewise, calcium oxalate crystals were observed in the pith of stem in all species in this study.

4. Conclusion

This study gives information about the anatomical features of the root, stem and leaf sections of *Carlina corymbosa*, *Carthamus dentatus* and *Picnomon acarna*. In the study, it was determined trichomes with different characteristics and this trichome diversity will contribute to the trichome micromorphology of Asteraceae. In addition, the results obtained from the study will constitute resource for the another research related to the anatomy of the Cardueae.

Author's Contributions

Ummahan Öz: Responsible of all processes; planning the research, obtaining and analyzing data, drafting and writing the article.

Ethics

There is no ethical issues after the publication of this article.

References

1. Davis, P. Flora of Turkey and the East Aegean Islands, Vol.5; Edinburgh University Press: Edinburgh, 1975.
2. El-Gazzar ,A, El-Husseini, N, Khafagi ,A, Mostafa, N. 2019. Computer-generated Keys to the Egypt.9.The Spiny Taxa of Asteraceae. *Egyptian Journal of Botany*; 59 (1): 107-138.
3. Seçmen, Ö, Gemici, Y, Görk, G, Bekat, L, Leblebici, E. Tohumlu Bitkiler Sistematigi; Ege Üniversitesi Yayınları, Fen Fakültesi Kitapları Serisi No: 116, İzmir, Turkey, 2011.
4. Kurt, A, Ozcan , M, Colak, N, Ozogul, Y, Glew, R, Ozogul, F, Ayaz, FA. 2019. Fatty Acids of Oil and Antioxidant Capacity of Phenolics from Fruits of 11 Cardueae (Carduoideae, Asteraceae) Taxa From Northeast Anatolia (Turkey). *Botanica Serbica*; 43(1): 31-45.
5. Ozcan, M, Akinci, N.2019. Micromorpho-anatomical Fruit Characteristics and Pappus Features of Representative Cardueae(Asteraceae) Taxa: Their Systematic Significance. *Flora*; 256: 16-35.
6. Dere, S, Aktas Akcin, T. 2017. Anatomical and Micromorphological Properties of Some *Tanacetum* L. (Asteraceae) Taxa from Turkey and their Systematic Implications. *Acta Botanica Croatica*; 76(2): 138-145.
7. Haratym, W, Weryszko-Chmielewska, E, Konarska, A. 2020. Microstructural and Histochemical Analysis of Aboveground Organs of *Centaurea cyanus* Used in Herbal Medicine. *Protoplasma*; 257: 285-298.
8. Karahan, F. 2020. Morphology, Anatomy, Palynology and Achene Micromorphology of *Bellis* L. (Asteraceae) Species from Turkey. *Acta Botanica Croatica*; 79(1): 59-67.
9. Makbul, S, Coskuncelebi , K, Beyazoğlu, O. 2011. Notes on the Stem Anatomy of *Scorzonera* (Asteraceae) Taxa from Northeast Turkey. *Phytologia Balcanica*; 17(1): 113-121.
10. Muravnik, L, Kostina, O, Shavarda, Alexey. 2016. Glandular trichomes of *Tussilago farfara* (Senecioneae, Asteraceae). *Planta*; 244: 737-752.
11. Muravnik, L, Kostina, O, Mosina, A. 2019. Glandular trichomes of the leaves in three *Doronicum* species (Senecioneae, Asteraceae): morphology, histochemistry and ultrastructure. *Protoplasma*; 256: 789-803.
12. Yağci Tuzun, C, Tarikahya, Hacıoglu, B, Bulbul, AS, Arslan, Y, Subasi, I. 2019. Comparative Anatomical Studies on Some Species of *Carthamus* L. in Turkey. *Fresenius Environmental Bulletin*; 28(5): 4072-4079
13. Zuccolotto, T, Bressan, J, Lourenço, A, Bruginiski, E, Veiga, A, Marinho, J, Raeski, P, Heiden, G, Salvador, M, Murakami, F, Budel, J, Campos, F. 2019. Chemical, Antioxidant, and Antimicrobial Evaluation of Essential oils and an Anatomical Study of the Aerial Parts from *Baccharis* Species (Asteraceae). *Chemistry & Biodiversity*; 16(4).
14. Gavrilovic, Milan, Rancic, D, Garcia-Jacas, N, Susanna, A, Dajic-Stevanovic, Z, Marin, P, Javackovic, P. 2020. Anatomy of Balkan *Amphoricarpos* Vis. (Cardueae, Asteraceae) taxa. *Biologia*; 75: 209-222.
15. Inceer, H, Ozcan, M. 2011. Leaf anatomy as an additional taxonomy tool for 18 taxa of *Matricaria* L. and *Tripleurospermum* Sch. Bip. (Anthemideae- Asteraceae) in Turkey. *Plant Systematics and Evolution*; 296:205-215.
16. Aydin, Ö, Coşkunçelebi, K, Güzel, ME. 2013. A contribution to taxonomy of *Centaurea* including *Psephellus* (Asteraceae) based on anatomical and molecular data. *Turkish Journal of Botany*. 37: 419-427.
17. Ozcan, M, Unver, M, Eminagaoglu, O. 2014. Comparative anatomical and ecological investigations on some *Centaurea* (Asteraceae) taxa from Turkey and their taxonomic significance. *Pakistan Journal of Botany*. 46(6): 1287-1301.
18. Ekeke ,C, Mensah, SI. 2015. Comparative Anatomy of Midrib and Its Significance in the Taxonomy of the Family Asteraceae from Nigeria. *Journal of Plant Sciences*; 10(5): 200-205.
19. Ozcan, M, Demiralay, M, Kahriman, A. 2015. Leaf anatomical notes on *Cirsium* Miller (Asteraceae, Carduoideae) from Turkey. *Plant Systematics and Evolution*; 301: 1995-2012.
20. Kartal, C. 2016. Calcium Oxalate Crystals in Some Species of the Tribe Cardueae (Asteraceae). *Botanical Sciences*; 94(1): 107-119.